

0830-C

NAS1.2: Sp2/3

NOV 13 1994

MAR 1 1995

#95-020101



Proceedings of the

International Symposium on

SPECTRAL SENSING RESEARCH

VOLUME I

10-15 July 1994

San Diego, California USA

COMPLETED

Proceedings of the
International Symposium on
SPECTRAL SENSING RESEARCH

VOLUME I

10-15 July 1994

San Diego, California USA

*Proceedings of the
International Symposium on Spectral Sensing Research '94
10-15 July 1994*

Sponsored by

U.S. Army Corps of Engineers (USACE)
Cold Regions Research and Engineering Laboratory (CRREL)
Topographic Engineering Center (TEC)
U.S. Army Night Vision and Electronic Sensor Directorate (NVESD)
U.S. Army Space and Strategic Defense Command (SSDC)
U.S. Army Research Laboratory (ARL)
U.S. Army Edgewood Research, Development and Engineering Center (ERDEC)
U.S. Army Research, Development and Standardization Group - United Kingdom (USARDSG-UK)
Air Force Office of Scientific Research (AFOSR)
U.S. Air Force Phillips Laboratory, Geophysics Directorate (PL/GD)
U.S. Air Force Systems Command (AFSC)
National Aeronautics and Space Administration (NASA)
Naval Research Laboratory (NRL)
National Oceanic and Atmospheric Administration (NOAA)
Wave Propagation Laboratory (WPL)
Nautical Charting Research and Development Laboratory (NCRDL)
Oak Ridge National Laboratory (ORNL)
Environmental Protection Agency (EPA)
Environmental Monitoring Systems Laboratory (EMSL)
U.S. Geological Survey (USGS)
NASA Stennis Space Center (SSC)

Under Contract No. DACA76-93-C-0028

PREFACE

These proceedings contain the papers presented at the International Symposium on Spectral Sensing Research '94 (ISSSR), held at the Doubletree Hotel at Horton Plaza, San Diego, California on 10–15 July 1994. Forty-eight papers are included in Volume I and forty-nine papers are included in Volume II of the proceedings. Thirteen papers are also included in the "proceedings only" portion of Volume II.

The ISSSR was sponsored by several U.S. government agencies and organized by the U.S. Army Corps of Engineers (USACE). Dr. Richard B. Gomez, Associate Director of Technology of the U.S. Army Topographic Engineering Center (TEC), was the ISSSR General Chair; Mr. John V.E. Hansen, Director of the Remote Sensing Laboratory at the U.S. Army Topographic Engineering Center, was the Steering Committee Chair; Dr. Jack N. Rinker, Senior Research Scientist at the U.S. Army Topographic Engineering Center, was the Technical Program Committee Chair; and Ms. Charlotte Lemen, U.S. Army Topographic Engineering Center, was the Organizing Committee Chair. The symposium theme was presented by Mr. Walter E. Boge, Director, U.S. Army Topographic Engineering Center. The keynote address was given by Professor John Richards, Head of the Department of Electrical Engineering and Deputy Rector at the University College, Australian Defence Force Academy, Australia. Science and Technology Corporation (STC) provided contractual support.

The theme of the ISSSR was "Dual-Use Technologies." The objective was to provide an international forum where people can meet to discuss scientific requirements, implementation issues, analysis problems, and scientific benefits of spectral sensing research, and to produce the symposium proceedings soon after the ISSSR meeting for the benefit of the scientific community. Members of the government, industry, and academia, as well as persons from allied nations, attended the symposium. Papers were presented in seven topical areas: (1) Data Collection; (2) Signal/Data Processing; (3) Spectral Analysis/Processing Systems and Tools; (4) Atmospheric Studies and Applications; (5) Oceanographic/Coastal Studies and Applications; (6) Terrestrial and Land Surface Studies and Applications; (7) Environmental Restoration and Disaster Evaluation.

On the day prior to the formal opening ceremonies of the symposium, attendees had the option of attending tutorials to enable them to update their technical knowledge and thus potentially increase their understanding of the technical presentations. Tutorials were given in the following topics: Introduction to Spectral Remote Sensing, *Lecturer*: Dr. Jack N. Rinker, U.S. Army Topographic Engineering Center; Spectral Measurements Demonstration, U.S. Army Topographic Engineering Center and University of Colorado; Imaging Spectrometer Data Analysis, *Lecturer*: Dr. Fred A. Kruse, University of Colorado; Spectral Sensors and Data Availability, *Lecturer*: Dr. Harlan L. McKim, U.S. Army Cold Regions Research and Engineering Laboratory.

Acknowledgment is made of the support and cooperation of the sponsoring organizations, steering committee members, technical program committee members, organizing committee members, session chairs, tutorial lecturers, and workshop chairs of the ISSSR; and of the technical contributions by both paper and poster presenters participating in the ISSSR. Special thanks are due to Professor John A. Richards, keynote speaker, Professor Emil Wolf, invited speaker, and Mr. Walter E. Boge, conference theme presenter.

Richard B. Gomez
Editor of the Proceedings

BLANK PAGE



INTERNATIONAL SYMPOSIUM ON SPECTRAL SENSING RESEARCH

**Doubletree Hotel at Horton Plaza, San Diego, California USA
10-15 July 1994**

MESSAGE FROM THE CHAIRMAN

Welcome to the *1994 International Symposium on Spectral Sensing Research (ISSSR94)*. This meeting, in San Diego, California, provides us all an opportunity to get to know what is going on in spectral sensing research and related topics within both the civil and military scientific communities. I look forward to meeting each and every one of you during your participation in the ISSSR94 activities.

As happened at our November 1992 ISSSR meeting (ISSSR92), the U.S. Army Corps of Engineers has brought together an innovative group of sponsors who have provided an outstanding agenda for this symposium. The ISSSR94 theme, "Dual-Use Technology," is of great interest to many in the remote sensing field. As before, the overwhelming response to the initial call for papers, the caliber of the scientific talent involved in the technical program and the outstanding efforts of the people who helped put the symposium together have assured a successful symposium.

The primary objective of ISSSR is to provide an international forum where people interested in the subject can meet to address the scientific and user requirements, discuss research issues and consider the scientific benefits of spectral sensing research and related topics.

The sponsors of ISSSR94 have provided a great opportunity for the participants of the symposium to share ideas and strengthen ties through fellowship. I believe this science oriented activity, with emphasis on dual-use technology, is going to go a long way in preparing us for the next generation of remote sensing systems.

I hope your stay here, in beautiful San Diego, will be both personally enjoyable and professionally rewarding. Again, welcome to the symposium. Have a great time, enjoy yourself and share the knowledge you gain here with those who could not make it to the symposium.

Richard B. Gomez
Symposium General Chairman

BLANK PAGE

CONTENTS

VOLUME I

Preface	iii
Message from Symposium General Chairman	v
Profile of Richard B. Gomez	xvii
Profile of Walter E. Boge	xviii
Profile of John V.E. Hansen	xix
Profile of Jack N. Rinker	xx
Profile of John Richards	xxi
General Information	xxii

TUTORIALS

Introduction to Spectral Remote Sensing	5
Jack N. Rinker, U.S. Army Topographic Engineering Center	
Imaging Spectrometer Data Analysis	44
Fred A. Kruse, University of Colorado	
Spectral Sensors and Data Availability	55
Harlan L. McKim, U.S. Army Corps of Engineers, Cold Regions Research and Engineering Laboratory	

OPENING SESSION

Conference Theme	59
Walter E. Boge, U.S. Army Topographic Engineering Center	
Keynote Address – Remote Sensing: An Australian Perspective on Opportunities and Challenges	62
John A. Richards, University College, The University of New South Wales, Australia	
Correlation-Induced Spectral Changes	71
Emil Wolf, University of Rochester	

SESSION I: DATA COLLECTION

Mapping and the Verification of Terrestrial Hyperspectral Information	77
John E. Estes, National Aeronautics and Space Administration/U.S. Geological Survey	
HYDICE: A Status Report	89
Lee J. Rickard, J. Fischer and M. Anderson, Naval Research Laboratory	
Operational Use of a Variable Interference Filter Pushbroom Scanning Multispectral Imager	93
James M. Anderson and X. Sun, University of Dundee, Scotland	
Development and Operation of a Real-Time Imaging Spectroradiometer	105
Mark Dombrowski, Surface Optics Corporation	
Spectral Significance of the MOMS-02 Sensor Flown Aboard STS-55/D2	116
Hermann Kaufmann and M. Berger, GeoResearch Center Potsdam, Germany; D. Meißner, German Aerospace AG, Germany	

Airborne Radioactivity Surveys for Routine and Emergency Applications	123
G.F. Schwarz, L. Rybach and E.E. Klingelé, Institut für Geophysik, ETH—Hoenggerberg, Switzerland	
Multispectral Background Measurements from an Airborne MWIR Sensor	133
Kevin D. Bishop, J.A. Granger and E.L. Jewett, Lockheed Palo Alto Research Labs	
A Hyperspectral Sensor and Investigation of Shallow Water Remote Sensing	149
Thomas B. McCord, Ronald G. Resmini, Michael Fené and Gregory C. Mooradian, SETS Technology, Inc.	
SMIFTS: A Flexible System for Collection of Hyperspectral Sensing Data in the 1–5 μm Region	160
Paul G. Lucey, Tim Williams, Keith A. Horton and John Hinrichs, University of Hawaii at Manoa	
High Resolution Multispectral Stereo Imager (HRMSI), A Step Toward the Future	168
George T. Elerding, Jerald R. Holt and Edgar E. Russell, Santa Barbara Research Center	
Wedge Imaging Spectrometer (WIS) Hyperspectral Data Collections Demonstrate Sensor Utility	180
Loren M. Woody and James C. Demro, Santa Barbara Research Center	
A State-of-the-Art Airborne Infrared/Ultraviolet Scanner for Oil Pollution Monitoring and Mapping	191
B.M. Sorensen, GER-Intradan, Denmark; S.-H. Chang, Geophysical and Environmental Research Corporation, USA; and T.E. Melhuish, Canadian Coast Guard, Canada	
Field Spectrometry: Techniques and Instrumentation	195
Brian Curtiss, Analytical Spectral Devices, Inc.; and Alexander F.H. Goetz, University of Colorado	
Comparative Study of Dielectric Constant Measurements of Soils Using Different Techniques	204
Ram M. Narayanan, Danny W. Rhoades, Paul D. Hoffmeyer, University of Nebraska; and John O. Curtis, U.S. Army Waterways Experiment Station	
A Field Portable Hyperspectral Imager: The Large Area Fast Spectrometer	216
Randall W. Zywicki, Keith A. More, Daedalus Enterprises, Inc.; J. Holloway and N. Witherspoon, Coastal Systems Station, Dahlgren Division	
TOPSAT: The Global Topography Mission	225
Thomas G. Farr, Howard A. Zebker, Jet Propulsion Laboratory; and David J. Harding, NASA Goddard Space Flight Center	

SESSION II: SIGNAL/DATA PROCESSING

Calibration and Atmospheric Compensation of Imaging Spectrometer Data for Vegetation, Geological and Water Applications and Research	229
Robert O. Green, Thomas G. Chrien, James E. Conel and Jeannette van den Bosch, Jet Propulsion Laboratory	
Mathematical Aspects in Modeling Material Reflectance Properties for Remote Sensing Applications	230
Michael D. Metzler, Environmental Research Institute of Michigan; James R. Baker, Virginia Polytechnic Institute and State University; and J.R. Maxwell, Environmental Research Institute of Michigan	

Scene/Object Classification Using Multispectral Data Fusion Algorithms	246
Thomas J. Kuzma, Laurence E. Lazofson, Howard C. Choe, E.B. Preston, and J.D. Chovan, Battelle	
An Assessment of the Effects of Data Compression on Multispectral Imagery	256
Ken Riehl Jr. and Carey D. Erdman, Itel Optical Systems	
Automatic Identification of Spectral Endmembers in Hyperspectral Image Sequences	267
Joseph C. Harsanyi, Applied Signal and Image Technology Company; William H. Farrand, Science Applications International Corporation; Joseph M. Hejl, Applied Signal and Image Technology Company; and Chen-I Chang, University of Maryland	
Subpixel Detection Methods: Spectral Unmixing, Correlation Processing, and When They Are Appropriate	278
Alan Schaum, Naval Research Laboratory; and Alan Stocker, Space Computer Corporation	
Predicting Sub-Pixel Target Detectability	287
Michael J. Duggin, Research Associates of Syracuse, Inc. and State University of New York; R. Richter, DLR, German Aerospace Research Institute, Institute of Optoelectronics, Germany; W.N. Philpot, Cornell University; and J. Lamicela, Research Associates of Syracuse, Inc.	
Automating Linear Mixture Analysis of Imaging Spectrometry Data	302
Joseph W. Boardman, University of Colorado	
From a Natural to a Behavioral Classification	310
Jean Paul Rasson, F. Orban-Ferauge and V. Granville, Laboratory GEOSATEL, F.U.N.D.P. University, Belgium	
Application of the Natural and the Behavioral Approaches for Supervised Remote Sensing Classification	311
F. Orban-Ferauge, Jean Paul Rasson and V. Granville, Laboratory GEOSATEL, F.U.N.D.P. University, Belgium	
Assessment of the Linear Mixing Model for Subpixel Materials Detection in Thermal Infrared Multispectral Scanner (TIMS) Images	312
Ronald G. Resmini, Jessica M. Sunshine, SETS Technology, Inc.; Alan Schaum, Naval Research Laboratory; Thomas B. McCord, Jennifer L. Forsythe, SETS Technology, Inc.; and Alan R. Gillespie, University of Washington	
Linear Estimation of Hyperspectral Mixed Pixel Components	333
Edmundo Simental and Elisa C. Gonzalez, U.S. Army Topographic Engineering Center	
SESSION III: SPECTRAL ANALYSIS/PROCESSING SYSTEMS AND TOOLS	
Effects of Spectral and Spatial Resolutions on NDVI	365
P.M. Teillet, Karl Staenz, Canada Centre for Remote Sensing, Canada; and D.J. Williams, MacDonald Dettwiler and Associates Ltd., Canada	
Application of Dark Object Subtraction to Multispectral Data	375
James B. Campbell and Xiangdong Liu, Virginia Polytechnic Institute and State University	

Temporal Measurements of High Resolution Spectral Signatures of Plants and Relationships Indicating Water Status	387
Charles Bostater, Florida Institute of Technology; Carlton Hall, The Bionetics Corporation; D. Vieglais, John F. Kennedy Space Center; J. Rebbman, Florida Institute of Technology; and M. Provancha, The Bionetics Corporation	
Spectral Manipulation for the Detection of Man-Made and Small Objects in Multi-Spectral Images	403
Vittala K. Shettigara and Gordon M. Sumerling, Defence Science and Technology Organisation, Australia	
Optimal Routing Techniques for Feedforward Neural Networks and Parallel Distributed Processors	416
Perry J. LaPotin, U.S. Army Cold Regions Research and Engineering Laboratory/University of Vermont; and Harlan L. McKim, U.S. Army Cold Regions Research and Engineering Laboratory	
Application of AVIRIS Data to Estimate Dynamic Range Demands on HYDICE	430
William S. Aldrich, William H. Farrand, William W. Stoner, Science Applications International Corporation; and Robert W. Basedow, Hughes Danbury Optical Systems, Inc.	
Target Detection in Multispectral Images Using Relative Entropy Thresholding	456
Mark L.G. Althouse, U.S. Army Edgewood Research, Development and Engineering Center; Chein-I Chang, University of Maryland; and Joseph C. Harsanyi, Applied Signal and Image Technology	
Quantifying Multispectral Imagery Interpretability	468
Carey D. Erdman, Ken Riehl, Jr., Lawrence A. Maver, Itek Optical Systems; Jon Leachtenauer, Ellen Mohr, John M. Irvine, Julie Odenweller, Environmental Research Institute of Michigan; Rulon Simmons, Eastman Kodak Company; and D. Hothem, Booz-Allen and Hamilton	
Hyperspectral Image Processing	477
Samuel Barr, U.S. Army Topographic Engineering Center	
Real-Time Analysis of Spectral and Spatial Data From Hyperspectral Imaging Sensors	491
Wally T. Jansen, WTJ Software Services	
A Hyperspectral Image Processing System-Hips™	496
Nicholas J. Susner, Juliana T. Lo and Thomas B. McCord, SETS Technology, Inc.	
Spectral Characteristics (0.4 μm – 2.5 μm) and the Detection of Camouflage Materials	497
Timothy D. Evans and Fonder Henley, U.S. Army Topographic Engineering Center	
A Rationale for Pixel Colorations of Evaporite Mineral Deposits in Thermal Imagery of Death Valley, California	516
John W. Eastes, U.S. Army Topographic Engineering Center	
The Impact of System MTF on Sub-Pixel Target Detection, and on Spectral Demixing For Sub-Pixel Discrimination	518
Michael J. Duggin, State University of New York and Research Associates of Syracuse, Inc.	

VOLUME II

SESSION IV: ATMOSPHERIC STUDIES AND APPLICATIONS

Remote Sensing of Aerosols Using Passive Infrared Spectroscopy	539
David K. Lynch and Andrew B. Christensen, The Aerospace Corporation	
Optical Remote Sensing of the Dayside Ionosphere from Space Through Observations of the O ⁺ 834 Å Dayglow	549
Kenneth F. Dymond, J. Michael Picone, Robert R. Meier, Robert P. McCoy, Owen Kelley, Naval Research Laboratory; and Ronald J. Thomas, New Mexico Institute of Mining and Technology	
Hyperspectral Observations of the Earth's Atmosphere and Surface from the MSX Satellite in the Spectral Region 200–900 NM	562
Donald E. Anderson, G.J. Romick, D. Morrison, J.F. Carbary, L.J. Paxton, C.-I. Meng, J.-H. Yee and G. Crowley, The Johns Hopkins University Applied Physics Laboratory	
Coincident Surface and Aircraft Spectral Resolution Sensing of Atmospheric Parameters: A Joint American-Mexican-Russian Research Program	570
Oleg B. Vasilyev, St. Petersburg State University, Russia; now at: UNAM, Cd. Universitaria, Del. Coyoacan, Mexico; Ronald M. Welch, South Dakota School of Mines & Technology; Amando Leyva Contreras, Agustin Muhlia Velazquez, and Ricardo Peralta y Fabi, UNAM, Cd. Universitaria, Del. Coyoacan, Mexico	
Estimation of Cirrus Cloud and Aerosol Scattering in Hyperspectral Image Data	582
E. Ben-Dor, Alexander F.H. Goetz, and A.T. Shapiro, University of Colorado	
Estimation of Atmospheric Conditions and Surface Temperatures from Multispectral Data	594
James R. Johnson, E-System Garland Division	
Sensitivity Analyses to Identify Key Parameters for Use with a Radiative Transfer Model-Based Atmospheric Correction	595
Sally Westmoreland, San Diego State University; and Frederick C. Mertz, Photon Research Associates, Inc.	
The 1994 GEISA Program for Management and Study of Spectroscopic Information	604
Nicole Husson, B. Bonnet, A. Chedin, N.A. Scott, Laboratoire de Météorologie Dynamique, France; Alexey A. Chursin, Vl. G. Tyuterev and V.F. Golovko, Institute of Atmospheric Optics, Russia	
A New Doppler Imager for Thermospheric Dynamics	612
Randall W. Zywicki, D.S. Dilworth, Daedalus Enterprises, Inc.; B.C. Kennedy, University of Michigan; E.J. Weber, Phillips Laboratory, Geophysics Directorate; and Keith A. More, Daedalus Enterprises, Inc.	
SSM/T-2 Brightness Temperature Signatures	628
Vincent J. Falcone, Michael K. Griffin, Phillips Laboratory, Geophysics Directorate; John D. Pickle, Ronald G. Isaacs, Atmospheric and Environmental Research, Inc.; and James Wang, NASA Goddard Space Flight Center	
Precipitable Water Estimated from SSM/I	635
Charles Norris, John Roads, Shyh Chen, Scripps Institution of Oceanography; and Paul Weber, Los Alamos National Laboratory	

Sensitivity of SSM/T-2 Channels to Water Vapor	636
Michael K. Griffin, Vincent J. Falcone, Phillips Laboratory, Geophysics Directorate; John D. Pickle, Ronald G. Isaacs, Atmospheric and Environmental Research, Inc.; and James Wang, NASA Goddard Space Flight Center	
Satellite Observed Cloud Patterns Associated With Precipitation	641
Graciela Alicia Catuogno and Inés Velasco, Universidad de Buenos Aires, Argentina	
The Software Package for Managing Large-Scale Spectroscopic Data Bases and Spectral Sensing Applications: GEISA Based Version	649
Alexey A. Chursin, V.F. Golovko, Vl. G. Tyuterev, Institute of Atmospheric Optics, Russia; Nicole Husson, B. Bonnet, A. Chedin, and N.A. Scott, Laboratoire de Météorologie Dynamique, France	
Water Vapor Dependent Thermodynamics of the Lower Atmosphere	658
Fred Walter, Scientific Components Company	
SESSION V: OCEANOGRAPHIC/COASTAL STUDIES AND APPLICATIONS	
Processing and Analysis of AVIRIS Imagery of the Coastal Ocean	661
Curtiss O. Davis, Naval Research Laboratory	
Simulating Radiative Transfer in Aquatic Systems and Contrasting Results from Ambient Environmental Spectroscopy: Estuarine and Near Coastal Waters	673
Charles Bostater, Wei-Ming Ma and Andrew Lamb, Florida Institute of Technology	
Spectral Reflectance Properties of Wetlands Plants	683
John E. Anderson, U.S. Army Topographic Engineering Center	
Airborne Visible Imaging Spectrometry Applied to Limnology: Chlorophyll Variation in Mono Lake	691
John M. Melack and Mary Gastil, University of California	
Laser-Induced Signatures in Oceanographic Spectral Sensing: Dynamics, Pollution and Baseline Studies	696
Alexander E. Dudelzak, Canadian Space Agency, Canada; Sergei M. Babichenko and Larisa V. Poryvkina, Institute of Ecology, Estonian Academy of Sciences, Estonia	
An Analytical Model for Remote Sensing of Chlorophyll α in Inland Waters	697
H.J. Hoogenboom, A.G. Dekker, Vrije Universiteit, The Netherlands; and G.A. Farrington, Integrated Terrestrial Systems, Canada	
A Synergistic Approach to Monitoring Coastal Environments by Using a Suite of Remotely Sensed Imagery and Ground-Based Measurements	705
Elijah W. Ramsey III, Richard H. Day and Kevin McRae, National Wetlands Research Center, National Biological Survey	
The Littoral Remote Sensing Modeling and Simulation System (LRS-MASS)	706
Lee J. Rickard, G. Keramidas and J. Spencer, Naval Research Laboratory	
Use of Principal Components to Characterize Upwelling off the Coast of California	707
Eugene Molinelli and G. Muncill, Planning Systems, Inc.	

SESSION VI: TERRESTRIAL AND LAND SURFACE STUDIES AND APPLICATIONS

Monitoring Vegetation Health Status With Steady-State Chlorophyll Fluorescence	737
Arnold F. Theisen and Barrett N. Rock, University of New Hampshire	
Remote Sensing Hypermedia Terrain Database	749
Brian D. Leighty, Knowledge Sciences, Inc.; Robert D. Leighty, Leighty and Associates, Inc.; George E. Lukes, Jack N. Rinker and Phyllis A. Corl, U.S. Army Topographic Engineering Center	
The Application of Almaz Radar Imagery to Petroleum Exploration	761
Richard F. Pascucci, Autometric, Incorporated	
Multispectral Measurements of Active Lava Flows in the MWIR (2.0–5.0 μm)	775
Kevin D. Bishop, J.A. Granger and E.L. Jewett, Lockheed Palo Alto Research Labs	
Rock-Soil Background Effects on Narrow Band Vegetation Indices	785
Christopher D. Elvidge, Zhikang Chen, Desert Research Institute, University of Nevada System; and Walrave T. Jansen, WTJ Software Services	
Derivation of Inputs to a Biogenic Emission Model from Spectral and Ancillary Data	805
Siamak Khorram, John A. Brockhaus, Jayantha Ediriwickrema and Heather Cheshire, North Carolina State University	
RASTER-J: A Multisensor Testbed for Environmental Research	813
Lee J. Rickard, G. Hoskins, Naval Research Laboratory; and A. Skroch, Falcon Research, Inc.	
Diachronic Study of Crop Spectral Response in Central Greece	821
Leonidas G. Toullos, National Agricultural Research Foundation, Greece; and N. Silleos, Aristotle University of Thessaloniki, Greece	
Spectral Change Detection in Coniferous Forest Using Landsat TM and Elevation Models	836
Per Syrén, Stockholm University, Sweden	
Using Imaging Spectrometry for Modeling Soil Erosion	842
Steven M. de Jong, Utrecht University, The Netherlands	
Using Multitemporal, Multispectral Remote Sensing Data to Monitor Land Degradation	848
Terrill W. Ray, California Institute of Technology; Thomas G. Farr, Eric M. De Jong, Ronald G. Blom and Robert E. Crippen, Jet Propulsion Laboratory	
Applications of Remote Sensing for Tectonic Purposes in El-Rouge Depression, Northwest of the Syrian Arab Republic	859
Moutaz Dalati, General Organization for Remote Sensing, Syria	

SESSION VII: ENVIRONMENTAL RESTORATION AND DISASTER EVALUATION

Multispectral Remote Techniques of Studying the Consequences of Chernobyl Catastrophe and Technogenic Activity in Belarus	869
Alexander Kovalyov, Belarusian Republican Scientific and Technical Centre of Environment Remote Sensing, Republic of Belarus	
Environmental Applications of Remote Sensing in the Greek Islands	870
John N. Hatzopoulos, University of the Aegean, Greece	

Mapping a Biochemical Stress Gradient Across a Coniferous Forest with Airborne Visible/Infrared Imaging Spectrometer (AVIRIS) Data	878
C. Banninger, Institute for Image Processing and Computer Graphics, Joanneum Research, Austria; L. Johnson and D. Peterson, NASA Ames Research Center	
Texture Analysis of Remotely Sensed Data for Waste Site Characterization	880
John M. Irvine and Garth Barbour, Environmental Research Institute of Michigan	
An Infrared Hyper-Imaging Spectrometer for Atmospheric Studies and Environmental Remediation	893
Mark Massie and Michele Hinnrichs, Pacific Advanced Technology	
An Examination of Mine Waste Contamination in the Coeur D'Alene River Valley, Idaho, Using Imaging Spectrometer Data	908
William H. Farrand, Science Applications International Corporation; and Joseph C. Harsanyi, Applied Signal and Image Technology Company	
Dual Use in GosNIIAS Airborne Laboratories—Capabilities of Multizonal Remote Sensing	919
Edward Falkov, I.M. Formanuk, and V.A. Kosinov, State Research Institute of Aviation Systems (GosNIIAS), Russia	
Monitoring of Surficial Deposits in the Gulf War Zone Using Satellite Data	929
Kamel M. Sheikho, Saudi Centre for Remote Sensing, Saudi Arabia	
Rapid <i>In-Situ</i> Assessment of Organic Contaminants in Aquatic Sediments with the REMOTS® UV Imaging Spectrometer	936
Donald C. Rhoads, Jo Ann Muramoto, Chris Coyle, Roger H. Ward, and Richard Anderson, Science Applications International Corporation	
Using Spectral Data and Stressed Vegetation to Evaluate Hazardous Waste Sites	945
M.B. Satterwhite and John E. Anderson, U.S. Army Topographic Engineering Center	
Role of Saudi Civil Defence in Monitoring and Protecting Environmental Pollution	946
F. Al-Khodairy, King Faisal Specialist Hospital and Research Centre, Saudi Arabia; Majdi H. Al-Tukhi, Center for Studies and Research, Saudi Arabia; M.A. Hannan and A. Al-Dakan, King Faisal Specialist Hospital and Research Center, Saudi Arabia	
Analysis of the 1993 Flood Using Digital Remotely Sensed Data	954
Donn Rodekohr, ERDAS, Inc.	

APPENDIX A: PROCEEDINGS ONLY

CCD Sensors Applicable in Tracking and Imaging Spectrometers: Study and Correction of Their Spectral Characteristics	A-3
Valentin Atanasov, Alexandar Krumov and Valentina Boycheva, Bulgarian Academy of Sciences, Bulgaria	
Study on the Intertransputer Connections for an Image Processing	A-10
Doyno Petkov, T. Zdravev and H. Nikolov, Bulgarian Academy of Sciences, Bulgaria	
A New Technique for Solving Classification Problems in Remote Sensing	A-16
Doyno Petkov, T. Zdravev and H. Nikolov, Bulgarian Academy of Sciences, Bulgaria	

Satellite Images Data Compression Using Multiresolution Analysis Based on Optimal Edge Detection	A-20
A. Serir and B. Sansal, Institut d'Electronique, Algeria	
Spatial Resolution of Multispectral Survey Systems for Different Atmospheric Conditions	A-31
V.V. Gogohia, Russian Academy of Sciences, Russia	
Second Generation Database of the Ionosphere Disturbance Indices	A-38
Tamara L. Gulyaeva, Russian Academy of Sciences, Russia	
Precipitation Amount Long-Term Variability Over Romanian's Territory	A-50
Maria Colette Iliescu, National Institute of Meteorology and Hydrology, Romania	
A Method for Direct Retrieving the Planetary-Scale Wave Parameters from Satellite Measurements of Thermal Outgoing Radiation	A-59
Igor A. Podgorny and Gustav M. Shved, St. Petersburg University, Russia	
Bathymetric Image Maps of Coastal Water Areas	A-70
Lee Estep, J. Lillycrop, U.S. Army Corps of Engineers, Waterways Experiment Station; R. Arnone, Naval Research Laboratory; and L. Parson, U.S. Army Corps of Engineers, Waterways Experiment Station	
Optimization of Water Quality Monitoring in Izmit Bay Using Landsat Spectral Radiance Differentials and SPOT Imageries	A-79
Hikmet Kurar and Krishnaier Natarajan, Turkish Council of Scientific and Industrial Research, Turkey	
Applications of Multispectral MM-Wave Technique for Diagnostics of the Deep Oceanic Processes and Critical Situations in the Atmosphere	A-89
Igor V. Cherny and G.M. Chernyavskiy, Russian Academy of Sciences, Russia	
A Review of Problems of Land Use and Cover Delineation Using SPOT and LANDSAT-TM Data of Sao Jose Dos Campos, Brazil	A-100
Sosthenes Kwadzo Kufogbe, University of Ghana, Ghana	
Detection of Rill Erosion with Digitized KFA-1000 Satellite Photographs	A-112
Fred Ernst, University of Çukurova, Turkey	
Temporal Environmental Changes in the Vicinity of Atatürk Dam Using Remote Sensing Techniques	A-118
Erhan Alparslan, M.T. Aygün and B. Bilge, TÜBİTAK, Marmara Research Centre, Turkey	

APPENDIX B

Author Index	B-3
--------------------	-----

APPENDIX C

List of Attendees	C-3
-------------------------	-----

BLANK PAGE

Profile of Symposium General Chairman

RICHARD B. GOMEZ



Dr. Richard B. Gomez is Associate Director of Technology of the U.S. Army Topographic Engineering Center (TEC), formerly the U.S. Army Engineer Topographic Laboratories (USAETL). He joined USAETL as Associate Technical Director (ATD) in March 1986. In January 1994, he was assigned to his current position, where he has oversight responsibilities over the Remote Sensing Laboratory, Geographic Information Laboratory, and the Simulation & Visualization Laboratory. From July 1992 to October 1993, Dr. Gomez was assigned to the Pentagon as Deputy for Space and Environmental Systems in the Office of the Under Secretary of Defense for Acquisition (Strategic and Space Systems, Missiles and Space Systems), Washington DC. In this

position, he serves as the Chairman of the Joint Environmental Satellite Coordinating Group (JESCG). As ATD at USAETL, Dr. Gomez was multi-hatted in the position, serving as the Director of the USAETL Research Institute (January 88 to June 89) and as the Deputy Director of the U.S. Army Space Technology and Research Office (ASTRO), Laboratory Command (September 1987 to January 1990). From November 1981 to March 1986, he served in the Office of the Chief of Engineers as Senior Army Scientist for the Environmental Sciences, Directorate of Research and Development. In this capacity, he was the ARMY POC to DoD on environmental science matters. Before that, he worked 14 years as a research scientist for the U.S. Army Atmospheric Sciences Laboratory (ASL) at White Sands Missile Range, New Mexico.

Dr. Gomez graduated from Bowie High School, El Paso, Texas, May 1960. He received his bachelor's degree in physics from Texas Western College in August 1963 and his master's degree in physics from the University of Texas at El Paso in May 1965. He joined Texas Instruments (TI), Dallas, Texas, in June 1965. In August 1967, he returned to El Paso to work for ASL. In January 1976, he earned his Ph.D. in physics from New Mexico State University, Las Cruces, New Mexico. Dr. Gomez is actively involved in many professional societies and has published extensively in scientific journals. He is a member of the Sigma Pi Sigma and is on the Board of Directors of the Society of Mexican-American Engineers and Scientists (1991-94).

Dr. Gomez's accomplishments gained him the cover story of the 1989 summer issue of the *National Hispanic Engineer* magazine. He received the 1989 Hispanic Engineer National Achievement Award as the outstanding Hispanic engineer in the award category of "Professional Achievement." In November 1988, Bowie High School presented him with the 1988 Outstanding Ex-Student Award. That same year, he received the Commissioners Court of El Paso Country Award. In May 1987, Dr. Gomez received the Gold Nugget Award for Outstanding Alumni from the College of Sciences, University of Texas at El Paso. The city of El Paso honored him in 1979 with the Key to the City Award, recognizing him as an Honorary Citizen of the city of El Paso, Texas. In 1978, Dr. Gomez received the prestigious U.S. Army Research and Development Achievement Award.

Dr. Gomez and his wife Edna Mae Salazar Gomez live in Fairfax, Virginia. They have four children, Eydie, Richard Michael, Ruth Marie and Valerie Marlene.

Profile of

WALTER E. BOGE



Mr. Walter E. Boge is director of the U.S. Army Topographic Engineering Center (TEC), formerly the U.S. Army Engineer Topographic Laboratories (USAETL), Alexandria, Virginia. As TEC's chief executive officer, Mr. Boge has overall management and leadership responsibility for a comprehensive program focused on the research, development and exploitation of topographic, geodetic, and remote sensing technologies for Army military and Corps of Engineers civil works applications.

Mr. Boge joined the Corps after graduating from the City College of New York in 1960 with a bachelor's degree in civil engineering and worked on developing improved map compilation equipment and techniques. From 1962-1963, he attended graduate school at Syracuse University, majoring in photogrammetry and geodesy. Upon return to the Corps, Mr. Boge was engaged in the development of new automated mapping equipment and digital image processing systems.

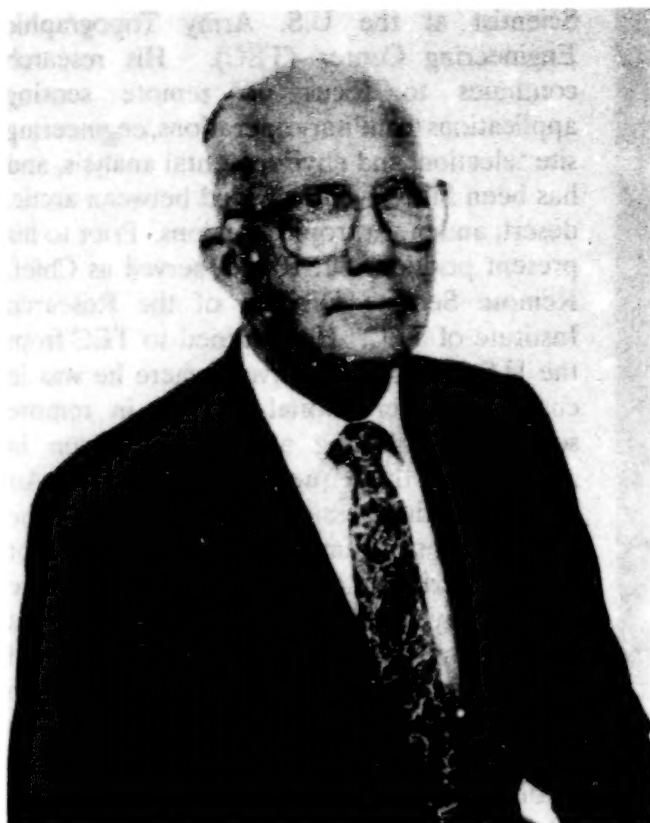
From 1972-1973, he continued graduate studies in photogrammetry and geodesy at Purdue University, receiving a master's degree in civil engineering and meeting all requirements except dissertation for a doctorate. Mr. Boge continued his career development at USAETL; covering many aspects of topographic mapping, surveying and remote sensing, achieving ever-increasing positions of responsibility. In 1983, he was named technical director with the responsibility of formulating and implementing the organization's research and development program. In December 1991, TEC's management structure was reorganized and Mr. Boge was named director.

Mr. Boge has been a member of the American Society of Photogrammetry and Remote Sensing (ASPRS) since 1962, serving in numerous positions, as well as contributing technical papers; winning the Talbert Abrams award in 1965. In addition to ASPRS, Mr. Boge is a member of the Society of American Military Engineers, the American Defense Preparedness Association, the Senior Executives Association, Chi Epsilon Civil Engineering Honor Society and Phi Kappa Psi Graduate Honor Society. He also is listed in *Who's Who in Engineering*.

Mr. Boge and his wife Lucy live in Fairfax County, Virginia. They have three sons.

Profile of Symposium Steering Committee Chairman

JOHN V.E. HANSEN



Mr. John V.E. Hansen is Director of the Army's Simulation and Visualization Laboratory at the U.S. Army Topographic Engineering Center (TEC). For the past five years, as Director of TEC's Research Institute, he directed its hyperspectral research activities. During Desert Storm, he directed Project Ostrich, which involved the exploitation of remote sensing systems to detect subsurface mines. He also served on the first (1992) ISSSR Steering Committee.

He was formerly Deputy Director of Technology Planning and Management at the Army's Laboratory Command, and contributed to the development of the Army's Technology Base Investment Strategy. His duties have also included serving on a number of Congressional subcommittees and DoD committees addressing technology forecasting, as well as management of the Defense Department's technology base. He was manager of the Army 21 technology forecasting initiative, and his recommendations

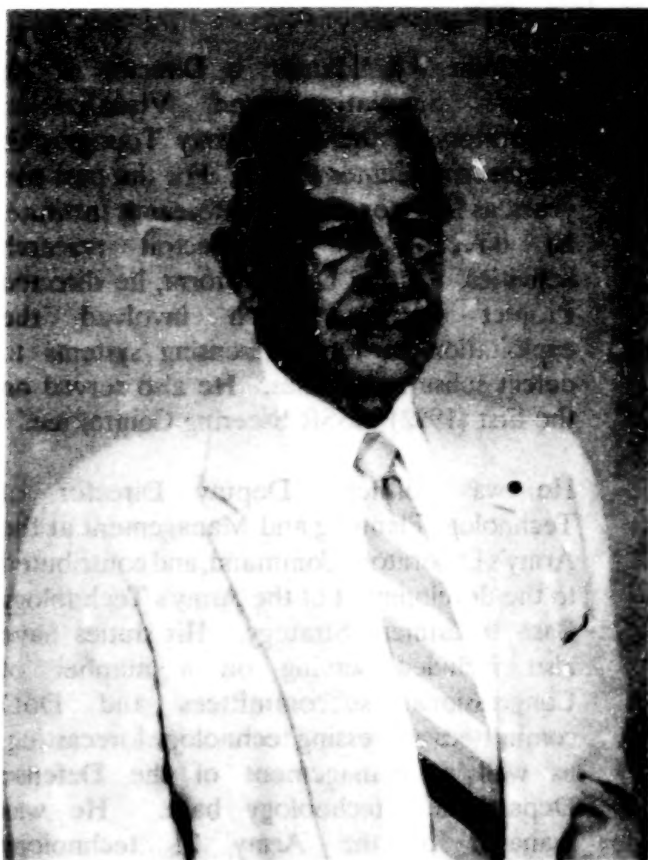
led to the Army's implementation of the Strategic Technologies for the Army of the Twenty-First Century (STAR 21). He served on the DoD committee developing the first Congressionally mandated DoD Critical Technologies Plan, as well as the first committee preparing the Army's Technology Base Master Plan. In 1990, he was personally assigned to the Undersecretary of the Army, visiting and reviewing all of the Army's technology base activities.

Prior to joining the Army, Mr. Hansen held a number of technical management activities in industry, serving as Division Manager in a major corporation. During the Vietnam era, he led the industry effort to develop the first lightweight ceramic armor systems. These were used in Vietnam on all combat helicopters, and resulted in a number of documented life saving incidents. His first assignment in the Army was as Director of the Army's laboratory responsible for protective systems for the individual soldier.

Mr. Hansen received his Chemical Engineering degree from the Polytechnic Institute of Brooklyn and is a Registered Professional Engineer. He has published more than 60 papers and articles, holds three patents, and taught a number of courses associated with technology forecasting and exploitation.

Profile of Symposium Technical Program Chairman

JACK N. RINKER



Dr. Jack N. Rinker is a Senior Research Scientist at the U.S. Army Topographic Engineering Center (TEC). His research continues to focus on remote sensing applications to military operations, engineering site selection, and environmental analysis, and has been fairly evenly divided between arctic, desert, and moist tropical regions. Prior to his present position, Dr. Rinker served as Chief, Remote Sensing Division of the Research Institute of TEC. He returned to TEC from the U.S. Geological Survey, where he was in charge of international training in remote sensing, establishing a similar program in Argentina at the request of the Argentina Air Force. Other assignments include: the development of remote sensing programs for Latin America, under the aegis of IAGS; the U.S. Army Cold Regions Research and Engineering Laboratory where he developed radio ice-sounding and crevasse detection techniques, led two international expeditions on the Greenland icecap, and was extensively involved in special studies for Vietnam and Navy Project Sanguine; and the U.S. Army

Snow, Ice and Permafrost Establishment where he developed the first instrumented field sites for testing and evaluating infrared thermal scanners.

Dr. Rinker's awards include the Army R&D Achievement Award (1991), the TEC Commander's Achievement Award (1990), and a Special Service Award for Desert Storm activities (1990/91). He has published extensively, and has been active in a number of professional societies, including: the Society of American Bacteriologists, the American Association for the Advancement of Science, the American Society of Photogrammetry and Remote Sensing, Society of Photographic Science and Engineering, Arctic Institute of North America, and the Glaciological Society.

Prior to WWII, Dr. Rinker attended DePauw University. After serving with the Navy in the Asiatic/Pacific theater of operations, he returned to Purdue University where he received a BS in science in 1947, an MS in microbiology and chemistry in 1950, and a PhD in 1956.

Dr. Rinker and his wife Betty live in Alexandria, Virginia. They have two daughters.

Profile of Symposium Keynote Speaker

JOHN RICHARDS

Professor John Richards is Head of the Department of Electrical Engineering and Deputy Rector at the University College, Australian Defence Force Academy.

He graduated from the University of New South Wales with the degrees of Bachelor of Engineering (Hons 1) and Doctor of Philosophy, both in electrical engineering, in 1968 and 1972 respectively.

From 1972 to 1977 he was with the Department of Electrical Engineering at the James Cook University of North Queensland returning to the School of Electrical Engineering and Computer Science at the University of New South Wales in late 1977. In 1981 he was appointed Director of the University's new Centre for Remote Sensing, a position he held concurrently with his post in electrical engineering until his move to the University College in June 1987. He has held sabbatical positions at Purdue University and the University of California, Santa Barbara in the United States of America.

In 1991 and 1992, Professor Richards was Deputy Chair of the Australian Research Council's Research Grants Committee and Chair of its discipline panel on Engineering, Earth and Applied Science. He is a member of the Fulbright National Selection Committee, a member of the Editorial Board of the international journal *Remote Sensing of Environment* and Deputy Chair of the Australian Space Council.

He is the author of two books and has published in the fields of remote sensing, imaging radar and parametric systems.

GENERAL INFORMATION

ORGANIZATION

Symposium General Chair:	Dr. Richard B. Gomez Associate Director of Technology U.S. Army Topographic Engineering Center
Steering Committee Chair:	Mr. John V.E. Hansen Remote Sensing Laboratory Director U.S. Army Topographic Engineering Center
Technical Program Chair:	Dr. Jack N. Rinker Senior Research Scientist U.S. Army Topographic Engineering Center

STEERING COMMITTEE

Mr. John V.E. Hansen (Chair), TEC
Dr. Douglas Amlin, ASC/REQR
Mr. Walter Boge, TEC
Mr. David P. Brannon, SSC
Dr. Rudy Buser, CECOMNVESD
Dr. Steven F. Clifford, NOAA/ERL/WPL R/E/WP
Dr. Darrell Collier, SSDC
Dr. John M. Ferriter, ERDEC
Dr. Richard B. Gomez, TEC
Dr. Herbert Gursky, NRL
Dr. Robert B. Honea, ORNL
Major James Kroll, AFOSR/NL
Mr. Donald L. Light, USGS
Dr. Lewis E. Link, CRREL
Mr. James R. Lucas, NOAA
Mr. Ross Lunetta, EPA
Dr. Robert A. McClatchey, PL/GD
Dr. Robert P. McCoy, NRL
Dr. Harlan L. McKim, CRREL
Mr. Kirkman Phelps, ERDEC
Dr. Lee J. Rickard, NRL
Dr. Jack N. Rinker, TEC
Dr. Philip R. Schwartz, NRL
Mr. Joe Swistak, TEC
Mr. Donald R. Veazey, ARL

TECHNICAL PROGRAM COMMITTEE

Dr. Jack N. Rinker (Chair), TEC
Mr. Mark Althouse, ERDEC
Dr. Douglas Amlin, ASC/REQ
Dr. James R. Baker, VA Tech
Dr. Lee K. Balick, EG&G
Dr. Henry Berger, TEC
Dr. James Cogan, ARL
Ms. Phyllis A. Corl (Secretary), TEC
Mr. Ron Gird, NOAA
Mr. Donn Holt, CIO
Dr. Frank Honey, SpecTerra Systems Pty Ltd.
Mr. Eddie Jacobs, BRDEC
Dr. Kenneth Johnston, NRL
Dr. Fred A. Kruse, U. of Colorado
Dr. Robert D. Leighty, Leighty & Associates, Inc.
Mr. Donald L. Light, USGS
Dr. Robert P. McCoy, NRL
Dr. Harlan L. McKim, CRREL
Dr. Ching -I. Meng, JHU/APL
Dr. John Price, U.S. Department of Agriculture
Dr. Lee J. Rickard, NRL
Dr. Barrett N. Rock, U. of New Hampshire
Lt Col Kevin Rose, USAF Landsat Office
Dr. Louiselle St-Laurent, Energy, Mines and Resources Canada
Dr. Karl Staenz, Canada Centre for Remote Sensing
Mr. Joe Swistak, TEC
Mr. Richard J. Szymber, ARL
Dr. Stephen Ungar, NASA
Mr. Robert E. Waldron, U.S. Department of Energy
Dr. Austin Yingst, BRDEC

ORGANIZING COMMITTEE

Ms. Charlotte Lemen (Chair), TEC
Mr. Timothy D. Evans, TEC

SYMPOSIUM ADMINISTRATION

Ms. Jeanne Hawtin, STC Administrator
Ms. Judy Cole, STC Coordinator
Ms. Sonya Herrin, STC Coordinator
Mr. Keith Hicks, STC Coordinator

SPONSORED BY

U.S. Army Corps of Engineers (USACE)
 Cold Regions Research and Engineering Laboratory (CRREL)
 Topographic Engineering Center (TEC)
U.S. Army Night Vision and Electronic Sensor Directorate (NVESD)
U.S. Army Space and Strategic Defense Command (SSDC)
U.S. Army Research Laboratory (ARL)
U.S. Army Edgewood Research, Development and Engineering Center (ERDEC)
U.S. Army Research, Development and Standardization Group - United Kingdom (USARDSG-UK)
Air Force Office of Scientific Research (AFOSR)
U.S. Air Force Phillips Laboratory, Geophysics Directorate (PL/GD)
U.S. Air Force Systems Command (AFSC)
National Aeronautics and Space Administration (NASA)
Naval Research Laboratory (NRL)
National Oceanic and Atmospheric Administration (NOAA)
 Wave Propagation Laboratory (WPL)
 Nautical Charting Research and Development Laboratory (NCRDL)
Oak Ridge National Laboratory (ORNL)
Environmental Protection Agency (EPA)
 Environmental Monitoring Systems Laboratory (EMSL)
U.S. Geological Survey (USGS)
NASA Stennis Space Center (SSC)

VOLUME I

TUTORIALS

OPENING SESSION

SESSION I - SESSION III

BLANK PAGE

TUTORIALS

BLANK PAGE

ISSSR TUTORIAL I¹

INTRODUCTION TO SPECTRAL REMOTE SENSING

J. N. Rinker
U. S. Army Topographic Engineering Center
Alexandria, Virginia 22315-3864, USA

ABSTRACT

This tutorial, the first of a linked set of four, provides an introduction to remote sensing as a tool for studying the earth, its land, water bodies, cultural components, and surrounding atmosphere. The basis for this capability is the recording of reflected, emitted, and luminesced photons, usually in the form of images, and the subsequent interpretation of image patterns for terrain information (manual analysis), and of spectral patterns for targeting, monitoring, and change detection (computer and digital analysis). Included are brief reviews of: radiation characteristics such as bandwidth, interference, absorption, reflectance, emittance, luminescence; optical attributes such as focus, and resolution; research results in spectral measurements; and application examples from various remote sensing systems. This leads to Tutorial II on spectral measurements; thence to Tutorial III on the digital analysis of imaging spectrometer data; and to Tutorial IV on the characteristics of available remote sensing systems.

1. INTRODUCTION

Remote sensing systems rely on a variety of energy forms such as pressure waves, or sonar (sound navigation and ranging), gravity, radio activity, and electrical and magnetic fields. The workhorse, however, is electromagnetic radiation; reflected, emitted, or luminesced. Such radiation comes from natural sources, such as the sun, from man-made sources such as flashbombs, lasers (light amplification by stimulated emission of radiation), or radio antennae as in radar (radio detection and ranging). How it is measured is of equal diversity and includes sensors such as the eye, photographic emulsions, photo cells, antennae, charge coupled devices, thermistors, etc. Most often, the results are presented as an image, or an assemblage of images, wherein each image portrays the terrain in a different band of the electromagnetic spectrum, e.g., multiband, multispectral, or hyperspectral.

Why the interest in multiband and hyperspectral remote sensing?—simply because these techniques provide more information. Materials respond differently in different parts of the electromagnetic spectrum. An image recorded in one band can depict patterns not discernable in images recorded in other bands. To illustrate this, Fig. 1 shows images of human torsos recorded with: A, reflected visible (400-700 nm); B, reflected near-infrared (700-800 nm); C, emitted thermal infrared (800-1400 nm); and D, transmitted x-ray radiation (0.1 nm range). In all cases, however, identification of the various features relied on shape patterns and their location. The visible light photograph (A) shows surface characteristics of the skin cover of the torso. That it is a torso is verified by its shape. The identification of the nipples also relies on shape patterns and locations. Near-infrared radiation (image B), having longer wavelengths, penetrates further into the skin and records subsurface differences in absorption; as evident in the interconnected pattern of dark lines, whose shape, size, and location identifies it as part of the vascular system. In the thermal infrared image (C), brightness differences result from temperature variations on the skin surface. The bright irregular pattern is caused by a tumor, the cells of which have a higher metabolic rate, and thus a higher temperature than normal

¹This tutorial is based on earlier publications (Rinker, 1990a and b), and the Tutorial for ISSSR 1992.

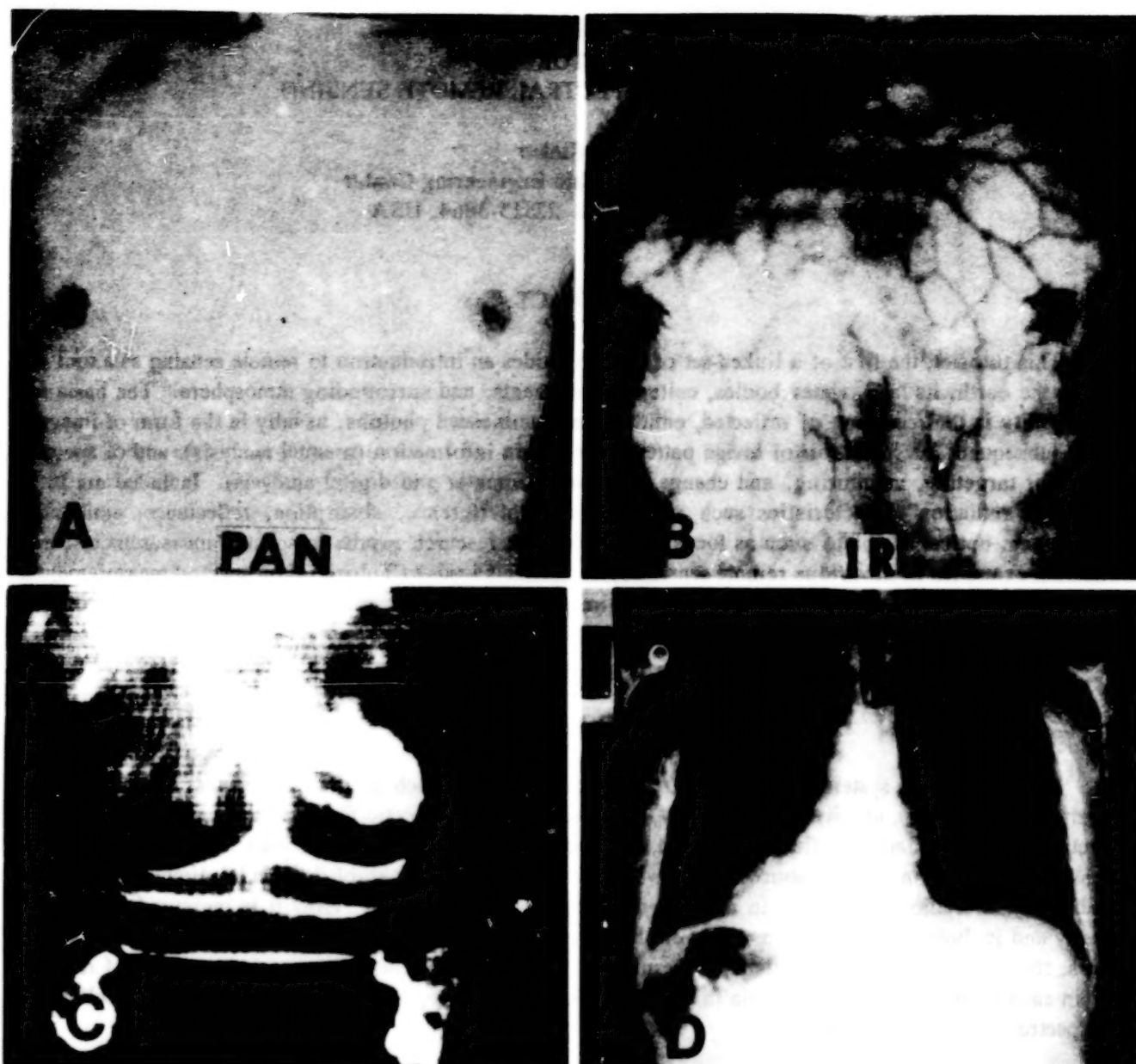


Figure 1. Human torsos as viewed in different spectral bands. Image A, a visible light record, shows only surface details of the skin, e.g., the pattern of the nipples, identifiable by shape and location. Image B was formed with reflected infrared energy, which penetrated the skin to depict the underlying vascular structure, identifiable by its shape and location. These images (A and B) are from an old Eastman Kodak Manual. Image C (Wallace, 1974 personal communication) is a record of thermal infrared energy wherein the brightness of tone is related to temperature. The bright irregular pattern on the breast results from a tumor. A tumor has a higher metabolic rate, and a slightly higher temperature than its surrounds. By conduction, it has warmed the skin over it and revealed its presence. The spectral band records it as a warmer object; the shape and location of the thermal pattern provides the identity. The bright linear patterns below the tumor represent warmer temperatures associated with folds in the skin. Image D, an x-ray record, shows internal structures within a torso, identifiable by their shapes and locations, as ribs, clavicle, joint, etc.

cells. By conduction, the tumor has made the skin over it warmer than the skin adjacent—revealing its presence. It is the shape and location of the thermal pattern, however, that suggest the presence of a tumor.

The shapes and locations of other equally light-toned, and warm areas, are indicative of folds in the skin. In the x-ray image (D), the brightness variations are caused by differences in tissue density through which the x-rays passed. But, it is the shapes and locations of the image patterns that provide identification, e.g., ribs, clavicle, sternum, etc.

Figure 2 is an example from the satellite remote sensing domain. The left image is a Landsat scene of a portion of the North African desert, showing only the surface patterns of the terrain. To the right is the same image, but with a superposed strip from the Shuttle Imaging Radar (SIR-A) imagery of the same area. The L-band microwave energy penetrated the surface deposits of sand and gravel to reveal an underlying pattern of an ancient drainage system (McCauley, 1982). The radar band provided the means for recording the details, and the shapes of the pattern elements provided identification. If one had but the radar image, would the conclusion arise that it was a buried drainage system? Radar does record surface drainage patterns. Band comparison can be as critical to the derivation of information, as can the contents within bands.

Because all materials reflect, absorb, or emit photons in ways characteristic of their molecular makeup, a high resolution trace of the intensity of the transmitted, reflected, emitted, or luminesced radiation versus wavelength forms a graphical record unique to a given material. Different materials cannot have identical spectral wave shapes of reflectance, emittance, and luminescence. Many of the characteristic absorption and emission bands occur in narrow wavelength ranges, 10 nm or less; and, unless the instruments have that kind of spectral resolution, these details cannot be recorded. Although many laboratory and field instruments exceed this spectral resolution, airborne systems have only recently entered this domain. From a laboratory point of view, the use of spectral measurements to identify and/or assay components of minerals, pigments, pharmaceutical and other organic and inorganic compounds, is old, established, and reliable. The reasoning goes that if such could be done from air or space, it would give remote sensing a similar capability.



Figure 2. The left image is a Landsat MSS scene over North Africa. To the right, an L-band radar image (SIR-A) is registered over the scene. The radar penetrated the surface deposits, to reveal a buried drainage system from an earlier time (McCauley, 1982).

1.1 TERRAIN ANALYSIS

Reliable, detailed information about the landscape in terms of composition, structure, properties, conditions, and use is fundamental to predicting terrain characteristics, be it for engineering site selection and evaluation, environmental impact studies, or military operations such as cross-country movement. Foremost to these applications, but more intuitively apparent in relation to cross-country movement, are questions such as: is it flat?—is it rolling?—is it a hill?—is it steep?—are the slopes smooth, stepped (thinly bedded, or massively bedded)?—is the surface dissected (drainageways as indicators of composition, as obstacles, as ambush sites, or for cover and concealment)?—are the channel slopes steep, or gentle? These questions involve shape, and for this purpose stereo imagery is the only source of accurate information. For example, an area can be covered with a vegetative mantle of grass and trees, and all that the spectral data will show will be reflectance traces of chlorophyll. In stereoscopic viewing, however, the shapes of the landform and drainage patterns can reveal that beneath the vegetal mantle rests a thinly interbedded series of gently dipping limestones and shales with unstable colluvial materials on the lower slopes.

Three-dimensional shapes are directly related to the composition, structure, physical properties, conditions and climatic regime of the resident materials, and thereby serve as indicators of these factors. Patterns in an image can be classified into landform, drainage (plan and elevation, i.e., cross section and gradient), erosion, deposition, vegetation, tone and texture, cultural, and "special," which includes such features as joints, faults, slumps, tears, mud flows, trim lines, etc. Topographic shape, i.e., landform, identifies landscape elements as plains, valleys, hills, mountains, escarpments, fans, terraces, etc., and their specific shapes provide clues about composition and physical properties. The shapes of the drainageways, in plan and elevation, convey information about soil type, soil texture, mantle thickness, homogeneity, and structural control. Thus, from an evaluation of these patterns, one can deduce compositional identities such as igneous, metamorphic, sedimentary (sandstone, limestone, shale, massive beds, thin beds, interbedded), soil types, and properties such as hard, soft, dusty, quick, sticky, unstable, etc. A fundamental principle is that like patterns, wherever they occur, indicate like materials and/or conditions, and unlike patterns indicate unlike materials and/or conditions. The basics of this manual analysis procedure are described in various publications (e.g., Belcher, 1943; Frost et al., 1953; Rinker and Corl, 1984). For obtaining this type of terrain information, the manual analysis of stereo imagery is still state-of-the-art. Digital analysis of spectral data contributes little direct information. Digital techniques such as band combinations, enhancement, etc., can, however, improve pattern boundaries for visual observation.

1.2 TARGETING

Targeting refers to the detection and, hopefully, the identification of specific features, items, or conditions. For success, the target must have some characteristic that differs from its background and which cannot be confused with any other feature in the field of view. For point targets, this is seldom the case. The prediction of detectability is based on physics, and more often than not, this can be done successfully. But, more often than not, identification is iffy, mostly because of signals that, in the spectral band of use, look like the target. For passive systems such as thermal infrared and thermal microwave, these issues are more complex than for active systems. In general, the more cluttered the image scene, the more difficult it is to identify point source targets. Detection based on shape, size, and arrangement includes examples such as roads, airports, dams, vehicles, crop/field patterns, structures, and urban areas; and such are usually easier to identify by manual analysis. In addition to shape, differences can also be based on color, spectral reflectance, spectral emittance (temperature), luminescence, acoustical reflectance and emittance, magnetic fields, etc. Application examples include road type (asphalt or cement concrete), diseased vegetation, stressed vegetation, flood boundaries, wetland areas, thermal springs, thermal plumes from power plants, oil slicks, hot spots in burned areas, alteration zones, number of lakes in a region, camouflaged sites, and military units and equipment. Included in targeting are the applications of change detection and monitoring, e.g., seasonal changes in wetlands, desertification, flood and fire damage, alteration of land use, forest clearing, extent of pack ice, etc. Although aerial photography and multiband images are used in these tasks, it is here that digital spectral imagery and computer techniques of digital analysis become important. Spectral data define the

molecular characteristics of the surfaces, whereas shape, especially stereoscopic shape, identifies object types. For example, the spectral reflectance characteristics of a sand sheet, barchan dunes, a dome dune field, and a sand-veneered playa are similar—similar to the extent that they would be grouped as an entity. Shape reveals that: two are plains, one of them to be avoided (the playa); the isolated hills are barchan dunes that can provide sites for cover and concealment, observation, etc., and with excellent support for vehicles on the interdunal surface; and, the dune field will support cross-country movement by HMV type vehicles, but not heavy trucks.

For targeting and change detection applications, military or civil, the more bands available to examine the scene, the better the chances for detection and identification. A camouflaged target can resemble the terrain visually, photographically, and thermally, but be a mismatch in the radar bands; or, match in the radio frequencies, but not in the thermal infrared; or match in radar and thermal infrared, but show a mismatch in its reflected solar spectral signature.

2. RADIATION - THE CARRIER OF INFORMATION

2.1 BASIC CHARACTERISTICS

Until 1819, electricity and magnetism were thought to be unrelated independent forces. In that year, the results of experiments by Hans Christian Oersted, a Danish physicist, proved that these two forces were not independent—but were intimately bound together. These two fields will always be present together, at mutual right angles, coalesced into an entity known as the electromagnetic field, with the electric field associated with voltage, and the magnetic field associated with current. In the 1860s, James Clerk Maxwell developed his famous set of four equations that established the relations between electricity and magnetism under all conditions; combined electricity, magnetism, and light into a single concept; and showed the existence of self-propagating electromagnetic waves. The propagation results because a time-varying electric field induces a time-varying magnetic field which, in turn, induces a time-varying electric field—and on to infinity, or until the energy content becomes vanishingly small. This continuous generation which takes place at the leading edge can occur only so fast, no more and no less, a defining rate at which each field can produce the other. It is this that establishes the speed of travel, and why it is a constant in a given medium. One result of Maxwell's equations, which astounded physicists at the time, was that the speed of propagation predicted by the equations for an electromagnetic field was the same value as the speed of light, which had already been measured. The speed of a wave motion is equal to the wavelength multiplied by the frequency. Equation 1 states it for electromagnetic waves. Figure 3 is a sketch of a changing electric field to illustrate concepts and terminology. For simplicity, the magnetic field, which would be in phase with the sketched waveform, but perpendicular to it, is not included.

Anything that influences either the electric component or the magnetic component alters the characteristics and response of the electromagnetic field. In passing through matter, the attribute that interacts with the magnetic field is called the relative permeability (symbol μ), and that which interacts with the electric field is called the relative permittivity (symbol ϵ). As shown in the Fig. 3 equation, this combined field travels through space at a constant speed for all frequencies. In condensed matter, however, the speed, or more properly the phase velocity, is slower for all frequencies, but not uniformly so, and is expressed by the following equation:

$$\text{Velocity} = \frac{c}{\sqrt{\mu\epsilon}} \quad (1)$$

c = speed of light in vacuum.

μ = mu, relative permeability.

ϵ = epsilon, relative permittivity (dielectric constant).

The quantity $\sqrt{\mu\epsilon}$ is the index of refraction.

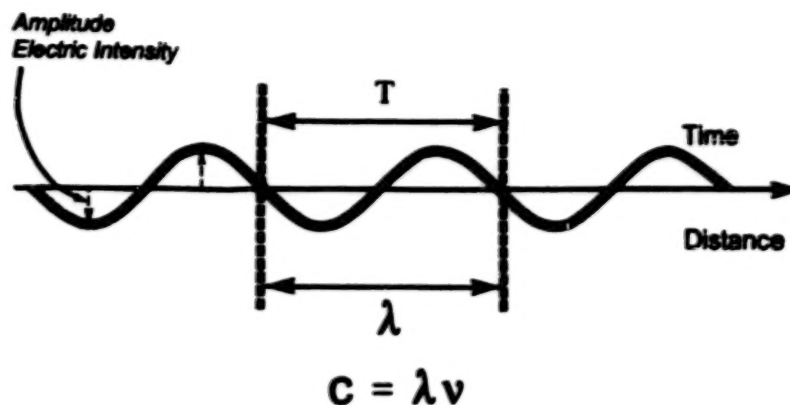


Figure 3. A representation of a time varying electric field. λ is wavelength. T is period (time per cycle), and c is speed of light, which in free space is about 3×10^{10} cm sec., or about 186,000 miles per second. A useful relation for quick calculations is that light travels about 1 ft per nanosecond (10^{-9} sec).

The magnetic permeability of a vacuum is set at 1. Because most materials have a permeability close to one, the magnetic component of the electromagnetic field is usually ignored, and the index of refraction is considered to be the square root of the dielectric constant. Thus, the defining characteristic of electromagnetic radiation is the frequency of oscillation of the electrical field, which runs from the infinitesimally small to the infinitely large.

This spread of frequencies, known as the electromagnetic (EM) spectrum, is portrayed in Fig. 4. The division into subunits of radio, microwave, infrared, etc., is strictly arbitrary, because there is no fundamental difference between them. The division is based, in part, on the different experimental techniques used, and in part on the fact that, historically, they were studied separately, and were once thought to be distinct entities. Spectral bands can be specified by numbers for frequency (cycles per second) and wavelength (Angstroms, nanometers, micra, feet, miles, etc.), or by words. Words that designate frequency locations are radio terms such as Low Frequency (LF), High Frequency (HF), Very High Frequency (VHF), Ultra High Frequency (UHF), and Extraordinary High Frequency (EHF), at which point they ran out of superlatives. On the wavelength side, amateur radio operators use the terms 1 m band, 10 m band, etc. General descriptors for various portions of the EM spectrum, going from high frequency to low, or from short wavelengths to long, include: gamma ray, x-ray, ultraviolet, visible, infrared, microwave, and radio. The visible part of the EM spectrum covers the approximate wavelength range of 400-700 nm. It is not a sharp cutoff at the long wavelength end, and many people can perceive photons with wavelengths well beyond 700 nm. The 400-500 nm band is called blue, the 500-600 nm band green, and the 600-700 nm band red. Wavelengths shorter than 400 nm fall in the ultraviolet region, and wavelengths longer than 700 nm are in the infrared domain, which extends out to a wavelength of 1 mm. Beyond this is the microwave region, which contains the radar bands. Over this extreme, from low frequency radio waves to high frequency γ -rays, there is an enormous difference in photon energy via the relation $E = h\nu$. We are immersed in an ocean of radio waves, but of such low energy that the effect on body tissue is little, or none—although subject to debate. At the high frequency end, γ -rays have such high energies that they are dangerous. Also shown at the top of Fig. 4 are the general locations of absorption due to electronic, rotational, and vibrational processes.

The sun, the most used energy source in remote sensing, is a blackbody radiator, operating at an average surface temperature of about 5800° K, and emitting energy from the short wavelengths of x-rays, through the ultraviolet, the visible, the infrared, and out to the longest wavelengths in the radio region. On an intensity *versus* wavelength plot, the curve peaks at about 480 nm, i.e., more energy is emitted at this wavelength than at any other. Some 96 percent of the sun's energy, however, is emitted at wavelengths shorter than 2.5 μ m. At wavelengths longer than this, one enters the thermal infrared domain and the need for different types of detectors. Although there is still a solar component, the amount is small compared to the

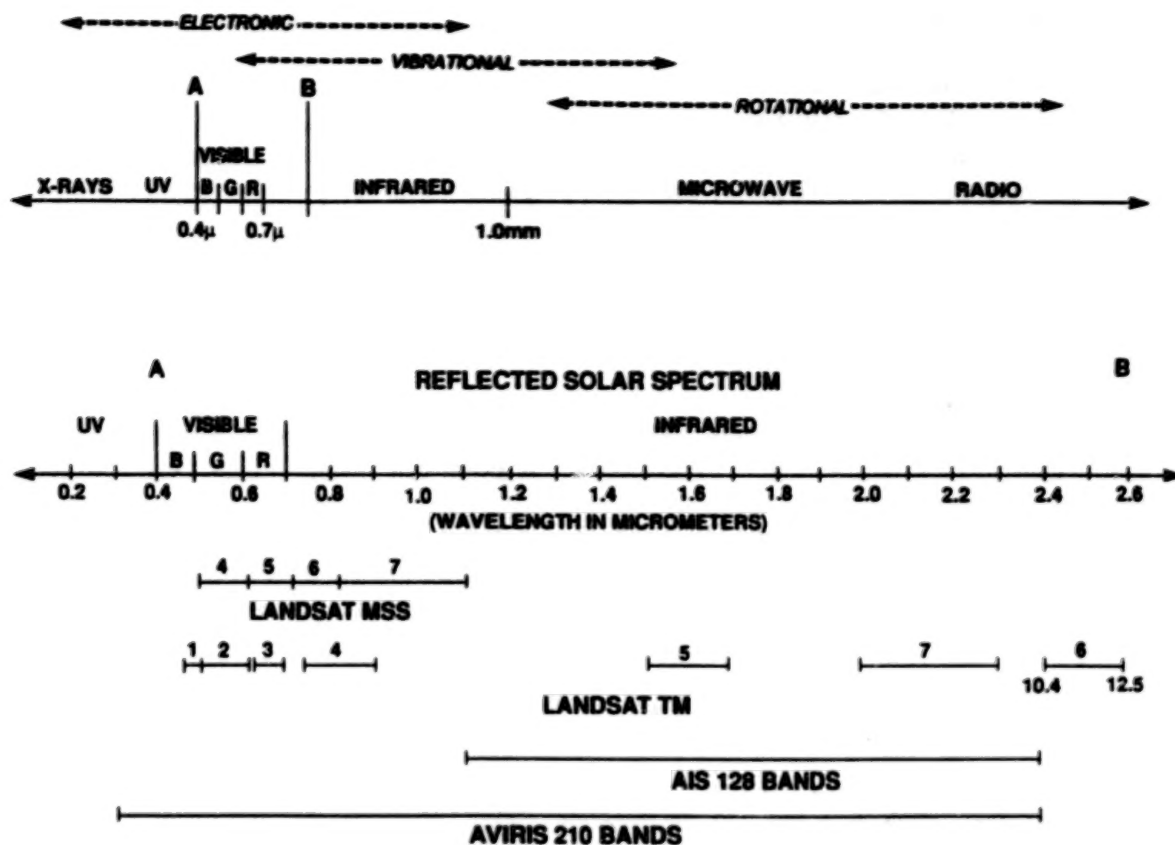


Figure 4. Electromagnetic spectrum. The top diagram locates various bands in a relative sense. Above it are general locations for electronic, rotational, and vibrational absorption processes. The next line down is an expansion of the AB portion. Below are approximate band locations for some of the operational multispectral and hyperspectral systems.

thermally emitted signal. For wavelengths shorter than about 350 nm, the atmosphere greatly attenuates the incoming photon flux. Thus, the reflected solar spectrum is generally considered to cover the 0.4 to 2.5 μm range; a spread that contains about 84 percent of the incoming solar energy, and which is probably the most used band in the electromagnetic spectrum.

2.1.1 Bandwidth and Pulse Duration

When electromagnetic energy is transmitted as a continuous series of pulses, the spread of frequencies required to emit the pulse is determined by time duration of the pulse. Pulse Duration (PD) times the Bandwidth (BW) is approximately equal to 1. A basic law of physics.

$$PD \cdot BW = 1 \quad (2)$$

Pulse Duration is the reciprocal of the Bandwidth, and *vice versa*. The narrower the band of frequencies, the longer the pulse duration. The shorter the pulse in time, the greater the spread of frequencies needed to get the energy out. As the time duration of the pulse becomes shorter, the pulse must shift to ever higher frequencies.

$$BW = \frac{1}{PD} \quad (3)$$

$$PD = \frac{1}{BW} \quad (4)$$

Wave packets can be created by adding together waves of different frequencies that have no beginning and no end. Taking a central frequency, and adding to it frequencies that are a little lower, and frequencies that are a little higher, the waves interfere with each other, constructively and destructively, to create a series of pulses, or wave packets, that travel through space. Between these packets, the electric and magnetic fields of the wave add vectorially to reduce the field to zero (destructive interference). The more frequencies added, the shorter the time duration of the pulse, and the less space it will occupy. Interference is a property of waves, whether they are visible light, radio frequencies radiating from an antenna, acoustical waves from a loud speaker, or pressure waves in water; and, it is basic to explanations for bandwidth, focus, and resolution.

For a monocyclus radar we developed for measuring thin ice thicknesses, the pulse had to be short enough to resolve the two reflections, one from the top (air/ice), and one from the bottom (ice/water) surfaces of an ice layer of 10-15 cm. At the speed of the signal in ice, this required a pulse of 2.5 nanoseconds duration, with a corresponding bandwidth of 500 megacycles. In 1962, that was considered a very short pulse. Since then, techniques and hardware have progressed to the point that ultrashort pulses can now be generated in the femtosecond domain (10^{-15} sec). Fork (1990) reports on pulse durations of 6 femtoseconds. To put this in perspective, a 1 sec pulse occupies 186,000 miles of space—a nanosecond pulse occupies 1 ft of space—and a 6 femtosecond pulse occupies about $1.8 \mu\text{m}$ of space—about twice the length of a bacterium such as *E. Coli*. Light forming such a brief pulse must contain the full complement of the visible spectrum (blue, green, red), plus ultraviolet and infrared frequencies.

2.1.2 Interference

In order to collect photons and record an image, some kind of an optical element is needed to bring them into the system, such as a lens, or an antenna. This introduces the factors of focus, resolution, beamwidth, and side lobes, all of which depend on constructive and destructive interference phenomena associated with waves. Figure 5A illustrates wave interference, or diffraction. A wave front passes through the two slits, S_1 and S_2 , and arrives at Point P. In the lower example, P_1 is exactly 10 wavelengths from S_1 , and from S_2 . The troughs and crests, produced simultaneously at the sources, arrive at P_1 at the same time so that they add together (constructive interference) to create a strong field, or wave, at P_1 , stronger, or brighter, than either of its components. These waves are said to be in phase. In the upper example, S_2 to P_2 is 10 wavelengths, and S_1 to P_2 is $10\frac{1}{2}$ wavelengths. When the waves arrive at P_2 , they are 180° , or $\frac{1}{2}$ cycle out of phase. A crest from S_2 arrives with a trough from S_1 . The fields cancel each other (destructive interference), and there is no field at P_2 —it is dark. If the difference between the two paths is one wavelength, or two, or three, they arrive in phase again, and form a brighter area, as in the lower illustration. A view of the image plane in Figure 5B would show a central bright spot surrounded by alternate dark and light zones, the light zones rapidly diminishing in brightness. The change from bright to dark to bright is a gradient, not a step, because the ratio between crest and trough varies constantly as one progresses along the image plane between the bright and dark extremes. Obviously, the waves cannot be brought to a focus at a precise point—they will spread out over an area. This interference pattern directly determines focus, resolution, instantaneous field of view (IFOV), or beamwidth, as in radar.

2.1.3 Focus

The term is widely understood in an intuitive sense. But, what is meant in an exact sense? In Fig. 6, a sequence of plane waves of light coming from point S in the object plane travels to the lens, passes through all parts of it, and proceeds on to point I in the image plane. In order for point S to be in focus in the image plane, the lens must be ground so that the number of wave cycles is exactly the same for every path through the lens to point I. The first point of contact of the lens with a wave front is the bulge of the lens on the axis. At that point, the wave enters the glass, slows in accordance with the index of refraction, and passes through the thickest part of the lens to emerge on the other side where it resumes its former speed and eventually arrives at I. Another part of the same wave front passes through the outer edge of the lens *en route* to I, and this path is longer than the one through the center of the lens. But, the longer time in the high speed air path, coupled to the shorter time in the slower speed glass path, adds up so that it arrives at I at exactly

the same time as that which went through the center of the lens. To be in focus, the number of waves between object and image points must be exactly the same through all parts of the lens. An excellent discussion on the nature of electrons and waves can be found in Pierce (1956).

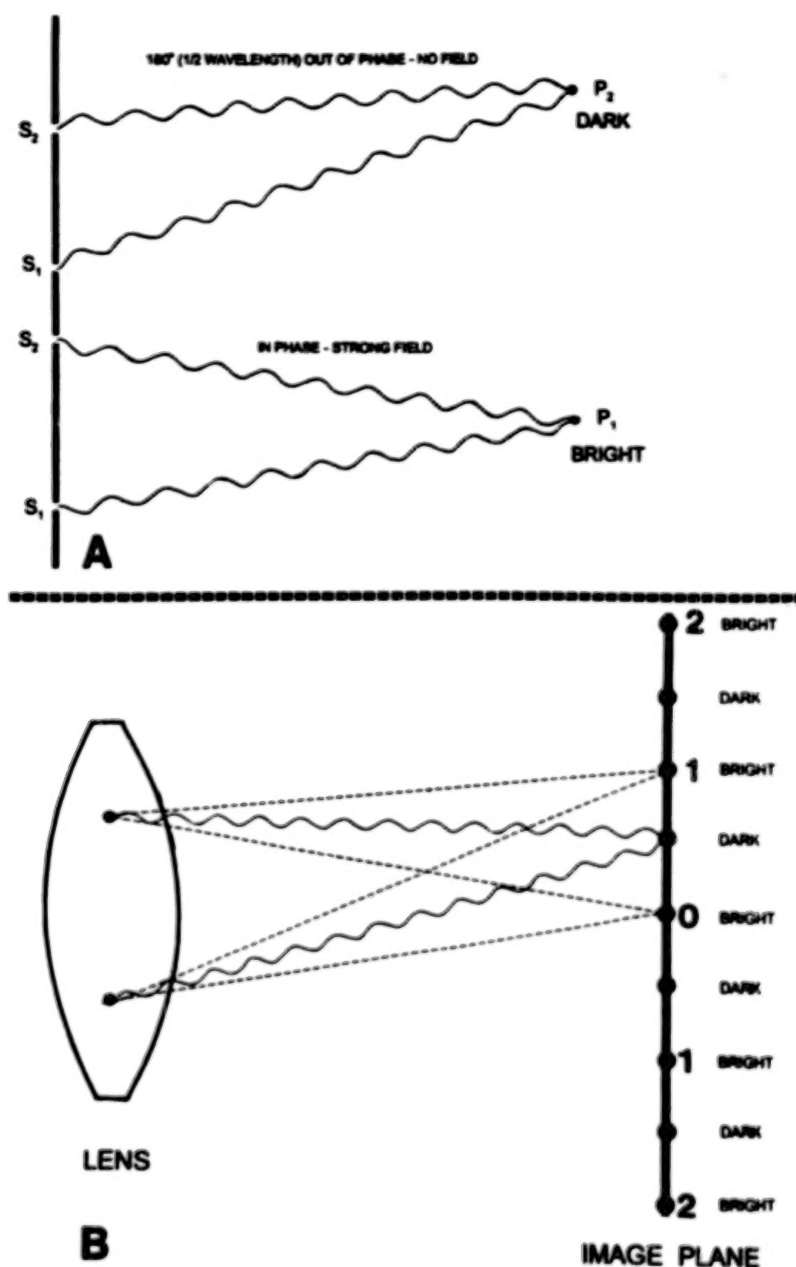


Figure 5. Interference. The lower part of A illustrates constructive interference, where each path has the same number of waves, 10 in this case, and combine at P_1 to produce a strong field. They are in phase. The upper drawing of A represents destructive interference. Path S_2-P_1 is 10 waves, and path S_1-P_1 is $10\frac{1}{2}$ waves, i.e., the waves are $\frac{1}{2}$ cycle out of phase. The crest of one meets the trough of the other, canceling the electric field at that point. In B, light from the lens, impinging on the image plane, forms a central bright zone surrounded by alternate dark and light zones. At 0, the waves arrive in phase and create a strong field. Going up or down, the path lengths begin to differ. Where they differ by one half a cycle, the fields cancel, and darkness results. Continuing up or down, the paths will eventually differ by 1 wavelength, and will add constructively to form a brighter zone. Intensity is maximum at 0, and decreases at each succeeding bright zone. The size of the central spot determines the resolution.

intensity of the light decreases until a zero field is encountered. At that place, the waves are one-half cycle out of phase, and the fields cancel each other—no light. Progressing further, up or down, the light becomes gradually brighter until it reaches another maximum at 1, where one path is one wavelength longer than the other. They are again in phase. Continuing up or down, the waves will slip into phase at 2 to produce another bright zone, and so on. If one could look at the image plane face on, there would be an intense bright spot at 0, surrounded by an alternating series of dark and bright circles. The spot at 0 is the brightest, i.e., it has the maximum amplitude. The first bright zone, or ring, surrounding 0 has an intensity of about one fifth of the max. The second bright zone is about one eighth of max. If we replace the lens with an antenna, as in radio or radar, these zones are called lobes. The one at 0 being the main lobe, the next being the first side lobe, the next the second side lobe, and so on. In his book, Kock (1965) provides excellent discussion and sketches associated with the fundamentals of wave motion, as well as photographs of the diffraction structure of acoustical waves and microwaves. The photographs show what the equations predict.

The central bright spot is the smallest point dimension that can be produced by the element, and represents the resolution of the lens, or antenna, except in the latter case it is called beam width. If two points are so close together that their central bright spots merge, they cannot be resolved. Also note that there is not a sharp division between field and no field, i.e., between bright and dark. Thus, if focused for maximum resolution, the image will have a somewhat fuzzy look. There are ways to estimate approximate limits for this central bright spot. Figure 7 (based on Pierce, 1956) shows a lens of diameter D focused on point 0, which is some distance L from the lens. Arbitrary points in the lens are a distance of $D/2$ apart. Point 0 represents the center of the bright spot, or main lobe, where the waves are in phase. Points 1 and 2 above and below 0 mark locations of the other lobes, or zones of brightness. The points between the numbers represent dark zones. The distance W represents the central area in which the in-phase waves arrive, or leave. Because L is so vastly greater than either W or λ , then very nearly:

$$\frac{W}{L} = \frac{\frac{\lambda}{2}}{\frac{D}{2}} = \frac{\lambda}{D} \quad (5)$$

$$W = \frac{L\lambda}{D} \quad (6)$$

W defines the resolution element formed by light coming from the lens D . It also defines the resolution element over which a collecting lens, or antenna, can receive photons of a given wavelength. It says that for a lens of diameter D , collecting photons of wavelength λ from a surface L distance away, the smallest recordable area (resolution cell) has a diameter of W . It also says that for an antenna of length D , emitting microwaves of wavelength λ , the width of the beam at distance L from the antenna is W . If L coincides with the surface being illuminated, then W is one dimension of the IFOV for that system. Also, the equation says that for a loudspeaker of diameter D emitting an acoustical signal (pressure wave) of wavelength λ (or frequency ν), the width of the beam L distance away is W . Holding D and L constant, but changing the tone to $\lambda/2$, i.e., doubling the frequency, which is an octave, W is one half its former value. Thus, the beam width is different for different tones coming from the same speaker. As a beamwidth example, take a radar with a 3 m long antenna operating at 10 cm wavelength. The width of the beam 10 km away will be about 330 m. A Synthetic Aperture Radar (SAR) allows one to synthesize what the radar interprets as a very long antenna—with resultant narrow beamwidths. Note the relation of the shape of the resolution element to the shape of the emitter, or collector. The narrowest part of the beam will be parallel with the longest dimension of element, and the widest part will be perpendicular to this. Table 1 lists some resolution elements for different systems. Beamwidth can also be derived in degrees if λ and D are expressed in the same units.

$$W(\text{degrees}) = \frac{51\lambda}{D} \quad (7)$$

TABLE 1. SOME RESOLUTION AND BEAMWIDTH EXAMPLES

Refer to Equation 6. λ refers to wavelength, ν to frequency, L to distance or range, D to diameter of lens or length of antenna, and W to resolution or beamwidth. The lower set is for acoustical waves. Values are approximate.

	λ	L	D	W
MICROSCOPE	0.55 μm	1 mm	2 mm	0.3 μm
BINOCULARS	0.55 μm	1 km	40 mm	14 mm
TELESCOPE	0.55 μm	3.5 X 10 ⁷ mi.	1 ft	63 mi.
RADAR	10 cm	2.5 km	3 m	83 mi.
RADAR	3 cm	2.5 km	3 m	25 mi.
	ν			
LOUDSPEAKER	20 kHz	10 ft	1 ft	0.5 ft
LOUDSPEAKER	11 kHz	10 ft	1 ft	5.1 ft
LOUDSPEAKER	11 kHz	10 ft	3 in.	20.4 ft
LOUDSPEAKER	1 kHz	10 ft	1 ft	56 ft

2.2 ABSORPTANCE AND REFLECTANCE

When electromagnetic energy falls on a material (gas, liquid, or solid) several things can happen. What happens depends on the electrical properties of the materials, i.e., the index of refraction, or dielectric constant. In turn, this is a function of the oscillation frequency of the incoming electric field. If, in going from one medium to another, the radiation encounters a change in electrical properties that takes place in a distance less than its characteristic wavelength, then something must happen to that radiation—it cannot continue as it was. It will undergo, singly or in combination, transmission, reflection (scattering), refraction, or absorption.

Incident radiation is absorbed if the photon energy matches an energy separation between two stationary states of the molecular components. Absorption characteristics, such as center frequency location, band depth, etc., carry the information needed to identify materials, and establish conditions, such as vegetal stress. In the laboratory, one can measure absorptance, as well as transmittance, reflectance, and emittance. With airborne and space systems, one can collect only those photons that have been reflected, and infer what has been absorbed by evaluating what is missing from the beam reflected to the sensor.

All frequencies can undergo conversion to thermal energy, a process of broad-band absorption, as in solar heating of the earth, solar cookers, and microwave ovens. Narrow band absorption is responsible for the colors seen from surfaces, or through filters. A yellow filter looks yellow because it absorbs the blue part of the visible spectrum, and passes the green and red bands—a combination that causes the sensation in our eye called yellow. Because a yellow filter does not transmit blue photons, it is also called a minus-blue filter. In order to absorb energy, the structural components, i.e., electrons, atoms, or molecules, must be capable of displacement motions that can occur in the time domain of the frequency of the radiation. Absorption of photons raises that component to a higher energy level, whereupon it will either return to its former lower energy state by emitting radiation, or transfer energy to other mechanisms. Absorption processes are classified as electronic, vibrational, rotational, and oscillatory; and the energy domains of these processes overlap. Electrons, being the lightest and fastest of the components, capable of resonating at very high frequencies, are involved in the absorption and emission of high frequency radiation, from gamma-rays to the near infrared. Molecular and atomic components, being massive, have slower displacement movements, and resonate only at lower frequencies. Vibrational absorption modes start in the visible and extend out into the millimeter wavelength domain. Rotational absorption begins in the middle infrared and extends out to radio waves. These regions are shown in Fig. 4.

When matter is condensed into a solid state, the electron orbitals are shoved together, become smeared, and lose the fine-structure details associated with electronic spectra. There is also loss of ability for rotational displacements. Vibrational processes become dominant, and the spectral bands of the fundamental modes occur in the middle and far infrared. For the most part, the only bands that can appear in the near infrared are those associated with overtones, or combinations of the fundamentals. Thus, the reflected solar region of the spectrum, the basis for hyperspectral sensing, carries little to no information about fundamental modes.

A normal, or fundamental, mode of vibration is one in which the component nuclei of the molecules undergo simple harmonic motion at the same frequency, in phase, but with different amplitudes. If one knows the molecular structure, there are quantum mechanical computations involving masses and force constants that can be used to determine the vibrational frequencies, and thus the frequencies of absorption. Conversely, one can measure the absorption spectra, and determine what must be the molecular structure. Details of such calculations are in various texts on spectroscopy, e.g., Hollas (1982). Background material, particularly with reference to minerals, can also be found in a series of excellent papers by Hunt and Salisbury (1970).

To show some of the relations between absorption and structure, consider the water molecule in Fig. 8. It is a bent molecule with C_2 symmetry, and has three normal modes of vibration, all in the infrared: ν_1 , symmetrical OH stretch; ν_2 , the H-O-H bend; and ν_3 , asymmetrical OH stretch. These are the fundamentals, and they take on different vibrational values for the vapor, liquid, and solid states. For the vapor state, these values, taken from Hollas (1982) and expressed as wave numbers are: $\nu_1 = 3657.1 \text{ cm}^{-1}$, $\nu_2 = 1594.8 \text{ cm}^{-1}$, and $\nu_3 = 3755.8 \text{ cm}^{-1}$. Equivalent wavelengths for these wave numbers, expressed in micra, are: 2.734, 6.270, and 2.662. Although single values of wave numbers are used in this discussion, the vibrations of a fundamental mode are spread over a range of values. Table 2 lists absorption bands for the vapor, liquid, and solid phases. Fundamental values for the liquid and solid states are from Hunt and Salisbury (1970). The lower part of the table lists absorption bands associated with overtones. The $2\nu_1$ band and the $\nu_2 + \nu_3$ band are characteristic absorption bands of water, and usually referred to as the $1.4 \mu\text{m}$ and $1.9 \mu\text{m}$ bands. When 1.4 and 1.9 are both present, it indicates undissociated water, i.e., plain water, such as water of hydration, water trapped in crystal lattices, or cellular water in tissue. The $1.4 \mu\text{m}$ band by itself indicates OH groups other than those associated with water, such as the hydroxyl group in alcohol.

The recording of the reflected component of radiation is the most common form of remote sensing, and the sun is the most frequently used source of illumination. The reflected solar spectrum ($0.4\text{--}2.5 \mu\text{m}$) supports sensors such as cameras, the Landsat Multispectral Scanner (MSS) and Thematic Mapper (TM) bands 1, 2, 3, 4, 5, and 7 (band 6 being a thermal infrared band), SPOT, and the hyperspectral systems, such as the Airborne Visible Infrared Imaging Spectrometer (AVIRIS). The tone differences that define boundaries of shapes, soil changes, and the highlight and shadow tones are due to different amounts of radiation reflected to the sensor from the various surfaces.

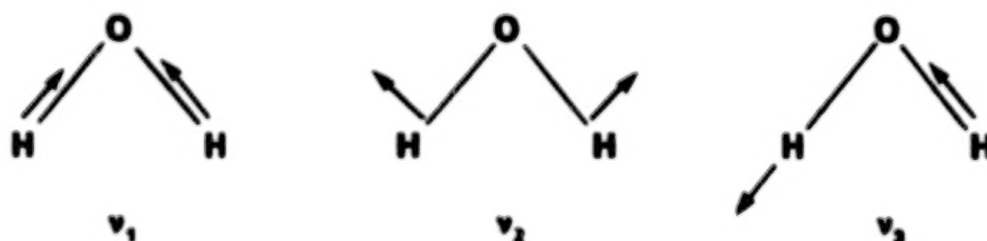


Figure 8. The three fundamental modes of vibration of a water molecule. The arrows indicate direction of the displacement. ν_1 refers to the symmetrical OH stretch, ν_2 refers to the H-O-H bend, and ν_3 refers to the asymmetrical OH stretch.

TABLE 2. ABSORPTION MODES

Wavelengths (in micra) associated with the fundamental and overtone vibration and absorption modes of the water molecule. The fundamental values for liquid and solid are from Hunt and Salisbury (1970), and for the vapor phase are from Hollas (1982). These are approximate values, because there is a spread of frequencies in the vibratory bands. Absorption spectra of the vapor phase will show numerous sharp bands caused by rotational fine structure. The loss of fine structure in the liquid and solid states is due to loss of rotational displacements.

Fundamentals (μm)			
Mode	Vapor	Liquid	Solid
ν_1	2.734	3.106	3.105
ν_2	6.270	6.079	6.06
ν_3	2.662	2.903	2.941
Overtones (μm)			
$2\nu_1 + \nu_3$	0.903	0.902	1.016
$\nu_1 + \nu_2 + \nu_3$	1.110	1.135	1.212
$\nu_1 + \nu_3$	1.349	1.379	1.510
$2\nu_3$	1.331	1.451	1.470
$2\nu_2 + \nu_3$	1.439	1.454	1.501
$\nu_2 + \nu_3$	1.869	1.965	1.988

The amount of radiation reflected from a surface depends on the wavelength of the light, its angle of incidence with the surface, the orientation of the sensor in relation to the surface and the illuminant, the material's molecular composition, and the surface structure. Molecular composition, however, sets the stage. A surface that reflects uniformly across the visible and photographic parts of the EM spectrum is called a neutral surface—i.e., it does not treat any one wavelength different from any other. For normal angles of illumination, no neutral material is a perfect reflector, i.e., 100 percent reflectance throughout the spectrum. Nor is it a perfect absorber, i.e., 0 percent reflectance. If it has a high reflectance, it is called white. If it has a low reflectance, it is called black. In between it is called gray.

Most materials reflect more at some wavelengths than at other wavelengths, e.g., a blue surface reflects blue light, and absorbs green and red, a yellow surface absorbs blue, and reflects green and red, and a green surface reflects green light, but absorbs blue and red. If three surfaces, e.g., blue, green, and red, reflect the same amount of photon energy, then a black and white photograph would show them with similar gray tones. Depending on the wavelength sensitivity of the film, they could be indistinguishable. A normal color film, however, is a multiband system. It has three bands, or channels, that separately document the intensities in the blue, green, and red bands, and displays the results as a color composite—showing that there are three different objects in the scene.

Figure 9 is a typical spectral reflectance response of healthy vegetation. In the visible part of the spectrum, the vegetation absorbs blue light, reflects some of the photons in the green band, and absorbs photons in the red band—thus, we see healthy leafy vegetal material as green, and it would be recorded as such in a normal color film. Healthy leafy vegetation is much more reflective in the infrared part of the spectrum, than in the visible; which is why, in black and white infrared photography, most vegetation shows as very bright tones. As indicated earlier, the dips at 1.4 and 1.9 μm are due to water absorption. As a plant loses water, these bands become shallower, and thereby provide an indicator of vegetation stress.

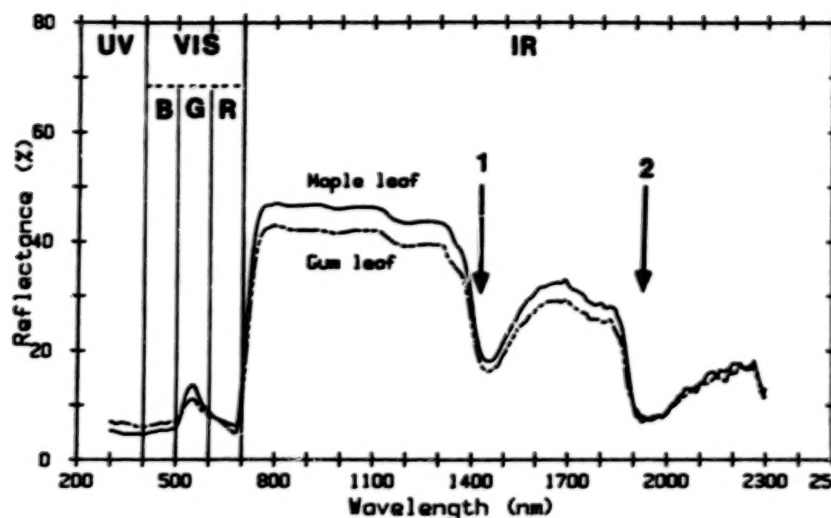


Figure 9. Reflectance characteristics of healthy vegetation. The reflectance in the visible part of the spectrum is mostly in the green band (500-600 nm), and is usually 10-15 percent. Reflectance increases rapidly in the infrared, reaching a maximum of around 35-50 percent. Arrows 1 and 2 indicate the water absorption bands at about 1400 nm and 1900 nm.

The infrared brightness of healthy vegetation has long been a useful characteristic for military targeting. In WW II, Eastman Kodak developed a film that could separate green painted camouflaged targets from surrounding green vegetation. Though a visual match, green paint is much less reflective in the infrared, than is vegetation. At that time, color films, such as Kodachrome and Ektachrome, were sensitive primarily to photons in the visible part of the spectrum. By extending the sensitivity of one of the three emulsion layers in Ektachrome film out to about 900 nm in the infrared region, Eastman Kodak developed the needed film, which was known as Camouflage Detection film, or CD film. With the proper filter, this film portrays green paint as green, and healthy vegetation as red. The emulsion with the extended sensitivity is the one sensitive to blue light, and which is coupled to the cyan dye. Increasing its sensitivity to infrared, out to 900 nm, also increased its sensitivity to the more energetic photons at double the frequency, or half the wavelength, i.e., 400-450 nm. The emulsion was about ten times more sensitive to blue light than to infrared. In order to tell which photons, blue or infrared, are responsible for the red tone, a yellow filter (Wratten 11, 12, or 13) is used to prevent blue light from entering the emulsion. With the blue light eliminated, the red response could be attributed to the vegetation—and any green painted object stuck out in stark contrast as green. Because the colors in an infrared photograph are not colors that eyes see in the scene, such a photograph is also called a false color image.

When vegetation is stressed, it loses much of its infrared reflectance. The stress can be induced by drought, flooding, chemical sprays, senescence, by biological infections such as the rust and wilt, or by infestations such as gypsy moths. The loss of infrared reflectance provides the basis for detecting the presence of stress, mapping its extent, and monitoring an area for change. Camouflage was, and still is, frequently made by cutting branches of trees and bushes to lay over the site—and this is effective, but only for a relatively short time. One response of the cut branch is that the leafy material loses its infrared reflectance faster than it loses its green reflectance. Even though looking equally green to the eye, the CD film shows the reflectance loss of the damaged vegetation as dark tones of red/green and green.

After WW II, CD film was evaluated for applications in geology, forestry, wetlands, land use mapping, and for detecting stressed vegetation. It became so useful that the consumer market constantly increased. Eastman Kodak improved the film, and changed its name to Ektachrome Infrared film (EIR). Adding infrared sensitivity makes a four channel system—blue, green, red, and infrared—analogue to Landsat TM bands 1, 2, 3, and 4. Taking the photograph through a yellow filter eliminates channel 1, the blue band, and the final

colors in the image result from mixes of intensities in the green, red, and infrared bands. With Landsat TM, the selection is made electronically. Of the seven bands available, one could select bands 1, 2, and 3, couple them to blue, green, and red guns and create a normal color image. One could also select bands 2, 3, and 4, couple them to the blue, green, and red guns, and create a false color composite image similar to the image from the EIR film with a yellow filter.

The quantity and quality of radiation falling on the terrain varies in relation to location, time of day, season, and atmospheric characteristics. On a clear day, the terrain is illuminated by two sources. One being a point source, the sun, and the other a diffuse hemispherical source, the sky. Skylight is blue, the result of atmospheric scattering of incoming short wavelength energy. Terrain exposed to sunlight is also exposed to skylight, receiving a double dose of blue. Terrain in shadow is illuminated with skylight only; thus, if one wants details within shadows, the blue component must be used. It is not exclusively blue light because sunlight of various colors can be reflected into a shaded area from vegetation, soils, rocks, buildings, etc.; but, blue is the major component. A yellow filter blocks blue light from contributing to the photograph, with the result that shadows are well defined with sharp edges and dark interiors—excellent for estimating canopy closure, or stem spacing and density, but poor for measuring canopy height where the ground must be seen. A black and white infrared film with a Wratten 87C filter that passes infrared radiation but excludes all visible light, gives the blackest shadows of all. Some filters pass two separate channels of radiation. A Wratten 47B (primary blue) passes blue light and infrared, absorbing green and the red. A Wratten 58 (primary green) passes green light and infrared, but rejects blue and red. Figure 10 shows the transmittance characteristics of these filters, and some results of different film/filter combinations. Coupled to the proper film, these filters provide a two channel system.

The set of aerial photographs in Fig. 10 compares an unfiltered Tri-X emulsion (XXX-0), which records all of the visual spectrum; infrared film with a Wratten 47B filter (IR-47B) which records both blue and infrared photons (a dual-channel system); and Infrared film with a Wratten 87C filter (87C), which excludes all the visible and records only the infrared (a single-channel system). These were taken some minutes apart. Although a few of the trees have started to drop leaves (early fall season), and some have changed color, much of the canopy shows as bright tones in the XXX-47B and IR-87C images because of the high infrared reflectance, as in location marked by Arrow 3. Cars in the shadow of the building are easily visible in XXX-0 photograph, somewhat visible in the IR-47B, and not discernable in the IR-87C image (Arrow 1). Arrow 2 points out one example of the bright sidewalks, visible in XXX-0 within the tree shadow, not discernable in the dual-channel XXX-47B, and reversed in tone in IR-87C.

In general, the reflectance of earth materials increases as one goes to longer wavelengths. In the ultraviolet and blue regions, most surfaces have a similar low reflectance. This is why photographs taken in ultraviolet, and in blue light tend to be flat—there is little contrast. Reflectance steadily increases going from blue, to green, to red, and to infrared. It is in the infrared region that brightness, contrast, and other interesting spectral features begin to develop. Figure 11 shows the reflectance characteristics of several playa surface materials, and indicates some of the more common absorption bands. The ordinates are percent reflectance. In the upper illustration, i.e., "A," the ordinate is not numbered because the individual reflectance records, which overlap, were offset vertically. In "A," the important indicative features are the locations of the various absorption bands along the wavelength axis. Strong water absorption bands at 1400 nm and 1900 nm are apparent for some of the materials. A record that shows both bands, i.e., 1400 nm and 1900 nm, indicates undissociated water such as water of hydration, or water trapped in the lattice. Molecular water, which is an important component in gypsum, has other absorption bands at 1000, 1200, and 1700 nm. These are overtones, i.e., combinations of the fundamental modes. These are marked as 1, 2, and 3. The lower illustration, "B," shows the effect of water on the reflectance properties of a silty loam playa soil. As the soil dries, the depth of the absorption bands becomes less, and the overall brightness increases.

A spectrometer measures light intensity on a wavelength basis. For reflectance measurements, this is usually done by measuring the amount of light of a given wavelength coming from the surface and comparing that value to the light itself, or to the light reflected from a reference surface of known reflectance

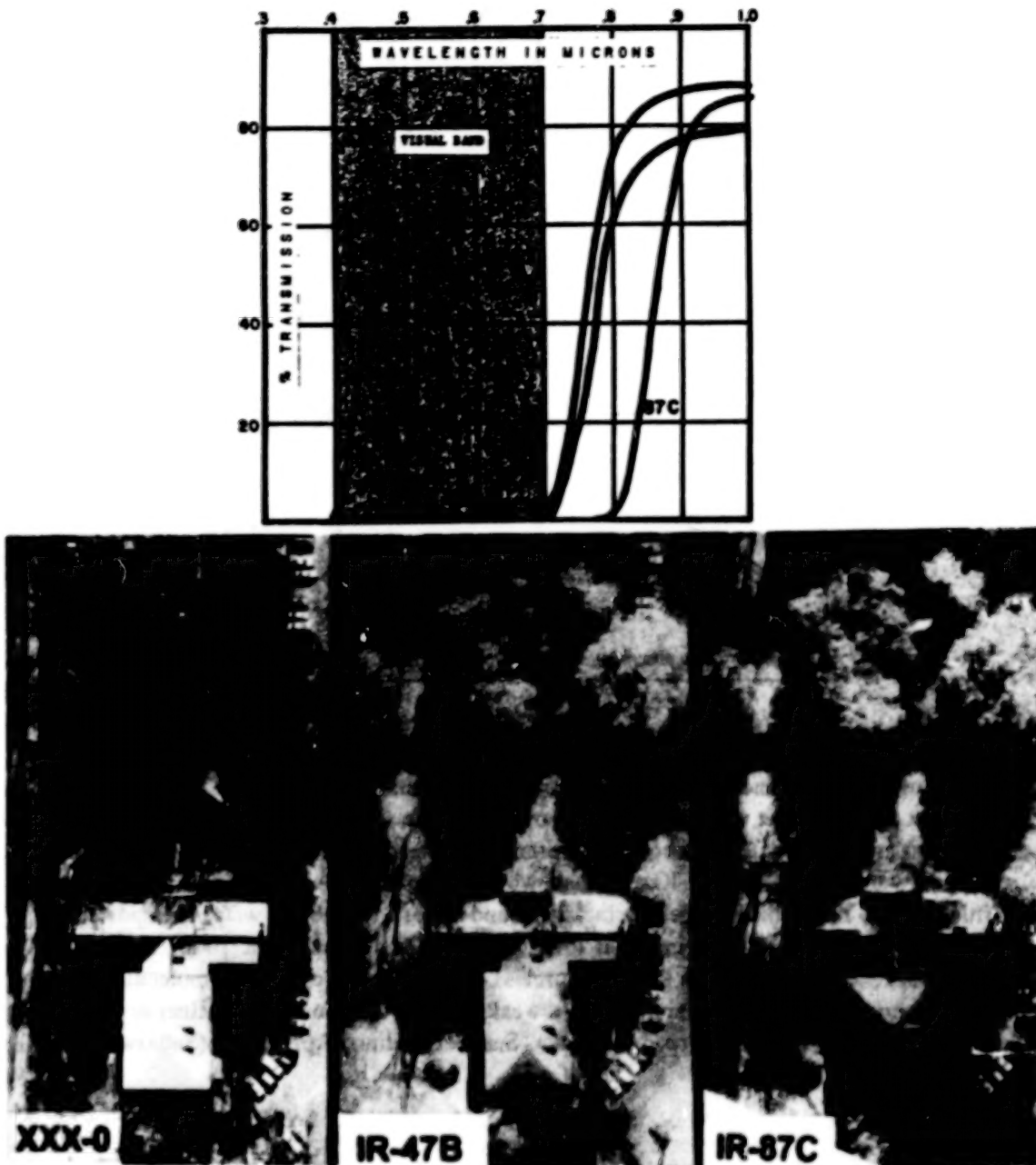


Figure 10. Top. Transmittance characteristics of Wratten filters 47B, 58, and 87C. The 87C passes only wavelengths greater than 800 nm. The 47B and 58 filters are two channel systems, passing the infrared band (> 700 nm), and about 45 percent of the blue band and 50 percent of the green band respectively. The bottom photos illustrate effects of these bands in recording shadow detail, or typing vegetation. Unfiltered Tri-X film (XXX-0) is a single broad band recorder, sensitive to blue, green, and red light. It depicts shadows as well as details within the shadows, which are illuminated with blue skylight. Arrow 1 points to automobiles within a shadow. They are visible, but less distinct in the IR-47B image, which records both the blue and infrared bands, and not visible in the IR-87C image which is the infrared band only. Arrow 2 marks sidewalk/grass contrast changes, and Arrow 3 marks area of high infrared reflectance in the trees. Infrared Aerographic film with an 87C filter (IR-87C) is a single broad band system, sensitive only to infrared photons—good for separating coniferous trees from deciduous ones, but useless for recording detail within shadows.

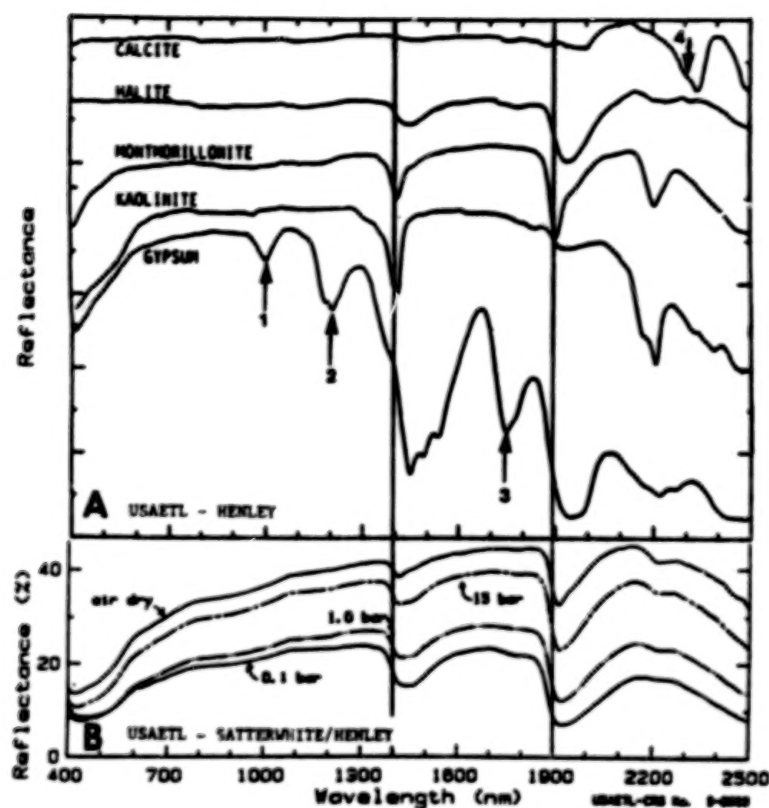


Figure 11. Playa surface reflectances. A. Reflectance measurements of playa surface minerals (Henley, 1988). The records are offset vertically to avoid overlap. The strong water absorption bands at 1400 and 1900 nm are apparent. When both are present, it indicates undissociated water (water of hydration, trapped water in the lattice). Kaolinite shows strong hydroxyl absorption at 1400 and 2200 nm but little at 1900 nm, which suggests a lack of bound water. Molecular water is important in gypsum, and its overtones and combinatorial tones account for the bands at 1000, 1200, and 1700 nm (Arrows 1, 2, 3). Calcite is fairly featureless except for the carbonate molecular vibration band at 2300 nm (Arrow 4), and sometimes a weak band at 2000 nm. B. Influence of moisture on a silty loam playa soil from Broadwell Lake, San Bernardino, April 1988 (Satterwhite and Henley, in edit).

characteristics. This comparison, or normalization, produces a plot of percent reflectance against wavelength. In the lab, physical setups can be varied to measure different kinds of reflectance, e.g., specular reflectance, bi-directional reflectance, total hemispherical reflectance, and diffuse minus specular. In the field, the sun is the usual light source, although halogen lamps are frequently used so that measurements can be made day or night, independent of sky conditions. Circumstances permitting, the procedure should be standardized. This includes a constant distance between spectrometer and the surface, and leveling the instrument and standard, and also target surface when possible. During the measurement cycle, stand away from the instrument to avoid adding a component of light reflected from clothing to the surface being measured. In addition to duplicate runs, take multiple measurements over the area or feature being measured. Do not assume homogeneity. To evaluate the spectrometer's performance in the field, keep a copy of the plot from the reference standard made right after the instrument was recalibrated. To check wavelength accuracy, one can use narrow band interference filters, clay minerals, etc.

A double field of view instrument collects measurements from both reference and target at the same time—one channel looking at the reference standard, and one channel looking at the target surface. Any variation in illumination during the measurement cycle is canceled because both surfaces are measured simultaneously. A single field of view instrument can collect only one set of measurements at a time. So,

measurements must be taken in sequence—first the standard, then the target. It takes a finite amount of time for an instrument to scan through the spectrum from 400 to 2500 nm, and if the illumination varies during the measurement cycles (reference and target), there will be an error in the results. If the spectral intensity distribution of the light falling on the target is not an exact match of that falling on the reference, then when the target data are normalized against the reference data, the resultant percent reflectance curve will not match that derived by a single field of view instrument. In the mid-latitudes, variation in solar intensity is significant in early morning and late afternoon. The least variation is in the noon zone, e.g., 1 to 1½ hours on either side of noon. In earlier field spectrometers, a measurement cycle could take over 10 minutes, which is ample time for variation to occur, particularly if one continues collecting measurements from other surfaces, and relying on the first reference reading for all. Measurement cycles were eventually shortened to seconds, and are now down to fractions of a second. Nevertheless, reference standards should be taken frequently.

2.2.1 Factors that influence reflectance

Although the molecular make-up of a material establishes the absorption characteristics, the recording of the reflected component is affected by: instrument calibration, variation in light characteristics (sun azimuth and altitude), atmospheric composition, surface structure, viewing angle in relation to the sun, surface attitude, etc. Instrument calibration is a separate issue. The intensity/wavelength distribution of sunlight at the earth surface varies with location, season, atmospheric composition, amount of atmosphere traversed, and time of day, changing most rapidly in morning and afternoon, and being more stable during midday, i.e., 1000 to 1400 hrs. Variation of irradiance with elevation is shown in Fig. 12A.

Surface structure and viewing angle are considered together because they are closely related in that the influence of surface structure is frequently dependent on viewing angle of the sensor in relation to the sun. Surface roughness can be defined in terms of wavelength of the radiation concerned. For a surface to be considered a high quality mirror, it must be flat to within about a quarter of a wavelength of the radiation to be used. Under this condition, most of the incoming radiation is reflected at an angle that equals the angle of incidence, i.e., specular reflection. If the surface variations exceed this, then proportionally more of the energy is scattered in other directions. This is called the diffuse component. As the surface variations increase, more energy is scattered in other directions, i.e., the diffuse component gets larger, and the specular component gets smaller. For remote sensors using reflected sunlight, the wavelengths fall between 400 nm and 2500 nm, or between 0.4 and 2.5 μm . Aside from still water, most surfaces have relief variations in excess of this, and are diffuse scatterers, e.g., leaves, bark, soil, rocks, concrete, paint, cloth, etc. Consequently, when viewing such surfaces from some point in space, the image tones can vary, even be reversed, as a function of viewing angle in relation to the sun. Looking at the ground in the up-sun direction, the sensor receives both a diffuse component and specular reflection component. Down-sun, the sensor receives diffuse minus specular, i.e., only the backscatter. If the surface variations have an orderly structure, the image patterns are influenced by sun azimuth as well. For example, the ridges and furrows of a freshly plowed field have relief on the order of 15 to 20 cm. Furthermore, it is an ordered relief, i.e., a pattern of parallel lines. If the sun's rays are parallel to the ridge pattern, the surfaces receive about the same amount of illumination and the image of the field would have an overall uniform tone. If the sun's rays are perpendicular to the ridge pattern, the field shows as a parallel series of highlights and shadows. X- and C-band radars would show a similar display. For L-band radar (25 cm wavelength), however, the plowed field would be a reflector, and would show as a dark area, an area of no return, from any angle of illumination.

Figure 12 shows the effect of changes in viewing angle of the sensor in relation to solar direction for a Halon standard (B), and for a coarse sand surface (C). For Fig. 12B, a leveled Halon standard was measured from two different viewing angles: with the spectrometer tilted 10° off vertical in the direction of the light source, which gave an increased component of specular reflection; and with the spectrometer tilted 10° off vertical away from the light source. A similar set of measurements for coarse sand particles (2-4 mm) is shown in Fig. 12C. These were normalized against the same reference, a vertical reading of the standard. The difference is not great, but it is 3-5 percent. These changes affect intensity only, not the location of absorption bands.

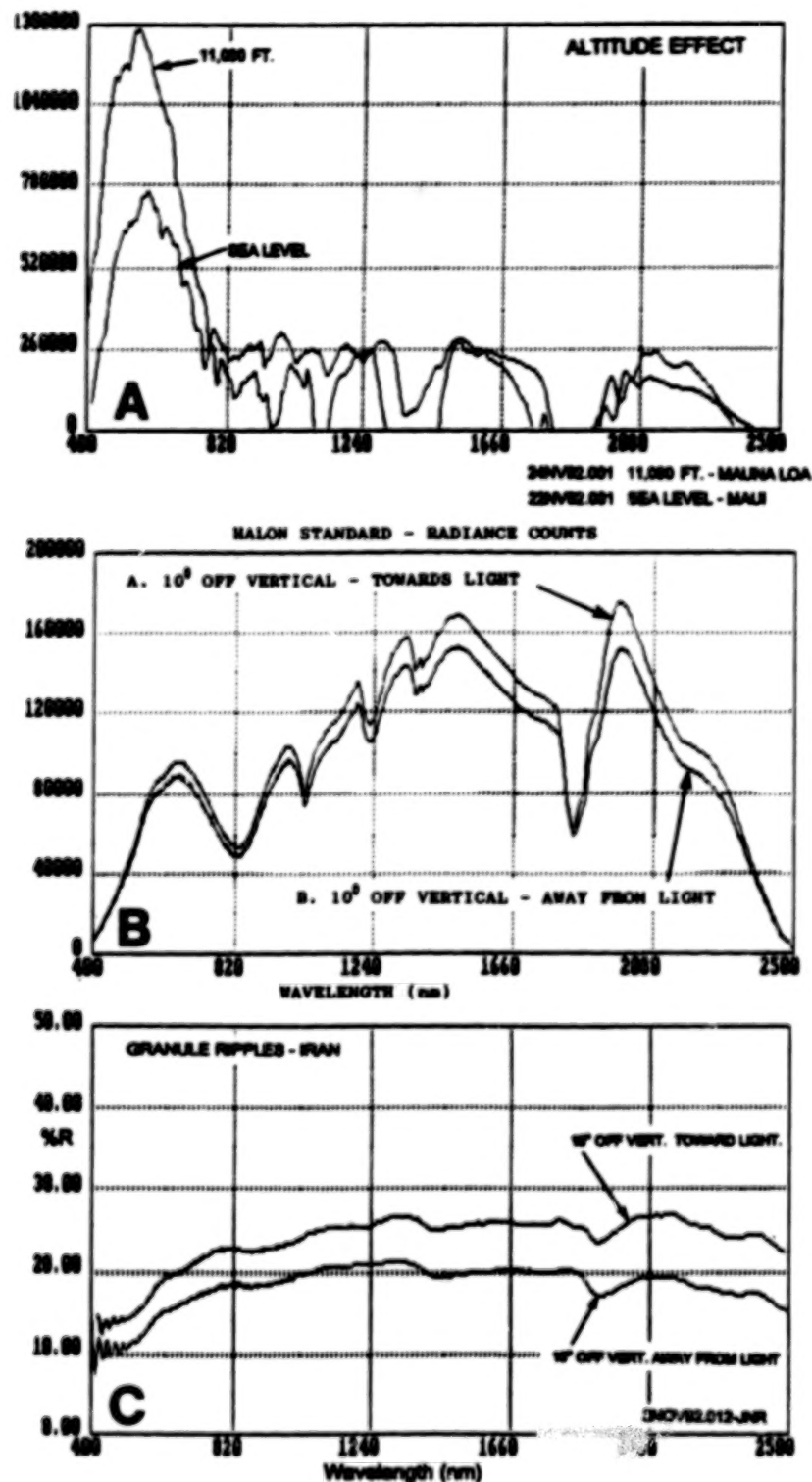


Figure 12. Variation of incoming solar radiation between sea level and 11,000 ft is shown in A. Variation caused by changes in viewing angle of the sensor in relation to the light source for a leveled Halon standard is shown in B. Results of a similar variation for a coarse sand surface (2-4 mm particle size) is shown in C. The two sand spectra were normalized against the same reference standard, a vertically measured Halon surface.

Figure 13 illustrates tone changes resulting from changes in viewing angle. The upper set of aerial photographs (A) is of an area on the south coast of Puerto Rico, showing water, beach sand, vegetation, shoals, etc. In exposure 164, this part of the frame has a viewing angle towards the sun, as indicated by the large bright area of sun glint, or "hotspot," on the water, which is the specular component of the sun's reflected radiation. Exposure 169 was taken several minutes later, while flying the adjacent parallel strip, and shows the same scene looking away from the sun. In 164, sun glint on the water masks shallow water bottom detail, which can be seen throughout the water area of image 169, especially in the sheltered bay, and shoal areas such as indicated by Arrow 1. On the other hand, sun glint makes the wave patterns conspicuous. On the point of land marked by Arrow 2, a small pond is depicted because of glint in image 164, but not visible in image



Figure 13. Influence of surface structure on reflectance. The upper set is of Puerto Rico. The right image (from frame 164) has a look angle towards the sun, whereas the left (from frame 169), which overlaps the same area and was taken some minutes later while flying the next line, has a look angle away from the sun. Because of these different viewing angles, there are changes in tone contrast. Without the sun glint there is an improvement in shallow bottom detail in the bay and in shoal areas (Arrow 1), loss of a small pond (Arrow 2), and loss of the wave pattern. The lower set of sequential air photos is of lava flows on the island of Hawaii. There was enough overlap to record the same piece of ground in each image, but from a different look angle in relation to the sun. A reversal of tones is evident throughout.

169. Exposed beach in the bay area of image 164 is easily identified, but not so in image 169. Part "B" of Fig. 13 shows tone changes associated with lava flows in a caldera on the island of Hawaii. The caldera edge is at the bottom of the images. The three frames are from sequential air photos showing the same scene as viewed towards the sun, directly above the feature, and away from the sun. Note the reversal of tones throughout the area of the flows.

2.3 EMITTANCE

Radiation absorbed by a material leads to other effects. For one, absorbed photons increase the internal energy, or temperature, of the material, which, in turn, increases the quantity and alters the wavelength distribution of the thermally emitted radiation, both infrared and microwave. This is the most common outcome of absorption, and is the basis for thermal, or passive, remote sensing in either the infrared or the microwave domain. During daylight hours, absorbed sunlight heats the terrain. During the night, the terrain cools by radiating into space, and would continue to cool except that the sun comes up and renews the heating cycle.

At temperatures above absolute zero (0°K or -273°C), all matter emits electromagnetic energy. If hot enough, such as a hot stovepipe, a tungsten light bulb, or the sun, the object emits enough energy to affect the eye, or a photographic emulsion. At normal earth surface temperatures (-50° to $+50^\circ \text{C}$), however, the amount of energy emitted is below the threshold level of either a photographic emulsion, or the eye. To detect such low levels of photons, special materials are used that are not only sensitive to infrared radiation, but which have some property, such as electrical resistance, that changes rapidly and significantly with variations in intensity of the incoming radiation. This signal is amplified, displayed on a cathode ray tube, and recorded on magnetic tape, or on photographic emulsions via a modulated glow tube, or other device. By convention, except for meteorological satellites, the images are printed so that light tones represent warmer surfaces, and dark tones represent cooler surfaces.

The amount of energy emitted from a surface, and its wavelength distribution, depend on temperature. The amount is equal to the fourth power of the absolute temperature multiplied by the emissivity. For a given temperature, the wavelength distribution curve will have a maximum intensity at a specific wavelength known as $\lambda_{\text{sub-max}}$. Regardless of temperature, 25 percent of the energy will be emitted at wavelengths shorter than $\lambda_{\text{sub-max}}$, and 75 percent at longer wavelengths. As the temperature gets higher, $\lambda_{\text{sub-max}}$ shifts to shorter wavelengths, e.g., at -150°C it is about $23.2 \mu\text{m}$, at 0°C it is about $10.5 \mu\text{m}$, and at 100°C it is about $7.7 \mu\text{m}$. At the sun's temperature, $\lambda_{\text{sub-max}}$ is about 480 nm . Also, as the temperature gets higher, the short wavelength edge of the distribution curve includes higher energy levels, i.e., it goes to shorter wavelengths, and the area under the curve (total energy emitted) gets rapidly larger. Keeping emissivity constant, a warmer body will emit more energy at all wavelengths than will a cooler body, and will incorporate a short wavelength increment denied the cooler material. Thermal infrared techniques are associated with two wavelength regions for which the atmosphere is transparent, i.e., atmospheric windows. These are the $3.5\text{-}5.5$ and $8\text{-}14 \mu\text{m}$ bands. For normal earth surface temperatures, i.e., -50° to $+50^\circ \text{C}$, the wavelength of peak emission is in the $8\text{-}14 \mu\text{m}$ band. About 40 percent of the energy is emitted in this band, and about 3 percent in the $3\text{-}5.5 \mu\text{m}$ band. For mapping thermal variations in the terrain the $8\text{-}14 \mu\text{m}$ band is the preferred choice. Above 250°C , the wavelength of peak emission enters the $3\text{-}5.5 \mu\text{m}$ band. For detecting hot targets, this band is the preferred choice. The signal/noise ratio, or the target/background contrast is much greater here. Emissivity, which is wavelength dependent, denotes how good an absorber, or emitter, a material is. Molecules emit energy only at those wavelengths they can absorb. A perfect absorber, or emitter, has an emissivity of 1. A material that absorbs 50 percent of the incoming radiation, and reflects 50 percent, has an emissivity of 0.5. So, if two materials have the same physical temperature, but differ in their emissivities, the one with the higher emissivity will emit more energy than the one with the lower, and will be brighter in the image. Many earth materials have emissivities in the $0.7\text{-}0.9$ range, which means they are fairly good absorbers. This being so, radiation emanating from them is pretty much of surface and near-surface origin. Radiation from molecules at depth is absorbed by molecules above, reradiated and absorbed by the next layer, and passed along until there are

molecules that can radiate into space. For infrared, the depth of the layer that radiates into space is a fraction of a millimeter. The effective depth of this layer increases with longer wavelengths, being perhaps 2.5 cm in the microwave L-band (23 cm).

This layer is an interface between the material below, and the atmosphere above, and is readily influenced by events on both sides. Below, energy transfer is associated with conduction and, in some cases, diffusion. Above, atmospheric variables take over. These can quickly, and radically, alter the radiation characteristics of the surfaces—eliminating, subduing, or increasing thermal contrast. Thus, thermal contrast is influenced by a variety of diurnal and seasonal variations in climatic and meteorological factors, such as wind, atmospheric pressure, dew, rain, humidity, incoming space radiation, etc. Wind can override subsurface conductive events and imprint its own temperature regime, which can create confusing thermal patterns in the form of wind shadows—i.e., surfaces in the lee can be much warmer, or cooler, than surfaces exposed to the wind.

Objects sticking up into the air take on the temperature characteristics of the air. At nighttime, when the air is warmer than the ground, which is cooling by radiation loss, these objects will appear as hot spots—giving signals similar to vehicles with their engines running, as in Fig. 14. As the night progresses, the air layer, cooled by contact with the cooler ground, becomes thicker, and sequentially cools taller and taller objects that project up into it. By late night the hot spots disappear, except for the tops of the tallest trees, or for natural or artificially maintained heat sources.

Also, cooler air is more dense, and, being more dense, it flows downslope to settle in the lows, which show as darker tones in the thermal imagery. Darker tones in the lows can also be caused by moist soil, which has a higher thermal conductivity than dry soil, and can lose heat faster. As a result, cool air drainage into the lows is sometimes mistaken for moist soils.

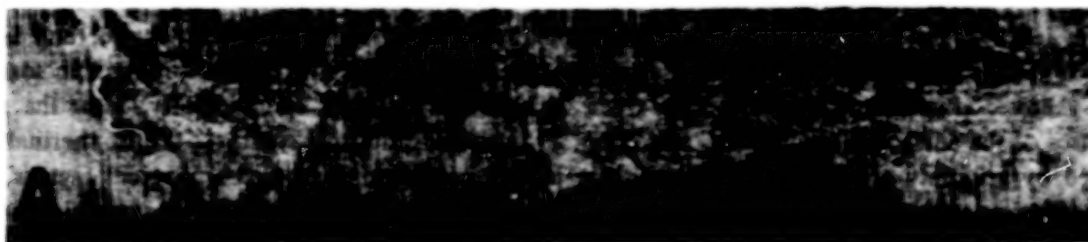
For detection of voids in the terrain, such as caves, tunnels, crevasses in an icecap, or buried installations, atmospheric pressure changes are critical. First, the interior temperatures are usually fairly constant, and are warmer or cooler than the ground surfaces at some time of the day. Also, infrared cannot penetrate the overburden to reveal the presence of the void. The best time to fly is when the void is exhaling, and the outpouring flow of warm air through various openings brings the temperature of the surrounds to above ambient, and they become detectable—i.e., one detects the openings, not the void. Such an outpouring can occur only when the atmospheric pressure is less than the air pressure in the void. Thus, the time to fly is on a descending pressure front (Rinker, 1975a). Figure 15 shows examples of this.

2.4 LUMINESCENCE

Another effect of photon absorption is luminescence. There are materials that can absorb photons of one frequency and emit photons of a lower frequency, i.e., lower energy, without any significant increase in temperature. These materials are said to be luminescent. An example is the emission of visible light from minerals when they are illuminated with "black" light, or ultraviolet radiation. Luminescence is an emission of radiation due to electronic transitions, and there are two kinds—fluorescence, which occurs from an excited single state, and phosphorescence, which results from an excited triple state. A distinction can also be made on the basis of time—i.e., how long does the light last after the excitation energy is turned off? This is called the decay time. In fluorescence, the decay time is very short, ranging from 10^{-9} to 10^{-3} seconds. For example, the fluorescence decay time of rhodamine B in water is about 2.5 nanoseconds (ns). In phosphorescence, the decay time is longer—sometimes much longer. Calcium sulphide, for example, can continue to glow for several hours after the excitation illumination is turned off.

Luminescent techniques require an energy source to excite, or raise the electrons to higher energy levels, and darkness in order to detect the luminesced photons. The sun meets both of these needs—as does the nighttime use of lasers. The sun does not emit a continuous spectrum, i.e., energy at all wavelengths, or frequencies. Although such is generated in the hot core, electronic absorption by elements and ionized atoms

Open Stream Compacted Snow Target -13° Conifers

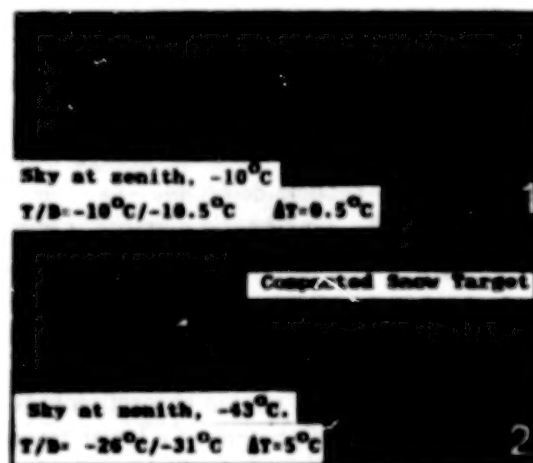


Adjacent Snow -14° W-6 (roof) -3° W-16 (engine on) Conifer
2031 HRS., 9 DEC. 1959. Air temp., -5°C . Surface wind, 6 mph.

Compacted Snow Target -15° Conifers Tree -10° W-20 -10°



Adjacent Snow -22° W-16 $+16^{\circ}$ Trail -15° Crusted Snow -17°
2036 HRS., 10 DEC. 1959. Air temp., -7°C . Surface wind, 0-1 mph.



D1: 2016 hrs., 2/14/60, clear.
D2: 2345 hrs., 2/13/60, thin overcast.

Figure 14. Thermal IR images over the USA Snow, Ice, and Permafrost Research Establishment (SIPRE) field site at Houghton, MI. Modified Michigan AN/AAR-9 scanner with a lead telluride, 3.5 micron filter. A and B show the potential for confusion between vehicles and isolated conifers in the mixed hardwood forest (Morgan et al., 1962). Image A also shows influence of surface wind on thermal contrast (1°C) between the compacted snow target and adjacent undisturbed snow. Image B had zero wind, and a stronger thermal contrast (7°C). Image C is from the same general area during the 1959-1960 winter flights (date/time details lost). The isolated light-tone spots are conifers in the mixed hardwood forest. Images D1 and D2 illustrate the influence of incoming long wave radiation on IR thermal contrast (Rinker, 1962). D1 (2016 hrs., 14 Feb 1960) had a target/background Delta T of 0.5°C , and D2 (2345 hrs., 13 Feb 1960) had a Delta T of 5°C for the same target/background. For D1: air temperature, -9°C ; compacted snow, -10°C ; undisturbed snow, -10.5°C ; sky at zenith, -10°C . For D2: air temperature, -19°C ; compacted snow, -26°C ; undisturbed snow, -31°C ; sky at zenith, -43°C .

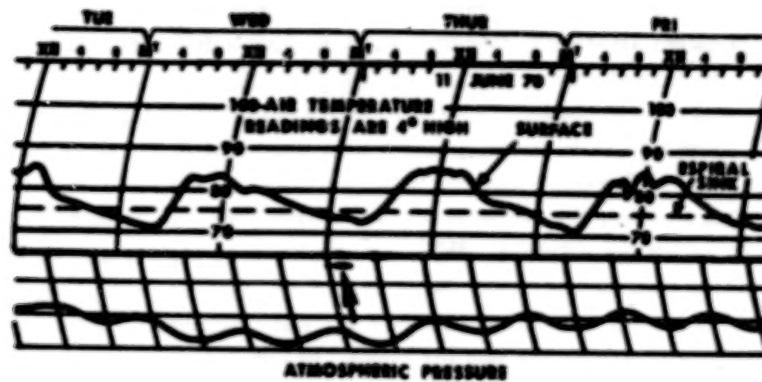


Figure 15. Influence of atmospheric pressure changes on void detection. Images of the Camuy Cave area in Puerto Rico. The top graph shows temperature traces for the surface and the interior of a sinkhole. The bottom graph is a barometric trace. The arrow indicates the time frame of the IR thermal flights, which is during a decreasing pressure phase. Photo A is an aerial oblique of Empalme sink, one of the sinkhole connections in the cave system. Thermal images B and C are of Empalme sink. Image B (Run 3, 0117 hrs) is at the beginning of the exhaling cycle, and the sinkhole is not discernable. Image C (Run 6, 0129 hrs) is later in the pressure drop and Empalme sink has developed a strong signal (Rinker, 1975a).

in the cooler outer envelope greatly reduces the intensities of many of the frequencies. When the sun is examined with a good spectroscope, one finds that there are gaps—many gaps—wherein energy is greatly reduced, or absent. These gaps of darkness are narrow in bandwidth, so narrow they are called lines—specifically, Fraunhofer lines in honor of their discoverer. The spectral bandwidths of these lines are measured in Angstrom Units, frequently in fractions of an Angstrom Unit. The ultraviolet, visible, and near infrared portions of the solar spectrum contain over 30,000 Fraunhofer lines, or lines of darkness. These lines provide the darkness needed for detection of the luminescence, and the sun's radiation provides the excitation energy on the short wavelength side of the lines.

A sensor system that can look at both the sun and the earth's surface with detectors sensitive to energy in these dark lines can detect the presence of luminesced photons from the earth's surface, or target. If, from the target, it detects a certain intensity in a dark line band, it cannot be reflected solar energy because such is not coming from the sun. The fill-in must, therefore, be due to luminesced photons from the target. Such is the function of the Fraunhofer Line Discriminator (FLD) previously mentioned (Hemphill and Settle, 1981, and Hemphill et al., 1989).

Such things as temperature and pH can alter the characteristics of the luminesced photons. Some materials that are under constant, or steady-state illumination, give a different luminescence signal after an hour or two, than they do to an instant measurement immediately after excitation. These changes show as an increase in intensity at longer wavelengths of emission and a decrease of the shorter wavelength components. In fact, some molecules show little luminescence when first illuminated, but develop an intense emission after steady-state illumination. These characteristics are usually associated with liquids and are indicative of changes caused by chemical reactions. Also, the recorded emission spectrum can be distorted in the short wavelength region by self-absorption within the solution. Whether or not these factors are of concern to remote sensing of earth surface and targeting materials is moot. Some materials, such as vegetation, have a near surface liquid component, and chemical reactions are taking place—e.g., photosynthesis. Furthermore, these surfaces are receiving steady state illumination from the sun for hours. In laboratory measurements, the illumination, i.e., the excitation mode, is of short duration. Another characteristic of luminescence is that for any specific wavelength of excitation, there is an emission spectra that can take place over a fairly broad wavelength band, and the decay times of the longer wavelengths can be considerably longer than those of the shorter wavelengths. The total is still a very short time. In laboratory experiments, decay time spectra have shown links to material types and conditions. Whether or not such has application in remote sensing remains to be determined. Abu-Zeid et al. (1987), and Quinn et al. (1988) studied decay characteristics of crude oil. From the standpoint of luminescence in general, Stoertz (1972a and b) demonstrated applicability to earth surface and target materials, and Hemphill and Settle (1981) presented a number of applications to earth resources studies.

No matter what sensor is used, there are other factors that influence the signal that one wants to detect. The atmosphere itself can remove energy from the sunlight, as well as add its own component—luminesced induced, thermally induced, or scattered. Sun angle and azimuth in relation to look angle and surface structure can change, and even reverse tonal contrast. Wind and atmospheric pressure changes alter infrared and microwave thermal contrast, and make it possible or impossible to detect some kinds of targets.

3. SENSORS - THE COLLECTORS OF RADIATION

Photographic emulsions were the earliest of the sensors to document landscape scenes, and human activities. By the late 1800s, emulsions went airborne, via balloons and kites, to replace the observer and his notepad for recording terrain characteristics and military items of interest. By WW I, cameras were in airplanes and routinely involved in reconnaissance and targeting. It was recognized early on that if one could sample different wavelengths of radiation, and compare them, one would have a better chance of detecting targets, as well as noting changes in the landscape—a multiband concept, although not called that, was now in place.

The first steps were taken in the late 1940s and the 1950s when the Army, along with other groups, divided the photographic portion of the electromagnetic spectrum into narrower bandpasses by means of various combinations of photographic emulsions and filters. The goal was to improve techniques for detecting targets and mapping conditions such as camouflage, vegetation type, vegetation stress, soil moisture, flood damage, wetland boundaries, to name a few (Rinker, 1975b), and the term multiband photography came into being to describe these efforts. Camouflage Detection Film, i.e., Ektachrome Infrared film, is one example of a successful film/filter combination, or multiband approach which later passed into the digital domain of Landsat as the False Color Composite. The bandpasses were still broad, however, ranging from 60 to 100 nm. Nevertheless, multiband photography was successfully used in various forms of targeting, and change detection.

Next came the Landsat MSS, which recorded reflected sunlight in four broad bands—two in the visible, each of which is 100 nm wide, and two in the infrared, with one being 100 nm wide and the other 1.1 μm . This was followed by the Landsat TM with six bands in the reflected solar region, and one in the thermal infrared, with the narrowest band being 60 nm for band 3. Spectral variations in the terrain within any of these bands are averaged out to arrive at a digital number (DN) representing the brightness for the whole band.

Extensions of the multispectral concept into the thermal infrared region of the spectrum include the Advanced Very High Resolution Radiometer (AVHRR), and the airborne Thermal Infrared Mapping System (TIMS) developed by Daedalus Enterprises, Inc.

In the early 1980s, a system came forth that greatly altered the existing concepts of multispectral remote sensing with reflected solar energy. This was the Airborne Imaging Spectrometer (AIS) developed by the Jet Propulsion Laboratory (JPL). Details of this system and some of the application results can be found in reports by LaBaw (1983), Vane and Goetz (1985), and Vane (1987). The AIS records reflected solar energy in some 128 channels, or images, within the 1.2-2.4 μm region of the spectrum and with a spectral bandwidth for each channel of less than 10 nm. The AIS evolved into the AVIRIS with some 220 raw data channels, or images, within the 0.4-2.45 μm portion of the spectrum. Resampling gives 210 spectral bands of radiometrically calibrated data. The IFOV is 1 milliradian, or about 10 m at operational altitude. Each image is a record of the intensity of reflected sunlight within a spectral bandwidth of less than 10 nm. After calibrations and corrections have been made, the intensity values of the 210 channels, for any given picture element (pixel), can be called up and sequentially displayed along the wavelength axis, as a spectrophotometric trace, i.e., radiometric intensity versus wavelength. Because of the narrowness of the bands, as well as their multiplicity, these systems are called hyperspectral, to differentiate them from the broad band systems, e.g., MSS, TM, SPOT, etc. Systems are also being developed that can operate in even narrower bands, i.e., the sub-nanometer range, for working with gaseous emissions and absorptions. These are called ultraspectral systems.

Since the advent of the AIS and the AVIRIS, other airborne narrow bandpass systems have been developed, and plans laid for satellite follow-ons. Details of these earlier concepts can be found in a Proceedings Issue of the Society of Photo-Optical Instrumentation Engineers (Vane, 1987b). Current capabilities and system characteristics will be covered in Tutorial IV.

Figure 16 portrays the image cube concept. The stack of images, seven for Landsat TM, and 210 in the case of AVIRIS, forms an image cube. The X and Y axes relate to ground, or pixel location, and the third axis to wavelength. Because of interest in all natural and man-made surfaces, and the need to work with diverse remote sensor data, the wavelength axis of the image cube should extend from the ultraviolet, through the reflected solar, thermal infrared, and microwave regions, out to at least L-band radar at about 23.5 cm wavelength, as shown in the figure. Moreover, we must be concerned with all photons—reflected, emitted, and luminesced—and be able to move back and forth along the image cube axis, incorporating, evaluating, and comparing whatever imagery bands and other data are available, such as Digital Terrain Elevation Data (DTED). Once the corrected image files are in the computer, the spectral patterns can be evaluated by placing the cursor on the site of interest and bringing up a record of the DN values of each of the involved channels. As a minimum, these data should be displayable as line spectra, intensity versus wavelength spectra, and, in the case of luminescence, as three-dimensional spectra (intensity, excitation, emittance), and as contour plots. The spectra can be evaluated in a number of ways, either directly, or by comparison to a computer library of spectral data bases and models. This will be covered in Tutorial III.

Because the atmosphere absorbs many wavelength components of the incoming sunlight, as well as of the reflected energy *en route* to the sensor, corrections are needed for many targets. If one is interested in vegetation, this involves the depths and shapes of water absorption bands. Because water vapor is a component of the atmosphere, the analyst does not know how much of the depth and shape of those water bands is due to atmospheric absorption, and how much is due to vegetation absorption. If corrections can be made to remove the atmospheric component via available models such as LowTran, then the residuum can be attributed to plant water. The notion has been expressed that 220 bands is overload, and that such a multiplicity of bands will lead to data constipation in the collection system, the transmission system, and the data reduction and manipulation systems; and, to ease this, unneeded bands should be eliminated from the collection system. But, which ones can be eliminated—which ones are unneeded? For a narrowly defined goal, the question is easier to answer. For targeting minerals, the geologist can get by with perhaps 30 bands. For determining crop quantity and quality, the agriculturalists can get by with perhaps 20 bands, only a portion of which overlap the geologists' needs. With the combined interests in terrain, targeting, and intelligence, there is need for

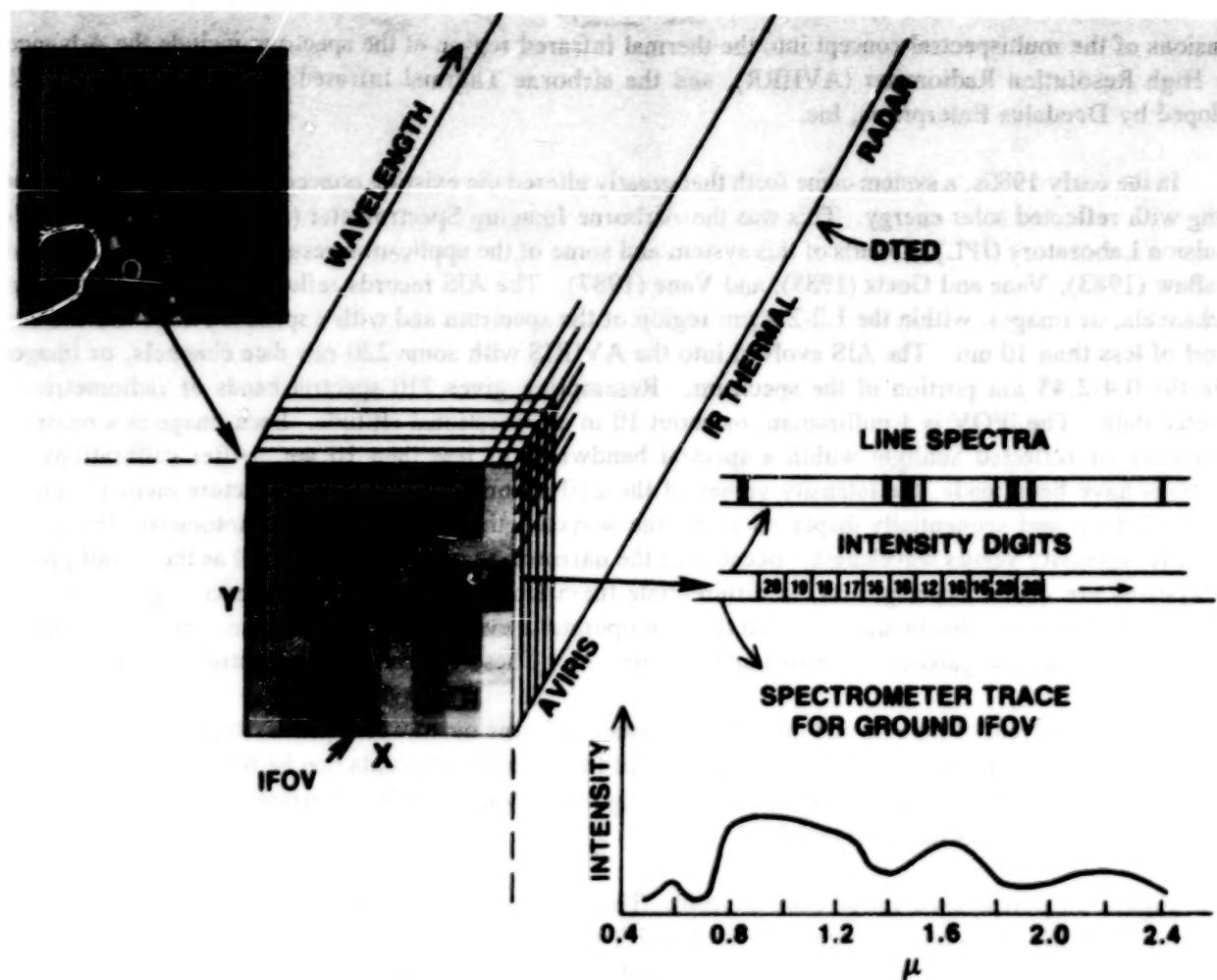


Figure 16. Image cube schematic. On the image cube, X and Y indicate ground coordinates, and the third axis is wavelength. This axis should extend from the ultraviolet out to the lowest frequency radar, and be able to incorporate other data such as Digital Terrain Elevation Data (DTED). For any pixel marked by the cursor, one can sequentially display the intensity values for the bands involved, e.g., MSS, TM, TMS, AVIRIS, etc., as a line display or as a radiance plot of intensity versus wavelength, either in terms of radiance values, or as normalized values as in this graph. These can be compared to computer stored spectral data bases to arrive at probable identities. Or, the scene can be searched for all locations that are a spectral match, within some variance range, for a given spectral signature.

information about identities, conditions, and properties associated with vegetation, soils, rocks, minerals, water bodies, and cultural objects including camouflage. Perhaps reductions can be made—perhaps there are bands that have no use for anybody—but, it is too early for positive declaration.

4. SPECTRAL DATA - INFLUENCING FACTORS - RESEARCH ISSUES

Spectral data from imaging spectrometers can be evaluated on the basis of: shape of the overall curve, or portions of it; intensity differences at any selected wavelength range; wavelength location of absorption bands; and, depth and shape of absorption bands. To link these to identities and conditions requires an extensive computer library of field and laboratory measurements of spectral reflectance, luminescence, and emittance throughout the reflected solar, and thermal infrared portions of the spectrum—and the software to make the evaluations and comparisons. Such a library needs excellent documentation, because these measured

values change with a variety of factors. For any given surface, the molecular makeup determines the basic characteristics of absorption, reflectance, luminescence, and emittance. These in turn, are modified by the structure of the surface, and its orientation in relation to the sensor and to the illuminating source. For example, maintaining a constant field of view and a constant viewing angle, while measuring spectral reflectance at different sun angles and elevations, can result in variances of plus or minus 10 percent. With reference to structure, vegetation can have smooth, crenelated, or wrinkled leaf surfaces, and the leaves and stems can have many different sizes and be arranged in many different ways. This means different highlight/shadow ratios, different amounts of transmitted and re-reflected infrared energy through the biomass, and different amounts of radiation reflecting up through the vegetation from the soil surface (Satterwhite and Rinker, 1986).

For a given mineral composition, the spectral signature of a fine textured soil can differ from that of a coarser textured soil. Then, there are the influences of conditions, such as age, growth phase, wet, dry, weathered, lichen covered, etc. New leaves have a different spectral signature than older leaves, wet soil is different than the same soil when dry, a weathered rock surface differs from a fresh surface. In reality, these are different chemical forms, which gets back to the earlier statement that the molecular makeup of a surface establishes the basics of reflectance and absorptance. Keeping the target surface and illumination/sensor angles constant, the spectral signature is further modified by climate, season, and meteorological variations. Changes in incoming short and long wave radiation from space, wind, and atmospheric pressure greatly alter radiometric signatures, as well as target/background contrasts in thermal imagery.

Multiplicity of measurements is necessary because there can be significant variation within any given class of targets, especially in field measurements. For example, one can measure 20 creosote bushes that look alike and are about the same size and age. But, the result will likely be 20 slightly different spectra—perhaps plus or minus 10 percent variance, or more, from a derived norm. The variations are mostly in intensity, not wavelength locations of absorption bands. Although the plants look alike, they are not identical—each has some variance in biomass, structure, openness, etc. These factors alter the characteristics of the energy reflected from the vegetal surfaces, as well as the characteristics of the contributing reflected soil component passing through, or reflected from the canopy.

For current systems and typical target areas, the IFOV (10 m for AVIRIS) encompasses a mixture of surfaces, and the resulting spectral signature is a composite of individual signatures—which presents another problem in relation to digital analysis of spectral data.

The intent is to call up the radiance plot of an area on a hyperspectral image, compare it to a spectral measurements library, and thereby identify the surface material. This can now be done—but, much research remains before the technique can be routinely and successfully applied, regardless of material type, location, or season. Basic to such a procedure is a documented library of field and laboratory spectral reflectance and luminescence measurements, coupled, where possible, to physical and chemical measurements. Issues for research or resolution include:

1. Continued development of image pattern data bases and spectral data bases (reflectance, emittance, luminescence), and an agreed to format.
2. Determination of diagnostic spectral features—pure and mixed spectra (UV, VIS, IR, Microwave).
 - a. Feature location (wavelength, frequency).
 - b. Intensity levels.
 - c. Waveform variations.
 - d. Statistical and mathematical analyses.
3. Development of formats for computer search and display of spectral data (radiance, reflectance, luminescence) as line spectra, x/y plots, three-dimensional plots, etc.

4. Atmospheric influences and atmospheric backout.
 - a. Test existing theoretical models against empirical data.
 - b. Develop and test empirical models.
 - c. Are atmospheric corrections needed for all targets?—for all locations?—for all seasons?—for all spectral bands?
5. Can scenes be self-calibrated against known spectral data?

Image patterns are indicative of surface materials and land cover. If such spectra are in the library, correct against them and apply the correction to the rest of the scene. This would remove atmospheric influence as well.
6. Mixed pixel problem. A sensor's IFOV usually contains some mix of objects, which results in an averaging of the reflectance returns.
 - a. How to deconvolute to find component spectra?
 - b. There is always a limited mix of components, and the mix varies with location. Can image patterns help determine the most probable mix?
 - c. Is deconvolution needed in all cases? Probably not. Many features, e.g., wetlands, bajadas, sand sheets, etc., have typical mixes of components of sand, soil, rock, water, and vegetation that identify them for what they are. The composite spectra, or mixed pixel, might be a preferred indicator for identifying such features, or detecting seasonal changes? Will knowing the mixed pixel signature of a given land cover assist in detecting camouflage?
7. Influence of steady-state solar illumination on luminescence.
8. Relation between Laser induced and solar induced luminescence.
9. Influence of season and conditions on luminescence.

5. SOME RESEARCH RESULTS AND APPLICATIONS

The first example illustrates the need for both reflectance and luminescence spectra. Figure 17A shows the reflectance characteristics of two fabrics, A and C, and of a typical green leaf, curve B. Note the deep water absorption bands at approximately 1.4 and 1.9 μm , which are typical of green turgid vegetation. Fabric C is a reasonable match in the visible and out to about 1100 nm. But, it distorts the 1400 nm water absorption band, misses the 1900 nm band, and would be easy to detect. Fabric A, however, mimics the vegetation throughout the spectral range. Based on the reflectance spectra, it would not be detectable against a vegetal background, and would, in fact, be classified as vegetation. At this point, one needs other spectral information, such as luminescence, or infrared thermal emittance. In Fig. 17B, the luminescence intensities of the fabrics, vegetation, and soils were plotted for the indicated Fraunhofer lines. Fabrics A and C not only have strong signals as compared to soils and vegetation, but have different distributions. Thus, they would be detectable in a milieu of soil and vegetation, and also distinguishable from each other. When bruised, the vegetation showed a strong luminescence that persisted for hours, indicating a possibility for detecting passage of traffic.

Figure 18A shows the reflectances of four differently dyed areas of a fabric. Although they, or their composite signal, would be distinguishable against a background of vegetation, the contrast would not be strong against a mixture of soil and different vegetation types and conditions. On a luminescence basis, however, the fabric has a signal intensity that not only greatly exceeds that of soils and vegetal backgrounds, but occurs at different wavelengths—making detection a certainty if the areal extent is sufficient. These relations are shown

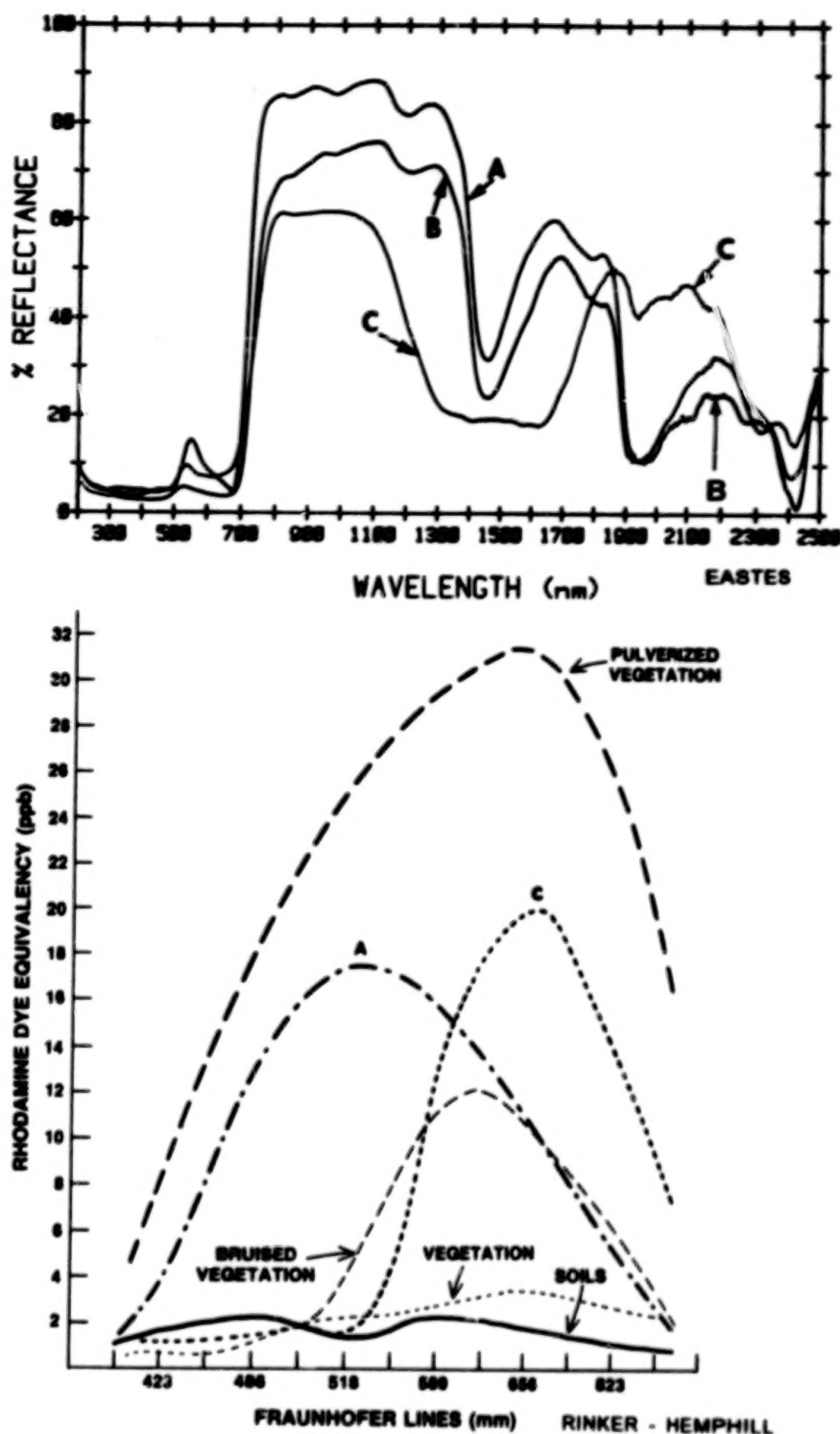


Figure 17. Fabric and vegetation reflectance/luminescence. At the top are spectral reflectances of two fabrics (A and C) and a green leaf (B). The measurements were taken by J.W. Eastes (TEC). Fabric A mimics vegetation, including the water absorption bands, and would be indistinguishable from it. Fabric C is a poor match, and would be easily detected. The lower graph is a plot of luminescence intensity in the Fraunhofer lines of the airborne FLD. These measurements were taken by J.N. Rinker (TEC) and W.R. Hemphill (USGS). Both fabrics show in strong contrast to soils and vegetation (bottom two traces), and also differ significantly from each other. Bruised vegetation gave a strong luminescence signal that persisted for many hours. Pulverized vegetation had even a higher intensity.

in graphs B and C. For airborne detection, the signal threshold is about 1,500 units, and the fabric's luminescence peak is 81,000 units—the "hottest" we had measured to date. In general, the luminescence seldom goes above 12,000 for healthy vegetation. As vegetation senesces, the luminescence increases, but rarely reaches 20,000. The vegetal sample in Fig. 18C, has a peak of 11,000. The iso-intensity contour plot, graph C, shows that the luminescence of the two samples, vegetal and fabric, occurs in different wavelength bands. The original fabric, designed by the U.S. Army Natick Laboratories, matched the luminescence background. What happened? What happened was, the fabric was laundered, and the soap brightener, which luminesces, coupled to the material.

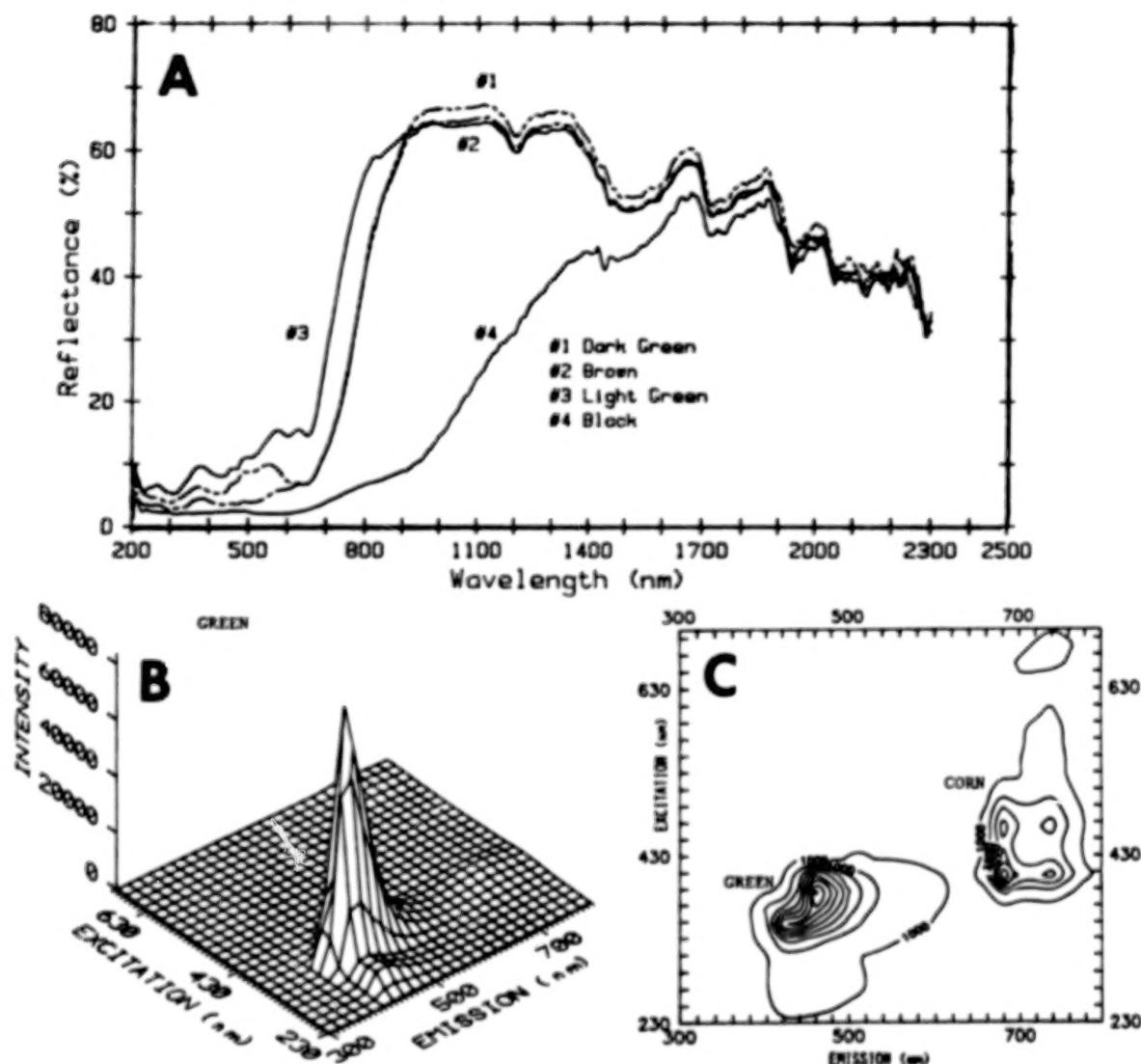


Figure 18. Comparison of fabric reflectance and luminescence. At the top are the reflectance characteristics of four dyed areas of a fabric. Although distinguishable from vegetation, there would not necessarily be a strong contrast, especially if the background provided a mixture of soils and different types and conditions of vegetation. Graph B is a luminescence plot of the green fabric, showing an exceedingly high signal, some 81,000 units. The detection threshold is considered to be 1,500 units. Graph C is an iso-intensity contour plot of the green fabric and of corn, which gives a response typical of healthy herbaceous vegetation. Against the 11,000 intensity units for typical herbaceous vegetation, and the flat response of soils, the fabric with its 81,000 intensity units is easily discernible. It would likely be the brightest object in the scene. This high intensity is attributed to brighteners in the laundry products, i.e. unwashed cloth does not give such a signal. Measurements by M.B. Satterwhite (TEC).

Figure 19 shows some of the differences that take place in vegetal luminescence as a function of drying and of aging. In each example, the upper graph is a three-dimensional display of emission versus excitation, and the lower graph is an iso-contour plot. Figure 19A is typical of healthy, turgid, green leaves, i.e., five distinct luminescence peaks—a group of four with one peak above them. Drying (Plot B) results in a loss of three peaks, reduced intensity in two, and the development of a peak in another area of the plot. Senescence (Plot C) results in the loss of the original five peaks, and the development of two new peaks. Table 3 summarizes these results.

An interesting observation was made by W.R. Hemphill, USGS (personal communication), that when looking out over the terrain with the FLD instrument, there was a strong luminescent signal just above the horizon. It was during the pollen season, and he wondered if the two were connected. Subsequent measurements at TEC confirmed the possibility, as shown in Fig. 20. Implicit in this illustration are a potential application and a potential problem. First, a possible technique for detecting and monitoring airborne pollen loads, i.e., measuring atmospheric quality; and second, a resulting problem—i.e., such an airborne load can reduce contrast, or otherwise interfere with the recording of terrain surface signals.

All materials have spectral reflectance characteristics; but, not all materials have luminescence characteristics. Although we have examined but a portion of what is available, some general statements can be made.

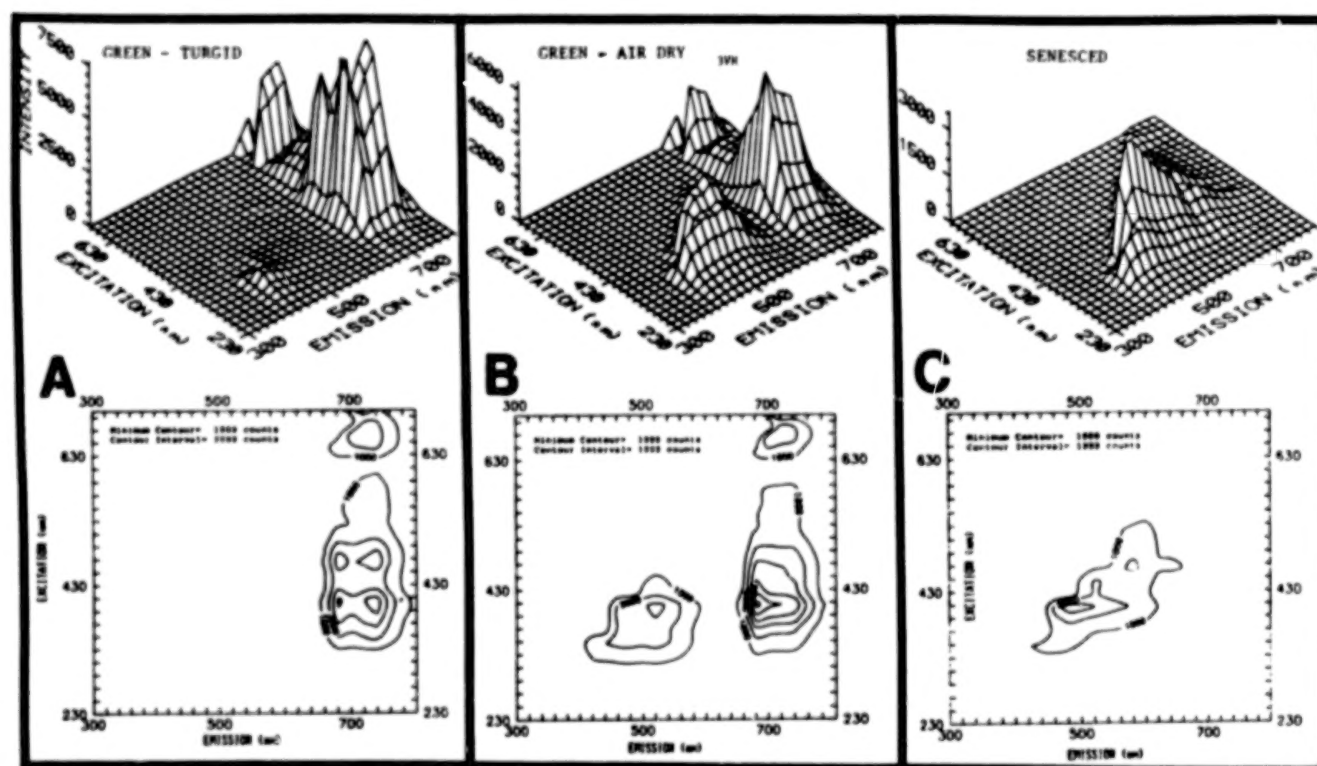


Figure 19. Luminescence characteristics of vegetation. Alteration of vegetal luminescence characteristics as functions of drying and aging. For samples measured so far, these are representative attributes. The upper graphs are three-dimensional displays of excitation wavelength versus emission wavelength versus intensity of the emission signal. The lower graphs are iso-contour plots of the same information. Set A shows the five distinct luminescence peaks—a cluster of four, with a fifth above them. This pattern is characteristic of healthy, turgid, green leaves. With loss of plant water (plot B), three of the lower four peaks fade, and a new peak appears in a different domain of the excitation/emission plot, i.e., in the 430/500 nm wavelength region. Plot C shows the effects of senescence. All of the original peaks are gone, and a new peak has emerged in the vicinity of the peak that developed in response to water stress (Plot B). Measurements by M.B. Satterwhite (TEC).

TABLE 3. LUMINESCENCE BAND CHARACTERISTICS OF VEGETATION

Approximate locations of peak intensities for healthy green vegetation (H), air dried vegetation (AD), and senesced vegetation (S), as taken from the contour plots in Fig. 15. The numbers express the excitation and emission wavelengths in nanometers (nm).

Excitation (nm)	Emission (nm)	H	AD	S
660	730	X	X	
470	680	X		
470	730	X		
400	680	X	X	
400	730	X		
400	500		X	X
470	580			X

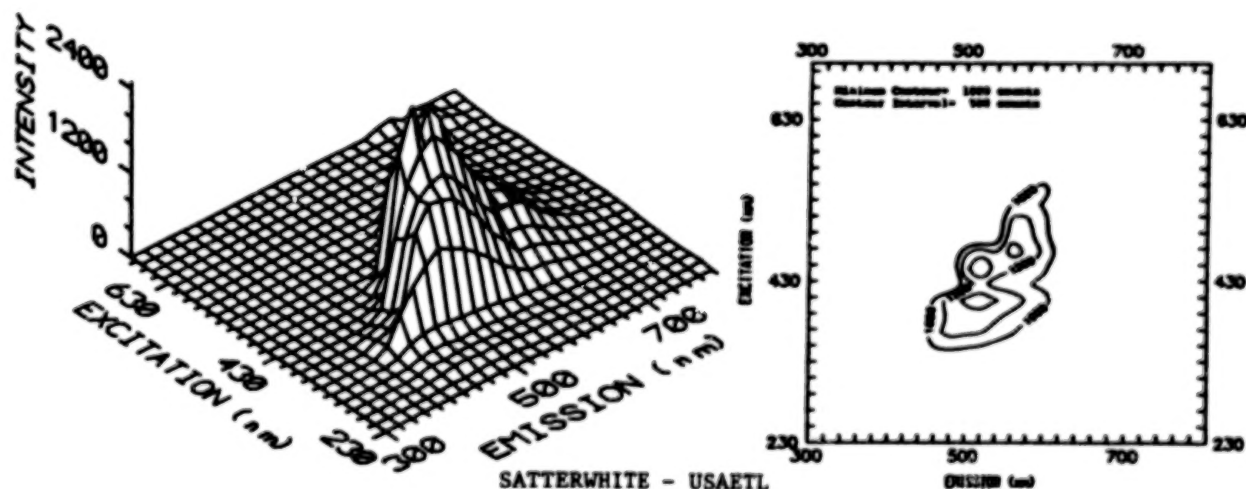


Figure 20. Luminescence characteristics of loblolly pine pollen. Other pollens also luminesce. Pollen of scrub pine is barely detectable, whereas that of cattails has a signal stronger than that of loblolly pollen. Loblolly pollen, however, consists of very small particle sizes and is readily airborne. This suggests a potential technique for monitoring atmospheric components, and also a potential interference problem for collecting terrain data. Measurements by M.B. Satterwhite (TEC).

Soils measured to date do not show useful luminescence. About 75 percent of the vegetal samples and 30 percent of the fabrics have detectable and diagnostic luminescence peaks. For healthy turgid vegetation, the luminescent peaks fall in the wavelength range between 640 and 800 nm. As vegetation dries out, these peaks decrease in intensity and peaks develop in the wavelength region between 400 and 600 nm. Intensity distributions are related to material type and condition, and the peak intensities can be sorted into fairly distinct groups based on emission wavelengths. As shown in Fig. 21, healthy herbaceous vegetation falls into one assemblage, and everything else, e.g., paints, fabrics, pollen, dry vegetation, senesced vegetation, etc., falls in another. So far, with reference to peak emissions, there are three diagnostically useful excitation bands. These are centered at 400, 460, and 660 nm. The important emission bands are centered at approximately 690 and 730 nm.

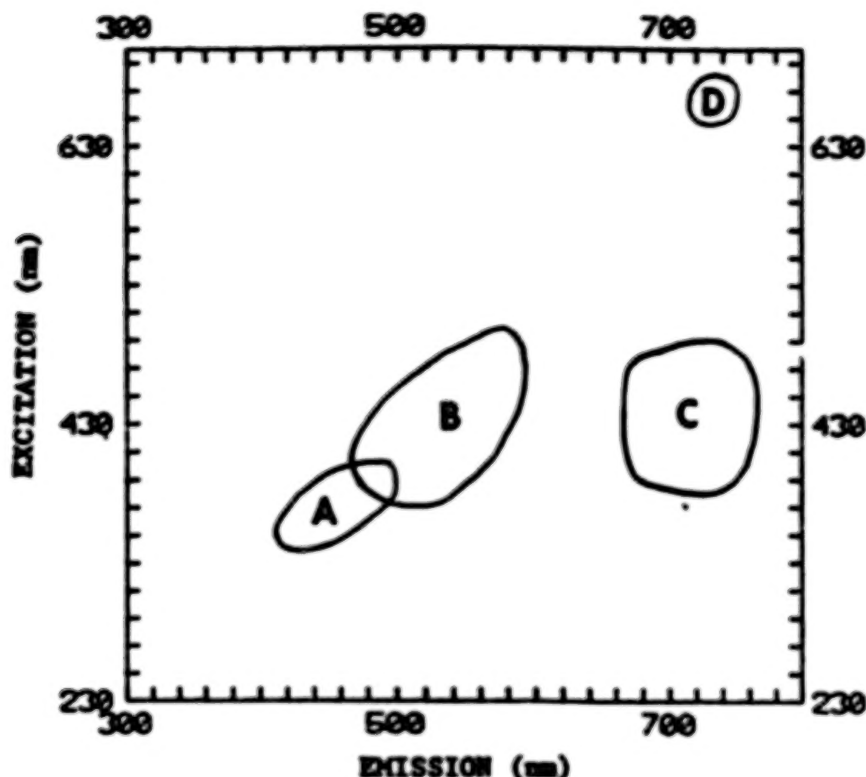


Figure 21. Luminescence classes. On a generalized basis, and for those materials that had usable luminescent peaks, the distributions of the peak intensities fall into the indicated areas. With one exception, so far at least, area A contains the fabrics. Area B, which overlaps A to some extent, contains the peaks of pollen, dry vegetation (pine and herbaceous), and senesced vegetation (pine and herbaceous). Area C contains the peaks of healthy vegetation (pine and herbaceous). Area D has a few secondary peaks associated with herbaceous vegetation. The most useful excitation bands are between 330 and 510 nm. The diagnostic emission peaks fall into two groups, 400-600 nm and 660-760 nm, with the latter containing all the healthy herbaceous samples.

Keep in mind that sensors cannot distinguish between reflected photons and luminesced photons. If sun induced luminesced photons are present, they will be recorded along with the reflected photons, causing a slightly higher DN value or slightly darker gray tone. It is not a large contribution; but, it is a contribution. A spectrometer trace made from a surface illuminated with full-spectrum light, such as the sun, or a halogen lamp, can differ from a record made of a surface illuminated with narrow-band energy at each measurement step. The former situation is characteristic of airborne systems such as AVIRIS, and of field spectrometers, whereas the latter is characteristic of many laboratory instruments, or airborne systems using lasers for illumination, or excitation. For example, luminesced photons from camouflage fabric (refer to Fig. 18) can add to the reflected photon stream to give a slightly higher intensity over the 400-600 nm range. This is shown in Fig. 22, which compares traces recorded from a surface in full illumination and in monochromatic illumination. There can be as much as 8-10 percent absolute difference and 35 percent relative difference. The slight increase in the near infrared region might also be caused by luminescence. It has long been known that vegetation luminesces in the near infrared as the result of the strong absorption at about 645 nm and at about 430 nm (refer to Fig. 19). These added luminesced photons could cause a slight increase in slope steepness of the rapidly increasing reflectance edge just beyond 700 nm, the so-called red edge.

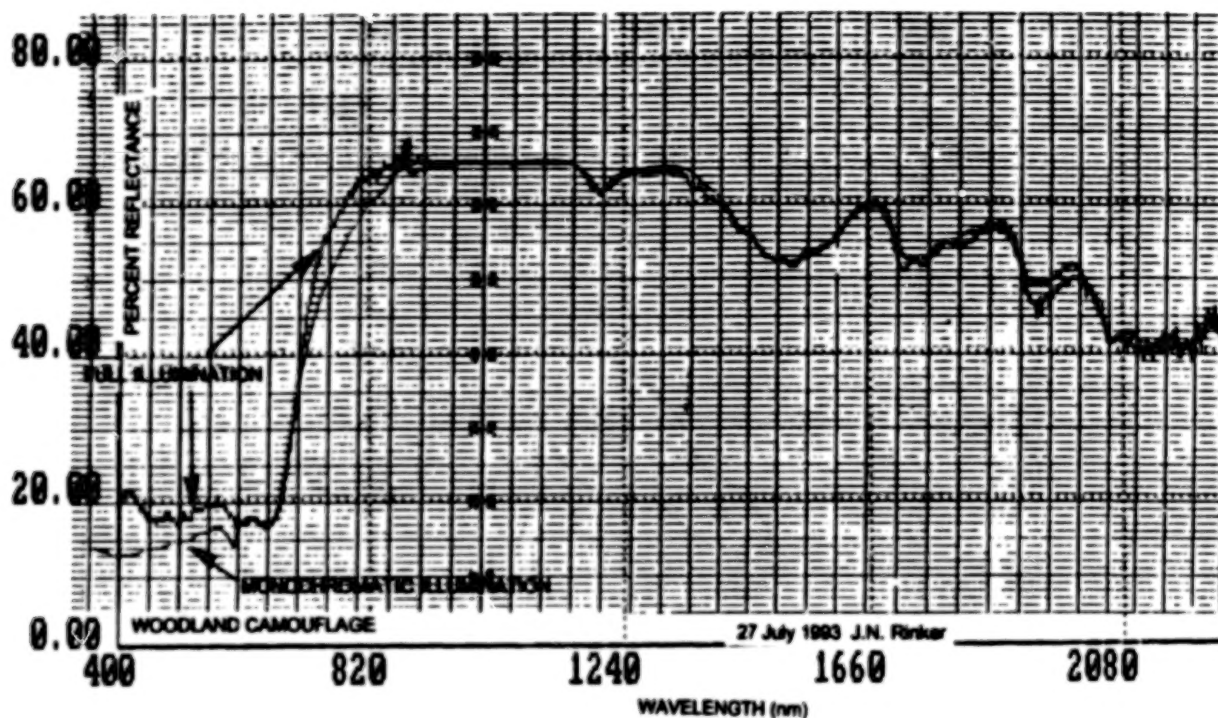


Figure 22. Percent reflectance of Woodland camouflage illuminated with full spectral illumination, or white light (Halogen lamp), and with monochromatic illumination. Full illumination excited the luminescence states, inducing emission of photons at longer wavelengths (refer to Fig. 18). These luminesced photons were incorporated into the stream of reflected photons to cause a slightly higher intensity than was achieved when the sample was illuminated with monochromatic light—most noticeable in the 400–620 nm wavelength region. For example, at 400 nm the sample being illuminated with white light showed a reflectance of about 20 percent. The same surface illuminated with monochromatic light showed about 13 percent reflectance. Once instrumentation differences are eliminated, the most likely cause for the disparity is the added component of luminesced photons. Vegetation also luminesces in the near infrared (refer to Fig. 19), and could easily show an increase in intensity in the 720–850 nm region as a result of luminesced photons. A Perkin Elmer Model 330 spectrometer was used for measurements under monochromatic illumination, and a GER instrument was used for measurements under full illumination.

6. SUMMARY

Remote sensing systems have proved ideal tools for studying earth and atmospheric characteristics, as well as for detecting processes previously unknown. One of the more important tools is the imaging spectrometer, particularly when it covers both the reflected solar band and the thermal infrared bands. An outstanding benefit of an imaging spectrometer is that it provides two domains of information for evaluation—image patterns for terrain information, and spectral patterns for targeting, monitoring, and change detection.

At present, imaging spectrometers provide only monoscopic imagery, so there is a reduction in the quantity and quality of information that can be derived on the basis of image pattern shapes; but, these shapes are present, and they can make significant direct contributions to an analysis, as well as assist in the evaluation of the spectral data. Furthermore, existing routines for combining bands to make color composite images, such as Landsat, or the Coastal Zone Color Scanner (CZCS), can be directly applied to hyperspectral data.

BEST COPY AVAILABLE

As are many agencies and academic institutions, TEC is collecting field and laboratory spectral measurements of soils, rocks, vegetation, and man-made materials; developing and testing classification and analytical software; and, in cooperation with the USGS group at Flagstaff, AZ, maintaining a series of instrumented test sites that collect around-the-clock measurements of target/background radiation characteristics and concurrent meteorological conditions (Rice and Krusinger, 1985). The resulting data bases (Table 4) support the climatic change program, empirical modeling for target/background contrast prediction and atmospheric backout, assisted target recognition, and digital analysis techniques for hyperspectral imagery.

Basic issues to resolve include: establishing variances within sets; determination of significant spectral bands (statistical, mathematical, empirical) and significant intensity variations; the importance of absorption band slope changes; atmospheric backout in relation to targets, areas, and conditions; self-calibration of imagery from known data base sets; mixed pixel problem; influence of steady state illumination on luminescence; and testing and validation of existing models.

The airborne systems are here, needed spectral data bases exist, and enough hyperspectral image sets (solar reflectance, luminescence, thermal IR) have been evaluated by various interest groups to come to some general conclusions. NASA and JPL have shown the applicability to targeting minerals. USGS, NASA, and USDA have shown applicability to minerals, petroleum, and vegetal characteristics. TEC has shown applicability to military targeting and terrain utilization. The capability exists to render direct assistance to critical national and worldwide problems such as narcotics, disaster evaluation, and global climatic change.

No technique is a panacea, no system does everything, and the hyperspectral, even in its broadest sense, has its limitations; but, from the standpoint of targeting, monitoring, and change detection, the technique has potential beyond any previous remote sensing endeavor. If the system ever achieves stereo imaging capability, we will have the best of both worlds, i.e., stereo image patterns for terrain information, and surface spectral patterns for molecular composition.

TABLE 4. EXISTING DATA BASES IN THE TEC INVENTORY

The temperate data base has nine years of continuous measurements; the subhumid, five years; and the arid, three years. The spectral data bases contain field and laboratory measurements of natural and man-made surfaces, and are collected with an equal or finer spectral resolution than that of the hyperspectral systems. These measurements can be averaged over any selected bandwidth to provide intensity values as they would be in Landsat MSS, TM, TIMS, AVIRIS, etc.

TEC Radiation/Meteorological Data Base - Temperate
TEC/USGS Radiation/Meteorological Data Base - Subhumid
TEC/USGS Radiation/Meteorological Data Base - Arid
TEC Spectral Reflectance Data Base - Solar Radiation (0.4-2.5 μm) ¹
TEC Spectral Reflectance Data Base - Thermal Infrared (2.5-14 μm) ²
TEC Spectral Luminescence Data Base
TEC/USGS Image Pattern Data Bases - Desert

¹Satterwhite and Henley (1990)

²Eastes (1991)

REFERENCES

- Abu-Zeid, M.E., K.S. Bhatia, M.A. Marafi, Y.Y. Makdisi, and M.F. Amer, 1987: Measurements of Fluorescence Decay of Crude Oil: A Potential Technique to Identify Oil Slicks, *Environ. Pollution*, **46**, 197-207.
- Belcher, D.J., 1943: The Engineering Significance of Soil Patterns. *Proc. 23rd Annual Meeting, Highway Research Board*, Washington, DC.
- Eastes, J.W., 1991: Thermal infrared spectra of natural and manmade materials: Implications for remote sensing. U.S. Army Engineer Topographic Laboratories Report, **ETL-0587**, Fort Belvoir, Virginia 22060-5546.
- Fork, R.L., H. Avramopoulos, and J.A. Valdmans, 1990: Ultrashort Light Pulses. *American Scientist*, **78**, No. 3, 216-223, May-June 1990.
- Frost, R.E., J.G. Johnstone, O.W. Mintzer, M. Parvis, P. Mantano, R.D. Miles, and J.R. Shepard, 1953: A Manual on the Airphoto Interpretation of Soils and Rocks for Engineering Purposes. School of Civil Engineering and Engineering Mechanics, Purdue University, West Lafayette, Indiana.
- Henley, J.P., 1988: Methods of determining playa surface conditions using remote sensing. *Technical papers of the 1988 ACSM-ASPRS Annual Convention*, Vol. 6, 108-117.
- Hemphill, W.R., and M. Settle (Eds.), 1981: Applications of luminescence techniques to Earth resources studies. A Lunar and Planetary Institute Workshop, December 10-12, 1980, LPI Technical Report **81-03**, Lunar and Planetary Institute, Houston, Texas.
- Hemphill, W.R., J.N. Rinker, A.F. Theisen, and R.H. Nelson, 1989: Potential military applications of passive detection of luminescent materials (U). U.S. Army Engineer Topographic Laboratories Report, **ETL-RI-1**, Fort Belvoir, Virginia 22060-5546.
- Hollas, J.M., 1982: *High Resolution Spectroscopy*, Butterworth & Company, Ltd., London, Boston.
- Hunt, G.R., and J.W. Salisbury, 1970: Visible and Near-Infrared Spectra of Minerals and Rocks: Silicate Minerals. *Modern Geology*, **1**, 283-300. First of a series of papers.
- Kock, W.E., 1965: *Sound Waves and Light Waves. The fundamentals of Wave Motion*. Anchor Books, Doubleday & Company, Inc., Garden City, New York.
- LaBaw, C., 1983: Airborne imaging spectrometer: An advanced concept instrument. *Proc. Soc. of Photographic Instrumentation Engineering*, paper 430.
- McCauley, J.F., G.G. Schaber, C.S. Breed, M.J. Grolier, C.V. Haynes, B. Issawi, C. Elachi, and R. Blom, 1982: Subsurface Valleys and Geoarcheology of the Eastern Sahara Revealed by Shuttle Radar. *Science*, **218**:4567, 1004-1019.
- Morgan, J.E., C.D. Miller, D.C. Parker, D.S. Fisher, J.H. McLerran, J.N. Rinker, and B.L. Hansen, 1962: Operation Cold Deck: A cold regions aerial infrared sensing program (U). U.S. Army Cold Regions Report **104**, Hanover, New Hampshire.
- Pierce, J.R., 1956: *Electrons, Waves and Messages*. Hanover House, Garden City, New York.

- Quinn, M.F., S. Joubian, F. Al-Bhatia, S. Al-Aruri, and O. Alameddine, 1988: Deconvolution Technique for Determining the Intrinsic Fluorescence Decay Lifetimes of Crude Oils, *Applied Spectroscopy*, **42**, 406.
- Rice, J.E., and A.E. Krusinger, 1985: A new and extensive thermal contrast data base. *Proc. IRIS Specialty Group on Targets, Background, and Discriminations*, Vol. II, 1-5.
- Rinker, J.N., 1962: Aerial detection of snow surface and undersnow targets. *Proc. Army Science Conf.*
- Rinker, J.N., 1975a: Airborne infrared thermal detection of caves and crevasses, *Photogrammetric Engineering and Remote Sensing*, **41:11**, 1391-1400.
- Rinker, J.N., 1975b: Some technical aspects of film emulsions in relation to the analysis and interpretation of aerial photographs. In *Aerial Reconnaissance for Archaeology*, D.R. Wilson (Ed.). Research Report No. 12, The Council for British Archaeology, 32-46.
- Rinker, J.N., and P.A. Corl, 1984: Air photo analysis, photo interpretation logic, and feature extraction. U.S. Army Engineer Topographic Laboratories Report, **ETL-0329**, Fort Belvoir, Virginia 22060-5546.
- Rinker, J.N., 1990a: Hyperspectral imagery - What is it? - What can it do? *Proc. Seventh USACE Remote Sensing Symposium*, 7-9 May 1990, Portland, Oregon.
- Rinker, J.N., 1990b: Hyperspectral imagery - A new technique for targeting and intelligence. *Proc. Army Science Conf.*, 12-15 June 1990, Durham, North Carolina.
- Satterwhite, M.B., and J.P. Henley, 1990: Hyperspectral signatures of vegetation, minerals, soils, rocks, and cultural features: Laboratory and field measurements. U.S. Army Engineer Topographic Laboratories Report, **ETL-0573**, Fort Belvoir, Virginia 22060-5546.
- Satterwhite, M.B., and J.N. Rinker, 1986: Time variant reflectance spectra of plant canopies as affected by in-canopy shadow. *Proc. Army Science Conf.*, Vol. IV, 17-19 June 1986, 41-55.
- Stoertz, G.F., 1972a: Visible fluorescence of Earth-surface materials and potential applications to remote sensing. **NTIS PB-210-621**.
- Stoertz, G.F., 1972b: Feasibility of differentiating target materials by their solar-stimulated fluorescence. **NTIS PB-210-641**.
- Vane, G. (Ed.), 1987a: *Proc. of the Third Airborne Imaging Spectrometer Data Analysis Workshop*. Jet Propulsion Laboratory, California Institute of Technology, JPL Publication 87-30.
- Vane, G. (Ed.), 1987b: Imaging Spectroscopy II. *Proc. Soc. of Photo-Optical Instrumentation Engineers*, Vol. 834.
- Vane, G., and A.F.H. Goetz, 1985: *Proc. Airborne Imaging Spectrometer Data Analysis Workshop*, Jet Propulsion Laboratory, California Institute of Technology, JPL Publication 85-41.

IMAGING SPECTROMETER DATA ANALYSIS - A TUTORIAL**

Fred A. Kruse
Center for the Study of Earth from Space (CSES)
Cooperative Institute for Research in Environmental Sciences (CIRES)
and
Department of Geological Sciences
University of Colorado, Boulder, CO 80309 USA

ABSTRACT

This tutorial is designed to provide an overview of selected methods for analysis of imaging spectrometer data. "Calibration" to reflectance is a prerequisite for most analysis approaches. A brief review of both empirical and model-based methods for recovery of apparent surface reflectance from the data is presented. Data analysis methods discussed include single pixel spectrum analysis, both empirical and feature based approaches to spectral classification of imaging spectrometer data, and the use of linear spectral unmixing to determine abundances of materials occurring with sub-pixel distributions.

1. INTRODUCTION

Visible/infrared optical remote sensing utilizes reflected solar energy to make measurements of the Earth's surface. Solar energy is scattered or absorbed based upon the physical properties and composition of the surface materials, and given sufficient spatial and spectral sensor resolution, these phenomena allow direct identification of individual materials. Multispectral remote sensing has been used routinely since the launch of Landsat in the early 1970s in disciplines as widely varying as geology, ecology, hydrology, oceanography, military applications, and many others. Imaging spectrometry or "hyperspectral" sensing has been available to government and university researchers for about 10 years, however, only recently have commercial and military end-users become aware of its potential.

1.1 WHAT IS IMAGING SPECTROMETRY (HYPERSPPECTRAL SENSING)

Broad-band remote sensing systems, such as the Landsat Multispectral Scanner (MSS, 4 bands) and Landsat Thematic Mapper (TM, 7 bands), drastically under sample the information content available from a reflectance spectrum by making only a few measurements in spectral bands up to several hundred nanometers wide. Imaging spectrometers, on the other hand, sample at close intervals (bands on the order of 10^{-2} nm wide) and have a sufficient number of spectral bands to allow construction of spectra that closely resemble those measured on laboratory instruments (Figure 1). Imaging spectrometry is defined as "the simultaneous acquisition of images in many narrow, contiguous spectral bands" (Goetz et al., 1985). Analysis of imaging spectrometer data allows extraction of a detailed spectrum for each picture element (pixel) of the image. High spectral resolution reflectance spectra collected by imaging spectrometers allow direct identification (and in some instances, abundance determinations) of individual materials based upon their reflectance characteristics including minerals (Goetz et al., 1985; Lang et al. 1987; Pieters and Mustard, 1988; Kruse, 1988; Kruse et al., 1993; Crowley, 1993; Boardman and Kruse, 1994), atmospheric constituent gases (Gao and Goetz, 1990; Carrère and Conel, 1993), vegetation (Gamon et al., 1993; Roberts et al., 1993; Elvidge et al., 1993), snow and ice (Nolin and Dozier, 1993), and dissolved and suspended constituents in lakes and other water bodies (Hamilton et al., 1993; Cardner et al., 1993).

** Presented at the International Symposium on Spectral Sensing Research '94 (ISSSR), San Diego, CA, 9 July 1994.

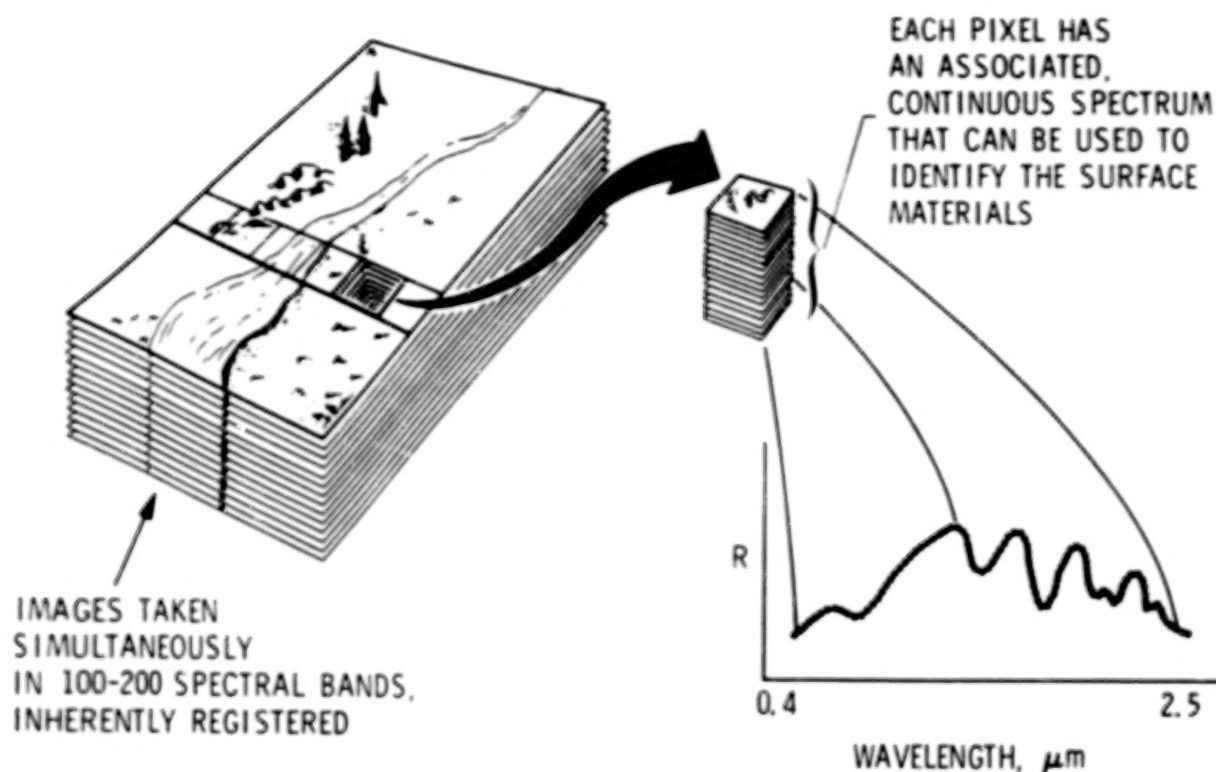


Figure 1. Schematic illustration of the imaging spectrometry concept. Images are acquired simultaneously of up to several hundred narrow spectral bands providing a complete reflectance spectrum for every pixel in the imaging spectrometer scene (from Vane, 1985).

1.2 REAL WORLD PROBLEMS

Theoretically, identification and mapping of individual materials using imaging spectroscopy should be quite easy. There are, however, significant factors that complicate the procedure. Remote sensing measurements of the Earth's surface are strongly influenced by the atmosphere (Goetz et al., 1985). Both scattering and absorption by gases and particulates affect the amount and wavelengths of light reaching the sensors. Absorption by atmospheric gases is dominated by water vapor with smaller contributions from carbon dioxide, ozone, and other gases (Gao and Goetz, 1990). Strong atmospheric water absorption bands make the atmosphere opaque in many regions (for example the 1.4 and 1.9 μm regions) and only small atmospheric windows are available for terrestrial remote sensing.

Additionally, visible/near-infrared remote sensing can provide compositional information only for approximately the top 50 μm of exposed surfaces (Buckingham and Sommer, 1983). Surface coatings or other differences between what is exposed at the surface versus what underlies the surface can mask near-surface spectral variation.

Determination of surface composition is also complicated by spectral mixing. Exposed surfaces are rarely composed of a single pure material. Intimate mixtures of varied materials are more common for naturally occurring materials such as rock and soils (Mustard and Pieters, 1987; Boardman, 1989) and surfaces covered by vegetation are influenced by such factors as canopy architecture, shading, and vegetation density (Milton et al., 1983; Collins et al., 1983; Peterson et al., 1988; Roberts et al., 1993). Additionally, within typical instrument fields of view (10-100 m) materials are spatially mixed and the signal reaching the sensor is an areal average of the individual component signatures (Boardman, 1989, 1991; Boardman and Kruse, 1993).

2. CALIBRATION TO REFLECTANCE IS A PREREQUISITE TO MOST ANALYSIS

The most critical step in most imaging spectrometer data analysis strategies is to convert the data to reflectance so that individual spectra can be compared directly with laboratory or field data for identification. This requires that accurate wavelength calibration be performed. Laboratory measurements made before and after data acquisition usually provide the initial wavelength calibration. An additional check on the wavelength calibration can be made by comparing the positions of known atmospheric absorption features to their locations in the imaging spectrometer data. Atmospheric carbon dioxide (CO₂) absorption bands located at 2.005, and 2.055 μm are useful for wavelength-calibration of the data in the infrared (Kneisyz et al., 1988; Vane, 1987). In the visible and photographic infrared portion of the spectrum, narrow atmospheric water bands at 0.69, 0.72, and 0.76 μm can be used to calibrate wavelengths.

Ideally, imaging spectrometer data should be calibrated to absolute reflectance using onboard calibration. Onboard calibration, however, is typically not available. In its absence, several approaches have been used to calibrate the data to reflectance relative to a reference spectrum, "relative reflectance".

Marsh and McKeon (1983) used a multiplier to scale GERS Mark I spectra (a single pixel column of spectra, not true imaging spectrometer data) to a constant value at 2.04 μm . They then subtracted the average normalized radiance value for each channel from each normalized spectrum to produce a "residual image". For these line data, the residual image consisted of a number of color-coded, stacked spectra that enhanced regions with varying spectral characteristics.

A similar procedure ("logarithmic residuals", Green and Craig, 1985) has been used by numerous investigators to successfully map mineral distributions with imaging spectrometer data. The mathematically similar "internal average relative reflectance" (IAR reflectance) calibration has also been used with considerable success in arid regions (Kruse, 1988; Ben-Dor et al., 1994). IAR reflectance is calculated by determining an average spectrum for an entire imaging spectrometer data set and dividing each spectrum in the data set by the average spectrum. The resulting spectra represent reflectance relative to the average spectrum and resemble laboratory spectra acquired of the same materials (Kruse, 1988).

While all of these methods produce calibrated images and spectra with characteristics similar to reflectance, it is crucial to remember that these techniques produce relative reflectance not absolute reflectance. Any data set reduced to reflectance by division by a reference spectrum (flat field, log residual, or IAR) may have artifacts introduced by the fact that the reference spectrum itself may have spectral characteristics related to specific absorption features. This can adversely affect the appearance of the reflectance spectra and limit their usefulness in comparisons with laboratory spectra. One advantage of the techniques described above is that the conversion to apparent reflectance does not require *a priori* knowledge of the site.

2.1 EMPIRICAL LINE CALIBRATION

An alternative to onboard calibration or reflectance conversions based on internal characteristics of the data is to use a standard area on the ground to calibrate the data to reflectance (Ballew, 1975; Roberts et al., 1985; Elvidge 1988; Kruse et al., 1990; 1993), however, this approach requires *a priori* knowledge of each site. The calibration to reflectance requires choosing two or more ground target regions with albedos that span a wide range and acquiring field or laboratory spectra to characterize them. The second step in the process involves picking multiple pixels in the airborne data set that are associated with each ground target. Then a linear regression is calculated for each band to determine the gains and offsets required to convert the DN to reflectance. Solving the system of linear equations provides estimates of the standard error for each parameter at each wavelength in addition to the gain and offset spectra for use in the calibration. Bands with large total errors should be considered for deletion from the data set and further analysis efforts. The gain spectrum of the remaining bands is essentially a solar irradiance curve. The offset value spectrum is usually a correction that increases in magnitude with wavelength, and is essentially a path radiance term.

The final step in the spectral calibration is to multiply the instrument DN values by the proper gain factor and to add the corresponding offset value. The result is the removal of atmospheric effects (both attenuation and scattering), viewing geometry effects, and residual instrument artifacts. While no such correction can be perfect, the empirical line calibration does allow conversion of the remotely sensed spectra into a form that can be readily compared with laboratory or field acquired spectra. This technique does require field or laboratory spectra of at least two regions in the area of interest. It also makes the assumption that all of the image pixels chosen to characterize each ground spectrum represent identical composition and reflectance response.

2.2 CALIBRATION USING AN ATMOSPHERIC MODEL

Ideally, researchers would like to be able to calibrate their data to absolute reflectance rather than relative reflectance without actually having to make ground measurements. One method that comes close to achieving this goal is a radiative transfer model-based technique "The Atmospheric Removal Program" (ATREM) developed by Gao and Goetz (1990) and Gao et al. (1993) using 224-channel Airborne Visible/Infrared Imaging Spectrometer (AVIRIS) data (Porter and Enmark, 1987). Several similar atmospheric model programs being developed and tested by other researchers (Teillet, 1989; Green, 1991; Carrère and Conel, 1993). The ATREM method involves using a three-channel ratioing method that utilizes the 0.94 and 1.1 μm water vapor bands to calculate water vapor on a pixel-by-pixel basis from the AVIRIS data. Apparent reflectance spectra are first obtained by dividing each AVIRIS spectrum by the solar irradiance curve above the atmosphere (Kneisyz et al., 1988). A number of theoretical water vapor transmittance spectra for the 0.94 and 1.1 μm water vapor bands are calculated for varying amounts of atmospheric water vapor using an approximate radiative transfer code called "Simulation of the Satellite Signal in the Solar Spectrum (5S)" (Tanre et al., 1986) and the Malkmus (1967) narrow band spectral model. The modeled spectra are run through the three-channel ratioing method to generate a lookup table of water vapor concentrations that can be used to convert the AVIRIS apparent reflectance measurements to total column water vapor. The output of this procedure is an image showing the spatial distribution of various water vapor concentrations as derived for each pixel of the AVIRIS data. The water vapor image is then used along with transmittance spectra derived for each of atmospheric gases CO_2 , O_3 , N_2O , CO , CH_4 , and O_2 using the Malkmus narrow band model and 5S model to produce scaled surface reflectance (Teillet, 1989; Gao and Goetz, 1990; Gao et al., 1993). This model-based technique produces total water vapor column images and reflectance calibrated AVIRIS data without *a priori* knowledge. This model has also successfully been applied to Geophysical and Environmental Research (GER) 63-band scanner data (Personal communication, Eyal Ben-Dor).

3. SELECTED DATA ANALYSIS METHODS

A great deal of spectral information can be extracted from either raw or calibrated imaging spectrometer data using "standard" image processing procedures but new techniques are required to take full advantage of the data. Successful discrimination of varied lithologies has been demonstrated using simple procedures such as color compositing, band ratios, and principal components (Feldman and Taranik, 1988) and more advanced procedures such as Chebyshev waveform analysis (Collins et al., 1983). Empirically-based procedures like those mentioned above, however, usually represent underutilization of the data, although they may actually enhance the information available from noisy data sets. Display of imaging spectrometer data is more complex than displaying three bands as a RGB color composite. The information present in the imaging spectrometer data simply cannot be fully displayed in one, or even 10, color images. A combination of spectral and spatial domains must be used to fully display the compositional information present in the data.

3.1 SINGLE PIXEL SPECTRUM BROWSING

Several public domain and commercial software packages are available that allow users to make direct comparisons between image and reference spectra (Mazer et al. 1988; Torson et al. 1989; Kruse et al., 1993). The first step after calibrating any imaging spectrometer data set is to look at the data in both the spatial and spectral domains. Ideally, this is done simultaneously by selecting a location on a single band or color composite and extracting the individual spectrum or by outlining a region of interest and extracting the average spectrum. Visual comparison is usually used to assess the calibration quality and to compare the extracted spectra to a spectral library or reference spectrum.

3.2 EMPIRICAL-BASED APPROACHES TO SPECTRAL CLASSIFICATION

The simplest way to produce maps showing the spatial distribution of specific materials using imaging spectrometer data is to empirically match image spectra to reference spectra. The reference spectra can be either laboratory or field spectra or extracted from the imaging spectrometer data. The "Spectral Angle Mapper" (SAM) is one algorithm designed to determine the similarity of spectra in multidimensional space (Boardman personal communication, 1991; Yuhas et al., 1993). This method assumes that the data have been reduced to apparent reflectance. The algorithm determines the similarity between two spectra by calculating the "angle" between them, treated as vectors in a space with dimensionality equal to the number of bands (nb).

A simplified explanation of this can be given by considering a reference spectrum and a test spectrum from 2-band data represented on a two-dimensional plot as two points. The lines connecting each spectrum-point and the origin contain all possible positions for that material, corresponding to the range of possible illuminations. Poorly illuminated pixels will fall closer to the origin (the dark point) than pixels with the same spectral signature but greater illumination. The angle between the vectors, however, is the same regardless of their length. The SAM algorithm generalizes this geometric interpretation to nb-dimensional space. The calculation consists of taking the arccosine of the dot product of the spectra. This measure of similarity is insensitive to gain factors because the angle between two vectors is invariant with respect to the lengths of the vectors. As a result, laboratory spectra can be directly compared to remotely sensed apparent reflectance spectra, which inherently have an unknown gain factor related to topographic illumination effects.

For each reference spectrum, the spectral angle is determined for every image spectrum and this value, in radians, is assigned to that pixel in an output SAM image for that reference material. The derived spectral angle image maps form a new data cube with the number of bands equal to the number of reference spectra used in the mapping. The results for each reference spectrum are typically viewed separately as gray-scale images or combined to form a color composite. Small spectral angles correspond to high similarity and these pixels are usually shown in brighter gray levels. Larger angles, corresponding to less similar spectral shapes, are shown in darker gray levels.

3.3 ABSORPTION FEATURE-BASED CHARACTERIZATION AND MAPPING

Many researchers have concentrated on the use of specific absorption features in reflectance spectra to identify specific materials (Green and Craig, 1985; Kruse et al., 1985; Yamaguchi and Lyon, 1986; Clark et al., 1987). Only recently have attempts been made to apply these techniques to imaging spectrometer data (Kruse, 1988; Clark et al., 1991; Abrams and Hook, 1990). The approach described here, an expert system, has been moderately successful in identifying mineralogy in arid terrains using AVIRIS data.

An expert system approach developed at CSES allows automated identification of Earth surface materials based on their spectral characteristics in imaging spectrometer data (Kruse et al., 1993). This expert system requires that the imaging spectrometer data be calibrated to reflectance because rules for identification are built using laboratory reflectance spectra. Once the data are properly calibrated, the procedure is to treat each pixel individually and sequentially to remove a continuum (normalize), binary encode the spectrum (Mazer et al., 1988), extract the features, and compare the binary encoding and features to the binary encoded reference spectrum and the feature rules built from the spectral library of reference materials. The result of these analyses is a new data cube consisting of a single image for each endmember contained in the spectral library (Kruse and Lefkoff, 1993). These images contain a value for each pixel indicating an empirical probability that a particular material will occur at that location. Probabilities range from 0.0 to 1.0 with 1.0 indicating a perfect match.

More specifically, the procedure is as follows. A spectral library of laboratory reference spectral reflectance measurements is used to develop a generalized knowledge base for analysis of visible and infrared reflectance spectra. Several libraries are available in the public domain (Clark et al., 1990; Grove et al., 1992). Spectral features are digitally extracted from a spectral library and numerical analysis and characterization of the digital reflectance measurements are used to establish quantitative

criteria for identifying materials.

Absorption feature information is extracted from laboratory spectra (and later each image spectrum) using the following automated techniques (Kruse et al., 1988; 1993).

- 1). A continuum is defined for each spectrum by finding the high points (local maxima) and fitting straight line segments between these points.
- 2). The continuum is divided into the original spectrum to normalize the absorption bands to a common reference. (See Clark and Roush, 1984 for a discussion of division versus subtraction of the continuum).
- 3). The minima of the continuum-removed spectrum are determined and the 10 strongest absorption features extracted.
- 4). The wavelength position, depth, full width at half the maximum depth (FWHM), and asymmetry for each of these 10 features are determined and tabulated. The asymmetry is defined as the sum of the reflectance values for feature channels to the right of the minimum divided by the sum of the reflectance values for feature channels to the left of the minimum. The base ten logarithm is taken of this value to maintain linearity. Symmetrical bands thus have an asymmetry value of zero (the area to the left and right of the band center are equal). Bands that are asymmetrical towards shorter wavelengths have negative asymmetry, while bands that are asymmetrical towards longer wavelengths have positive asymmetry. The magnitude of the asymmetry value indicates the degree of asymmetry.

The information derived from the analysis of the spectral library are interactively reviewed simultaneously in both tabular and graphical format to determine if features extracted from the digital spectra are representative of the material measured or were due to impurities. The four parameters derived using the feature extraction procedure are used in conjunction with published spectral information to determine the critical absorption bands and absorption band characteristics for identification of specific materials. Facts and rules are formulated based on the analysis of the reference spectra.

The final step is to apply the rules to an imaging spectrometer data set to automatically identify materials and to map their spatial distributions. The absorption feature positions and shapes of each reflectance spectrum for each picture element (pixel) are characterized using the automated techniques described previously for individual laboratory spectra. The final products of the expert system analysis are a "continuum-removed" cube with "n" bands containing all of the continuum-removed spectra calculated from the reflectance data, a "feature" cube containing the wavelength positions, depths, FWHMs, and asymmetries for each pixel for the ten strongest absorption features, and an "analysis cube" showing the location and probability of occurrence of the reference materials based on a weighted combination of binary encoding, and feature analysis in the expert system. The analysis cube also contains four images that help with evaluation of the expert system mapping success. These are 1) the "final decision best endmember" image showing the single best match for each pixel, 2) the "sum of decisions" image showing the sum of all probabilities for each pixel, 3) the "number of decisions greater than or equal to 50%" image showing those areas with endmembers with high probabilities, and 4) the "no match" image showing those areas with maximum probabilities less than or equal to 10%.

Interactive display and analyses of the probability images and the additional images described above permits determination of the spatial extent of specific minerals and identification of problem areas where the expert system may have identified multiple minerals, or no minerals at all. These images form the starting point for detailed analyses using techniques such as linear spectral unmixing.

3.4 SPECTRAL UNMIXING

Identification of the main constituents of the surface is only the first step in mapping using imaging spectrometer data because natural surfaces are rarely composed of a single uniform material. These surfaces are more commonly made up of mixtures or assemblages of intimately mixed minerals, alteration products, or weathered constituents; and vegetation, water, and shadows. Spectral mixing is a consequence of the mixing of materials having different spectral properties within the ground field-of-view (GFOV) of a single image pixel. Several researchers have investigated mixing scales and linearity. Singer and McCord (1979) found that if the scale of the mixing is large (macroscopic), then the mixing occurs in a linear fashion. For microscopic or intimate mixtures, the mixing is generally nonlinear (Nash and Conel, 1974; Singer, 1981).

Boardman (1989, 1991) addressed the macroscopic mixing problem using singular value matrix decomposition (SVD) to determine the scale of spatial mixing and to linearly unmix AVIRIS data. This technique assumes that most mixing is on the macroscopic scale, and thus linear. For most situations, however, there is a significant amount of intimate mixing and therefore the linear unmixing techniques are at best an approximation. Abundances determined using these techniques are not as accurate as those determined using non-linear techniques, however, to the first order, they appear to adequately represent the surface conditions.

A spectral library of constituent spectra or "endmembers" typically forms the initial data matrix for the analysis. Ideally, these endmembers, when linearly combined should be able to match all possible spectra in the imaging spectrometer data. An inverse of the spectral library matrix is formed by multiplying together the transposes of the orthogonal matrices and the reciprocal values of the diagonal matrix (Boardman, 1989). A simple vector-matrix multiplication between the inverse library matrix and an observed mixed image spectrum gives an estimate of the abundance of the library endmembers for the unknown spectrum.

Data are typically first examined using unconstrained unmixing in which the derived abundances are free to take on any value including negative ones. The output of the unmixing process is an image data cube with the same spatial dimensions as the input data, with the "spectral" output bands representing the abundances of the endmembers. The analysis also usually produces two additional images, one showing the sum of the abundances at each pixel, and the other the root-mean-square (rms) error values at each pixel. Interactive analysis of the abundance cube, the sum image, and the rms error image is used to determine if the endmembers explain most of the spectral variation. Subsequent inclusion of new endmembers and iteration are used until the rms error is small and the results converge to non-negative values that sum to one or less (100%). Alternatively, fully constrained unmixing may be used, but this is much more computationally intensive.

4. CONCLUSIONS

This paper presents an overview of several commonly used imaging spectrometer data analysis techniques. There are as many different approaches, however, to working with these data as there are spectral bands in a typical data set. A complete analysis usually combines the use of spatial and spectral processing, analysis, and interpretation. The reader is referred to the current literature for detailed discussion of the many options.

REFERENCES

- Ballew, G., 1975, A method for converting Landsat I MSS data to reflectance by means of ground calibration sites: Stanford Remote Sensing Laboratory Technical Report 75-5, Stanford, CA.
- Ben-Dor, E., and Kruse, F. A., 1994, The relationship between the size of spatial subsets of GER 63 channel scanner data and the quality of the Internal Average Relative Reflectance (IARR) correction technique: International Journal of Remote Sensing, v. 15, no. 3, p. 683-690.
- Boardman, J. W., 1989, Inversion of imaging spectrometry data using singular value decomposition: in Proceedings, IGARSS '89, 12th Canadian Symposium on Remote Sensing, 4, pp. 2069-2072.
- Boardman, J. W., 1991, Sedimentary Facies Analysis Using Imaging Spectrometry: A Geophysical Inverse problem: Unpublished Ph. D. Thesis, University of Colorado, Boulder, 212 p.
- Boardman, J. W., and Kruse, F. A., 1994, Automated spectral analysis: A geological example using AVIRIS data, northern Grapevine Mountains, Nevada: in Proceedings, Tenth Thematic Conference, Geologic Remote Sensing, 9-12 May 1994, San Antonio, Texas, p. I-407 - I-418.
- Buckingham, W. F., and Sommer, S. E., 1983, Mineralogical characterization of rock surfaces formed by hydrothermal alteration and weathering-Application to remote sensing: Economic Geology, v. 78, no. 4, p. 664-674.
- Carder, K. L., Reinersman, P., Chen, R. F., Muller-Karger, F., Davis, C. O., and Hamilton M. K., 1993: AVIRIS calibration and application in coastal oceanic environments: Remote Sensing of Environment, v. 44, nos. 2-3, p. 205 - 216.
- Carrère, V., and Conel, J., 1993, Recovery of atmospheric water vapor total column abundance from imaging spectrometer data around 940 nm - Sensitivity analysis and application to Airborne Visible/Infrared Imaging Spectrometer (AVIRIS) data: Remote Sensing of Environment, v. 44, nos. 2-3, p. 179 - 204.
- Clark, R. N., and Roush, T. L., 1984, Reflectance spectroscopy: Quantitative analysis techniques for remote sensing applications: Journal of Geophysical Research, v. 89, no. B7, pp. 6329-6340.
- Clark, R. N., King, T. V. V., Klejwa, M., and Swayze, G. A., 1990, High spectral resolution spectroscopy of minerals: Journal of Geophysical Research, v. 95, no. B8, p. 12653-12680.
- Clark, R. N., King, T. V. V., and Gorelick, N. S., 1987, Automatic continuum analysis of reflectance spectra: in Proceedings, Third AIS workshop, 2-4 June, 1987, JPL Publication 87-30, Jet Propulsion Laboratory, Pasadena, California, p. 138-142.
- Clark, R. N., Swayze, G. A., Gallagher, A., Gorelick, N., and Kruse, F. A., 1991, Mapping with imaging spectrometer data using the complete band shape least-squares algorithm simultaneously fit to multiple spectral features from multiple materials: in Proceedings, 3rd Airborne Visible/Infrared Imaging Spectrometer (AVIRIS) workshop, JPL Publication 91-28, p. 2-3.
- Collins, W. et al., 1983, Airborne biogeochemical mapping of hidden mineral deposits: Economic Geology, v. 78, p. 737-749.
- Crowley, J. K., 1993 Mapping playa evaporite mineral with AVIRIS data: A first report from Death Valley, California: Remote Sensing of Environment, v. 44, nos. 2-3, p. 337 - 356.

- Elvidge, C. D., 1988, Vegetation reflectance features in AVIRIS data: in Proceedings, International Symposium on Remote Sensing of Environment, Sixth Thematic Conference, "Remote Sensing for Exploration Geology", Houston, Tx, 16--19 May, 1988, Environmental Research Institute of Michigan, Ann Arbor, p. 169-182.
- Elvidge, C. D., Chen, Z., and Groeneveld, D. P., 1993, Detection of trace quantities of green vegetation in 1990 AVIRIS data: Remote Sensing of Environment, v. 44, nos. 2-3, p. 271 - 280.
- Feldman, S., and Taranik, J. V., 1988, Comparison of techniques for discriminating hydrothermal alteration minerals with Airborne Imaging spectrometer data: Remote Sensing of Environment, 24, 1, 67-83.
- Gamon, J. A., Field, C. B., Roberts, D. A., Ustin, S. L., and Valentini, R., 1993, Functional patterns in an annual grassland during and AVIRIS overflight: Remote Sensing of Environment, v. 44, nos. 2-3, p. 239 - 254.
- Gao B. and Goetz, A. F. H., 1990, Column atmospheric water vapor and vegetation liquid water retrievals from airborne imaging spectrometer data: Journal of Geophysical Research, v 95, no. D4, p. 3549-3564.
- Gao, B., Heidebrecht, K. B., and Goetz, A. G. H., 1993, Derivation of scaled surface reflectances from AVIRIS data: Remote Sensing of Environment, v. 44, nos. 2-3, p. 165-178.
- Goetz, A. F. H., Vane, G., Solomon, J. E., and Rock, B. N., 1985, Imaging spectrometry for earth remote sensing: Science, 228, 1147-1153.
- Green, A. A., and Craig, M. D., 1985, Analysis of aircraft spectrometer data with logarithmic residuals: in Proceedings, AIS workshop, 8-10 April, 1985, JPL Publication 85-41, Jet Propulsion Laboratory, Pasadena, California, p. 111-119.
- Green, R. O., 1991, Retrieval of reflectance from AVIRIS-measured radiance using a radiative transfer code: in Proceedings, 3rd Airborne Visible/Infrared Imaging Spectrometer (AVIRIS) workshop, JPL Publication 91-28, p. 200-210.
- Grove, C. I., Hook, S. J., and Paylor, E. D., Laboratory reflectance spectra of 160 minerals, 0.4 to 2.5 micrometers: JPL Publication 92-2.
- Hamilton, M. K., Davis, C. O., Rhea, W. J., Pilorz, S. H., and Carder, K. L., 1993, Estimating chlorophyll content and bathymetry of Lake Tahoe using AVIRIS data: Remote Sensing of Environment, v. 44, nos. 2-3, p. 217 - 230.
- Hook, S. J., and Rast, M., 1990, Mineralogic mapping using Airborne Visible/Infrared Imaging Spectrometer (AVIRIS) shortwave infrared (SWIR) data acquired over Cuprite, Nevada: in Proceedings, 2nd Airborne Visible/Infrared Imaging Spectrometer (AVIRIS) workshop, JPL Publication 90-54, p. 199-207.
- Kneisyz, F. X., Shettle, E. P., Abreau, L. W., Chetwynd, J. H., Anderson, G. P., Gallery, W. O., Selby, E. A., and Clough, S. A., 1988, Users guide to LOWTRAN 7, AFGL-TR-8-0177, Airforce Geophysics Laboratory, Bedford, MA.
- Kruse, F. A., Raines, G. L., and Watson, Kenneth, 1985, Analytical techniques for extracting geologic information from multichannel airborne spectroradiometer and airborne imaging spectrometer data: in Proceedings, International Symposium on Remote Sensing of Environment, Fourth Thematic Conference, "Remote Sensing for Exploration Geology", San Francisco, California, 1-4 April, 1985, p. 309-324.

- Kruse, F. A., 1988, Use of Airborne Imaging Spectrometer data to map minerals associated with hydrothermally altered rocks in the northern Grapevine Mountains, Nevada and California: Remote Sensing of Environment, v. 24, no. 1, pp. 31-51.
- Kruse, F. A., Kierein-Young, K. S., and Boardman, J. W., 1990, Mineral mapping at Cuprite, Nevada with a 63 channel imaging spectrometer: Photogrammetric Engineering and Remote Sensing, v. 56, no. 1, pp. 83-92.
- Kruse, F. A., Lefkoff, A. B., Boardman, J. B., Heidebrecht, K. B., Shapiro, A. T., Barloon, P. J., and Goetz, A. F. H., 1993, The Spectral Image Processing System (SIPS) - Interactive Visualization and Analysis of Imaging Spectrometer Data: Remote Sensing of Environment, Special issue on AVIRIS, May-June 1993, v. 44, p. 145 - 163.
- Kruse, F. A., Lefkoff, A. B., and Dietz, J. B., 1993, Expert System-Based Mineral Mapping in northern Death Valley, California/Nevada using the Airborne Visible/Infrared Imaging Spectrometer (AVIRIS): Remote Sensing of Environment, Special issue on AVIRIS, May-June 1993, v. 44, p. 309 - 336.
- Kruse, F. A., and Lefkoff, A. B., 1993, Knowledge-based geologic mapping with imaging spectrometers: Remote Sensing Reviews, Special Issue on NASA Innovative Research Program (IRP) results, v. 8, p. 3 - 28.
- Lang, H. R., Adams, S. L., Conel, J. E., McGuffie, B. A., Paylor, E. D., and Walker, R. E., 1987, Multispectral remote sensing as stratigraphic tool, Wind River Basin and Big Horn Basin areas, Wyoming: American Association of Petroleum Geologists Bulletin, 71, 4, 389-402.
- Nash, E. B., and Conel, J. E. (1974) Spectral reflectance systematics for mixtures of powdered hypersthene, labradorite, and ilmenite, Journal of Geophysical Research, 79, 1615-1621.
- Nolin, a. W., and Dozier, J., 1993, Estimating snow grain size using AVIRIS data: Remote Sensing of Environment, v. 44, nos. 2-3, p. 231 - 238.
- Malkmus, W., 1967, Random Lorentz band model with exponential-tailed S line intensity distribution function: J. Opt. Soc. Am., v 57, p. 323-329.
- Marsh, S. E., and McKeon, J. B., 1983, Integrated analysis of high-resolution field and airborne spectroradiometer data for alteration mapping: Economic Geology, v. 78, no. 4, p. 618-632.
- Mazer, A. S., Martin, M., Lee, M., and Solomon, J. E., 1988, Image processing software for imaging spectrometry data analysis: Remote Sensing of Environment, v. 24, no. 1, pp. 201-210.
- Milton, N. M., Collins, W., Chang, S. H., and Schmidt, R. G., 1983, Remote detection of metal anomalies on Pilot Mountain, N. Carolina: Economic Geology, v. 78, p. 605-617.
- Mustard, J. F., and Pieters, C. M., 1987, Abundance and distribution of ultramafic microbreccia in Moses Rock dike: Quantitative application of mapping spectroscopy: Journal of Geophysical Research, 92, B10, 10376-10390.
- Peterson, D. L., Aber, J. D., Matson, P. A., Card, D. H., Swanberg, N., Wessman, C., and Spanner, M., 1988, Remote sensing of forest canopy and leaf biochemical contents: Remote Sensing of Environment, v. 24, no. 1, pp. 85 - 108.
- Porter, W. M., and Enmark, H. T., 1987 A system overview of the Airborne Visible/Infrared Imaging Spectrometer (AVIRIS): in Proceedings, 31st Annual International Technical Symposium, Society of Photo-Optical Instrumentation Engineers, v. 834, pp. 22-31.

- Roberts, D. A., Yamaguchi, Y., and Lyon, R. J. P. (1985), Calibration of Airborne Imaging Spectrometer Data to percent reflectance using field spectral measurements: in Proceedings, Nineteenth International Symposium on Remote Sensing of Environment, Ann Arbor, Michigan, October 21-25, 1985.
- Singer, R. B., 1981, Near-infrared spectral reflectance of mineral mixtures: Systematic combinations of pyroxenes, olivine, and iron oxides: Journal of Geophysical Research, 86, 7967-7982.
- Singer, R. B., and McCord, T. B., 1979, Mars: Large scale mixing of bright and dark surface materials and implications for analysis of spectral reflectance: in Proceedings Lunar and Planetary Science Conference, 10th, p. 1835-1848.
- Tanre, D., Deroo, C., Duhaut, P., Herman, M., Morcrette, J. J., Perbos, J., and Deschamps, P. Y., 1986, Simulation of the Satellite Signal in the Solar Spectrum (5S), Users's Guide (U. S. T. de Lille, 59655 Villeneuve d'Ascq, France: Laboratoire d'Optique Atmospherique).
- Teillet, P. M., 1989, Surface reflectance retrieval using atmospheric correction algorithms: in Proceedings of IGARSS'89 and the 12th Canadian Symposium on Remote Sensing, Vancouver, Canada, p. 864-867.
- Torson, J. M. (1989), Interactive image cube visualization and analysis: in Proceedings, Chapel Hill Workshop on Volume Visualization, 18-19 May, 1989, University of North Carolina at Chapel Hill.
- Vane, Gregg, 1987, First results from the Airborne Visible/Infrared Imaging Spectrometer (AVIRIS): in Proceedings, 31st Annual International Technical Symposium, Society of Photo-Optical Instrumentation Engineers, v. 834, p. 166-174.
- Vane, G., 1985, High spectral resolution remote sensing of the earth, Sensors, V.2, p. 11-20.
- Yamaguchi, Yasushi, and Lyon, R. J. P., 1986, Identification of clay minerals by feature coding of near-infrared spectra: in Proceedings, International Symposium on Remote Sensing of Environment, Fifth Thematic Conference, "Remote Sensing for Exploration Geology", Reno, Nevada, 29 September- 2 October, 1986, Environmental Research Institute of Michigan, Ann Arbor, p. 627-636.
- Yuhas, R. H. and Goetz, A. F. H., 1993, Comparison of airborne (AVIRIS) and Spaceborne (TM) imagery data for discriminating among semi-arid landscape endmembers: in Proceedings, Ninth Thematic Conference on Geologic Remote Sensing, Environmental Research Institute of Michigan, Ann Arbor, MI., p. 503 - 511.

ISSSR TUTORIAL

SPECTRAL SENSORS AND DATA AVAILABILITY

Harlan L. McKim
U.S. Army Corps of Engineers
Cold Regions Research and Engineering Laboratory
Hanover, NH 03755-1290
(603) 646-4479

Data availability from present and future satellite and airborne sensor systems will be discussed at the ISSSR workshop. We will examine the aircraft availability, frequency of data acquisition, the volume of information obtained from the sensor and hardware systems, and software required to analyze, store and display data sets. The availability of both multispectral and hyperspectral systems will be displayed and discussed. Application of these data sets to assess environmental, water, and natural resource areas will be demonstrated.

Manuscript not available at time of printing. Please contact author for further information.

BLANK PAGE

OPENING SESSION

BLANK PAGE

CONFERENCE THEME

Walter E. Boge
U.S. Army Topographic Engineering Center

Good morning, ladies and gentlemen. It is both an honor and a pleasure to be here with you this morning at the opening session of the second International Symposium on Spectral Sensing Research (ISSSR).

About a year and a half ago, many of us attended the first ISSSR in Maui, Hawaii, which was aimed at gathering researchers world wide to present and exchange information on spectral phenomenology. The aftermath of that successful symposium was a pathway for using spectral sensor technology as a tool to better measure and understand the earth's environment. It also provided the venue for scientists, engineers, and technicians to use spectral sensing technology to protect the environment and help preserve the earth's natural resources.

I predict that this week's meeting in beautiful San Diego will be even more successful than the first. Our focus this year is on "Dual-Use" technology. From a U.S. Government perspective, dual-use means not only to we share emerging knowledge between the government and the private sector; it also means that the government deliberately works to develop technology that also has civil and commercial utility. Dual-use involves the establishment of partnerships of federal (military and civil) agencies with state and local governments, private enterprise, and other countries. With regard to ISSSR, I see the term dual-use to include the free exchange of technical information and development of interpersonal agreements among the participants. When entered into in a cooperative and professional manner, these partnerships become truly "win-win" enterprises.

A significant part of existing remote and spectral sensing technology was originally developed for military or national security objectives. Even before the onset of the space age in the late fifties, military developers were creating sensors that extended beyond the visible spectrum. Infra-Red and Side Looking RADAR are but two examples. These technological advances were eventually passed on to non-military users and provided a good portion of the framework in spectral sensing that we have today.

U.S. Government civil agencies such as NASA have also made major contributions to our knowledge and its application for measuring and monitoring natural and manmade phenomenon on, in, or near the earth's surface. This is also true of other governments around the world, who more and more are extending the envelope of our knowledge in spectral technology.

I believe that we now have a golden opportunity to get on the spectral sensor research road together--military, civil, and

private sectors--right from the start rather than after the fact. This applies not only to the U.S. or other countries working in isolation as has too often been the case in the past; but to international cooperative programs. The current U.S. administration has not only given the okay to proceed in this direction; but has mandated that it be done.

It is, therefore, important that you recognize the significance of the papers that will be presented in the next four days. Many of them were selected by our Technical Committee because they are oriented towards promoting and exploiting dual-use technologies. As you are well aware, the rate of knowledge growth in spectral sensing is exponential. It is up to us, the experts in the field, to work collectively to develop and guide this knowledge so that we all gain. Working together, we can develop, test, evaluate, and employ spectral sensors that can scan the environment in multiple wavelengths, and at variable spectral, spatial, and temporal resolutions. This year's conference will concentrate on this theme of international cooperation.

During the week, we will hear speakers from many different countries representing different perspectives on spectral technology. We will hear about new sensor systems capable of measuring hundreds of spectral bands with high spatial resolution. We will hear of sensors being developed to measure many atmospheric and ionospheric parameters and meteorological conditions. We will hear about commercial satellites being built today that will acquire imagery with resolution of one meter before the year 2000. And, we will hear about special purpose satellites being developed to provide unique data sets and coverage--both spectrally and spatially.

As these systems transition from theory to reality (no joke here), we, the community, must learn how to best utilize this enormous amount of data intelligently--and deal with technical and political issues of data storage and sharing, measurement standards, analysis algorithms, and the like. Each iota of spectral information from these sensors must be tagged and calibrated. We have to agree on standards in collection, analysis, processing, and display. And, these standards need to be applied in design and building of these systems, not after the fact.

To my knowledge, there are not many collection and processing systems that meet the criteria I have just outlined. And, in my opinion, it is in this area where we can make the most progress in the next few days--but, only if we work in a collaborative dual-use mode.

I said earlier that spectral technology is growing exponentially and will provide us leap ahead abilities to detect,

identify, locate, and record many of the entities in our environment. This week, we will address this technology in detail and from any different perspectives. Let us use this forum to recognize the synergistic potential of communicating and cooperating together to enhance our overall knowledge in spectral science.

I thank you very much for your time and sincerely wish you all have a very successful symposium.

REMOTE SENSING: AN AUSTRALIAN PERSPECTIVE ON OPPORTUNITIES AND CHALLENGES

John A. Richards

Department of Electrical Engineering
University College
The University of New South Wales
Australian Defence Force Academy
CANBERRA ACT 2600
AUSTRALIA

1. INTRODUCTION

This paper takes a largely non-technical view of Australia's remote sensing activities concentrating on matters of policy and organisation. Its purpose is to provide summary information on the nature of the technology in our country and to highlight current challenges. Such a coverage is appropriate from two points of view. First, the newly established Australian Space Council has recently set its priorities for remote sensing for the next five years. Secondly, it is expected that ISSSR in 1995 will be held in Australia, so that it is useful to provide a national perspective in preparation for that event.

The paper is structured around five key points.

First, the national context just mentioned is developed so that the nature of remote sensing in Australia can be understood in preparation for what is to follow in the remainder of the paper. Included in this is a comment on those US space programs in which Australians have participated.

Thirdly, and perhaps most importantly, some of the impediments that have been identified to the widespread adoption of remote sensing for *operational* purposes in Australia are discussed. In all likelihood some of these impediments are common with most other nations and account, particularly, for the poor uptake of the technology in the renewable resources sector. Other countries possibly share the same problems - hopefully there will be a commonality in identifiable solutions.

The Australian Space Council, its mission, objectives and programs are then discussed, followed by a commentary on its recommendations in relation to earth observation - recommendations designed to secure operational benefits from remote sensing and to overcome the impediments identified.

2. MILESTONES IN AUSTRALIAN REMOTE SENSING

Australia has been involved in satellite remote sensing since the launch of Landsat 1. Early work was largely focussed on applications in the mining industry, although some of the initial research also looked at the suitability of Landsat MSS technology for photogrammetric purposes as well. We have moved now to a position where the technology is widely applied over many fields, but those in mining still dominate.

For the first six years Australia was, with much of the world, dependent on EROS Data Center products and the on-board storage capacity of the earlier Landsats. But in 1978 the then Australian Landsat Station was established - later renamed the Australian Centre for Remote Sensing (ACRES). It was upgraded in 1985 to install X-band down link capacity for Landsat TM and SPOT reception, and was upgraded again in 1991 and 1992 for European ERS-1 and Japanese JERS-1 radar satellite data reception and processing.

Apart from aircraft and weather programs ACRES is Australia's single source of satellite remote sensing data.

During the last two decades a number of specific-purpose organisations have been set up in Australia - four quite different types are discussed here, although clearly there are others as well.

In 1981, the Centre for Remote Sensing at the University of New South Wales was established as the first such university centre in Australia. It was modelled to an extent on the very successful Laboratory for Applications of Remote Sensing (LARS) at Purdue University. Since then a number of other strongly focussed university centres have appeared.

In 1984, the CSIRO (the Australian Government's R & D Agency) set up its Office of Space Science and Applications (COSSA) as a vehicle for coordinating space-related activities over the very many relevant divisions of that large and diverse organisation. COSSA also acts to develop space policy for the CSIRO.

A very innovative development came to fruition in 1993, in the formation of the Leeuwin Centre - a cooperative venture in the State of Western Australia, involving CSIRO Divisions, tertiary education institutions, State Government agencies and industry, all brought together in a special purpose building. The synergy so created is paying dividends even in the short time since its formation.

Just this year the first operational X-band remote sensing data reception facility outside the Federal Government came on line, in the southernmost state of Tasmania. The Tasmanian Earth Resources Satellite Station (TERSS) represents the culmination of many years of development by the CSIRO Division of Oceanography, with support from the National Space Program, to establish a facility with coverage to the south of Australia, over the Southern Ocean and extending to the coast of Antarctica.

3. PARTICIPATION IN US SPACE PROGRAMS

Australian Government, R & D agencies and universities have participated in many major US satellite remote sensing programs and aircraft missions, as well as in programs in Europe and Japan.

Those earth surface activities Australia has taken part in have extended from the early ERTS-1 (Landsat 1) science program through the Shuttle Imaging Radar missions and, in the future, will include the Mission to Planet Earth.

The NASA C-130 was deployed in Australia in 1985 to carry out an extensive campaign over many different applications using the TIMS, TMS (NS001) and AIS instruments, while just last year the NASA DC-8 was in Australia carrying the JPL multifrequency, multipolarisation radar, involving 65 experimental sites over its two week mission. Intended outcomes from this cooperation will include joint CSIRO-NASA radar analysis software, a joint CSIRO-NASA workshop and a possible follow-up mission in 1995 [1].

Cooperative programs such as these are seen as essential elements in Australia's national remote sensing agenda. Substantial funding is invested in them by Australian organisations, but they have many benefits. First, they provide significant opportunities for applications personnel, scientists and researchers to benefit from technologies not ordinarily available in Australia. Secondly, they act to form strategic alliances between US and Australian colleagues and their agencies.

4. AUSTRALIAN REMOTE SENSING RESEARCH

To illustrate something of the research being carried out in Australia on imaging spectrometer data processing, reference will be restricted just to work being undertaken at the University of New South Wales. This should be regarded only as a small sample of the interests of many of Australia's research agencies. Of particular importance is work also being carried out at the CSIRO Division of Exploration and Mining addressed to applications of imaging spectrometry in the mining industry.

Much of our work at the University of New South Wales has been based on exploiting the sparseness properties of the correlation and thus covariance matrix of the data from instruments such as AVIRIS. This has led efficient binary codes for use in library searching [2] and to streamlined procedures for applying traditional image processing methods such as maximum likelihood classification and principal components analysis [3,4].

While our work, and that at the CSIRO, addresses image interpretation and handling issues, several imaging spectrometers are planned for design and construction in Australia in the coming years, with one focussed specifically on the need to map surficial cover.

5. CHARACTERISING AUSTRALIAN REMOTE SENSING

Even with such a brief overview of Australian remote sensing activities, it is possible nevertheless to characterise the nature of the current Australian remote sensing scene.

Australia doesn't manufacture satellites, although it was in fact the third nation, after the former Soviet Union and the United States, to launch a satellite. WRESAT was launched in 1967 by the then Weapons Research Establishment (now the Defence Science and Technology Organisation).

Australia doesn't manufacture rockets nor does it at present provide launches, although launch facilities were provided for Britain and Europe in the 1950s, 1960s and early 1970s at Woomera in South Australia. It is possible that the Woomera launch facility could be made operational again, but for the present it does not represent a cornerstone of Australian space activity.

Thus Australia is not at the "big" technology end of space, although it is involved in some instrumentation programs. Rather Australia is best characterised as a nation of *data users* in remote sensing.

Unfortunately, however, some two decades after our entry into the business of satellite remote sensing the number of operational agencies making regular use of satellite and aircraft remote sensing is disappointingly small. In a country as ideally suited to remote sensing as Australia, with its large land mass, concentrated population centres and extensive coastal economic zone, one must question why this is the case and why there is not a vibrant value adding sector servicing private and government needs.

There are several reasons why we must be properly concerned about the current circumstances. First, Australia spends \$700M per annum on space goods and services, covering communications technology, meteorology and remote sensing. Secondly, it is largely dependent on overseas space programs. Although Australia has its own communications satellites, it has no weather or remote sensing satellites.

Against these however, is the fact that Australia has a highly educated and skilled workforce in all the appropriate areas for exploiting earth observation technologies, and of course their integration into GIS systems.

Without doing something about a less optimal operational penetration of the technology into the public and private sectors Australia risks losing the full range of commercial, economic and social benefits to be gained from earth observation technologies.

To improve the penetration of earth observation technology into operational strategies it is important to understand those factors that have impeded uptake of the technology.

First, adoption of the technology has been poor in those sectors that could benefit most from it. Not only is this the result of entrenched traditional attitudes, but those responsible for promoting the technology have somehow missed the mark - possibly because of ineffective awareness and training programs. Certainly Australia has excellent formal education schemes in the universities but it may have missed the opportunity to expose the technology to end users in a way that is strongly focussed on their needs.

Secondly, data delivery has been a major impediment - possibly *the* major impediment - both in terms of cost and quantity. Purchase of full Landsat scenes at several thousand dollars each makes little sense to the small land owner or Local Government Authority, particularly when frequent *multitemporal* coverage is required.

Thirdly, Australian earth observation involvement has been very much of the nature of a technology driven program, rather than in response to identified market needs. We have done very little by way of market assessment and development, both in relation to domestic and international opportunities.

Finally, our user-government liaison committees of the past have been too oriented to public sector applications, the relevance of which must now be brought into question. We are now moving to the stage where private sector users must be given higher profile in providing advice to government.

6. THE AUSTRALIAN SPACE COUNCIL

Having so identified the problems, a way forward must be determined. What steps should Australia take to obviate the inhibitors and risks to the adoption of remote sensing technologies for operational strategies in support of economic and commercial benefits? This is where the establishment of the Australian Space Council is relevant, since its programs are designed in part to meet this need.

6.1 Formation and Mission

In 1992 the Australian Federal Government undertook a major review of Australia's National Space Program [5]. The review looked at past performances and identifiable needs; a companion report also considered cost-effectiveness issues [6]. A major recommendation from the primary review was for the establishment of the Australian Space Council. The Council was set up informally in 1993, but only recently imbedded in Federal Legislation. It is a high level body having 14 members consisting of Deputy Secretaries of Federal Government Departments, senior industry members, academics, a CSIRO Institute Director, an Independent Chairman and the Executive Director of the Australian Space Office (which is the administrative organisation responsible for implementing and supporting the Integrated National Space Program).

The Mission of the Australian Space Council and its objectives are shown in Table 1. In exercising its objectives the Minister of State has asked Council to apply itself to the preparation of a living (or rolling) five year plan for space activities in Australia. The first version of the plan has now been prepared and is with the Minister, before being released publicly.

Table 1. The Australian Space Council

MISSION:

To secure for Australia net benefits from the development and use of space related science, technology and industry.

OBJECTIVES:

To promote activities that make a cost-effective contribution to the public good.

To promote the development of space-related industries, based on comparative and competitive advantages.

To support government international policy objectives through space activities.

To foster space related research.

To develop an appreciation, by client groups and the public, of the Integrated National Space Program and the rationale, content and implementation of the Five Year Plan.

To develop the fundamental material for the Plan, Council established four working groups, chosen to reflect those fields assessed as offering the greatest opportunities for deriving economic and commercial benefits from space technology. Three (Earth Observation, Communications, Launch Services) are of an applied nature and one (Space Science) deals with more fundamental material.

In relation to launch services it should be noted that Australia has strategic geographical advantages for launch, particularly for light satellites. To the north of our country there are several low latitude sites suitable for equatorial launch services, while at Woomera in South Australia, substantial infrastructure is already in place that could readily be supplemented to allow polar launches.

The remainder of this treatment concentrates on the Earth Observation working group, since its work bears directly on the interests of ISSSR.

6.2 Recommendations for Earth Observation

The central recommendation in relation to earth observation is to strengthen Australia's value adding commercial sector - ie the consultant industry that makes a business out of selling goods and services that have substantial value added to them beyond the purchase price of the raw satellite data.

While this recommendation is aimed first at developing value adding opportunities, it is seen also as an essential precursor to effective future support for public good applications and for future technology developments.

There are four major enabling factors that need to put be in place to stimulate development of value adding activities, as depicted in Figure 1.

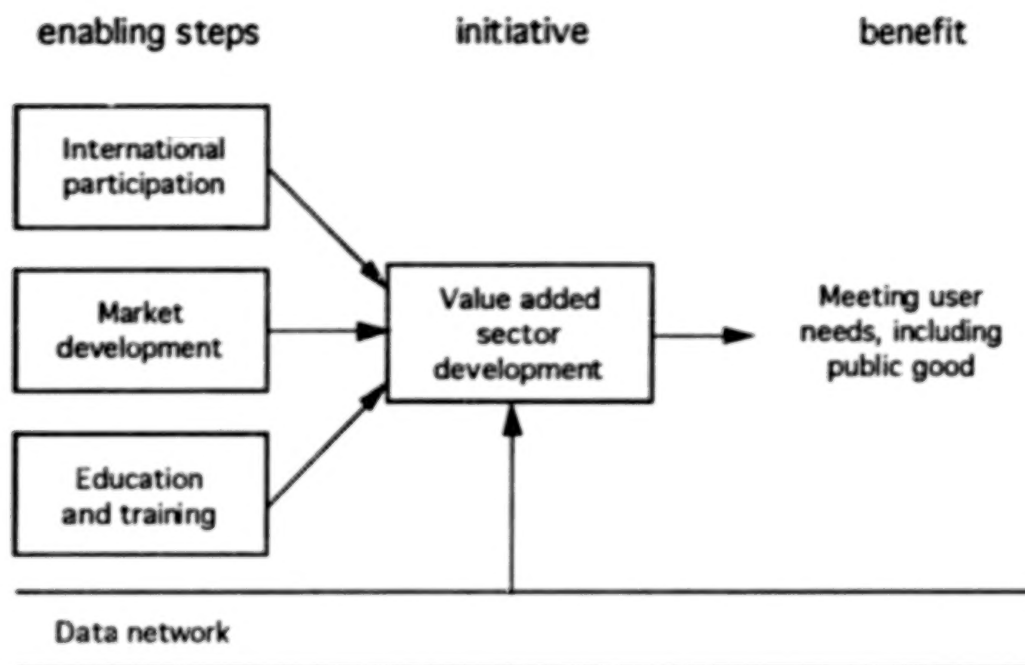


Figure 1. Recommendations for developing Australia's earth observation value adding sector

First, market opportunities must be identified, and strategies put in place for developing and exploiting the market. Australia has excellent fundamental knowledge and application skills. Additionally, domestically and in the region there are major assessed markets for value added remote sensing products and services. The two have to be bridged to enable the commercial sector to grow.

It is pointless expending resources on market development if, in the short term, access to data is not secured. Given that the operational data Australia uses is largely acquired by overseas agencies we must confirm our international standing so that we can have assurance of supply and some influence on data policies. In other words we must be seen to be contributing genuinely to international needs. Two aspects are important: first, Australia must maintain a presence in international planning and policy bodies such as CEOS (Committee on Earth Observation Satellites) and ESA. We have already and plan to maintain active memberships in both. Secondly, we must remain a supplier of instrumentation to international spacecraft so that we are seen to be part of the group of data providing nations. Through a number of historical ties, our major efforts of recent times have been participation in the Along Track Scanning Radiometer and its later variants. These are infrared scanners, carried currently on ERS-1. Subsequently they will contribute to ERS-2 and ENVISAT.

Thirdly, we must improve the penetration of the technology into the user sectors. We can only do this effectively if we adopt a "needs focussed" education and training strategy. If we are concerned about the lack of uptake of fairly simple technologies such as are offered by Landsat and SPOT, we must be doubly concerned about the more complicated technologies such as imaging radar and imaging spectrometry. Educating the user sector is thus of increasing importance and will be one way of opening up markets for products and services.

Finally and critically, we must address the data distribution issue, and particularly the constraints of current data delivery by magnetic or optical media.

We now have available the technology to deliver data electronically and, provided it is available in geocoded form, this would also allow data to be purchased in quantities "as required" by particular applications. The local government agency or small landowner, for example, would then be able to purchase say 10 km x 10 km at a fraction of the price now paid for full scenes, even after premiums have been added to reflect the higher costs that might be associated with data handling at the supplier end.

Of course, electronic delivery should not be restricted just to satellite data but to all the spatial and other data types (even spectral libraries) that are used by resource managers in decision making. This suggests then an arrangement such as that shown in Figure 2. The Australian Space Council believes that there could be a commercial opportunity in providing this service based on the Public Switched Telecommunications Network. The owner of the service would provide the directory function (on a fee for service basis) and could derive revenue through tariffs added to data transfers.

With such an arrangement there would be benefits that go beyond ease of data delivery and pricing. For example if pricing can be structured so that users would find it uneconomical to hold their own archives, the expensive task of data maintenance would remain with the agencies best equipped to carry out that maintenance - ie the data gatherers themselves. Further, the complete system would operate as a subscriber based GIS, working alongside any other electronically delivered information service on the public common carrier telecommunications network.

In this telecommunications-linked geographically distributed GIS, the need for substantial amounts of local storage is replaced by telecommunications channels to the data suppliers, in which the data suppliers themselves take full responsibility for data maintenance.

We anticipate that a full, public subscriber spatial information management system to be possible under such an arrangement, in which the value adding companies can also make available their derived products to end users over the network.

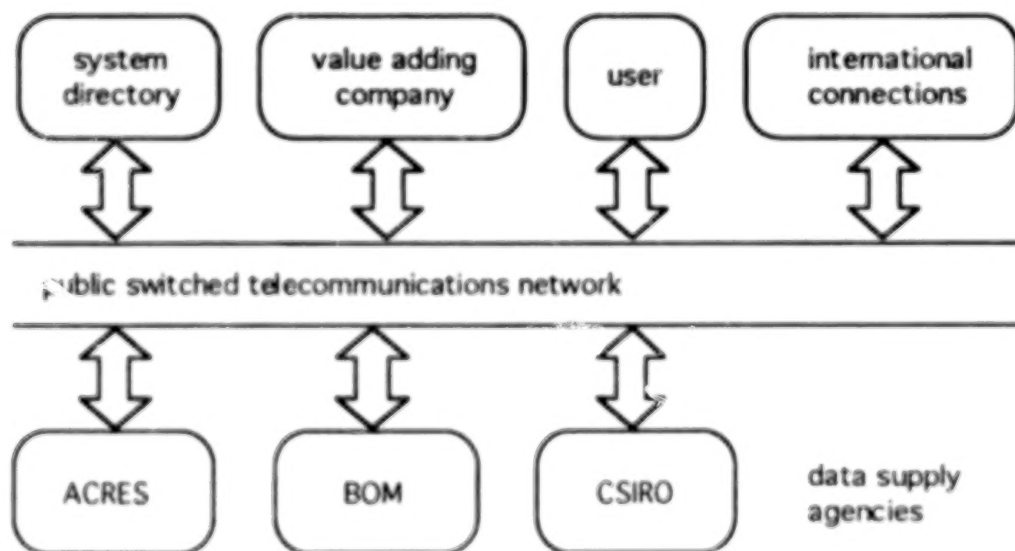


Figure 2. Proposed Australian Earth Observation Network

7. CONCLUDING REMARKS

The involvement of a nation like Australia, in a space program such as remote sensing can be represented very effectively in the form of a vertical market diagram such as that shown in Figure 3, taken from an Australian Space Council report. Moving down the

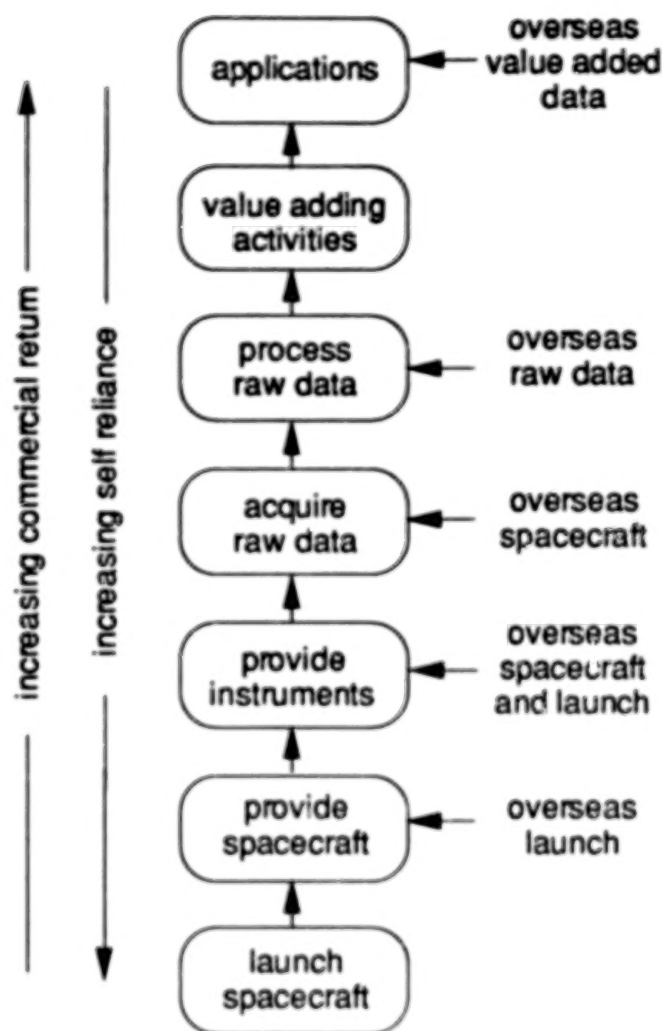


Figure 3. Commercial value and self reliance in a space industry

which to exploit the products of newer instruments. Beyond that it is possible we may look towards platform development, but again that development must be based on needs that have been identified by commercial and public sector users.

Our new space policy direction in Australia is very much "needs focussed" rather than being technology driven. To this extent we are looking to those activities that suggest commercial, economic or social benefits, and to partnerships with other countries so that we can make worthwhile contributions to the global need.

8. REFERENCES

1. A.K. Milne, I.J. Tapley and J.L. Smith, AirSAR Downunder: Report and Preliminary Results of the September 1993 Australian Mission. *Seventh Australasian Remote Sensing Conference*, Melbourne, 1-4 March 1994, pp. 199-204.
2. X. Jia & J.A. Richards, Binary coding of imaging spectrometry data for fast spectral matching and classification. *Remote Sensing of Environment*, 43, pp. 47-53, 1993.

diagram corresponds to increasing a nation's self reliance in matters of space technology, while moving upwards is consistent with improved commercial returns.

The current recommendations of the Australian Space Council are designed to exploit the high return, top end of that market, and thus secure the public and commercial end-user sectors. For the future however, Australia must move down the diagram to improve security of our program, noting the fragility of depending, in the longer term, on overseas supply of data.

We will seek to explore further satellite instrumentation development, although that should not be done in isolation. This is why it is so important to consolidate the value added sector first - so that we have proper guidance on the choice of instruments and the specification of their characteristics that match identified user needs, and so that we have a base from

3. X. Jia & J.A. Richards, Efficient maximum likelihood classification for imaging spectrometer data sets. accepted for publication in *IEEE Trans on Geoscience and Remote Sensing*.
4. X. Jia & J.A. Richards, Efficient hyperspectral remote sensing image display and classification using segmented principal components transformation. *Seventh Australasian Remote Sensing Conference*, Melbourne, 1-4 March, 1994, pp. 351-358.
5. Department of Industry Technology and Commerce, *An Integrated National Space Program*. Report by the Expert Panel, Australian Space Office, Canberra, 1992.
6. Bureau of Industry Economics, An Economic Evaluation of the National Space Program. *Bureau of Industry Economics Research Report 43*, Commonwealth of Australia, 1992.

CORRELATION-INDUCED SPECTRAL CHANGES

Emil Wolf

University of Rochester, Rochester, NY 14627, USA

This paper presents a general review of a rapidly developing new field of statistical optics, with special relevance to spectroscopy.

Traditional spectroscopy is concerned with radiation from sources which are essentially spatially incoherent. Since the invention of the laser in 1960, spectroscopy of radiation from sources which are spatially highly coherent have also been gradually developed. From the statistical point of view these two kinds of sources represent extreme cases. In recent years sources have been produced whose statistical properties are not yet fully understood, (e.g. undulators and soft x-ray lasers), but some of them are known to be spatially neither fully coherent nor fully incoherent, i.e. they are partially coherent (Kim, K.-Je, 1986, Trebes *et al.* 1993). Moreover, it is known that partially coherent secondary sources may be produced even from spatially incoherent sources by the process of propagation (Born and Wolf, 1980).

In a paper published some years ago (Wolf, 1986) it was shown that, in general, the spectrum of radiation from a partially coherent source may change on propagation, even in free space. For example, the spectral lines may undergo shifts, broadening or narrowing and new lines may be created and some may be suppressed. These predictions have been verified by a number of laboratory experiments (cf. Wolf, 1991, 1992, 1993, Kandpal *et al.* 1994). Similar effects have also been shown to exist when light is scattered by a random medium whose response function is suitably correlated at pairs of space-time points. More than 100 papers on correlation-induced spectral changes have been published by now. This effect has potential applications to remote sensing. In particular the changes in the spectrum of radiation obtained by superposing partially correlated beams may be

BLANK PAGE

used to obtain information about the source of the radiation and about some of the physical properties of scattering media. Recently a new method was proposed based on this effect, for determining small angular separation of distant objects from spectral measurements with an interferometer which has a fixed baseline (James *et al.*, submitted).

ACKNOWLEDGMENT

Some of the research described in this paper was supported by the Army Research Office under the University Research Initiative Program, by the National Science Foundation and by the New York State Science and Technology Foundation.

REFERENCES

- Born, M. and Wolf, E., 1980, *Principles of Optics*, Pergamon Press, Oxford, 6th ed., Sec. 10.4.2.
- James, D. F. V., Kandpal, H. C. and Wolf, E. "A new method for determining the angular separation of double stars", submitted to *Astrophys. J.*
- Kandpal, H. C., Vaishya, J. S. and Joshi, K. C., 1994, *Opt. Eng.* **33**, 6.
- Kim, K.-Je, 1986, *Nuclear Instr. and Meth. in Phys. Res.* **A246**, 71.
- Trebes, J. E., Nugent, K. A., Mrowska, S., London, R. A., Barbee, T. W., Carter, M. R., Koch, J. A., MacGowan, B. J., Matthews, D. L., da Silva, L. B., Stone, G. F. and Feit, M. D., 1993, *Phys. Rev. Lett.* **68**, 588.
- Wolf, E., 1986, *Phys. Rev. Lett.* **56**, 1370.
- Wolf, E., 1994. In *International Trends in Optics*, J. W. Goodman (Ed.), Academic Press, 221.

Wolf, E., 1992. In *Proc. Symp. Huygens' Principle 1690 - 1990 - Theory and Applications*, H. Blok, H. A. Ferwerda and H. K. Kuiken (Eds.), North-Holland, Amsterdam, 113.

Wolf, E. 1993. In *Recent Developments in Quantum Optics*, R. Inguva (Ed.), Plenum, New York, 355.

BLANK PAGE

SESSION I
DATA COLLECTION

BLANK PAGE

MAPPING AND THE VERIFICATION OF TERRESTRIAL HYPERSPECTRAL INFORMATION

John E. Estes¹
Senior Visiting Scientist
NASA/USGS
Reston, VA 22092

ABSTRACT

Hyperspectral information, to be adequately verified, require detailed information on the type and condition of components of our environment. Baselines against which to evaluate the performance of various sensor bands and processing combinations for extracting features from given landscapes. Such baseline data often exist in spatial or map format. While maps can be employed to aid in verifying the information extraction potential of hyperspectral data; hyperspectral data can be employed to create map feature information.

Adequate maps do not exist for many areas of the world today. Depending upon scale, thematic content, and timeliness this is equally true in both developed and developing countries. Many people find this hard to believe. We assume that the map we require exists, contains the information we seek, is accurate, and up-to-date. Yet, much of today's map data are, for many purposes, too outdated. Reasons for our lack of current map data are varied, complex, and include issues related to: national security, national sovereignty, institutional infrastructures, public sector private sector competition, international copyright agreements, and even religion. More resource must be directed at the development of innovative ways to create and update map data. Hyperspectral imaging and associated processing technique hold some promise in this area. What is required is the resources and institutional support to address the use of maps for verifying hyperspectral data, and the use of hyperspectral data for mapping in a meaningful way.

1. INTRODUCTION

Hyperspectral information, to be adequately verified, require detailed information on the type and condition of components of our environment. Baselines, as you will, against which to evaluate the performance of various sensor bands and processing combinations for extracting features from given landscapes. Such baseline data often exist or are used in spatial or map format. In addition, while maps can be employed to aid in verifying the information extraction potential of hyperspectral data; hyperspectral data can also be employed to create map feature information.

There is a revolution going on today in the mapping sciences. A revolution that is, in effect, taking mapping from green eyeshades, scribe, and peelcoat into the digital realm of computers,

¹Support for this effort from both the University of California, Santa Barbara, NASA grant, NAGW 1743 and the Universities Space Research Association's, NAGW 3173.

geospatial analysis and Geographic Information Systems (GIS). This revolution is being driven by the need for improved information concerning the nature, rates, and areal extent of changes occurring in the world around us. Changes which cross and touch all levels of society. In addition to their use as "ground truth" in image analysis, maps depicting the spatial arrangement and areal extent of components of our global environment are important as we seek to improve: investments made by private enterprise, military operations, environmental planning, resources management, and public policy decision making. Yet, adequate maps do not exist for many areas of the world today. Depending upon scale, thematic content, and timeliness this is equally true in both developed and developing countries.

Many people find this hard to believe. We assume that the map we require exists, contains the information we seek, is accurate, and up-to-date. But, as soon as a map is made, or data about the earth is collected it is dated. Some mapped information is more perishable than others, e.g. continental outlines as opposed to forest clear cutting. The value of data is many times related to its currency. Yet, much of today's map data are, for many purposes, too outdated. Reasons for this lack of current map data are varied, complex, and include issues related to: national security, national sovereignty, institutional infrastructures, public sector and private sector competition, international copyright agreements, and even religion.

Now, more than ever, we need to break through the myths that surround mapping. Myths that perpetuate the notion that: the maps we need exist, are accessible, up-to-date, accurate, and inexpensive; mapping is easy; and, there is little research to do in the mapping sciences. We all need to become more aware that mapping is an important, complex, expensive, and time consuming task. A task that, we believe, we are not performing today in an acceptable fashion. We need to put more resource into research directed at innovative ways to create and update map data. Hyperspectral imaging and associated processing techniques hold some promise in this area. What is required is the resources and institutional support to address the use of maps for verifying hyperspectral data, and the use of hyperspectral data for mapping in a meaningful way.

The myth that the world is "well mapped" is perpetuated in a variety of subtle ways: from the road maps we use, to the atlases we possess. Just because people can use road maps to guide them from one place to another does not mean that those maps will accurately depict how many acres of agriculturally active land one will pass through. Nor will a road map or an atlas typically provide information on timber volumes, or how fast urban areas are gaining or losing population. The myth is further perpetuated by the material we see and read in news media and scientific literature concerning the state of various parts of the Earth System: declining forests, expanding deserts, or the loss of soil productivity and biological diversity. We may know how many acres of old growth forest existed in the Pacific Northwest, in say 1985 -- but we really need to know what the acreage of old growth forest is today. How much reliance can we place on any published figures? What are the current facts? The facts are: we often really do not know.

Do we as individuals need science quality spatial information for the land and coastal zone areas of the world? Most of us might waffle on our own specific need for this kind of data/information, or may only need such data for specific areas of interest to us. Do we as a nation need this kind of information? Most of us might say yes. Do we as a nation have this kind of information? Most of us might say yes. The right answer is, we do not currently have the types of map data we require for either the United States or the world at scales and accuracy and timeliness necessary to support optimum use in either tactical military or environmental

planning, resources management or in the public policy decision making process. Yet, decisions still get made. Decisions based often on inadequate, imperfect data. Results of such decisions can be seen all around us.

2. THE PROBLEM

With respect to the land surface of the globe there is currently no comprehensive, coordinated, operational science quality global measurement, mapping, monitoring, and modeling program in existence (Estes, et al. 1992). A key feature making this statement true is the inclusion of the word *mapping*. Today, no civil organization in the Federal Government of the United States has a global mapping charter; no civil agency globally has the resources, or the backing of its respective government, to aggressively develop a major, high resolution, science based global scale mapping effort. As I understand the current situation the facts are that:

- (1) Large scale, science-based datasets do not exist for most of the earth at the present time, even in highly developed countries;
- (2) Development of such datasets is labor intensive, in terms of both scientific and technical personnel and is, therefore, labor expensive;
- (3) Although such datasets could support a wide variety of useful applications specific to a given locale, no single use can generally justify the cost of their development;
- (4) In many developing countries, even well-understood environmental changes with local causes and effects, that in the aggregate may represent a global concern, often have very low priority with officials compared to such issues as food, health care, and safety of the people. Global change issues and environmental concerns are often treated as rumors from more fortunate neighbors;
- (5) In a number of countries, the high resolution datasets needed by the world community are classified and are not permitted to leave the country in any form. In some instances where such data are exchanged with "friendly" nations, restrictive agreements limit access to these data; and
- (6) Even in highly developed countries, where scientific understanding is widespread, it is often difficult to generate the political and financial support for the correction of widely recognized environmental problems (Mooneyhan, 1993).

In many developing countries even the most basic information related to resources and the environment do not exist. A second type of problem that complicates the acquisition of high resolution science quality datasets is the classification of certain data for "internal use" only. Some of the worst case examples of this particular problem are in countries where entire data archives have been lost or destroyed by actions during revolution, wars, and/or civil disturbances. Examples include: Cambodia; Laos; Afghanistan; Liberia; Angola; Chad; Uganda; and Somalia. Other examples are countries in which high resolution spatial (large scale map) information and almost all information relative to the physical and human environment has been under internal embargo for decades. These include large areas of the world that have been under communist

rule for many years, such as what was the former USSR, Bulgaria, Romania, North Korea, the People's Republic of China, and Cuba. While the situation with respect to some of these nations seems to be improving with recent changes, it could be decades before information whose reliability has been verified is available to the world community for global research and applications oriented studies.

There are still other countries that have high resolution spatial information and the freedom to release it, but simply choose not to share it with the international science community. Both India and Brazil have been in this category for a long time. Both now, however, seem to be relaxing their environmental data/information policies somewhat following the United Nations Conference on Environmental and Development (UNCED) meeting in Rio de Janeiro in 1992.

There also exist situations where a country is not constrained by either lack of resources or by data classification policies, but simply does not place high enough political priority on long term environmental investments to cause large scale, science quality, baseline datasets to be generated for general utility. Therefore, the information is not available to either indigenous environmental planners, scientists and/or resource managers who are concerned with managing change on a site, at a local or national scale, or the international science community, which is concerned with change on a regional, continental, or global scale. Most of the so called "developed countries" fall in this category. Here in the United States, as in most industrialized nations, large scale, site specific datasets are often generated for one-time studies or for the solution of a specific local problem. At present, very few of these datasets ever make their way into databases that can be accessed by the interested community at large. As a result, although much of an area may be covered, the coverage consists of data that is thematically incompatible both within a given theme or between themes, was compiled at different scales, or was collected in different time series. The result is that the datasets that cover the area cannot be combined for larger area studies or applications. In addition, because these data often reside in non-networked local databases (a map drawer in a planning agency or on the agency's tape rack) the data for all practical purposes are lost to the community. This is, in essence, the map equivalent of the scientific gray literature or worse.

Another trend affecting access to map data is the move by a number of nations to operate their mapping agencies on a full cost recovery basis. The cartographic coverage of the United States, produced by U.S. Geological Survey (USGS) National Mapping Division (NMD) is essentially provided at the marginal cost of filling a user request. The move towards full cost recovery by other nations is beginning to have an adverse effect on access to the map data they produce. Both developed and developing nation resource planning, management, environmental agencies, and the scientific and educational communities are finding it increasingly difficult to justify the costs associated with the systematic acquisition of map coverages at local to national scales, let alone regional, continental, or global. This situation appears of particular concern in areas that once relied on former colonial powers for their mapping needs.

As a result of all of this, more money continues to be spent on the generation of site and local scale datasets than might be needed to develop science quality baseline datasets for an entire country. The loss to the community, however, is far more than just the money. Many local projects with funding levels too low to produce their own datasets, are either abandoned or poorly done. The result is usually detrimental to the local environment and collectively to the global environment. In addition, large area studies (either regional or global) continue to suffer for the lack of high resolution information for: (1) baseline model development; (2) calibration

of remote measurements; and (3) verification of indices of change.

3. DISCUSSION

Science quality, global land surface cover maps are important for a number of reasons. If we are asked to maintain current global environmental conditions or, to look for subtle changes, it would seem logical that we would need a information on the areal extent of key components of the Earth System as a baseline. As the science community continues to take point measurements of key environmental parameters e.g. biomass, carbon loading, and albedo (CEES, 1992) there is a need to areally extrapolate these measurements to gain global predictions for specific cover type classes. Error terms associated with areal extent of global land-cover types today far exceed the errors in precision with which many land-related global change measurements are made. In addition, if point measurements of such parameters are to adequately represent the universe being sampled, then for some of these measured parameters areal extent and spatial distribution information is critical to derive meaningful sample designs. Yet, today, we appear primarily focused on the making of measurements not the refining of maps.

The author is not the only individual who recognize the lack of data as a major problem for "global" science. Eric Rodenburg in "Eyeless in GALA" (1992) writes: "Those who seek data on the condition of the world's environment are often shocked by the depth of ignorance they find." The authors of International Geosphere Biosphere Program's report, relating global land-use and land-cover change (Turner et al., 1993) state that: "At present we are unable to answer even the even the most basic questions..."

Today then, we find that specific information on the status of mapping the globe is scarce and found in widely scattered sources e.g. NASA, 1988; United Nations, 1990; CEES, 1992; Wolf and Wingham, 1992; Townshend (ed.), 1992. From these sources we learn that as of 1987 only 33.3 percent of the world's land surface area was covered by topographic maps at a scale larger than 1:25,000 (see Figure 1). Only 56.1 percent of the world's land surface is covered at scale larger than 1:50,000 and 58.9 percent at scales larger than 1:100,000 some 90.2 percent is covered at a scale of 1:250,000 (United Nations, 1990). Neither the currency nor the accuracy of this coverage is directly addressed. We are told, however, that as of 1968 only 7.7 percent of the world's land surface was covered at 1:25,000 or greater; 23.4 percent at 1:50,000; 38.2 percent at 1:100,000 and 81 percent at 1:250,000. So it appears that slow, steady progress is being made.

A survey of global digital evaluation data done by Wolf and Wingham (1992) resulted in the first "...global inventory of digital, elevation data stocks of known reliability." These authors conducted a survey that they report as "...accurate over 11 percent of the Earth's surface, and shows data held for 10 percent of the Earth's surface area." The authors go on to state that, "For 11 percent of the surface area of the Earth the status of data is known, for the remaining 89 percent the status is unknown" (Wolf and Wingham, 1992). If we take the potential for significant changes to occur over time, this already small number is reduced even further.

While a number of global scale thematic datasets have been developed for land cover, there is little agreement among primary sources and a distinct lack of information upon which to judge the accuracy of the data. While existing sources have proven to be "useful first order

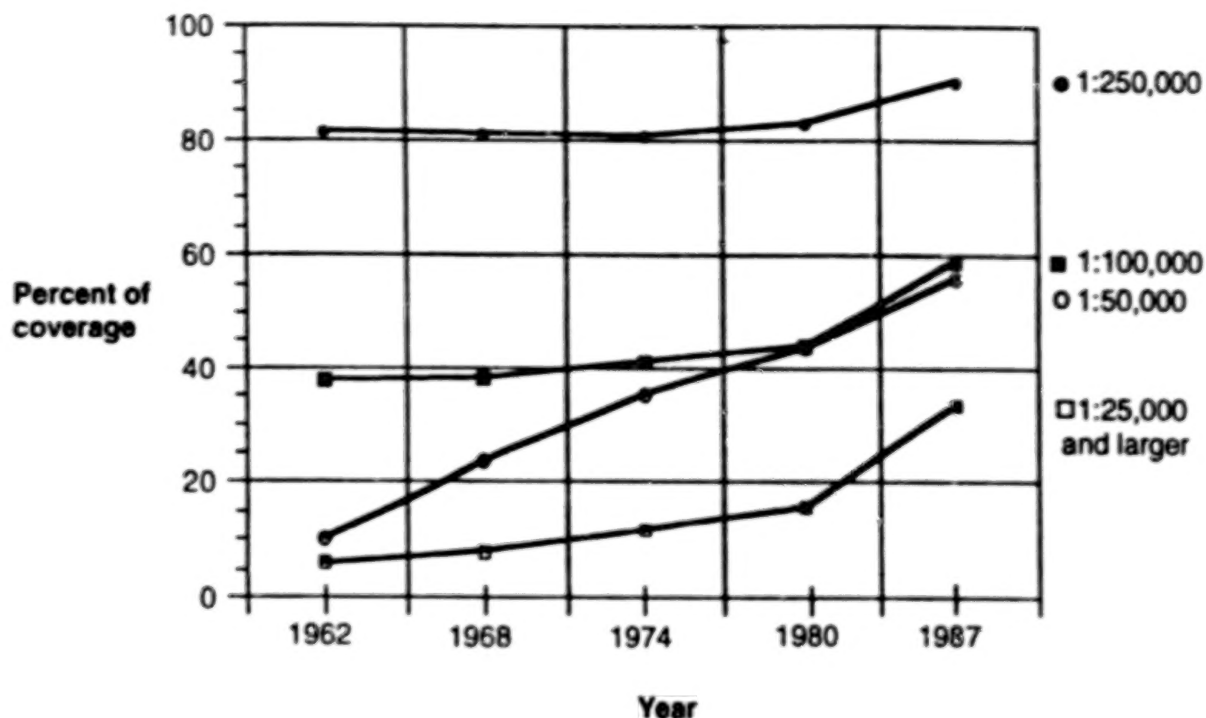


Figure 1: Percent total world land area mapped in each scale category, 1968-1987 (U.N.).

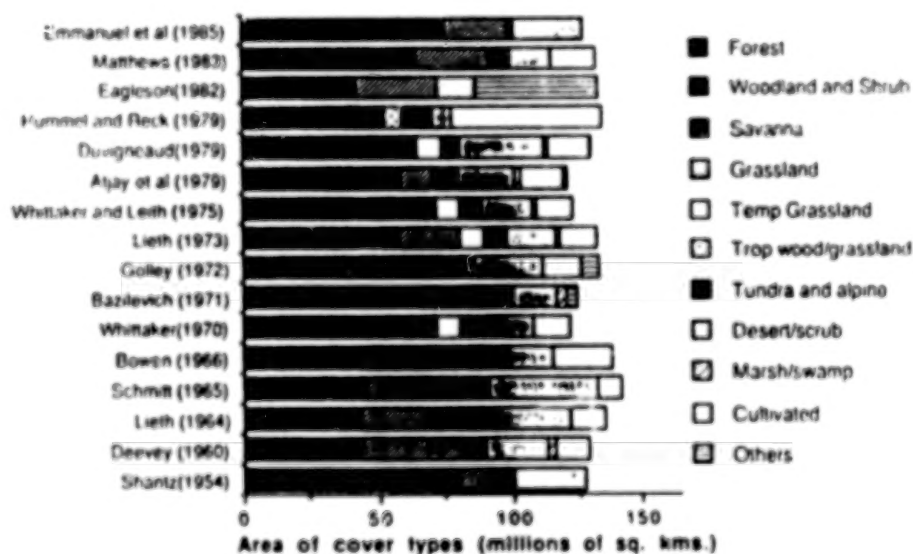


Fig. 2: Variations in estimates of global land cover classes based on calculations from cartographic sources. Differences in the total cover relate to the inclusion or exclusion of categories such as ice fields and deserts (Townshend, ed., 1992).

delineations of land cover" (Townshend, 1992), they are basically unreliable. As seen in Figure 2 from Townshend, 1992, comparisons of these global land cover classifications for the period 1954 to 1985 show variations of as much as 100 percent in major cover types (e.g. forests) among different sources. Townshend (1992) goes on to state that the "... shortcomings of these cartographic approaches suggests the strong need to develop land cover datasets derived from remotely sensed data."

Why aren't we doing more to establish global baselines now? There is some work going on here -- notably the International Geosphere Biosphere Program's (IGBP) global land cover project and the USGS EROS Data Center's (EDC) global land cover dataset activities. These are important, but they are in an early stage, not sufficiently funded nor staffed and the work is at a resolution too coarse for many site, local, and national level needs. What is required is agency and international support and coordination to produce and keep current high resolution science quality datasets. We have the tools. We have the technology. Yet, we continue to lack the ability to influence key policy makers to provide the resources and develop the infrastructure to accomplish the task.

We, as a nation, should not take comfort in the current state of our own mapping. By 1990 the National Mapping Division (NMD) of the USGS had completed the 1:24,000 scale topographic quadrangle map coverage of the United States, excluding Alaska. Yet, as of April 1993 only 14 percent of the area of the United States is covered with 1:24,000 scale maps that are less than 10 years old, while 9 percent of the United States is covered by 1:24,000 scale maps more than 40 years old. As of June 1993 only 11 percent of the United States is covered by digital base cartographic products, while there are variations in the coverage by specific data layers. At 1:100,000, 65 percent of the country is covered by digital cartographic products from the USGS, while 100 percent of the United States is covered at scales of 1:250,000.

This should not be read as an indictment of the NMD or other agencies such as the Environmental Protection Agency (EPA), or the U.S. Department of Agriculture (USDA), Soil Conservation Service (SCS). Those of us who have worked with NMD and personnel from other agencies involved in map production know that these people are trying to do their best within the constraints of a system where policy makers often does not truly appreciate the difficulties inherent in the cartographic process. It is also true that upper agency management appears, by and large, to either misunderstand or fails to comprehend the range of scientific, technical, managerial, and policy issues involved in mapping a country the size of the United States. A number of personnel in these agencies and organizations are doing what they can to dispel the mapping myths that are commonly held by their management, the Administration, and Congress but they are constrained by the system in which they operate. They need all of our help. I may disagree with some of the specific things Federal agencies, and others are trying to do, but at least they are trying. And some are trying very hard.

The United States has endorsed the concept of a national spatial data infrastructure (NSDI) National Research Council, 1993. We have a Federal Geographic Data Committee (FGDC) looking at ways to improve this infrastructure. FGDC discussing the concept of a national spatial data framework (FGDC, in preparation). A concept where within given standards various scales of maps can be nested to form a mosaic of multi-scalar digital, thematic coverages for the United States. Why aren't we, as a nation, pursuing the same tack on a global scale? It is equally important. The national security of our nation and the environmental well-being of all people argue that a global spatial data infrastructure and a world geographic data

committee should be established and that global baseline mapping at high resolution should be pursued. Why do we currently find ourselves in this position? Why, with all the technological advancements that we have made, do we still lack global baselines of large scale land surface information? The answers to these questions are not complex, and yet they are not simple either.

The production of maps is a complex and expensive task. Today the average cost to produce a 1:24,000-scale USGS quadrangle map is some \$40,000. There are some 55,000 of these maps in the conterminous United States and Hawaii. Some 1,000 man hours of labor are required in the production process. It costs the USGS some \$20,000 to completely revise a 1:250,000 scale map. So, mapping is not easy and it is not cheap. On the research side we could easily expend the budget of a national lab on a global mapping activity. I am not suggesting that a national lab do the job, I am only indicating what I believe is the relative magnitude of the resources required.

That there is considerable research left to do in mapping cannot be denied. We have not even come close to answering the basic questions in cartography associated with error/accuracy, scale or time to name a few (Estes et al., 1993). Such research is made all the more urgent by the rapidly expanding use of geographic information system (GIS) technology. GIS's are dependent on the accuracy and currency of the base cartographic products that form the foundation of each system's database. As use of these systems expands, more of us are coming to realize that the basic data we require is either not there, not current, or not in a form which we can readily utilize. GIS will increasingly drive the demand for larger scale resolution map products.

As previously stated, there is currently no civil United States Government agency with an international land related mapping charter. In the United States, the Defense Mapping Agency has the charter to map foreign nations for United States Government use. We are, therefore, largely dependent upon the military and/or intelligence communities of our own and other countries for access to large scale, science quality mapping products of foreign nations. Other nations are even more restrictive with respect to access to their maps than we are. We must remember that maps have multiple uses. Because one major use of maps relates to military operations, nations around the world treat maps as critical national security assets.

4. THE MAPPING PARADOX

There is a growing recognition that the environmental and/or economic health of nations are also factors affecting our national security. Indeed, the recently passed Land Remote Sensing Policy Act of 1992 (Public Law 102-555), Section 2. (1) finds: "The continuous collection and utilization of land remote sensing data from space are of major benefit in studying and understanding human impacts on the global environment, in managing the Earth's natural resources, in carrying out national security functions, and in planning and conducting many other activities of scientific, economic, and social importance." While an image from a satellite is not a map, it is important to note that mapping can and is being done from satellite systems. It is significant that P.L. 102-555 puts understanding of human impacts on our global environment and management of the Earth's natural resources on a par with national security. This, along with other items such as the Vice President's book "Earth in the Balance" (Gore, 1993), signal a growing awareness of the importance of understanding of the Earth as a system on the part

of the Administration and the Congress.

The economic and environmental health of all the world's nations are key factors affecting the national security of the United States. Better maps depicting a wide variety of themes are a fundamental requirement if we are to improve our economic well being, environmental quality, and management of our nation and the Earth as a whole. Yet, when the reasons for our lack of maps are examined carefully, other than non-existence we find that national security is the major factor inhibiting access to map products. Thus we have a paradox. We need large scale, science-based maps to: improve our understanding of the Earth as an integrated system; plan the wise use of the resources base of nations, and assess and monitor environmental quality at scales from local to global. Improvements in environmental quality and the economic well-being of nations around the world can enhance the quality of life and improve global economic conditions. These factors can have the effect of improving our national security. On the other hand, the widespread availability of large scale, science-based maps can represent a tactical military threat. It cannot be denied that maps have, and will continue to play, a key role in military operations. Yet, the problems associated with the management of the Earth as a global community are much more complex than those associated with specific military actions. Control of the flow of information has value in specific tactical military situations. This control to be effective must apply to maps in general as it is difficult to predict where advantages in specific knowledge will be significant. Such controls, however, represent restrictions that inhibit scientists, planners, and resource managers as they attempt to improve our general level of understanding of the global system; search for the environmental indices that facilitate early detection of global change, and try to model those environmental factors that can lead to a more sustainable future. So we have the mapping paradox -- the classic double edged sword. Maps used one way can improve national security, but used another way are a threat to national security.

One approach to this paradox might be that we should have such maps, but access to them should be restricted. This is the intelligence community model. The intelligence community wants to control access to data/information. There are good and valid reasons for this position. These reasons include the reduction in potential threats to the security of a nation by not allowing other nations, or in some cases even their own nationals, access to maps of sufficient quality to support terrorist or military operations. If we agree that information and the control of its flow to decision makers represents power, we have another reason for controlling access to information. We should be aware here that, from a decision maker's standpoint, the concept of plausible deniability applies in a very real way. If someone does not know, or cannot prove, that a decision-maker has access to a critical piece of knowledge when a decision is made, the decision maker has a better chance of not being held directly responsible for unintended or intended consequences that might flow from that decision. This concept has served rulers and politicians well throughout history.

Another major problem is how we deal with the reality that data/information concerning resources and our environment is a basis for power. The intelligence community knows data are power, but so also do international organizations, civil agencies, academics, industries, and non-governmental organizations. How do we convince the affected parties -- all of us -- that the problems associated with understanding the Earth as a system are so critical that we must break down the barriers to the development and flow of science quality information? Barriers to open the flow of data we face today inhibit our understanding of our global resource base and the factors that affect the quality of our environment. We need open access to map products on a

global scale.

5. CONCLUSIONS AND RECOMMENDATIONS

Governments engage in programs of systematic mapping in response to a wide variety of national, regional, and local needs -- military, administrative, socio-economic, and environmental. The Federal agencies I most often deal with are trying, within the limitations of their charters and their resources, to support the spatial analysis user community. Yet, when I compare the need with current activity, I conclude that changes must occur. We must need better map products in support of a wide variety of spatial data users. Agencies must be given expanded charters and significantly increased resources if we are to improve the quantity, quality, timeliness and spatial coverage of our mapping. Such maps can help to reduce our current ignorance regarding important local, regional, national and global conditions.

We must reinvigorate our national mapping community. A United States civil agency must be given the lead in global environmental mapping and the resources to do the job. I recommend that this agency be the National Mapping Division of the USGS. NMD should be chartered with the task of leading coordinated civil Federal research, development, and operational global mapping activities. This lead should be accomplished with advice from the National Academy of Science, professional societies, and should enlist the talents of personnel in other Federal agencies, academia, and private industry. This effort should also interface with and support, to the extent practical, international mapping efforts.

In addition, I believe we must:

- Begin to develop a set of specifications for baseline, country level, spatial information; and
- Encourage international donor and national scientific, mapping, and environmental agencies and non-governmental organizations to work towards the production of internally consistent, publicly available spatial datasets on at the country level.

Finally, every effort must be made to communicate to the public, politicians and policy makers, key agency personnel, the science community, and private industry that: (1) spatial information/maps currently needed to fully support military operations, environmental planning and resource management efforts are lacking for most parts of the world; (2) there is a great deal of science still to do in mapping spatially specific, environmental development and resource management information that deserves support; and, (3) improved mapping of baseline environmental information even with today's advanced technologies remains a difficult task.

In today's rapidly changing world, an improved understanding of the delicate balance between economic development and environmental security on both the local and global levels is essential. Can hyperspectral data help to improve our chances of achieving such a balance? Hyperspectral sensor systems and the data they generate are important for the future of mapping, in particular, and for increasing our understanding of the Earth system in general. Advanced pattern recognition algorithms operating on these data will provide the basic input to the maps of the future. Features extracted from hyperspectral data will permit us to update existing maps in a more timely fashion; and hopefully lead to improved decision making and a

safe, secure, and sustainable global environment.

ACKNOWLEDGEMENTS

The author wishes to acknowledge the support for this effort from both the University of California, Santa Barbara, NASA grant, NAGW 1743 and the Universities Space Research Association's, NAGW 3173. Major portions of this paper are taken directly from Estes and Mooneyhan (1994) listed in the references to this paper.

REFERENCES

- Committee on Earth and Environmental Sciences. "The U.S. Global Change Data and Information Management Program Plan," National Science Foundation, Washington, D.C., 94pgs.
- Estes, John E., November 1992. "Global Change: Remote Sensings' Challenge," paper presented at the 6th Australia-Asian Remote Sensing Conference, Wellington, New Zealand.
- Estes, John E., Jeffrey L. Star, and Frank W. Davis, 1993. "Remote Sensing and GIS Integration: Towards a Prioritized Research Agenda," paper presented at the 24 International Remote Sensing Symposium, Graz, Austria.
- Estes, J.E. and W. Mooneyhan, 1994. "Of Myths and Maps," Photogrammetric Engineering and Remote Sensing, Vol. 60, No. 5, (in press).
- Fox, Robert, and Ira Mehlman, 1992. "Crowding out the Future World Population Growth," U.S. Immigration, and "Pressures on National Resources," Federation for American Immigration Reform.
- Gore, Albert, 1992. "Earth in the Balance," Houghton Mifflin Company, Boston, Massachusetts, 407 p.
- Mooneyhan, D.W., August 1993. "International Science Data Set Acquisition for Early Detection," talk presented at Aspen Global Change Institute.
- Murakami, Hiroshi, 1993. "Global Mapping: Global Geographic Datasets for Environmental Studies," Proceedings International Workshop on Global GIS, Toyko, Japan, International Society for Photogrammetry and Remote Sensing, pp. 8-14.
- National Aeronautics and Space Administration Advisory Council (Earth System Science Committee), 1988. "Earth System Science: A Closer View," NASA, Washington, D.C. 208 pgs.
- National Research Council, 1993, "Towards a Coordinated Spatial Data Infrastructure for the Nation," National Academy Press, Washington, D.C., 171 pgs.

- Platt, R.R., April 1945. Official Topographic Maps, A World Index, Geographical Review, Vol. XXXV, No.2.
- Rodenburg, Eric, 1992. "Eyeless in GAIA, The State of Global Environmental Monitoring," World Resources Institute, 19 pgs.
- Townshend, John R.G., (ed.), 1992. "Improved Global Data for Land Applications a Proposal for a New High Resolution Data Set," Global Change IGBP Report No. 20, The International Geosphere-Biosphere Programme: A Study of Global Change (IGBP) of the International Council of Science Unions (ICSU), Stockholm.
- Turner II, B.L., R.H. Moss, and D.L. Skole, February 1993. "Relating Land-Use and Global Land-Cover Change: A Proposal for an IGBP-HDP Core Project," Global Change IGBP Report No. 24, HDP Report No. 5, Stockholm, by International Geosphere-Biosphere Programme: A Study of Global Change and Human Dimensions of Global Environmental Change Programme.
- United Nations, 1990, World Cartography, Vol. XX, New York.
- U.S. Global Change Research Program, 1993. "Our Changing Planet: The FY 1993 U.S. Global Change Research Program, Washington, D.C., Committee on Earth and Environmental Sciences, c/o National Science Foundation, Washington, D.C., 79 pgs.
- Wolf, Michael, and Duncan Wingham, 1992. "WP 4010: A Survey of the world's digital, elevation data," Dorking, Surrey, England, Department of Electronic and Electrical Engineering, University College, London, 87 pgs. John Power

HYDICE: A STATUS REPORT

L. J. Rickard, J. Fischer, and M. Anderson
Naval Research Laboratory
Washington, DC 20375-5351, USA

ABSTRACT

HYDICE (the Hyperspectral Digital Imagery Collection Experiment) is a dual-use program to build and operate an advanced airborne imaging spectrometer. Scheduled to be operating at the end of 1994, it will provide high quality hyperspectral data for use by a number of U.S. civil agencies, as well as DoD. The program focus is to determine the utility of such data for a wide range of applications, as well as for support of basic research. The current status of the system under construction and the plans for its operation are reviewed.

1. THE HYDICE PROGRAM

In hyperspectral remote sensing, the spectroscopic and imaging functions of remote sensing are combined into a single system. Thus, every image pixel contains a spectrum, and every spectral channel contains an image. This technique has been explored for more than a decade, with effort being roughly equally apportioned among addressing instrumental limitations, developing data handling techniques, and investigating applications. Sensitivity and calibration accuracy have been the primary limiting factors in the exploitation of the spectral domain, and spatial resolution has often limited the exploitation of the image domain. The richness of spectral phenomenology makes both collection and analysis very complex; one must traverse a huge volume of data to address even well constrained problems. Similarly, the number of environmental variables that must be controlled, modelled, or otherwise accounted for makes calibration laborious.

Thus, while the potential of hyperspectral remote sensing for a wide variety of practical applications has been long recognized, it still has been seen primarily as a research activity. However, the combination of this large body of research experience with recent advances in instrumentation and in analytical approaches may now make it possible to develop a truly operational hyperspectral system, suitable for use in a broad range of applications. The Hyperspectral Digital Imagery Collection Experiment (HYDICE) is an attempt to explore this possibility. By providing major improvements in spatial resolution, signal-to-noise ratio, and radiometric accuracy, we hope that HYDICE will provide a unique platform for determining the applicability of hyperspectral remote sensing to problems originating in civil and military applications, as well as basic research.

The HYDICE program is being conducted under the FY91 Congressional Dual-Use Initiative. The Dual-Use Initiative is intended to transition military technology to the civil sector, as represented by agencies of the U.S. Government. With the Naval Research Laboratory (NRL) acting as executive agent, hyperspectral imaging technology will be made available to experimenters from

- Department of Agriculture
- Environmental Protection Agency
- Department of Energy
- U. S. Geological Survey
- National Oceanic and Atmospheric Administration
- National Aeronautics and Space Administration
- U. S. Army Corps of Engineers
- Arms Control and Disarmament Agency

These experimenters will explore the utility of hyperspectral data for problems in agriculture, geology, ocean sciences, and the environment. NRL will itself pursue a scientific program emphasizing coastal ocean processes, ocean optics, and the marine atmospheric boundary layer; in addition, it will address applications of interest to naval operations in coastal waters, such as bathymetry and water clarity measurements.

It is important to recognize that the success of HYDICE as a dual-use program (if we may speak of success in advance of actually fielding the system) has been due in large part to early commitments by both civil and military partners. All of the civil agency partners agreed to support collection activity in FY 95, guaranteeing a user base to be identified as the transition target. They also provided up front support through the reduction of their anticipated needs into system requirements understandable to the DoD acquisition process. This was particularly important for HYDICE, as it was the breadth of these requirements that justified design decisions that would otherwise have been dismissed as unjustifiably costly. On the military side, the commitment to involve the civil users throughout the acquisition process - developing the Request for Proposals, reviewing the submitted proposals, interacting with the prime contractor at the design reviews and interim workshops, doing system analysis and modeling to assess particular design decisions, and developing the acceptance and characterization test plans - has meant agreeing to a management process more cumbersome than traditional DoD program management, and may arguably have resulted in a more costly system. Yet it has also produced a broad, highly supportive user community, and (we anticipate) a very capable instrument.

The HYDICE system is being constructed by Hughes Danbury Optical Systems (HDOS), with major subcontracts to Hughes Santa Barbara Research Center (SBRC) for the focal plane array, and to FCD, Inc. for the thermal control system. (Technical details are summarized below.) The system includes the sensor, its supporting mount, thermal control system, and electronics, and its data recording and basic post-flight reduction system. The system is currently scheduled to be delivered in the fall of 1994 to the Environmental Research Institute of Michigan (ERIM), who will integrate it into a CV-580 that is currently used for SAR observations. The instrumented aircraft is scheduled to conclude acceptance testing in December 1994. Additional system characterization tests will no doubt be required, but regular user observations should commence early in 1995. At that time, collection plans from each of the participating agencies will be melded into a set of collection missions. The HYDICE program basically provides the opportunities to use the system; thus, *e.g.*, each agency will be responsible for whatever *in situ* data collection is required to support its own experiments. The raw data will be radiometrically corrected and delivered to the experimenter, along with supporting data from the aircraft, including whatever data is required to perform geometric corrections. The HYDICE program will also provide a basic analysis kit suitable for standard image processing workstations.

It is important to understand that, while we have attempted to make significant improvements over existing systems, especially in the areas of spatial resolution, signal-to-noise ratio, and radiometric accuracy, the HYDICE program is not primarily a research program to build an imaging spectrometer. Rather, the instrument is being built to make possible the research program of using an advanced imaging spectrometer to evaluate the utility of the data and to determine how to build truly operational systems. We have thus made a number of design decisions that support reliable end-to-end operation by a wide range of users, some with little experience in airborne collection. The Dual Use Initiative only provides for a collection period of less than three years, and we must make efficient use of it. Accordingly, much of the HYDICE design reflects efforts to reduce risk in construction, integration, and operation.

2. THE HYDICE SYSTEM

An overview of the HYDICE instrument was presented at the April 1993 SPIE meeting (Rickard *et al.* 1994). In this paper, we shall only briefly summarize the basic elements, updating the system characteristics to reflect the subsequent changes.

One of the primary improvements over earlier systems is the adoption of a pushbroom, rather than whiskbroom, approach. This is the fundamental means for achieving our sensitivity advantage; the difference in dwell-time per pixel alone accounts for a potential factor of 11 advantage in predicted SNR over AVIRIS. In order to capitalize on this without proliferating subsystems, the instrument uses a biprism to accomplish spectral dispersion, and a novel focal plane array capable of operating over the full spectral range (400 to 2500 nm). We thus use a single optical path design, and so avoid the expense and alignment complexities of multiple spectrometers, enhance radiometric stability, and reduce polarization effects.

Installed in the CV-580 and operating at the nominal altitude of 6 km, the sensor will achieve a spatial resolution of 3m. The foreoptics have an 8.94 degree field of view, so that the spectrometer slit makes a swath of approximately 1 km on the ground. Because of the dispersion properties of the prism, the spectral resolution varies with wavelength; the average channel bandwidth is 10 nm. The optical subsystem is fairly compact: 32 inches tall, 18.3 inches across at maximum diameter, and 180 lb. It will rest on a Zeiss T-AS three-axis stabilization platform and will be covered with a thermal shroud to enable operation at a constant temperature of 10 °C. The instrument will operate only in the nadir-looking mode, although it can be tilted somewhat to account for aircraft angle of attack.

HYDICE will use a 320×210 element InSb array, with $40 \mu\text{m} \times 40 \mu\text{m}$ pixels. The array will be operated at 65 K, using a split cycle Stirling mechanical cooler. Good response is obtained over the full spectral range through the use of an improved passivation technique (to inhibit flashing) and a wedge-shaped anti-reflection coating (to optimize performance for each wavelength). The readout integrated circuit has been designed to have three regions of different saturation charge, enabling the system to meet simultaneously the requirements of high signal-to-noise over faint targets and linear performance over highly reflective targets (effectively to reflectances $\sim 85\%$). The output is digitized to 12 bits.

In characterizing the signal-to-noise performance, we have adopted a standard spectral radiance curve at the sensor aperture. This curve betrays our original interests in designing a system for maritime applications, as it assumes operation at 6 km altitude (3 m pixels) over a target of 5% reflectance (roughly corresponding to seawater) illuminated by the sun at a 60° zenith angle, and assuming a standard mid-latitude atmosphere. The resulting radiance ranges from $\sim 3.3 \mu\text{W cm}^{-2} \text{sr}^{-1} \text{nm}^{-1}$ in the blue to $\sim 0.1 \mu\text{W cm}^{-2} \text{sr}^{-1} \text{nm}^{-1}$ at $2 \mu\text{m}$. We must emphasize that these are very stressing assumptions. The predicted signal-to-noise for that assumed radiance curve is most easily characterized by average values for the three FPA regions:

- for 400 - 1000 nm, $\langle S/N \rangle = 244$;
- for 1000 - 1900 nm, $\langle S/N \rangle = 135$;
- for 1900 - 2500 nm, $\langle S/N \rangle = 37$.

It is particularly important that there is considerable SNR in the water vapor bands at 0.9 and $1.1 \mu\text{m}$. This should enable us to do high-quality retrievals of atmospheric water vapor over the ocean. Indeed, the combination of high SNR and high spectral resolution should enable us to obtain significant vertical resolution in water vapor distribution. In addition, sensitive fits to the blue-to-near-IR continuum will enable us to extract aerosol distributions.

A major emphasis in the design was the need to achieve high radiometric accuracy. At typical operating altitudes over the ocean, almost all of the observed signal originates in the atmosphere rather than from the water. In-flight calibration will be made through the full optical system (including aircraft window) by use of a 15 cm PTFE integrating sphere, with radiance stabilization and monitoring. Pre- and post-flight calibration will be done with an identical ground calibration unit. Baseline calibration will be done with a 30 cm barium sulphate integrating sphere. All three units will be calibrated against a precision radiometric source at HDOS, which is itself tied to standards at NPL and NIST. The final absolute spectral radiance calibration accuracy

will range from $\pm 0.9\%$ in the 400-1000 nm region, to $\pm 1.6\%$ in the 1000-1900 nm region, to $\pm 2.4\%$ in the 1900-2500 nm region.

ACKNOWLEDGEMENTS

The HYDICE Program would never have existed without the vision, energy, and managerial skill of its first program manager, LCDR Mark Landers. His unflagging commitment to hyperspectral remote sensing as the means to many ends was the force that brought together so many disparate communities into this one program.

We wish to thank the members of the HDOS HYDICE team, especially R. Basedow, P. Silvergate, E. Zalewski, W. Rappoport, R. Rockwell, D. Rosenberg, K. Shu, and R. Whittlesey. J. Colwell, L. Watts, W. Stoner, and W. Aldritch at SAIC contributed material to the program and system descriptions above. We wish to thank T. Chrien, R. Green, J. Simmonds, and G. Vane, who have been very generous in sharing their extensive experiences from the JPL AVIRIS program, and who continue to provide us with greatly appreciated support. We also wish to thank the members of the HYDICE Technical Advisory Group -- J. Dozier, A. Goetz, H. Kieffer, T. McCord, B. Rock, J. Salisbury, D. Schuresko, P. Slater, J. Taranik, and P. Weber -- upon whose many contributions the program has relied so heavily.

REFERENCE

- Rickard, L. J., Basedow, R., Zalewski, E., Silvergate, P., and Landers, M., 1994: HYDICE: The Hyperspectral Digital Imagery Collection Experiment. In *Imaging Spectroscopy of the Terrestrial Environment*, G. Vane (Ed.), Proc. SPIE 1937, 173-179.

OPERATIONAL USE OF A VARIABLE INTERFERENCE FILTER PUSHBROOM SCANNING MULTISPECTRAL IMAGER

J.M.Anderson and X.Sun

Department of Applied Physics and Electronic and Manufacturing Engineering

University of Dundee

Dundee, Scotland, UK, DD1 4HN.

ABSTRACT

A variable interference filter based multispectral imaging system (VIFIS) has been developed by the authors over the last few years, the design of which had as its prime objective the widening of the availability of the technique of multispectral scanning. This has resulted in a low-cost system which can be flown at short notice in almost any aircraft. A brief description of the principles of operation of the instrument and its current configuration will be given and some of the experiences of the authors in its operation over a variety of sites under various conditions described.

1. INTRODUCTION

The authors have had some experience of several multispectral scanning systems over the past ten years or so. In the UK four systems have been available to researchers over this time period, for the most part under the sponsorship of the Natural Environment Research Council (NERC). NERC have also supported the development of the VIFIS system.

1.1 ESTABLISHED SYSTEMS

The Natural Environmental Research Council in the UK has organised for some time an annual Airborne Campaign during which a variety of instruments are flown at the request of environmental researchers throughout the UK. This has obvious advantages in efficiency of scale and makes the technique of multispectral scanning available to scientists who would otherwise be denied the resultant data. The disadvantages are that a large number of "clients" must be satisfied simultaneously within a weather window appearing within a predetermined campaign time slot or slots. This is difficult even in a small nation like the UK because of fast changing weather patterns both spatially and temporally. Surface truth measurements can also prove difficult to organise when weather conditions force several postponements of flights since helpers tend to evaporate after several abortive call-outs, especially when water truth measurements are required.

Nevertheless much valuable data has been acquired during these campaigns, using for the most part a hired Deadalus AADS1268 scanner. There has also been very limited use of the AVIRIS system (once) and the MONITEQ system (once). More recently the CASI system has been flown and now that NERC has acquired its own system it is likely that more flexible deployment will be possible.

1.2 BACKGROUND TO THE DEVELOPMENT OF VIFIS

For several years the first author has been particularly interested in the study of water circulation in his home estuary, that of the River Tay in Scotland. This is a particularly complex system, displaying a variety of frontal systems which are very dependent on tidal range, season of the year, fresh water flow volume and tidal

state. Several successful participations in the NERC campaigns had shown the way towards the understanding of the functioning of the estuary but it was soon realised that the type of data required, spread closely over many tidal cycles would place undue demands on a nationally organised service. The question of developing a home built system was therefore addressed and VIFIS proved to provide the answer.

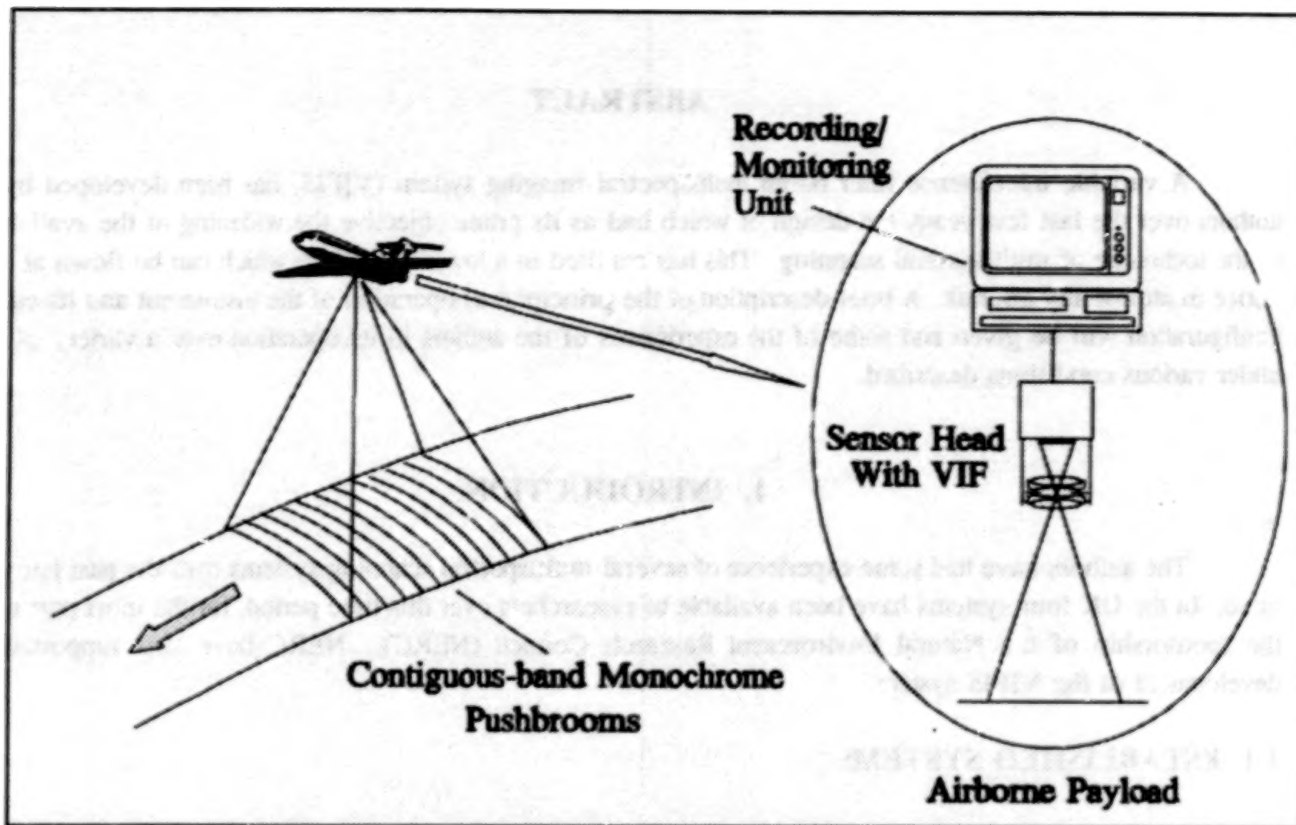


Figure 1. Schematic of operation of the VIFIS system.

2. THE VIFIS SYSTEM

A brief description of the principle of operation of the system will now be given along with an outline of the format of the system as operated at present.

2.1 PRINCIPLE OF OPERATION

The principle of operation of the system has been fully described elsewhere (Sun and Anderson, 1993) and only a brief description will be given here. The linear interference filter is fitted either to the image plane or an intermediate image plane of a video camera in an orientation such that changes in pass band are as shown in Figure 1. As the aircraft passes over the study area it can be seen that a particular strip of the surface is imaged successively in gradually increasing wavebands. Monochrome images in any given waveband within the range of the filter can then be assembled by combining the data from contiguous strips, the data being extracted from several hundred video frames. At present it is convenient to store the raw data on a Hi-8 video recorder and to process the data in the laboratory. Since, however the processing is carried out in near real time there is no reason why this cannot be done in the air if sufficient digital storage is available.

2.2 DESCRIPTION OF SYSTEM

The instrument in its current operational format consists of three synchronised cameras each covering a section of the spectral region between 405nm to 890nm, with considerable overlap between the three cameras. This design offers several advantages over a single camera with three CCD arrays in terms of wider spectral coverage, flatter spectral response and more accurate focus. Being modular also provides increased flexibility and reduced cost comparing to a purpose designed beam splitter approach. In cases where only a particular region of the spectrum is required a single camera can be used although where bidirectional reflectance spectral data are desirable more than one camera would have to be used. A separate VCR could be used for each channel or camera output but it is generally more convenient to treat the output from the three cameras as a single RGB output (either via a portable computer with suitable frame grabber and image processing board or via an RGB to Y/C converter) and use a single recorder. Spectral and radiometric calibration are carried out at the NERC field spectroscopy unit.

The present software produces the processed data in several formats. The first consists of images which represent the raw video scenes. This is of course almost free from geometric distortion since each scene consists essentially of a snapshot of the surface through the filter and, unlike the raw data from other scanners, which use dispersive elements, is an immediately recognisable image. These images are of course what are seen in the video monitor during the data collection. The second format consists of panoramas of six selected bands now typically sized as 2560 by 576 pixels. The third format illustrates a selected area of the image in as many bands as are necessary to give the required spectral coverage. It is then possible to select any pixel (or group of pixels) and display a spectrum of up to 60 contiguous bands over the complete spectrum.

3. APPLICATIONS

The original design objectives included the need that the system be easily deployed in a variety of aircraft. The examples now given will illustrate the versatility of the instrument which has flown on platforms ranging from a CESNA 150 to a twin engine Banderanti. This has involved making the system independent of aircraft power systems where necessary and capable of being deployed from a window clamp support or a foot-step clamp support where no convenient floor port was available.

3.1 COASTAL REGION, VANCOUVER

This example shows results obtained from a survey of the coast and inshore waters of a nature reserve near Boundary Bay, Vancouver, Canada taken on 26 June 1992. The area is a major feeding ground for geese and comprises a large area of eel grass covered at high tide. Flights were carried out using a CESNA 185 fitted with floor ports concurrently with ground truth measurements taken from a Coast Guard hovercraft. No logistic difficulties were encountered. Figure 2 shows 6 bands of track recovery images which cover a section of the Fraser River plume. The higher albedo of the sediment laden fresh water is clearly shown. In this case it is convenient to derive a spectral data set using the primary data, an example of which is shown in Figure 3, since the water bodies on either side of the front can be assumed to be reasonably homogeneous and a primary data set represents a simultaneous snapshot of the conditions. The spectrum shown in Figure 4 uses the data in the upper left image to acquire the sea water spectrum and the lower right image to derive that of the river sediment laden river water.

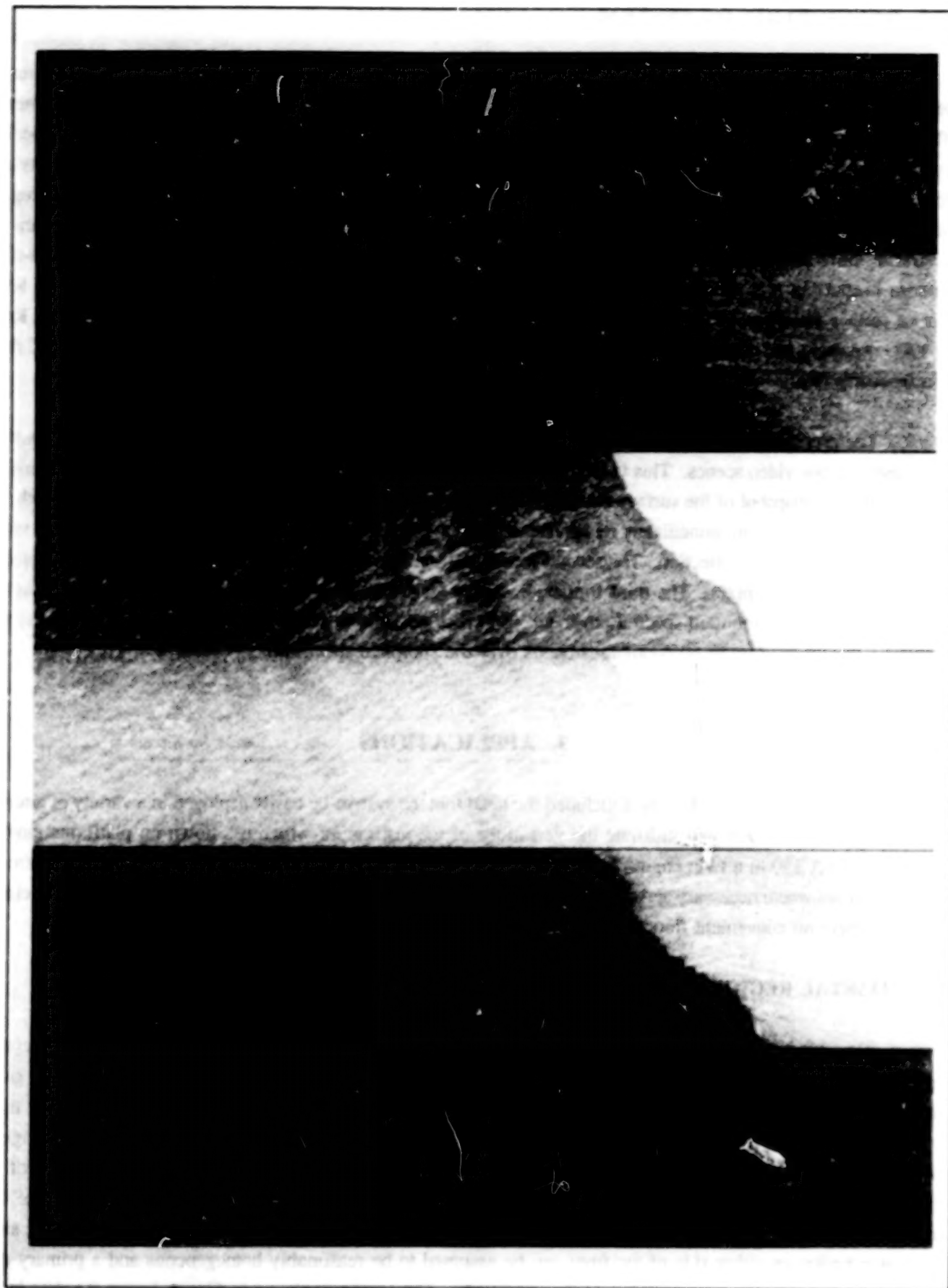


Figure 2. Six bands of track recovery images covering a section of Fraser River plume.

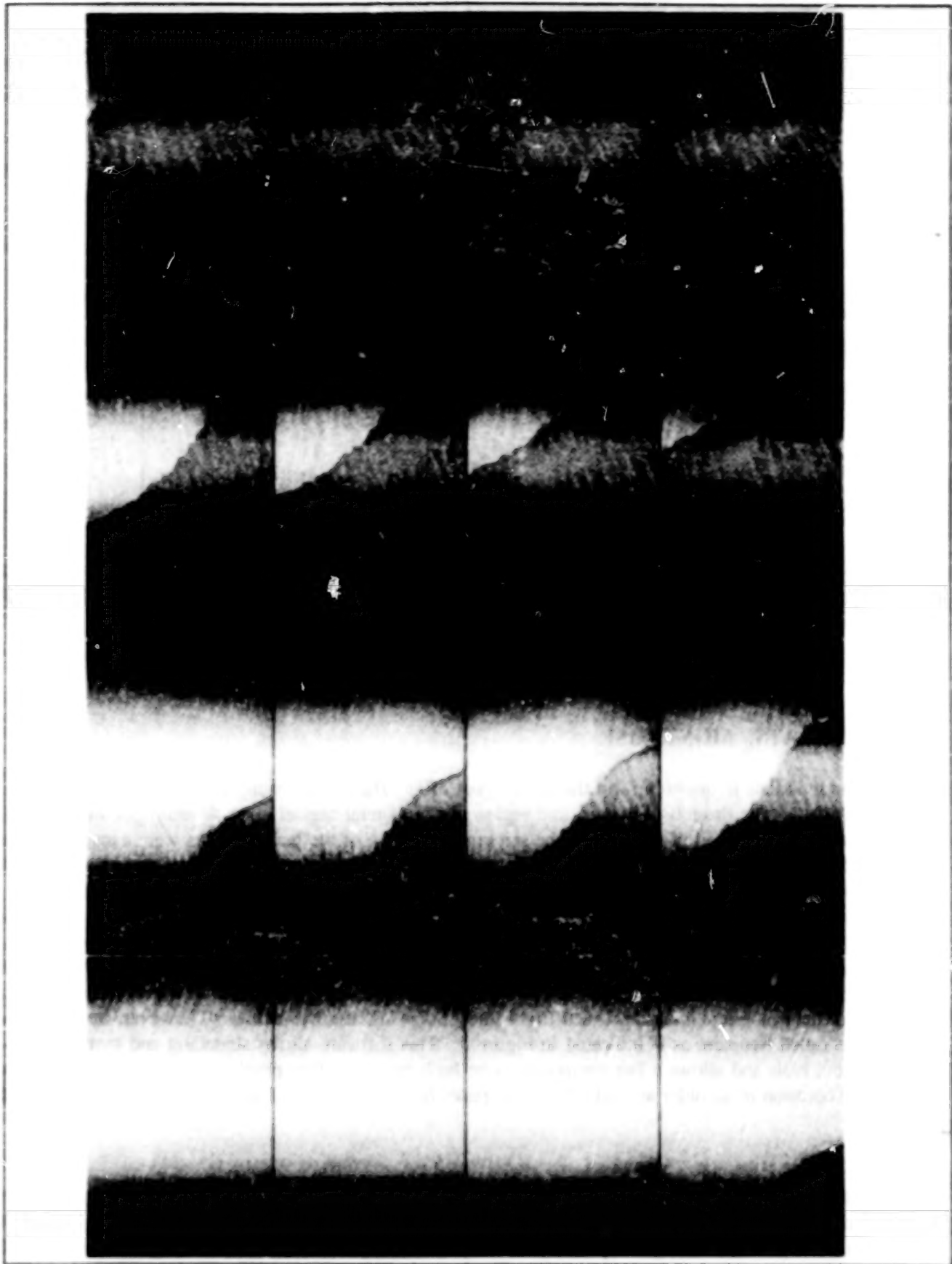


Figure 3. A sequence of sixteen frames of VIFIS primary images acquired across the Fraser River plume with frame sampling interval of ten frames

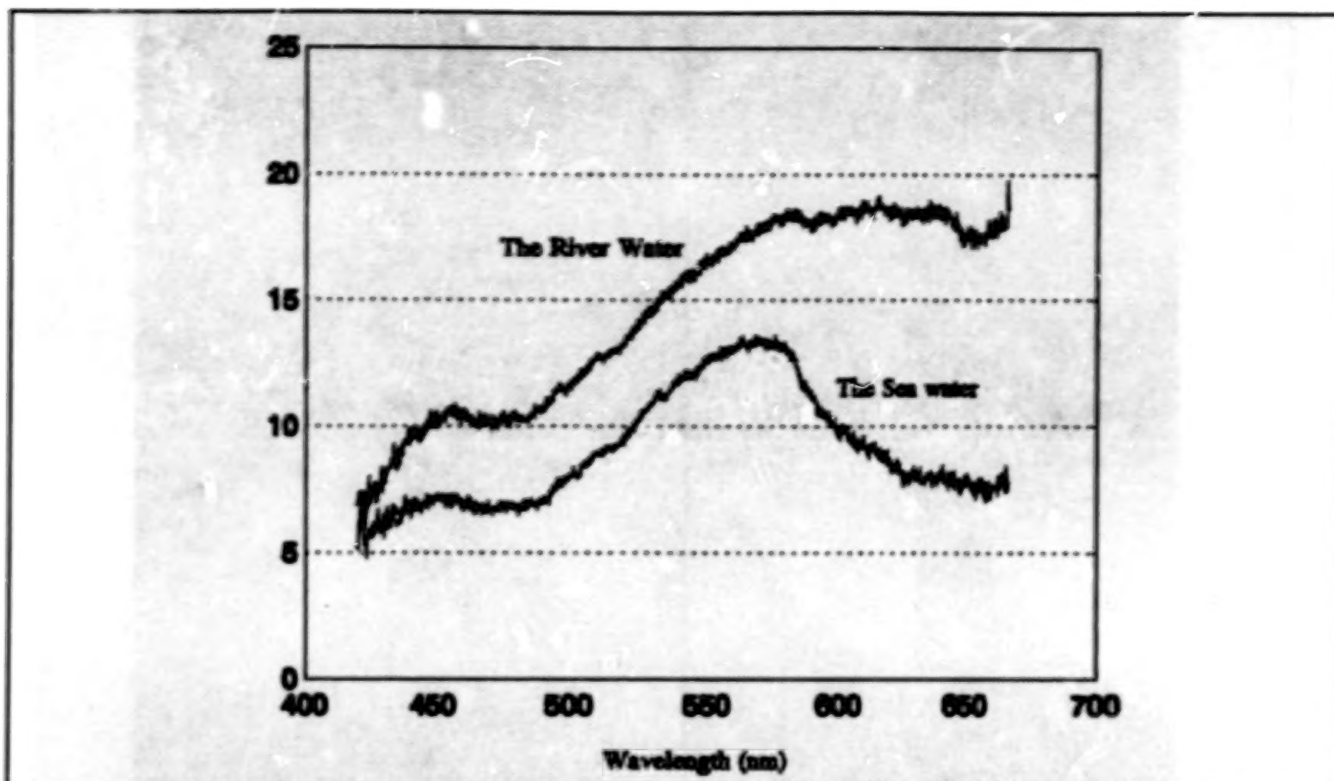


Figure 4. The examples of the VIFIS frame spectral plots of the fresh surface water and coast sea water.

3.2 MUD FLATS, MONTROSE

The mud flats question form the largest part of an estuary known as the Montrose Basin on the east coast of Scotland. The Basin is of interest as a region of commercial mussel beds and multispectral scanning has been suggested as a method of monitoring the size and condition of the beds. Flights were carried out using a CESNA 152 with a window mounted camera system. Markers of approximately two square metres were laid out in the regions of interest. Even when the weather appeared fairly good at ground level some turbulence was experienced over the Basin itself, making it difficult for the pilot to hold a succession of straight parallel flight lines. Since the widest field of view available in this case was 18 degrees (to avoid the intrusion of the aircraft undercarriage and wing strut) it was necessary to fly at 2000m and even then over 10 flight lines were needed to cover the Basin. A reasonable composite of the Basin proved difficult because of the overlap and variable distortion of the panoramic images on each flight line. Some success was achieved, however, by using a piece of software called Neopaint as is indicated in Figure 5. This software allows stretching and reorientation on a point to point basis and allows a fair composite to be built up. A further problem experienced was due to the use on one occasion of an older aircraft. The door panel had some play and the resulting vibration affected the data.

The important results were successful, however, as can be seen from Figure 6. This shows an area around a marker along with 72 spectral-window sub-images, each of which is with 80 by 108 pixels and cut from VIFIS primary video sequence, covering the spectrum. The centre of the spectral-window sub-images varies from 430nm to 650nm. Such spectral window sub-images make the spectral analysis possible even the data acquired in the worse flying conditions. The resultant spectra for the two points shown along with that of the white marker are illustrated in Figure 7. The apparent noise on the spectrum of the marker is due to the limits of spatial resolution since the approximate area on the ground corresponding to one pixel is one square metre and aircraft departure

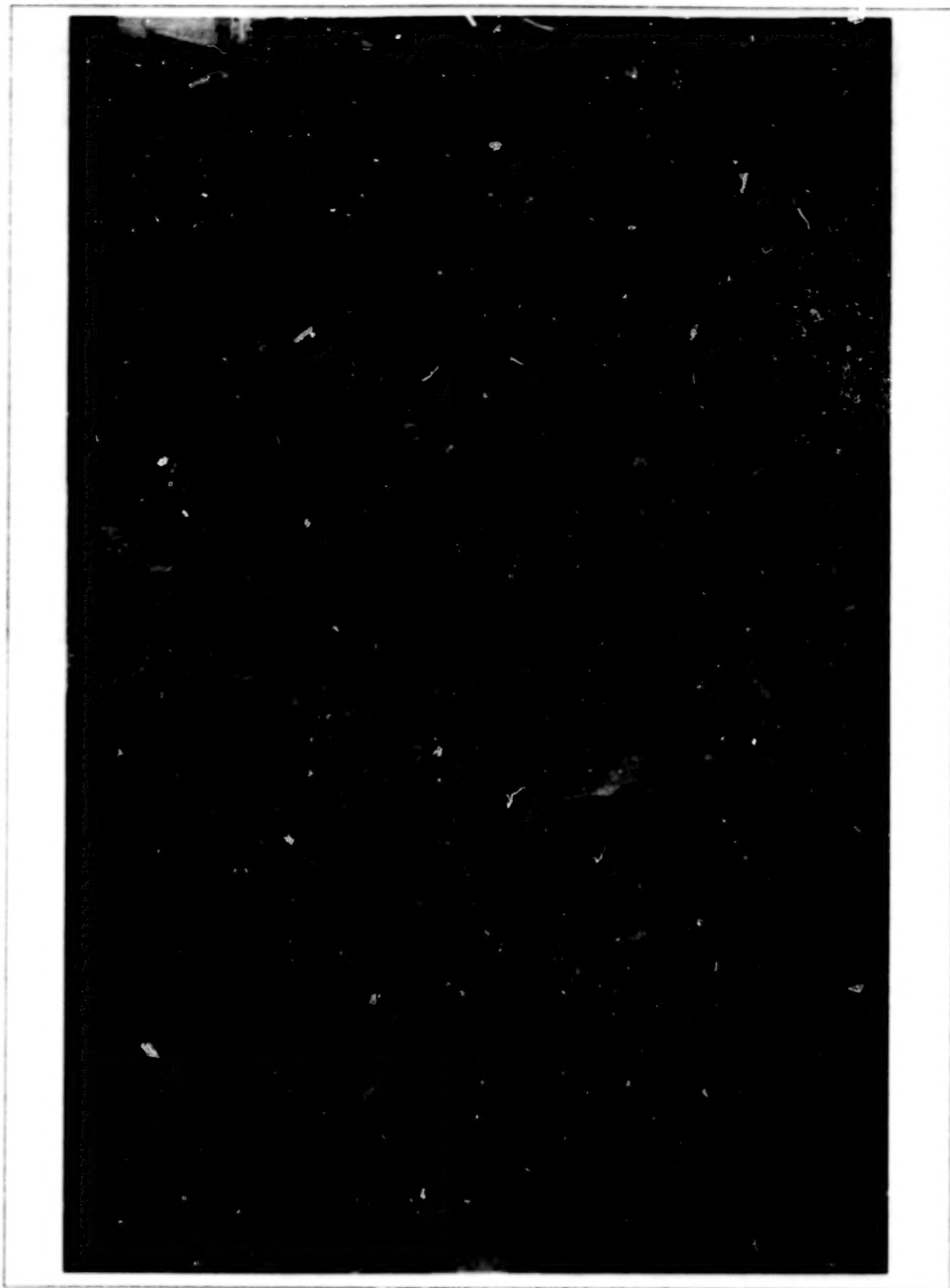


Figure 5. The composite image of Montrose Basin.

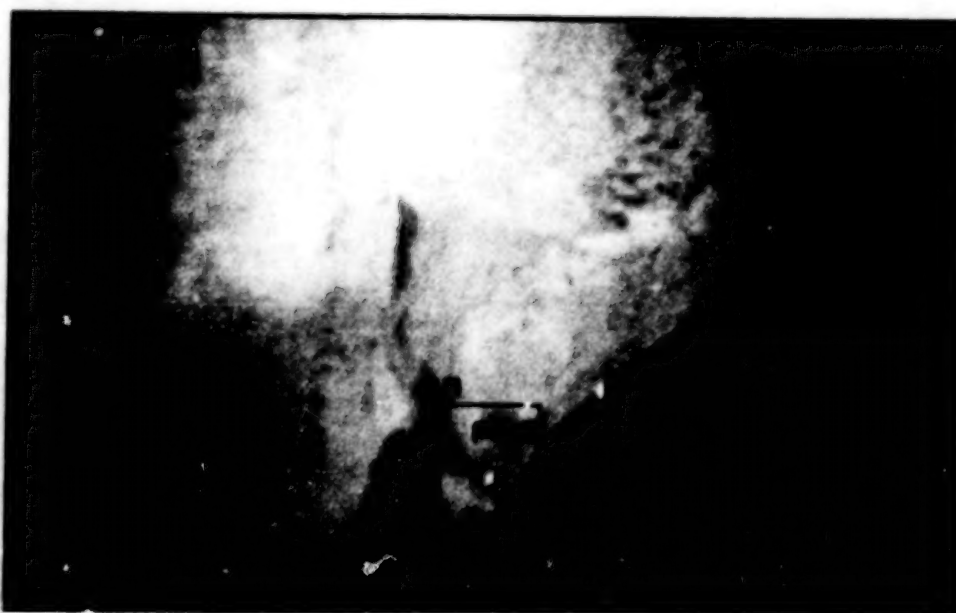
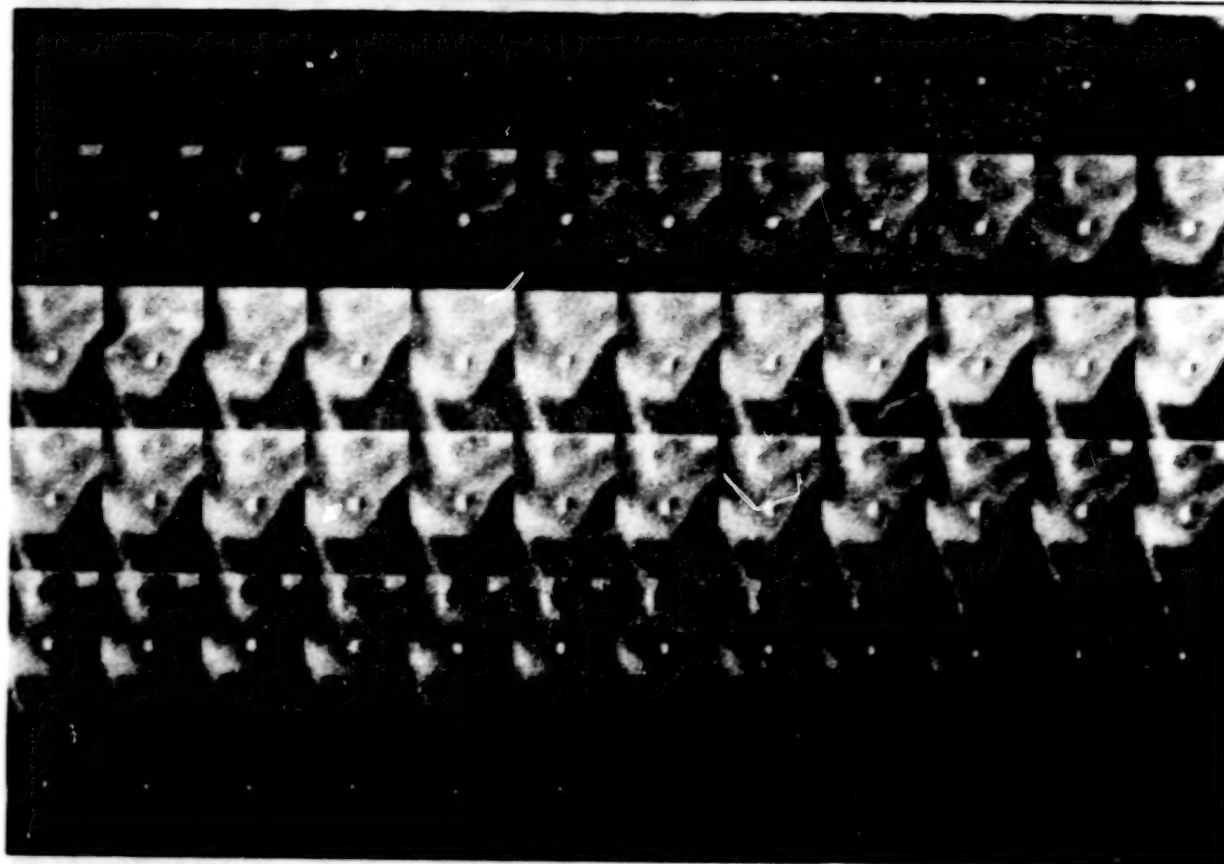


Figure 6. A sequence of primary spectral-window sub-images cut from primary video frame sequence. (A) 72 sub-images; (B) One of the frames in the primary video sequence.

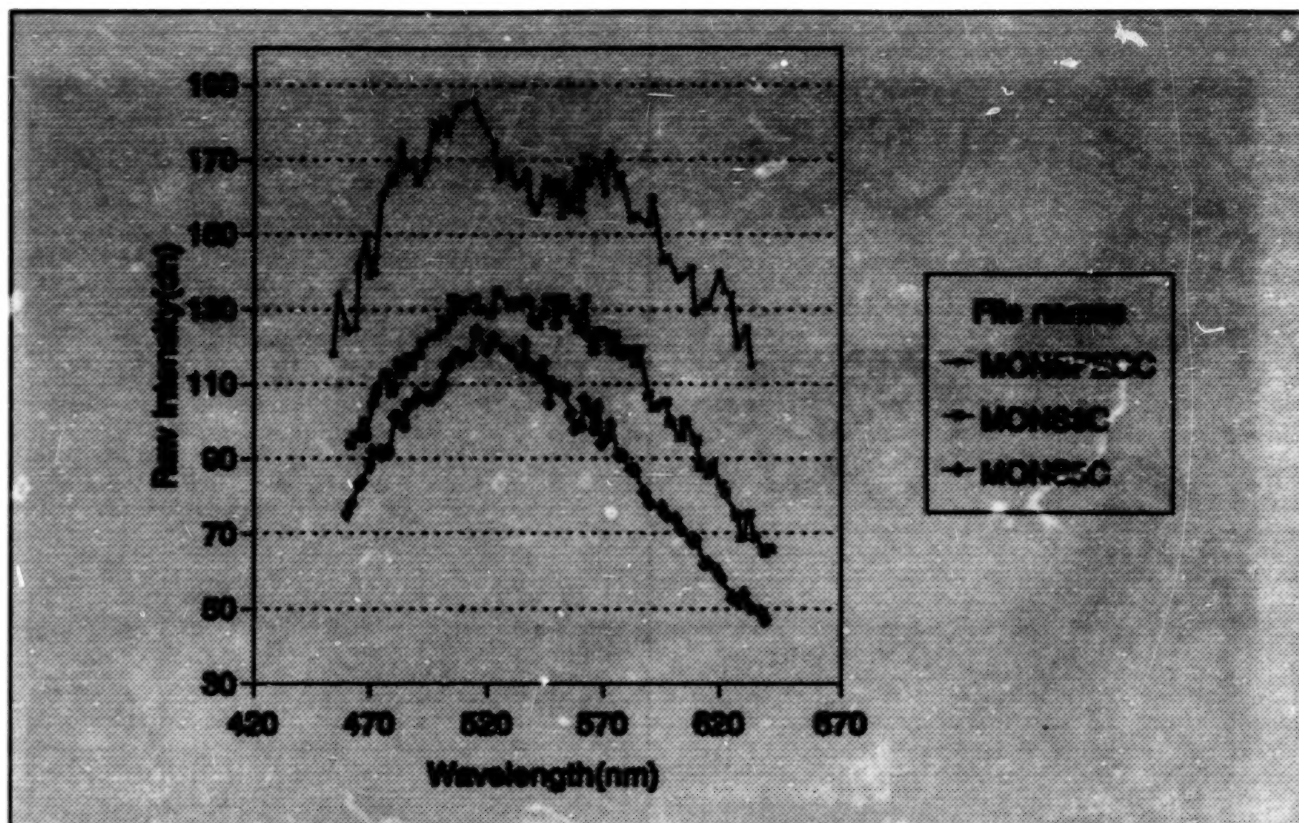


Figure 7. The spectral digital count plots of the marker and nearby regions indicated in Figure 6.

from a straight line path over the several seconds of image acquisition required to form a track recovery image will mean that the image of the marker will tend to drift on to several adjoining pixels. Accurate identification of the regions of mussel beds awaits further ground truth measurements of spectra under a variety of conditions.

3.3 BOSTON HARBOUR

This example is given because of the way it illustrates a set of directional spectral images where the intensity difference is dominated by directional effects rather than wavelength effects. This can provide high contrast water surface remote sensing by making use of sunglint. Surface anomalies due to factors affecting the surface roughness can be picked up by track recovery based on the direction of the surface from the nadir position. In practice this means the selection of appropriate columns for front and rear sunglint conditions. The example shown in Figure 8 is taken from a series of flights over the Boston harbour area with the instrument mounted in a CESNA 205 fitted with camera ports. The centres of the wavelength bands of the six panoramas are 447.6, 478.4, 513.7, 550.0, 585.4 and 621.8nm corresponding to 16.9, 10.7, 3.2, -4.4, -12, and -19.2 degrees from nadir. This flight was taken during front-sunglint circumstances. A small stream to the left of the panorama shows up in the first image. A ship's wake can also be seen as can a smooth region possibly due to an oil slick.

3.4 SOUTHAMPTON, ENGLAND

This example is given since it represents the first attempt to fly three cameras synchronised to one another (Figure 9). Two of the cameras are fitted with linear variable interference filters, between them covering the range 440 to 890nm. The third camera is a panchromatic one in this case to look for panchromatic bidirectional effects and serve as the reference of spectral reflectant ratio measurement. A serial engineering tests for the new system are still going on. The resultant data will be published when available.

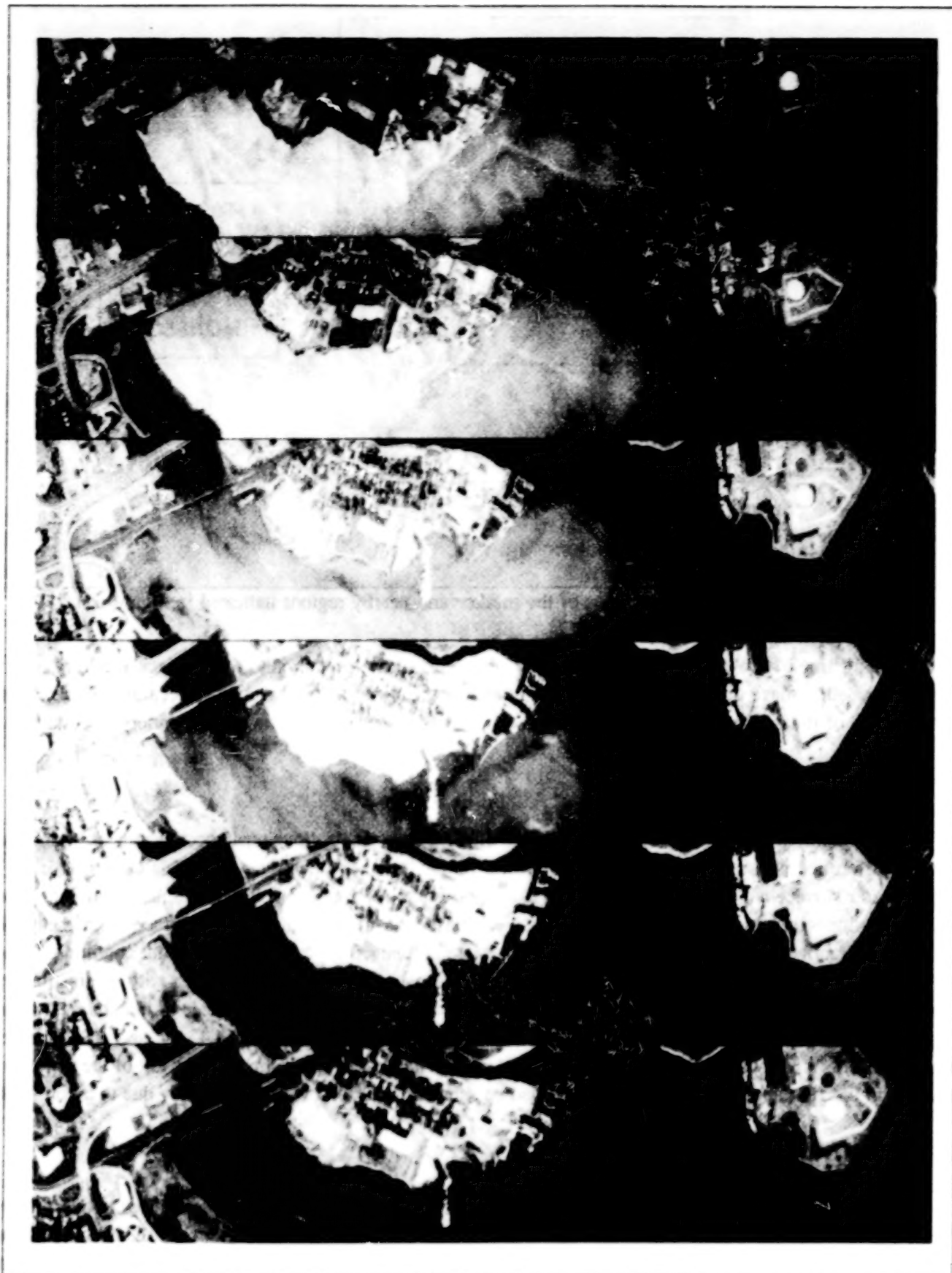


Figure 8. Six bands of VIFIS track-recovery-images acquired over Boston Harbor. Front Sun-glint circumstances were encountered.



Figure 9. A miniaturized modular VIFIS system are currently under engineering test. It is clamped on the foot-step of a CESNA 150 aircraft.

DISCUSSION

Over the past two years considerable experience has been acquired in flying the VIFIS system. Development continues based on the resulting operational feedback. The advantages and disadvantages over currently available commercially available systems will now be discussed.

4.1 COST OF SYSTEM

Since the system is not available commercially it is difficult to put an actual cost on a complete system since this will depend on individual needs and preferences. The basic system would consist of a single camera (not a camcorder!) modified by placing a linear interference filter either directly in the image plane or in an intermediate image plane. A VCR would also be required along with the appropriate portable power supplies. This need not cost more than \$2000 in total for the parts. Processing the data requires a frame grabber and the writing of some software. This need not be too elaborate if near real time conversion is not required.

Commercially available systems are of course orders of magnitude more expensive and unless budgeting is no problem usually involve the development or modification of suitable software to get the data into some kind of recognisable image.

4.2 EASE OF DEPLOYMENT

Because of the very small size of the camera(s) any two-seater aircraft is the minimum requirement. The

authors have yet to try a small remote controlled craft but this is feasible. Experience based on flights throughout the UK, Canada, the US and Brazil has shown that very little time is required (at the most a few hours) to ready the system in a previously unused aircraft. A light survey aircraft fitted with floor ports such as a CESNA 185 or 205 is probably the optimum choice when cost and convenience is balanced.

4.3 OPERATIONAL MODES

One mode of operation involves the derivation of track recovery images which are then interpreted as single spectral band images along with the resulting spectra from individual pixels or groups of pixels or, where sunglint conditions are encountered, selected look directions are used to examine surface features.

A second mode of operation is that used when the primary video images are analysed to produce spectra in the case of a homogeneous water body. These primary images, being relatively distortion free also have the potential of being used for geometric correction procedures. The spectral-window sub-images also consists of geometric distortion free spectral image for interested target analysis. The primary images can also be used straight from the VCR as convenient quick-look imagery.

A third mode of operation is to look at bidirectional reflectance effects. Various possibilities exist because of the flexibility of the new modular system. For examples, one method would be to use a single pass band filter and to use selected look directions. Another would involve using two of the modular camera units fitted with identical filters placed in the aircraft in such a way that the filters were oriented in opposite directions along the flight line.

ACKNOWLEDGEMENTS

The authors would like to acknowledge the support afforded by the National Environmental Research Council and by the Field Spectroscopy Unit at Southampton for their help in calibrating the instruments. We would also like to thank Prof Arthur Roberts of Simon Fraser University for the flights in Vancouver and Dick Hordon of Flight Landata for the flights over Boston.

REFERENCE

ARTICLE IN JOURNAL

X.Sun and J.M.Anderson, 1993. A Spatially Variable Light-Frequency-Selective Component-Based, Airborne Pushbroom Imaging Spectrometer for the Water Environment, Photogrammetric Engineering and Remote Sensing, Vol. 59, No. 3, pp. 399-406.

DEVELOPMENT AND OPERATION OF A REAL-TIME IMAGING SPECTRORADIOMETER

Mark Dombrowski
Surface Optics Corporation
San Diego, CA, 92131, U.S.A.

ABSTRACT

Many imaging applications require quantitative determination of a scene's spectral radiance. This paper describes a new system capable of near real-time spectroradiometric imagery. Operating at a full-spectrum update rate of 30Hz, this imager is capable of collecting a 20 point spectrum from 400 nm to 700 nm, with a 10 nm nominal bandwidth, over an image of 256 x 192 pixels. At a slightly reduced update rate of 15Hz, 30 point spectra can be collected. A 15Hz maximum update version is available with extended coverage to 900 nm. Although this full scene information is available, to make such a tremendous amount of data more manageable, internal processing electronics compute in real time the tristimulus integrals X, Y, and Z; along with standard RGB, these colorimetric integrals are available either as tristimulus values, or as chromaticity coordinates x, y, and Y. To allow the imager to simulate sensors with many different spectral responses, any arbitrary response function may be loaded into the imager including delta functions to allow single wavelength viewing. More powerful exploitation of the gathered spectral radiances is currently being developed in the form of real-time spectral matched filtering. This technique allows application of spectral matched-filtering algorithms of varying sensitivity to identify pixels whose relative spectral radiance distribution matches a sought-after spectral radiance distribution. The luminous dynamic range of the instrument is about 1 cd/m² to 10⁵ cd/m²; reduced frame rates allow operation down to less than 10⁻³cd/m².

The unique challenges of design and calibration are described. Average pixel readout rates of 30MHz, for full frame readout rates of 600Hz present the first challenge, with the processing rate of 400+ million integer operations per second presenting the second. Spatial and spectral calibration of 49,152 pixels and up to 1,000 spectral positions mandate novel decoupling methods to keep the required calibration memory to a reasonable size. Large luminous dynamic range also requires care to maintain precision operation with minimum memory size.

1. INTRODUCTION

High spectral resolution imagery is becoming an important tool for many applications; earth resource monitoring, resource management, medical diagnostics, non-destruction test and identification, and defense can all benefit from exploitation of material spectral characteristics. Until now, only limited portions of a scene's information have been available through varied imagers; true spectroradiometric data can be gleaned through spot radiometers, which, used in conjunction with scanning systems can slowly build up spectroradiometric images. Moving line-scan systems can also slowly build such images. Rotating discrete filter-wheel systems can also yield qualitative, low spectral resolution, low update rate spectral images, which, with much work, can be corrected to near radiometric form.

Surface Optics Corporation's (SOC) new Real Time Imaging Spectroradiometer (RTISR) is a technological breakthrough employing state-of-the-art optics, sensors and electronics in an innovative way. In summary the RTISR is a system which:

- quantitatively measures spectral radiances throughout a scene with
- a spatial format and resolution of 256 horizontal pixels by 192 vertical pixels,

- using a 29°H X 22°V computer controlled 10:1 zoom lens;
- offers a spectral resolution of 7 nm to 14 nm linearly varying over a spectral range of from 400 nm to 700 nm (or 900nm),
- over a radiometric range from 1 to 10^5 cd/m² ($<10^3$ cd/m² at reduced frame rates)
- convolves each pixel's spectral radiance with any arbitrary spectral response function (six simultaneously);
- provides quantitative outputs in a real-time imaging video format and through serial and parallel interface busses;
- is capable of both full operational control by computer, and of full operation manually without intervention of computer, and of completely autonomous operation.

Key features of the RTISR are:

A set of six high-speed digital processors, particularly appropriate to radiometric calculations, are used in parallel, to achieve the extraordinarily high processing rates required.

A system which is completely calibrated both spectrally and radiometrically for each pixel element as a function of instrument mode and settings (e.g., image intensifier gain, gating, zoom setting, filter position and rotation rate, etc.).

Great flexibility in data acquisition and processing performance. For example, the design allows complete spectral data to be obtained for any pixel; spectral images can be viewed individually, scanned, or integrated together with any arbitrary spectral response function to allow quantitative emulation of any sensor, including the human eye. Further development is currently aimed at implementation of real-time spectral matched filtering through a wide variety of filtering algorithms to aid in identification of materials in a scene with specific spectral characteristics.

The RTISR uses refractive optics and CVF technology to produce spectral images on a two-dimensional array. This results in simultaneous acquisition of spatial imagery for each spectral increment, and near simultaneous acquisition of all spectral points for each pixel. Further, the CVF approach is highly polarization insensitive as contrasted to monochromator based systems which can exhibit a high degree of polarization sensitivity. Table 1 summarizes the key specifications of the SOC real time imaging spectroradiometer.

2. SYSTEM DESCRIPTION

Requirements placed on the real-time imaging spectroradiometer (RTISR) by the sheer volume of data which must be accurately processed are quite stringent. Pixel resolution, frame-rate, and spectral resolution mandate the instrument perform over 400 million calculations per second. These high digital rates are indeed demanding. Coupled with the radiometric challenges of spectral imagery, the Surface Optics Corporation's engineering and scientific development team undertook an unprecedented task of building a compact, rugged RTISR designed for field use.

Table 1. RTISR Specifications

ITEM	SPECIFICATION
Spectral Range	400-700 nm (900 nm)
Spectral Bandwidth	7-14 nm (19 nm)
Spectral Selection	0.3 nm
No. Frequency Bands	20 or 30
Field of View (FOV)	29° x 22°
Instantaneous FOV	2.0 mr 1:1 zoom to 0.2 mr 10:1 zoom
No. Pixels H x V	256 x 192
Frame Update Rate	30 Hz (ultimate)
Radiometric Dynamic Range	1 to 10 ⁵ Cd/m ²
Output	
Video:	RS-170
Digital:	12 bit x 3 Muxed Data
Computer:	RS-232, IEEE-488 I/O Control
Computer	IBM PC compatible

SOC's imaging spectroradiometer has four distinct subfunctions as shown in Figure 1: An optical system (1) which captures and spectrally filters an image which is focused on a micro-channel plate/high speed CCPD detector assembly (2) whose output is electronically processed (3) and formatted (4) for output to video or computer.

In operation, a scene is imaged onto a gated, variable gain, proximity focused Micro Channel Plate (MCP) system operates in high light level conditions by changing a precision iris or intensifier gain. Output of the image intensifier is re-imaged onto a very high-speed CCPD array by a fiberoptic bundle. Output from the CCPD array is fed into the processing electronics where, with previously stored spectral and radiometric calibration data, each pixel is individually spectroradiometrically calibrated. Further processing allows convolution with arbitrary response functions. Default response curves produce R, G, and B output on three channels, with the tristimulus integrals X, Y, and Z output on the other three; post processing allows conversion to chromaticity coordinates x, y and Y. These integrals, computed on a pixel-by-pixel basis, are then formatted into standard RS-170 video format, encoded with scaling information, and made available through six BNC connectors. All functions can be controlled and data accessed via an IEEE-488 bus or a back-panel keypad. Following is a detailed discussion of system operation and performance.

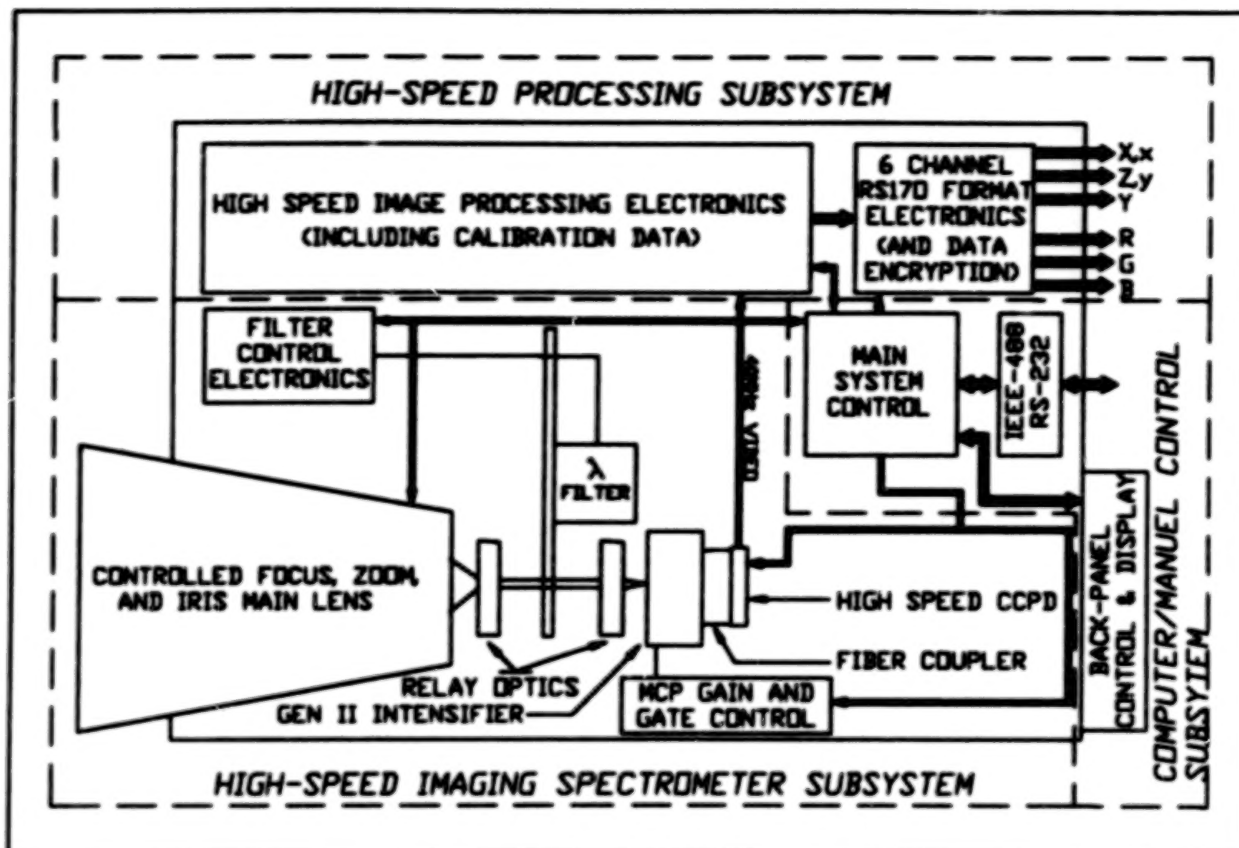


Figure 1. SOC's Real-Time Imaging Spectroradiometer Layout.

2.1 IMAGING SPECTROMETER

As mentioned above, the "eye" of the RTISR is a high speed imaging spectrometer. Through a system-controlled-lens assembly, the viewed scene is imaged onto the photocathode of a gated, variable-gain, proximity focused MCP image intensifier; the intensifier is necessary due to low photon fluxes encountered at minimum luminance, and because of the speed of rotation of the filterwheel. Dispersion across the array is less than ± 9 nm (alternate collection and processing techniques can produce a spectrally pure image with each pixel seeing the same wavelength within ± 0.5 nm). The exact part of the spectrum being viewed by any pixel for a given filter rotational position is calibrated. Output from the image intensifier is re-imaged onto a high-speed 256 x 256 pixel CCPD array.

2.2 FILTERS

A narrowband circular variable filter provides spectral information. Varying bandpass centerwavelength from less than 400 nm to greater than 700 nm as the CVF is rotated by 180° , this filter exhibits a passband that varies from about 7 nm at 400 nm to about 14 nm at 700 nm. A similar CVF is bonded with this filter to provide 2 scans from 400 to 700 nm as the filter rotates one complete revolution. An optional NIR CVF can also be bonded to the visible filter; this filter has spectral resolution varying from about 14 nm at 700 nm to about 19 nm at 900 nm, allowing spectral operation out to the limit of the intensifier, or about 950 nm. To meet 30 Hz frame rate, the CVF must spin at 15 Hz, or a spectral rate of 9,000 nm/second. This number is important in determining the maximum allowed integration time on the array. Given a bandpass of $\Delta\lambda \sim 10$ nm, centerwavelength changes one full bandwidth in 10 nm/(9,000

nm/second), or 1,100 μ s. Allowing centerwavelength to change by only $\Delta\lambda/2.5$ (an amount which produces negligible increase in filter bandwidth) yields a maximum integration time of about 300 μ s. Hence the need for gating of the intensifier. As the light level decreases below that which provides good SNR for the above maximum integration time, the CVF is automatically (or manually) slowed down to allow increase in integration time without compromising spectral resolution.

Rotational velocity of the CVF is controlled by the system, either automatically or manually in conjunction with the intensifier gate time. Rotational position of the CVF is encoded at a resolution of .09°, or .15nm. Encoding position with such fine resolution allows implementation of a spectral resolution enhancement process, detailed in the processing electronics section. Gating of the intensifier is synchronized with the encoded position of the filter wheel, allowing accurate determination of the spectral content of any given frame, an absolute necessity if spectroradiometric imaging is to be performed properly.

2.3 INTENSIFIER

Since the RTISR operates over a large range of light levels and with relatively fine spectral resolution, amplification of the photon flux leaving the CVF is an absolute necessity. Amplification is accomplished with a MCP image intensifier. A proximity focused rather than electrostatically focused intensifier is used to ensure a distortion free image. Fast gating is employed to allow repeatably precise gating times of 100 ns to 400ms. Gating also allows collection of system dark level information for each and every pixel in the detector array. Exhibiting a luminous gain of between 10,000 fl/fc and 20,000 fl/fc, a single stage MCP provides adequate gain. As detailed below in Section 4, the high gain necessary to operate in low light levels would fundamentally limit the achievable SNR at high light levels if gain were not decreased. Hence, the MCP gain is variable, controlled automatically by the system or manually by the operator. Special attention must be paid to the construction of this intensifier to ensure that the high speed at which this intensifier must operate does not induce surface charge depletion in the channels of the MCP, thereby reducing channel gain and destroying radiometric accuracy.

2.4 IMAGE ARRAY

The image generated on the phosphor screen of the image intensifier is re-imaged onto the detector array. In order for the system to operate at high frame rates and good spectral resolution, an extremely high-speed detector is necessary. The frame rate at which the CCPD must run is calculated as the radiometer frame rate times the spectral range divided by the spectral increment, or $30\text{Hz} \times 300 \text{ nm}/d\lambda\text{nm}$. With $d\lambda = 15.7 \text{ nm}$ the required frame rate is 570 Hz. This high frame rate is achieved using a charge-coupled photodiode (CCPD) array of 256 x 256 pixels with 8 video ports operating at a 5 MHz clock rate producing a 40 MHz pixel rate. Resetting after 192 lines provides desired 4:3 aspect ratio with an effective frame rate, including overhead but excluding integration time, of 700 Hz; integration time brings overall frame rate to 600Hz.

3. ENERGY THROUGHPUT CALCULATIONS

In order to define the performance boundaries of the RTISR, detailed analysis of photon flux levels throughout the imaging system have been performed. These calculations begin with a previously required upper end luminance level of 10^5 cd/m^2 . Assuming standard solar illumination and noting that the peak sea-level solar illuminance is about $1.25 \times 10^5 \text{ lumens/m}^2$, maximum luminance of a perfectly white lambertian reflector at sea level would be about $4 \times 10^4 \text{ cd/m}^2$. Note that the assumption of lambertian reflectance was made and will continue to be made for analysis purposes only; this assumption is a convenience for converting luminance values to spectral radiance values, and is not a limitation of performance. At an illuminance level of $1.25 \times 10^5 \text{ lumens/m}^2$, corresponding solar spectral irradiance peaks at about 500 nm at $1500 \text{ W/m}^2/\mu\text{m}$, and

over the visible band changes less than 50% from its peak value. Hence, using the maximum luminance specification in conjunction with the above parameters yields a maximum spectral radiance level for the imaging spectroradiometer of about 1.2×10^{-4} W/cm²/nm/sr. For noise calculations, to be performed later, note that at 500 nm in a 10 nm band, this maximum spectral radiance corresponds to a photon flux of 3×10^{15} photons/sec/cm²/sr.

Having established the maximum (and also then the minimum) spectral radiance level under which the RTISR will operate, system configuration can be used to elicit system performance. The first step is to calculate the exposure level on the imaging array. Given a lens collecting area A_l and a pixel IFOV of Ω_p steradians, assumed small, the spectral power level on a pixel (or more precisely on the area of the intensifier's photocathode which corresponds to that pixel on the array) is found simply as

$$P(\lambda) = L(\lambda) \Omega_p A_l \quad \left[\frac{W}{nm} \right] \quad (1)$$

where $L(\lambda)$ is spectral radiance. With a spectral filter of width $\Delta\lambda$ and peak transmission T_f placed in front of the intensifier, power incident on a pixel is approximated as

$$P = L(\lambda) \Omega_p A_l \Delta\lambda T_f \quad [W] \quad (2)$$

Note that this is an approximation since explicit knowledge of the filter response curve is necessary to integrate the spectral power level; a square filter was implicitly assumed. This yields an answer that is not absolutely correct, but is within a small percentage of the true answer.

If now a gain of G is applied for a time Δt to this power by the image intensifier, "radiant energy" at the output phosphor screen is found as

$$I = L(\lambda) \Omega_p A_l \Delta\lambda T_f G \Delta t \pi \quad [J] \quad (3)$$

Intensifier tube luminous gains are generally specified in terms of output luminance for a given input illuminance, such that G has units of footlamberts/footcandle or equivalent. Assuming the output is Lambertian, multiplying by π converts the Joules/sr to Joules. Care must be taken in applying this gain in spectral system since input and output spectral distribution of photons is not necessarily the same. The factor $G\pi$ is understood to represent the photon gain of the intensifier -- output photons per input photon. This gain is, of course, a function of wavelength but is fairly constant over the range of 400 nm to 700 nm (using an appropriate photocathode). This output is then re-imaged onto the detector array by a fiber optic bundle with a coupling efficiency η_f of about 0.6. At the array, this energy is incident over a pixel of area A_p . Therefore, the exposure level at the detector is given by

$$E = \frac{L(\lambda) \Omega_p A_l \Delta\lambda T_f G \Delta t \eta_f \pi}{A_p} \quad \left[\frac{J}{cm^2} \right] \quad (4)$$

Equation (4) is the desired throughput equation relating array exposure level to input radiance.

By now simply applying values to the variables in Equation (4), system performance can be quantified. The instantaneous collection area of the lens is $A_i = .55 \text{ cm}^2$ ($F/1.8$, $f = 15 \text{ mm}$). $\Delta\lambda$ is taken as 10 nm. Peak transmission of the CVF and optical train is about $T_r = 0.2$ and η_i is about 0.6.

Using a tapped CCPD array results in pixel solid angle of collection different than might be assumed by just dividing the system total FOV by the number of horizontal or vertical pixels. Since the array is a device with non photoreceptive taps lying between each column of photoreceptors, some collected energy will not contribute to array output signal. Each array pixel measures $40\mu\text{m}$ V x $24\mu\text{m}$ H, with equal vertical and horizontal separation of $40\mu\text{m}$. Horizontal length and vertical height of the array is 1.02 cm ($256 \times 40\mu\text{m}$). Hence the 29° HFOV must be made along the horizontal axis of the array such that each pixel views an area of $29^\circ/256 = .11^\circ$, or 2.0mr. Each pixel sees only one-half this horizontal IFOV, however, due to the video taps. Vertical pixels view an angle of $22^\circ/192$, or 2.0 mr. Therefore, effective radiometer IFOV is 2.0 mr x 2.0 mr. For the throughput calculation, however, a given pixel views a solid angle of about $9.6 \times 10^{-6} \text{ sr}$. Pixel area is $963 \mu\text{m}^2$.

Substituting the above parameters into Equation (4) yields

$$E = .9 L(\lambda) G \Delta t \left[\frac{J}{\text{cm}^2} \right] \quad (5)$$

or rearranging,

$$G \Delta t = \frac{E}{.9 L(\lambda)} \quad [\text{sec}] \quad (6)$$

Array saturation exposure is about $0.4 \mu\text{J}/\text{cm}^2$. Using this value in conjunction with the maximum spectral radiance found above yields a minimum gain-time product of 3.5 ms. Substituting the maximum exposure time of 300 μs as derived in Section 1.2.1, minimum intensifier gain is found as 12 to achieve array saturation at maximum frame rate and maximum spectral radiance. Available single MCP proximity focused intensifiers have gains variable from about 20 to 10,000. The system exhibits an electronically limited SNR of 10 at 1.5% of saturation. Hence, overall system dynamic range from an array exposure standpoint is 6×10^4 at a 30 Hz frame rate.

4. PHOTON STATISTIC LIMITATIONS

To fully characterize the operable range of the instrument, the fundamental physical phenomena which limit the achievable SNR at low levels must be understood. As calculated at the beginning of Section 1.3, photon flux in a 10 nm bandwidth around 500 nm at maximum luminance is about $3 \times 10^{15} \text{ photons/sec/cm}^2/\text{sr}$. For a 0.55 cm^2 instantaneous lens collection area, pixel solid angle of $9.6 \times 10^{-6} \text{ sr}$, and filter peak transmission of 0.2, maximum photon flux striking the area of the intensifier's photocathode corresponding to a given array pixel is $1.4 \times 10^9 \text{ photons/sec}$. At an exposure time of 300 μs , total number of photons hitting the array that contribute to exposure of the array is 4.2×10^5 . Arrival of temporally incoherent photons at a given point is governed by Bose-Einstein statistics, which under most conditions can be approximated as Poisson statistics; hence, the RMS fluctuation in the number of photons arriving at the intensifier while it is gated on is just the square root of the number of photons, or 380, yielding a maximum signal-to-noise ratio on an exposure-to-exposure basis of 380. This is the quantum mechanical limit of the system operating as described. However,

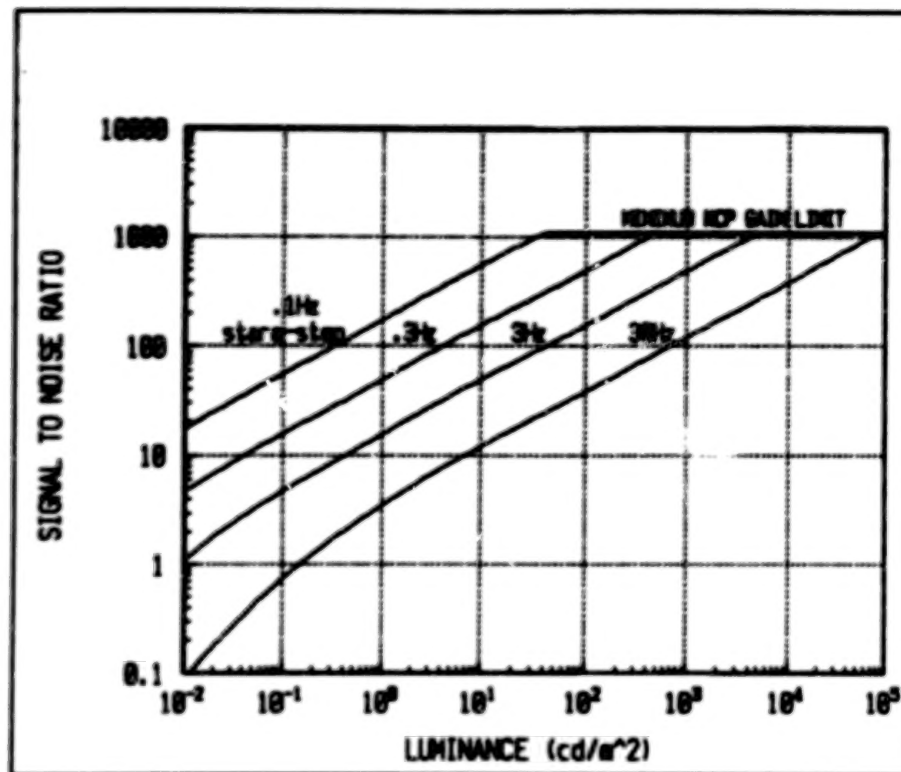


Figure 2. Photon and Electronics Limit of Instrument.

frame-to-frame statistically limited SNR will be higher. Since, at 30 Hz frame rate, 20 individual exposures will be integrated with the tristimulus curves to yield the resultant signal, frame-to-frame SNR is increased by 3 to 1140 (weighting of each spectral point is not constant, so the increase in SNR is not $\sqrt{20}$). Recalling from the last section that a 300 μ s exposure at maximum luminance would require an intensifier gain of 12, but that the minimum realizable gain is actually 20, true maximum realizable SNR is dropped to about 1000 because of decreased exposure time necessary to avoid saturation. When input radiance is decrease by 5 decades, average input photon flux decreases to 4.2 photons in the 300 μ s exposure time. Overall frame-to-frame SNR is now a meager 6.0. Decreasing frame rate to allow increased integration times allows increased SNR operation in low light levels. Statistically and electronically limited SNR versus luminance level and frame rate is shown in Figure 2. Here, 20 array exposures per frame were assumed.

5. ELECTRONICS

Necessary 700 Hz array frame rate is admittedly a challenging requirement; however, the brunt of system requirements is really borne by the processing electronics which must accept the raw output from the array, and knowing the filter wheel position at each exposure and MCP gain and gating, transform this raw data on a pixel-by-pixel basis to radiometrically calibrated spectral data, finally integrating 20 or more such exposures with appropriate response curves to yield tristimulus and RGB values for each and every 49,152 selected array pixels. A challenging proposition this is, but not impossible. At a 30 Hz frame update rate with 20 spectral points per frame, and 6 independent outputs, over 400 million calculations - albeit 16-bit integer - must be performed every second. Compare this with a CRAY 1S CPT (a small Cray) capable of performing 23 million floating point operations per second and the magnitude of the challenge is apparent.

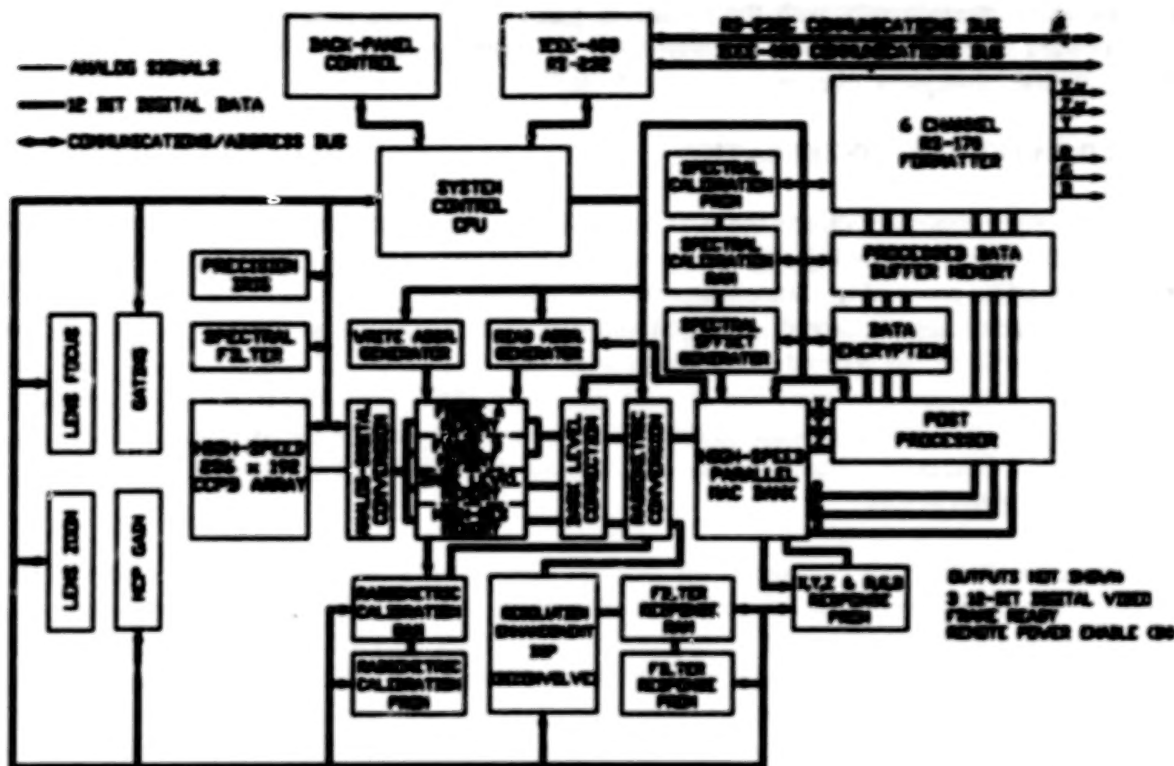


Figure 3. Electronics Block Diagram.

Fortunately, high-speed digital signal processing components are now readily available with architecture devoted solely to performing calculations on digital data. High speed subtractors, multipliers, and multiply-accumulators (MACs), operating at 30 MHz, perform the necessary calibrations and integrations in series and parallel.

Figure 3 presents a block diagram of the RTISR's processing and control electronics section. An instrument controller, accessed either via an IEEE-488 bus, an RS-232 bus, or by a removable backpanel keypad, is responsible for setting and monitoring the major subsystems, i.e., MCP gain and gate, CVF rotation rate and position, lens zoom position, array pixel dump, calibration and processing, post processing, and RS-170 formatting. Note that in addition to the main processing bank, a secondary processor is shown. At standard frame rate, user will have access to spectral data stored in memory consisting of 20 or 30 spectral points separated by 10 nm or 16 nm and taken at about 10 nm resolution. If so desired, however, the user can greatly enhance spectral resolution by allowing the system to slow filterwheel rotation, take more spectral data points from selected areas of the image (up to 1000 spectral data points separated by 0.3 nm from 256 pixels), and finally deconvolve filter response from the data to achieve resolutions below that of the filter; this is the task of the additional processor. Fully deconvolved spectra for a given pixel would be available at a 1/3 Hz rate (limited by array readout rate) over the IEEE-488 or RS-232 bus.

5.1 CONVERSION AND STORAGE

Few aspects of SOC's instrument are unchallenging; conversion of the analog pixel data to digital data is not one of them. Leaving the array at a 40 MHz rate, each pixel must be digitized to 12 bits resolution. Four 10 MHz, 12 bit converters digitize at the required 40 MHz rate. Output of these converters is directed to one of two full-frame, high-speed static RAM memories, capable of storing 30 complete spectral images

at 12 bits; each frame memory is effectively 2 MByte. Added to each bank is a second section which stores a set of data taken intermittently with the intensifier gated off to yield dark level information. The last component of the main memory bank is the high resolution memory capable of holding 1000 spectral points from 256 pixels for subsequent filter response deconvolution.

5.2 CALIBRATION AND INTEGRATION

As the system controller directs the A/D conversion section to fill one image bank of the memory, it simultaneously directs the processing system to read from the other previously filled bank, calibrate the data, and perform appropriate processing. Since 6 separate integrals must be computed (X,Y,Z and R,G,B), 6 MACs are used, one for each integral. Stored in PROM and downloaded into the appropriate processor's external RAM at power-up will be the spectral tristimulus curves and RGB curves, although the user can input any desired spectral response curve into any one of these processors. Also stored in PROM and downloaded into high-speed RAM will be spectral calibration data (i.e., centerwavelength of filter for a given pixel at a given filter rotation) and radiometric calibration data (i.e., digitizer counts for a given spectral radiance at a given filter position for a given pixel).

In operation, MACs will compute their required integral for a given pixel by first determining the wavelength offset within their internally stored response curves of the first spectral data point for that pixel; this is accomplished through the spectral calibration RAM. The first spectral data point is then accessed and dark level subtracted by a simple arithmetic unit. Dark level corrected data is then radiometrically calibrated by another arithmetic unit accessing the radiometric calibration RAM and gate time associated with each spectral image. Radiometrically calibrated data is then input to the MAC which multiplies it by the appropriate response value at that wavelength and stores this value in its accumulator. Subsequently processed spectral pixels are then added to this value, effecting numeric integration of the spectral data and response curve. At the user's discretion and dependent on the rate of change of scene spectral features, varying coefficients of integration can be applied to each spectral point to effect either trapezoidal (1st order) or Simpson (2nd order) approximation of these integrals. Also at the users discretion, any default response curve can be replaced via either computer bus with any desired response function, including delta functions to view a given wavelength, or other sensor response functions for sensor emulation. Ability to view a given wavelength is also selectable by the backpanel keypad.

Integrated pixel values are then output to a post processor, again comprising simple arithmetic units which convert X, Y, and Z, to x, y, and Y if so desired. Post processed pixels are then sent to 1 of 2 banks of output video memory which also contain the scaling factors necessary to radiometrically interpret the scene video data.

Digital data is then converted to analog by a relatively slow (compared to the rest of the system) 6 MHz Digital to Analog converter. Analog signals are then properly formatted by a RS-170 formatting subsystem which outputs the required six video signals on separate BNC connectors. 12 bit digital video data is also available on a separate connector.

6. FURTHER DEVELOPMENT

The technology described above has produced an instrument capable of very high-speed collection, calibration, and processing of spectral images from 400 nm to 700 nm, or to 900 nm. SOC is currently working on extension of this technology to allow spectral coverage from 400 nm to over 12 μ m. Since no photocathode is available with a work function sufficiently low to allow thermally generated photons to liberate photoelectrons, the MWIR and LWIR version of this instrument will not include an image intensifier; hence, alternate techniques will be used to effectively freeze the rotation of the filter wheel. Save for this difference (and the fact that cooled InSb and HgCdTe arrays will replace the Silicon array), The imaging spectrometer

heads for the MWIR and LWIR will be nearly the same as the VIS/NIR head. Stable radiance sources will also be included in the next generation of imaging spectroradiometers to increase the time between recalibration.

Spectral-matched filtering, a technique whereby each pixel's relative spectral radiance distribution can be compared to a sought-after spectral radiance distribution with matching pixels appearing bright while mismatched pixels appear dim, is also being implemented in the next generation of imaging spectroradiometers. By far the most powerful aspect of the instruments, spectral matched filtering will employ hardware implementation of a wide range of filtering algorithms. Some are as simple as merely treating a pixel's spectral radiance as a 20 (or 30) dimensional vector and computing the dot product between it and the sought-after radiance's spectral radiance "vector". Such algorithms provide a relatively "broad" filter, requiring only gross similarity between measured and desired spectrum to show a match. This is apparent when considering that a 20-dimensional vector can lie in any of 2^{20} sectors (just as a three-dimensional vector can lie in any of eight cartesian octants), but because measured spectral radiances can never be negative, spectral radiance vectors are constrained to lie in only 1 of these 2^{20} sectors. Other filtering algorithms will be implementable to allow varying sensitivity, from broad filters to extremely narrow filters. Such power will allow identification or classification of materials throughout a scene based on the materials' reflectance, emittance, and transmittance characteristics -- characteristics inseparably connected to the material's macroscopic and microscopic structure and material composition. Implementation of these techniques more than triple the processing requirement for the system.

7. CONCLUSIONS

This paper has described the development and key features of a new real-time imaging spectroradiometer. The basic system provides a 20 point spectral image of 256 x 192 pixels from 400 to 700 nm with a full spectrum update rate of 30Hz. The internal processing electronics calibrates each spectral pixel element, and computes in real time the tristimulus integrals and RGB output. The user also has the option to input an arbitrary spectral response function to provide the capability to simulate various sensors or to perform spectral matched filter functions. The availability of high spectral resolution data in a real-time image format is anticipated to have many applications in the defense, earth resources, and medical communities.

SPECTRAL SIGNIFICANCE OF THE MOMS-02 SENSOR FLOWN ABOARD STS-55/D2

H. Kaufmann, and M. Berger
GeoResearchCenter Potsdam, Remote Sensing Section
D-14407 Potsdam, Germany

D. Meißner
German Aerospace AG, RSX-24 Section
D-81663 Munich, Germany

ABSTRACT

A second generation instrument of the "Modular Optoelectronic Multispectral/Stereo Scanner" was flown during the D2 mission aboard Space Shuttle flight STS-55. The newly designed sensor provides multispectral coverage in 4 wavebands including the visible and near-infrared range and is additionally equipped with a three line along-track stereo device recording for/aft and nadir panchromatic data. During a 9 days mission in April/May 1993 approximately 8 mio. km² of data have been recorded in different modes from a mean altitude of 296km that results in a GIFOV of 4.5m x 4.5m for the nadir looking panchromatic module and 13.5m x 13.5m for the multispectral - and tilted panchromatic modules.

Data of the newly designed multispectral and panchromatic bands of MOMS-02 have been investigated with regard to their technical performance and their spectral significance. Different algorithms are used for preprocessing of raw data and merge of panchromatic and multispectral information. First results indicate a 10-15% less correlation for MOMS-02 bands as compared to those of operational sensors with broader band design. Entropy, SNR and PSF performances are comparable to operational sensors like HRV or TM. However, data of band 3 (red part of the spectrum) are weaker in their performance, especially in the SNR. First imagery are presented on the basis of a merging concept for high resolving panchromatic and multispectral data.

1. INTRODUCTION

MOMS-02, was developed by the German Aerospace (DASA) under contract to the German Aerospace Research Establishment (DLR) and the German Space Agency (DARA) (Meißner et. al., 1994). MOMS-02 has been designed under consultancy of a scientific user group of different universities and research centers (Ackermann et. al., 1989). It is financed by the German Federal Minister for Research and Technology (BMFT). MOMS-02 was flown aboard the Space Shuttle flight STS-55 in the frame of the D2 mission. STS-55 was launched on April 26, 1993, for a ten days mission with an orbit inclination of 28.5° (Bodechtel et. al., 1994). Main advanced performance of the MOMS-02 system are the along-track three-fold stereo capability, a high resolution panchromatic capability and a narrow banded multispectral VIS/NIR design. Table 1 lists orbit - and sensor parameters of STS-55 /D2 MOMS-02.

Table 1: Orbit- and Sensor-Parameters of STS-55/D2 MOMS-02

<u>Orbit-Parameter</u>	
○ Orbit mean altitude	296 km
○ Inclination	28.5°
○ Platform	Space Shuttle STS-55
○ Launch date	April 26, 1993; 9 days mission
<u>Sensor-Parameter</u>	
● Swath widths (mode dependent)	37 km or 78 km
● GIFOV	4.5m x 4.5m HR-nadir 13.5m x 13.5m XS; for/aft
● Detectors	6000 elements (Fairchild)
● Spectral range of bands	<div>XS #1.....449 - 511 nm</div> <div>XS #2.....532 - 576 nm</div> <div>XS #3.....645 - 677 nm</div> <div>XS #4.....772 - 815 nm</div> <div>nadir pan HR #5.....512 - 765 nm</div> <div>for + 21.4° pan #6.....524 - 763 nm</div> <div>aft - 21.4° pan #7.....524 - 763 nm</div>
● Radiometric resolution	8 bit out of 12
● Data compression (on-board, band 5)	8 to 6 bit
● Acquisition modes	
mode 1.....bands 5,6,7	(HR + ST, stereo)
mode 2.....bands 1,2,3,4	(XS, multispectral)
mode 3.....bands 3,4,6,7	(2 XS + for/aft ST)
mode 4.....bands 1,3,4,6	(3 XS + for ST)
mode 5.....bands 1,3,4,7	(3 XS + aft ST)
mode 6.....bands 2,3,4,5	(3 XS + HR)
mode 7.....bands 1,3,4,5	(3 XS + HR)
● Data recording / storage	DDR-100 HDT Recorder Capacity: 5.5 hrs
● Data rate	100 Mbit/s

2. ANALYSIS OF RAW DATA

Raw data have been analyzed with regard to striping effects and their band to band registration. For evaluation, data of two different orbits (28-arid, Saudi Arabia and 126-semi-arid, Zimbabwe) were selected, that have been recorded to the beginning and at the end of the mission.

To evaluate the striping characteristics a Fast Fourier Transformation (FFT) was used, supported by visual inspection. Striping effects with a period of 2 in scan direction and a period of 3 in flight direction are present in bands 1 and 2 but mostly accentuated in the HR-panchromatic band. Striping in scan direction is identified as odd/even effect that is due to separate read-out of the odd and even pixels and their different electronic paths. Striping in flight direction is due to a malfunction of the multiplexer. Striping as well as noisy frequencies are mainly due to unstable temperature conditions during the shuttle mission and vary from scene to scene dependent from the time periods given for heating up the system. In addition, the multispectral bands are not perfectly registered to each other. The reason for this might be a slight bend of the center plate where the lenses are mounted on. The accuracy of band to band registration can vary from scene to scene indicating an instability of the center plate during the mission. The shift may also be due to 'blind' elements on the CCD arrays.

To correct for the mentioned problems, first an adapted histogram matching algorithm was applied to MOMS-02 raw data that gave reasonable results in compensating the odd/even effect and the multiplexer problem. Each image was divided into 6 subscenes to separate the striping effects. Radiometric calibration was applied by matching the subscenes to the scene with the highest mean level. Thereafter, the subscenes were re-merged. Fourier filtering with sharp ideal filters may only be used to correct for unsystematic errors, e.g. in band 3. Because of artefact generation it was not applied here.

After radiometric corrections, data of the two multispectral modules covering bands 1/2 and 3/4 have been co-registered using a polynomial of first degree and nearest neighbour resampling method. The resulting data are then analyzed without further processing in comparison to operational sensors.

3. ANALYSIS OF SYSTEM CORRECTED DATA

The radiometrically and geometrically corrected raw data have been used to evaluate the entropy, signal to noise ratio (SNR), spatial resolution / point spread function (PSF), and interband correlation. Since analysis is presently based on recorded mission data, a comparison to complementary data of operational sensors like HRV (high resolution visible) and TM (thematic mapper) seems to be a reasonable approach. However, one has to keep in mind that radiometric and geometric preprocessing as well as resampling of multisensor data is different and results just present a relative measure of performance. To meet the objective, complementary data of similar acquisition dates have been co-registered to MOMS-02 data and corrected for sun elevation by the cosine law. The following table lists the investigated data sets.

Table 2: Data investigated

SENSOR	ORBIT - PATH/ROW	DATE OF ACQ.
MOMS-02	126 Scene 5 and 6	May, 4th. 1993
MOMS-02	28 Scene 10 and 11	April, 28th. 1993
LANDSAT TM	170/72	April, 12th. 1993
LANDSAT TM	172/41	July, 6th. 1984
SPOT HRV	134/386	May, 14th. 1993

3.1 ENTROPY, SNR AND PSF

The entropy is a quantitative measure of image information content and was calculated for several subscenes of orbit 126: Zambia-Zimbabwe-Mocambique and orbit 28: Saudi-Arabia (Berger and Kaufmann, 1994). The mean relative entropy (ratio of corresponding bands) is as follows.

Table 3: Relative entropy

MOMS-02 / HRV	bands	value	MOMS-02 / TM	bands	value
	--	---		1/1	0.92
	2/1	1.11		2/2	1.10
	3/2	0.90		3/3	0.86
	4/3	0.97		4/4	0.94

The results of MOMS are comparable to HRV and TM differing at a maximum of 0.5 bits/pixel. MOMS band 3 of arid scenes differs about 1.5 bits/pixels versus TM band 3. This might be due to the band width of MOMS band 3 which is effectively narrower than originally defined (Kaufmann et. al., 1989). To calculate the effective signal to noise ratio (SNR) of image data an automated estimate similar as described in Bo-Cai (1993) was used. Since data-takes over Southern Africa temporary cover the harvesting season and comparative data are not available for exactly the same day, only data of an arid area (orbit 28) were used for calculation. Results (relative SNRs) are comparable apart from band 3, who's noisy impression has already been discussed.

Table 4: Relative SNR calculations

MOMS-02/TM	bands	value
	1/1	1.04
	2/2	0.87
	3/3	0.52
	4/4	1.01

The point spread function (PSF) is a measure of contrast and spatial resolution and related to the modular transfer function (MTF). It was calculated by extracting several profiles cutting three well known sharp edges in different directions (Berger and Kaufmann, 1994). The first deviation of each profile was Gaussian fitted by the assumption that the PSF will have a Gaussian distribution (Hallada et. al., 1986). Thus the PSF is defined by the half width of the Gaussian fit. Per edge the mean of PSF's were calculated.

Like entropy and SNR the results for MOMS-02, HRV and TM are similar. Especially as compared to the pilot-system MOMS-01 (Bodechtel et. al., 1985), the performance of the -02 system has improved enormously. Following table lists the results in pixel units with the corresponding standard deviations.

Table 5: PSF calculations

	MOMS				HRV			TM			
Band Number	1	2	3	4	1	2	3	1	2	3	4
Mean PSF [Pixel]	1.62	1.73	1.44	1.76	1.16	1.96	1.51	1.25	1.33	1.57	1.45
Stand. Deviation	0.31	0.22	0.17	0.33	0.21	0.32	0.20	0.23	0.33	0.18	0.23

3.2 SPECTRAL FEATURE ANALYSIS

The analysis of signatures is based on spectral curves measured with lab- and field-spectrometers. Targets addressed are those, showing characteristic features in the visible and near-infrared range like healthy green and stressed vegetation as well as rock samples containing iron-oxides and -hydroxides. First, insolation characteristics and atmospheric attenuations are applied to the curves. Then, for various combinations of the above mentioned targets mean, standard deviation and interband correlations have been calculated for nominal bandpassed of MOMS-02, HRV and TM. The results indicate a 5-25% more resolved recording of spectral features through MOMS (dependent on the band ratios observed) as compared to the broader banded design of HRV and TM.

For the analysis of real data, several subscenes of TM and MOMS data of an arid area in Saudi-Arabia have been radiometrically adapted and co-registered. An analysis of the Zimbabwean target for different vegetation canopies is unfeasible due to time gaps of different sensor recordings and daily changes of surface because of extended harvesting activities.

Interband correlations as a measure of spectral variations in images show slightly more spectral variances of app. 10-15% for MOMS data as compared to TM bands. This fact is visualized through more saturated colors in merged products if processed in equal manner. The results are in accordance with simulations based on high resolving field-spectra of vegetation (Koch et al., 1993) as well as rock samples used for MOMS-02 band design (Kaufmann et al., 1989) and confirm the improvement by the new arrangement of band centers and widths.

4. IMAGE PROCESSING

Processing of MOMS-02 imagery is dependent on the respective mode in which data have been acquired. Besides DTM-generation of the three line stereo mode and distinct combinations of multispectral data, major interest is focused on the combination of high resolving panchromatic (stereoscopic) data (4.5m) with multispectral data (13.5m) that were recorded simultaneously in modes 3, 6 and 7. The most meaningful merging concept was originally developed for exploration purposes (Kaufmann, 1988), and has now been adapted to combine MOMS-02 data of different spatial resolutions. The concept is based on a reversible color space transformation that offers the opportunity to separate hues and saturations of a color composite from its intensities (apparent albedo). Those intensities are then substituted for the high resolving panchromatic data.

The panchromatic bandpass of MOMS-02 has been extended towards longer wavelengths to include a section of that wavelength range, where vegetation is characterized by a strong increase in reflectivity (Kaufmann et al., 1989). Vegetated areas are now displayed in brighter tones and thus more suitable for color merge, than if imaged in darker tones as provided e.g. by HRV pan.

Shown are data acquired during orbit 126, crossing Zambia, Zimbabwe and Mocambique in Southern Africa. The scenes are located South of the capital city of Harare. Fig 1 shows the panchromatic band of MOMS-02 where agricultural fields, roads and even single trees are well accentuated. Vegetation is present all over the image apart from the very strong reflecting areas. Grass, bush- and woodland can be well differentiated by their pattern and moderate apparent albedo and are clearly to be separated from the water reservoirs to the North and South. Fig. 2 is composed of multispectral bands 2 (green range), 3 (red range) and 4 (infrared range) coded blue red and green respectively, merged with high resolving panchromatic data. It shows the Manyame river to the South and numerous small fields covered by scattered trees and bushes in shades of green. Already harvested fields are displayed in brownish colors. Note the dark green shaded areas to the South. Because of the high resolution of the panchromatic band these can be identified as wet grass lands and clearly separated from woodlands characterized by a very similar spectral behavior but a much rougher pattern.

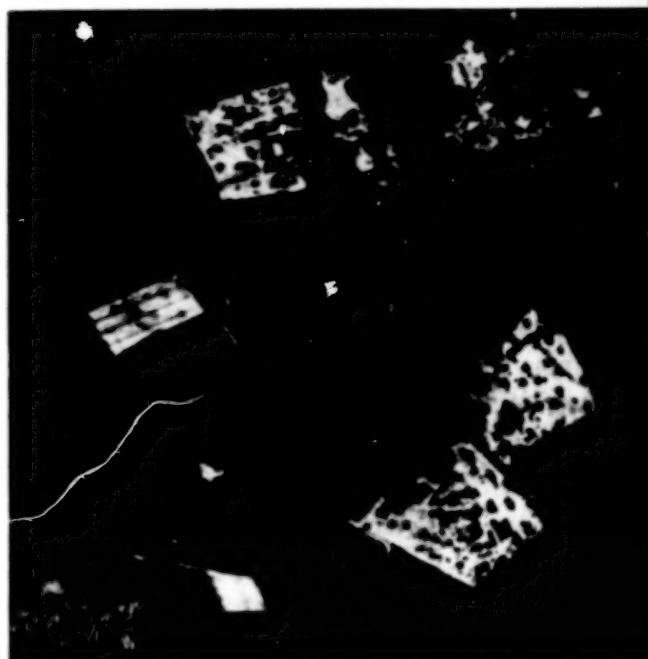


Fig 1: Panchromatic band of MOMS-02
Size of area about 2.2km x 2.2 km



Fig.2: Color composite of bands 2, 4, and 3 (BGR)
merged with the HR-panchromatic band.
Size of area about 2.2km x 2.2 km

5. CONCLUSIONS AND FUTURE ASPECTS

The analysis of MOMS-02 data is based on imagery taken during the STS-55/D2 mission in April/May 1993. To get a measure of the instruments performance, several algorithms and approaches have been used and investigated in conjunction with operational sensors. However, mainly due to thermal problems of the system, quality of this experimental data may vary significantly from one orbit to another.

In principle, the first space mission of MOMS-02 on STS-55/D2 has proven very successful. Presently, the system is refurbished and will be integrated onto the Russian MIR platform end of '96. In the frame of PRIRODA, an environmental earth observation mission, MOMS-02P will acquire data within the latitudes $\pm 51.6^\circ$ with a repetition rate of 2 to 7 days for an 18 months period.

Acknowledgement

The MOMS scientific program and this investigations are funded by the Ministry of Research and Technology (BMFT).

References

- Ackermann, F., Bodechtel, J., Dorrer, E., Ebner, H., Kaufmann, H., Koch, B., Konecny, G., Lanzl, F., Seige, P., Winkenbach, H., and Zilger, J. 1989, MOMS-02 D2 Wissenschaftsplan. DLR, Oberpfaffenhofen, FRG, 81 pp.
- Berger, M., and Kaufmann, H., 1994, Performance verification of spectral and panchromatic modules of the MOMS-02 sensor flown aboard STS-55 / D2-mission. *Proc. of IGARSS Symp.*, Pasadena, CA, USA, in print.
- Bo-Cai, G., 1993, An operational method for estimating SNRs from data acquired with imaging spectrometers. *Remote Sensing of Environment*, **43**, 23-33.
- Bodechtel, J., Kaufmann, H., Koch, B., Berger, M., Lei, Q., and Lörcher, G. 1994, MOMS-02/D2 First results and future applications. *International Journal of Remote Sensing*, in print.
- Bodechtel, J., Zilger, J., and Salomonson, V. V., 1985, Preliminary results of a quantitative comparison of the spectral signatures of Landsat TM & MOMS. *Proc. of the 3rd. Int. Colloquium on Spectral Signatures in Remote Sensing*, ESA SP-247, Les Arcs, France, 335-341.
- Hallada, A. W., Nickeson, J. E., Newcomer, J. A., and Strebel D., 1986, A comparison of MOMS and TM imaging systems, *Goddard Space Flight Center, Science Applications Research, Contr. NAS 5-28200*, Task Assignment 143.
- Kaufmann, H., 1988, Mineral exploration along the Aqaba-Levant structure by use of TM data - concepts, processing and results. *International Journal of Remote Sensing*, **9/10-11**, 1639-1658.
- Kaufmann, H., Meißner, D., Bodechtel, J., and Behr, F.J., 1989, Design of spectral and panchromatic bands for the German MOMS-02 sensor. *Photogrammetric Engineering and Remote Sensing*, **55/6**, 875-881.
- Koch, B., Schneider, Th., and Ammer U., 1993, Expected radiometric and spectral significance of MOMS-02 data for vegetation mapping - Calculations based on system parameters applied on spectral field measurements. *Remote Sensing of Environment*, **46**, 73-88.
- Meißner, D., Süßenguth, G., et al., 1993, MOMS-02 auf D2 - Endbericht. DASA-MBB, Doc.No.: **MOMS-02.RP.0100.0**, München, FRG, 91 pp.

AIRBORNE RADIOACTIVITY SURVEYS FOR ROUTINE AND EMERGENCY APPLICATIONS

G.F. Schwarz, L. Rybach, E.E. Klingelé
Institute of Geophysics, ETH-Hoenggerberg
CH-8093 Zürich, Switzerland

ABSTRACT

Helicopter surveys permit rapid evaluation with complete areal coverage of the terrestrial gamma radiation from natural and artificial radioisotopes in the topmost layer of the ground. In order to identify possible radiation level changes around the five Swiss nuclear installations (four power plants and one research facility) the surrounding regions of each site are surveyed annually. In addition, regions with elevated natural radioactivity are mapped within the framework of the Swiss National Geophysical Survey. In case of accidents in nuclear power plants with radioactive material, or from debris of nuclear-powered satellites, the system would be used to locate the radioactive sources.

The measuring system consists of a helicopter-borne gamma ray spectrometer with automatic gain control covering the energy range from 40 keV to 3000 keV and a PC-based data acquisition system. The detectors are composed of four 4"x4"x16" sodium iodide crystals with a total volume of 16.8 l.

As the main part of the surveyed area lies in the Swiss Alps, common calibration and reduction procedures can only be used after several modifications and additional correction steps in the extreme topographic conditions of the Swiss Alps. The data processing procedures adopted in this projects, in particular to reduce the effects of topography on airborne gamma-ray spectrometry measurements, are described.

The results show a very good fit with the lithology of surface rocks and can be used for geological overview mapping. The measurements in the environs of the nuclear installations enabled the detection of artificial radiation at all sites with exception of the Gösgen power plant.

1. INTRODUCTION

Regional and local gamma-ray radiation maps are of key importance for a variety of purposes: location and monitoring of contamination, basic data for radiation biology (variation of the natural exposure rate in the context of the effects of low doses), information relevant to prospecting for raw materials (for example potassium alteration) and geological mapping.

Since areal radiometric surveys are expensive and time consuming, they are advantageously carried out airborne. Airborne surveys permit rapid evaluation of radiation levels of large areas. In inaccessible regions, surveys with complete areal coverage are only possible from the air. Because of the larger ground clearance and the higher speed, the coverage per unit time of an airborne system is about 2500 times larger than of a comparable ground system. This is of key importance in radiological accidents. Although the costs for the measuring instruments and the flights are relatively high, the resulting cost per surveyed area is clearly lower than for a comparable terrestrial survey. Three projects actually make use of airborne radiometric measurements in Switzerland.

The first project aims at a better evaluation of the natural radiation level in Switzerland. The Swiss Geophysical Commission (SGPK) decided to map selected regions with elevated natural radioactivity within the framework of the Swiss National Geophysical Survey (Schwarz et al., 1992a). The main attention was given to the crystalline rocks of the Central Massifs of the Swiss Alps because of their relatively high natural radioactivity. The area covered by this survey is about 3000 km².

The second project financed by the Swiss Federal Nuclear Safety Inspectorate (HSK) concerns on artificial radioactivity. The surrounding regions (approx. 50 km²) of the four nuclear power plants (Beznau, Gösgen, Leibstadt and Mühleberg) and the Swiss nuclear research facility (Paul Scherrer Institute) are surveyed annually since four years. The measurements aim to monitor the dose-rate distribution and to provide a documented reference base (Schwarz et al., 1989, 1990, 1991, 1992 and 1993). From 1994 on the surveys will be carried out biannually.

In addition to the mentioned two projects the airborne measuring system is mobilized in case of accidents with radioactive material or from debris of nuclear-powered satellites. The emergency measurements are done by military helicopters under the control of the Swiss National Emergency Operation Center (NAZ).

The methodology developments (Schwarz, 1991) as well as the measurements were carried out by the Institute of Geophysics of the Swiss Federal Institute of Technology (Zürich). The measuring equipment was assembled, developed and calibrated at the Institute of Geophysics.

2. DATA ACQUISITION

The measuring system consists of a helicopter-borne gamma ray spectrometer with data control and storage and flight positioning instrumentation. The intention in the development of the measuring equipment was to construct a system with high data quality and security that is easy to operate and to maintain. This aim was achieved by using a spectrometer with automatic gain control and a PC-based data acquisition system. Figure 1 shows the block diagram of the complete system. The system is presented in more detail below.

The spectrometer (Exploranium GR-820) used in the system was originally designed for uranium exploration. It covers the gamma ray energy range of 40 keV to 3000 keV with 255 channels. An additional channel is used for the registration of high energy cosmic radiation. The main advantage of the spectrometer is the automatic gain control. In older systems the gain control was accomplished by using temperature stabilization methods. The new spectrometer system monitors each of the input detectors during operation and uses the peak of the natural potassium isotope ⁴⁰K as stabilization peak for the gain control. The automatic gain control eliminates the need of heating systems to keep the detector temperature constant, which reduces logistic problems significantly. Furthermore the drift is reduced and there is no more need of manually calibrating the spectrometer.

The detector package consists of four 4"x4"x16" sized prismatic thallium doped sodium iodide crystals. Each crystal is equipped with its own photomultiplier tube (PMT). The whole package is heat and shock isolated and includes the high voltage power supplies and controls for the PMT's.

The data acquisition system is based on an industrial PC equipped with rack keyboard and 9"-monitor. It synchronizes and controls the measurements. The spectrometer data are collected together with time, radar altitude, barometric pressure, temperature and attitude angles every second. The measured data are stored on JEIDA memory cards with a storage capacity of 2 Mb. This storage medium in credit card size works without moving mechanical parts and is therefore insensitive against vibrations, humidity and temperature changes.

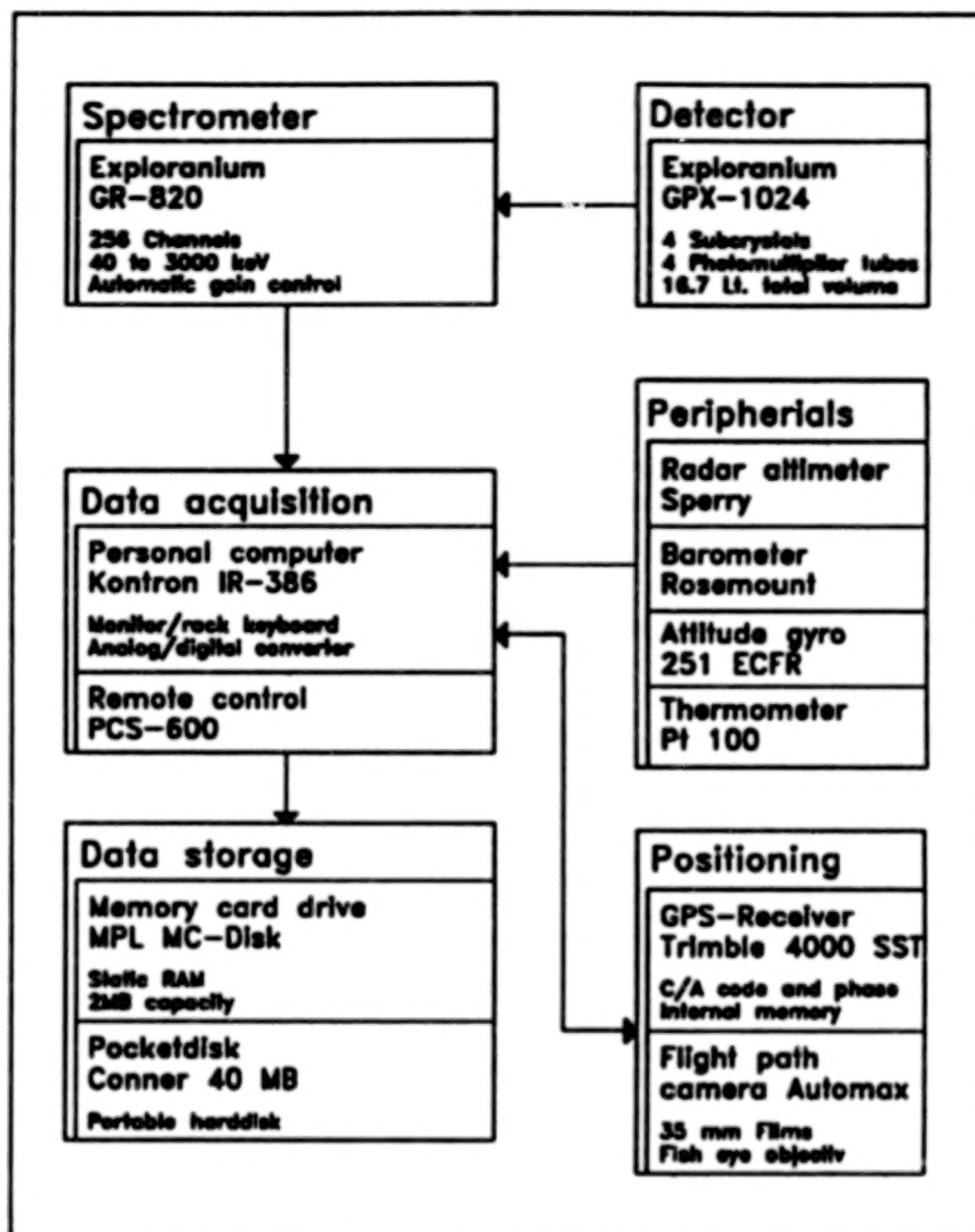


Figure 1. Block diagram of the measuring system

In order to achieve uniform coverage of the surveyed area the flights are carried out on a regular grid of flight lines. The flight line spacing depends on the flight altitude and on the desired ground coverage. It is desirable to fly as low as possible (92 m in flat terrain resp. 122 m in mountainous areas) because of the absorption of gamma-rays by the air. For overview surveys usually a flight line spacing of 500 m is used. Detailed surveys are flown with 250 m line spacing. The precision of the positioning is of ± 5 m after post processing the GPS data using a reference station. The on-line positions available during the flights are intentionally disturbed by the U.S. Department of Defense up to ± 100 m for civil users (selective availability).

The quality check takes place directly after landing. For this purpose the complete processing software including the modules for corrections and map outputs has been implemented on a transportable personal computer. This enables not only the quality control of the acquired raw data, but also the complete processing directly in the field, a facility of great importance in the event of a radiological accident.

3. PROCESSING OF RAW DATA

Since NaI-detectors have a relatively poor energy resolution the data processing is based on specified energy windows in which the registered counts are integrated. The energy windows are centered on spectral regions of special interest. The energy windows have to be sufficiently separated from each other to keep interactions small.

The region centered at the 1460 keV peak of K^{40} is used for the determination of the potassium content. Uranium is detected using the 1765 keV line of the daughter product Bi^{214} . For thorium the 2615 keV line of Tl^{208} is used. The energy windows are located at higher gamma ray energies where the absorption by air is less important. The artificial isotopes Cs^{137} and the Co^{60} are determined using energy windows centered at 660 keV and 1250 keV. Figure 2 shows a spectrum measured in the Magadino plain (TI). The peak at 660 keV which can be identified in the spectrum originates mainly from the release of the Chernobyl accident.

Three additional windows cover larger parts of the spectrum. The total count window covers the complete spectrum and is representative for the total amount of gamma radiation. The low (below 1400 keV) and the high energy part of the spectrum are registered in separate windows as an indicator for artificial radiation (see chapter 5.).

The gamma radiation registered by the detector in a helicopter is composed of the contributions from soil, atmosphere, aircraft and cosmic radiation:

- Cosmic radiation: During the absorption process of the cosmic high energy particle radiation gamma radiation is produced, which is registered by the spectrometer. The intensity of the cosmic radiation depends mainly on the thickness of the atmosphere above the measurement location and therefore on air pressure and altitude above sea level.

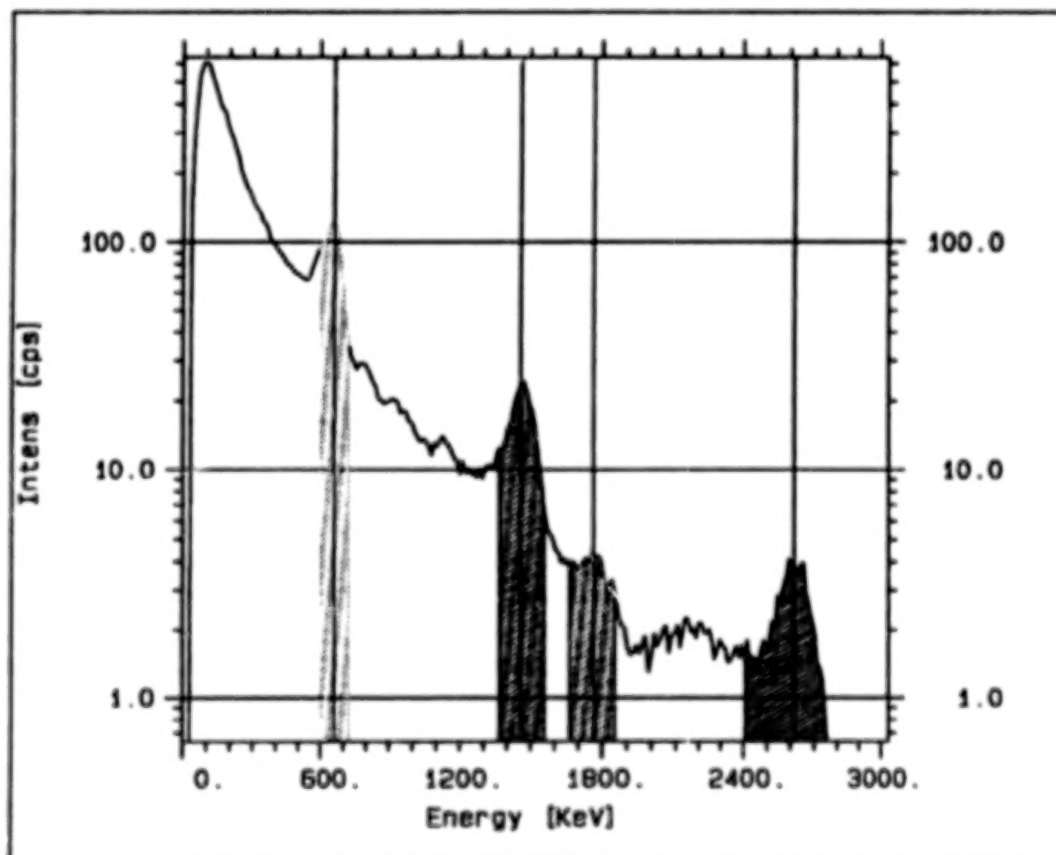


Figure 2. Spectrum of the γ -radiation in the Magadino plain (TI) as measured in July 1991.

- **Atmospheric radiation:** The most important radiation source in the atmosphere is the isotope Rn^{222} of the inert gas radon. It originates from the decay of uranium. The concentration of radon in the air depends on meteorological conditions and is strongly variable.
- **Background radiation from aircraft and detector:** In the aircraft as well as in the detector material itself small amounts of radioactive material are present. The helicopter background is assumed to be constant.
- **Terrestrial radiation:** Terrestrial radiation is mostly produced by the decay of the four natural radio isotopes U^{235} , U^{238} , Th^{232} and K^{40} . Sometimes contributions of long living decay- and activation-products from nuclear weapon tests and/or nuclear facilities as Cs^{137} and Co^{60} add to the natural contributions.

The aim of airborne radiometric measurements is the determination of the radionuclide content of ground using the information of the direct terrestrial gamma radiation. All other contributions are perturbing and have to be removed. These contributions are determined by flights above large lakes, where the ground radiation is completely absorbed by water. Whereas the helicopter background and atmospheric radiation is assumed constant, the contribution of the cosmic radiation increases with increasing height. Therefore the calibration flights are carried out at different altitudes above sea level.

The gamma ray spectrum received during field measurements is very complex. It is composed of the contributions of several radio isotopes. The spectrum is further complicated by scattering and absorption, which can occur in the ground, in the air and in the detector itself. To reduce the radiation intensities measured from the air to the ground activity a second set of corrections is needed. These corrections are called normalization corrections and are carried out applying the following steps:

- **Spectral stripping:** Gamma rays are scattered in the detector crystals, in the air and also in the soil. The scattering changes the energy of the radiation and therefore the original spectrum. The spectral stripping reduces the data to the primary (direct) radiation contribution by removing the effects of scattering and contributions from other isotopes.
- **Altitude correction:** The effects of a varying flight altitude are removed with the altitude correction. These variations represent the most significant perturbation to airborne radiometric measurements. The gamma ray intensity decreases rapidly with increasing ground clearance because of absorption of gamma rays in the air.
- **Topographical correction:** The effects of topographic relief can be neglected in flat or slightly hilly areas. In narrow valleys, which are abundant in the Swiss Alps, topography can produce a strong increase of the count rates by as much as 100%. These effects can be corrected adequately in most practical circumstances with the topographical correction (Schwarz et al. 1992b).
- **Conversion to general units:** In a last step the detector-specific count rates are converted to the corresponding soil activity or radionuclide concentrations. For this conversion the detector sensitivity is needed. In case of uranium and thorium, radioactive equilibrium is assumed.

Contrary to the background corrections, the normalization corrections need assumptions on the distribution of the radioactive source(s). The topographical and the altitude corrections as well as the conversion to general units can only be carried out when the activity distribution is known. Normally the natural radioisotopes are homogeneously distributed in the ground. Their activity distribution can therefore be considered as known, which is not the case regarding artificial isotopes. This is the reason why the normalization corrections with exception of the spectral stripping and the altitude correction generally apply only to the natural isotopes.

The methods developed for processing and correction allow a routine processing of airborne radiometric data acquired even in areas with high topographic relief. The complete processing software including the modules for corrections and map outputs has been implemented on a personal computer. This enables not only the quality control of the acquired raw data, but also the complete processing directly in the field, a facility of great importance

in the event of a radiological accident. The software is menu driven and easy to use and easy to learn even for non computer specialists. It contains a total of 32'000 lines of source code. An overview of the software modules is given in Table I. Details are given in Schwarz (1991).

4. CALIBRATION

The spectral stripping factors, the attenuation coefficient of air and the detector efficiency and sensitivity are determined ideally on large concrete calibration pads with a precisely known radioisotope content (Purvanec & Novak, 1983). Unfortunately there are no such calibration pads available in central Europe.

The stripping factors were determined using radioactive point sources with small activities around 37 kBq. The precise activity of the calibration sources must not be known, since only ratios are used in the calculations. For each energy window a corresponding calibration source is needed. The factors determined with point sources have been corrected mathematically to account for the different geometry of the pads (Grasty, 1975; Schwarz, 1991).

The determination of the detector sensitivity is based on the detector efficiency and model calculation of the gamma ray flux. For detector efficiency determination a Cs^{137} and a Co^{60} source (each of 1.9 GBq) were used. The measurements were carried out with the helicopter at different source distances. The measured count rate of the point source leads to the detector efficiency and the attenuation coefficient of the air at the corresponding gamma energies. The detector efficiency at other energies can be derived by extrapolation using an approximation of the efficiency curve of sodium iodide detectors (Grasty, 1975). In a last step the detector sensitivity at flight altitude is calculated from the detector efficiency and gamma ray flux calculations (Schwarz, 1991; Løvborg et al., 1975).

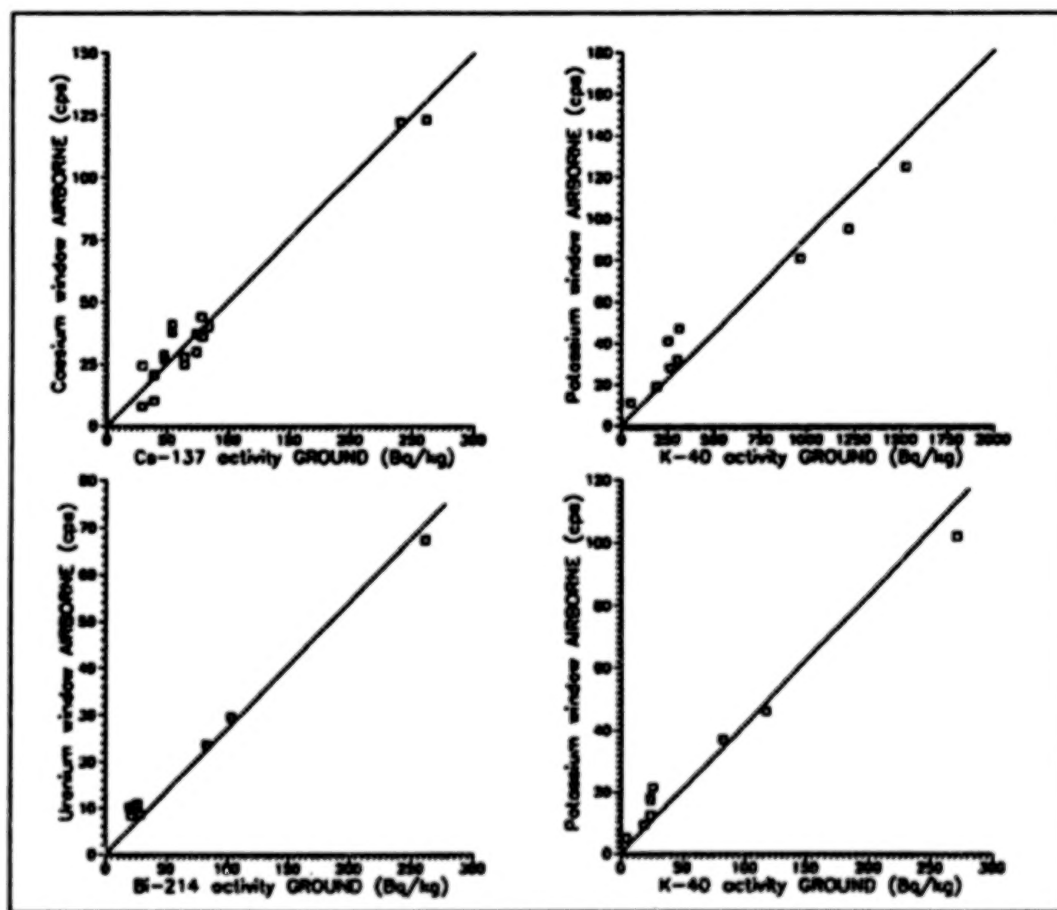


Figure 3. Experimentally determined detector sensitivities

The results of this calibration procedure were controlled by high precision in-situ gamma spectrometric measurements together with gamma spectrometric measurements of natural isotopes on rock samples (Labhart & Rybach, 1971). The corrected count rates measured with the airborne system are plotted against the determinations of ground activity in Fig. 3. As can be seen from Fig. 3 the data show a reasonably good correlation between the airborne and the ground measurements.

TABLE 1. SUMMARY OF THE DETECTOR SENSITIVITY DETERMINATIONS.

Window	Radio nuclide	Activity [Bq/kg]	Z_{eff} Model [cps]	Z_{eff} Exp. [cps]	Ground dose rate [nSv/h]
Cesium	Cs ¹³⁷	100	-	50	17
Potassium	K ⁴⁰	100	9	7	5
Uranium	Bi ²¹⁴	100	27	27	52
Thorium	Pb ²⁰⁸	100	41	42	73

The ratio count rate/ground activity allows to determine the detector sensitivity for the specific flight altitude (100 m in this case) for each energy window. As can be seen from Table 1 the experimentally found values are in good agreement with the values derived from point sources. The advantage of the calibration using point sources is that it is not limited to isotopes abundant in the natural environment.

5. MAP GENERATION

Unlike a camera, a gamma-ray detector does not have a fixed field of view since it can receive radiation from any angle. For airborne gamma-ray observations, the field of view of a detector is commonly thought as the circular area beneath the aircraft contributing to a fixed percentage of the total detected radiation (generally 75%). This area corresponds approximately to the area of the smallest resolvable structure (Pitkin & Duval, 1980) and is chosen as pixel size.

The field of view at a flight altitude of 90 m is about 125 x 125 m so this pixel size is used for the representation. Since the distance between two measurements is 25 m at a typical flight speed of 25 m/s, a pixel represents the average of five measurements. This averaging also reduces the error of the radiometric data which always show a large statistical scattering.

The generally used line spacing is 250 m, so only half of the pixels will contain data without interpolation. Since the gamma ray field contains abrupt steps and the statistical error of airborne radiometric data is very large, the interpolation cannot be performed with standard methods. A simple method proposed by Green (1987) was therefore chosen for the interpolation.

The unassigned pixels are filled with the average of the surrounding neighbors if they have at least three already assigned neighbors. This procedure is repeated until the grid is completely filled. It has to be mentioned that the original values are not changed by this interpolation procedure.

Figure 4 shows the total activity map of the surroundings of the nuclear power plant Beznau (KKB) and of the research facility Paul Scherrer Institute (PSI). The total intensity of γ -radiation as measured from the helicopter is plotted in detector specific counts per second. For reproduction reasons the map is plotted in black and white. Of course, color maps can also be produced. The highest intensities (the two black spots) are measured over the two sub-units of the PSI. They are caused by the direct radiation of the storage areas for radioactive components

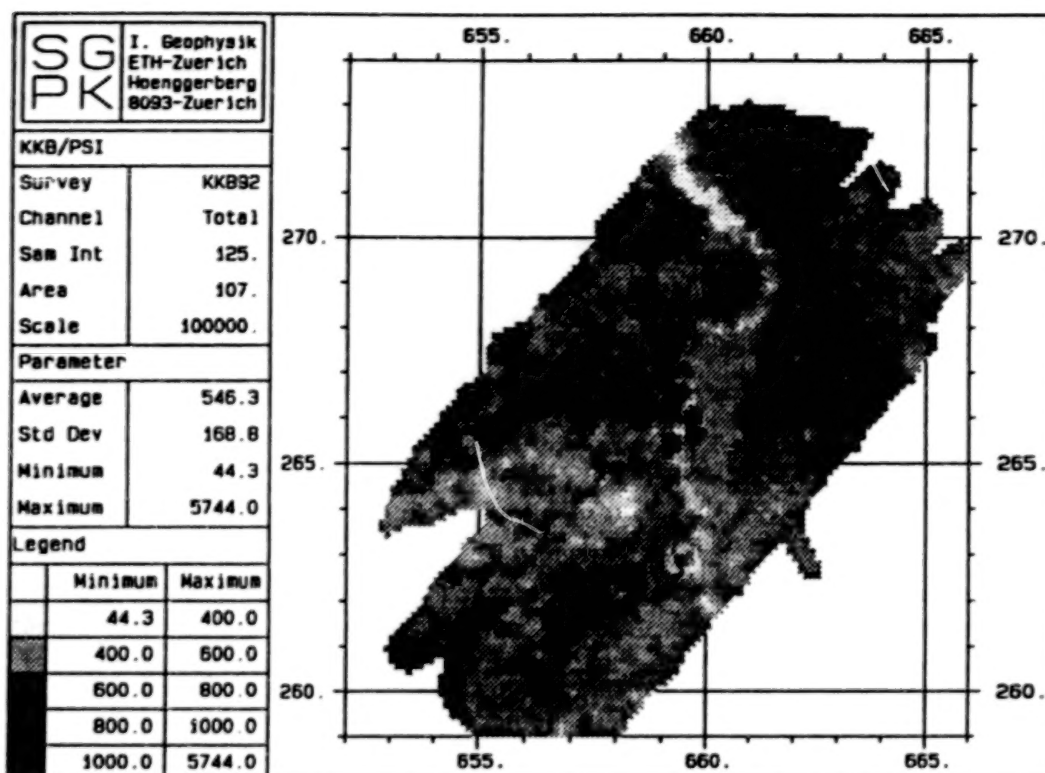


Figure 4. Total count map of the KKB/PSI survey

(PSI-West) respectively for radioactive waste (PSI-East). The water of the river Aare strongly absorbs the ground radiation, which is why the course of the river stands out in white. Even differences in vegetation cover are visible; meadows (light grey) show generally higher values than forests (dark grey).

When converting the airborne count rates to ground activities two perturbing effects have to be considered. For a constant ground activity a lower count rate is measured over forests than over meadows due to the additional absorption by trees. This attenuation varies between 5% and 25% depending on the biomass of the forest. Soil humidity and rain also influence the measurements up to 10%. This second effect is especially troublesome because the soil humidity varies with time.

Both effects can be distinctly reduced with the aid of ratios. The ratio of two windows is less affected by an additional absorber than the single window values, since the ratio is only affected by the difference of the attenuation coefficients in the two windows. Especially sensitive to artificial radiation is the so called Man Made Gross Count (V_{MMGC}) ratio (Hoover, 1988).

$$MMGC1 = \sum_{400\text{keV}}^{1390\text{keV}} I_E$$

$$MMGC2 = \sum_{1400\text{keV}}^{3000\text{keV}} I_E$$

$$V_{MMGC} = \frac{MMGC1}{MMGC2}$$

It uses the fact that the common artificial radio nuclides all radiate at gamma energies below 1400 keV, the natural isotopes on the other hand emit gamma quanta of higher energy too. The ratio of the low energy part of the spectrum (MMGC1) to its high energy part (MMGC2) corresponds therefore to the ratio of artificial to natural radioactivity. An example of representation of MMGC ratio is shown on Fig. 5.

Because of the strong correlation between the radioelements due to geochemical reasons, the maps of the natural radioisotopes are all very similar. Working with ratios of natural radioisotopes will therefore not only reduce disturbing effects, but also reduce the contrast of the image. An appropriate method to increase the contrast and with it the interpretability of an image is called histogram equalization (Haberlacker, 1985). After histogram equalization every color covers the same area on the map. The visual impression of such a representation is optimal. As a consequence the color scale becomes nonlinear.

The histogram equalization is particularly useful producing ternary maps. In this representation the maps of potassium, uranium and thorium are merged into a single map. The color red is assigned to the potassium window. Uranium and thorium are colored green and blue respectively. Regions with a high relative potassium content will appear in red color shades on the map. Correspondingly areas with a high relative uranium or thorium content will appear in green or blue shades. Regions with equally balanced radioisotopes will be plotted as gray or white shades depending on the total activity. Ternary maps can almost be read like a geological maps, especially in regions with crystalline rocks (Schwarz et al., 1992a).

6. CONCLUDING REMARKS

The methods developed for processing and correction allow a routine treatment of airborne radiometric data acquired even in areas with high topographic relief. The results for the areas processed so far show a very good fit with geology and can be used for geological overview mapping.

The airborne radiometric survey conducted so far covers about ten percent of the area of Switzerland. However, the typical geologic-lithologic units (Jura, Molasse Basin, Central Massifs) have been investigated; the results of the survey allow to describe the mean radioactivity level in Switzerland and its variation in broad outline (Schwarz et al., 1992a). Together with in-situ ground measurements and data from rock samples the airborne survey can serve as a good base for the compilation of a radiometric (dose rate) map of whole Switzerland including the contributions of artificial isotopes and cosmic radiation. The measurements in the environs of the Swiss nuclear installations showed that all sites (with the exception of the Gösgen power plant) can be identified clearly on the MMGC-ratio maps.

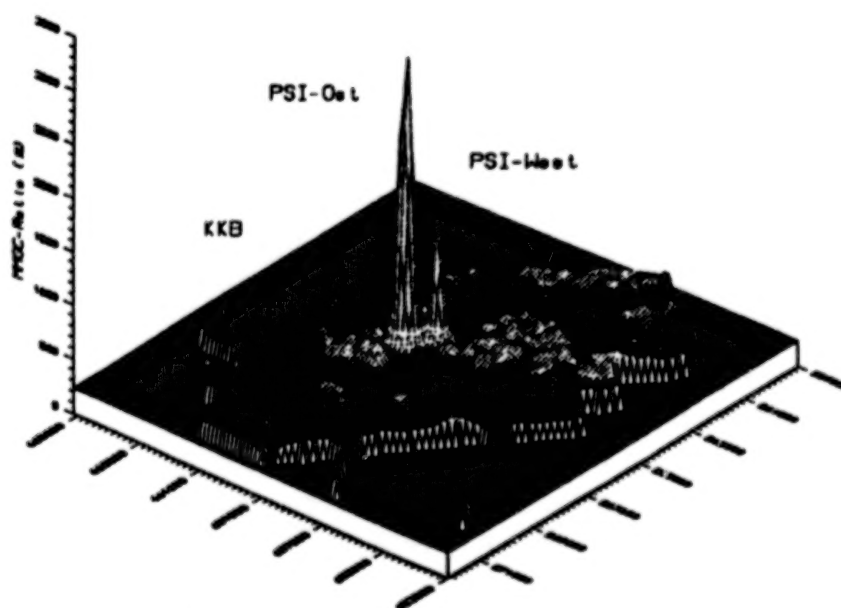


Figure 5. 3D-representation of the MMGC-ratio of the region of Würenlingen/AG (looking from north west).
The highest peak corresponds to a ground dose rate of 2 mSv/a.

Figure 5 shows a three dimensional representation of the MMGC-ratio of the surroundings of Würenlingen/AG (looking from north east). The two locations of the Paul Scherrer Institute PSI-Ost and PSI-West show up particularly well. The signal is caused by the direct radiation of the storage areas for radioactive components (PSI-West) and radioactive waste (PSI-Ost). The smaller peak is caused by the Beznau nuclear power plant. The highest peak corresponds to a ground dose rate of 2 mSv/a.

At sites of operating boiling water reactors (BWR) the high energy radiation of the activation product N^{16} is clearly visible in the data. No artificial radioactivity, that could not be explained by Chernobyl or nuclear weapon test, was detected outside of the fenced sites of the nuclear installations. The repeated measurements in the last four years (Schwarz et al., 1989, 1990, 1991, 1992 and 1993) showed that the radioactivity level in the environs remained more or less constant within the measurement errors.

7. REFERENCES

- Grasty, R.L., 1975: Uranium measurements by airborne gamma-ray spectrometry. *Geophysics* **40**, 503-519.
- Green, A.A., 1987: Leveling airborne gamma-radiation data using between-channel correlation information. *Geophysics*, **52**, 1557-1562.
- Haberäcker, P., 1985: *Digitale Bildverarbeitung, Grundlagen und Anwendungen*. Hanser Studienbücher, München/Wien.
- Hoover, R.A., 1988: An aerial radiological survey of the River Bend Station and surrounding area. National Technical Information Service, U.S. Department of Commerce, Springfield (Virginia).
- Löbhart, T.P., Rybach, L., 1971: Abundance and distribution of uranium and thorium in the syenite of Piz Giv (Aar-Massif, Switzerland). *Chemical Geology* **7**, 237-251.
- Løvborg, L., Bøtter-Jensen, L., Christiansen, 1975: Gamma-ray measurements in an area of high natural radioactivity, Proc. of the third international symposium on the natural radiation environment, Houston (Texas), CONF-780422, US DOE Technique Information Center.
- Pitkin, J.A., Duval, J.S., 1980: Design parameters for aerial gamma-ray surveys. *Geophysics* **45**, 1427-1439.
- Purvance, D., Novak, E., 1983: General procedure for calibration and reduction of aerial gamma-ray measurements: Specification BFEC 1250-B. U.S. Department of Energy, Rep. GJBX-16(83) DE84004974.
- Schwarz, G.F., 1991: Methodische Entwicklungen zur Aerogammaspektrometrie. Beiträge zur Geologie der Schweiz, Geophysik Nr.23, Schweizerische Geophysikalische Kommission (Available from: Institut für Geophysik ETHZ, CH-8093 Zürich).
- Schwarz, G.F., Klingelé, E.K., Rybach, L., 1992a: Airborne radiometric mapping in Switzerland. Beiträge zur Geologie der Schweiz, Geophysik Nr.25, Schweizerische Geophysikalische Kommission (Available from: Institut für Geophysik ETHZ, CH-8093 Zürich).
- Schwarz, G.F., Klingelé, E.K., Rybach, L., 1992b: How to handle rugged topography in airborne gamma-ray spectrometry surveys, *First break* **10**, 11-17.
- Schwarz, G.F., Klingelé, E.K., Rybach, L., 1989, 1990, 1991, 1992, 1993: Aeroradiometrische Messungen in der Umgebung der schweizerischen Kernanlagen; Bericht zuhanden der Hauptabteilung für die Sicherheit der Kernanlagen (Available from: Institut für Geophysik ETHZ, CH-8093 Zürich)

MULTISPECTRAL BACKGROUND MEASUREMENTS FROM AN AIRBORNE MWIR SENSOR

K.D. Bishop, J.A. Granger, E.L. Jewett
Lockheed Palo Alto Research Labs
Palo Alto, California 94304

ABSTRACT

A wide variety of Multispectral MWIR background measurements have been collected over the past 12 months as a part of the Airborne Instrument Program (AIP). Data from these collections include: diffuse and specular surface reflections from cloud tops and alpine lakes, lava flow mapping on the island of Hawaii, demonstration of stereoscopic imaging techniques, and a Multispectral pushbroom tour of the diverse micro-environments of the Hawaiian islands. The sensor provides 45 channel spectral data over the 2-5 mm band combining aspects of the solar reflective (short wave) and thermal (long wave) IR. Both pushbroom and scanning data collection and image reconstruction techniques will be applied to a wide variety of MWIR backgrounds. Applications of MWIR multispectral differencing for feature enhancement, narrow band absorption feature identification and agricultural assessment/identification will also be demonstrated.

1. INTRODUCTION AND SYSTEM DESCRIPTION

The Airborne Instrument Program (AIP) is a Multispectral Mid-Wave Infrared (MWIR) data collection activity conducted by the Lockheed Palo Alto Research Labs in conjunction with the NASA Johnson Space Center's WB-57F high altitude research aircraft program. The data presented here summarize the flight experiments between March and August of 1993.

1.1 AIRCRAFT PLATFORM

Based at Ellington Field, an offsite extension of the NASA Johnson Space Center in Houston Texas, the WB-57F is a high altitude, two-place, twin-engine aircraft with a maximum ceiling of 19 km (62,000 ft). The F-model is a descendant of the earlier B-57, originally modified for high altitude reconnaissance (larger wingspan, more powerful engines), with the bomb bay areas converted over to house scientific instrument packages such as the AIP sensor. Due to fuel efficiency and operational safety constraints, the aircraft is typically operated at altitudes of either 14 km or 18 km with the latter requiring the use of full body pressure suits by the aircrew. Cruising speed, at 14 km, is typically 390 knots with a maximum flight duration, limited primarily by fuel capacity, of approximately 6 hours. The aircraft cockpit is two-seat with a pilot and instrument operator/navigator making up the flight crew.

1.2 AIP SENSOR PAYLOAD

The instrument itself is both a scanning spectrometer and staring radiometer utilizing common pointing optics, imaging lens and Indium doped Silicon photoconductive 45x90 element detector array. An internal motor driven mirror is commanded into or out of the optical path to bypass the spectrometer and reflect the incoming light directly into the imaging lens and onto the focal plane to provide a two dimensional staring capability as well as a multichannel (currently approximately 60 useful channels) MWIR spectrometer. The spectrometer utilizes a narrow reflective slit as a field stop and a two-element prism to provide spectral dispersion. Additionally, two motorized 5-position filter wheels, one containing 4 bandpass filters and an open, and the other with 4 neutral density filters and an open, are housed within the vacuum-cryocooled dewar enclosing the telescope optics. Spectral resolution, determined by the projection of the prism dispersion onto the multi-element detector array,

ranges from 25 nm at 2.2 μm to 70 nm near 5 μm . The total spectral coverage of the spectrometer extends from 2.0 to 6.3 μm , however for most down-looking applications, typically 50-60 of the 90 focal plane columns receive useable signal levels due to atmospheric absorption. As the focal plane array (FPA) is oriented with the dispersion direction along the 45 element (row) axis, a frame of spectrometer data consists of 50-60 narrow band line images of the projected footprint of the reflective entrance slit.

A diagram of the AIP optical system is presented as Fig. 1 below. The task of pointing and acquiring an object of interest are performed by a Stabilized Mirror Pointing System (SMPS) in conjunction with visible-band TV cameras feeding into a monitor in the instrument operator's console. Operator joystick commands, a pre-programmed position/angle timeline, or a closed loop video tracker system can all be used to control instrument pointing over a range of 30 deg forward to 20 deg aft in pitch (along the axis of the aircraft) and 90 deg either side of straight down (NADIR) in roll. Additionally, a commercial Short Wave Infrared (SWIR) camera utilizing a Pt:Si detector array and Charge Couple Device (CCD) readout structure is installed in the system as an alternate tracking source to the wide and narrow field TV cameras.

To sweep the projection of the spectrometer entrance slit across the target area, a motorized, commandable, fine scan mirror system may be used as an alternative to the simple fixed angle/aircraft motion pushbroom commonly used on down looking systems. The angular resolution or detector instantaneous field-of-view (IFOV) is 1.17×10^{-3} rad/detector element for the radiometer or the spatial axis of the spectrometer. The projected angular width of the entrance slit is currently 360 μrad , having been recently increased from 150 μrad at the time of these data collections. The practical angular resolution of the scan-axis of the spectrometer however is generally a function of scan mirror angular rate and/or aircraft velocity. External optical elements are sized for 45x45 detector array with some oversizing in the scan direction to allow for scan mirror motion, bringing the total Field of View (FOV) to 53 mrad or 3 deg.

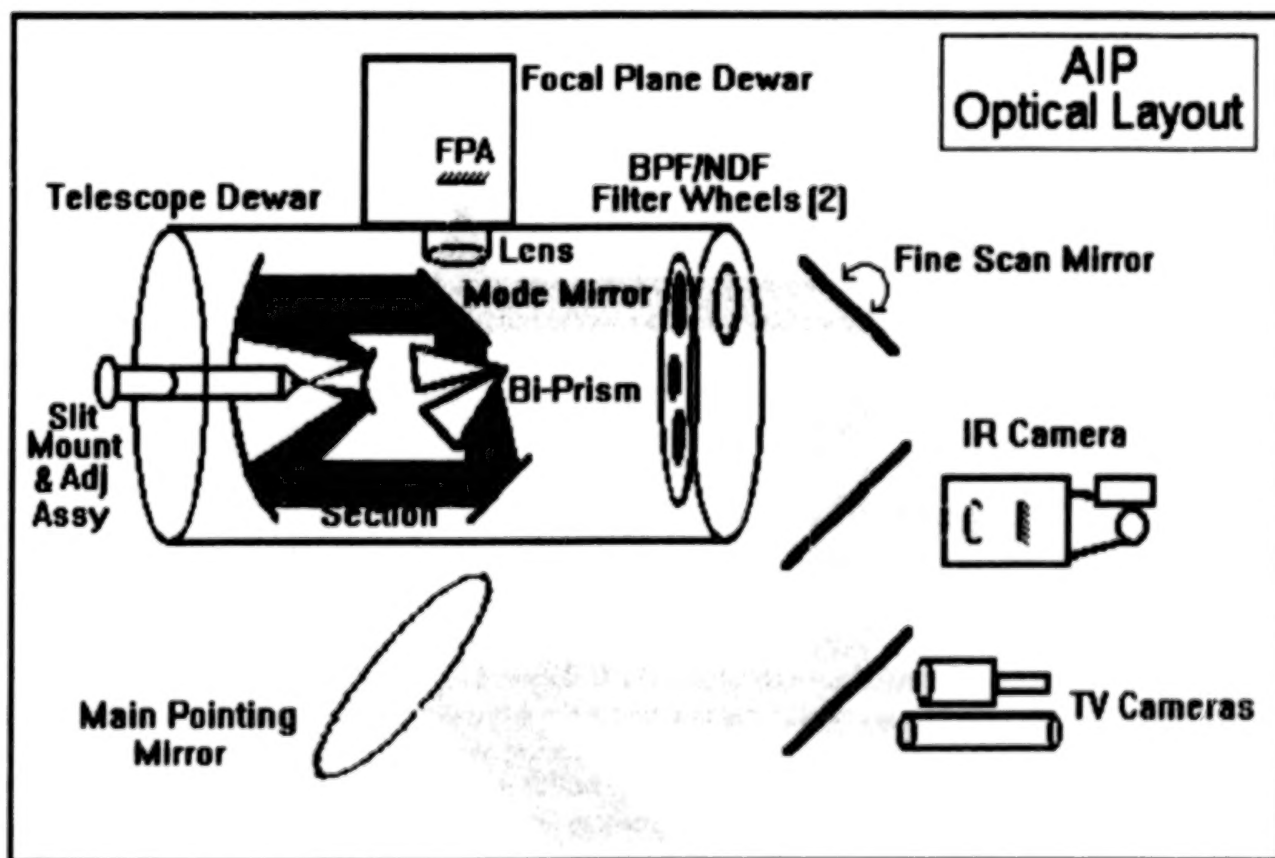


Figure 1. AIP Optical System Diagram. Radiometer and Spectrometer Paths Shown in Two-Tone Gray Scale

2. 1993 DATA COLLECTIONS

During March through August of 1993, the AIP program was heavily involved in the acquisition of multispectral MWIR data on natural terrestrial sources. Some of these measurements were aimed at characterizing potential false alarm sources for overhead systems, particularly the direct solar specular reflection off cloud or high altitude lake surfaces. A thermal mapping experiment on the currently active lava flow areas on the island of Hawaii, and a demonstration of stereoscopic imaging techniques possible with the AIP system were also conducted during this period. In addition, a multispectral pushbroom mapping 'tour' of the Hawaiian islands, collected 25 May 1993, obtained data on a wide variety of agricultural, urban and geologic environments. A summary of each of these experiments, complete with examples of the MWIR imagery and spectra, is presented in the following paragraphs.

2.1 SOLAR REFLECTIONS OFF HIGH ALTITUDE ICE CLOUDS

The occurrence of strong solar reflections off thick, high altitude cloud layers has long been recognized as a potential source of false alarm for overhead detection systems. In a measurement conducted 4 Mar 1993, the AIP sensor obtained approximately 500 seconds of data, both in the scanning spectrometer and staring radiometer modes, on the direct solar specular reflection off high altitude ice clouds. Using the on-board TV/video closed loop tracking capability, the system was able to 'lock' onto and follow the image of the solar disk as reflected off the cloud tops. The aircraft continued to fly parallel to the long axis of the cloud layer which was oriented approximately 90 degrees to the solar azimuth. These data were collected off a formation of thick cirrus/cirrostratus over west Texas, just outside the city of Abilene. Immediately prior to take off, the NASA weather facility at Ellington Field provided information on cloud location, structure and an estimate of cloud altitudes in the region of 6-7 km (19-24,000 feet) for the tops, with a cloud base down to 4-5 km.

Figure 2 is a TV/visible band image of the cloud reflected solar disk as seen in the instrument operator's cockpit monitor. The square in the middle of the image defines the video tracker gate, within which the cursor, at the very center of the image, marks the track point. (i.e. the point in the video frame chosen by the tracker to fix the line of sight.) Also indicated in Fig. 2 are the pointing mirror (SMPS) angles of 6 degrees forward and 53 deg up (relative to nadir). Figure 3 is a false color 45x45 element staring IR radiometer image of the solar disk as seen through a 2.68 - 2.97 μm bandpass filter. Peak in-band radiance is 112 $\mu\text{W}/\text{cm}^2\text{-SR}$ in this frame (Fig. 3), but varies throughout the data set from negligible signal to detector saturation as the thickness of the cloud layer changes. The image reversal, seen between the TV and IR images, is simply a function of the orientation and readout structure of the focal plane relative to the TV camera.

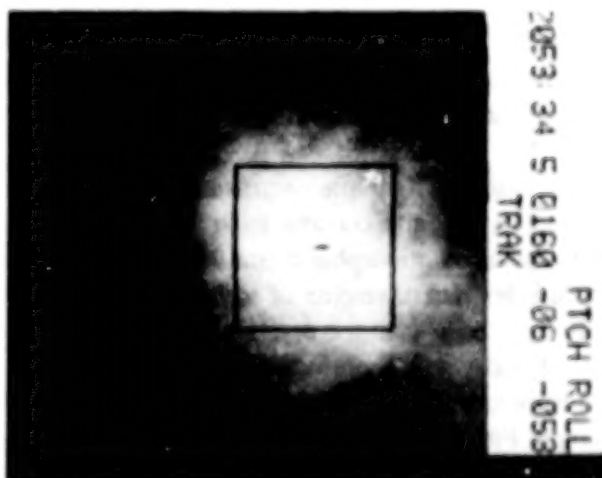


Figure 2 - TV Video (Visible) Image of Solar Disk as Reflected Off a High Altitude Cloud Layer

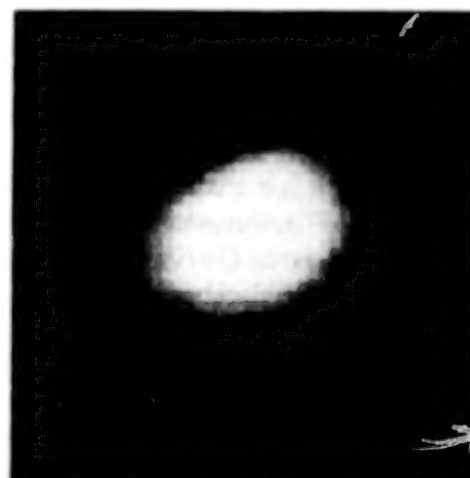


Figure 3 - False Color IR Radiometer Image : 2.68-2.97 μm Band

Cloud Reflected Spectra vs Model

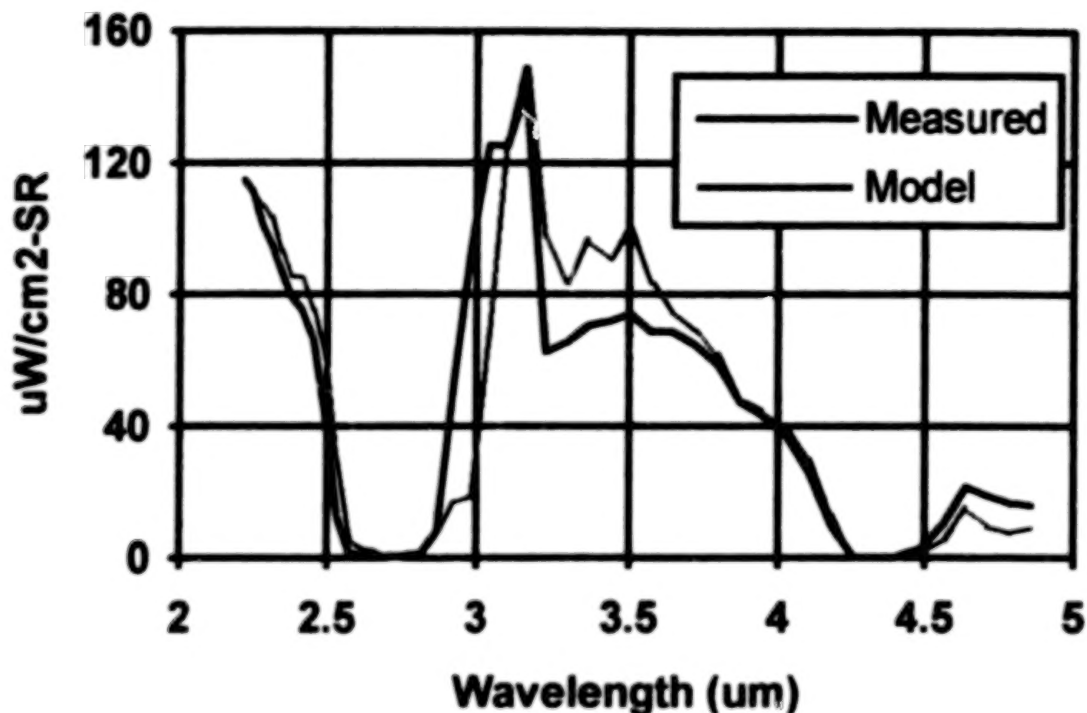


Figure 4 - Cloud Reflected Spectra vs Model. Comparison of 4 Mar 1993
Measured Cloud Reflected Solar Spectra with Ice Crystal Model

An example of the measured cloud reflected solar spectra from the 4 Mar 1993 flight is displayed in Fig 4 above. The strong atmospheric absorption features at 2.8 (H_2O) and 4.3 μm (CO_2), are readily apparent in the reflected spectra, and indicate that even above 6-7 km there is enough CO_2 and water vapor in the atmospheric path to almost completely attenuate the reflected solar energy in these bands. The actual peak in the reflected spectra occurs not at the short wavelength (2.2 μm) end of the spectra, as might be expected from the Sun itself which is commonly approximated as a 5900 K blackbody, but just past the H_2O absorption band, near 3.0 μm .

Also shown in Fig 4 is a prediction of the reflected solar spectra based on a simple solar/ice cloud reflectance model. Utilizing AFGL cirrus/cirrostratus ice crystal particle size, typing and concentration measurements as summarized by Anderson (1979), a LOWTRAN 5B spectrally enhanced atmospheric transmission model, an assumed 5900 K solar blackbody source spectra, and refractive index measurements of ice as summarized by Liou (1980), a model was constructed assuming horizontally oriented planar ice crystals to be the primary reflection mechanism. The presence of these 'hexagonal plate' crystals, with a preferred horizontal orientation within the cloud, is further confirmed by laser backscatter and de-polarization measurements as summarized by Platt (1980). Ice crystal reflectance is then modeled as a simple Fresnel calculation based on the spectrally varying index of refraction and angle of incidence θ reconstructed from sensor and aircraft telemetry. The resulting spectra, also illustrated in Fig 4, is in excellent agreement with the measured data below 2.9 μm , between 3.1-3.2 μm , and beyond 3.6 μm . In the 2.9-3.1 μm region, the rapid and dramatic change in the index of refraction of ice, and the variability of its spectral features with conditions (temperature, pressure)

surrounding formation of the crystals, combine with in-exact modeling of the atmospheric transmission in the tail edge of the H₂O absorption band to result in significant uncertainties in the model and thus the poorer agreement between data and model shown in this area of Fig 4. Between 3.2-3.6 mm, the differences between data and model (up to 33% at 3.5 μ m) result from inaccuracies in the atmospheric transmission model due largely to the lack of local meteorological data.

A normalizing factor was required to provide the close agreement between data and model depicted in Fig 4. This factor may be physically interpreted as representing the fraction of the projected area of the pixel footprint occupied by reflecting ice crystals, and can be approximated by a rather simple dimensional argument. Based on the AFGL ice crystal sizing, concentration and typing data reported by Anderson (1979), a typical size for the planar hexagonal plate crystal is 100-300 μ m with concentrations ranging from 500-2000 / m³ in dense cirrostratus. Using a crystal area of $(100 \times 10^{-6})^2$ m² and multiplying by a concentration of 10³/m³, an 'obscuration factor' of 10⁻³/m of depth into the cloud results. Multiplication of this factor by an appropriate 'reflection depth' (i.e. the distance over which the reflection occurs) will result in the desired estimate.

Based primarily on a review of the available flight TV/video and operator observations while passing through the cloud formations, a reflection depth of 100 m was chosen resulting in a total 'pixel/ice crystal fill factor' of 10⁻³ which compares quite well with the actual 1.5×10^{-3} factor used (in Fig 4) with a single (front) surface ice crystal reflection, or 8×10^{-4} for a double (front/back) surface reflector. In either case the normalizing factor is within 50% of the first-order estimate.

In comparison, typical LIDAR-measured optical extinction coefficients range from 0.3-1.4 /km for thin cirrus 10-30 /km for alto-stratus (Carswell (1980)). As the observed cloud was more similar in density to alto-stratus, the 100 m reflection depth, and hence the area factor of 10⁻³, seems reasonable.

In all, the cloud/solar reflection experiment produced a large set of multispectral MWIR data of apparently high quality and utility in the development of cloud reflectance models and the understanding of potential problems posed to overhead remote sensing systems by direct cloud/solar specular reflection. A complete data package including video tapes, calibrated multispectral data, mission description and data quality assessment/analysis reports is available to interested potential users.

2.2 THERMAL MAPPING OF ACTIVE LAVA FLOWS

In May 1993, the AIP sensor and NASA WB-57F were deployed to Barber's Point Naval Air Station, Oahu in order to make multispectral MWIR thermal mapping measurements of the currently active lava flow areas on the island of Hawaii. Utilizing USGS geological and topological mapping data, a plan was developed for the collection of parallel flight tracks covering an area of approximately 5 km wide by 13 km long extending from just above the Pu'u O'o vent, a subsidiary vent of Kilauea, down to the sea. As the flow is almost entirely contained in an intricate network of underground flow tubes, the thermal mapping of the upwelling heat flow and surface temperature gradients are the primary indicators of the flow patterns below. Occasionally a collapse in the roof of the underground flow tube or 'skylight' can be seen visually under low light conditions (night); otherwise the flow areas are essentially a featureless expanse of solidified volcanic rock.

With the WB-57F at an altitude of 18.3 km (60,000 feet), the AIP spectrometer's projected footprint is just over 21 m in the cross-track direction and the distance traveled by the aircraft, cruising nominally at 390 knots, in one integration time, at a nominal 40 Hz frame rate, is about 5 m. Thus each frame of data for an individual pixel represents the spectra obtained from a region roughly 5 m long by 21 m wide as projected onto the ground below. The total width of the single flight-line swath is just under 1 km. To assure complete area coverage and sufficient track to track overlap for the spatial registration and mosaic construction to follow, a total of 10 separate flight tracks were collected between 11 p.m. and 1:30 a.m. local time.

Figure 5 at right is a single band false color thermal IR (4.7 μm) mosaic reconstruction of the active flow areas between the Episode 51 vents, near Pu'u O'o, and the Pacific. The composite image was produced by the registration and superposition of data from 7 of the 10 flight tracks. Track-track seams are still faintly visible in the final image. To properly reconstruct the spatial along-track axis, a graphical display of the data at a 4:1 aspect ratio was used to represent the distance traveled by the sensor line-of-sight in a single frame time in proportion to the apparent width of a pixel footprint in the cross-track direction. In this fashion, the data at right represents the radiometry collected over a 2500 frame by 225 pixel (12.3 x 4.8 km) area.

Detector saturation effects are evident in the image as white horizontal lines or 'spill-over' of charge within the focal plane's Charge-Coupled-Device (CCD) readout; the heaviest region of which occurs directly over the main vent and lava pool at Pu'u O'o as seen in the upper right of the mosaic. The chain of small sources extending through the main vent and diagonally across the upper portion of the image are the fissures and vents marking the East Rift Zone. The Kilauea summit could be reached by following the chain back up the slope, approximately 17 km to the left. The Kupaianaha vent, scene of the 1986-90 eruptions which buried Kalapana and the Royal Gardens subdivision, would be found about 3 km further to the right.

Immediately below the main vent, the apparent flow is diffuse, covering an area 1.5 x 3 km with several localized hot spots or 'skylights' (small areas of exposed flow usually caused by collapse of a piece of the solidified 'roof' over the flow) as evidenced by detector saturation. The flow begins to converge on a single, clearly defined channel mid-way down the slope (around the 2,000 ft elevation level). The flow then divides first into two channels and ultimately a complex network of flow tubes before separating again into two major flow channels.

The left of these two arms of the flow exits directly to the shoreline forming a triangular delta at the mouth. The right channel, initially narrower and more distinct, divides into a maze of tunnels and empties into the ocean in at least two, but probably more, locations. A massive delta of lava 0.5 km wide by 300 m deep forms at the rightmost entrance to the sea. Thermal plumes in the ocean surface spread more than 1 km in any direction outward from the discharge point, and can be clearly be seen at the bottom of the image.

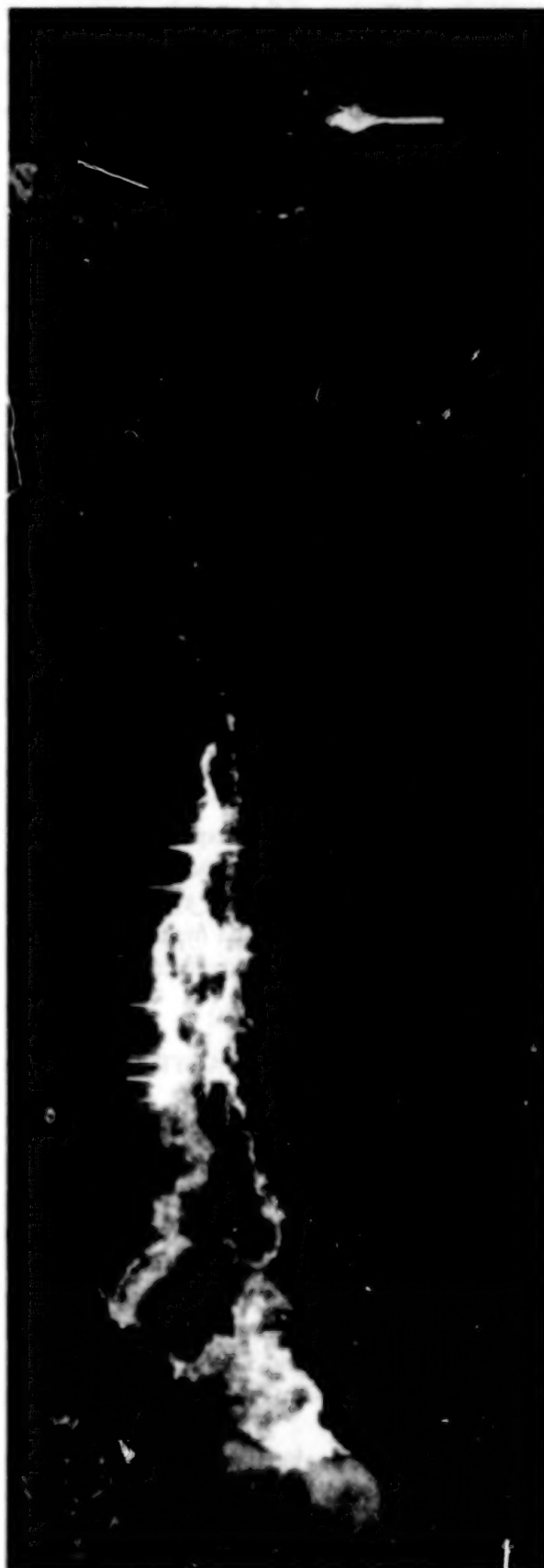


Figure 5 - False Color IR Map of the Active Flow Areas between Pu'u O'o and the Sea

The image in Fig 5 is a single-band spatial reconstruction. A total of 45 such mosaics have been constructed and included in a complete data package (reports, calibrated MWIR spectrometer data, video tape, aircraft and sensor telemetry, etc...) based on the Hawaii lava thermal mapping experiment.

2.3 A MULTISPECTRAL 'TOUR' OF THE HAWAIIAN ISLANDS

Another experiment conducted during the May 1993 deployment involved the collection of a multispectral pushbroom 'tour' of the various cultural, agricultural and geologic features of the Hawaiian islands. A total of 6 pre-planned flight lines over the islands of Hawaii, Oahu, Maui and Kauai were flown on 25 May 1993 between 10 am to 12 p.m. local time. The sensor was configured in the down-looking (nadir) spectrometer mode utilizing the aircraft motion to sweep or 'pushbroom' the projection of the spectrometer entrance slit across the scene below. As the aircraft was flown at an altitude of 14.6 km (48,000 feet), the cross-track pixel footprint, at sea level, of each detector was 17.1 m for a total cross-track swath width of 770 m. The nominal aircraft cruising speed was 390 kts.

The first track, over the island of Hawaii, traces a line between the peaks of Mauna Loa and Mauna Kea at 20 deg east of north for a distance of about 60 km (some 12,400 frames of data at a nominal 40 Hz rate) covering portions of the Hawaii Volcanoes National Park, and the Mauna Loa and Mauna Kea Forest Reserves. The terrain is steeply sloped with surface elevation ranging from 2 to over 4 km at the Mauna Kea peak. Centuries of volcanic activity have produced a quilt-like landscape of superimposed flows of varying age and color from the jet black recent flows (less than 200 years old) to the ash-white of the ancient cinder, as seen in the visible. Vegetation is limited to a fairly narrow band at the foot of the Mauna Kea slope between 2-3 km in elevation.

In contrast to the rather barren landscape of central Hawaii, the Maui track, second of the six, was chosen to pass over the fertile northeast corner of the island near Hana, through the rainforests of the Koolau Forest Reserve, and eventually back to sea over the cane fields of Paia. The total track length is about 50 km. The rainforest areas are steeply sloped between 0.3-0.6 km in elevation with numerous streams and gullies carving out the hillsides. The farming and township areas cover gently sloping hills and coastlines below 0.3 km.

Three of the six tracks were collected over the island of Oahu for its diversity of urban and rural cultural features and wide variety of land/water interfaces. The first of the Oahu tracks begins near the center of Pearl Harbor, crosses Hickam AFB and Honolulu International Airport and continues southeast toward Waikiki Beach, crossing out to sea again just beyond Diamond Head Crater. The mid point of the track crosses over the Keahi Lagoon with its coral reefs, mud flats and intersecting seaplane runways. The second Oahu track crosses the coastline heading in from the sea just above Barbers Point, at the southwestern tip of the island, and continues on through the heart of Pearl Harbor, passing over the wreck of the *USS Utah*, and finally into the foothills beyond Aiea. The third flight line over Oahu begins out to sea just below Ewa Beach heading northwest over the WWII airfield at Ewa, Makakilo City and the dry brush covered hills and gulches separating the southwest corner of the island from the western coastline towns of Nanakuli and Maili, and continues finally out to sea again just north of Maili.

The last of the tracks collected 25 May was flown over the island of Kauai. The track begins over the island heading 20° north of west from Hanalei, across the northern tip of Olokele Canyon and the Alakai Swamp, a swamp filled basin over 1.5 km (5,000 feet) above sea level, and continues on over the northern tip of Waimea Canyon, and out to sea over the Na Pali-Kona Forest Reserve on the northwest corner of the island. Much of the terrain is covered by swamp and dense tropical rainforest. Near the beginning of the track there is considerable farming area surrounding the Kapaia Reservoir. Surface elevation ranges from near sea level to 1.5 km (5,000 feet) with deep canyons and valleys carved by numerous rivers. Surface water is very plentiful in these areas near central Kauai as the peak, near the center of the island, is reputedly the wettest place on Earth, receiving an annual rainfall of more than 10 m (400 inches).

As examples of the MWIR imagery, Fig. 6 below is a set of three false color IR images from a section of the first of the Oahu tracks over the aircraft parking areas at Hickam Field just west of downtown Honolulu. The top strip is a spatial reconstruction of a thermal IR (4.95 μm) channel for some 640 frames of data covering an area approximately 3 km long by 770 m wide. Two aircraft parking areas are located just to the right of center of the image and appear as a large bright rectangular region oriented 30-45 deg off vertical, and a smaller dark rectangle, lower and to the right of the first, in the top strip of Fig 6. Two aircraft appear as small dark shapes against the bright (in the thermal IR) asphalt tarmac immediately to the right and just above the center of the image. On the second parking ramp three aircraft are faintly visible as slightly brighter in contrast to the dark, concrete parking ramp.

The second strip in Fig 6. is again a false color IR reconstruction, but here depicting the difference between the long wavelength (thermal IR at 4.95 μm) and short wavelength (solar/reflective IR at 2.35 μm) channels to highlight spectral differences in reflectance and emission characteristics and bring out the contrast between the aircraft and the surrounding background. The aircraft on the darker concrete parking ramp, nearly invisible in the thermal IR, now stand out against the colder, higher reflectance surface. The aircraft on the asphalt ramp, above and to the left, adequately visible before in contrast to the warmer background, are essentially unchanged.

The third strip of Fig 6 is the false color IR spatial reconstruction of the same scene as seen through a narrow band spectral difference between a 3.51 μm 'window' band and a 3.34-3.40 μm CH_3 stretch absorption band common to a wide variety of organic solvents. As expected between bands about 0.1 μm apart, the majority of the differenced scene is featureless as reflectivity and emissivity changes should be negligible. However a few buildings in the scene show a stark contrast between the closely spaced bands and stand out as dark shapes against the neutral background. Clearly these are narrow band absorption features and are most likely associated with the recent application of paint or roofing materials (tar and gravel for example).

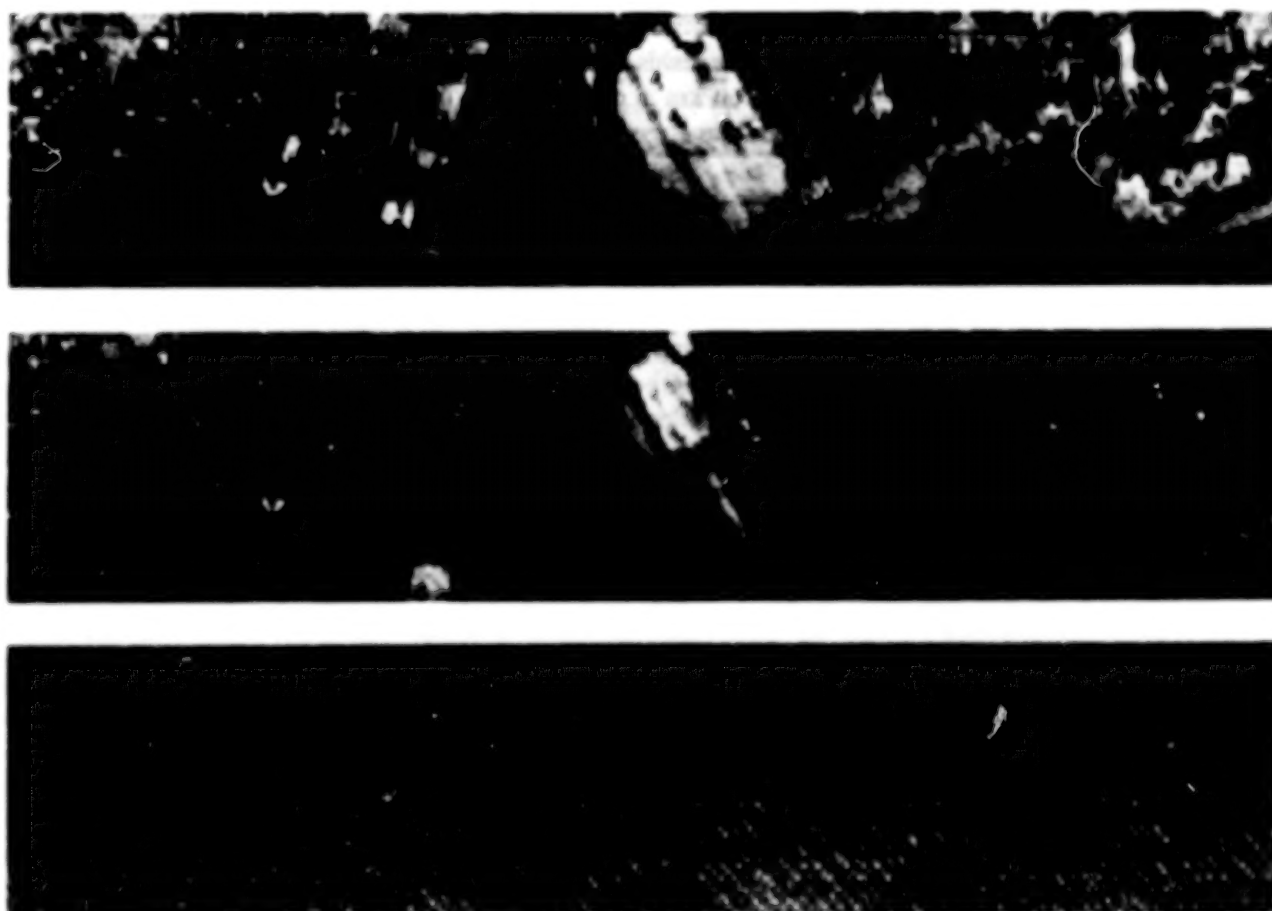


Figure 6 - Reconstructed Thermal IR and Wide and Narrow Band Deltas Over Parking Areas at Hickam

Figure 7 is again a three strip false color IR spatial reconstruction in the thermal and mid-wave IR (4.95 and 3.51 μm respectively) of various scenes collected over the islands of Hawaii, Maui and Oahu. The top strip shows the thermal IR (4.95 μm) contrast between lava flows of considerably different age. The dark region in the center and lower right of the top strip represent the lava from the fairly recent flow of 1842. The bright areas, such as the one to the right intersected by a dirt road, seen in the top strip of Fig 7, are composed of the centuries-old, decomposed volcanic cinder which is quite high in reflectance in the visible and MWIR.

The middle strip of Fig 7 was collected over a farming area on western Maui near Paia. Near the middle of the strip, an irregularly shaped field stands out in sharp contrast to its surroundings. The customary Hawaiian sugar cane harvesting process begins with burning off the leaves, grass and stubble before cutting the sugar filled stalks. As sugar cane is not an annual crop, taking years for a field to mature, the planting, growing and harvesting cycle is continuous throughout the year, rotating from field to field. The middle strip of Fig 7 then is probably a recently burned cane field in preparation for harvesting. The visible contrast, as seen in the TV camera data which is not shown here, is opposite to that of the thermal IR with the field appearing quite dark in contrast to its surroundings; which is again consistent with the field having been recently burnt in preparation for harvest.

A mid-wave (3.51 μm) band was chosen for the bottom strip of Fig. 7 in order to bring out the contrast in ocean surface disturbances (swells) along the western Oahu coastline near the town of Maile. Several swell cycles are apparent with a spacing on the order of 100 m. This type of contrast between ocean surface features is only seen

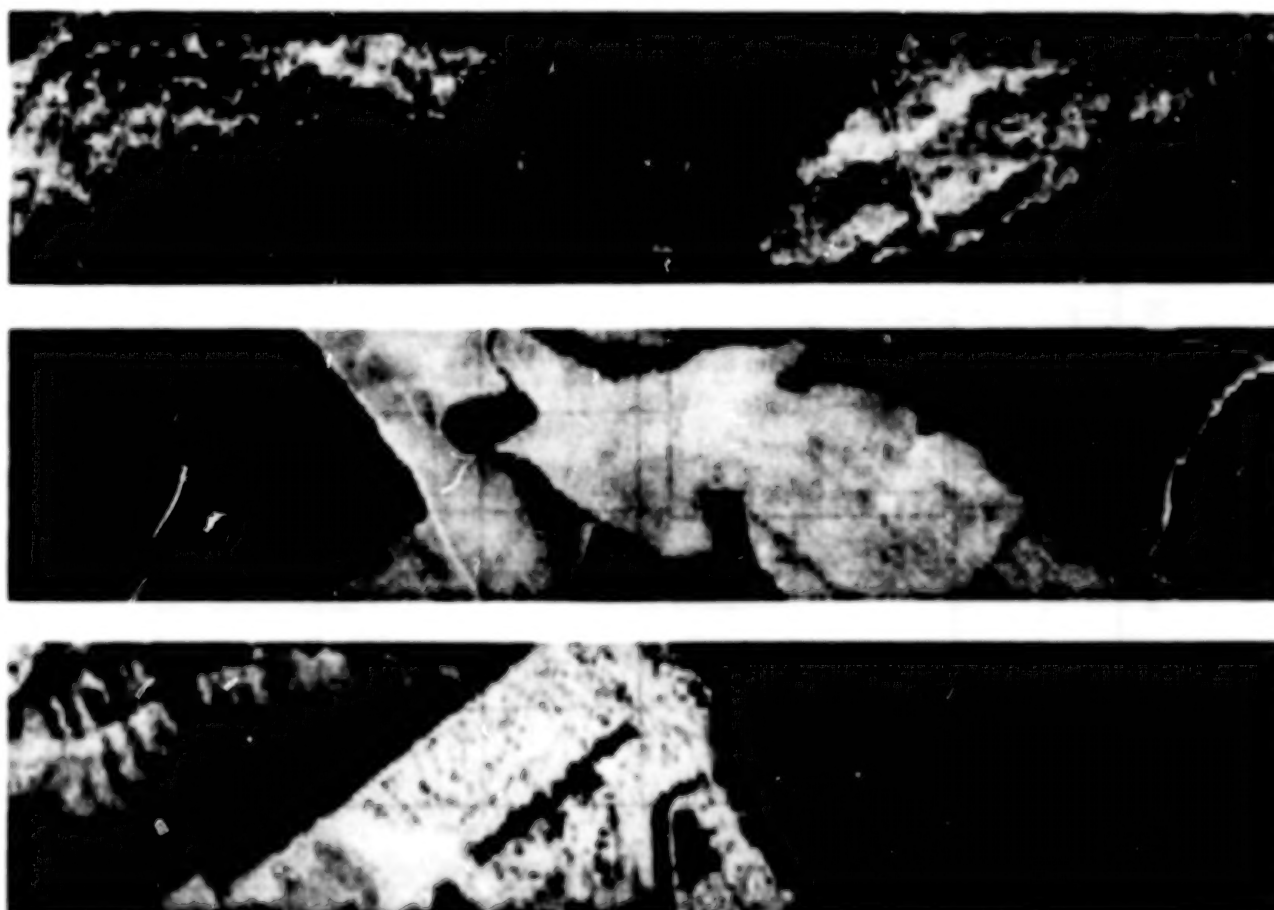


Figure 7 - MWIR Background Contrasts : Varying Age Lava Flows - 1843 Flow Dark vs. Bright Ancient Cinder; Maui Sugar Cane Fields - Bright Region Burnt in Preparation for Harvest; and Ocean Swells off Oahu - Periodic Swell Patterns Stand Out in the 3.5 μm Band Image

over a fairly narrow band between 3.4-3.8 μm . Outside this range, the ocean surface is essentially featureless throughout the MWIR (2-6 μm). The southern portion of the town of Maile can also be seen, in contrast to the shaded slope of the hillsides behind, with roads appearing as thin bright lines, canals as wide dark shapes and the irregular arrangement of roof tops (and materials) appearing as a 'popcorn' pattern of light and dark denoting a predominantly residential area.

In terms of spectral information, Fig. 8 below illustrates some of the MWIR background spectra obtained during the Hawaii pushbroom tour of 25 May. These spectral curves include the ocean background off the Maui coast, ocean swells (as seen above in Fig. 7) off western Oahu, cumulus clouds over Oahu, and the burnt and surrounding sugar cane fields on Maui (also seen in Fig 7). All backgrounds are sunlit, collected over a period of two hours between 10 am and 12 p.m. local time.

Among the most interesting spectra of Fig. 8 are the clouds and the contrast between the ocean background and surface swells. The cloud spectra has by far the strongest short wavelength (solar reflected) component, which remains strong through the mid wave (3.3-4.0 μm), and falls off above 4.5 μm in relation to the other backgrounds, indicating a high reflectance but relatively cold surface temperature. For comparison, a 280 K blackbody integrated over the AIP spectral channel width at 5.0 μm would produce an in-band radiance of 9.4 $\mu\text{W}/\text{cm}^2\text{-SR}$ vs about 10 from the cloud spectra of Fig 8. The only significant difference between the ocean surface and swell spectra lies in the 3.4-3.8 μm range. Outside this band the curves are nearly identical. Given this rather obvious contrast, the utility of the mid-wave (3.5 μm) band for ship wake or other ocean surface disturbance detection seems promising.

Various Sunlit Background Spectra

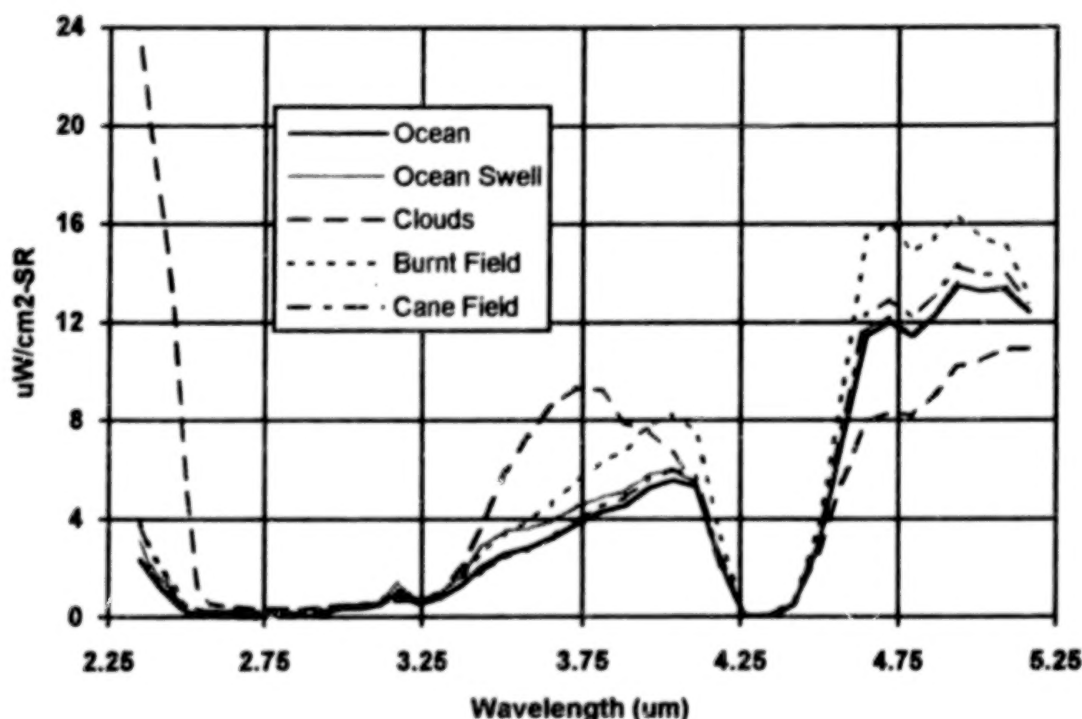


Figure 8 - Various Sunlit Background Spectra : Ocean Background (off Maui), Ocean Swells (off Western Oahu), Cumulus Clouds (Oahu), Burnt Sugar Cane Field and Surrounding Cane Fields (NW Maui)

Lava and Construction Material Spectra

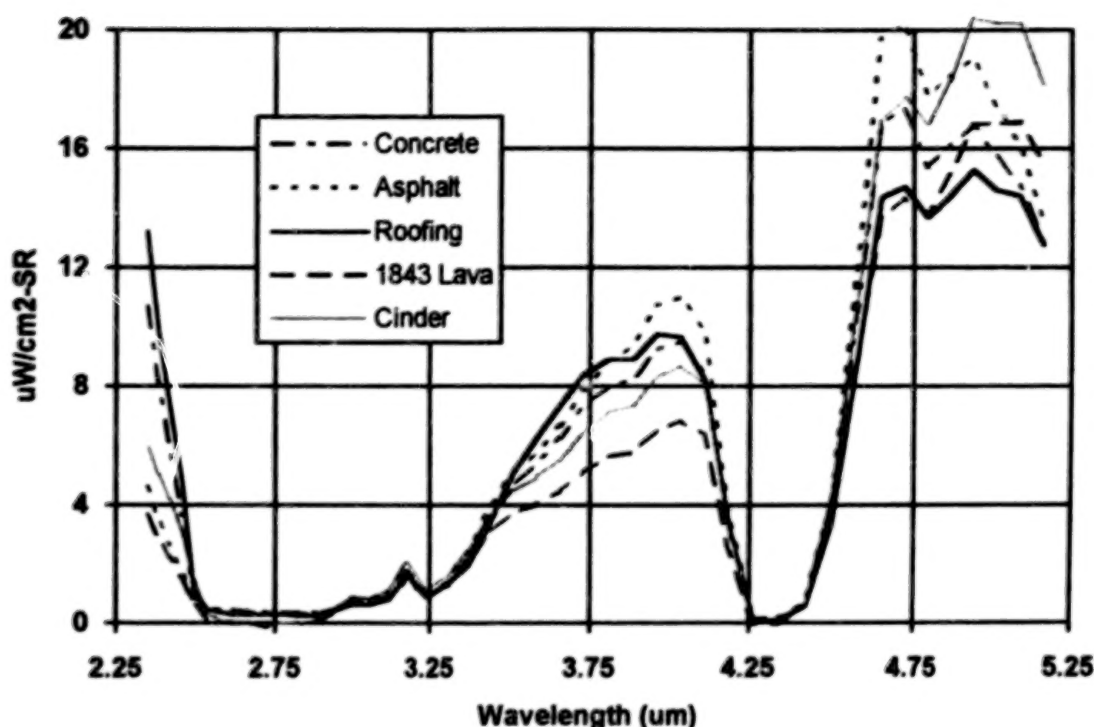


Figure 9 : Sunlit Lava Flow and Construction Material Spectra - Recent (1843) Lava Flow and Ancient Volcanic Cinder (Hawaii), Concrete and Asphalt Parking Areas (Hickam AFB, Oahu) and Roofing Material (Probably Tar and Gravel, Near Hickam AFB)

Figure 9 depicts spectra from the 'quilt-like' volcanic flow areas between Mauna Loa and Mauna Kea on Hawaii, as well as roadway and roof construction materials near Hickam AFB/Honolulu International on Oahu. The lava flow spectra contrast sharply with age as the wear and weathering tend to break down the rock and bleach out the surface coloration. In the visible (TV camera) image the ancient (pre-dating established records) flow appears light in contrast to the dark of the recent flow (1843, little difference in observed coloration or MWIR contrast is seen between flows of the 1800's and 1900's). The shortwave (reflected solar) portion of spectra in Fig 9 is then as expected with the ancient flow higher than the 1843 flow from 2.25 μm to the CO_2 absorption band at 4.3 μm .

Curiously though, in the thermal IR range (above 4.5 μm) where the newer, darker flow would be expected to dominate by virtue of a higher emissivity, the light volcanic cinder still provides a stronger IR signal. In this case the gross difference in reflectance (and thus the solar contribution) overpowers the difference in emissivity (thermal emission). At 5.0 μm , the solar irradiance, not accounting for atmospheric absorption, is about 24 $\mu\text{W}/\text{cm}^2$. Assuming a Bi-Directional Reflectance Distribution Function (BRDF) of 0.5 this could account for as much as 4-12 $\mu\text{W}/\text{cm}^2\text{-SR}$ depending on the exact atmospheric transmission. The actual difference between lava flow spectra is 3 $\mu\text{W}/\text{cm}^2\text{-SR}$ at 5.0 μm .

In all, the Hawaii multispectral pushbroom tour produced a wealth of multispectral (MWIR) background information on the diverse environments of the Hawaiian islands. A complete data package, including calibrated

spectrometer data, a technical summary report, aircraft and sensor telemetry data, and cockpit (TV camera) and false color IR video tapes are available to assist further investigation into this remarkable data set.

2.4 STEREOSCOPIC DATA COLLECTION TECHNIQUES, SOLAR REFLECTIONS OFF ALPINE LAKES

In late summer, 1993 a multi-purpose flight experiment was conducted to investigate solar reflections off alpine lake surfaces and to test alternative stereoscopic data collection techniques made possible by the AIP sensor's tracking, pointing and scanning capabilities. Conducted 16-17 August over an area of the Sierra Nevada Mountains near King's Canyon National Park, the experiment consisted of three separate mission profiles : a tracking overflight of a mountain peak near Mt. Whitney (Mt. Hale), a scanning pushbroom sweep along the eastern Sierra ridge line, and a forward looking pushbroom over a string of alpine lakes at the solar specular angle.

The scanning pushbroom technique, relies upon the sensor's fine scan mirror (FSM) to provide continuous sweeps of the terrain below while the aircraft motion provides the angular separation from scan to scan. Scan rate and aircraft velocity were chosen to provide approximately 50% overlap between consecutive scans. As the external optics, primarily the main pointing mirror, are sized for little more than the 3 degree cone represented by the projected footprints of the 45x45 detector radiometer mode coverage of the focal plane, the scan amplitude was limited to 3 degrees. Thus the actual angular separation between reconstructed scan images is small (about 1.5 degrees). While the topology of the area overflown (the steeply sloped eastern ridge of the Sierras in the John Muir Wilderness area) is quite dramatic, the resulting images are not of sufficient angular separation to be considered truly stereoscopic in nature.

Of greater interest however is the TV-tracking overflight of the rugged Mt Hale peak. The intent of this experiment was to demonstrate a wide angle stereoscopic collection capability as the line of sight of the system was fixed on the sharp Mt. Hale ridge by the closed loop TV-tracker while the aircraft overflew the peak. In this way, data could be collected over almost 50 degrees of angle (from forward to aft pointing mirror gimbal limit). In order to track on an object as loosely defined as a mountain peak or ridge line, the TV tracker was operated in a correlation track mode (i.e. with the video signal of a subarea of the wide field visible camera used as a reference pattern which is periodically updated to allow for slow continuous change in the shape or contrast of the reference target). Figure 10 at right is a TV/Visible band image of the Mt. Hale ridge line as seen through the wide field TV camera. The ridge line was acquired and autotrack initialed about 20 degrees forward of vertical in terms of pointing mirror angle. Loss of tracker lock occurred at the pointing mirror aft gimbal limit of 20 degrees aft.

Figure 11 is a series of false color IR reconstructions of the shortest wavelength spectral channel ($2.21 \mu\text{m}$) utilizing the fine scan mirror to continuously sweep the ridge line. The spatial contraction of the ridge line with pointing angle is quite obvious through the progression of the six images of Fig 11.

In Fig 11, a 0.75:1 aspect ratio was needed to accurately reconstruct the 2-D spatial image from the line spectrometer scans. This is performed graphically in Fig. 11 by displaying 3 image pixels per frame in the



Figure 10 : TV/VIS Image of Mt Hale Ridge

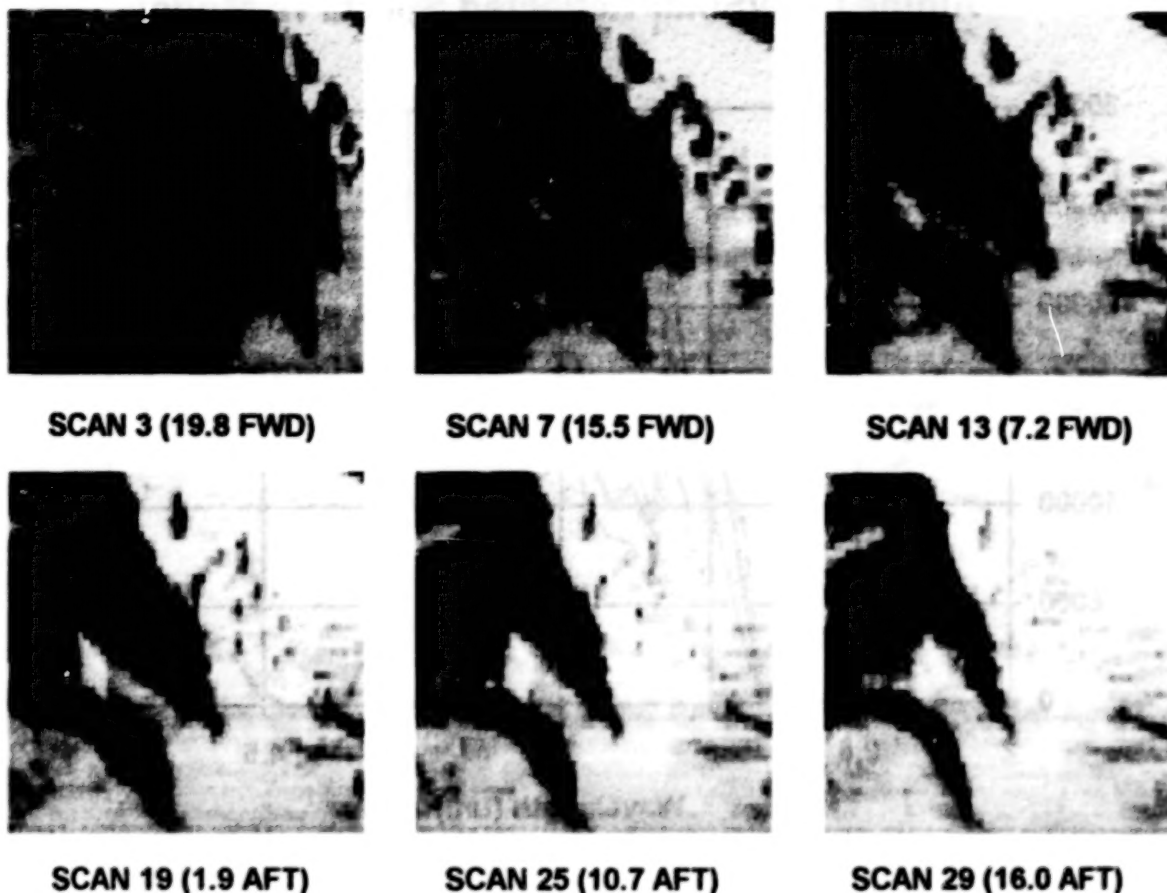


Figure 11 - Reconstructed Stereoscopic Images of the Mt Hale Ridge in the $2.21 \mu\text{m}$ Spectral Channel. Progression of Images Span a Range of -20 (Forward) to +16 Degrees (Aft) in SMPS Pitch

time-scan axis (left right) vs 4 image pixels per detector in the spatial axis (top-bottom).

The primary goal of the flight experiments of mid-Aug 1993 was to characterize and quantify the strong solar specular reflection off alpine lake surfaces. To this end a mission timeline was designed to provide a forward looking pushbroom sweep over a string of high altitude lakes in an area just north of Mount Whitney. By coordinating aircraft heading, SMPS pointing mirror angle and local time of day, a line of sight with a direct specular path to the sun was established and then traced southward along with the aircraft motion.

While direct specular reflections were seen off quite a number of lakes and streams, the actual reflecting surfaces were small pools of clear or moving water near the lake shores as the exposed lake surfaces were almost completely frozen. The area was chosen precisely for its combination of closely spaced small to moderate sized lakes at elevations over 3 km (10,000 feet). The nearly solid frozen condition of the lake surfaces was something of a surprise in mid-August, but is apparently typical at these altitudes.

Figure 12 depicts the measured solar specular reflection data in comparison with variants on a basic model similar to the one used for the cloud specular reflections data of early March. As was the case with the cloud/solar reflections, a peak in the measured spectra occurs in the $3.1 \mu\text{m}$ range where a sharp rise in the index of refraction of water (and ice as well) greatly increases the surface reflectance.

Alpine Lake/Solar Reflected Spectra vs Model

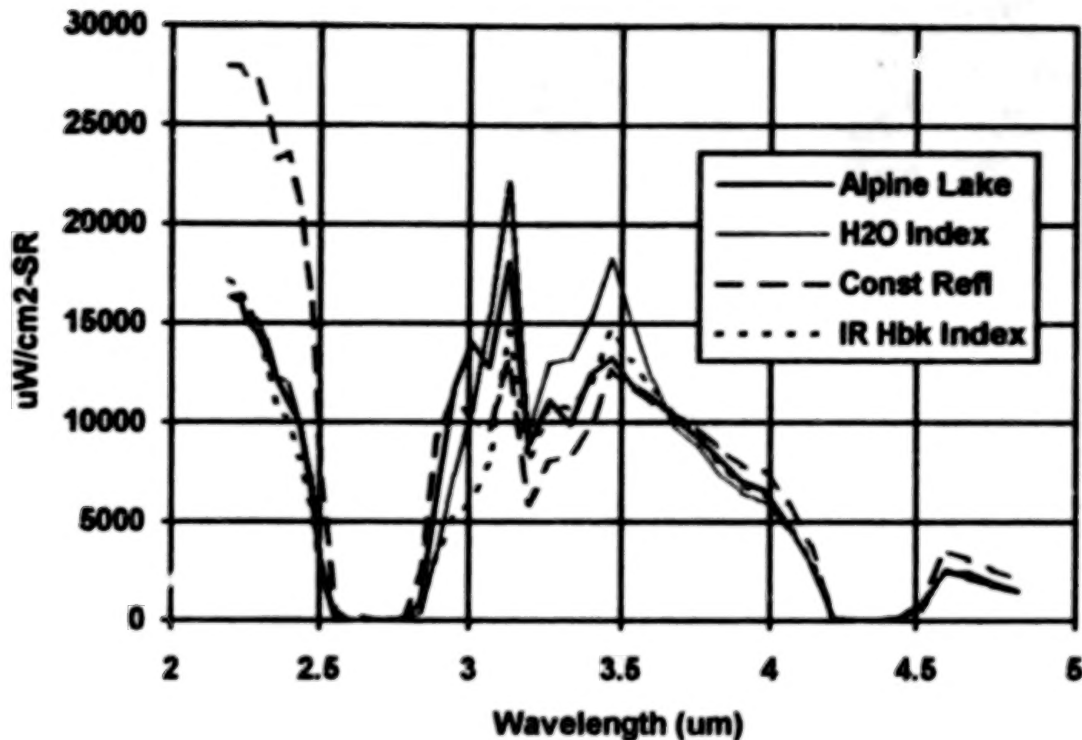


Figure 12 : Comparison of Measured Solar Reflected Spectra vs Models - 17 Aug Alpine Lakes Collect

The simplest of the models shown, denoted 'Const Refl' in Fig. 12, is based on a 5900 K blackbody, as observed through a LOWTRAN 5B modeled atmospheric path. The lake surface reflectance, estimated at 2% by a normal incidence approximation of the Fresnel formulae, is assumed to be spectrally constant. While providing a reasonably good fit to the data beyond 2.9 μm , this model overestimates the reflected solar radiance at shortwave end of the spectra by a little less than a factor of two.

Slightly more sophisticated versions of the model use spectrally varying refractive indices for water as reported by *The IR Handbook* (ERIM, 1989) and Liou (1980). The resulting curves, labeled 'IR Hdbk Index' and 'H2O Index' respectively in Fig. 12, provide a much better fit to the observed data, essentially bracketing the measured spectra. Clearly then, the accuracy of the model is defined by the refractive index data used. In fact it is equally possible to extract an alternative refractive index measurement from the observed spectral reflectance.

In each case, the model curves were normalized to the measured data at 3.6 μm , by a factor of approximately 30% which physically represents the percentage of an individual pixel footprint filled with clear water surface. Given the nearly frozen lake surface conditions seen in the wide field TV video, that ratio seems reasonable.

The stereoscopic data collection techniques and alpine lakes solar reflection data set includes the complete calibrated spectrometer data from all three mission timelines, a summary technical report, cockpit TV and false color IR video tapes along with the necessary aircraft and sensor telemetry and topological mapping data needed for a more in-depth analysis of the both the sensor stereo capabilities and the solar specular reflection phenomenon off alpine lake surfaces; and is available to interested users.

3 SUMMARY AND RECOMMENDATIONS

Over the past year, the Airborne Instrument Program has collected a wide variety of multispectral mid-wave infrared data on a unique collection of both natural and urban backgrounds. To date the analysis effort applied to these data has been from a sensor data quality perspective rather than a complete investigation into the various aspects of background phenomenology. These data, and other potential collection experiments, need to be exploited and brought to bear on the problems of modern infrared remote sensing, particularly the areas of background and potential false alarm source characterization, as well as environmental/earth science uses such as: thermal mapping of volcanic flow patterns for change detection, ocean/lake thermal gradient mapping for water quality/discharge assessment, multispectral differencing based detection of aerosol discharges of toxic solvents, and agricultural assessment of ingested plant water content or disease infestation. A wide variety of applications are possible as the system is uniquely situated to provide multispectral data on both the physics of the solar reflective and thermal emissive regions of the infrared, while also providing the spatial imaging capability needed for localized classification, identification and mapping.

REFERENCES

- Anderson, A.D., 1979 : A Survey of Cirrus Ice Crystal Measurements by AFGL Aircraft
Lockheed Missiles and Space Company, Palo Alto Research Labs, LMSC D-678536
- Carswell, A.I., 1980 : Lidar Measurements In Clouds
Clouds Their Formation, Optical Properties and Effects (Proceedings of Symposium of the same title)
Hobbs P.V. and A. Deepak Editors, Academic Press 1981, 363-397
- Liou, K.N., 1980 : Some Aspects of the Optical Properties of Ice Clouds
Clouds Their Formation, Optical Properties and Effects (Proceedings of Symposium of the same title)
Hobbs P.V. and A. Deepak Editors, Academic Press 1981, 315-345
- Platt, C.M.R., 1980 : Transmission and Reflectivity of Ice Clouds by Active Probing
Clouds Their Formation, Optical Properties and Effects (Proceedings of Symposium of the same title)
Hobbs P.V. and A. Deepak Editors, Academic Press 1981, 407-431
- Wolfe, W.L. and G.J. Zissis (Editors), 3rd Printing 1989 : *The Infrared Handbook (Revised Edition)*
Infrared Information Analysis Center, Environmental Research Institute of Michigan

The Following References, not explicitly cited in the paper, were used as sources of mapping or topological detail :

- Clague, D.A., and C. Heliker, 1992 : The Ten Year Eruption of Kilauea Volcano
Earthquakes and Volcanoes, Vol 23, No 6, 1992, 244-254
U.S. Geological Survey, U.S. Government Printing Office 1993-774-049/66074
- U.S. Geological Survey, 1986 : *Hawaii Volcanoes National Park and Vicinity*, Map 19155-D3-PF-100

- U.S. Geological Survey, 1958 : *Sequoia and Kings Canyon National Park and Vicinity*, Map 36118-E7-PF-125-00
- U.S. Geological Survey, 1956 : *Mount Whitney*, Map 36118-E3-TF-062-00
- U.S. Geological Survey, 1948 : *Mount Goddard*, Map 37118-A5-TF-062-00
- U.S. Geological Survey, 1978 : *Hawaii County (Sheets 1,3)*, Map 19155-F1-LB-100-00
- U.S. Geological Survey, 1957 : *Maui*, Map 20155-E8-TF-250-00
- U.S. Geological Survey, 1978 : *Honolulu County*, Map 21157-C7-LB-100-00
- U.S. Geological Survey, 1978 : *Kauai County*, Map 21159-H3-LB-100-00

BIBLIOGRAPHY

The following references provide useful background material, additional technical detail or striking color photography :

- Anderson, A.D., 1978 : Ice Crystal Type Versus Formation Temperature and Altitude
Lockheed Missiles and Space Company, Palo Alto Research Labs, LMSC D-615857
- Clague, D.A., and C. Heliker, 1992 : The Ten-Year Eruption of Kilauea Volcano
Earthquakes and Volcanoes, Vol 23, No 6, 1992, 244-254
U.S. Geological Survey, U.S. Government Printing Office, 1993-774-049/66074
- deGruy M., Hollis, R., and J. TenBruggencate, 1990 : *HAWAII'S KILAUEA VOLCANO The Flow to The Sea*
C.F. Boone Publishing Co, Sun City West, Arizona, 81 pp.
- Heliker C., 1989 : Volcanic and Seismic Hazards of the Island of Hawaii
U.S. Geological Survey, U.S. Government Printing Office, 1991-287-376
- Heliker C., and D. Weisel, 1990 : *Kilauea The Newest Land On Earth*
Bishop Museum Press, Honolulu, Hawaii, 76 pp.
- Jewett, E.L., and K.D. Bishop, 1993 : AIP Data User's Manual
Lockheed Missiles and Space Company, Palo Alto Research Labs
- Jewett, E.L., Granger J.A., and K.D. Bishop, 1993 : AIP Technical Reports - *Cloud Specular Reflections, Kilauea Volcano Thermal Mapping, Hawaiian Daytime Backgrounds, Alpine Lake Specular Reflections and Multispectral Stereoscopic Imagery*,
Lockheed Missiles and Space Company, Palo Alto Research Labs
- Tilling, R.I., 1991 : *Volcanoes*
U.S. Geological Survey, U.S. Government Printing Office, 1992-316-653

A HYPERSPECTRAL SENSOR AND INVESTIGATION OF SHALLOW WATER REMOTE SENSING

Thomas B. McCord, Ronald G. Resmini,
Michael Fené, and Gregory C. Mooradian

SETS Technology, Inc.
300 Kahelu Avenue, Suite #10
Mililani, Hawaii 96789-3911, USA

ABSTRACT

An airborne, two-dimensional Si-CCD hyperspectral imaging spectrometer will be flown over several maritime sites in Hawaii (e.g., Hanalei Bay, Kauai; and Kahoolawe) in June and July, 1994. The sensor will acquire imagery in the 433 nm to 832 nm range in 288 simultaneous spectral channels. Instrument limited resolution is ~6 nm and the number of spectral channels is selectable via on-chip and/or software controlled pixel binning. All spectral channels are measured simultaneously for a (spatial) line of 385 pixels in length. Typical operation incorporates on-chip binning of four pixels spectrally and two pixels spatially. This increases the signal-to-noise ratio (SNR) and reduces data rate, permitting 20 minutes of continuous data recording before placing data on the 5 GB tape. The aircraft motion sweeps the pixel line along the flight path in a "push broom" fashion, thus building up a strip of image data simultaneously at all spectral channels. SNRs are expected to be $\geq 200:1$ for upwelling underwater radiance and $\geq 570:1$ for a land surface with an albedo of 20%. The instantaneous field of view at 1 kilometer is 1 meter. The sensor is optimized for shallow water and littoral region remote sensing for a variety of civilian and defense applications including bathymetry, suspended sediment concentration mapping, reef monitoring, pigment and algae bloom mapping, bottom-type identification, and mine and unexploded ordnance detection. Radiative transfer and sensor performance models indicate that subsurface features will be visible through depths of 50 meters for Jerlov Type IA water and to depths of 14 meters for Type III water. Where possible, calibrated ground and underwater targets will be deployed. Over the next several years, the sensor system will be enhanced to provide image stabilization, real time processing and extended spectral range to the short-wave infrared (SWIR). A description of the sensor system is presented.

1. INTRODUCTION

SETS Technology, Inc. and Science Applications International Corporation, San Diego, Calif. (SAIC-SD), under funding from the Advanced Research Projects Agency's (ARPA) Hawaii Center for Excellence in Research in Ocean Sciences (CEROS) program, have developed and are flying the Advanced Airborne Hyperspectral Imaging Spectrometer (AAHIS). AAHIS is a hyperspectral imaging sensor covering the extended visible spectral range, 433 nm to 832 nm, in 288 spectral channels and is optimized for shallow water and littoral region remote sensing. All spectral channels are measured simultaneously for a line 385 pixels long; the aircraft motion sweeps the pixel line along the flight path, as shown in Fig. 1, thus building an image one line at a time.

A first generation, experimental imaging spectrometer covering approximately 400 nm to 900 nm was previously built and flown by SAIC-SD (Speer et al., 1992). SETS collaborated with SAIC-SD to exploit the data sets acquired by the first generation SAIC-SD sensor and to assist in the definition of specifications and applications for future sensor development. SETS was subsequently funded with SAIC-SD as a subcontractor and team partner, to build the AAHIS sensor and to fly the

new sensor over several candidate sites in Hawaii. The objectives are to demonstrate the value of using hyperspectral imaging for a variety of shallow-water, beach, and near-shore land remote sensing applications.

A hyperspectral imaging spectrometer acquires images in tens to hundreds of spectral channels. A convenient data structure to represent hyperspectral data is the image cube (Fig. 1). Image cubes are four-dimensional—two spatial, one spectral, and one intensity. Generally, the number of spectral channels is large enough such that a plot of the reflectances against all wavelengths for a single pixel is indeed a continuous reflectance spectrum.

Construction of the AAHIS sensor is complete. The new sensor has undergone a lab-bench sensor characterization and performance assessment and is being test flown over San Diego, Calif. AAHIS will be installed in a Hawaii-based Piper Aztec aircraft in late June 1994 to be flown over several test sites.

2. AAHIS SYSTEM

The AAHIS system block diagram is given in Fig. 2. The two-dimensional (one spatial, one spectral) Si-CCD-based AAHIS system is controlled with a Macintosh Quadra 800 computer. Data are stored on an internal 1.2 GB hard drive during data collects; between collects, the data are written to a 5 GB tape drive. The AAHIS "push broom" is boresighted to the center of the field of view of a color Si-CCD spotter camera which records to SVHS tape. The computer-controlled spectrometer and spotter camera systems are powered by an inverter attached to the aircraft power system.

3. AAHIS SYSTEM ANALYSIS MODEL

Several AAHIS system parameters are given in the left-hand column of Table 1. Using the SAIC *Remote Sensing Program* (ver. 3.0) and the typical operational parameters specified in the right-hand column of Table 1, it is predicted that AAHIS will detect—with an SNR of 569—the light reflected from an object with an albedo of 20% at 440 nm. In a similar calculation, we predict an SNR of 188 from viewing very clear Jerlov IA water (Jerlov, 1976) at 440 nm with no target. A screen-dump of the SAIC *Remote Sensing Program* showing several additional parameters used in these calculations—and additional predicted sensor performance measures—is given in Table 2. A plot of SNR over the entire operational range of AAHIS is given in Fig. 3 for subaerially exposed materials with albedos of 5% and 20%.

4. AAHIS DEPTH PERFORMANCE

The depth at which objects can be submerged and still be sensed via AAHIS is a function of several parameters including object albedo, water quality, diffuse attenuation coefficient (K), and beam attenuation coefficient (c). Consider an object with an albedo of 5% which AAHIS detects with an SNR of 235 at 440 nm. The SNR increases to ~400 at 700 nm primarily due to increased CCD quantum efficiency (Fig. 3). This same object will be detectable with a predicted SNR of 10 while submerged under: 36.4 m of Jerlov Type IA water with $K = 0.03 \text{ m}^{-1}$ and $c = 0.06 \text{ m}^{-1}$; 15.2 m of Jerlov Type II water with $K = 0.07 \text{ m}^{-1}$ and $c = 0.15 \text{ m}^{-1}$; and 6.8 m of Jerlov Type III water with $K = 0.12 \text{ m}^{-1}$ and $c = 0.375 \text{ m}^{-1}$.

5. DATA PROCESSING AND ANALYSIS

Image processing and analysis will be conducted using SETS Technology's HIPSTM (Hyperspectral Image Processing System) software. A versatile image processing system, HIPSTM is specially designed for processing and analyzing data from multi- and hyperspectral imaging spectrometers. Overall data processing flow is indicated in Fig. 4. Atmospheric corrections will be applied to the data using complete sensor characterization and calibration information, LOWTRAN (Kneizys et al., 1983) and calibration panels. Underwater calibration panels and models of radiative transfer through a water column (e.g., Bierwirth et al., 1993) will be used for the detection and identification of submerged objects, the classification of the seafloor, and optical bathymetry. STARSTM (Spectrometric Target Analysis and Recognition System), a HIPSTM module, will be used to apply spectral mixing analysis (Adams et al., 1986; Resmini et al., 1994) to AAHIS data. Spectral mixture analysis uses purely spectral information and assumes the radiance of a pixel is a linear combination of radiances from a small number of materials which are generally observable within the scene. Spectral mixture analysis performs image classification and provides quantitative abundance maps of image components.

AAHIS images, thematic maps, and bathymetric measurements will be georegistered to basemaps using the ArcInfoTM geographic information system. Timely information derived from the analysis of AAHIS data products can also be used for mission planning.

6. THE FUTURE

Over the next two years, AAHIS will be enhanced with image stabilization, a wider spectral range through the SWIR, more automated mission control and data handling, and real time processing. SETS envisions establishing a low cost, airborne hyperspectral imaging service based on the AAHIS sensor.

7. SUMMARY

SETS Technology, Inc. and Science Applications International Corp., San Diego, Calif., have developed a hyperspectral imaging spectrometer which will be flown in a small aircraft in Hawaii in summer, 1994. Sensor development was funded by the Advanced Research Projects Agency's Hawaii Center for Excellence in Research in Ocean Science program, which is intended to support maritime defense and environmental ocean research. The Advanced Airborne Hyperspectral Imaging Spectrometer—AAHIS—covers the spectral range from 433 nm to 832 nm in 288 simultaneous spectral channels. AAHIS has superior signal-to-noise ratio and an instantaneous field of view of 1 m at 1 km. The sensor is optimized for shallow-water remote sensing for a variety of maritime defense and civilian applications including reef inventory, algae bloom mapping, bottom-type identification, and mine detection. SETS Technology's HIPSTM (Hyperspectral Image Processing System) with the STARSTM (Spectrometric Target Analysis and Recognition System) and other software modules will be used to process AAHIS data. Where possible, ground and underwater calibration targets will be deployed. AAHIS is to be used for a variety of applications in Hawaii and is available for use elsewhere. Over the next two years of the project, the sensor system will be enhanced with image stabilization, more automated tasking and data handling, and a wider spectral range through the SWIR.

REFERENCES

- Adams, J.B., Smith, M.O., and Johnson, P.E. (1986), Spectral mixture modeling: A new analysis of rock and soil types at the Viking Lander 1 site. *J. Geophys. Res.*, v. 91, no. B8, pp. 8098-8112.
- Bierwirth, P.N., Lee, T.J., and Burne, R.V. (1993), Shallow sea-floor reflectance and water depth derived by unmixing multispectral imagery. *Photogramm. Eng. and Rem. Sen.*, v. 59, no. 3, pp. 331-338.
- Jerlov, N.G. (1976), *Marine Optics*, Elsevier Publishing, New York, NY.
- Kneizys, F.X., Shettle, E.P., Gallery, W.O., and et al. (1983), Atmospheric transmittance/radiance: Computer code LOWTRAN 6. Environmental Research Paper #846, Technical Report AFGL-TR-83-0187, NTIS AD A137796, Air Force Geophysics Laboratory, Bedford, MA.
- Resmini, R.G., Sunshine, J.M., Schaum, A., McCord, T.B., Forsythe, J.L., and Gillespie, A.R. (1994), Assessment of the linear mixing model for subpixel materials detection in Thermal Infrared Multispectral Scanner (TIMS) images. *Proceedings of the International Symposium on Spectral Sensing Research*, 1994, San Diego, CA, this volume.
- Speer, B., Coyle, C., Anderson, R., and Mooradian, G. (1992), Compact, high resolution airborne hyperspectral imaging sensor at SAIC. *Proceedings of the International Symposium on Spectral Sensing Research*, Maui, Hawaii, November, 1992, v. 2, pp. 948-955.

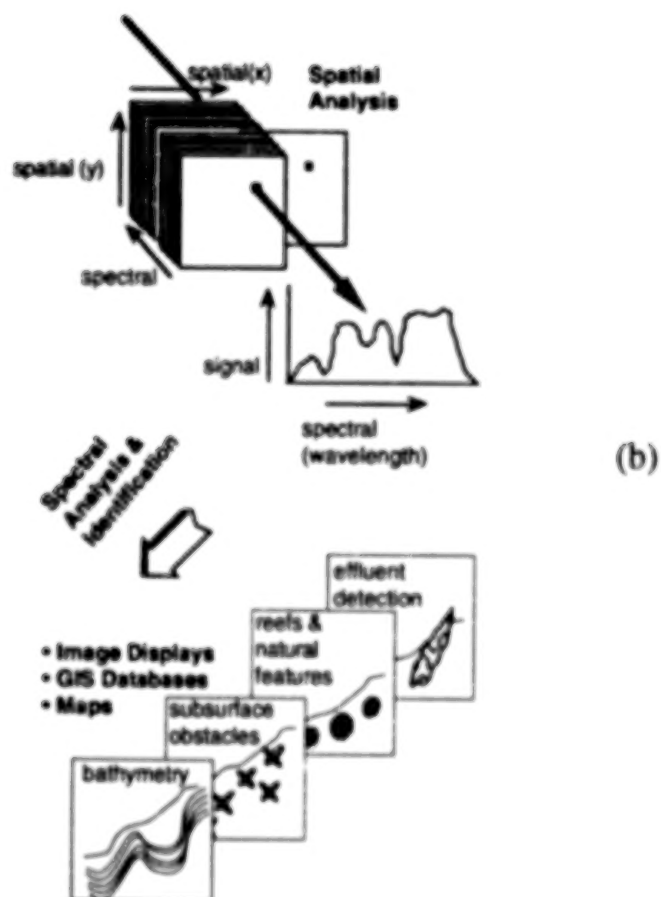
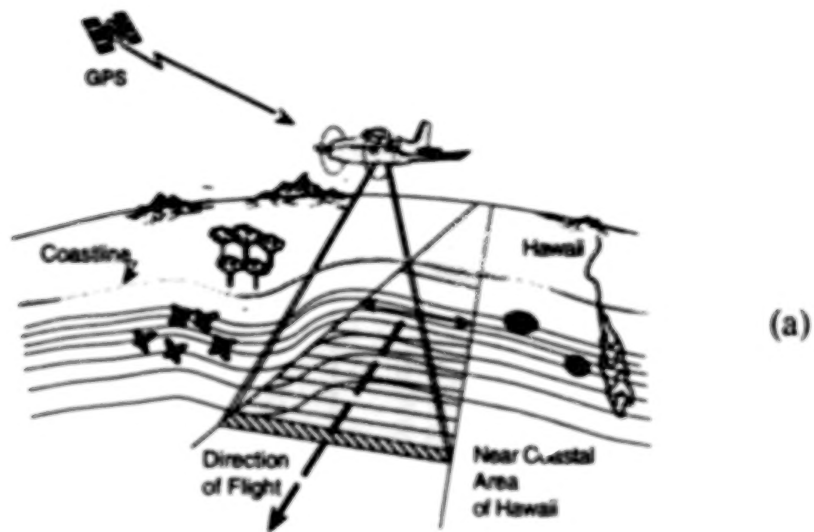
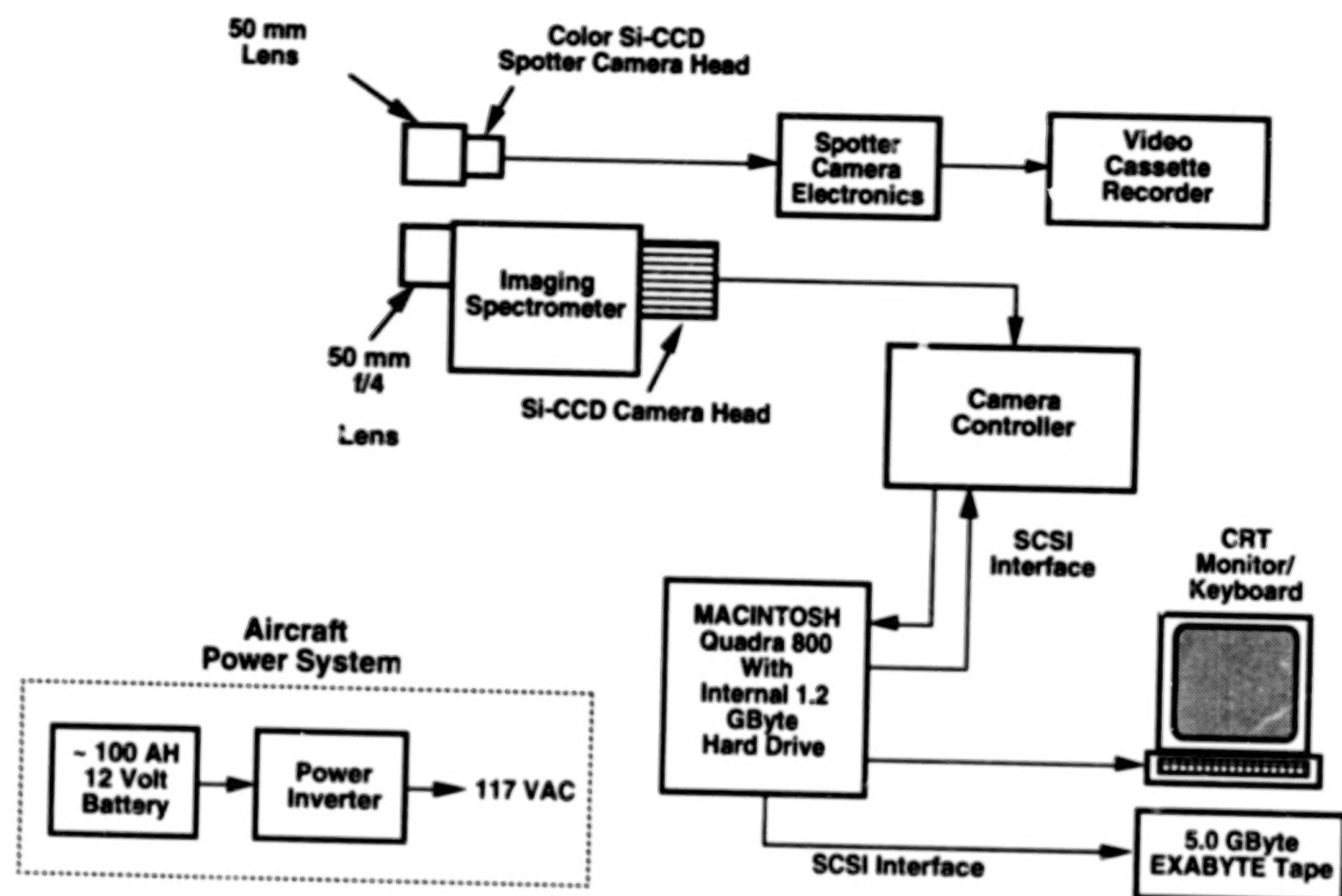


Figure 1. AAHIS and shallow-water remote sensing.

Figure 2. AAHIS system block diagram



BLANK PAGE

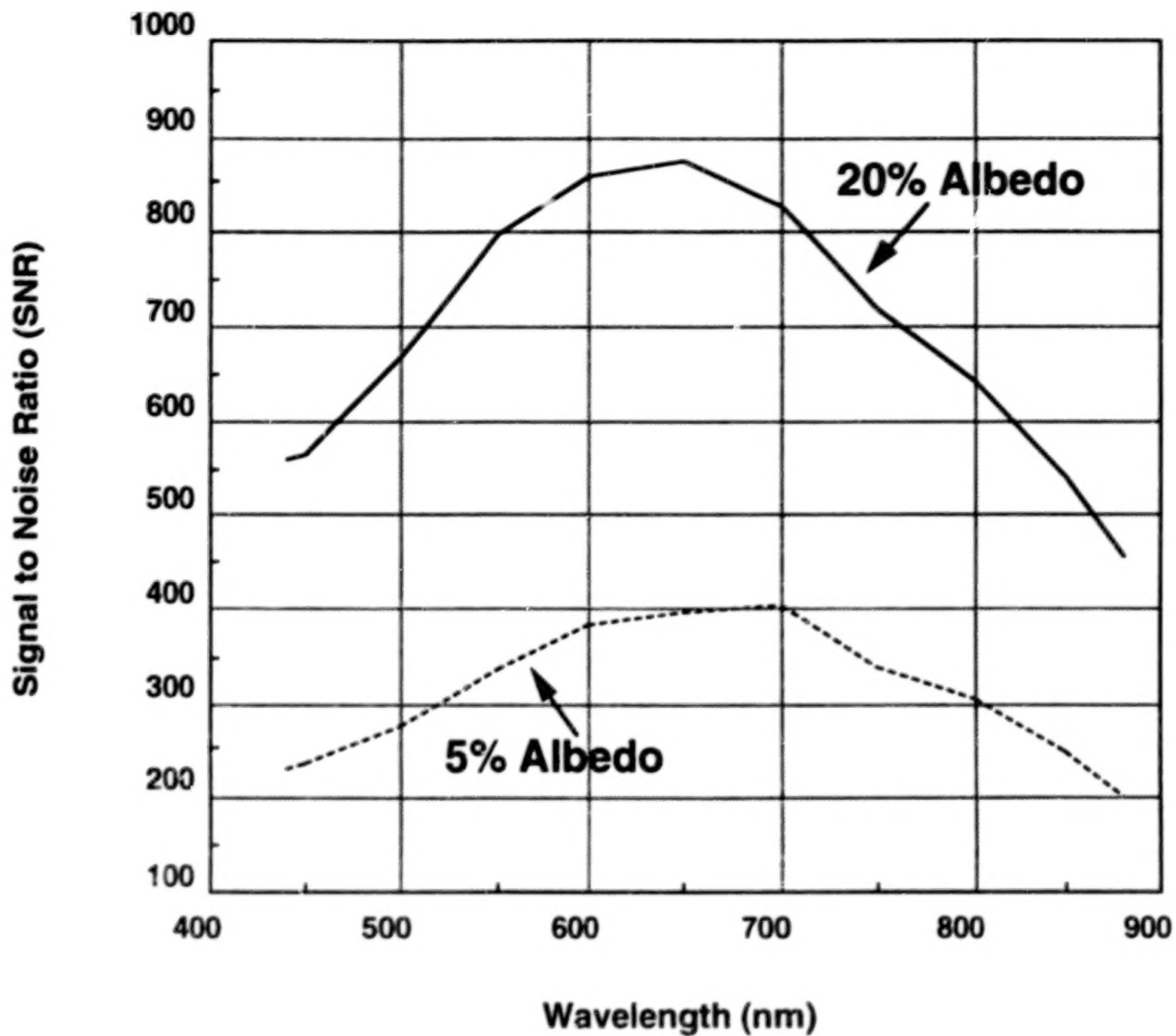


Figure 3: Signal to noise ratio (SNR) over the entire operational range of AAHIS for subaerially exposed materials with albedos of 5% and 20%.

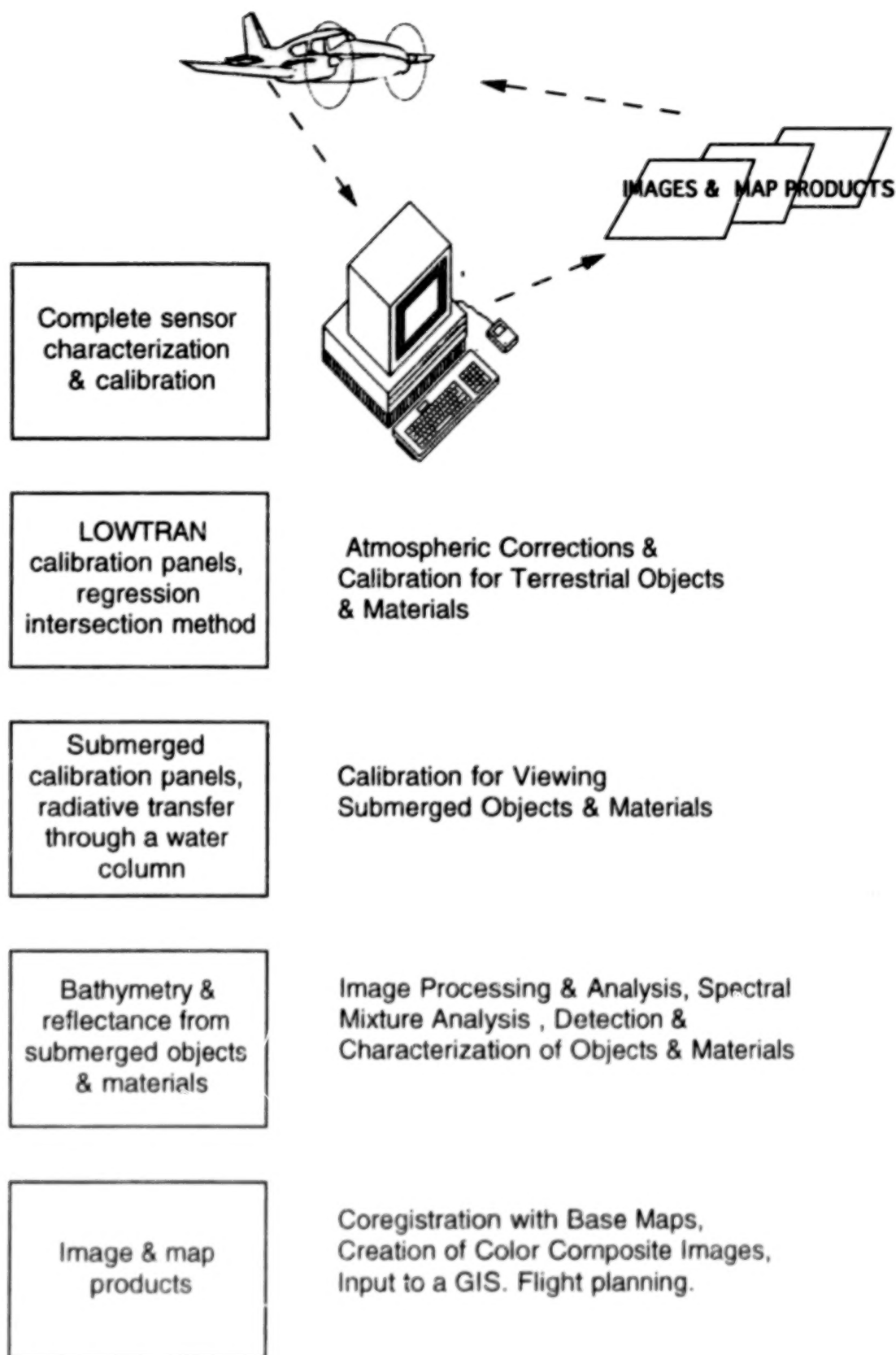


Figure 4. AAHIS Data Processing Flow

BLANK PAGE

157

Table 1. AAHIS System Analysis Model	
System Parameters	Nominal Operational Parameters at 38 fps
<i>Optical Focal Length: 50 mm</i>	<i>Aircraft Altitude: 1 km</i>
<i>f/#: 4</i>	<i>Aircraft Speed: 78 kts</i>
<i>CCD pixels: 385 (spatial) x 288 (spectral)</i>	<i>IFOV/GSD Along Track: 1.03 m</i>
<i>Pixel Size/Spacing: 22 μ</i>	<i>IFOV Cross Track: 0.54 m</i>
<i>Spectral Range: 433–832 nm</i>	<i>On-Chip Spatial Binning: 2</i>
<i>Spectral Resolution: 6 nm</i>	<i>GSD Cross Track: 1.09 m</i>
<i>Sensor Field Angle: 11.4°</i>	<i>On-Chip Spectral Binning: 4</i>
<i>Camera Frame Rate: <55 frames/sec (nominal 38 fps)</i>	<i>Software Spectral Binning: 2</i>
<i>Frame Transfer Time: 1.4 ms</i>	<i>Optical Bandwidth: 11 nm</i>
<i>Integration Time: 25 ms at 38 fps</i>	<i>Data Recording Rate: 1.1 MB/sec</i>
<i>SNR (20% albedo): 569 (55dB)</i>	

157

Table 1. AAHIS System Analysis Model Cont.

Optical Focal Length	Focal length of foreoptics
f/#	Focal ratio of foreoptics
CCD pixels	Number of pixels in CCD array, in spatial and spectral directions
Pixel Size/Spacing	CCD array pixel spacing, in spatial and spectral directions
Spectral Range	Shortwave to longwave limit of instrument
Spectral Resolution	Minimum distance resolvable in spectral domain
Sensor Field Angle	Full field angle; corresponds to swath width
Camera Frame Rate	Number of CCD frames acquired per second (fps); i.e. number of ground track scan lines acquired per second
Frame Transfer Time	Time between frames needed to read out the CCD array
Integration Time	Time for collection of photons
Aircraft Speed	Speed of the Piper Aztec aircraft
Aircraft Altitude	Aircraft altitude
IFOV/GSD Along Track	Instantaneous field of view, on the ground, along the flight path, and ground sample distance along the flight path
IFOV Cross Track	Spatial resolution on the ground, normal to flight path
GSD Cross Track	Ground sample distance normal to flight path
On-chip Spectral Binning	Number of pixels along spectral direction summed in hardware to form one hyperspectral channel
Software Spectral Binning	Number of pixels along spectral direction summed in software to form one hyperspectral channel
Optical Bandwidth	Optical bandwidth of each hyperspectral channel
Spatial Binning	Number of pixels along spatial direction summed to form one hyperspectral channel
Data Recording Rate	Number of bytes per second generated by the instrument

BLANK PAGE

Table 2. AAHIS SNR Cases

GROUND

SAIC REMOTE SENSING PROGRAM VER. 3.0

W(avelength (nm)..... 440	A(ltitude of recr (km)..... 1.00
N(OSC water (-1..7,8=Gnd).... 8	Scan angle (deg)..... 5.70
K(bar, atten coeff (1/m).... NA	V(elocity (km/sec)..... 0.04
Pigment conc, C (mg/m^3).... NA	R(esol'n @ nadir s (m)..... 1.00
	l (m)..... 1.09
G(round albedo (%)..... 20.00	D(etector diameter (cm)..... 1.25
M(eteorological range (km).... 50.00	B(andwidth (nm)..... 11.00
O(zone (cm NTP) (TAB=HELP).. 0.28	qU(antum efficiency..... 0.15
	T(ransmission..... 0.35
	P(ixel read noise (p.e.).... 20.00
L(atitude (deg N)..... 21.00	Eff. surface albedo (%)..... 20.00
Longitude (deg W)..... 158.00	[Lw]n (mW/cm^2/um/ster).... 10.662
Date (MM/DD/YY)..... 05/15/94	Total pix sig (mW/cm^2/um).. 44.473
Time (local HH.MM)..... 11.00	Target pix sig (mW/cm^2/um).. 24.127
Z(enith/solar (deg)..... 7.03	Total pix signal (dB p.e.).. 57.75
clocking F(actor (0-1)..... 0.96	Target pixel sig (dB p.e.).. 55.10
E(ffective operation..... Pushbrom	Target SNR(dB)..... 26.22
I(ntegration time (msec).... 24.615	Electronic SNR (dB)..... 48.59

WATER

W(avelength (nm)..... 440	A(ltitude of recr (km)..... 1.00
N(OSC water (-1..7,8=Gnd) .. 1	Scan angle (deg)..... 5.70
K(bar, atten coeff (1/m).... 0.037	V(elocity (km/sec)..... 0.04
Pigment conc, C (mg/m^3).... 0.148	R(esol'n @ nadir s (m)..... 1.00
	l (m)..... 1.09
G(round albedo (%)..... 5.20	D(etector diameter (cm)..... 1.25
M(eteorological range (km).... 50.00	B(andwidth (nm)..... 11.00
O(zone (cm NTP) (TAB=HELP).. 0.28	qU(antum efficiency..... 0.15
	T(ransmission..... 0.35
	P(ixel read noise (p.e.).... 20.00
L(atitude (deg N)..... 21.00	Eff. surface albedo (%)..... 5.20
Longitude (deg W)..... 158.00	[Lw]n (mW/cm^2/um/ster).... 1.160
Date (MM/DD/YY)..... 05/15/94	Total pix sig (mW/cm^2/um).. 22.386
Time (local HH.MM)..... 11.00	Target pix sig (mW/cm^2/um).. 2.625
Z(enith/solar (deg)..... 7.03	Total pix signal (dB p.e.).. 54.77
clocking F(actor (0-1)..... 0.96	Target pixel sig (dB p.e.).. 45.46
E(ffective operation..... Pushbrom	Target SNR(dB)..... 18.08
I(ntegration time (msec).... 24.615	Electronic SNR (dB)..... 38.96

SNR(ground) = 569

SNR(water) = 188

Note: SNR for signal shot noise limited conditions is (Target pixel sig(dB p.e.))^{1/2}

SMIFTS: A FLEXIBLE SYSTEM FOR COLLECTION OF HYPERSENSITIVE SENSING DATA IN THE 1-5 μ m REGION¹

Paul G. Lucey, Tim Williams, Keith Horton and John Hinrichs
Hawaii Institute of Geophysics and Planetology
University of Hawaii at Manoa
Honolulu, HI, 96822, USA

ABSTRACT

The SMIFTS sensor developed at the University of Hawaii is a pushbroom imaging spectrometer which collects hyperspectral data in the 1-5 μ m region. The SMIFTS sensor has been deployed on a number of platforms for a variety of hyperspectral imaging experiments; a helicopter for down-looking airborne experiments, an astronomical telescope for planetary observations and a large tripod for ground based data collects.

1.0 INTRODUCTION

The SMIFTS project is an ARPA/ONR project aimed at determining the utility of a novel hyperspectral measurement technology for hyperspectral applications. SMIFTS is an acronym for spatially modulated, imaging, Fourier transform spectrometer. This system utilizes a 2-D InSb detector array and a spatially modulated interferometer to produce an unusually flexible imaging spectrometer for collection of hyperspectral imaging data in the 1-5 μ m region of the spectrum. During the course of continuing sensor characterization, the sensor has been deployed upon several platforms: helicopters, astronomical telescopes, and on the ground using a large tripod. This paper briefly describes the present capabilities of the system in these data collection environments and aspects of the sensor characteristics which have been measured to date.

2.0 SENSOR CHARACTERISTICS

The sensor, shown in Fig. 1, has characteristics which are summarized in Tables 1 and 2. The SMIFTS sensor is a cryogenically cooled Sagnac interferometer utilizing a 256x256 element InSb detector array. The interferometer is equipped with a variable width input slit aperture and the sensor is operated as an imaging spectrometer. That is, each frame derived from the FPA has one axis of spectral information and one axis of spatial information. The slit is scanned across the target to obtain the second axis of spatial information. When deployed in a helicopter or on the ground the sensor is equipped with a 150mm focal length off-axis paraboloid telescope, internal to a liquid-nitrogen cooled radiation shield. This optic yields a .6 mrad cross-track IFOV, and a swath width of 6 degrees divided into 256 pixels. The along-track IFOV is adjustable according to experiment requirements, from .6 mrad to 10 mrad. Digitization is 12-bits. The spectrometer is operated in two modes with differing spectral characteristics. The first mode collects data from 1-5 μ m with a spectral resolution of 100 cm^{-1} , yielding 75 spectral channels. The second mode collects data from 3.2 to 5.3 μ m at a spectral resolution of 50 cm^{-1} in 35 spectral channels. These two modes are offered to increase the spectral resolution for experiments focussing on the 3-5 μ m region. A graphical representation of the spectral range and resolution is shown in Fig. 2, compared to the NASA modis airborne simulator, the closest analog to the SMIFTS system currently deployed. The signal to noise ratios achieved by the sensor are measured in the field during regular calibration observations of an extended area blackbody source and a stabilized integrating sphere. Peak SNR's are in the vicinity of 400 for signals filling one-half of the detector well.

¹ This work was supported by ONR contract No. N00014-91-C-0028

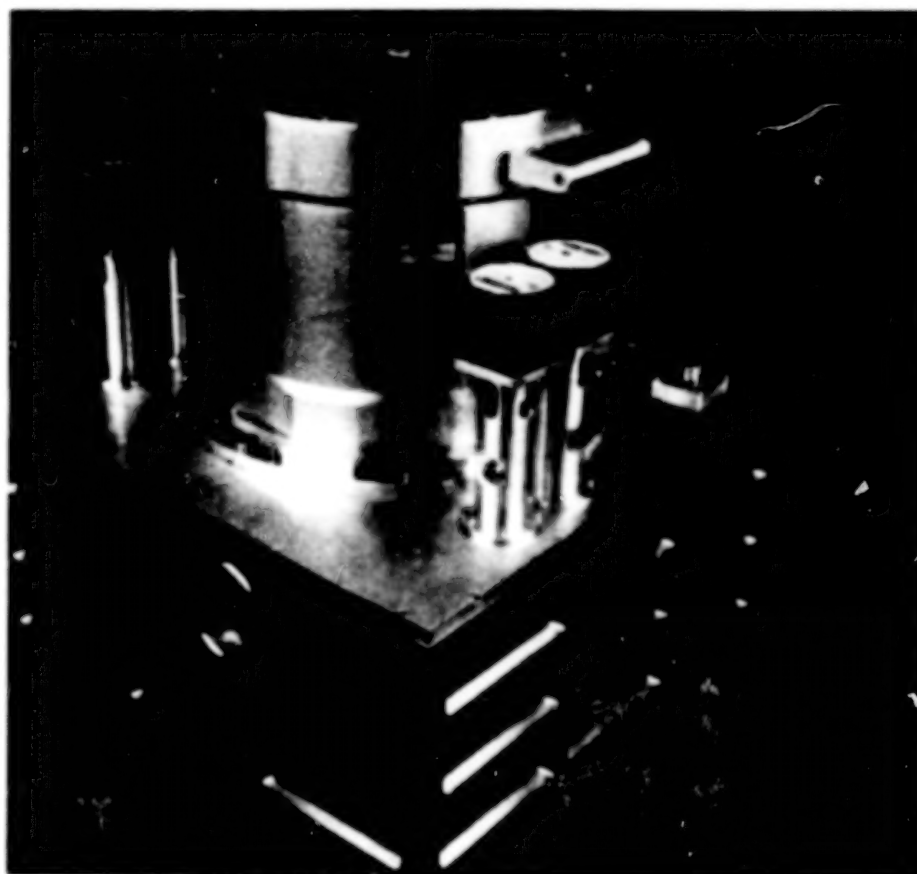


Figure 1. SMIFTS sensor

Table 1. SMIFTS Sensor description

Spectrometer type	All reflective Sagnac interferometer
FPA	InSb, 256x256 element, Amber Engineering
Input optics	Off-axis parabola, 150 mm f.l.
Cooling	Cryogenic nitrogen, FPA/Spectrometer to 55K, Input optics to 77K
Digitization	12 bits
IFOV	0.6 mrad cross-slit, variable 0-10 mrad along slit
Swath width	6 degrees, 256 pixels
Swath length	to 30,000 pixels

BLANK PAGE

Table 2. SMIFTS Data Characteristics

	Mode I	Mode II
Spectral range	1-5.3 μm	3.2-5.3 μm
Spectral resolution	100 cm^{-1}	50 cm^{-1}
Spectral channels	75	35
SNR	~400	
Precision	~1%	
Radiometric accuracy	~10%	
IFOV	.6 mrad	
Swath width	6 degrees, 256 pixels	

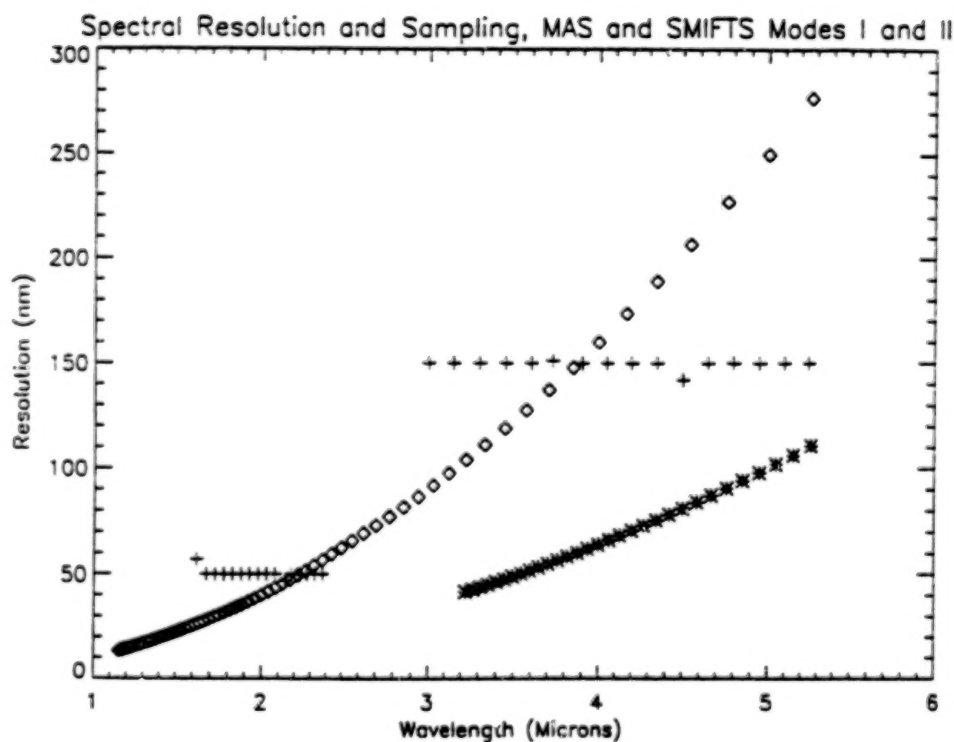


Figure 2. Spectral range and resolution of SMIFTS (diamonds and stars) compared to NASA MODIS Airborne simulator (crosses)

Typical plots of SNR's are shown in Fig. 3. The data collection system limits both the frame rate and the total number of frames collected. Data can be collected at up to 7 frames per second via DMA connection of the Amber electronics parallel output to a 4.5 Gbyte high speed disc array acting as data recorder.

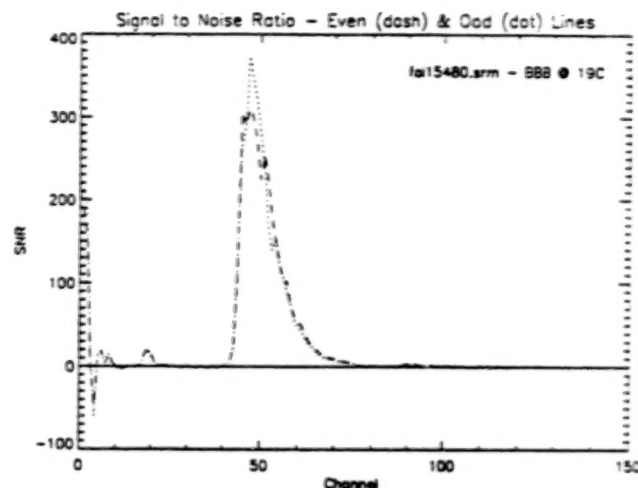


Figure 3. Measured SNR from observations of calibration sources during data collects. This example was taken in 3-5 μm mode of a 19 degree centigrade blackbody. "Odd" and "Even" lines represent lines which are output from the Amber dual amplifiers which have slightly different noise characteristics.

The swath length is limited by the data recorder capacity to 30,000 frames. Integration times are adjustable from 100 ms to 1 second. After data collection, data is down-loaded from the disc array to magneto-optical disks for transfer to data processing systems. A schematic of this system is shown in Fig. 4.

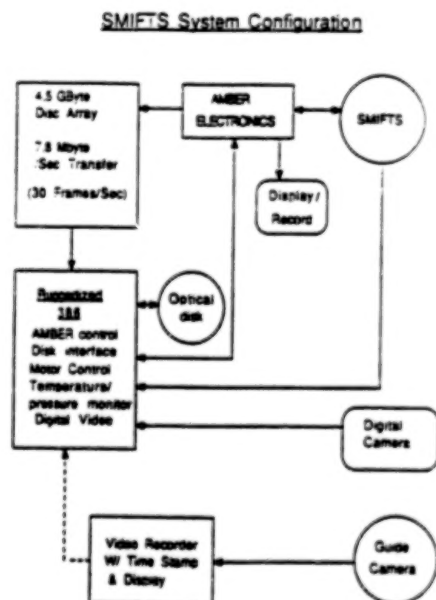


Figure 4. SMIFTS data collection system schematic.

3.0 DEPLOYMENT ON GROUND PLATFORMS

The system described above has been used for ground based collections by installing the sensor on a large tripod equipped with one axis of scan. A photo of the sensor in this configuration is shown in Fig. 5. An image obtained during a data collect at Redstone Arsenal is shown in Fig. 6.

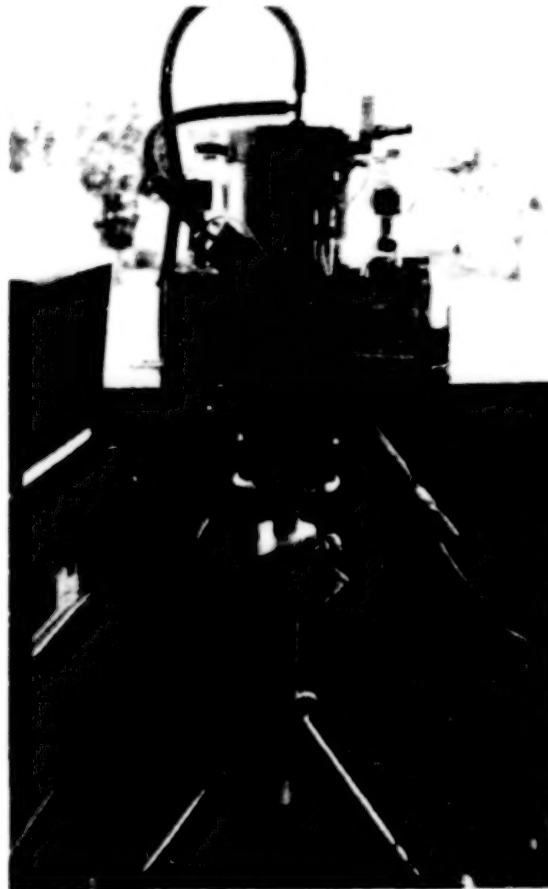


Figure 5. SMIFT3 sensor on the ground data collect motorized tripod.

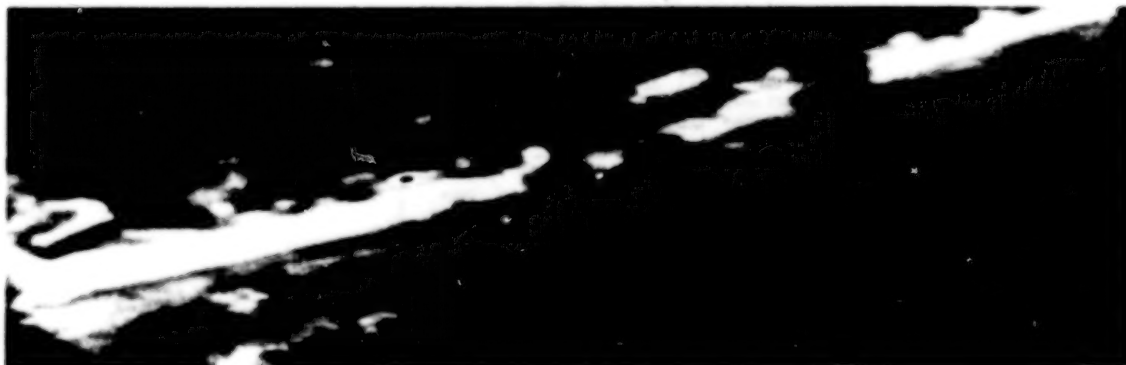


Figure 6. A $4.7\ \mu\text{m}$ daytime image of a forested area with a dirt road and a few vehicles from the 300 ft. tower at Redstone Arsenal

4.0 AIRBORNE DEPLOYMENT

The system is used in a commercial Bell Longranger for airborne deployment (Fig. 7). Three test flight series have been completed. The sensor itself is mounted on an Aeroflex gyroscopically stabilized mount to remove aircraft pitch and roll. The data collection system is compactly packaged, and the sensor, data collection system and sensor operator occupy the passenger compartment of the helicopter.



Figure 7. SMIFTS sensor aloft

A fold mirror extending out one door directs the light from the target into the SMIFTS (Figure 8). In addition to the system as described above, subsystems have been added to aid in analysis of the data. There are two boresighted cameras augmenting the system. The first is a wide angle color video camera which is operated continuously during data collection. The second is a wide-band monochrome digital CCD camera with a field of view matched to the SMIFTS FOV. These latter data are used to measure and correct for aircraft translations during data collection, and to serve as a digital base map for SMIFTS data.

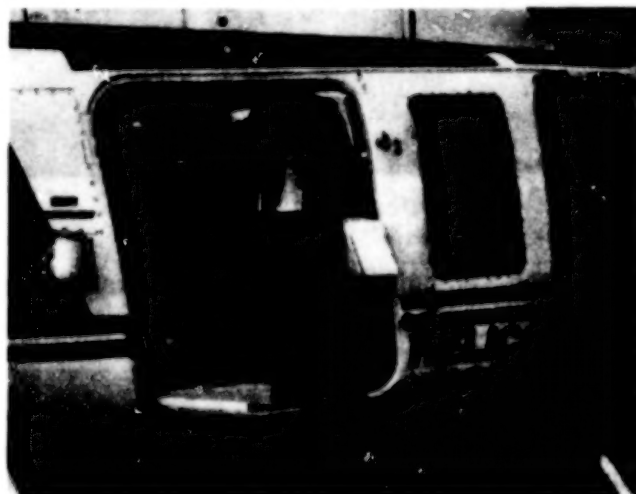


Figure 8. Detail of SMIFTS in Bell Longranger

Regular recording of GPS positions are also performed. An image from the first test flight series is shown in Fig. 9.

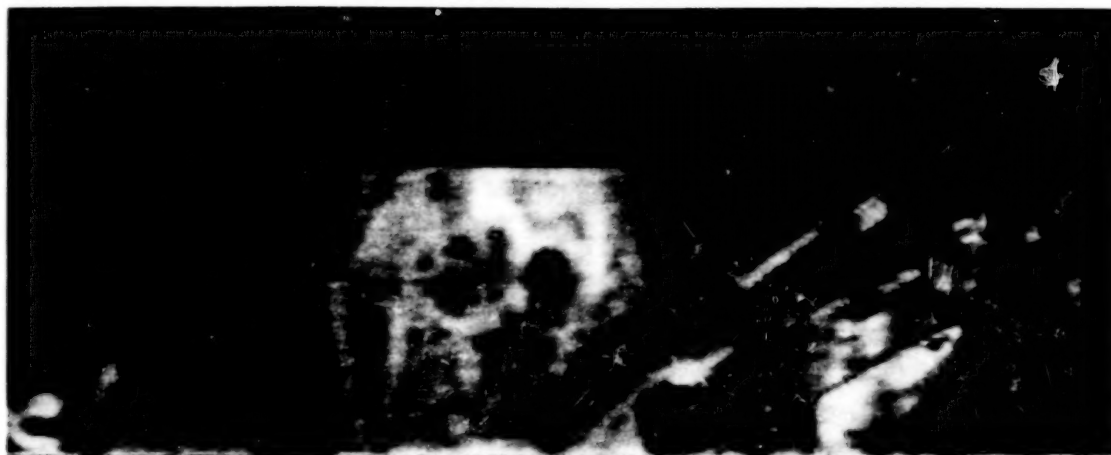


Figure 9. Image from airborne test flight. Along track compression is due to oversampling.

5.0 LARGE TELESCOPE DEPLOYMENT

The SMIFTS sensor was originally designed for tracking telescopes, and has been used at Mauna Kea Observatory on a 60 cm telescope. Fig. 10 shows the system in an early configuration, on this telescope.



Figure 10. SMIFTS sensor on a 60-cm telescope at Mauna kea Observatory, Hawaii.

6.0 FIELD CALIBRATION

Field calibrations include regular measurement of the dark response of the FPA using a cold stop internal to the dewar, and regular observations of the extended area blackbody for 3-5 μm observations and a calibrated Spectralon integrating sphere for 1-2.5 μm observations. Wavelength calibration is accomplished with observations of the calibration sources through transmission filters with abundant absorption lines.

A plastic filter is used in the 3-5 μm region, and rare-earth doped glasses in the 1-2.5 μm region. Responsivity nonuniformity is also measured with the extended area blackbody and integrating sphere.

7.0 EXAMPLE SPECTRA

Representative spectra obtained at Redstone Arsenal are shown in Figs. 11 and 12.

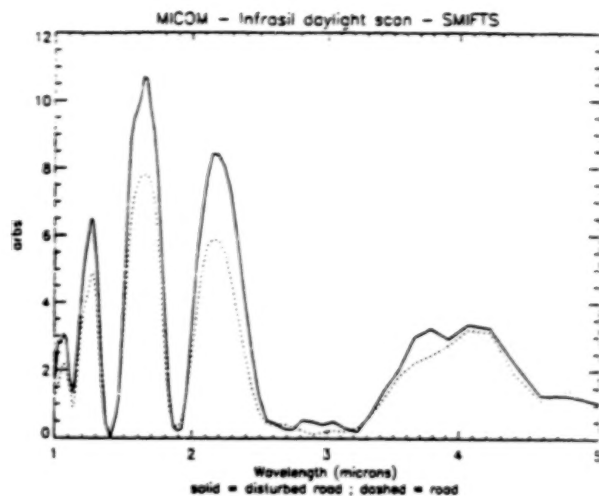


Figure 11. Raw spectra in daytime 1-5 μm mode obtained at Redstone Arsenal.

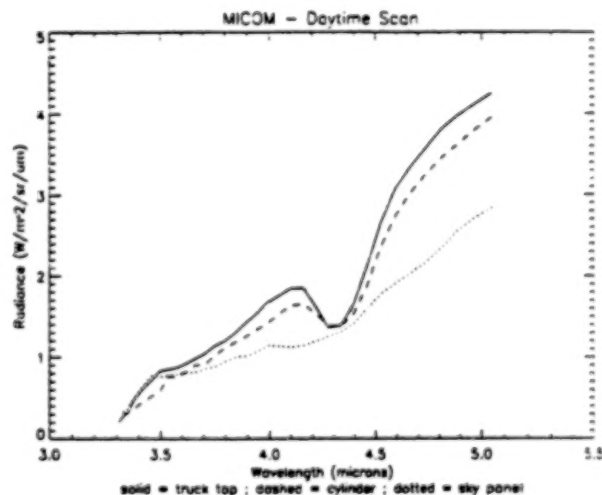


Figure 12. Radiance spectra obtained during the day at Redstone Arsenal.

8.0 CONCLUSION

The SMIFTS SWIR/MWIR hyperspectral measurement system allows a variety of experiments to be performed for hyperspectral research, ranging from controlled experiments at test ranges to airborne imaging spectroscopy.

HIGH RESOLUTION MULTISPECTRAL STEREO IMAGER (HRMSI), A STEP TOWARD THE FUTURE

George T. Elerding, Jerald R. Holt, and Edgar E. Russell
Santa Barbara Research Center
Goleta, CA 93117

ABSTRACT

The High Resolution Multispectral Stereo Imager (HRMSI), originally planned for the Landsat 7 platform, would have represented a significant step forward in the remote sensing capabilities of the United States. This sensor, conceived in response to the Landsat 7 Request for Proposal issued by the U.S. Air Force/NASA team, would have provided high-quality monoscopic and stereoscopic visible panchromatic imagery at 5 meters ground sample distance (GSD) and visible/near-infrared (VNIR) multispectral imagery in four bands at 10 meters GSD. Up to 532 mono/177 stereo scenes per day could have been collected from the Landsat orbit (705.3 km) over a swath of up to 60 km.

This paper describes the requirements for HRMSI and the design choices selected to satisfy those requirements. Selected design details are presented to illustrate the requirements/performance issues, design alternatives and tradeoffs. Areas covered include optical design, focal-plane concepts, signal handling, gimbal design, and data compression.

While no longer in active development, HRMSI sensor evolution continues in alternative concepts based on, but not explicitly following, the HRMSI design. These systems include wide-swath, large-area-coverage concepts as well as narrow field-of-view higher resolution systems, and many extend the HRMSI capabilities into the short-wavelength infrared (SWIR).

1. LANDSAT 7 SYSTEM OVERVIEW

The Landsat 7 system consists of a Space Segment and a Ground Segment designed to satisfy operational and performance requirements. The spacecraft is based on the Landsat 6 General Electric (now Martin Marietta) bus, with added capabilities in attitude control and communications. Two sensors were proposed: an upgraded Enhanced Thematic Mapper and a new sensor designated as the High Resolution Multispectral Stereo Imager. The system was conceived in response to the Landsat 7 requirements issued as a part of the Landsat 7 Request for Proposal issued by the Defense Landsat Program Office (DLPO).

The system is capable of collecting imagery from both instruments simultaneously, and directing payload data either to direct downlinks (at X-band), a Tracking and Data Relay Satellite System (TDRSS) relay (at Ku-band), or to onboard recorders. Command and control of the system would be via an East Coast mission operations facility. Payload data would be processed at the EROS Data Center in Sioux Falls, SD, as an adjunct to NASA's Earth Observing System.

1.1 PAYLOAD MISSIONS

The two instruments conceived in response to the Landsat 7 Request For Proposal provided a mix of Landsat continuity and enhanced capabilities prioritized by the DLPO and NASA. Requirements for continuity of equivalent data (not an identical sensor) were satisfied by the Enhanced Thematic Mapper Plus (ETM+) instrument, with design characteristics similar to the Enhanced Thematic Mapper delivered for Landsat 6. ETM+ enhancements included smaller GSDs in the long-wavelength infrared (LWIR) band. In addition, the calibration capability, producibility improvements, and upgraded electronics/data formatting and error detection/correction.

The HRMSI instrument responded to the primary enhancement requirements areas of higher spatial resolution, collection of stereo data, and decreased revisit time. The additional calibration capability improvements on ETM+ responded to the request for better radiometric accuracy.

These two payloads support the traditional Landsat missions of global land and near-shore monitoring with added missions of terrain relief generation, support of map-making, and other Department of Defense needs.

1.2 SYSTEM COMMUNICATIONS

A primary enhancement to the system over that planned for Landsat 6 was the inclusion of a TDRSS link, as existed in Landsats 4 and 5, but at 300 Mbps. This allowed for simultaneous real-time transmission of both payloads, or a combination of a real-time transmission and downlink of data recorded onboard previously. In addition, the data rate of the X-band downlink was increased to 150 Mbps per channel for each of the three channels. In normal operation, two downlink channels could be used simultaneously, although no preclusion existed for the use of all three simultaneously.

These communications enhancements significantly increased the capacity of the system to deliver data to the ground, via TDRSS to the United States, or via direct downlink to International Ground Stations or other receiving facilities.

2. HRMSI REQUIREMENTS SUMMARY

Table 1 presents the key requirements to be satisfied by the HRMSI sensor design. The most exacting performance requirements were associated with modulation transfer function (MTF), signal-to-noise ratio (SNR), and pointing stability. A second set of implied constraints on power and weight significantly influenced the design alternatives and effort required to satisfy these tight performance requirements.

3. HRMSI DESIGN CONCEPTS

In response to these requirements, iterated of course during the initial months of the program, the HRMSI design was established. HRMSI consists of a sensor module and an electronics module, to be described in detail in the following sections. A cutaway view of the sensor module design is shown in Fig. 1. Key elements of the concept are highlighted by callouts in the figure.

TABLE 1. HRMSI KEY REQUIREMENTS

Instrument Parameter	Specified Value			Notes
Spectral Bands/SNR	<u>Bandpass</u>	<u>SNR Low</u>	<u>SNR High</u>	Panchromatic (Pan) band narrower than ETM+; Spectral bandpasses of visible and near infrared (VNIR) bands same as ETM+; SNR specified for low and high radiance conditions
Pan Band	0.50–0.74 μm	24	94	
Band 1	0.45–0.51 μm	43	102	
Band 2	0.51–0.60 μm	47	129	
Band 3	0.63–0.69 μm	35	113	
Band 4	0.76–0.90 μm	43	153	
Ground Sample Distance (GSD)	Pan: 5 m at $\pm 25^\circ$ along-track (AT) and 0° cross-track (CT) VNIR: 10 m GSD at $\pm 25^\circ$ AT and 0° CT			Pan: effective pitch (cross-track) = 7 μm ; 0.733 ms sampling period VNIR: effective pitch = 14 μm ; 1.466 ms sampling period
Nonuniformity	< 1% across array; < 0.5% across 100 pixel segments within SCA			Reference source for uniformity measurement/calibration
Radiometric Calibration	Better than 6.5% Absolute			Based on transfer of ETM+ calibration
Swath	60 km nominal at $\pm 25^\circ$ AT and 0° CT			Compression mode dependent
Pointing Capability	$\pm 30^\circ$ AT and $\pm 38^\circ$ CT with 0.35° increments			Momentum compensation on both axes
Pointing Accuracy (stability)	1 arc-sec (random) and 1.5 arc-sec (slowly varying)			Servo-controlled direct drive on both axes
MTF	Pan: 0.197 AT and CT VNIR: 0.275 AT and CT			At Nyquist frequencies: 71.4 (CT) and 80.6 (AT) cycles/mm for Pan; 35.7 (CT) and 40.3 (AT) cycles/mm for VNIR
Output Data Rate (Mbps)	Two 75 Mbps channels in CCSDS format with BCH error detection/correction and embedded ancillary telemetry data			Data compression selectable among uncompressed, lossless (RICE algorithm), and nonlinear DPCM (4, 5, or 6 bits/pixel) options

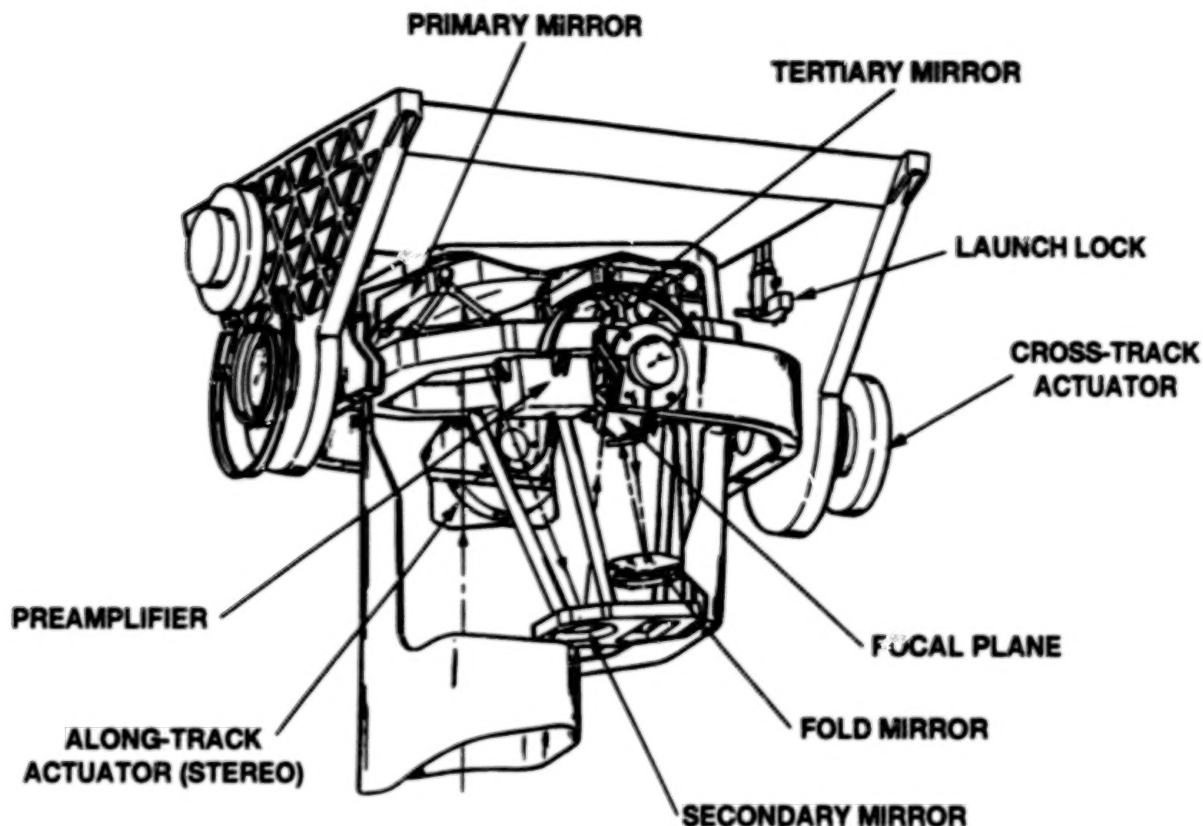


Figure 1. Cutaway view of HRMSI sensor module.

3.1 OVERVIEW

Key features of the HRMSI design are summarized in Table 2. As illustrated in Fig. 1, HRMSI consists of two major modules mounted on the payload mounting platform. The sensor module contains an Earth-pointing telescope assembly mounted on a two-axis gimbal for stereo and cross-track imaging. The telescope itself contains the focal plane assembly (FPA), two preamplifier modules with clock and bias circuits, and a fail-safe dark-shutter assembly mounted close to the focal plane to establish a zero radiance reference signal level. An Attitude Displacement Assembly (ADA) package containing three orthogonal accelerometers is mounted on the telescope bulkhead. The ADA is used to characterize jitter-induced pointing changes to allow image data registration during ground processing. Also mounted on the edge of the payload mounting platform are the stow cover and reference source assemblies used for contamination protection during launch and for on-orbit, detector-to-detector responsivity characterization, respectively.

The second module, denoted the electronics module, contains: the post-amplifiers; data buffers and data compression circuitry; data formatter; redundant command, spacecraft interface and control processors; redundant gimbal drivers; redundant power supplies; focal plane and gimbal heater controllers; dark-shutter drivers; and launch lock controller. The electronics module is mounted on the nadir face of the L7 spacecraft in close proximity to the sensor module. The overall temperature of the electronics module is controlled by a suitable view to space through a cutout in the thermal blanketing that otherwise covers the module.

3.2 SENSOR MODULE

The sensor module consists of two primary subassemblies: the telescope and the gimbal. The telescope subassembly includes the telescope, the focal plane with control heaters and dark shutter, the preamplifiers with replacement heaters, and the ADA. The gimbal assembly consists of the mainframe with heater, the gimbal, the rotary actuators, and the launch locks. The modular design allows all major components and subassemblies to be assembled and tested in parallel with other assemblies. The telescope can be pointed in both the along-track plane ($\pm 30^\circ$) and the cross-track plane ($\pm 38^\circ$) for scene imaging and to 90° cross-track to access stow and reference source positions.

TABLE 2. HRMSI DESIGN CHARACTERISTICS

Instrument Parameter	Design Value	Notes
Sensor Type	Two-axis pointable telescope	Inner gimbal along-track
Optics	4.6° × 1.34° field, near diffraction limited, 20.6 cm exit pupil diameter, f/5.38	Three-mirror, all reflecting unobscured; graphite epoxy structure with lightweighted Zerodur mirrors
Detectors/Focal Plane Assembly	Two staggered sensor-chip assemblies; each has one panchromatic band with 6272 active detectors and four VNIR bands with 3124 active detectors each	Silicon photodiode detectors arranged for each band in staggered, bilinear (odd/even) arrays, with a readout CCD for each odd and even array. VNIR channels have on-chip mux with single output.
Quantization	Pan: 9 bits; VNIR: 10 bits	Not quantization limited; 4 selectable gains
Electronics	Conventional with mask programmable gate arrays	Parallel 4.4-MHz channels
Data Compression	Nonlinear DPCM with 4, 5, and 6 bit per pixel modes; Lossless RICE compression	Gate array DPCM implementation; NASA-sponsored custom RICE IC implementation
Calibration	ETM+ radiometric calibration transferred to the HRMSI via viewing common scenes; detector-to-detector responsivity variations characterized by viewing reference source assembly	ETM+ will use solar diffuser on aperture door and partial aperture stability monitor; reference source assembly is designed as solar diffuser
Size (cm/in.)	111/43.7 × 110/43.3 × 105/41.3 Sensor Module; 74.2/29.2 × 63.5/25.0 × 35.6/14.0 Electronics Module	
Mass (kg/lb)	79.6/175 Sensor Module; 59/130 Electronics Module	
Power, watts	212 W imaging; 211 W slewing w/o imaging data	244 W slewing w/imaging data to maintain TDRSS synch

3.2.1. TELESCOPE ASSEMBLY

HRMSI utilizes a wide field of view three-mirror anastigmat (TMA) to provide diffraction limited imagery across the focal plane. The key features of this all reflective, three-mirror telescope are listed in Table 3. An optical schematic of the design, illustrating along-scan and cross-scan views, is shown in Figure 2.

The design is diffraction limited with an MTF of at least 0.64 across the entire field. Geometric rms blur sizes were computed across the FOV, as were 80% encircled energy and rms wavefront error. Wavefront error, comparable to the rms spot size, averages 0.049 waves rms across the field. These analyses confirm the excellent optical characteristics of this design form.

TABLE 3. OPTICAL FEATURES PROVIDED BY THE HRMSI DESIGN

Feature	Benefit
All Reflective	No chromatic aberration minimal radiation effects
Unobscured	Enhanced MTF, improved SNR, better control of stray light
High Resolution	Diffraction limited across FOV
Telecentric in Image Space	Minimizes centroid shifts and reduces any shift in spectral bandpass
Mirrors Share Common Axis	Facilitates alignment
Low Thermal Expansion Mirror Substrates	High Thermal stability

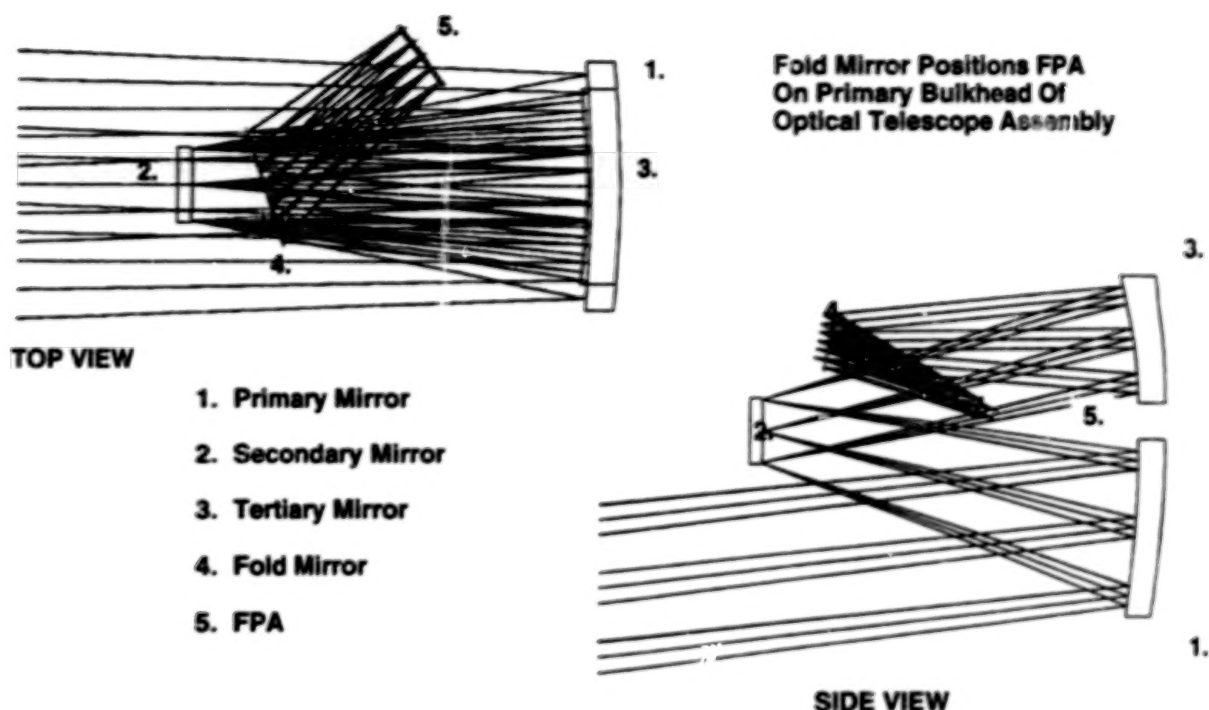


Figure 2. Optical schematic for the HRMSI Reflective Triplet; along-track view (a), cross-track view (b).

The 20.6-cm diameter telescope assembly consists of four Zerodur mirrors supported kinematically within a graphite/epoxy housing. The housing also supports the focal plane, dark shutters, preamplifiers, and attitude displacement assembly.

SPECTRAL SEPARATION

The spectral filtering is provided with a filter element located above the detector array chip on each of the two sensor-chip assemblies (SCAs) which comprise the HRMSI focal-plane assembly. Each filter element consists of five filter strips bonded together to form a single element. The filters are mounted in a bezel with opaque masking to reduce stray radiation at the focal plane. The spectral characteristics of the filter strips are selected such that the overall spectral response (including the detectors and telescope mirrors) meet the requirements summarized in Table 1.

3.2.2 GIMBAL ASSEMBLY

Pointing of the sensor is controlled by two brushless torquers with integral Inductosyn encoders. The along-track (stereo) torquer rotates the telescope within the gimbal $\pm 30^\circ$. The cross-track torquer rotates the gimbal and telescope $\pm 38^\circ$ as a unit for imaging and to 90° for stow or calibration.

The direct telescope drive system for both axes of HRMSI consists of a brushless dc torquer and 21-bit Inductosyn encoder. Momentum compensation is accomplished at an axis parallel to the output shaft by a rotating mass driven at 200 times gimbal speed. Table 4 gives the gimbal drive performance requirements. The HRMSI direct-drive system meets these requirements and has the following important attributes:

- Mechanically simple
- Duplex pair bearings
- Direct-drive brushless torque motor — no gears and negligible drive friction
- Base referenced position servo loops — open-loop crossover frequency = 5 Hz
- Line of sight follows base motion below crossover frequency
- Line of sight isolated above crossover frequency
- Discrete steps in servo with analog feedback
- Inductosyn zero crossings at 0.35° increments
- Modular counter-rotating mass compensation
- Compensation is easily adjustable

TABLE 4. GIMBAL/TELESCOPE POINTING REQUIREMENTS

	Along-Track Axis	Cross-Track Axis
Range	$\pm 30^\circ$	$\pm 38^\circ$ plus to 90° for stow/calibration
Step Size	$0.352^\circ \pm 0.05^\circ$	$0.352^\circ \pm 0.05^\circ$
Slew Rate	50° in <16.67 sec	50° in <25.0 sec
Random Error	± 1.0 arc-sec (1σ)	± 1.0 arc-sec (1σ)
Slowly Varying Error	± 1.5 arc-sec (1σ), rate <0.034 arc-sec/min	± 1.5 arc-sec (1σ), rate <0.034 arc-sec/min
Jitter	Jitter angular velocity ≤ 85 (TBR) arc-sec/sec; Jitter amplitude ≤ 5 (TBR) arc-sec from 2 to 125 Hz in presence of S/C jitter	Jitter angular velocity ≤ 85 (TBR) arc-sec/sec; Jitter amplitude ≤ 5 (TBR) arc-sec from 2 to 125 Hz in presence of S/C jitter
Life	200,000 slews	200,000 slews
Note 1:	Uncompensated Angular Momentum: $< \pm 2.0$ (TBR) oz-in-sec peak (short term) $< \pm 0.2$ (TBR) oz-in-sec average (long term)	
Note 2:	Reaction Torque: $< \pm 1.2$ (TBR) in-oz peak (short term); $< \pm 0.2$ (TBR) in-oz average (long term)	

3.2.3 FOCAL-PLANE ASSEMBLY (FPA)

The HRMSI focal-plane layout is shown in Fig. 3. The focal plane contains two separate sensor-chip assemblies (SCAs) each having five bilinear silicon photodiode detector arrays with charge-coupled device (CCD) readouts, each servicing a separate spectral band. Each bilinear array consists of a staggered combination of an odd and an even subarray. The FPA configuration of the two SCAs has the panchromatic (Pan) band arrays (with the smallest detectors that provide the highest spatial resolution) positioned nearest to the optical axis to optimize imaging performance. There are 12,544 active Pan band detectors and 6,248 active detectors in each of the four VNIR bands. A small number of these detectors (<100) provide overlap for registration purposes and to accommodate cross-track ground velocity.

3.2.4 ON-BOARD CALIBRATION

The dark shutters, used to establish the zero radiance calibration condition on each SCA when closed, are shown in the open (de-energized) position in the figure. Each shutter has a fail-safe actuator that can be used to drive the dark shutter to its open position if necessary.

The RSA is a solar diffuser that provides a uniform illumination of the focal plane when the sensor is positioned to view the solar illuminated diffuser near the north pole. The RSA viewing geometry for detector-to-detector responsivity characterization is accessed by gimbaling the sensor approximately 90° cross-track and 15° along-track to view the solar diffuser.

3.3 ELECTRONICS MODULE

A simplified block diagram of the electronics is shown in Fig. 4. Except for synchronization of the clocks and transfer signals, the detector signals from the two SCAs and from each of the bands within an SCA are independent. The scene data are transferred simultaneously into the adjacent readout CCDs on the SCAs. Each CCD transfers data from the dark, test, and active pixels through the on-chip output amplifiers.

The serial detector data from each on-chip output amplifier are processed through separate preamp buffer amplifiers. Each preamplifier has an associated cable driver for routing the scene signals to the postamps located in the electronics module. Averaged signals from the dark (shielded) detector elements (located on the output end of each array) are sensed each scan line and used to form a channel offset signal which is subtracted from the detector array signals (scene plus offset) of each channel, thereby reducing the required dynamic range of the analog-to-digital converters (ADCs). A 12-bit ADC dedicated to each individual channel then provides 9-bit quantization at a 4.4 Msample/s rate for panchromatic data and 10-bit quantization at a 2.2 Msample/s rate for VNIR data.

The two outputs from the panchromatic array of an SCA are stored in a $128 \text{ K} \times 10$ -bit RAM buffer memory. Four separate groups with half this amount of memory ($64 \text{ K} \times 10$) are used to store data from each of the four VNIR arrays of an SCA. Regardless of the compression mode, raw data is routed by a switch matrix through a data compressor which has been selected and programmed to either compress or bypass (not compress) the data. With data compression selected, either lossy (nonlinear DPCM implemented by gate arrays with uploadable parameter values) or lossless (RICE algorithm implemented with a space-qualified NASA-sponsored

application-specific integrated circuit design) data compression is performed. This data is then stored in first-in first-out memories. Next, blocks of 992 bytes of data, consisting of source packets with scene or engineering data, are passed through the BCH (1023, 993, 3) error encoder. Finally, formatted CCSDS-compatible frames are made available at the two HRMSI telemetry channel interfaces. ECL shift registers are used to load the output word buffer preparatory for readout by the spacecraft into one of the downlink channels or into the on-board tape storage.

The HRMSI electronics, from the FPA CCD clocks through to the data output buffer, operate in a fully synchronous mode. Timing signals are generated by hard-wired logic that decodes timing pulses from a single count-down chain clocked by the 74.914-MHz master spacecraft crystal oscillator.

Redundant 1750-A microprocessors provide command and payload correction data decoding, housekeeping data acquisition, and transfer frame header generation. A slightly modified microprocessor assembly developed for the Moderate Resolution Imaging Spectrometer instrument (containing circuitry for multiple serial ports and an expandable parallel port network) would be used for HRMSI. This assembly, including all of the support chips, is radiation-hardened and has an operating frequency of 9.36 MHz.

Commanding of the HRMSI actuators for along-track positioning, cross-track positioning, and dark-shutter operation is performed by the microprocessor via parallel ports. As discussed previously, the along track and cross-track positioning is performed by dc brushless motors with integral encoders. Driver electronics are identical for both actuators. Closed-loop position control is provided within the motor-driver electronics, with position telemetry from the position encoder also monitored by the digital housekeeping circuitry for insertion into the instrument output data format.

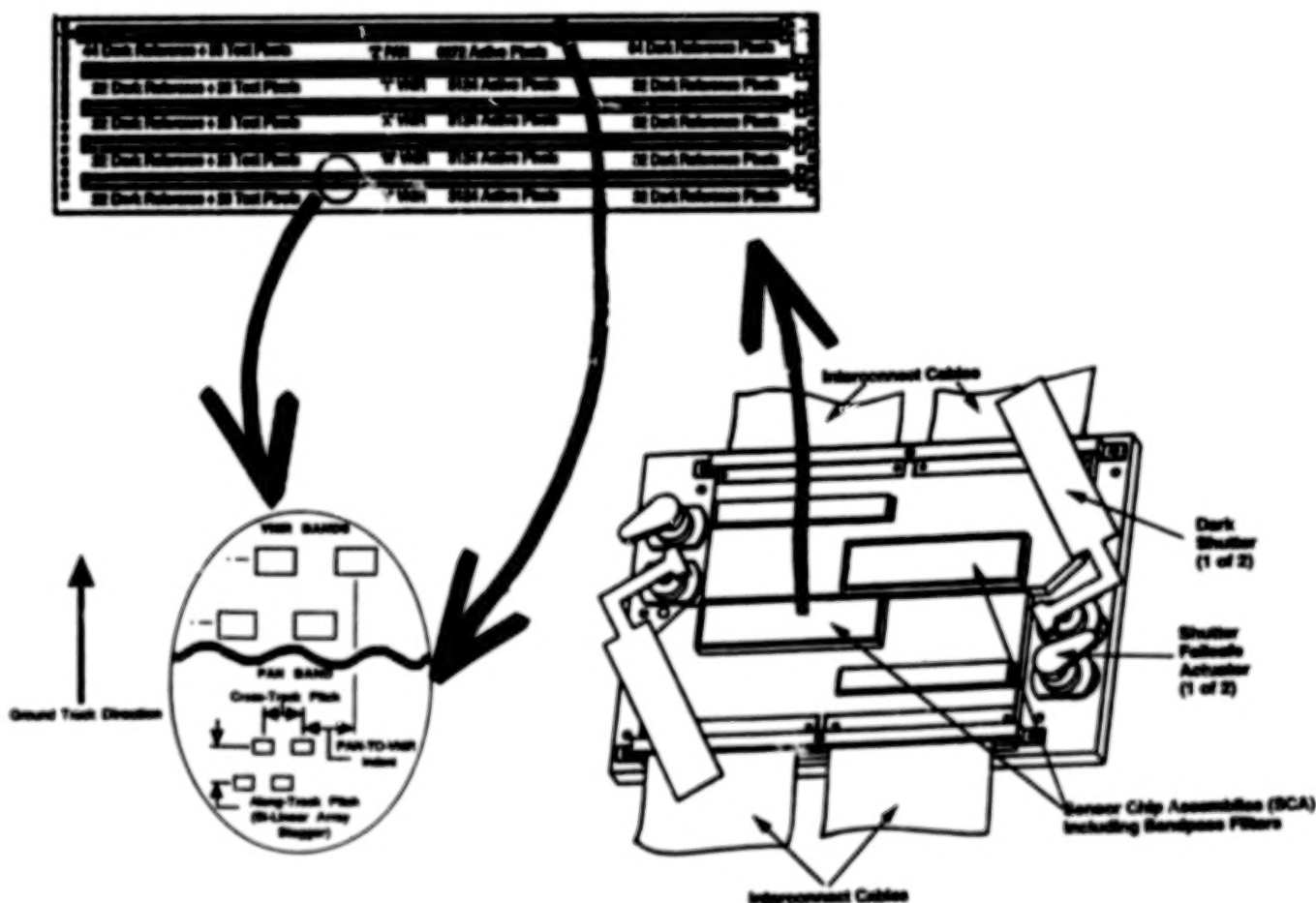


Figure 3. HRMSI Focal-Plane layout showing complete Focal-Plane Assembly and Sensor-Chip assembly detail.

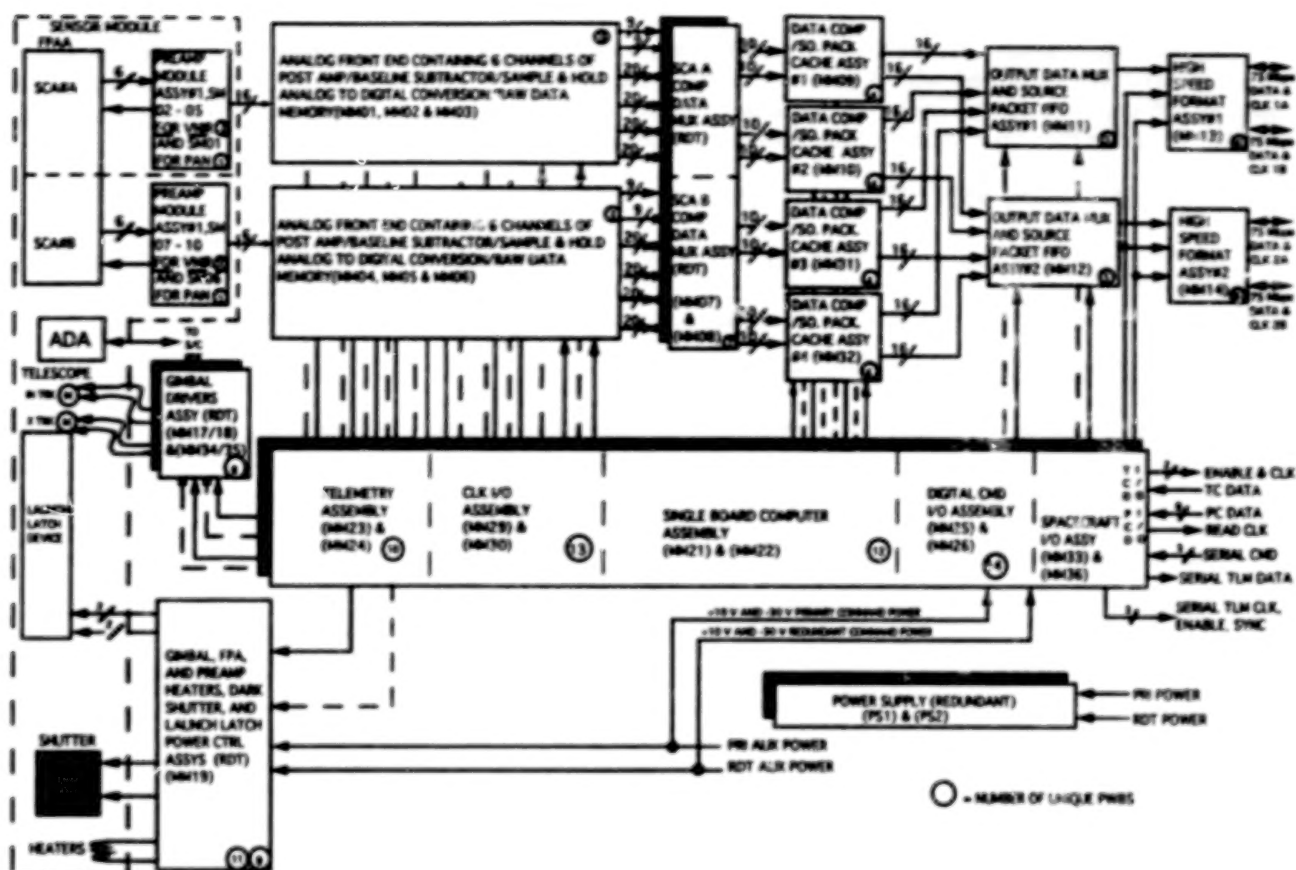


Figure 4. HRMSI electronics block diagram.

Shuttering of the optical path to provide a dark (zero radiance) reference is performed by a rotary actuator configured as a large-angle stepper motor. A return spring ensures that the shutter is removed from the optical path when an actuator is not powered. The driver circuit consists of a current-limiting switch (similar to the position actuators). As a further precaution, a similar circuit is provided for the fail-safe actuators which can be energized to unblock the optical path if the dark shutter were to fail in the closed position.

The design includes redundant power supplies to isolate and convert spacecraft bus power to usable power forms. Each of these will support the 212 W required for the highest power operating mode (imaging with slewing).

3.3.1 HRMSI FLIGHT SOFTWARE (HFSW)

Flight software residing in PROM decodes and executes ground commands, controls and monitors instrument subsystems, manages data compression, and oversees the packet formatting process. Flight code can also be copied and executed from RAM or uploaded from the ground. The design, implementation, and verification of the flight software is planned in accordance with MIL-STD-2167 and MIL-STD-2166. The flight software uses the ADA programming language.

The HFSW included the following functional capabilities:

- Receipt, validation, and execution of payload commands from the space vehicle
- Control of instrument subsystems and functions, including analog conditioning electronics (gain select), telescope pointing (gimbal actuators), dark-shutter assembly, and data routing through the instrument
- Telemetry collection, formatting, and transmission to the space vehicle
- Control of data compression operational states
- Downloading of data compression parameters or tables
- Formatting and transmission of auxiliary data packets

4. KEY TECHNICAL ISSUES AND THEIR RESOLUTION

In the requirements analysis and instrument preliminary design process, a number of key technical issues were addressed and resolved which were related to requirements, predicted performance, interfaces, and programmatic considerations. These are discussed briefly in the following subsections. It is in this solving of problems arena that the major benefit of the now completed HRMSI activities was derived.

4.1 PERFORMANCE-DRIVEN DESIGN DECISIONS

Many of the issues addressed were related to the stringent requirements placed on and evolved for the instrument performance. Often, external restrictions on allowable size, weight, and power limited the scope of potential solutions to those of a more esoteric nature rather than simpler "brute force" approaches.

MODULATION TRANSFER FUNCTION (MTF)

The MTF requirements outlined in Table 1 allowed little or no margin at end of life in some bands. Potential solutions to this condition included additional aperture, focal-plane design changes, and optimization of optical design and fabrication. Due to size/weight constraints, the choice of larger aperture was strongly resisted. In the end, a number of small changes were made, including increasing the aperture from 18 cm to 20.6 cm to allow more leeway in trading off MTF and SNR.

SIGNAL-TO-NOISE RATIO (SNR)

In a similar fashion, there was little or no margin in SNR at end of life on orbit. Options to mitigate this problem included increased aperture and selection of a focal plane with higher responsivity/quantum efficiency. Again, the increased aperture was not desired due to weight penalty. Few focal-plane alternatives were practical during this process; however, by increasing the readout conversion gain, the relative contribution of the electronics channel noise was reduced. Thus, the final optimization took advantage of the slightly increased aperture and efforts to minimize contributions of the noise sources to ensure that the performance requirements would be met.

DYNAMIC RANGE/BLOOMING

While the specified full-scale scene levels represented maximum reflectances predicted from typical imagery, radiance levels much larger than the full-scale scene radiance levels, e.g., due to solar glint, had to be accommodated. While the saturation of pixels imaging such high radiances was acceptable, significant spill over or "blooming" to adjacent pixels was not. The CCD-type readout is particularly susceptible to blooming over wide areas due to the sequential transfer of charge serially out of the array. The design choice was to build in blooming control into the photodiode/CCD unit-cell design to mitigate the effects from radiances up to 100 times the nominal saturation level.

In addition to this, four ground-selectable gain levels were built into the analog signal channels. While not a protection for blooming, they nevertheless allowed optimal use of the instrument dynamic range and quantization (9 bits pan, 10 bits VNIR data). Relative gains of $\times 0.5$, $\times 1.0$, $\times 1.33$, and $\times 2$ are implemented in the design. The lowest gain selection of a higher gain allows optimization for data near the lower end of the dynamic range or to compensate for responsivity degradation over time.

FIELD OF VIEW (FOV)

During the HRMSI concept development process, the design team attempted to respond to the desire to provide as much area coverage as feasible. This translated into as wide a field of view as possible. SBRC had studied, fabricated prototypes, and evaluated diffraction-limited, all-reflective designs up to 15° FOV and beyond. To achieve the 60-km swath goal from 700-km altitude, a near 5° FOV is required. Due to chromatic aberration, focus variation with temperature, and radiation darkening considerations, refractive alternatives were rejected; the three-mirror off-axis approach described in an earlier section was the approach of choice. Fields of view beyond the nominal 5° range were ruled out due to downlink data rate limitations (150 Mbps) and practical data compression/image-quality limitations. Significant effort during the program was undertaken to trade off optical designs and allocations of errors to optimize performance and balance this against fabrication effort and margins. The final design provided excellent performance with challenging but feasible fabrication and alignment implications.

SPECTRAL UNIFORMITY

In the examination of predicted focal-plane performance, certain nuances of spectral response were investigated. There were tight tolerances placed on spectral uniformity; that is the uniformity of the spectral response along each array. Variations in passivation layers on the detectors caused interferometric effects which caused "ripples" in the output as a function of wavelength. A method was devised and demonstrated that effectively eliminated such spectral variations for HRMSI. This technique is currently in the patent application process.

GIMBAL/POINTING PERFORMANCE

Required gimbal performance was driven by the stereo mission data requirements. The initial design utilized a harmonic drive which offered relative simplicity and reasonable pointing performance. As the pointing requirements were refined and evolved, the harmonic drive was ultimately replaced with a direct-drive servo system with dual inductosyn position readouts. In addition, to maintain pointing stability over each orbit, the gimbal frame was fitted with heating elements to balance the thermal gradients to approximately 1°C and thereby limit diurnal thermal distortions to acceptable levels.

The use of dual inductosyn tracks, one providing 252 and one providing 256 zero crossings per revolution, allowed absolute readout of position using differential data. In a degraded mode, should one inductosyn fail, the remaining unit would still provide an excellent relative positioning capability.

COMPLEXITY

The design process is always required to balance complexity with cost, schedule, and risk. The HRMSI design was no exception, with continual tradeoffs being made. In the focal-plane area, a design with 20 outputs (2 for each band for each SCA) was traded against a 12-output concept (2 for Pan and 1 for each VNIR band for each SCA). The first alternative implied more analog channels but less complexity in the FPA output circuitry and lower VNIR data rates. The second alternative required multiplexing on-chip for the VNIR bands, but fewer analog channels and FPA interfaces. In the end, the choice went to the simpler 12-channel approach due to perceived cost benefits.

The focal-plane choice itself involved the tradeoff between the use of many shorter SCAs or fewer longer SCAs. Kodak, Loral, Westinghouse, and other suppliers have produced various sized arrays that could serve as a conceptual basis for the HRMSI SCAs. The choice was to go with the Kodak baseline which utilized two SCAs for the focal plane. This seemed the best balance of overall complexity and risk, selecting long arrays within the focal plane with attendant simpler mechanical design/fabrication and electrical interfacing.

RELIABILITY

Reliability is often also a tradeoff between complexity and predicted reliability in space. Certain functional elements, whose loss would dictate complete mission loss, were duplicated. These elements included the power supply, the flight processor, the gimbal drivers, and the compression data multiplexer. More robust and complicated alternatives were considered to further reduce the presence of single-point failure sites, including a complete foreground/background duplication of all digital electronics and even spare switchable analog channels. Cost and schedule considerations led to the simpler approach described here.

FLEXIBILITY/UTILITY

In the proposal process, it was clear that HRMSI should serve two fairly disparate user bases: an operational one that could tolerate some radiometric degradation in order to enhance collection quantity, and a scientific one to when preservation of data quality takes precedence over quantity. This led to the inclusion of two types of data compression: differential pulse code modulation (DPCM) and RICE. The DPCM compression provided guaranteed swath width at quantifiable and characterizable image-quality degradation. The lossless RICE compression guaranteed perfect image transmission at the expense of a variable swath width and ultimate image-collection quantity.

DATA COMPATIBILITY AND QUALITY

There was a strong requirement to provide data from the ETM+ sensor that would allow direct comparison and equivalency with the TM sensors of Landsats 4 and 5 and the ETM sensor on Landsat 6. This requirement did not apply specifically to the format of the data. In fact, the strong desire to minimize protocol differences between HRMSI and ETM+ and to address compatibility with NASA's Earth Observing System Data

and Information System (EOSDIS), led to the adoption of the Consultative Committee for Space Data Standards (CCSDS) protocols for data transmission. Specifically, Grade 3 Service was adopted, which provided for standard synchronization and data blocking at the highest protocol levels, while allowing for detailed lower level formats to be driven by instrument operational and architectural considerations.

Grade 2 Service, while providing more robust error detection and correction, had to be traded in favor of the Grade 3 Service due to high overhead and transmission channel data rate limitations (75 Mbps). To partially compensate for channel bit error rates, a BCH (1023,993,3) error detection/correction code (EDAC) was added, with interleaving to level 8 to protect against burst errors. This provided an overall space-to-ground bit error rate (BER) of 10^{-6} . This additional BER protection was important for HRMSI, because impact of bit errors on the compressed data is substantially more than on uncompressed data. Resulting codeblock error rate was less than 10^{-9} .

CALIBRATION

From the beginning, it was intended to utilize ETM+ and HRMSI in an on-orbit cross-calibration approach that minimized the extra complexity for HRMSI of dedicated calibration hardware. Two functions were required, however, internal to HRMSI to support both radiometric and imaging performance. The first was a dark shutter to allow for collection of sensor output for a zero-radiance condition. This data would be employed for gain and offset corrections of each detector/channel by collecting dark-shutter data before and after each image sequence.

The second function was a Reference Source Assembly (RSA) to characterize the uniformity of response across the entire focal plane. The original concept employed a number of lamps that could be activated in combinations to provide a near uniform irradiance for each array. Following a tradeoff study assessing performance, complexity, and cost, the RSA approach using lamps was replaced with a solar diffuser that could be used near the north pole during any orbit. Contamination and reflectance degradation issues relative to the diffuser material were not significant issues, because the diffuser was to be used only for uniformity measurements.

Simultaneous viewing of well-characterized scenes by both HRMSI and ETM+ would have been used to transfer the radiometric calibration of ETM+ to HRMSI. Accurate transfer of calibration requires good characterization of the relative spectral response of both instruments and knowledge of the scene spectral radiance variation across the corresponding spectral bands.

4.2 INTERFACE, COST, AND SCHEDULE-DRIVEN DESIGN DECISIONS

As discussed in the sections above, certain interface dictates strongly influenced the instrument design and the tradeoffs performed during the design process. In particular, the TDRSS interface limited data rate to 75 Mbps per output channel (150 Mbps total per instrument). The bit error rate across the TDRSS link (10^{-5}) led to the inclusion of EDAC in the instrument output. Serious constraints on allowable volume, weight, and power led to particular design choices and evaluation of alternatives that minimized impact on these scarce spacecraft resources.

Also as discussed above, schedule and cost implications were always a part of the design tradeoff process, at times being the dominant influence on the outcome. This was particularly true in the complexity, reliability, and single-point failure trades. It also drove the original philosophy on electronics architecture and technology level.

5. DERIVATIVE FUTURE CONCEPTS

While the HRMSI-specific effort on Landsat 7 is now no longer active, we continue to build on the lessons learned on the HRMSI effort as we analyze new alternatives for other programs and concepts for new programs. Where these systems require long linear arrays, the HRMSI experience allows quick evaluation of the tradeoffs on SCA size vs. complexity as well as an experienced understanding of the performance nuances of the detectors/readouts/arrays themselves. In the electronics area, the HRMSI experience has contributed to IR&D efforts to develop standardized integrated circuits for focal-plane clocks, biases, timing, and analog interface/signal processing. Having studied wide field-of-view optical systems, and fabricated IR&D prototypes, we now have actual experience in the practical aspects of designing, specifying, and planning for actual production of such optics. The basic three-mirror, off-axis concept has utility out to beyond 15° .

Derivatives of HRMSI have served as the conceptual basis for proposed designs on two studies for DoD, and one commercial high-resolution application. In each case the particulars may be different, but the HRMSI legacy is evident. In at least one of these systems no gimbal was required. However, the approach for the

telescope, focal plane, and electronics was not seriously impacted by this alternative, even with the addition of SWIR capability.

One of the issues with a pointing telescope system such as HRMSI is the addition of cooling for longer wavelength bands. We have studied concepts for solution of this problem which would be affordable and provide required performance, utilizing both radiative and mechanical coolers. However, it also appears that for moderate resolution systems, providing good SWIR performance in an uncooled approach is now feasible.

6. CONCLUSION

HRMSI as a real, operating entity would have provided significantly useful data in the panchromatic and visible/near Infrared bands, with high-quality stereo imagery. While no longer a part of the revised Landsat 7 program, the effort on HRMSI has nevertheless served as a stepping stone for future programs. Each of the team members, including government customers, Martin Marietta as prime contractor, and SBRC as instrument designer/builder, has gained significant understanding of the issues, roadblocks, tradeoffs and alternatives that form a part of the development of such a high-performance, flexible space instrument. While we would rather be continuing on with the original program, we nevertheless can build on this experience in future programs.

ACKNOWLEDGMENT

Special thanks are given to the entire HRMSI management and design team who spent tireless hours responding to program and technical challenges.

WEDGE IMAGING SPECTROMETER (WIS) HYPERSPECTRAL DATA COLLECTIONS DEMONSTRATE SENSOR UTILITY

Loren M. Woody and James C. Demro
Santa Barbara Research Center
Goleta, CA 93117

ABSTRACT

Santa Barbara Research Center's (SBRC's) Wedge Imaging Spectrometer (WIS) offers the flexibility and high performance of an imaging spectrometer in a compact package. The technology was realized in an SBRC-funded demonstration using a 1-cm² wedge filter and detector array in the 400 to 1000 nm spectral range. Subsequently, through IR&D and contracts sponsored by ARPA, DNA, and USACETEC, airborne flight demonstrations over a variety of scenes were made. Analysis of the data revealed that discrimination amongst crops could be made, automatic detection of features could be attained using a combination of spatial and spectral data processing algorithms, and color processing could be used to highlight environment pollution events. These results were obtained on data corrected only for gain and offset.

The WIS design consists of a linear spectral wedge filter mated directly to an area detector array, providing a single, integrated assembly that performs spectral selection and signal detection without requiring the aft optics needed by imaging spectrometers based on gratings and prisms. The resulting instrument is smaller, lighter, more rugged, and less costly than comparable instruments based on conventional technologies.

Currently, VNIR and SWIR instruments are under development, each with two filters whose spectral bandwidths are optimized for specific spectral features, including (VNIR) vegetation, plant litter, iron oxides, biological events near the "red edge," and (SWIR) discrimination of rocks, soils, and direct identification of surface materials.

The compact, rugged nature of the WIS brings routine acquisition of hyperspectral imagery into the realm of financial feasibility.

1. WEDGE IMAGING SPECTROMETER DESIGN

Santa Barbara Research Center's (SBRC) patented Wedge Imaging Spectrometer (WIS) offers the flexibility and high performance of an imaging spectrometer in a compact package. The design consists of a linear spectral wedge filter on a substrate mated directly to an appropriate detector array, thus providing a single, integrated assembly that performs spectral selection and signal detection without requiring the aft optics needed by imaging spectrometers based on gratings and prisms.

The linear spectral wedge filter is the key to the WIS. It is a thin-film optical device that transmits light at a center wavelength that depends on the spatial position of the illumination. If an array of detectors is placed behind this device, each detector will receive light from the scene at a different center wavelength. Hence, the array output is the sampled spectrum of the scene. By mating the wedge filter to an area array, the scene information will vary spatially in one direction and spectrally in the other. Moving the filter/array assembly perpendicular to the spatial dimension builds a spatial image (two-dimensional) in each of the detected spectral bands, resulting in an imaging spectrometer. The WIS sensor samples each ground point in all spectral bands by using the forward motion of the aircraft to "pushbroom" the ground image across the WIS detector array. The data are then registered in post-processing to superimpose the spectral bands.

The configuration of the wedge focal plane assembly is shown in Fig. 1. The assembly used in the demonstrations which collected the imagery shown in this paper consisted of a single filter mounted on a 128 × 64 detector array (64 spectral bands) with a wavelength range of 0.4 to 1.0 μm . However, the next-generation assemblies, which are currently being developed under SBRC IR&D funding, will have two filters. Each filter will cover less than a spectral octave, easing fabrication, and will be fabricated with differing spectral resolutions, enabling optimization for specific applications. The characteristics of the next-generation instrument are shown in Table 1.

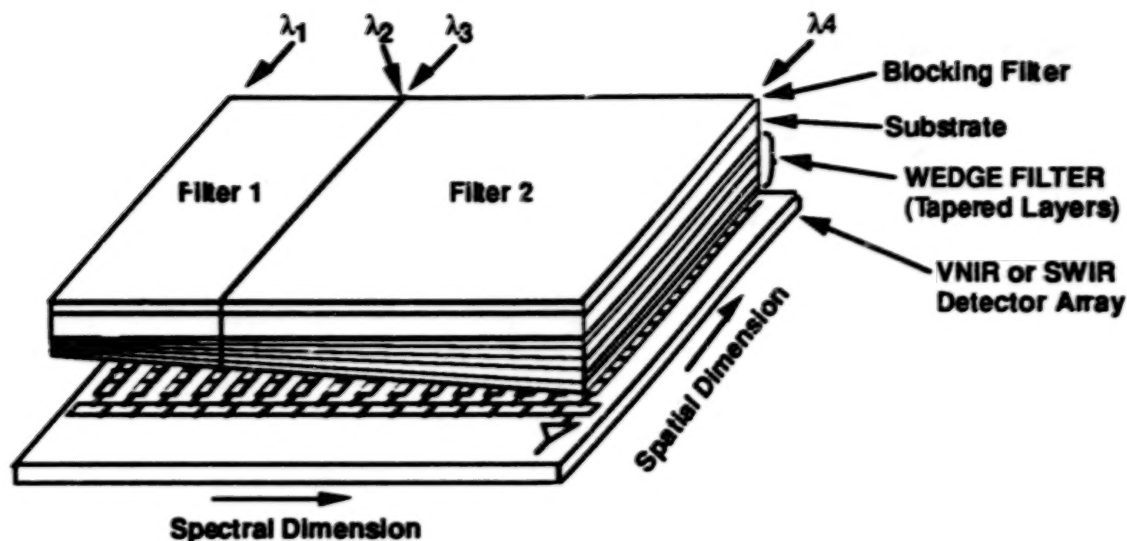


Figure 1. Generalized configuration of the wedge focal plane assembly.

TABLE 1. CHARACTERISTICS OF THE NEXT-GENERATION VNIR AND SWIR WIS INSTRUMENTS

Parameter	VNIR Instrument		SWIR Instrument	
Filter	1	2	3	4
Spectral Range (μm)	0.4-0.6	0.6-1.0	1.0-1.80	1.95-2.50
Number of Bands	17	67	41	45
Spectral Resolution (nm)	9.6-14.4	5.4-8.6	20.0-37.8	18.0-25.0
Detector Array	512 \times 512		512 \times 128	
Detector Material	Si CCD		InSb	

In addition to reductions in size, cost, and complexity, the WIS also provides a degree of spectral flexibility not offered by standard sensor designs. The instrument output can be tailored by weighted aggregation of the spectral bands to derive band sets that directly meet users' needs, without having to utilize the full spectrometric sensor output. This weighted aggregation can be reprogrammed to form new band sets after the sensor is in operation, providing flexibility to meet changes in users' needs after instrument fabrication.

2. DATA COLLECTION

The WIS demonstration flight instrumentation consists of the sensor head assembly with video camcorder, electronics module, data acquisition system, sensor monitor, camcorder monitor, a global positioning system (GPS) receiver, a rotary-stage controller (for yaw correction), and a hand-held controller, as shown in Fig. 2.

The WIS instrument was flown during 1992 on both of the Saberliner 40s owned by Hughes Aircraft and operated by Hughes Aeronautical Operations (HAO). The rugged, modular nature of the WIS flight system design is amenable to integration on almost any airborne platform. However, the maturity of the FAA-approved interface definition, the existence of a backup aircraft should the need arise, and the corresponding reduction of risk and development costs made this the most attractive option.

Table 2 summarizes the sensor characteristics that comprise the critical weight, volume, and power aircraft interface specifications. Equipment locations are driven by operator-interface requirements and aircraft center-of-gravity considerations. Proper consideration of the center of gravity of the Saberliner 40 can make a significant difference in attitude stability as well as fuel consumption at the lower end of the flight envelope.

All external power for this system is standard 120V, 60 Hz, and is provided by the aircraft. Regulation and conversion are accomplished internal to the WIS system. Power interface is by normal grounded plugs and sockets, and all signal and data interfaces are designed with front-panel access for ease of installation. All operating interfaces (power, signal, data) for the airborne system are the same as in the laboratory. The complete system can be installed or removed from the aircraft in less than a day.

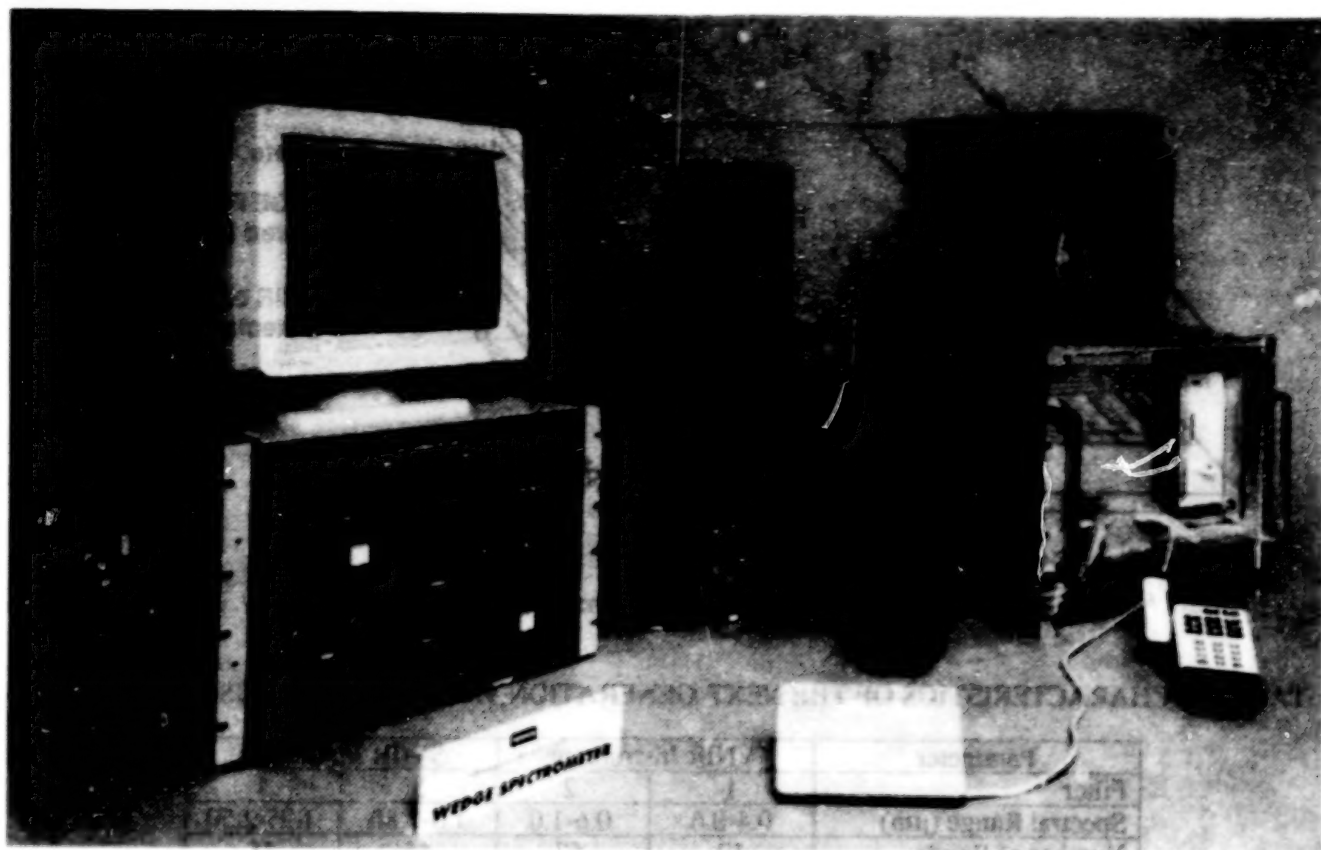


Figure 2. WIS flight instrumentation modules.

TABLE 2. SENSOR/AIRCRAFT MECHANICAL AND ELECTRICAL INTERFACE SPECIFICATION

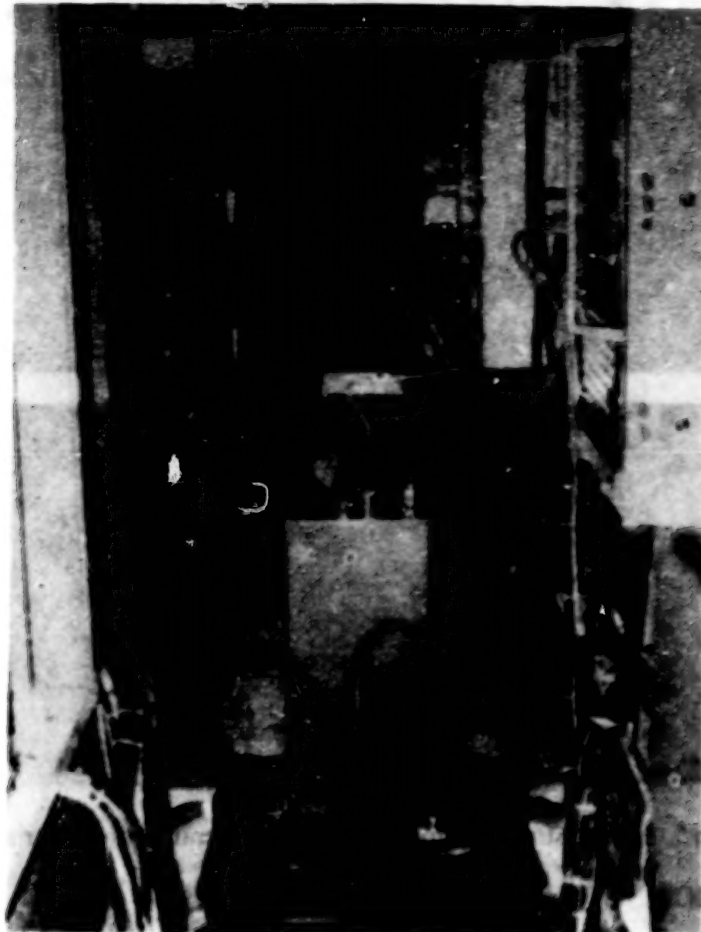
Item	Weight (lb)	Volume (ft ³)	Power (W)
Data Acquisition System	60	3.8	130
Main Electronics - VNIR	67	3.2	50
Sensor/Mount Assembly - VNIR	31	2.0	N/A
Optional "Radiance Camera"	10	0.3	70
Video Camera	2	0.1	5.3
Video Monitor - Camera	23	1.8	100
Video Monitor - VNIR	27	1.9	100
Total (max)	220	13.1	455

The interface to the aircraft included purchase and modification of an emergency escape hatch located on the underside of the aircraft. The principal change was to incorporate a 6-inch diameter, half-inch thick window made of BK7 optical glass. If VNIR and SWIR instruments were to be flown together, both instruments should share a common optical aperture. In this event, it would be necessary to replace the BK7 with fused silica to ensure adequate optical transmission out to 2.5 μm . A bolt-on retainer with an O-ring allows easy replacement of the window. Fig. 3 shows the flight demonstration sensor head mounted on the hatch.

3. DATA EXPLOITATION

3.1 BAND-TO-BAND REGISTRATION

To perform any form of hyperspectral processing, it is necessary to ensure that each spectral band's sample corresponding to image coordinates (x,y) actually was collected from identically the same region on the ground. Typically, aircraft attitude and velocity are recorded with the scene data and then used in post-collection processing. However, aircraft data were not available for the demonstration flights, and so the WIS data were collected in the best manner possible and post-collection processing was applied to re-register the band images.



97-7-97(3)

Figure 3. WIS flight demonstration sensor head mounted on hatch.

Since the WIS collects a spatial image of the scene at each frame time, a correlation can be performed between successive frames of data to establish apparent line-of-sight (LOS) motion. As shown in Fig. 4, successive frames of imagery show virtually identical data, just shifted slightly spatially (predominantly one pixel to the right, as shown by the crossbar in the "H"). This LOS motion estimate can then be used to control an image-resampling routine to force band-to-band registration. Using this algorithm, about 0.5 pixel worst-case band-to-band registration was achieved for the data set of Fig. 2, without aircraft attitude information.

As an example of the ability of this algorithm to re-register the imagery, Fig. 5 shows a "before" and "after" pair of images for bands 20, 30, and 40 (left to right). In the upper image set ("before"), the scene objects for selected points in the band 30 image wander significantly in the other bands (taken at earlier and later times), principally due to a combination of aircraft roll, pitch, and velocity variations. However, the re-registered imagery, shown in the lower image set, has clearly corrected the majority of this attitude variation, with an effective band-to-band registration of about 0.5 to 1 pixel.

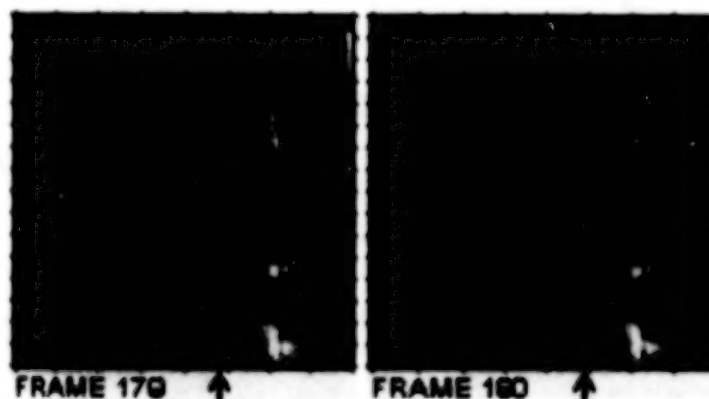


Figure 4. Positional shift of objects in consecutive frames used to estimate LOS motion.

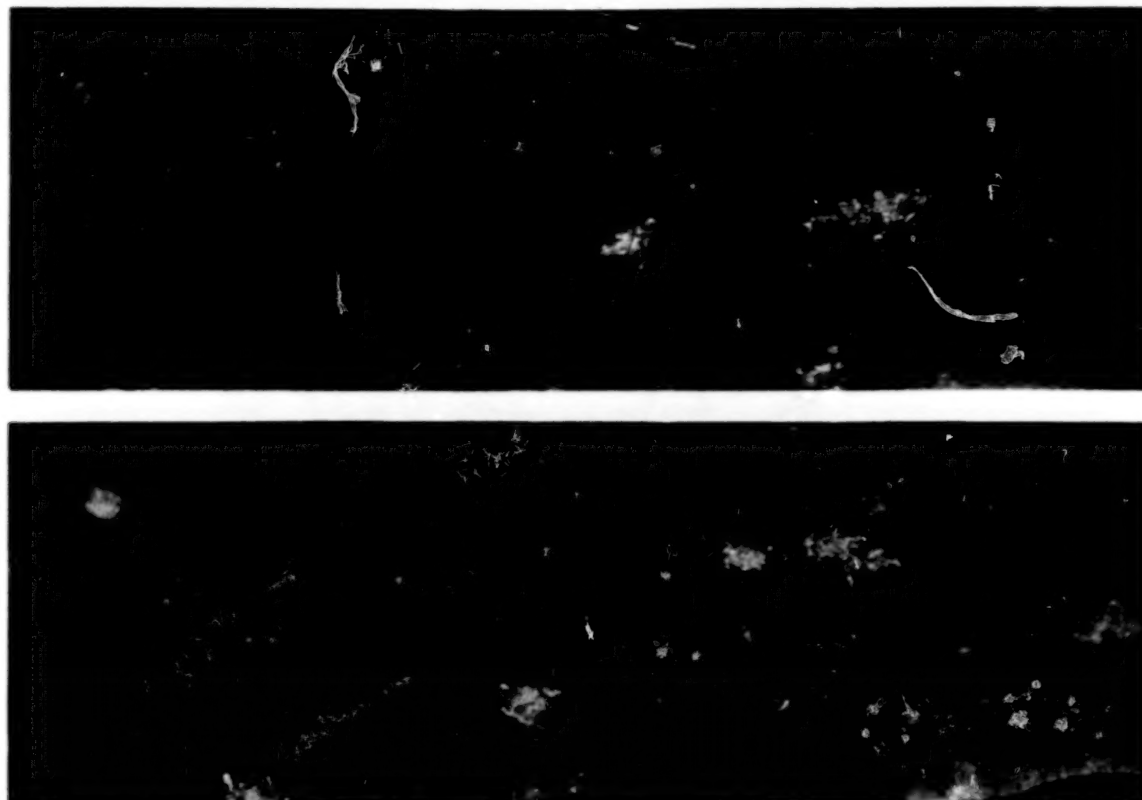


Figure 5. Re-registration algorithm corrects aircraft attitude variation.

3.2 CROP DISCRIMINATION

Data were collected over a large farm, located west of Bakersfield, California. Fig. 6 shows a WIS image of some of the fields taken from band 40 (about 795 nm). (Fields labeled "Fall Lettuce" and "Spring Carrots" were fallow when the data were collected.) These data were registered, and spectra of selected points were extracted. At least two spectra were evaluated for each material selected from the scene. No ground truth spectral data were available, hence the spectra were uncorrected for any effects other than gain and offset. Nonetheless, the common spectra for each material type were highly correlated, and the spectra of different types were distinctly different. Fig. 7 shows the spectra for all types. Note that the spectra from the two types of cotton are distinguishable.

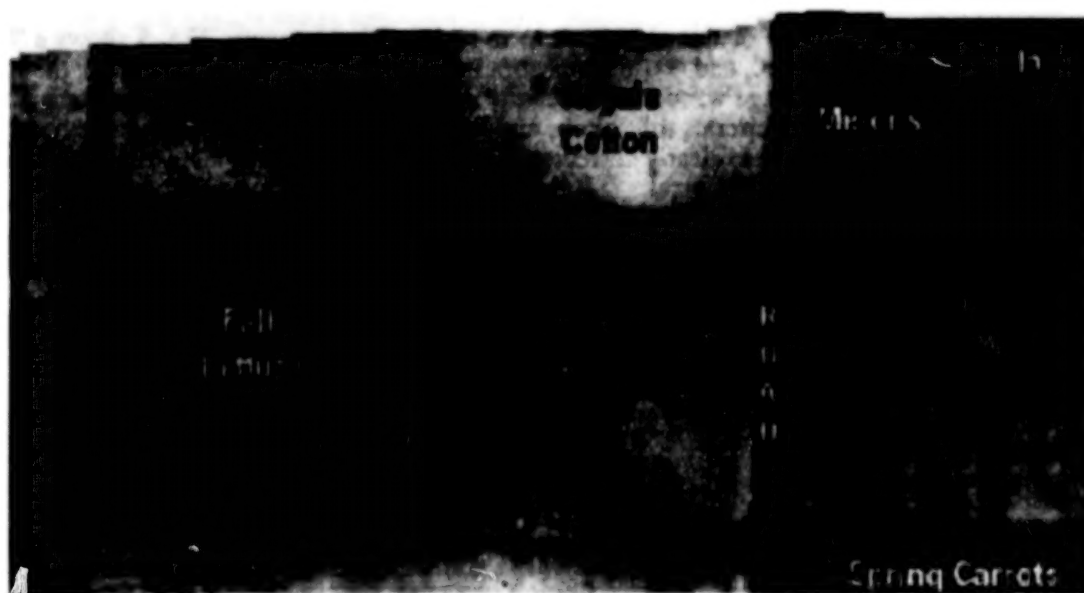


Figure 6. Band 40 (795 nm) imagery of fields on a large farm.

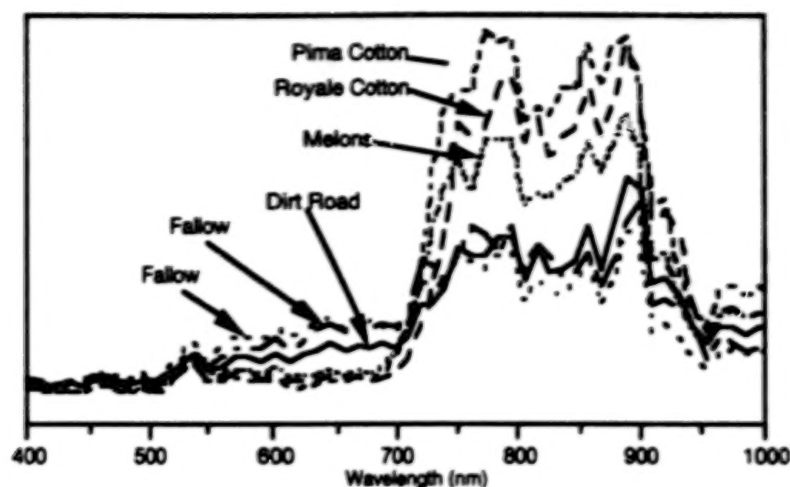


Figure 7. Spectra extracted from WIS data collected over a farm scene.

3.3 AUTOMATIC DETECTION ALGORITHM

Figure 8 shows a scene collected over Camp Pendleton, CA, with three AV-8 Harrier aircraft near a landing pad, as well as a photograph of the scene within the sensor's field of view. A spatial processing algorithm isolated the regions inside the boxes as potential locations of the jets. The jets were actually in regions 10, 11, and 13. Subsequently, the 64 spectral values defining the spectrum from every point in each of the regions were extracted, and Principal Components Analysis (PCA) was used to select a single spectrum that best represents all of the spectra in each region. The results of this analysis for each of the 10 regions isolated from band 30 data are shown in Fig. 9.

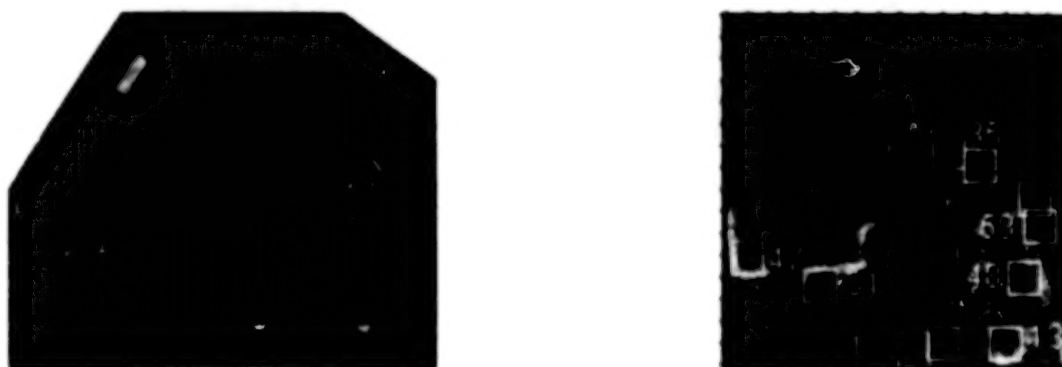


Figure 8. Three Harrier jets. Imagery is from band 30 (690 nm) at 1-meter resolution.

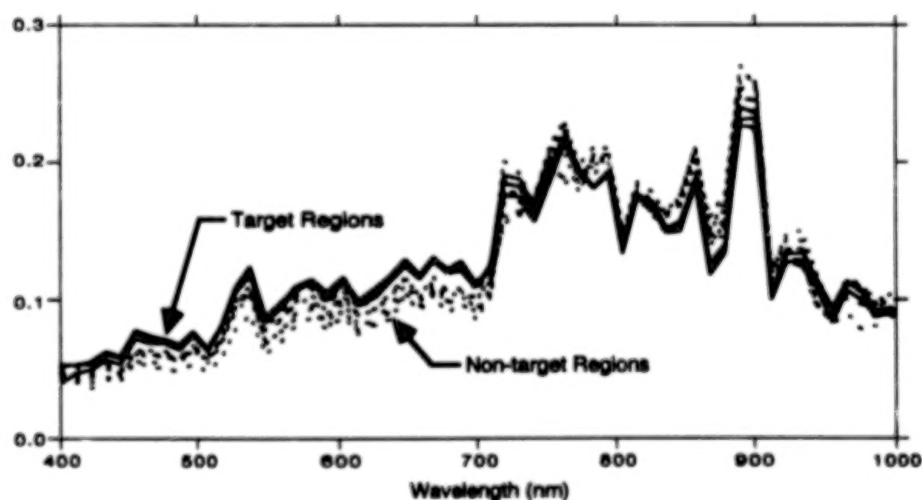


Figure 9. First principal components of each of the 10 cued regions.

To estimate a "reference" spectral signature for subsequent processing, the three target first-principal spectra were averaged, since no ground truth data were available. A ratio was then formed of each region's first principal component spectra to the reference spectrum for evaluation of normalized spectral features. The results are shown in Fig. 10, in which two spectral locations where the three target signatures are maximally different from the other signatures occur in bands 14 and 47 (about 520 and 870 nm). The difference between the target signatures and the other signatures is also of opposite sign at these locations, leading to a simple definition for a discriminant function: the signature (ratio) for a region at band 47 minus that at band 14.

If this discriminant function is examined for each region, as shown in Fig. 11, the target regions can be separated. In this case, selection of a discriminant value midway between the discriminant values for region 13 (0.030) and region 47 (0.238) yields a threshold of 0.135, which cleanly separates the target from non-target regions.

The utility of this discriminant function in separating target from non-target regions selected from other band images was then tested by using the cued regions identified by spatial processing in band 20 (580 nm), band 40 (795 nm), and band 50 (900 nm). These images and their cued regions are shown in Fig. 12. As shown in Fig. 13, the discriminant function derived from band 30 data also correctly identifies these target regions.

3.4 FLIGHT TEST DATA AGAINST A DESERT SCENE

Several data collections were made over Fallon, NV. As shown in Fig. 14a, the scene contained hydroseed, Saudi camouflage, a tarpaulin, a wall in a "bullseye," and desert background of varying brightness. Fig. 14b shows the spectra extracted from this scene. Although the data are uncalibrated, spectral differences among the different materials and similarities among similar materials are clearly demonstrated.

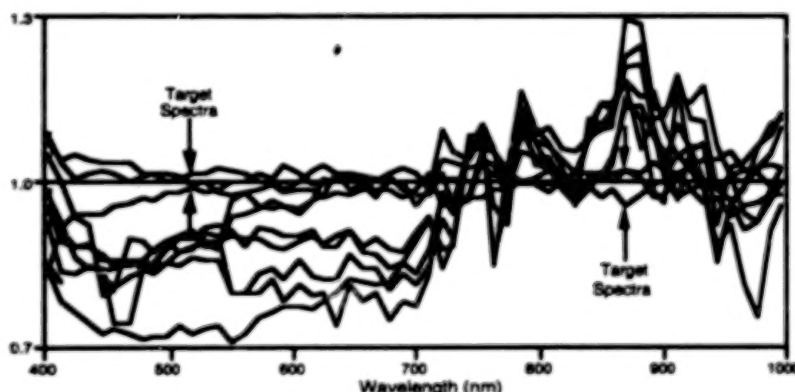


Figure 10. Ratio of each first principal component spectrum to the reference spectrum.

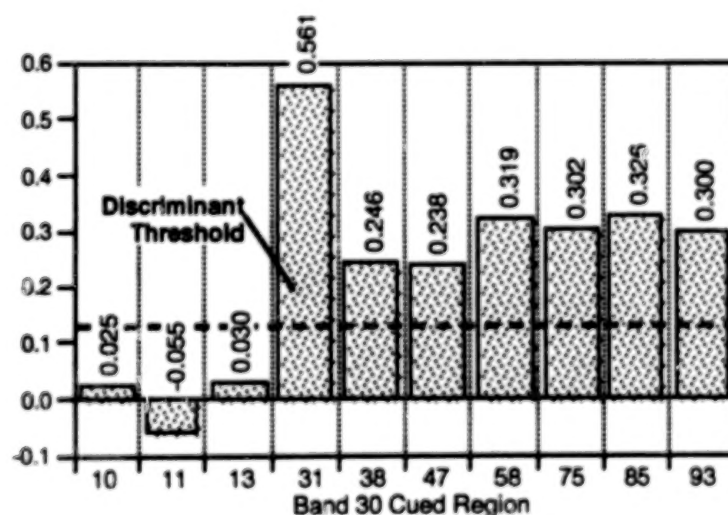


Figure 11. Discriminant function separates target from non-target regions in band 30.



a. Band 20 cued regions



b. Band 40 cued regions



c. Band 50 cued regions.

Figure 12. Cued regions for bands 20, 40, and 50.

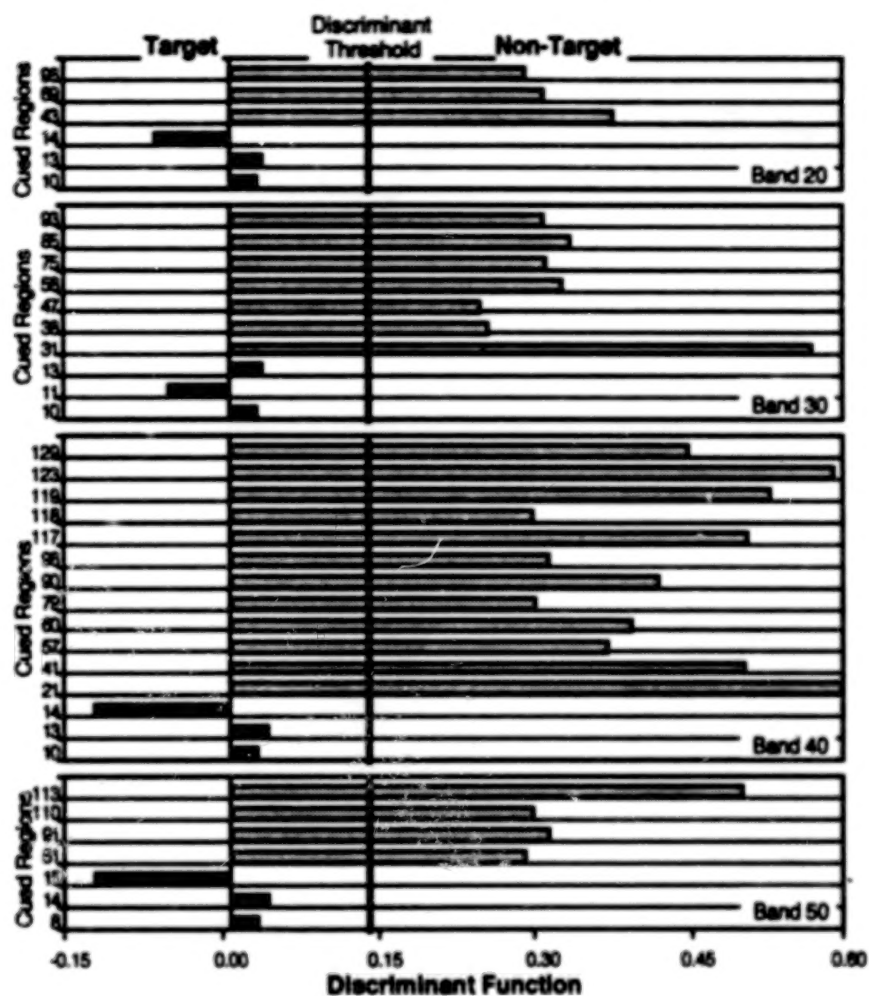


Figure 13. Same discriminant function reliably selects targets from other bands.

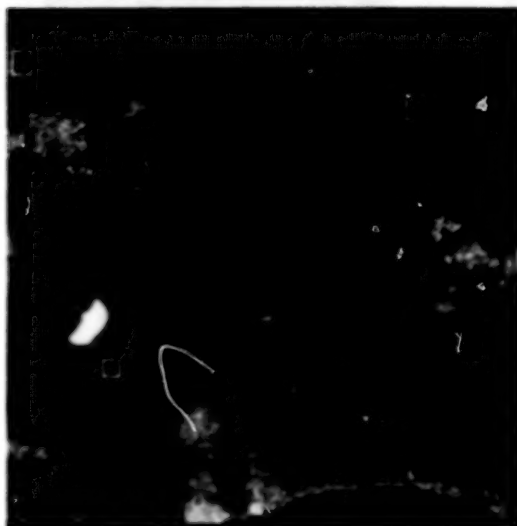


Figure 14a. WIS imagery collected on one flight pass over Fallon, NV.

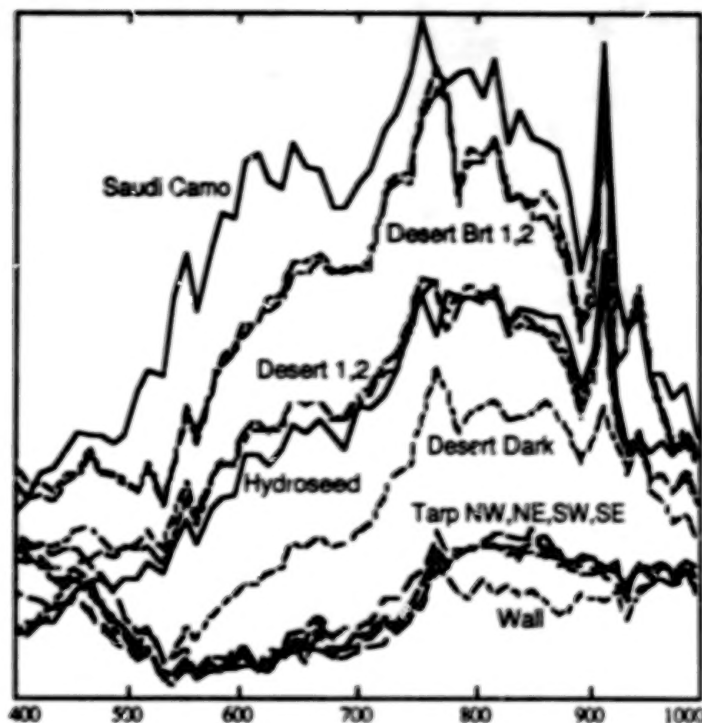


Figure 14b. Spectra extracted from scene in Fig 13a.

Another data set from over Fallon, NV, shown in Fig. 15, illustrates a variety of techniques for displaying spectral variation over a spatial distribution. The spectra presented are taken sequentially along a vertical (spatial) line bisecting the indicated building. The plot of spectra (upper right) shows some variation between the spectra, but it is difficult to identify which spectra correspond to what points in the scene. On the other hand, the surface plot (and the related shaded surface plot) allow identification of both spectral and spatial variation along the selected transect.

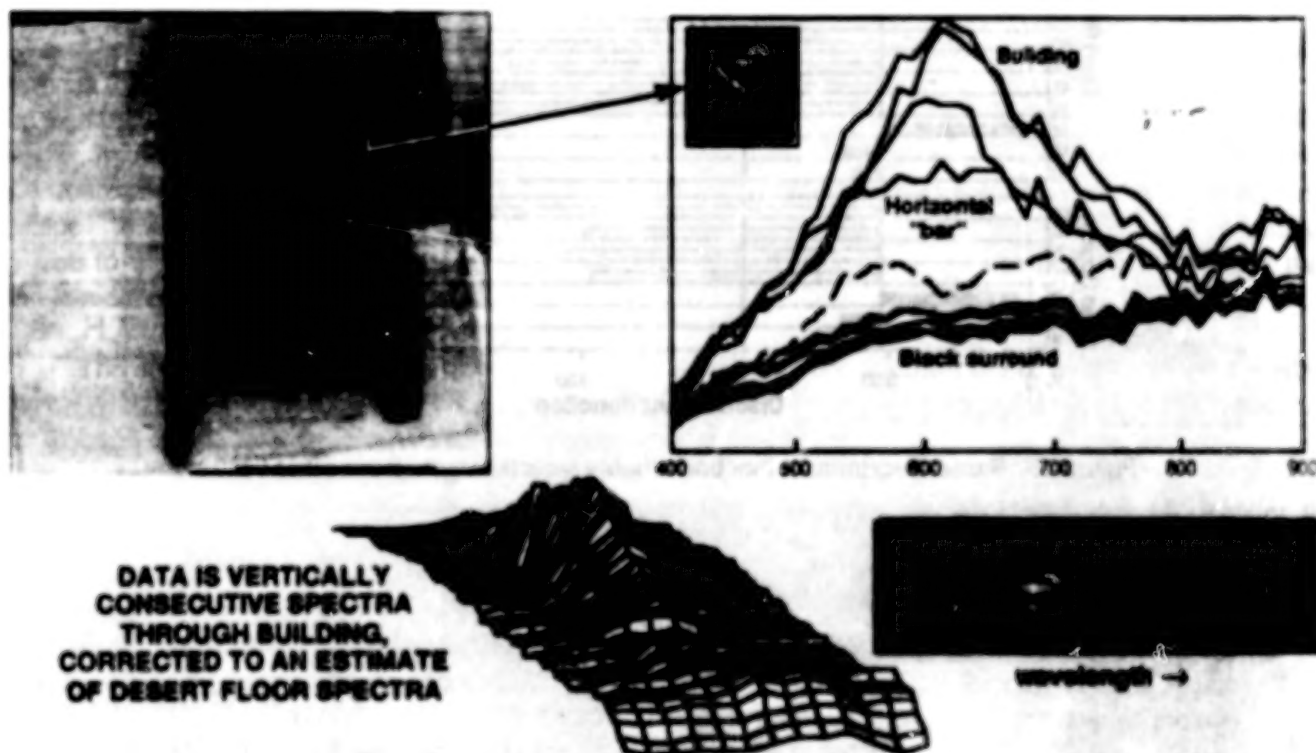


Figure 15. WIS imagery and extracted spectra for a different pass over Fallon, NV.

4. OPERATIONAL CONCEPTS

In the next-generation flight system, each of the 84 VNIR spectral bands comprise 512 spatial resolution elements. The corresponding nominal ground coverage and spatial resolution are a function of the principal data collection parameters: altitude, velocity, detector integration time, and optics focal length. In addition, since the desired data collection parameters may force the use of a ground velocity that is too fast for a given aircraft, the WIS data acquisition system allows a selected number of data frames to be skipped for every frame that is recorded. This data-rate reduction capability provides the ability to match a desired ground resolution (and implied aircraft altitude) to a reasonable aircraft velocity, given the WIS flight demonstration instrument's fixed detector integration time (and implied ground velocity). Fig. 16 shows these tradeoffs of aircraft velocity, altitude, ground resolution, and data-rate reduction (or skip) factor.

As an example, at an altitude of 5 kft, the sensor provides a 1.0 m ground sample distance (GSD), with a data swath width of 512 m and a swath length of up to about 1000 m. For an aircraft speed of 130 kt, with a 15 ms signal integration time and no data-rate reduction (SKIP = 1, which matches the 1 m GSD to the 130 kt velocity), the raw data rate is about 280 Mbps for a VNIR-only system, or effectively about 46 Mbps if only the desired 84 VNIR bands are collected. The data rate would roughly double for a VNIR/SWIR system. Since the integration time can be adjusted over a range of about 10 to 100 ms, these parameters can be tailored for a given collection scenario, allowing selection of an appropriate aircraft velocity for a desired ground spatial resolution (GSD).

Finally, this next-generation VNIR WIS, currently under development at SBRC, will cover the VNIR spectral region with spectral sample spacings (shown in Fig. 17) chosen to support the phenomenology of applications such as: agriculture, mineralogy and geology, and environmental monitoring. This instrument will be flying capability demonstrations during Fall 1994. A companion SWIR WIS, also under development, will undergo laboratory evaluations during the same time period, with airborne demonstrations shortly thereafter.

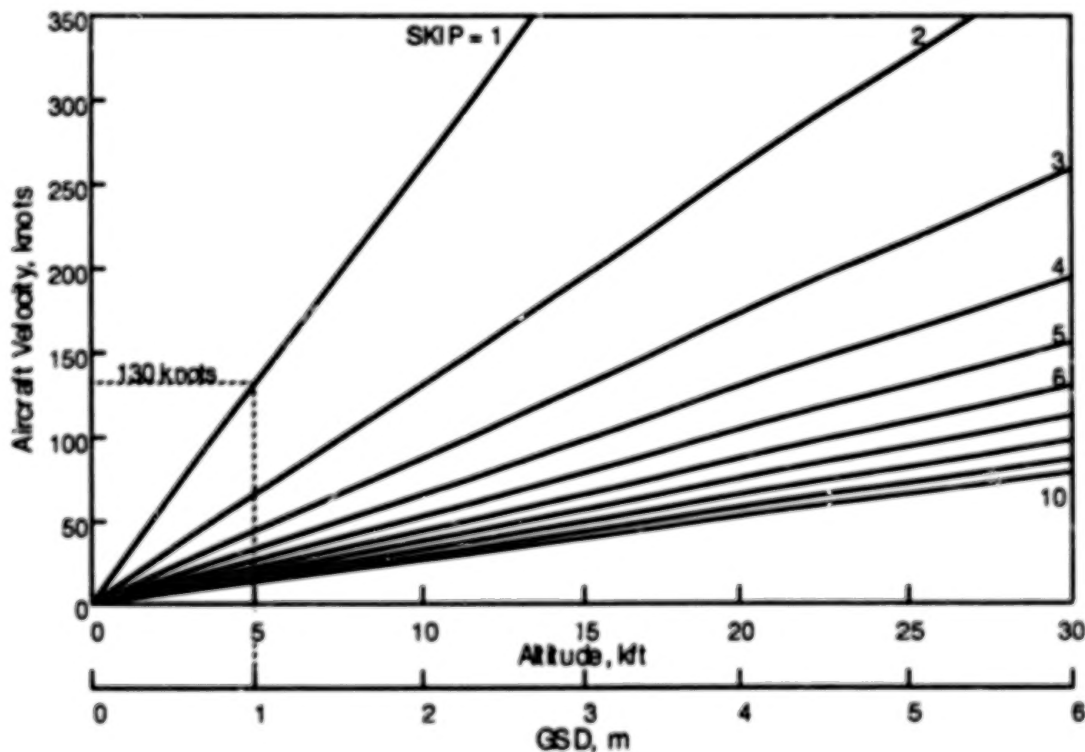


Figure 16. Subsampling rates, altitude, and aircraft velocity limits.

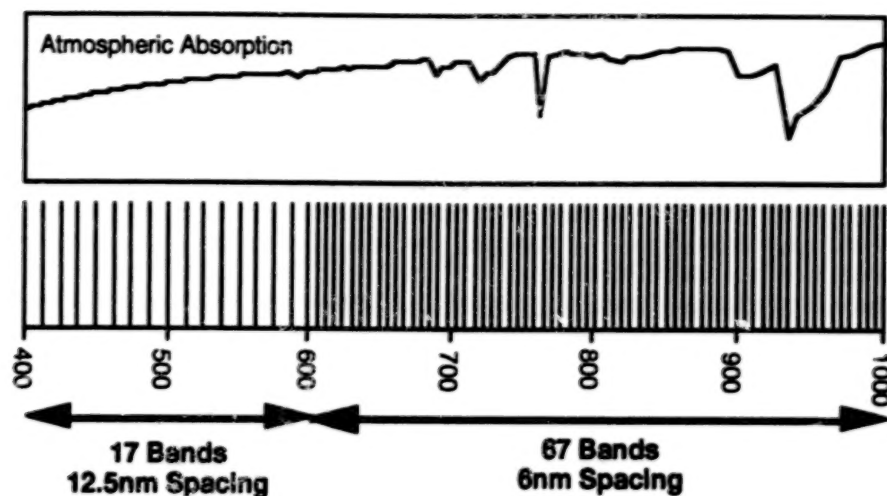


Figure 17. Spectral coverage of next-generation VNIR WIS.

A STATE-OF-THE-ART AIRBORNE INFRARED/ULTRAVIOLET SCANNER FOR OIL POLLUTION MONITORING AND MAPPING

B.M. Sorensen
GER-Intradan, Naerum (Copenhagen), Denmark

S.-H. Chang
Geophysical and Environmental Research Corporation
Millbrook, New York, U.S.A.

T.E. Melhuish
Canadian Coast Guard
Ottawa, Ontario, Canada

ABSTRACT

For more than 15 years, the basic components in airborne marine oil pollution surveillance systems have comprised a Side Looking Airborne Radar (SLAR) and an IR/UV scanner. While the SLAR has been dramatically upgraded since the late seventies, it is only recently that a new scanner technology has been introduced. It is based on a Kennedy mirror which has increased the scan efficiency in spite of a significant size and weight reduction of the scan head compared to conventional scanners. The system includes a real time monitor and is controlled by a Sun Workstation. The scanner is presented including a description of the real-time facility to automatically georeference, mosaic, manipulate, enhance and interpret the data.

1.0 INTRODUCTION

The very first compact operational airborne marine oil pollution surveillance systems built in the late seventies comprised a SLAR, and Infrared/Ultraviolet (IR/UV) scanner with some auxiliary equipment. Today, 15 years later, these two sensors still constitute the core of most oil spill surveillance packages in use in the world.

The SLAR has the advantage of being an (almost) all-weather sensor but it is limited to detecting oil on the sea surface. However, once an oil-like feature has been detected, it has to be identified as oil-mapped and quantified. For this, an IR/UV scanner is used for all but the volume determination. The scanners can discriminate between thin and thick layers of oil, but cannot quantify them. SLARs have been upgraded considerably over the years while conventional flat mirror scanners have undergone little change.

In early 1993, the Canadian Coast Guard (CCG) defined requirements for an IR/UV scanner which is a new generation in terms of configuration, data processing/display, georeferencing and operator friendliness. The system is presented below as the CCG scanner.

2.0 OVERVIEW

2.1 SCANNER

The system is based on a proven, high efficiency, Kennedy-type scanner coupled to custom radiometers and modular electronics subsystems. The radiometer features efficient coupling of in-band radiation to state-of-the art, high-stability, low-noise detectors, insignificant stray radiation and integral preamplifiers on both channels. The dual nature of the probe enables the user to generate the required images in real-time, and to track and identify oil spills, while superimposing the UV and IR images.

2.2 ANALYSIS SYSTEM

The analysis system is designed to address 24-hour, day/night surveillance. The system facilitates the entire surveillance process from data acquisition to hardcopy generation *on board* the aircraft. All data acquisition, processing, and interpretation can be done entirely while the aircraft is on station. The system performs this process rapidly by allowing repeated mapping of critical areas, facilitating an efficient and timely assessment of broad area targets. The recorded data can also be processed on the ground using either the same system, or more traditional image processing and analysis tools and techniques.

The concept of the system is to provide a complete interactive environment for:

1. Verifying, viewing and interpreting real-time sensor data in the aircraft.
2. Continuous recording of sensor data along with capture of full resolution freeze frames.
3. Precision target location and description
 - Target detection
 - Target location

Target boundary definition
Target track estimation

4. Generation of output map & information products from analyzed imagery.
5. Full capability post-mission replay of acquired scanner imagery on ground station.
6. Pre-mission planning, post-mission operations review, and operations documentation.

3.0 TECHNICAL DESCRIPTION

3.1 SCANNER

3.1.1. Scanner Module

The Scanner Module consists of the scanner shock mount, the image acquisition optics (rotating polygonal mirror, 60° folding mirrors, 15° folding mirrors, parabolic mirror, a beam splitter, and the aperture), gyroscopes and mounts, polygonal mirror drive motor, encoder, and optional blackbodies.

3.1.2. Spectrometer Module

The Spectrometer Module is comprised of the UV Collimator focusing optics, the UV detector, the thermal collimator and the 8μ to 12μ detector and optics. The preamplifier electronics are included in this module along with all mirrors, splitters, and optics necessary for each band.

3.1.3. Data Acquisition Module

The Data Acquisition Module consists of the analog-to-digital circuitry for each band, the integrate and hold electronics, and appropriate buffers. This module also includes various system and subsystem controllers including blackbody control, gyroscope control, encoder and motor feed back.

3.1.4. Computer Module

The computer module is a Sun compatible workstation with CD-ROM, 3¼" floppy disk, 8 mm Exabyte tape drive and internal hard drive. The workstation functions as both a data channel between the scanner, navigation device, and tape drive controller, and as a real time display.

3.1.5. Real-time Monitor

The real-time monitor continuously refreshes display of both channels simultaneously. They are displayed in waterfall mode, with either interactive or automatic contrast adjustment. Gyroscopic and thermal baseline corrections are performed in real time.

3.2 ENHANCEMENT PACKAGE

The primary functions of the software and hardware enhancement package can be divided into several general categories:

1. Control and recording of sensor data
2. Real-time data display and image enhancement
3. Selective recording/printing of georeferenced data

These functions are integrated in a windowed environment providing rapid, flexible access to features suitable for the non-technical user. The primary features of these functions are given below:

3.2.1. Control and Recording of Sensor Data

Interactive control of the recording of scanner data is provided with a Sun workstation acting as an intelligent interface to an 8 mm Exabyte data recorder. Point-and-click operation of record start, stop and pause is provided. Data playback capability provides the capability to review recorded data in-flight.

3.2.2. Real-time Data Display and Image Enhancement

Real-time display of both sensor and aircraft navigational data is provided. Sensor data are presented as a scrolling "waterfall" display of both UV and IR data bands, with non-destructive overlay of navigational data and a map graticule. Freeze frame images can be "grabbed" and printed using an on-board color printer.

FIELD SPECTROMETRY: TECHNIQUES AND INSTRUMENTATION

Brian Curtiss
Analytical Spectral Devices, Inc
4760 Walnut Street Suite 105
Boulder, CO 80301-2561, USA

Alexander F. H. Goetz
University of Colorado
Center for the Study of Earth from Space/
Cooperative Institute for Research in the Environmental Sciences
Boulder, Colorado 80309-0449, USA

ABSTRACT

Applications such as aircraft and satellite sensor calibration, development of remote sensing data exploitation methods, remote sensing feasibility studies, and geologic mapping greatly benefit from the use of field spectrometry. The collection of accurate spectra in the field requires an awareness of the influences of the various sources of illumination, atmospheric characteristics and stability, winds, instrument field of view, target viewing and illumination geometry, instrument scanning time, and the spatial and temporal variability of the target characteristics. The first step in the development of a field experiment is the definition of the overall experimental design. Unfortunately, the formulation of an appropriate experimental design is not always obvious. Issues such as the timing of the data collection, spatial scale of the field measurement, target viewing and illumination geometry, and the collection of ancillary data sets must be considered in light of the objectives of the study. The lack of the appropriate ancillary data sets that often makes previously collected data sets unusable for a new application. Frequently, the experimental design must be modified to account for the characteristics of the available instrumentation. Instrument characteristics, such as signal to noise ratio, radiometric calibration, spectral resolution, spectrum acquisition time, and angular field of view, all place limitations on the types of spectral measurements that can be made in the field. For example, vegetation canopy spectra collected using a slow scanning instrument will sometimes have small wind-induced "absorption" features in those portions of the spectra when the instrument was viewing more shadow.

1. INTRODUCTION

Field spectrometry is the quantitative measurement of radiance, irradiance, reflectance or transmission in the field. Portable, battery powered spectroradiometers are typically used to make these measurements. In this paper, the discussion will be limited to: 1) visible to near infrared wavelengths, 300 to 2500 nm; 2) examination of geological, man-made, and vegetative materials; and, 3) instrumentation acquiring a continuous spectrum.

There are many reasons why it is desirable to perform spectral measurement in the field, not all related to remote sensing. Field spectra of ground targets that are homogeneous at the scale of the imaging sensor and collected using ambient solar illumination can be used to convert radiance images to reflectance (Conel et al., 1987a & 1987b). Often, field spectra of target materials are collected to allow for more precise image analysis and interpretation (Goetz and Srivastava, 1985). Field spectroscopy is also used as a tool to perform feasibility studies to understand if and how a process or material of interest can be detected using remote sensing. Field spectra of both the material(s) of interest and spectra of other materials present in the environment can be used to address such questions as: 1) What spectral resolution is required for detection?; 2) What spatial resolution is required for detection?; 3) What is the best time of year/day for detection?; and 4) What signal-to-noise ratio is required for detection? Aside from remote sensing applications, field spectrometers are used to make direct material identifications in the field rather than collecting samples for later laboratory analysis.

2. ILLUMINATION

2.1 ASSUMPTIONS

In order to determine the reflectance or transmittance of a material, two measurements are required: the spectral response of a reference sample and that of the target material. The reflectance or transmittance spectrum is then computed by dividing the spectral response of the target material by that of a reference sample. Using this method, all parameters which are multiplicative in nature and present in both the spectral response of a reference sample and the target material, are ratioed out. These parameters include the spectral

irradiance of the illumination source and the optical throughput of the field spectrometer. Thus, when determining the reflectance or transmittance of a material in the field, an inherent assumption is the characteristics of the illumination are the same for the reference and target materials. Variability of the illumination characteristics between the time the reference and target materials are measured will result in errors in the resultant spectra.

2.2 CHARACTERISTICS OF NATURAL ILLUMINATION

Spectral measurements are typically made in the field using ambient solar illumination. In the field, the target material is illuminated by three or more sources (see Fig. 1), each with its own spectral characteristics (Curtiss and Ustin, 1988). Unless the target is in a shadow, the direct solar illumination is the dominant source of illumination. Parameters such as solar elevation angle and atmospheric conditions will effect the overall intensity and spectral characteristics of direct solar illumination. Diffuse skylight illumination can contribute as much as 5-10% of the total illumination reaching a surface. At shorter wavelengths, diffuse skylight can contribute as much as 20-25% of the total. The spectral characteristics of the illumination scattered off of surrounding objects is determined by their reflectance characteristics. In the case of a forest clearing, as much as 20% of the illumination in the 750 - 1200 nm wavelength range can be attributed to sunlight scattered off the surrounding forest canopy (Curtiss and Ustin, 1988). One important source of surroundings scattered light is the person and the instrumentation making the measurement. Objects in the surroundings also effect the overall illumination of the target surface by obscuring a portion of the diffuse skylight and, possibly, shading the target from direct solar illumination. The magnitude of both the diffuse skylight and scattered from surrounding illumination components is determined by the solid angle subtended by these sources when viewed from the reference frame of the target surface. The surface texture of the material being measured also effect the relative proportion of the various sources of illumination. When compared to a smooth surface, a surface with a rough texture will tend to have a higher proportion of illumination from the diffuse and scattered-from-surroundings sources relative to the direct solar illumination (Curtiss and Ustin, 1988).

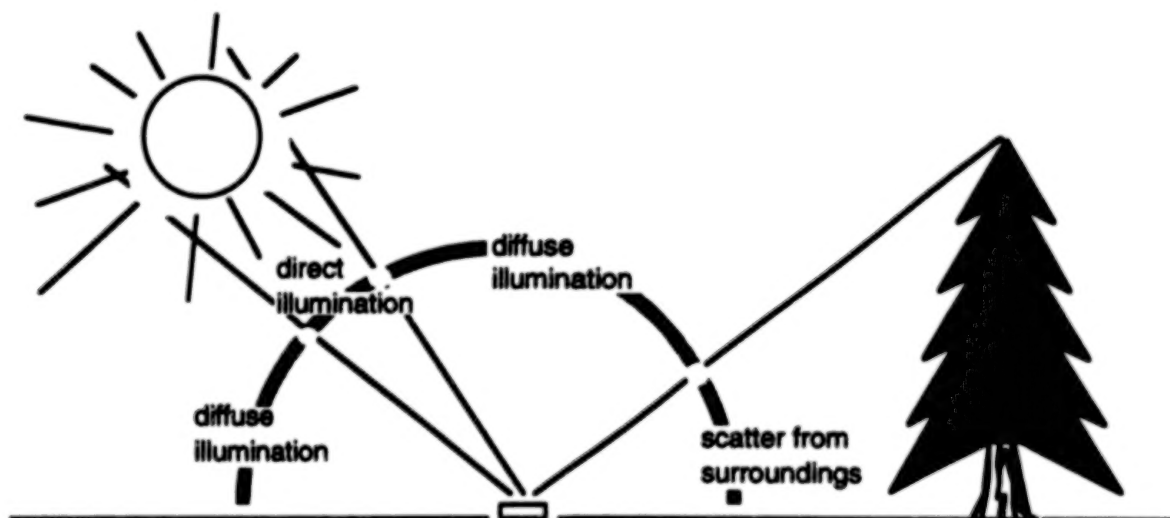


Figure 1. The major sources of illumination. Note that it is possible to have several sources of light scattered off of surrounding objects, each with its own unique spectral distribution.

2.3 CHARACTERISTICS OF ARTIFICIAL ILLUMINATION

While in most cases it is desirable to use ambient solar illumination to maintain equivalence between field spectral measurements and remotely sensed images, there are some cases where the use of artificial illumination is desirable. The use of artificial illumination allows: 1) more control over illumination and viewing geometry; 2) more control over sample geometry; 3) measurements during non-optimal conditions (e.g. cloud cover or at night); and 4) measurement of reflectance and transmittance in the deep atmospheric absorption bands. Several problems with using artificial illumination include: 1) difficulty in maintaining a constant distance between the sample or reference and the light source when measuring samples with irregular geometry; and 2) lights can 'cook' vegetation samples (water loss, chlorophyll degradation). A typical lamp configuration for indoor use is shown in Figure 2. Alternatively, the light source can be either incorporated into the field spectrometer (often precluding the use of solar illumination) or can be provided in the form of an optional accessory that mounts to the light collecting optics of the instrument.

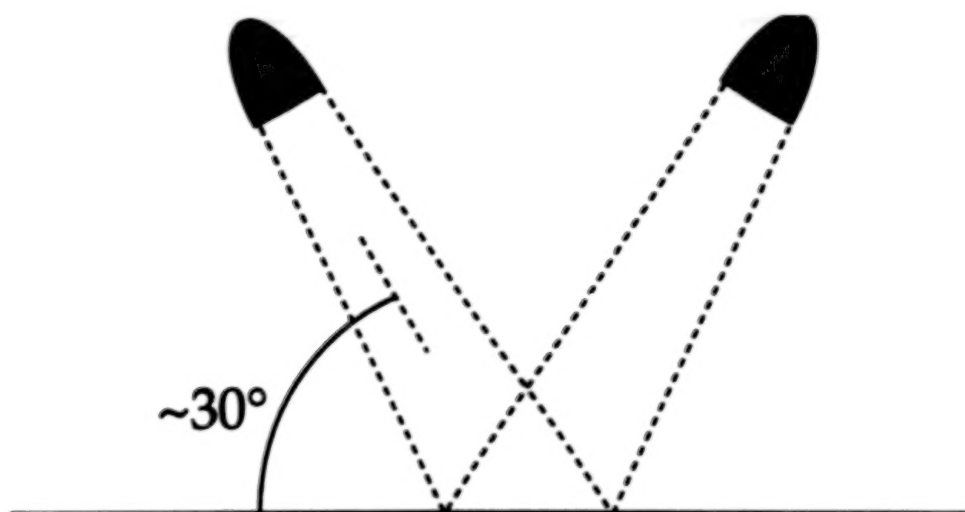


Figure 2. A typical lamp configuration for artificial illumination; the sample is viewed with the collecting optics of the spectrometer nadir to the sample. Use 1 or 2 200 to 500 Watt quartz-halogen cycle tungsten filament lamps ($\sim 3400^\circ\text{K}$ color temperature) in housings with aluminum reflectors about 1 meter above the surface being measured.

3. ATMOSPHERIC CHARACTERISTICS

3.1 ATMOSPHERIC TRANSMISSION

Absorbing molecules in the atmosphere strongly modify the incoming solar irradiance (Goetz, 1992). All of absorption features described in this section will increase in intensity as the atmospheric path length of the incoming solar radiation increases (e.g. with changing solar elevation angle). By far, water vapor is the strongest modifier of the incoming solar spectrum (Gao and Goetz, 1990). Water vapor has absorption features spanning the solar reflected region of the spectrum (see Fig. 3), and varies both spatially and temporally. Carbon dioxide has strong features in the 2000-2200 nm range (see Fig. 4), a region of major interest for the identification of layered silicate minerals (Goetz, 1992). Carbon dioxide is a well mixed gas, thus the intensity of the absorption features associated with carbon dioxide are not as variable as those of water vapor, but they do decrease with increasing altitude. Other major atmospheric components that influence the atmospheric transmission spectrum are shown in Figure 5.

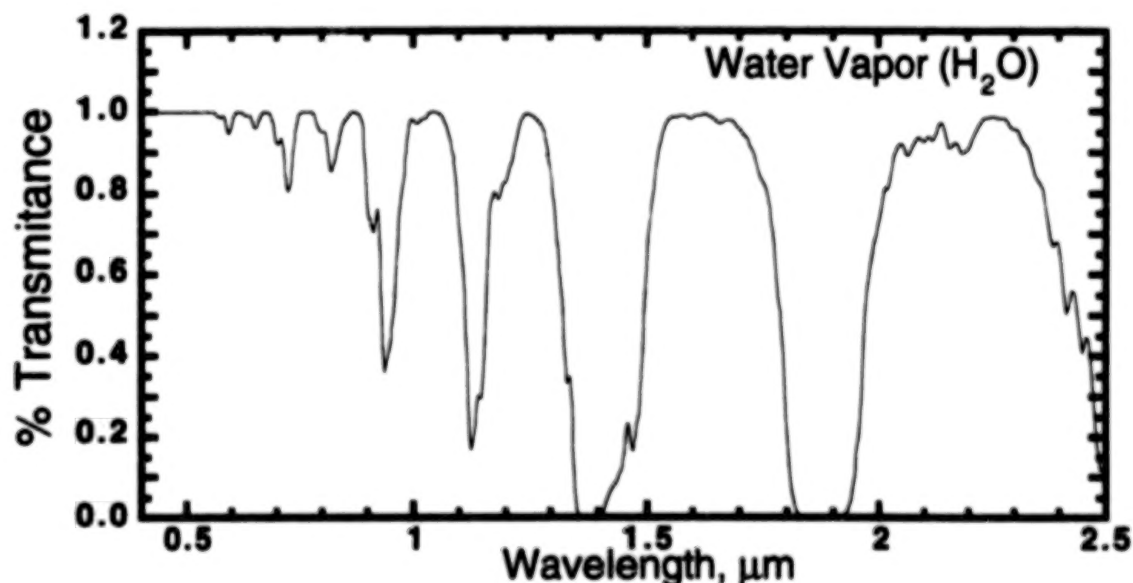


Figure 3. Transmission spectrum of water vapor for typical atmospheric conditions.

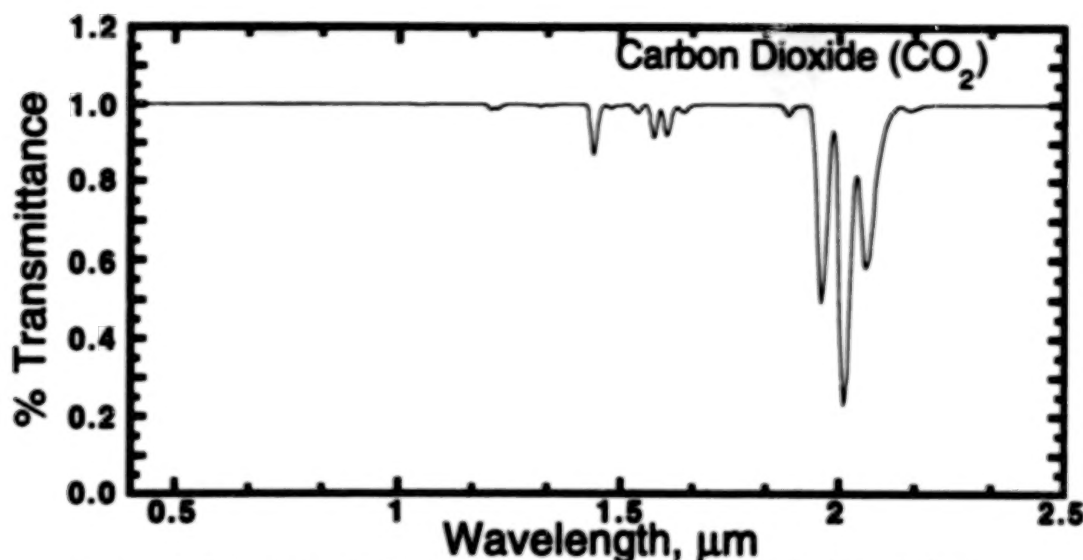


Figure 4. Transmission spectrum of carbon dioxide for typical atmospheric conditions.

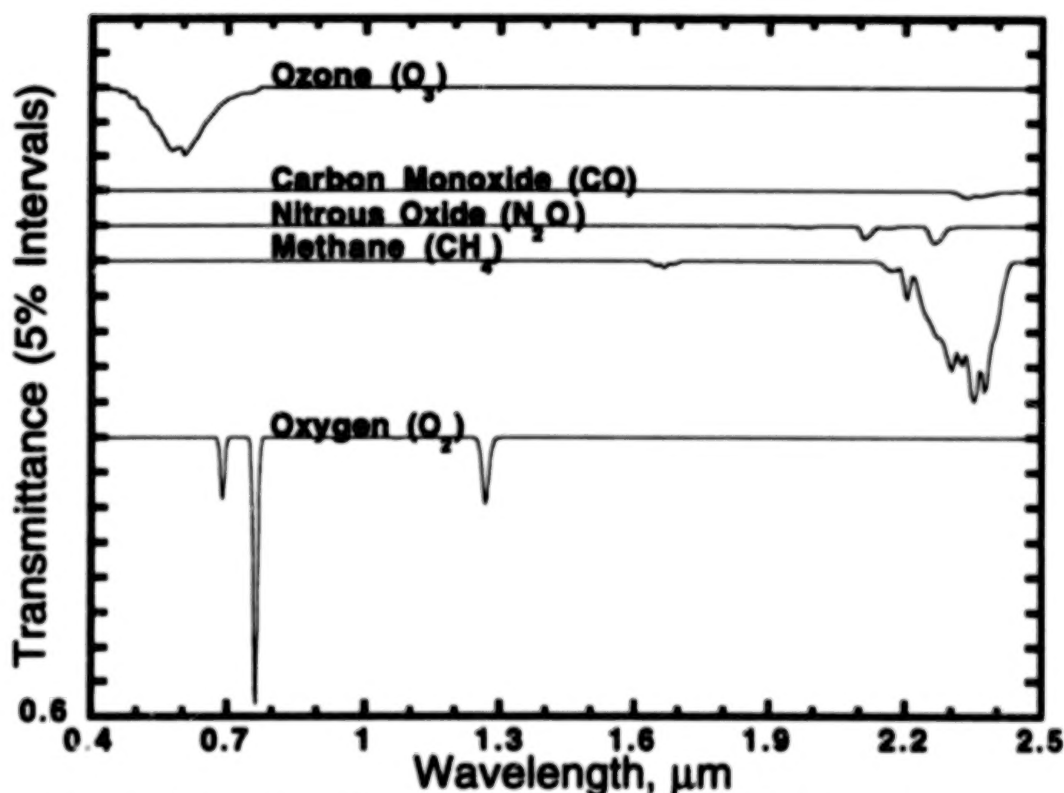


Figure 5. Transmission spectrum of various gases for a typical atmospheric conditions.

3.2 CLOUDS

The presence of partial cloud cover is indicative of highly spatially and temporally variable atmospheric water vapor (Gao and Goetz, 1992). Because of the large influence of water vapor on the atmospheric transmission (see Fig. 3), variability of atmospheric water vapor between the time when the reference and target measurements are made will result in errors in the resultant spectrum. This error can be reduced by minimizing the length of time between the measurement of the reference sample and the target.

While they are difficult to see and often appear inconsequential, the presence of cirrus clouds tends to produce significant variability in atmospheric water vapor (Gao and Goetz, 1992). The field spectrometer itself can be used to measure the magnitude of the effect. Simply standardize the instrument on the reference panel, then continue to view the reference panel with the instrument. If the atmospheric conditions are stable, the computed reflectance of the panel will be a flat spectrum with near 100% reflectance. If atmospheric conditions are unstable, the computed reflectance of the panel will vary over time and will show absorption

minima or maxima (depending on whether atmospheric water vapor is increasing or decreasing) at the wavelengths corresponding to the water vapor absorption features. In this way, it can be determined whether spectral data with sufficient accuracy can be acquired.

In addition to the errors produced by time varying atmospheric water vapor, partial cloud cover also greatly increases the intensity of diffuse skylight illumination (Curtiss and Ustin, 1988). This tends to "fill in" shadows and reduce the contrast between surfaces with dissimilar surface textures. If the goal is to collect field spectra for image calibration or interpretation, spectra should be collected under illumination conditions similar to those at the time the image was collected.

3.3 WIND

Wind can be a source of error if the material being measured moves during the time the spectrum is acquired. If a spectrum is slowly scanned, changes in the amount of shadow in the instrument field-of-view will result in erroneous "features" in the spectrum. Vegetation canopies, with their large proportion of shadow, are especially susceptible to wind induced errors. Instruments using an array detector or that scan the spectrum rapidly are not significantly affected by wind.

4. CHARACTERISTICS OF TARGET MATERIALS

4.1 VEGETATION

Because of the complex three dimensional geometry of a plant canopy, light returned from the canopy is a complex mixture of multiply reflected and/or transmitted components (Curtiss, 1990; Curtiss and Maecher, 1991; Curtiss and Ustin, 1989). The canopy level optical signal is dependence upon illumination and viewing geometry, canopy structure, leaf optical properties, and the optical properties of other vegetative and non-vegetative components within and below the canopy. The strong dependence on illumination and viewing geometry can be seen in Figure 6. Both the overall brightness of the canopy and the shape of the spectral signature (e.g. the red to infrared ratio for the canopies in Figure 6) are dependent on the illumination and viewing geometry. Thus, it is only by controlling the viewing and illumination geometry, that changes in canopy reflectance attributable to the canopy itself can be detected.

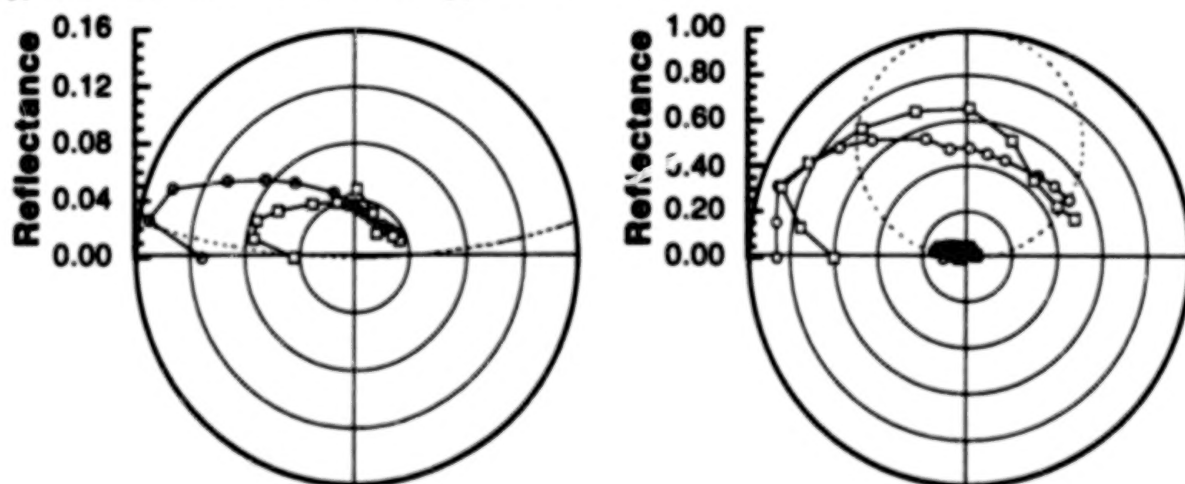


Figure 6. Bi-directional reflectance functions (BRDF) of a conifer, Mugo Pine, (circles) and a broadleaf shrub, Viburnum, (squares). For reference, the BRDF of a Lambertian reflector is plotted as a dashed line. The left plot is for a red band (650 nm) and the right plot is for a near infrared band (850 nm). Both canopies were illuminated from the left at an elevation of about 30°.

True differences in canopy reflectance between several canopies may be due to either differences in canopy structure or in leaf/needle optical properties (Curtiss and Maecher, 1991). Using the data presented in Figure 6 as an example, for almost all viewing geometries, a conifer canopy will appear darker in the infrared than the broadleaf canopy even though the reflectance of the individual needles and leaves may be almost identical. Observed differences in canopy level reflectance may be attributable to differences in either leaf level optical properties or other, larger scale, structural properties of the canopy. Important structural properties include leaf/needle size, leaf/needle density at the branch level, number of years of needles retained (conifers), and branching angles. When differences are observed between canopies of the same species, almost always due to differences in canopy or branch level structure.

The absorption features seen in vegetation spectra are all related to organic compounds common to majority of plant species (Peterson et al., 1988; Gao and Goetz, 1992). Thus, the information about a plant canopy is contained in the relative intensity of the various absorption features rather than in the presence

absence of a specific absorption feature. The major spectral absorption features can be attributed to plant pigments (chlorophylls, xanthophyll, and carotenoids) and water. Other, minor, absorption features are attributable to other chemical components; these include cellulose, lignin, proteins, starches, and sugars. Non-photosynthetic components of the canopy have spectra which are dominated by absorption features attributed to lignin and cellulose.

4.2 ROCKS, SOILS, AND MAN-MADE MATERIALS

Unlike vegetation, the shape of the spectral signature of rocks and soil tend to be invariant with varying viewing geometry. Due to changes in the amount of shadow in the field-of-view of the spectrometer, the overall brightness of the observed spectrum does change with illumination and viewing geometry. Absorption features in the spectra of rocks and minerals (See Figure 7) are due to the presence of specific molecular groups and are often diagnostic of the minerals present in the sample (Abrams et al., 1877; Hunt, 1980)

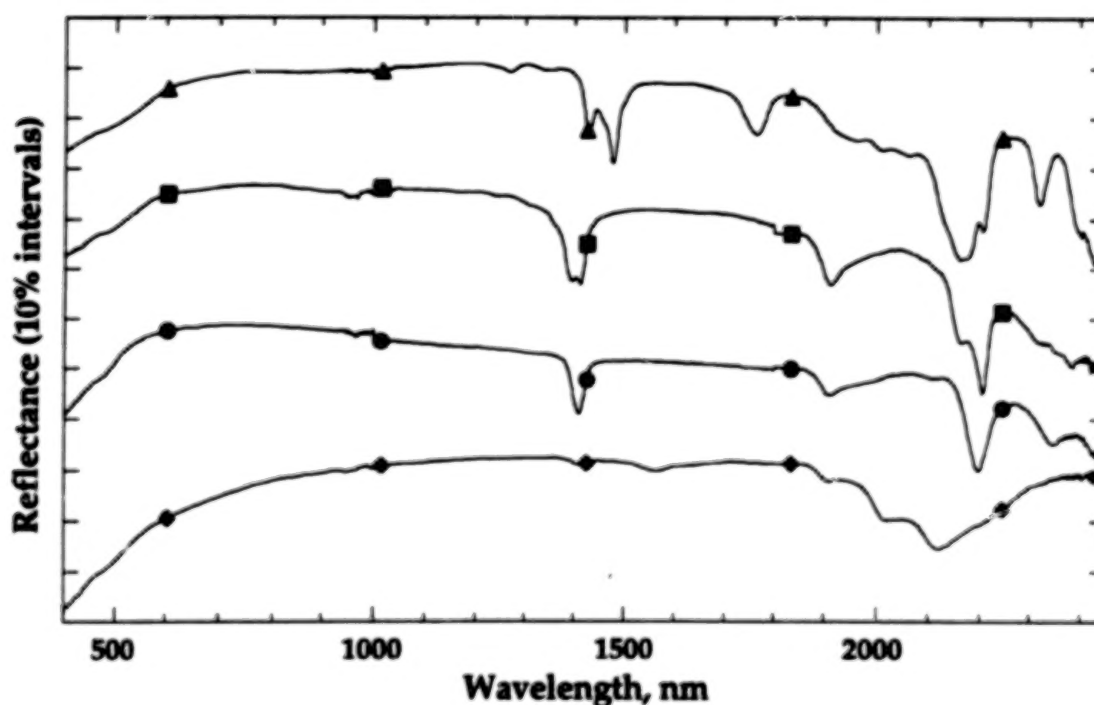


Figure 7. Reflectance spectra of alunite (triangles), kaolinite (squares), illite (circles), and buddingtonite (diamonds) measured with a FieldSpec™ FR field portable spectroradiometer.

The dependence of the optical properties of man-made objects on the viewing and illumination geometry will fall somewhere between that for vegetation and rocks/soils. This will depend on the amount of light transmission through elements of the target and on the surface texture of the object. The reflectance spectra of objects with translucent elements and highly textured surfaces have an angular dependence more like vegetation, while those with opaque elements have an angular dependence more like spectra of rocks and soils.

5. INSTRUMENTATION

5.1 SPECTRAL RESOLUTION VS. SPECTRAL SAMPLING INTERVAL

While the terms "spectral resolution" and "spectral sampling interval" are often used interchangeably, they refer to very different characteristics of a spectrometer. Spectral resolution is a measure of the narrowest spectral feature that can be resolved by a spectrometer. It is also defined as the full width at half maximum (FWHM) response to a spectral line source. The spectral sampling interval of a spectrometer is the interval, in wavelength units, between data points in the measured spectrum.

For hyperspectral remote sensing applications, a spectral resolution of about 10 nm and a spectral sampling interval of about 2 to 3 nm is required (Goetz and Calvin, 1987; Goetz, 1992b). The requirement for 10 nm spectral resolution is driven by the spectral resolution of the hyperspectral sensor (about 10 nm). A spectral sampling interval of about 2 to 3 nm provides 3-4 data points in the field spectral data. This oversampling of the spectrum results in less degradation of spectral resolution when resampling the field spectral data to match the wavelengths of the hyperspectral sensor channels. Also, analysis methods utilizing derivative spectra greatly benefit from the oversampling of the spectrum.

5.2 SPECTROMETER DESIGN

Spectrometers used in currently available field spectrometers are either based upon a fixed grating and an array detector, or a single element detector and a scanning grating. One of the drawbacks of an array based spectrometer is the signal-to-noise ratio (SNR) is tied to the sampling interval as well as the spectral resolution (Smith, 1992), while in a scanning spectrometer the SNR is independent of spectral sampling interval. Array detectors in the 350 to 1000 nm region of the spectrum (VNIR) have sufficient sensitivity to allow spectra to be collected with spectral resolutions well above the 10 nm resolution required for hyperspectral remote sensing studies. Thus, in the VNIR, fixed grating, array detector, based spectrometers provide the best performance for most remote sensing applications. Typical VNIR spectrometer designs provide 3 to 5 nm spectral resolution with a spectral sampling interval of better than 2 nm.

Due to the rapid fall-off in energy of the solar spectrum in the 1000 to 2500 nm region of the spectrum (SWIR), spectrometer design is strongly driven by the need to maintain an acceptable SNR. In general, a loss of SNR is not acceptable in exchange for decreased spectral sampling interval. Thus, the use of an array detector in the SWIR spectral region generally precludes the oversampling of the spectrum. While scanning spectrometers do not have this limitation, they have the drawback of not measuring all wavelengths simultaneously. This can result in errors due to changes in the target during the measurement of the spectrum (see Section 3.3). This limitation is overcome by rapidly scanning the spectrum.

Traditionally, scanning SWIR spectrometers have used lead sulfide (PbS) detectors. Due to the lack of sufficient frequency response, the use of PbS detectors precludes rapid scanning. Indium gallium arsenide (InGaAs) detectors have the high frequency response required for rapid scanning (less than 100 milliseconds to scan from 1000 to 2500 nm). InGaAs detectors have the added advantage of having a higher sensitivity than PbS and, also, do not require an optical chopper as does PbS. These increases in performance over PbS allow the design of a rapid scanning spectrometer with equivalent or better SNR performance than a PbS array detector based spectrometer. A scanning design has the added advantage of being having a spectral sampling interval that is less than one fifth the spectral resolution without a reduction in SNR.

While it is possible to include the illumination source within the spectrometer, this limits the applications that can be addressed and the types of targets that can be measured. Because of the need to hold illumination and viewing geometry constant between the field and image spectral data, field spectra collected for either hyperspectral sensor calibration or for direct comparison with hyperspectral image data are best collected using ambient solar illumination. The use of a built-in light source also precludes the measurement of radiance or irradiance. Additionally, targets such as vegetation with a complex three dimensional structure can only be measured in the field using solar illumination.

5.3 SPECTROMETER FIELD OF VIEW

Existing field spectrometers use one of two basic approaches to collect light energy and deliver it to the spectrometer. In some spectrometer designs, foreoptics are used to form an image of the target upon the entrance slit of the spectrometer. This approach results in a ground field of view (GFOV) that has the same shape as the spectrometer entrance slit (often a rectangle with a height to width ratio of more than 10:1). If more than one spectrometer is used in an instrument (e.g. a VNIR and SWIR spectrometer), it is often difficult to ensure both spectrometers are viewing the same GFOV. The use of optical fibers to deliver the light to the spectrometer results in a circular GFOV. The use of more than one spectrometer is accommodated by splitting the optical fiber bundle within the instrument to deliver light to the various spectrometers. The size of the GFOV is determined by the angular field of view of the instrument and the distance to the target. While optics can be added to modify the angular field of view of a field instrument, this is often practical only for those instruments utilizing optical fibers for light collection.

6. EXPERIMENTAL DESIGN

6.1 TIME OF DAY / YEAR

The timing of the field data collection is important if field spectra are to be used to calibrate or interpret a hyperspectral image. Reflectance spectra used to interpret a hyperspectral image should be collected under illumination conditions similar to those when the image was acquired. Time of day and date are the major controlling factors of direct illumination geometry, while atmospheric conditions relating to scattering and clouds are the major factors controlling the geometry and relative intensity of indirect illumination (Curtiss and Ustin, 1988). If field spectra are to be used to convert a hyperspectral sensor image to reflectance, spectra should be acquired simultaneously with image acquisition. If this is not possible, a water vapor correction should be made to the image prior to its conversion to reflectance (Gao and Goetz, 1990).

6.2 SAMPLING STRATEGY

The selection of a particular sampling strategy should be based upon the objectives of the study. If the objective is to determine the detectability of either a target material or of a process effecting the spectral signature of a target material, the sampling strategy must encompass examples of the target material under all expected conditions as well as all other background materials. Consideration must be given to all the processes modifying target and background spectral signatures; these include illumination, slope and aspect, and target surface architecture. Adequate collection of vegetation is even more problematic due to the wide range of processes that effect their spectral signature. These include soil chemical properties, soil reflectance, water availability, time of day, time of year, cloud cover, temperature, and relative humidity.

If the purpose of a study is to understand how a process effects the spectral signature of a target without consideration of how background materials and other sources of variability effect the spectral signature, variance from sources other than the one of interest should be minimized in the selected targets. This is achieved by carefully controlling viewing and illumination geometry, often in a laboratory. This type of study is often performed as a feasibility study prior to a full study evolving collection of spectra of background material.

6.3 VIEWING GEOMETRY

The selection of an appropriate viewing geometry depends upon whether the spectra are used for image analysis or for a feasibility study. For image analysis, a viewing geometry similar to the airborne sensor is required. For a feasibility study it is possible to eliminate much of the confounding variance typically present in an image data set by fixing the viewing and illumination geometry.

For vegetation, spectra can be acquired at the spatial scale of the leaf/needle, branch, or canopy. Canopy level spectra are most suitable for image analysis and interpretation. Rarely can leaf/needle or branch level spectra be used to directly to interpret an image. Leaf/needle and branch level spectra are useful to understand how the canopy level spectra are influenced by changes in leaf/needle and branch spectral changes as opposed to changes in the canopy structure.

6.4 ANCILLARY DATA SETS

Collection of appropriate ancillary data sets is as important as the collection of field spectra. The measurement of processes and material properties directly influencing, or correlated with, the collected spectra are essential to the understanding of the variance observed in a hyperspectral image data set. It is often necessary to collect a set of spectra with ancillary data in order to validate predictions made using the main field spectra plus image data set.

REFERENCES

- Abrams, M.J., R. Ashley, L.C. Rowan, A.F.H. Goetz, and A.B. Kahle (1977) Mapping of hydrothermal alteration in the Cuprite Mining District, Nevada, using aircraft scanner imagery for the 0.46 - 2.36 μm spectral region, *Geol.*, **5**, 713-718.
- Conel J.E., C.J. Bruegge and B. Curtiss (1987a) Correcting Airborne Imaging Spectrometer measurements for the atmosphere: a comparison of methods. *Proc. 31st. S.P.I.E. International Technical Symposium on Optical and Optoelectronic Applied Science and Engineering*.
- Conel J.E., R.O. Green, G. Vane, C.J. Bruegge, R.E. Alley and B. Curtiss (1987b) AIS-2 Radiometry and a comparison of methods for the recovery of ground reflectance. *Proc. of the Third Airborne Imaging Spectrometer Data Analysis Workshop*.
- Curtiss B. (1990) From leaf to landscape: The parameterization of vegetation canopy radiative transfer models from remote sensing data. *Proc. Ann. Meeting of the Ecol. Society of Amer.*
- Curtiss B. and A.G. Maecher (1991) Changes in forest canopy reflectance associated with chronic exposure to high concentrations of soil trace metals. *Proc. of the 8th Thematic Conference on Geologic Remote Sensing*, Denver, Colorado.
- Curtiss B. and S.L. Ustin (1988) Spectral changes in Ponderosa Pine associated with natural ozone exposure. *Proc. U.S. Forest Service Forest Response Program Annual Meeting*, Corpus Christi, Texas, February 23 - 26.
- Curtiss B. and S.L. Ustin (1989a) The Remote Detection of Early Stages of Air Pollution Injury in Coniferous Forests using imaging Spectrometry. *Proc. European Joint Research Center Remote Sensing of Forests Workshop*. Ispara, Italy.
- Gao, B.-C. and A.F.H. Goetz (1990) Column atmospheric water vapor retrievals from airborne imaging spectrometer data, *J. Geophys. Res.-Atmospheres*, **95**, 3549-3564.

- Gao, B.-C., and A.F.H. Goetz (1992) A Linear Spectral Matching Technique for Retrieving Equivalent Water Thickness and Biochemical Constituents of Green Vegetation, *Proc. of the Third Airborne Annual JPL Geoscience Workshop (AVIRIS, TIMS, and AIRSAR)*, Jet Propulsion Laboratory, Pasadena, CA.
- Goetz, A.F.H. (1992a) Imaging Spectrometry for Earth Remote Sensing, in *Imaging Spectroscopy: Fundamentals and Prospective Applications*, F. Toselli and J. Bodechtel, Eds., pp. 1-19, Brussels and Luxembourg.
- Goetz, A.F.H. (1992b) Principles of Narrow Band Spectrometry, in *The Visible and IR: Instruments and Data Analysis in Imaging Spectroscopy: Fundamentals and Prospective Applications*, F. Toselli and J. Bodechtel, Eds., pp. 21-32, Brussels and Luxembourg.
- Goetz, A.F.H. and W.M. Calvin (1987) Imaging spectrometry: Spectral resolution and analytical identification of spectral features, *Imaging Spectros. II*, G.Vane, Ed., *Proc. SPIE*, 834, 158-165.
- Goetz, A.F.H. and V. Srivastava (1985) Mineralogical mapping in the Cuprite mining district, Nevada, *Proceedings of the Airborne Imaging Spectrometer Data Analysis Workshop*, April 1985, *JPL Publication*, no. 85-41.
- Hunt, G.R. (1980) Electromagnetic radiation: The communications link in remote sensing. In *Remote Sensing in Geology*, B.S. Siegal and A.R. Gillespie, eds, Wiley, NY, pp 5-45.
- Peterson, D.L., J.D. Aber, P.A. Matson, D.H. Card, N. Swanberg, C.A. Wessman and M. Spanner (1988) Remote sensing of forest canopy and leaf biochemical contents, *Rem. Sens. Environ.*, 24, 85-108.
- Smith, M.W. (1992) Design and initial performance evaluation of a portable short wave infrared spectrometer, *Proc. SPIE*, Vol. 1762-14., San Diego, CA.

COMPARATIVE STUDY OF DIELECTRIC CONSTANT MEASUREMENTS OF SOILS USING DIFFERENT TECHNIQUES ¹

Ram M. Narayanan, Danny W. Rhoades and Paul D. Hoffmeyer
University of Nebraska
Lincoln, NE 68588-0511, USA

John O. Curtis
U.S. Army Waterways Experiment Station
Vicksburg, MS 39180-6199, USA

ABSTRACT

The dielectric properties of soils and their relationship to soil physical properties such as soil moisture, texture and mineralogy are of great interest in remote sensing of soil properties as well as in subsurface probing applications. Although various experimental studies have been carried out in the past to characterize the dielectric properties of soils, there has been no attempt to compare one set of measurements at one laboratory to another independent set of measurements on the same soil samples at another laboratory. In order to quantify the variability associated with independent dielectric constant measurements, the University of Nebraska and the U.S. Army Waterways Experiment Station (WES) characterized the dielectric properties of seven different soil types at each of their laboratories. The soils chosen for this study represented wide variability in texture and soil-water relationship, and were obtained from various geographical locations within the U.S. At the University of Nebraska, the complex dielectric constant was measured using different sample holders for different frequency ranges from 200 MHz to 18 GHz. A coaxial sample holder was used in the frequency range 200 MHz to 1.5 GHz, while waveguide sample holders were used at S-Band and C-Band frequencies. Measurements at X-Band and Ku-Band frequencies were done using the free-space technique. The WES measurements were made using a broadband coaxial sample holder and a network analyzer system capable of sweeping over a frequency range extending from 45 MHz to 26.5 GHz. Our study indicates that soil density variations due to sample preparation can, in some cases, cause significant variations in the soil dielectric constant at the same volumetric moisture levels. We conclude that soil dielectric constant measurements reported in literature have to be interpreted with caution.

1. INTRODUCTION

The dielectric properties of soils are of primary importance in various types of remote sensing systems that operate in the VHF, UHF, microwave and millimeter-wave frequency ranges. The radar reflectivity of a soil surface depends on its dielectric constant, as does its radiometric emissivity. In subsurface probing applications, the penetration depth of the electromagnetic energy is a function of the loss tangent, i.e., the ratio of the imaginary part to the real part of the dielectric constant. Thus, characterization of the dielectric constant of soil is essential in theoretical and simulation studies in various military and civilian applications. However, modeling the dielectric properties of soils is a formidable task owing to the very complicated nature of soil structure. Various factors that affect the dielectric constant include the soil texture, volumetric moisture, porosity, density and the shape of the soil particles. In addition, the amount of bound water, i.e., water molecules contained within the first few molecular layers surrounding the soil particles, also determines the overall dielectric constant of soil, especially under low moisture conditions.

¹This research was supported by the U. S. Army Waterways Experiment Station under Contract DACA39-93-M-4645.

There have been numerous experimental studies of the dielectric characteristics of soils as a function of various soil properties. However, inconsistencies have been noted between experimental measurements reported by different researchers, especially with regard to the absolute value of the dielectric constant at a particular volumetric soil moisture, as well as the dependence on soil texture. One of the primary reasons for these discrepancies has been attributed to the lack of precise and quantitative controls during soil sample preparation. This paper summarizes results on comparative measurements made on identical soil samples at the University of Nebraska and the U.S. Army Waterways Experiment Station.

2. REVIEW OF PRIOR WORK

This section reviews and summarizes a few earlier comprehensive studies of the dielectric properties of soils in the VHF and microwave frequency ranges. The investigations presented here are only representative, and not exhaustive.

Detailed laboratory measurements on ten different soil types and their mixtures were performed by Lundien (1971) in the 1.0 to 1.5 GHz frequency range. Moisture contents ranged from 0.2% (almost dry) to approximately 50% for some of the clays. The measurement technique involved an interferometric method with the soil sample being placed at an angle of 45° to the incident beam. Although strong correlations were observed between the volumetric moisture content and the dielectric constant of soil, soil type or texture appeared to have little effect on the real part of the dielectric constant. The conductivity, on the other hand, was found to differ for the three primary soil types of sand, clay and silt. Within the narrow frequency range of measurement, no appreciable frequency dependence was observed. Furthermore, the dielectric properties were found to be independent of the soil compactive effort, thereby confirming that the soil-water dielectric properties were governed primarily by volumetric moisture content.

Hoekstra and Delaney (1974) measured the dielectric constant of four types of soils (which included a sand, a silt and two clays) over the frequency range 100 MHz to 26 GHz. The gravimetric moisture contents ranged from 0 to 15%, while temperatures ranged from +24 to -20° C. The measurements at lower frequencies, i.e., between 100 MHz and 4 GHz were accomplished using a time domain reflection (TDR) technique wherein the soil samples were packed in a coaxial line 20 cm long with a inner diameter of 7 mm. Higher frequency measurements over the 3.95 to 26.5 GHz range were made using specific waveguide transmission lines with the samples being placed against a short circuit. The authors concluded that two closely spaced relaxations appear to be associated with water in all types of soils, with the dominant relaxation occurring between 1 and 4 GHz. The real part of the dielectric constant, ϵ'_r showed a positive temperature coefficient, i.e., $d\epsilon'_r/dT$ was positive. Also, the real as well as the imaginary parts of the dielectric constant, ϵ'_r and ϵ''_r respectively, increased with increasing volumetric moisture content m_v , although the nature of the dependency was different at different frequencies.

Dielectric properties of two basic soil types, both clay loams, were determined as a function of frequency, moisture content and density by Hipp (1974). Measurements were made for frequencies from 30 MHz to 4 GHz, for gravimetric moisture contents from 0 to 20%, and for dry soil densities from 1.2 to 1.8 gm/cc. The sample holder was a 7.5 cm length of rigid 14 mm precision coaxial airline filled with the soil material. An admittance bridge was used in the frequency range 30 MHz to 1 GHz, while a standing wave ratio (SWR) indicator was used in the frequency range 1 GHz to 4 GHz. Results indicated that the dielectric constant of dry soil was essentially independent of texture, as long as the soil density and measurement frequency were kept constant. Although variations were observed with respect to the moisture content dependence, the author concluded that qualitative variations of the electromagnetic parameters of the two clay loams were very similar. This result is not surprising, since both soils investigated were similar texturally.

Wang and Schmugge (1980) investigated the dielectric properties of soils at 1.4 GHz and 5 GHz made available from various measurement programs published in literature. It was observed that, in general, the dielectric constant increased slowly with moisture content up to a transition point, beyond which the increase was more rapid. This transition moisture was found to vary with soil type or texture,

was positively correlated with the clay content, and was negatively correlated with the sand content. The authors also compared various mixing formulas for computing the dielectric constant of the soil-air-water mixture with measured data, but without much success owing to the complex nature of the soil system. An empirical model wherein the transition moisture was used as a curve-fitting adjustable parameter was observed to agree reasonably well with the large data set available. Since the transition moisture correlated well with the wilting point, the authors concluded that their model provided a means of estimating the soil dielectric properties on the basis of textural information.

The research group at the University of Kansas completed a comprehensive experimental and theoretical study on the relationship between soil dielectric properties and its physical characteristics (Hallikainen et.al., 1985; Dobson et.al., 1985). Experimental observations at frequencies in the 1-18 GHz range were conducted on five texturally dissimilar soils at volumetric water contents ranging from 0% to approximately 40%. Waveguide dielectric measurement systems were used in the 1-2 and 4-6 GHz range, while a free-space method was employed in the 4-18 GHz frequency range. Comparisons of both methods at 6 GHz yielded dielectric constant values that were quite close. It appeared that soil texture does indeed have an effect on the dielectric behavior of soils, especially at frequencies below 5 GHz. The experimental observations were used to guide the development of a semi-empirical mixing model, which was found to yield acceptable fits to the measured data. In addition, four-component theoretical model developed using a dielectric constant for bound water that was different from free water and ice, also yielded values that correlated well with the observed effects of soil type and frequency.

3. MATERIALS AND METHODS

3.1 SOIL PHYSICAL CHARACTERISTICS

Dielectric constant measurements were made on seven soils selected from a set of eighteen benchmark soils, whose characteristics are summarized in Table 1. The soils exhibited wide variability in their properties and represent various geographical regions within the U.S. Table 2 shows various soil-moisture relationships for the soils considered in this study. Soil horizon is a layer of soil or soil material approximately parallel to the land surface, differing from adjacent layers in physical, chemical, or biological characteristics. The "A" horizon is formed at or adjacent to the surface in which humified organic matter associated with the mineral fraction is accumulated. Only characteristics of the "A" horizon are tabulated because of the low penetration depth of the electromagnetic energy. Gravimetric moisture contents, m_g , were measured at soil water potential ψ_w of -0.1, -1.0, and -5.0 bars. These data were then fitted into the empirical relation

$$\psi_w = a10^{bm_g} \quad (1)$$

where a and b are constants. Best-fit values of a and b for each soil type are also shown, from which the field capacity (m_g at $\psi_w = -0.333$ bar), wilting point (m_g at $\psi_w = -15$ bars), and hygroscopic moisture (m_g at $\psi_w = -31$ bars) are computed and tabulated. At field capacity, water drains freely because of gravitational effects; at wilting point, plants are not able to absorb water fast enough from the soil for their needs; at hygroscopic moisture, water is held tightly by the attraction of soil particles. Actual values of the wilting point and the hygroscopic moisture may be vastly different from the estimated values shown in Table 2, primarily because these values have been extrapolated outside the soil water potential values used in obtaining the best-fit values a and b in (1).

The volumetric moisture, m_v , was obtained using the relation

$$m_v = \rho m_g \quad (2)$$

where ρ is the soil density at the specified m_g value. This relationship accounts for any soil particle volume changes such as swelling or shrinkage due to addition of water.

TABLE 1. CHARACTERISTICS OF BENCHMARK SOILS

Soil #	Soil Order	Great or Subgroup	Series	Mineralogy*	Location	Horizon	Clay Content	Silt Content	Organic Carbon
							%	%	%
01	Mollisol	Typic Haploxerall	Walla Walla	Q,P,K-sp,H/M,U	Oregon	A	18	67	1.09
02	Mollisol	Udic Hapoboroll	Barnes	Q,P,U,Py	North Dakota	B	15	69	0.53
03	Mollisol	Typic Hapludoll	Clarion	Q,P,H/M,S	Iowa	A	26	36	2.17
04	Mollisol	Torrertic Paleustoll	Pullman	Q,P,K-sp,U,A	Texas	B	28	36	0.96
05	Mollisol	Typic Arguidoll	Sharpsburg	Q,P,K-sp,H/M,U	Nebraska	A	21	28	1.31
06	Alfisol	Typic Paleudalf	Crider	Q,P,K-sp,H/M,U	Kentucky	B	22	30	0.83
07	Alfisol	Typic Hapludalf	Miami	Q,P,K-sp,H/M,U	Indiana	A	34	51	0.92
08	Alfisol	Typic Xerorthent	Yolo	Q,P,K-sp,H/M,U	California	B	43	44	0.71
09	Ultisol	Typic Paleudult	Frederick	Q,K-sp,K	Virginia	A	36	62	1.69
10	Ultisol	Typic Hapludult	Cecil	Q,P,H/M,K,S	North Carolina	B	38	60	1.03
11	Ultisol	Typic Paleaquult	Rains	Q,P,K-sp,H/M,K,G?	South Carolina	A	25	73	2.14
12	Aridisol	Typic Haplargid	Mohave	Q,K-sp,H/M,C,S	Arizona	B	22	50	1.23
13	Aridisol	Ustollic Haplargid	Fort Collins	Q,P,H/M,C,U	Colorado	A	34	34	0.58
14	Entisol	Typic Ustipsamment	Valentine	Q,P,K-sp,H/M,U	Nebraska	B	26	54	1.31
15	Vertisol	Udic Pellustert	Houston Black	Q,P,H/M,U,S	Texas	A	26	54	0.86
16	Spodosol	Dystril Eutrochrept	Caribou	Q,P,K-sp,H/M,K,U	Maine	A	19	62	2.19
17	Oxisol	Ustoxic Humitrop	Kole Kole	Q,H/M,K,U,G	Hawaii	B	37	51	0.25
18	Inceptisol	Tropeptic Eutrustox	Wahiawa	H,K	Hawaii	A	10	20	3.20

*Q=quartz, P=plagioclase feldspar, K-sp=potassium feldspar, H/M=hematite and/or magnetite, C=calcite, K-kaolinite, S=smectite, U=unspecified clay, Py=pyrolustie, A=apatite, G=gibbsite.

TABLE 2. SOIL MOISTURE RELATIONSHIPS

Soil #	Gravimetric Moisture Content, m_g (%), at			Constants in $\psi_w = a10^b m_g$		Field* Capacity (%)	Wilting** Point (%)	Hygroscopic*** Moisture (%)
	$\psi_w = -0.1$ bar	$\psi_w = -1$ bar	$\psi_w = -5$ bar	a	b			
02	29.5	18.8	14.4	-955	-0.158	21.9	11.4	9.4
06	34.3	20.1	14.0	-198	-0.114	24.3	9.8	7.1
09	29.3	15.8	10.6	-132	-0.134	19.4	7.1	4.7
12	22.6	16.1	13.1	-5471	-0.232	18.2	11.0	9.7
15	36.8	27.7	23.2	-15065	-0.150	31.0	20.0	17.9
17	46.6	29.4	21.8	-506	-0.092	34.6	16.6	13.2
18	41.5	30.7	25.2	-7988	-0.127	34.5	21.5	19.0

* m_g at $\psi_w = -0.333$ bar** m_g at $\psi_w = -15$ bar*** m_g at $\psi_w = -31$ bar

BLANK PAGE

3.2 UNIVERSITY OF NEBRASKA TEST SETUPS

At the University of Nebraska, separate measurements setups were used to characterize the dielectric properties of soils in the 200 MHz-18 GHz frequency range. The various measurement techniques used depended upon the specific frequency range, and are listed below:

1. 200 MHz to 1.5 GHz: Coaxial sample holder
2. 2.6 to 3.95 GHz: S-Band waveguide sample holder
3. 3.95 to 5.85 GHz: C-Band waveguide sample holder
4. 8 to 12 GHz: Free-space technique using X-Band antennas
5. 12 to 18 GHz: Free-space technique using Ku-Band antennas

In all of the above cases, the Hewlett-Packard 8720B Automatic Vector Network Analyzer was used as the test source and the receiver. Swept frequency measurements were performed at 1601 equally-spaced frequency points within each measurement band specified above.

3.2.1 Coaxial Cavity Method

A block diagram of the measurement setup is shown in Fig. 1. The sample holder used in the measurements had an overall length of 7.45 cm with an inner diameter of 1.689 cm and an outer diameter of 3.876 cm. The region between the inner and outer conductors was filled with the soil material at the appropriate wetness conditions, and the reflection and transmission coefficients viz., S_{11} and S_{21} respectively were measured at the air-dielectric interface planes by using appropriate de-embedding techniques to account for the phase shifts introduced by the lengths of the air line between the measurement planes and calibration planes. The values of ϵ'_r and ϵ''_r were determined from the measured values of S_{11} and S_{21} for a sample of finite length using the method outlined in Weir (1974). To resolve the phase ambiguity, the group delay of the signal through the sample was used.

3.2.2 Waveguide Cavity Method

The waveguide cavity method is very similar to the coaxial setup described above, and a block diagram is shown in Fig. 2. The major differences are the cavity geometry and the mode of propagation. While the coaxial cavity uses the TEM mode of propagation for which the cutoff wavelength λ_c is infinite, the waveguide method uses the TE_{10} mode whose free-space cutoff wavelength is given by

$$\lambda_c = 2a \quad (3)$$

where a is the larger dimension of the waveguide. For the S-Band measurement, waveguide WR-284 of inner dimensions 7.214 x 3.404 cm was used, giving us a cutoff wavelength of 14.427 cm. The S-Band sample holder was 2.98 cm long. For the C-Band system, waveguide WR-187 was used with inner dimensions 4.755 x 2.215 cm; thus the cutoff wavelength was 9.55 cm. The sample holder length was 2.00 cm. The algorithm to invert for the complex dielectric constant from S_{11} and S_{21} is described in Weir (1974).

3.2.3 Free-Space Method

The free space system at X-Band and Ku-Band frequencies used two horn antennas and a soil dielectric slab. A block diagram of the setup is shown in Fig. 3. The antenna separation was approximately 70 cm and the sample chamber size was 25.0 cm square. The soil slab thickness was 0.9525 cm. The maximum far-field distance for the X-Band antennas was 35.0 cm, while the value for the Ku-Band antennas was 27.0 cm. The maximum spot sizes at X and Ku-Bands were 23.6 cm and 15.1 cm respectively; thus the illuminated spots on the soil were contained within the overall sample chamber. To account for multiple reflections, spatial averaging was used by moving the pulley system connected to the transmit and the receive horns. In addition, frequency averaging was employed to nullify multiple reflection effects. The plane electromagnetic wave was normally incident on the soil sample and the cutoff wavelength was set to infinity. The algorithm described in Hallikainen et al. (1985) was used to obtain the ϵ'_r and ϵ''_r values.

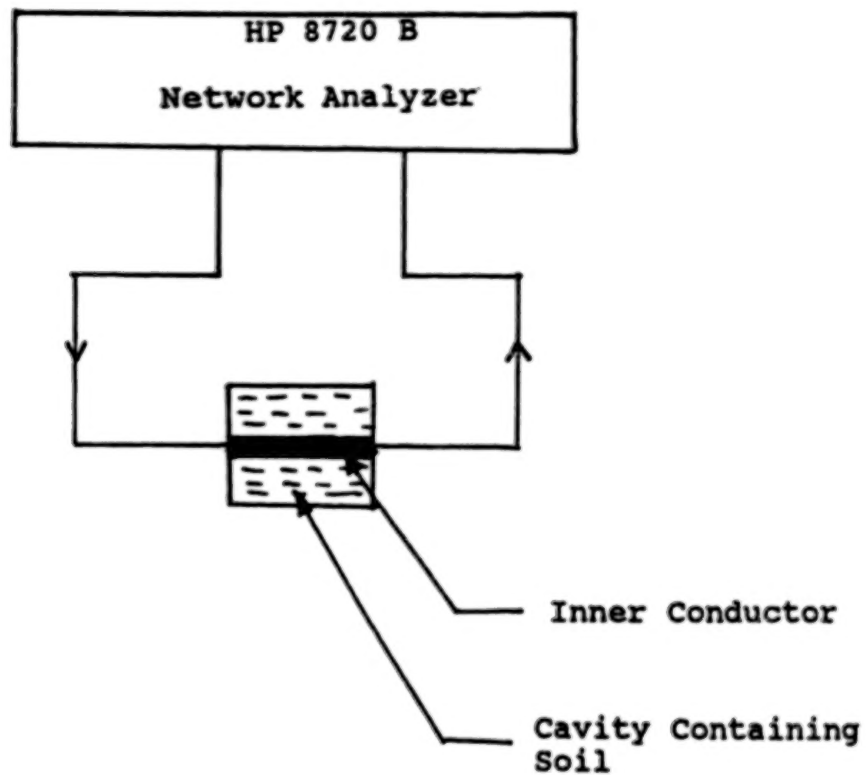


Figure 1. Block diagram of coaxial cavity measurement setup.

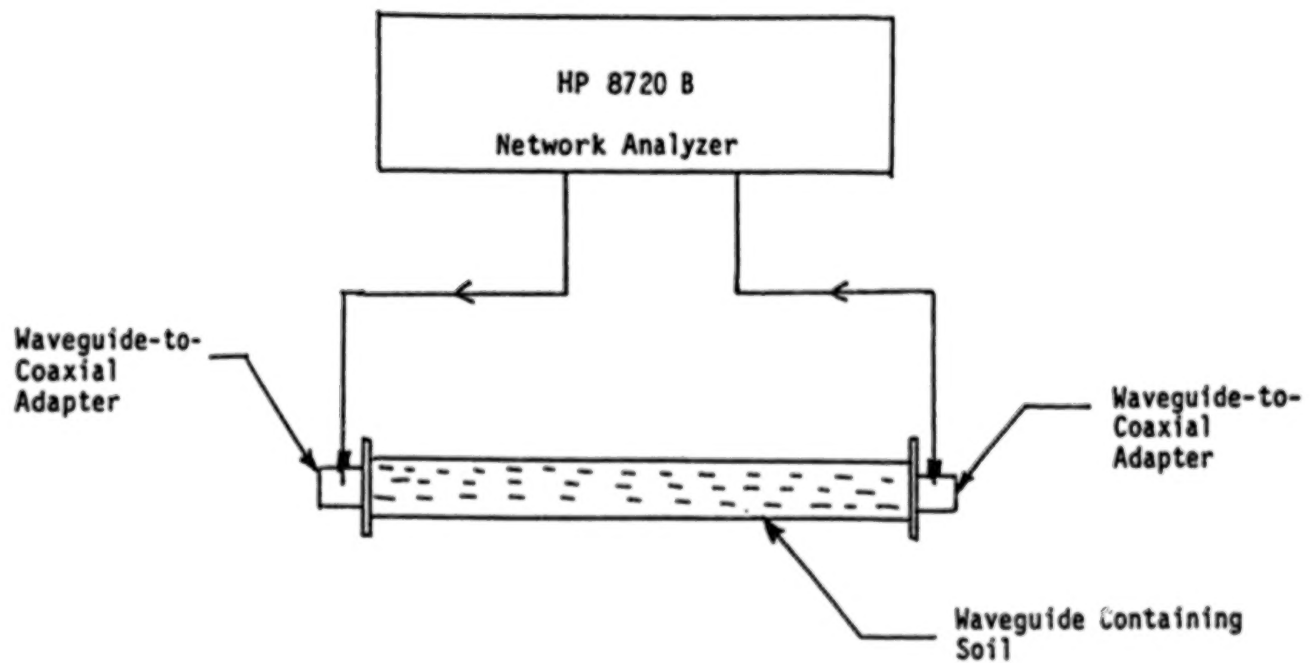


Figure 2. Block diagram of waveguide cavity measurement setup.

3.2.4 Sample Preparation

The soils were oven-dried to 105° C, and ground to the same dry bulk density. Distilled water was then added so as to achieve the required gravimetric moisture content value. The soil-water system was thoroughly mixed, and allowed to equilibrate for 24 hours before the dielectric measurements were made. A density measurement was made just prior to the dielectric measurements. In the case of the coaxial and waveguide methods, the soil was carefully packed inside the sample holders, without any undue compactive effort that would alter the soil density. For the free-space method, care was taken to ensure that the soil surface was kept as smooth as possible, and the rms soil roughness was less than 1 mm. After every measurement at a specified m_v value, the soil was oven-dried and the same procedure repeated.

3.3 WATERWAYS EXPERIMENT STATION TEST SETUP

3.3.1 Coaxial Apparatus

At the U.S. Army Engineer Waterways Experiment Station, a unique coaxial apparatus of square cross section was developed and employed to measure the complex dielectric constant of liquids and fine-grained solid/liquid mixtures over a 45 MHz-26.5 GHz frequency range (Curtis, 1993). The measurements used for this study were conducted with a modification of the earlier setup that made use of some new electronic hardware to ensure more stable calibrations and new sample holders to overcome some concerns about data integrity at both the lowest and highest frequency values (Curtis, 1994). A block diagram of the measurement setup is shown in Fig. 4, which reveals that the core of the WES measurement system is a synthesized sweeper and an S-parameter test set driven by a Hewlett Packard 8510C Vector Network Analyzer. The software used to control the network analyzer and to calculate the complex dielectric constant was developed at the WES.

Sample holders were machined from brass stock and provided square cross-sectional sample volumes having lengths of either 15 mm or 100 mm with a cross section of 7.5 mm by 7.5 mm. The center conductors consisted of pieces of copper bus wire soldered to 50-ohm SMA-type connectors at each end of the sample holder. The short sample holders were fabricated to achieve the transmission of measurable signals at the high end of the frequency sweep but were too sensitive to calibration drift and the computational algorithm to be used with confidence at the lowest frequencies. Data reported in the next section were, therefore, chosen in the following way: 100 mm sample holder results were reported between 45 MHz and 3 GHz; 15 mm data were reported for frequencies above 3 GHz.

A Caron Model 2065 Circulating Bath was used to provide sample temperature control. The bath was connected to a hollowed aluminum heat source/sink with insulated plastic tubing. As the circulating 50/50 antifreeze solution controlled the physical temperature of the source/sink, it also controlled the temperature of the brass sample holder, which was positioned in a slot in the top of the source/sink.

3.3.2 Sample Preparation

The soil sample was made homogeneous by drying, pulverizing and mixing thoroughly. The soil sample was nearly saturated and placed inside the dry, empty sample holder which has been weighed previously. The sample and the holder were weighed, then sealed and connected to the measurement system. Dielectric constant measurements were then made at specified temperatures after allowing adequate time for the system to reach equilibrium (generally about 10 min.). After all the measurements were completed, the sample was carefully removed, dried and weighed to determine its dry density and to facilitate calculation of volumetric moisture. This procedure allowed one to accurately measure the volumetric moisture, and reduces the chances of error inherent in the measurement techniques which involve packing of sample holders.

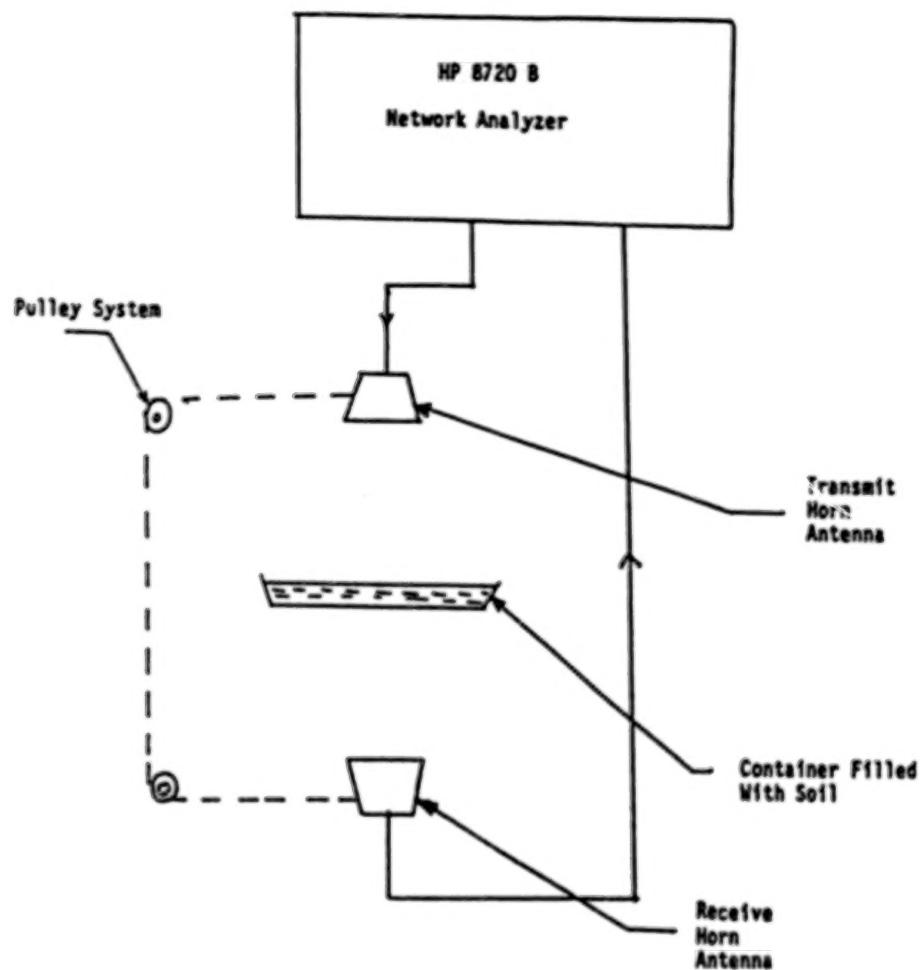


Figure 3. Block diagram of free-space measurement setup.

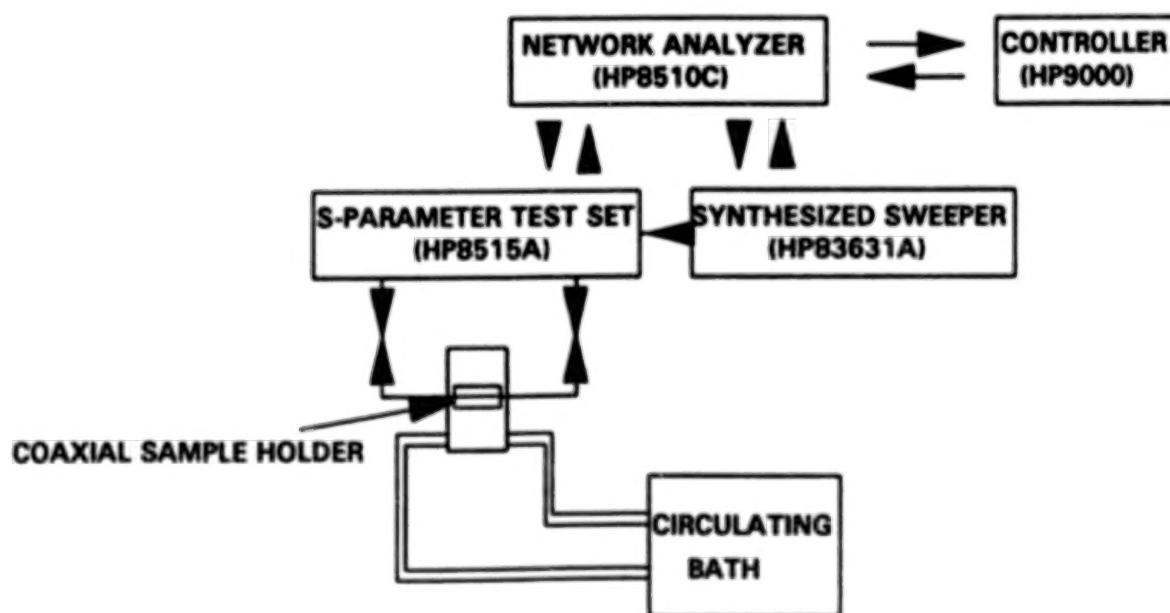


Figure 4. Block diagram of WES coaxial measurement setup.

4. RESULTS AND DISCUSSION

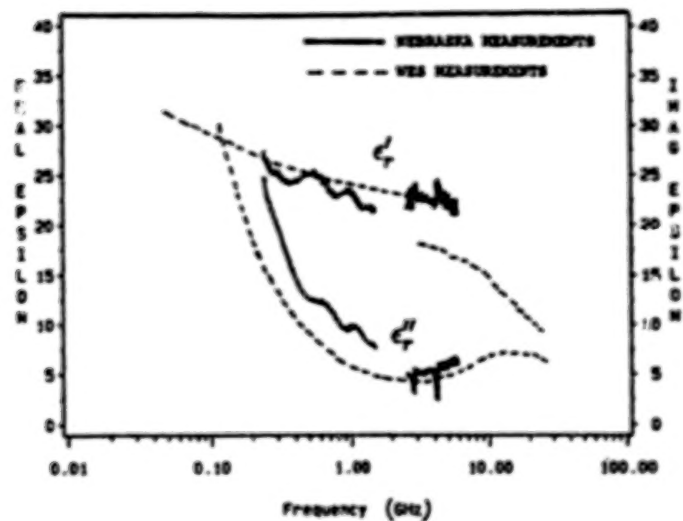
While measurements at both laboratories did show the expected increase in the dielectric constant as the soil moisture increased, there were discrepancies in the absolute value of the real and imaginary parts of the dielectric constant. A few comparisons are discussed in this section.

One of the major parameters that determines the absolute value of the dielectric constant is the soil density. Accurate control and determination of soil density were found to be crucial factors in the accurate characterization of the soil dielectric properties. A detailed experimental analysis of the range of variations in soil density revealed that this parameter can vary as much as 10% around its average value for typical cohesionless soils (Tiedemann, 1973). Our measurements to characterize the density variations indicated that the standard deviations were of the order of 6% of the mean, and that a large part of the variability could be attributed to the manner in which each individual packed the sample holder. These variations are significant in the University of Nebraska measurements since the wet density was measured just prior to introducing the samples in the holder. The WES measurements had better characterization of the soil density because the sample holder was weighed prior to as well as after introducing the soil samples, and the volume of the sample holder was accurately known. However, even in the WES measurements, accurate control of soil density was not possible, and variations of the order of 5% around the mean dry density were found. It has been determined from studies on soils (Hipp, 1974) and minerals (Nelson et al., 1989) that the real and the imaginary parts of the dielectric constant increase with increasing density, and the rate of increase is approximately comparable on a percentage basis.

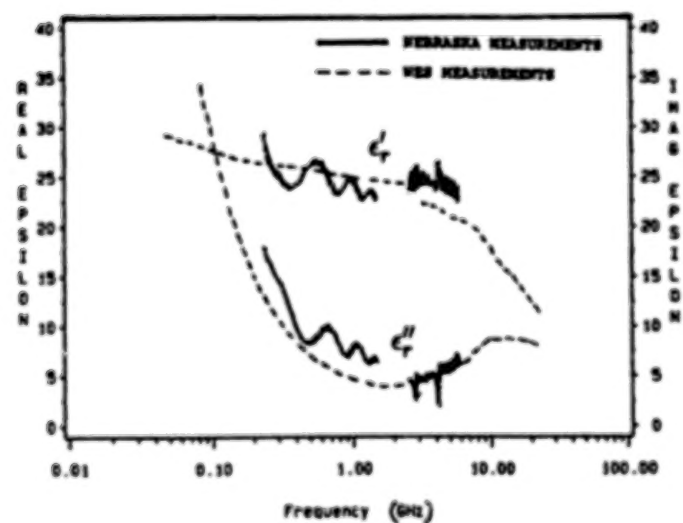
Comparative plots of the real and imaginary parts of the dielectric constant are shown in Fig. 5. In Fig. 5(a), these curves are plotted for the Barnes soil at approximately 25% gravimetric moisture. The Nebraska measurements assume a volumetric moisture of 36.6% based on a wet density of 1.831 gm/cc. The WES measurements were made at volumetric moisture levels of 39.2% for frequencies less than 3 GHz, and 35.4% for frequencies greater than 3 GHz. In both cases the gravimetric moisture was 24.4%, while the dry density values were 1.61 and 1.45 gm/cc respectively. It is observed that the WES measurements do not show any discontinuity around 3 GHz for the imaginary part despite the almost 4% variation in volumetric moisture, while the Nebraska measurements show higher values at frequencies less than 2 GHz, and comparable values at frequencies greater than 3 GHz. In the case of the real part, however, the WES measurements show a marked discontinuity at 3 GHz, attributable to the volumetric moisture difference, while the Nebraska measurements follow the WES curve at lower frequencies.

In Fig. 5(b) are shown similar characteristics for the Frederick soil at 25% gravimetric moisture. The WES parameters are: volumetric moisture of 40.25% for both measurements, while the dry densities are 1.67 and 1.55 gm/cc for lower (less than 3 GHz) and higher (greater than 3 GHz) frequencies respectively. The Nebraska parameters are: volumetric moisture of 36.8% with wet and dry densities of 1.84 and 1.28 gm/cc respectively. Here too, the WES curve shows a discontinuity near 3 GHz in respect of the real part, despite the almost identical moisture contents.

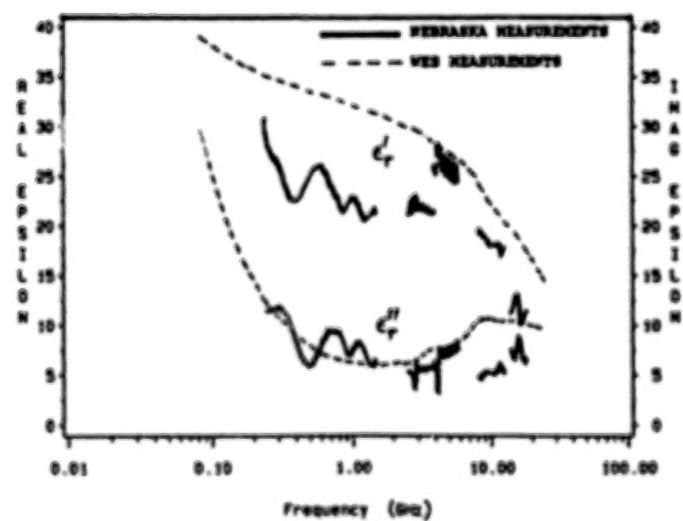
Figure 5(c) shows similar plots for the Kole Kole soil at high gravimetric moisture content values: 30% for Nebraska, and between 34.3% at low frequencies and 38.1% at high frequencies for the WES measurements. The volumetric moisture content for the Nebraska measurements are 42.3% with wet and dry densities of 1.83 and 1.32 gm/cc. The WES volumetric moisture contents are 49.7% at lower frequencies and 54.3% at higher frequencies, while corresponding dry densities are 1.45 and 1.43 gm/cc. There exists no discernible discontinuity in the WES data at 3 GHz, despite the 4.6% difference in volumetric moisture. The Nebraska measurements show great differences and variability, part of which could be attributed to its lower volumetric moisture in relation to the WES measurements. However, the Nebraska measurements also clearly show discontinuous behavior on going from one sample holder (i.e., frequency range) to another.



(a)



(b)



(c)

Figure 5. Comparison between Nebraska and WES measurements for (a) soil 02-Barnes, (b) soil 09-Frederick, and (c) soil 17-Kole Kole.

5. CONCLUSIONS

Our results indicate that the soil density does have a small, albeit discernible impact on its dielectric properties. While the overall levels are indeed determined by the volumetric moisture content, there can be measureable variation due the changes in soil density. Soil density variations usually appear during sample preparation wherein control of density is difficult. Thus, measurements of dielectric constant at specified volumetric moisture levels have to be interpreted with caution if corresponding soil density data are not provided. From a physical viewpoint, a change in the density at the same volumetric moisture content indicates a change in the porosity, i.e., volume fraction of air-filled voids. Therefore, if the density varies, it follows that the dielectric characteristics are also expected to change. However, the impact is more discernible on the real part than on the imaginary part of the dielectric constant, since the latter is dominated primarily by the loss tangent of water, while the former has contributions from each constituent of the soil-air-water system. Further studies are recommended to quantify the effects of soil density on the soil dielectric properties.

REFERENCES

- Curtis, J. O., 1993: Microwave dielectric behavior of soils, Report 2: A unique coaxial measurement apparatus. Technical Report EL-93-25, US Army Corps of Engineers Waterways Experiment Station, Vicksburg, Mississippi.
- Curtis, J. O., 1994: Soil texture and broadband dielectric properties. *Proc. of the Unexploded Ordnance (UXO) Detection and Range-Remediation Conf.*, Golden, Colorado.
- Dobson, M. C., F. T. Ulaby, M. T. Hallikainen and M. A. El-Rayes, 1985: Microwave dielectric behavior of wet soil - Part II: Dielectric mixing models. *IEEE Transactions on Geoscience and Remote Sensing*, **GE-23**, 25-34.
- Hallikainen, M. T., F. T. Ulaby, M. C. Dobson, M. A. El-Rayes and L. K. Wu, 1985: Microwave dielectric behavior of wet soil - Part I: Empirical models and experimental observations. *IEEE Transactions on Geoscience and Remote Sensing*, **GE-23**, 25-34.
- Hipp, J. E., 1974: Soil electromagnetic parameters as a function of frequency, soil density and soil moisture. *Proceedings of the IEEE*, **62**, 98-103.
- Hoekstra, P., and A. Delaney, 1974: Dielectric properties of soil at UHF and microwave frequencies. *Journal of Geophysical Research*, **79**, 1699-1708.
- Lundien, J. R., 1971: Terrain analysis by electromagnetic means, Report 5: Laboratory measurement of electromagnetic propagation constraints in the 1.0 to 1.5 GHz microwave spectral region. Technical Report 3-693, US Army Corps of Engineers Waterways Experiment Station, Vicksburg, Mississippi.
- Nelson, S., D. Lindroth and R. Blake, 1989: Dielectric properties of selected purified minerals at 1 to 22 GHz. *Journal of Microwave Power and Electromagnetic Energy*, **24**, 213-220.
- Tiedemann, D. A., 1973: Variability of laboratory relative density test results. In *Evaluation of Relative Density and its Role in Geotechnical Projects Involving Cohesionless Soils*, E. T. Selig and R. S. Ladd (Eds.), ASTM, Philadelphia, Pennsylvania, 61-73.
- Wang, J. R., and T. J. Schmugge, 1980: An empirical model for the complex dielectric permittivity of soils as a function of water content. *IEEE Transactions on Geoscience and Remote Sensing*, **GE-18**, 288-295.
- Weir, W. B., 1974: Automatic measurement of complex dielectric constant and permeability at microwave frequencies. *Proceedings of the IEEE*, **62**, 33-36.

A FIELD PORTABLE HYPERSPECTRAL IMAGER: THE LARGE AREA FAST SPECTROMETER

R.W. Zywicki¹, K.A. More¹, J. Holloway² and N. Witherspoon²

1. ABSTRACT

The US. Navy and Marine Corps have identified the need for a fast field-portable imaging spectrometer. This instrument will allow Marine Corps and Navy personnel to collect data to be used to detect, from a cluttered background, targets ranging from mines to tanks and rocket launchers. The background clutter can range from rocks and small bushes that clutter minefield scenes to dense foliage that conceal large vehicles. Multispectral scene analysis can be used on the spectrometer scene data to detect targets in camouflaged or concealed backgrounds. Additionally, hyperspectral scene data can be acquired in a fast, accurate and portable fashion.

During the Phase I SBIR effort a Large Area Fast Spectrometer (LAFS) was designed and the feasibility of producing an operational prototype was demonstrated by computer simulation and experimental measurement of the key optical technologies. This innovative design combines a high throughput imaging spectrograph with a high frame rate electronic camera system, broadband primary optics and a scanning system to form a high performance imaging spectrometer. During the Phase II SBIR effort, an operational, field portable prototype is being developed, manufactured and tested. The prototype will be capable of measuring a 256 point spectra over 256 x 252 spatial points in a scene, in a 400-1100 nm wavelength band. Data acquisition will be accomplished in 1.5 seconds and stored within 16 seconds.

The Phase II SBIR prototype will allow hyperspectral image measurement in the field, facilitating target recognition research. The need for multispectral imaging capabilities resides in many government agencies such as DOD, DOE, NASA, EPA, USDA and also in commercial organizations. The hyperspectral imaging technologies developed in this program have direct application to areas such as environmental monitoring, factory product inspection, and general purpose hyperspectral remote sensing.

2. INTRODUCTION

During the Phase I effort we found that there are widespread requirements for medium resolution field spectrometers that have an integral imaging capability. This imaging capability allows a system to reject clutter within the instrument field of view by allowing the user to spatially discern between the object of interest and the surrounding background.

The most significant innovation of the Phase I effort was the design of a simple, rugged imaging spectrometer that overcomes the limitations of earlier scanned point spectrometers and filtered imagers. It does so by simultaneously measuring the spectra of 256 points along a line of imagery, and builds up a complete spectral image by scanning the scene in the orthogonal direction. In this design, we take advantage of the inherent sensitivity advantage of a 2-D sensor array for acquiring scene imagery in parallel, while also utilizing the high spectral resolution of a plane grating Littrow spectrometer.

¹Daedalus Enterprises Incorporated, Ann Arbor MI 48106-1869 USA

²Coastal Systems Station, Dahlgren Division, Panama City FL 32407-7001 USA

The second significant outcome of the Phase I program was the integration of this optical design with an extremely high speed imaging system. Based around a commercial 200 frame per second camera, a high speed single board PC and a large capacity digital data storage system, the prototype LAFS instrument will acquire 16 MBytes of hyperspectral image data in 1.5 seconds. Integrated together, the optical and image acquisition systems form a compact, portable hyperspectral imager.

To demonstrate the technical feasibility of this design, Daedalus conducted detailed investigations into the expected performance of a Phase II prototype. These included:

- Analytic and computerized two-dimensional linear systems modeling of the imaging and image acquisition process,
- Computerized signal and noise calculations based around real optical, detector and solar data,
- Broadband ray trace simulations of the imaging performance of the optical system,
- Experimental investigations of the spatial and spectral resolution performance of the imaging spectrometer.

The results of these investigations showed that overall system design was feasible and would exhibit excellent spectral performance, good system sensitivity and good spatial resolution. The limiting factor in spatial resolution will be the number of pixels in the detector array, and not the resolving power of the optics. This fact suggests that as higher pixel count high speed imagers become available commercially, the LAFS design could be extended to significantly higher spatial and spectral resolutions.

3. SYSTEM OVERVIEW

3.1 SYSTEM DESIGN

The LAFS system is primarily a compact pushbroom scanner combined with a precision sweep mirror. A block diagram outlining the system design is shown in Fig. 1. The optical head is comprised of a visible/near infrared imaging spectrometer, a computer controlled scan mirror and a high speed CCD camera. This assembly is controlled from an electronics chassis that provides system power from rechargeable batteries, provides system control and acquires, stores and displays hyperspectral imagery.

A layout of the LAFS system components is shown in Fig. 2.

The principle method of data acquisition is as follows:

- The primary optics form an image of the target onto the vertical input slit of the spectrometer.
- The plane grating Littrow spectrometer re-images a "column" of spatial imagery onto the Y axis of the silicon CCD camera, spectrally dispersing the image along the X axis.
- The camera integrates for a pre-set period from 7 to 112 ms, digitizes the data, and passes the camera frame to the frame grabber memory.
- The scan mirror is rapidly moved to the next look angle, and the process is repeated until the field is fully scanned.

The resultant block of imagery is stored in frame grabber memory as a 16 MByte "Data Cube" as shown in Fig. 3.

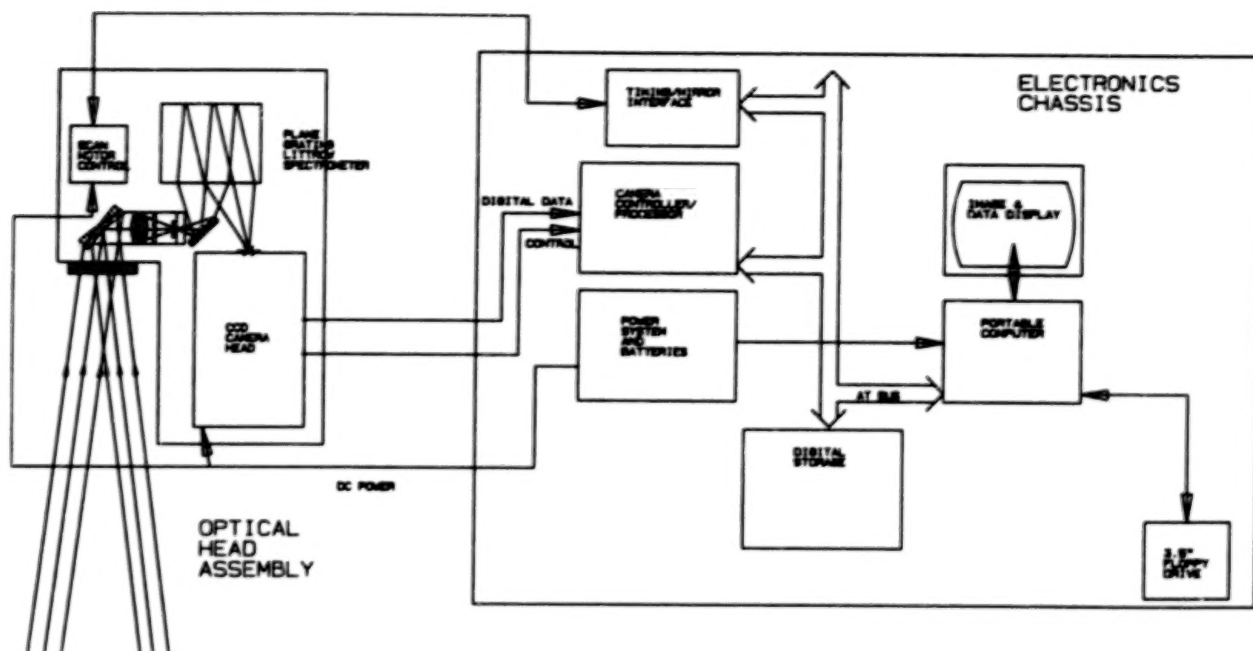


Figure 1. LAFS System Block Diagram.

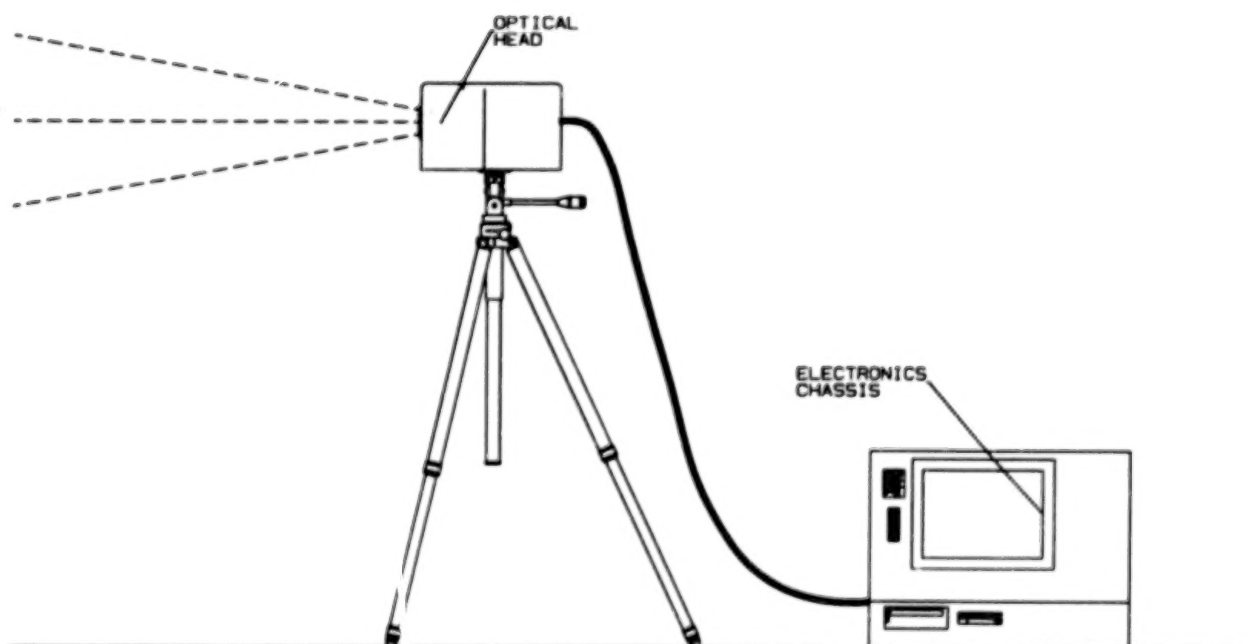


Figure 2. LAFS System Layout.

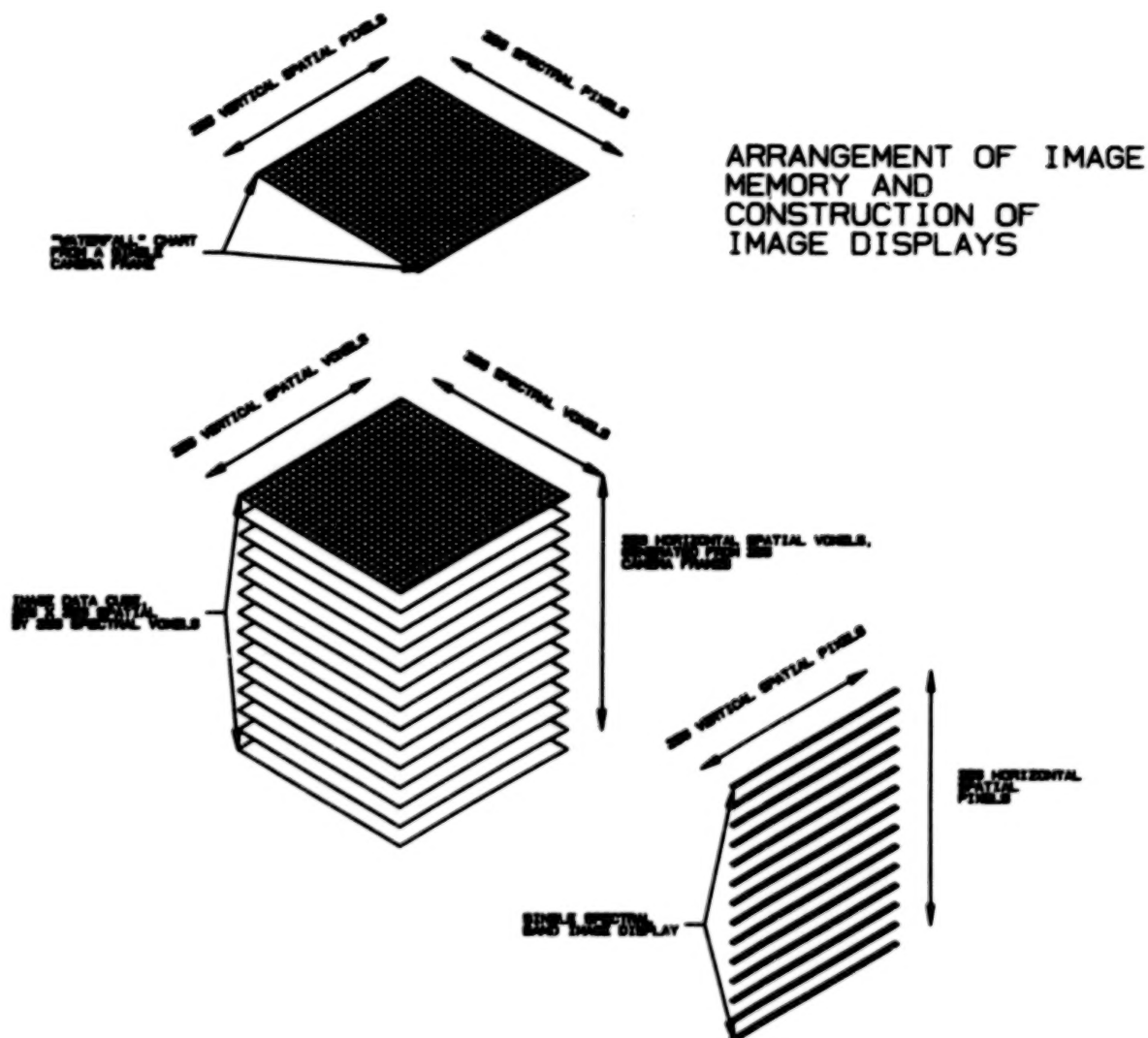


Figure 3. Arrangement of Image Memory and Construction of Image Displays.

Following are the technical specifications for the LAFS Phase II prototype.

Parameter	Value
Spatial Coverage:	15° x 15° with 15 mm lens 7.5° x 7.5° with 30 mm lens
Spatial Resolution:	252 x 256 pixels, 1.0 milliradians each with 15 mm lens 0.5 milliradians each with 30 mm lens
Spectral Coverage:	400 to 1100 nm
Spectral Bands:	256 bands, 2.75 nm bandwidth
Spectral Resolution:	< 5.5 nm
Acquisition Time:	1.8 seconds minimum
Storage Time:	< 16 seconds for all spatial and spectral data
Operation Time:	>4 hours per battery charge

4. BREADBOARD TESTS

As a part of the development sequence, we constructed a breadboard testbed of the LAPS system using:

- the deliverable camera, frame grabber and mirror subsystems,
- laboratory optics and,
- a laboratory PC and power supplies.

Along with the hardware for the breadboard we developed significant portions of the system software. This entailed designing and coding what will become a "bare-bones" version of the final system code including:

- basic image acquisition with integration time control functions,
- image storage and retrieval macros,
- a rudimentary image extraction and display routine and
- connection to an extensive library of generalized image processing functions.

The optical performance of the breadboard compares to the deliverable system as follows:

<u>Parameter</u>	<u>Deliverable System</u>	<u>Breadboard Tests</u>
Total Field Of View	7.5° and 15°	3°
Single Channel Bandwidth	2.7 nm	1.4 nm
Relative Aperture	f/2.0	f/3.0
Relative Optical Throughput	4.5	1

In the laboratory, we acquired a set of test images using a variety of targets and light sources. Figs. 4 and 5 show single band (approximately 2 nm) images extracted from the same data set. The full-field illumination is from an incandescent lamp, and a HeNe laser illuminated spot near the center of the target. Fig. 5, the image at 633 nm clearly shows the HeNe at the center of the field, whereas Fig. 4 at 546 nm does not. Note that the optics used in this breadboard are by no means optimized for this application, and the poor spatial resolution of these images represent the best focus compromise across the full spectral band.

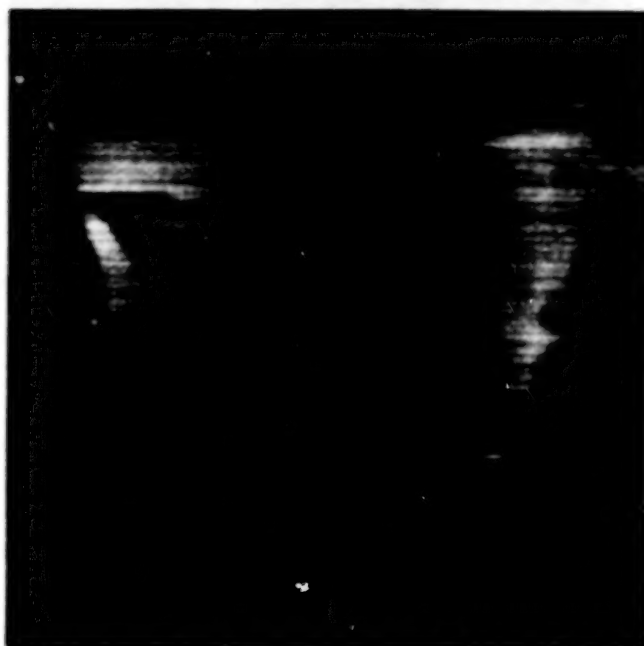


Figure 4. Lab Target with HeNe Laser: Green (546 nm) Band.



Figure 5. Lab Target with HeNe Laser: Red (633 nm) Band.

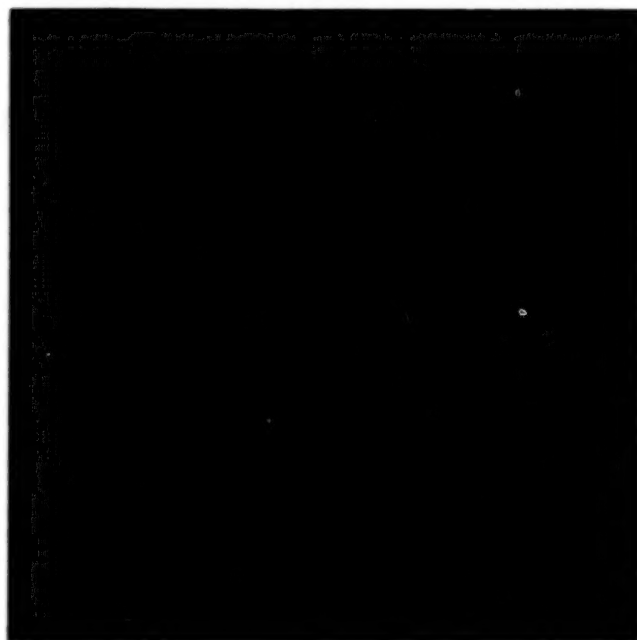


Figure 6. Simulated Minefield: Green (546 nm) Band.

The breadboard was then used to acquire field imagery of a simulated minefield, using inert government issue landmines painted camouflage green. The images shown in Figs. 6 and 7 were taken at a 100' range with a 3° total field of view. The scan time was 1.8 seconds under mostly sunny skies.

The most significant feature of these images is the significant difference in image contrast between the green and near infrared bands. In Fig. 6, the green mines blend well with the background vegetation. In Fig. 7, the increased near infrared reflectance of the vegetation brings out the mines in the imagery. The signal performance of the deliverable system will be considerably better than these breadboard images, since the breadboard optical throughput is only 22% of what is expected of the deliverable prototype.

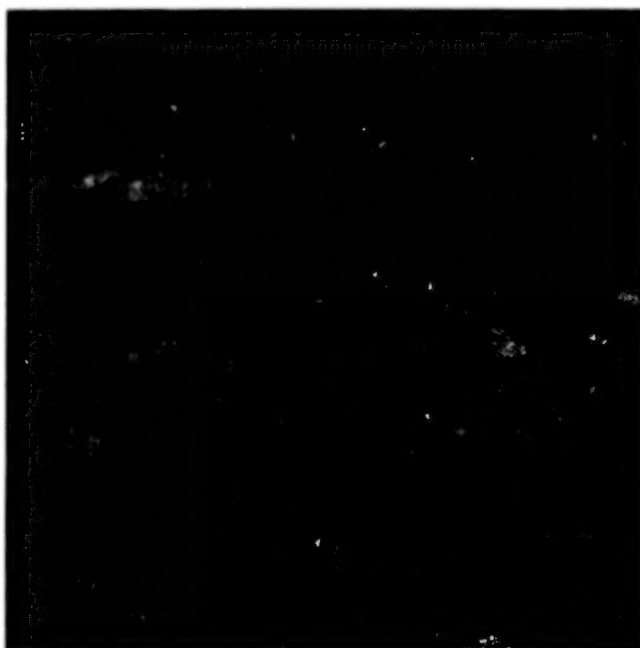


Figure 7. Simulated Minefield: Near Infrared (756 nm) Band.

5. APPLICATIONS

5.1 PORTABLE HYPERSPECTRAL IMAGER

Hyperspectral scanners that have spectral resolution of 3 to 5 nm in the visible are now being developed for airborne platforms by Daedalus and others, and are planned for satellite platforms. The remote sensing community will need a portable field imaging spectroradiometer for ground truth measurements and for studies to define airborne hyperspectral data collection. Programs such as HYDICE will develop these applications and it is anticipated that some of these applications will then require ground truth data with the high spatial resolution achievable with the LAFS instrument.

A second application is for the Marine Corps as a portable mine detection system. The Coastal Systems Station plans to use the LAFS for detection of land mines by means of a multispectral signature. Once the mine and background spectral signatures are known, then the Large Area Fast Spectroradiometer can be reconfigured for the mine detection application. The true potential of this system's ability to reject clutter both spatially and spectrally can be seen in applications such as this where a user is attempting to discriminate and identify an object within a spatially complex scene. In this type of application, the object of interest may have a distinct spectral signature, but may only extend across a small portion of the instrument's field of view. In a non-imaging spectrometer, the unique spectral information of the object is masked by the spectrum of the background, making detection difficult or impossible. By creating a hyperspectral image of the scene, the spectra of small portions of the field of view can be studied individually, without interference from the surrounding.

This configuration may require binning in the CCD camera and other data processing tasks to speed frame time and data processing and display time. Other needs, such as mounting the head so it can be elevated to look down through vegetation or to conduct mine field searches far in advance of any troop movement may require further head miniaturization or a fiber optic path between the collection optics and the scanning spectrometer. The system that will be delivered to the Marine Corps will allow the Coastal Systems Station to define the requirements and modifications needed to convert the Large Area Fast Spectroradiometer into a portable mine detection system.

5.2 AIRBORNE HYPERSPECTRAL SCANNER

High signal-to-noise ratio in rotating mirror scanner systems can only be achieved by using large mirrors at low scan speeds, thus, scanners have a very low V/H due to the slow scan speed. They are also large and heavy. These factors limit the spatial resolution and the type of aircraft in which rotating systems can be flown. As a result, there is a need for a new approach that will reduce the size and complexity of a hyperspectral scanner and at the same time improve the signal-to-noise ratio.

A hyperspectral pushbroom scanner based on the LAFS design is a solution to this problem. Such a system, as shown in Fig. 8, would use a focal plane array detector which offers a large detector area to give high signal-to-noise ratio with a modest optical collecting area. The core optical design for a visible/near infrared spectrometer would largely be based on the optical architecture of the LAFS instrument, and would benefit greatly from lessons learned in the Phase II program. For operation in the mid-wave infrared, a preliminary study of an imaging spectrometer with an InSb focal plane has been completed. With recent advances in infrared CCD technology, we hope to extend this technology farther into the infrared in order to cover the full spectral range of our current standard products, 0.4 - 14 μm .

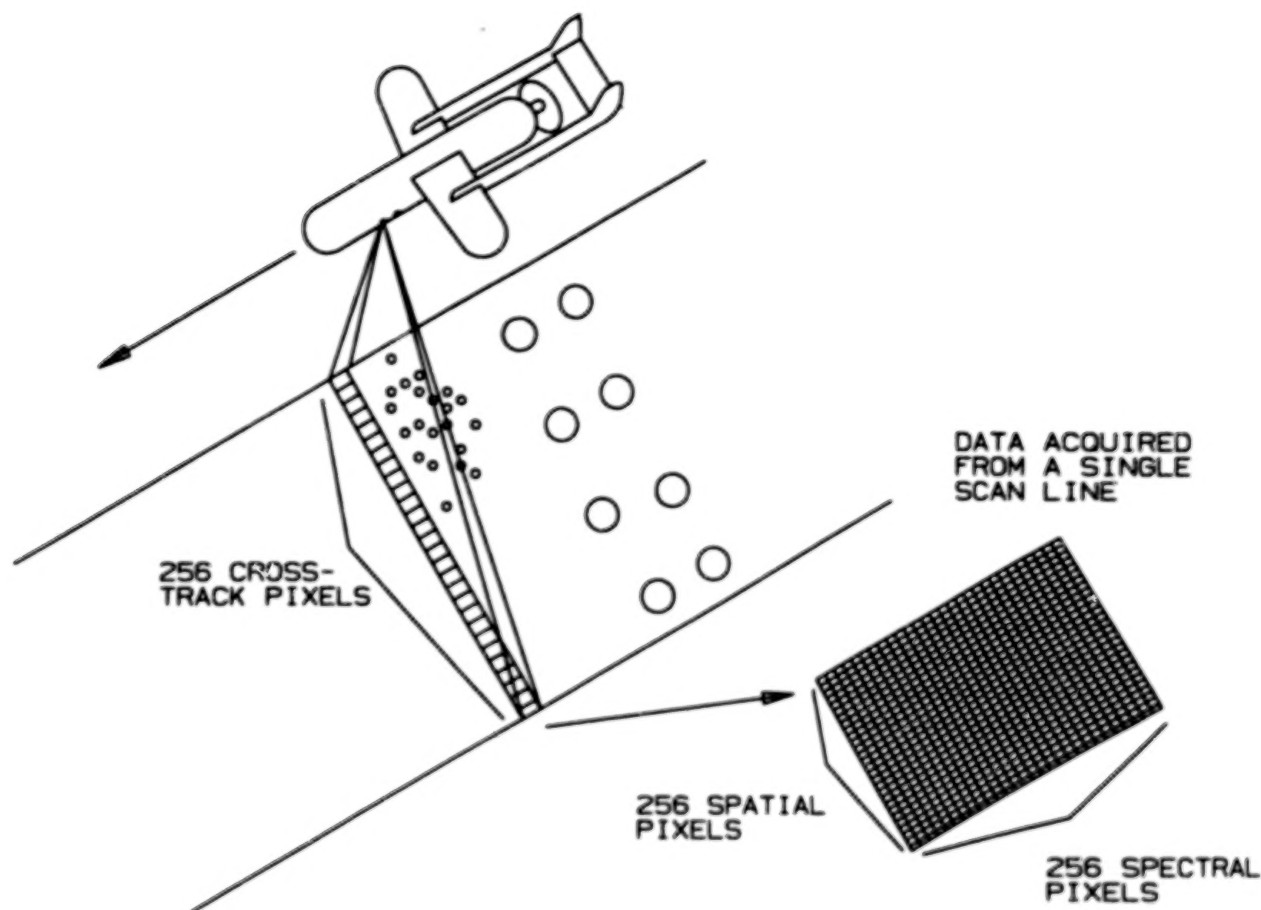


Figure 8. Data Acquisition Geometry for an Airborne Hyperspectral Pushbroom Scanner.

5.3 PROCESS CONTROL

Several raw material processes move the materials over a belt conveyor for human inspection to remove unacceptable materials. Examples are spoiled vegetables in a cannery or frozen packaging plant, low grade ore in bauxite, and burned flakes in cereal. Robots or auto-routing of materials are being developed to eliminate hand picking or re-routing of unacceptable material. To complete the automation, a sensor is needed to automatically recognize the unacceptable material. Both active and passive techniques are being evaluated. These include spectral identification of fluorescence in active systems and passive multispectral detection. The spectral identification requires a spectral image to separate the good materials from the bad, and the conveyor flow of the products require line imaging for continuous monitoring. These make the imaging spectrometer of LAFS a candidate for this application.

6. CONCLUSIONS

The LAFS system represents a new class of field portable spectrometers: the hyperspectral imager. It provides field spectra with fine spatial resolution: previously these spectra would be acquired with single-point spectrometers that blend target and background signatures. The system is rugged, field portable, fast and operationally flexible. The design has a wide range of applications and the architecture is scalable to incorporate future higher resolution sensors, variable field optics and faster processors.

7. ACKNOWLEDGMENTS

This work was performed for the United States Marine Corps under contract N61331-93-C-0053, Naval Coastal System Station, Dahlgren Division, Panama City Florida.

TOPSAT: THE GLOBAL TOPOGRAPHY MISSION¹

Thomas G. Farr and Howard A. Zebker
Jet Propulsion Laboratory
California Institute of Technology
Pasadena, CA 91109
(818) 354-8780

David J. Harding
NASA Goddard Space Flight Center
Greenbelt, MD

An accurate description of the surface elevation of the Earth is of fundamental importance to many branches of Earth science. In 1990, the NASA-Italian Space Agency Joint Topographic Science Working Group recommended a dedicated space mission as the best way to obtain a global, uniform high-quality topographic data set. The Global Topography Mission, or TOPSAT, would include an interferometric synthetic aperture radar (INSAR), a Multi-Beam Laser Altimeter (MBLA), and a Global Positioning System (GPS) receiver. The INSAR will obtain a global digital elevation data set in less than 6 months, with high spatial resolution (30 m) and high vertical accuracy (less than 5 m). The MBLA will obtain a globally distributed grid of narrow altimeter swaths (5 beams cross-track with 30 m diameter footprints) of very high vertical accuracy (less than 1 m in low-relief terrain) for verifying the geodetic control of the INSAR data, for mapping of the polar ice sheets, and for measurement of vegetation height and surface roughness in selected areas. The GPS data will provide accurate (~ 10 cm) spacecraft orbit determination to ensure that the elevation data are acquired in a consistent, Earth center of mass reference frame. The Global Topography Mission can be accomplished within the framework of NASA's "Earth Probe" program and be ready to launch in the 1998-2000 time frame.

Manuscript not available at time of printing. Please contact authors for further information.

¹Part of this work was carried out by the Jet Propulsion Laboratory, California Institute of Technology, under contract with NASA.

BLANK PAGE

SESSION II
SIGNAL/DATA PROCESSING

BLANK PAGE

**CALIBRATION AND ATMOSPHERIC COMPENSATION OF IMAGING
SPECTROMETER DATA FOR VEGETATION, GEOLOGICAL
AND WATER APPLICATIONS AND RESEARCH**

Robert O. Green, Thomas G. Chrien, James E. Conel and Jeannette van den Bosch
Jet Propulsion Laboratory
California Institute of Technology
Pasadena, CA 91109
(818) 354-9136

Calibration and atmospheric compensation of remote sensing data is required to quantitatively identify, measure and monitor materials on the surface. This is true of imaging spectrometers measuring molecular absorption and scattering characteristics in the 400 to 2500 nanometer region at high resolution.

First, the requirements for absolute spectral, radiometric and geometric calibration of an imaging spectrometer are reviewed for vegetation, geological and water applications. As an example, absolute calibration and validation of the performance of the Airborne Visible-Infrared Imaging Spectrometer is presented.

Second, an approach for compensation for the atmosphere based on imaging spectrometer derived estimates of total path water vapor, Rayleigh scattering and aerosol scattering is given. Examples of derived apparent reflectance for a vegetation, geological and water target are presented. Use of the derived reflectance is discussed for applications and research in these disciplines.

Manuscript not available at time of printing. Please contact authors for further information.

MATHEMATICAL ASPECTS IN MODELING MATERIAL REFLECTANCE PROPERTIES FOR REMOTE SENSING APPLICATIONS

M.D. Metzler
Environmental Research Institute of Michigan
Ann Arbor, MI 48105

J.R. Baker
Virginia Polytechnic Institute and State University*
Blacksburg, VA 24061

J.R. Maxwell
Environmental Research Institute of Michigan
Ann Arbor, MI 48105

ABSTRACT

This study examines several facets in mathematical modeling of surface reflectivities and emissivities, based upon the bidirectional reflectance distribution function (BRDF). Mathematical expressions are derived and presented for spectral values for horizontal and tilted surfaces. Further formulations for normalized band effective values are given. The expressions presented are most applicable to solid surfaces, particularly man-made surfaces. The formulations provided in this paper in some cases are inappropriate, in that uncertainties in other analysis components (sensor, atmosphere, background) negate the need for such rigor. In many cases, however, meaningful error will result if these directional and band normalization concepts are ignored. We have implemented these as algorithms in engineering software, and performed several tests of their efficacy. Not unexpectedly, we find that the algorithms work well when the assumptions upon which they are based are fulfilled, and when we have reliable input parameters to use. They work less well in other circumstances, but are in many cases surprisingly robust. We believe the form and format of the equations may be of use to a large number of analysts. We are undertaking studies to ascertain and define errors associated with these models, and the measurements upon which model parameters are derived. We are also continuing study of alternate model formulations, and alternatives in implementing the models.

1. INTRODUCTION

This paper defines the mathematical basis for modeling of optical properties of materials (reflectivities and emissivities). It contains a discussion of the physical basis for spectro-radiometric exploitation. Included for reference are data and algorithms used to implement spectro-radiometry. The parameters produced allow a user to estimate the spectral radiance, surface temperature, and other electro-optical properties of imaged materials.

2. REMOTE SPECTRO-RADIOMETRY

Figure 1 illustrates the major components of the spectral radiance detected by a sensor. A number of these are unrelated to the imaged material(s), and the material component itself is substantially modified by the radiometric environment. Because most of the effects cannot be directly sensed or separated, they must be modeled in terms of parameters that can be sensed or estimated. Those effects and the approach used to model them are discussed below.

*CIA Officer-in-Residence. The views presented in this paper are those of the authors, and do not necessarily represent those of the Central Intelligence Agency.

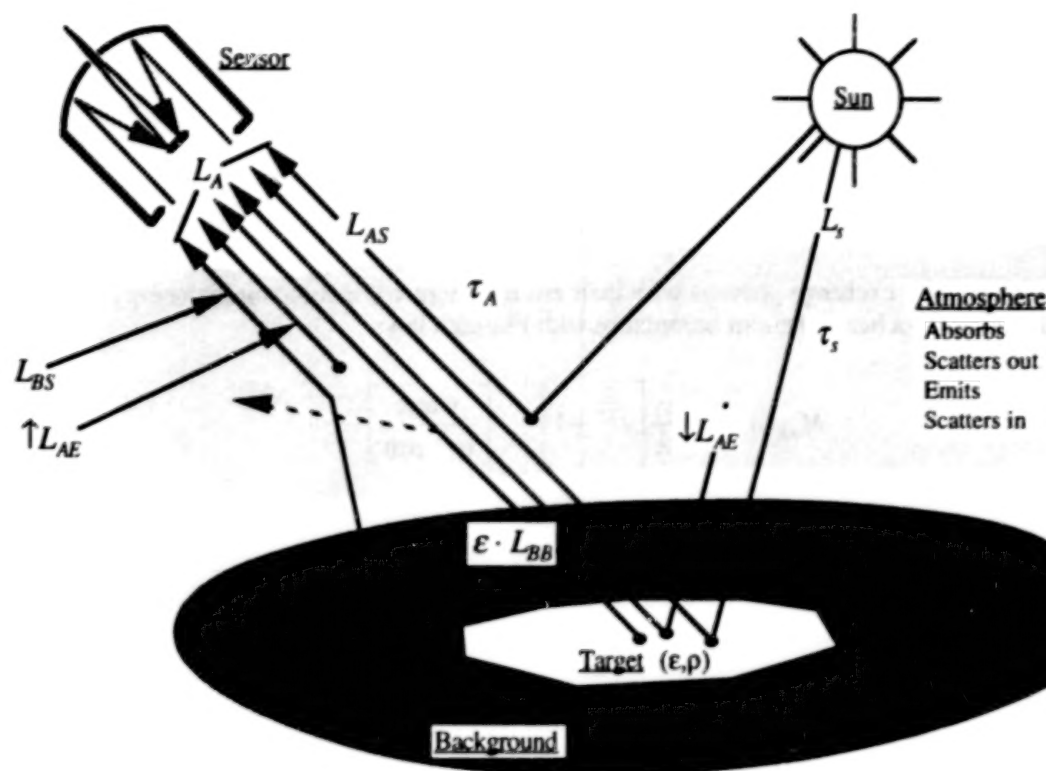


Figure 1. Radiometric Environment

2.1 SOLAR EFFECTS

If materials are observed in the presence of sunlight, a major component of their spectral radiance will be due to reflected solar radiance.

For Lambertian materials, the effective down-welling solar spectral radiance is given by:

$$\tau_s(\lambda) L_s(\lambda) = \tau_s(\lambda) \cdot \Gamma \cdot \cos(\theta_s) L_{BB}(\lambda, T_s) \left[\frac{\text{watts}}{\text{m}^2 \cdot \mu\text{m} \cdot \text{ster}} \right] \quad (1)$$

where

- Γ = solid angle ratio for mean Sun = 2.1645×10^{-5}
- θ_s = solar zenith angle
- $\tau_s(\lambda)$ = atmospheric transmission to the sun along the solar zenith angle
- $L_{BB}(\lambda, T_s)$ = spectral radiance of blackbody at T_s - see (2) and (4)
- T_s = effective solar radiative temperature (6000 K)

Insolation can be reflected not only from materials but also by atmospheric constituents. The latter effect, denoted $L_{AS}(\lambda)$ in Fig. 1, is termed scattering-in and is similar in effect to up-welling atmospheric emission. The magnitude of the scatter-in flux exhibits a complex dependency on line-of-sight-sun geometry, scattering constituent (primarily aerosol) density,¹ vertical distribution, and angular (phase) scattering function.

¹High densities lead to high probability of multiple scattering and invalidation of all but the most complex models

2.2 MATERIAL RADIANCE

The effect of material temperature that is sensed remotely is spectral radiance (the infrared analog of brightness), which is a measure of the flux radiated per unit material area per unit spectral (wavelength) interval into a unit solid angle. The magnitude of the emitted spectral radiance of a real material is characterized in terms of its deviation from the ideal quantum-mechanical blackbody.

2.2.1 Blackbody Emission

Materials continually exchange photons with their environment while maintaining energy equilibrium. Ideal blackbodies radiate into a hemisphere in accordance with Planck's law:

$$M_{BB}(\lambda, T) = \frac{c_1}{\lambda} \left[e^{\frac{c_2}{\lambda T}} - 1 \right]^{-1} \left[\frac{\text{watts}}{\text{m}^2 \cdot \mu\text{m}} \right] \quad (2)$$

where:

$M_{BB}(\lambda, T)$ = spectral emission of a blackbody at λ and T , per unit wavelength interval

λ = wavelength of emission, μm

$$c_1 = 2\pi c^2 h = 3.741832 \times 10^8 \left[\frac{\text{watts} \cdot \mu\text{m}^5}{\text{m}^2 \cdot \mu\text{m}} \right]$$

$$c_2 = \frac{hc}{k_B} = 1.438786 \times 10^4 [\mu\text{m} \cdot \text{K}]$$

T = absolute surface temperature, K

Most objects, however, are not ideal blackbodies and emit somewhat less than indicated by (2). The measure of effectiveness is emissivity (ϵ), which can be a function of wavelength and such other factors as observation angle and surface temperature. Material thermal emission is thus given by:

$$M(\lambda, T) = \epsilon(\lambda) M_{BB}(\lambda, T) \left[\frac{\text{watts}}{\text{m}^2 \cdot \mu\text{m}} \right] \quad (3)$$

If emissivity is spectrally uniform over the wavelength band of interest, the resulting emission is called "graybody".

2.2.2 Thermal Radiance

Sensors generally do not collect all of the material emission into a hemisphere. The measure of material emission into a solid angle less than a hemisphere is called spectral radiance. For diffuse or Lambertian surfaces, thermal spectral radiance is independent of viewing angle or sensor aperture. For non-Lambertian materials, spectral radiance is a function of relative viewing angle. The dependence is usually subsumed in the emissivity term so that as in Fig. 1, the material thermal spectral radiance can be taken as consisting of a blackbody thermal spectral radiance, $M_{BB}(\lambda, T)$, modified by the appropriate emissivity, i.e.

$$L(\theta, \phi, \lambda, T) = \epsilon(\theta, \phi, \lambda) L_{BB}(\lambda, T) \left[\frac{\text{watts}}{\text{m}^2 \cdot \mu\text{m} \cdot \text{ster}} \right] \quad (4)$$

2.2.3 Reflected Radiance

For solid bodies (i.e., those with transmission = 0), there is a complementary relationship between reflectivity (ρ) and emissivity (ϵ) known as Kirchhoff's Law:

$$\rho + \varepsilon = 1 \quad (5)$$

Most solid bodies have $\varepsilon < 1$, and therefore both reflect incident energy and emit thermal energy.

For materials viewed through the Earth's atmosphere, the spectral radiance that is reflected consists of the down-welling spectral radiance of the atmosphere and the attenuated solar spectral radiance. The reflected spectral radiance may be expressed as:

$$L_p(\lambda) = \sum \rho_i \cdot \downarrow L_i(\lambda) \left[\frac{\text{watts}}{\text{m}^2 \cdot \mu\text{m} \cdot \text{ster}} \right] \quad (6)$$

where $\downarrow L_i(\lambda)$ is the down-welling spectral radiance from source i and ρ_i is the material reflectivity appropriate for the geometry and spectral characteristics of source i . For Lambertian materials, the Lambertian reflectivity may be used for all reflected sources; but for materials with a specular component of reflectivity, care must be exercised in selecting ρ_i , especially where point sources, such as the sun, irradiate the material. Figure 1 shows different reflectivities for solar and atmospheric down-welling radiance.

2.3 ATMOSPHERIC EFFECTS

The material spectral radiance given by (4) and (6) is considerably modified by the atmosphere along the line of sight (LOS) to the sensor. The atmospheric gases and aerosols (suspended particulates) attenuate the material radiance by absorption and scattering-out of photons. The same species emit thermal energy in all directions, adding to the apparent material radiance. The amounts of attenuation and emission are strong functions of meteorological conditions. The net spectral radiance reaching a sensor, therefore, can vary widely for a given amount of material radiance.

The effects described in this section have been the subject of considerable study by various agencies and universities, resulting in a number of models, such as the LOWTRAN series developed by the Air Force Geophysical Laboratory (Kneizys et al., 1980, 1983). The literature associated with that series describes in considerable detail the physics reviewed in this section and typical computer codes developed for quantitative estimates of spectral atmospheric transmission and emission.

2.3.1 Transmission

Two effects must be considered when estimating atmospheric transmissions: absorption and scattering out. Atmospheric gases and aerosols contribute to both mechanisms. Absorption refers to the capture of a fraction of the incident photon flux. For gases, the capture is associated with quantum transitions, and the amount of absorption is strongly dependent on the exact wavelength of the incident flux, as well as the quantity of the particular gas and its temperature and pressure.

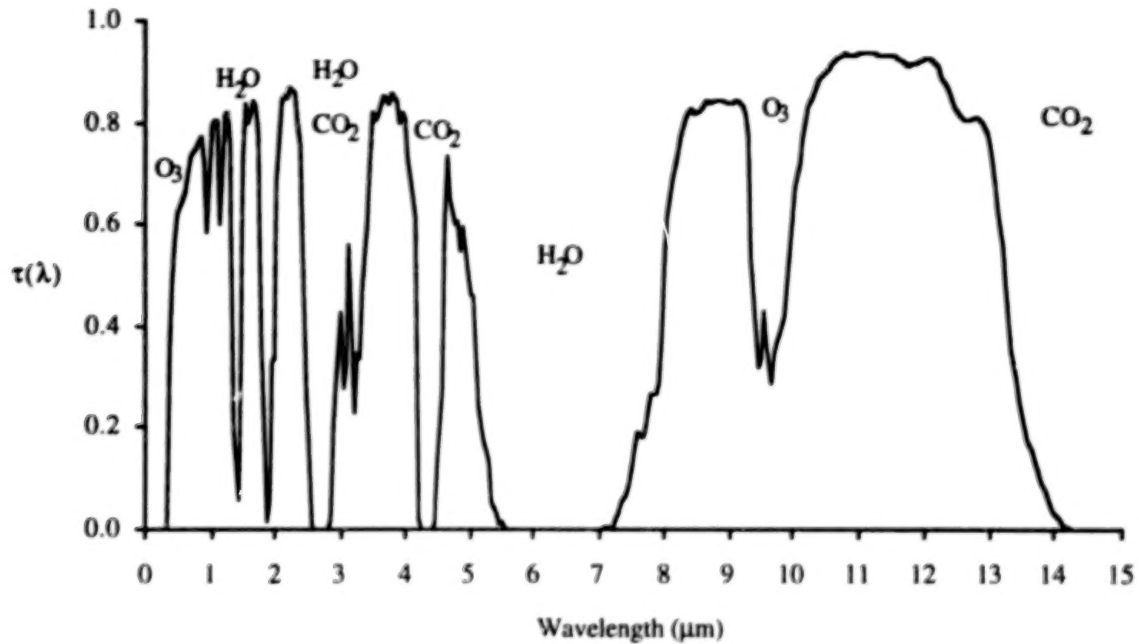


Figure 2. Example Atmospheric Transmission

Both atmospheric gases and aerosols also scatter photons out of the LOS between the material and the sensor. The Rayleigh scattering associated with atmospheric gases is spectrally dependent ($\sim \lambda^{-4}$) but Mie scattering associated with aerosols can be substantial. Transmission for a typical atmosphere (nadir view through entire atmosphere) is provided in Fig. 2.

2.3.2 Atmospheric Emission

The constituents of the atmosphere emit photons to maintain thermal equilibrium while absorbing quanta. While the emission is thermal in character, the atmospheric emissivity, being linked to absorption, is markedly non-uniform, so that the net emission bears only a small resemblance to that of a black-or-graybody. A portion of the energy emitted by the constituents along the LOS is collected by a sensor, along with the attenuated material spectral radiance. This up-welling atmospheric spectral radiance is denoted $\uparrow L_{AE}(\lambda)$. Some of the atmospheric emission is directed downward. This down-welling spectral radiance, $\downarrow L_{AE}(\lambda)$, is reflected by materials and augments the thermal spectral radiance emitted by such materials.

For specular materials, the down-welling spectral radiance of interest is that associated with Snell's law *vis-a-vis* the sensor LOS and the normal to the material surface. If a variety of materials of different orientations is to be studied in the same scene, a variety of such down-welling spectral radiances, denoted $\downarrow L_{AE}(\lambda, \theta)$, must be available, where θ is the nadir angle of the portion of the atmosphere in question.

For Lambertian materials, the "hemispheric (down-welling) spectral radiance" is appropriate. It represents the weighted relative contribution of spectral radiance from constituents of the atmosphere at different angles from nadir. Assuming axial symmetry about the zenith, it may be approximated as

$$L_{AE}(\lambda) = \int_0^{\pi/2} \downarrow L_{AE}(\lambda, \theta) \cdot \sin(\theta) \cdot \cos(\theta) d\theta \left[\frac{\text{watts}}{\text{m}^2 \cdot \mu\text{m} \cdot \text{ster}} \right] \quad (7)$$

Most materials are neither purely specular nor purely Lambertian and require a weighted mix of the two forms of down-welling radiance (specular and diffuse) in order to estimate reflected radiance.

Atmospheric propagation models compute up-welling and down-welling atmospheric radiance from the same input data as that required to compute atmospheric transmission.

2.4 OTHER ENVIRONMENTAL EFFECTS

Various other effects modify the spectral radiance reaching the sensor from the LOS to the material. The presence of any significant cloud cover in the scene, even if the LOS is not obscured, can substantially modify the spectral radiance of a material as sensed from above. The cloud blocks off the down-welling radiance from the atmosphere above it, while radiating, substantially as a blackbody, its own thermal emission.

Strong local sources can substantially alter the radiance that is sensed. Hot chimneys, burn-off flares, exhaust gases, etc., can be reflected, especially by suitably oriented specular materials. Burn-off flares and exhaust gases can also affect atmospheric transmission and emission.

2.5 APERTURE RADIANCE

The total spectral radiance reaching a sensor aperture from the direction of the material is termed the aperture radiance. This term is denoted $L_A(\lambda)$ and is given by:

$$L_A(\lambda) = \tau_a(\lambda) \left[\epsilon(\lambda) L_{BB}(\lambda, T_m) + \rho_A(\lambda) \downarrow L_{AE}(\lambda) + \rho_s(\lambda) \tau_s(\lambda) L_s(\lambda) \right] + L_{AS}(\lambda) + L_{BS}(\lambda) + \uparrow L_{AE}(\lambda) \quad (8)$$

$\left[\frac{\text{watts}}{\text{m}^2 \cdot \mu\text{m} \cdot \text{ster}} \right]$

It is composed of the following elements (assuming the material is not shadowed and is directly illuminated by the sun):

$L_{AS}(\lambda)$	= scattered-in insolation
$L_{BS}(\lambda)$	= scattered-in terrain radiance
$\uparrow L_{AE}(\lambda)$	= up-welling atmospheric radiance
$\rho_A(\lambda) \tau_a(\lambda) \downarrow L_{AE}(\lambda)$	= attenuated reflected down-welling atmospheric radiance
$\rho_s(\lambda) \tau_a(\lambda) \tau_s(\lambda) L_s(\lambda)$	= attenuated reflected solar radiance
$\epsilon(\lambda) \tau_a(\lambda) L_{BB}(\lambda, T_M)$	= attenuated material thermal radiance

in which,

$\rho_A(\lambda)$	= spectral effective directional diffuse reflectivity
$\rho_s(\lambda)$	= spectral bidirectional reflectivity at the solar angle
$\epsilon(\lambda)$	= spectral directional emissivity
$\tau_a(\lambda)$	= spectral atmospheric transmission to the receiver along the sensor zenith angle
$\tau_s(\lambda)$	= spectral atmospheric transmission to the sun along the solar zenith angle
$\downarrow L_{AE}(\lambda)$	= spectral down-welling atmospheric radiance
$L_s(\lambda)$	= spectral exo-atmospheric solar radiance
$L_{BB}(\lambda, T_M)$	= spectral blackbody radiance at the material temperature T_M

As noted above, several additional factors might be encountered, but they are too particularized for a general treatment.

2.6 SENSOR CONSIDERATIONS

From the radiometric point of view, the most important sensor considerations are the system spectral response and the calibration accuracy. The system spectral response determines the portion of the input scene radiance to which sensors can respond. Examples of the general shape for system spectral response functions for panchromatic, multispectral, and hyperspectral systems are shown in Fig. 3.

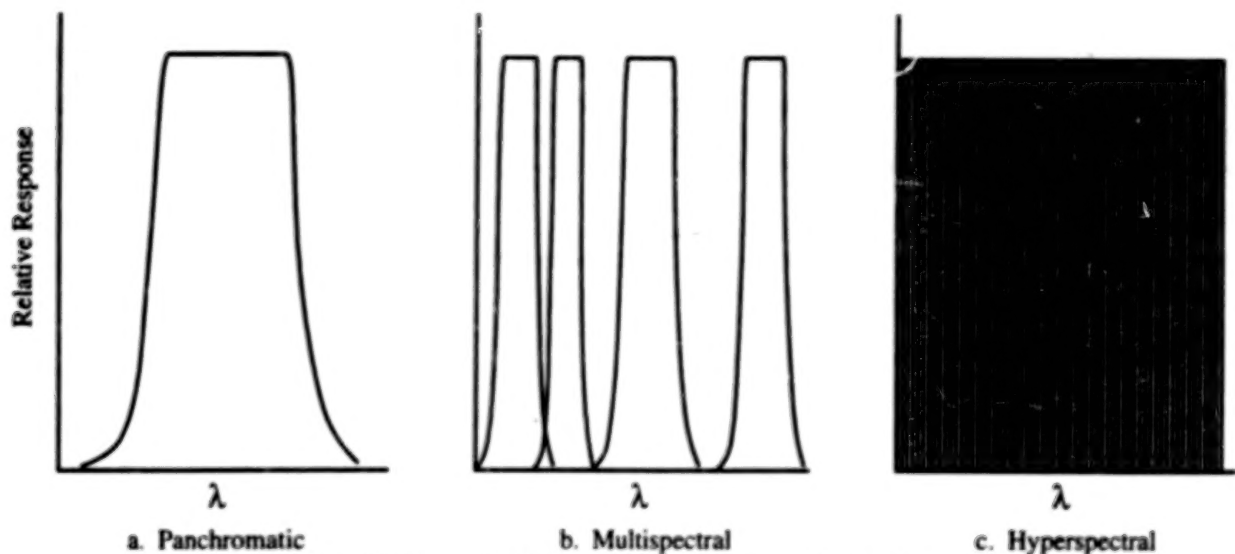


Figure 3. Example System Spectral Response Functions

2.7 RADIOMETRY CONSIDERATIONS

In-band radiance as measured by a sensor is denoted L_{MEAS} and corresponds to the spectral product integration of $L_A(\lambda)$ from (8), times the system spectral response, $r(\lambda)$. This in-band aperture radiance is given by:

$$L_{MEAS} = \int r(\lambda) L_A(\lambda) d\lambda$$

$$= \int r(\lambda) \left\{ \begin{aligned} &\rho_s(\lambda) [\tau_a(\lambda) \tau_s(\lambda) L_s(\lambda)] + \rho_A(\lambda) [\tau_a(\lambda) \downarrow L_{AE}(\lambda)] \\ &+ \epsilon(\lambda) [\tau_a(\lambda) L_{BB}(\lambda, T_M)] + [\uparrow L_{AE}(\lambda)] + [L_{AS}(\lambda)] + [L_{AS}(\lambda)] \end{aligned} \right\} d\lambda \quad \left[\frac{\text{watts}}{\text{m}^2 \cdot \text{ster}} \right] \quad (9)$$

Given estimates or measured values for the atmospheric terms and material temperature, (9) may be solved for material reflectivity and emissivity. Likewise, if atmospheric and material emissivity/reflectivity parameters are known, a material temperature may be derived.

3 OPTICAL PROPERTIES OF MATERIALS

The purpose of this section is to adequately define *material* optical properties and to describe the measurement techniques needed for obtaining these properties. For remote sensing in the reflective portion of the electromagnetic spectrum, from about 0.3 to 3.5 μm , it is primarily reflectance properties of materials which induce signals in the source radiation. In the thermal portion of the spectrum, from 3.5 to 15 μm , it is a combination of thermal properties (heat capacity, density, etc.) and optical properties (solar absorptance and thermal emittance) which provide useful signals in the otherwise uninteresting world of 300 K blackbody radiation. The remote sensor operating parameters should be chosen to operate where the signals from materials of interest are distinctive and recognizable from all of the others. The dependence of the signals on the source, receiver, sensor, and meteorological parameters should be known and understood. Detectable characteristics of the electromagnetic field (amplitude, polarization, wavelength, and coherence) are familiar, but an understanding of the optical properties of materials and how they manifest themselves in the field at a remote sensor is needed, in order to develop useful remote sensing techniques.

3.1 REFLECTANCE PROPERTIES OF MATERIALS

The reflectance of a surface generally depends on the aspect angle of the source, its polarization and wavelength, and on the viewing angle of the receiver, with polarizations generally modified when reflection occurs. Nicodemus et al. (1977) summarized reflectance parameterization and notation.

3.1.1 Bidirectional Reflectance Distribution Function

The bidirectional reflectance distribution (BRDF) is defined as the ratio of the radiance reflected by the sample in the direction of the receiver, (θ_r, ϕ_r) , to the irradiance incident on the sample from direction (θ_i, ϕ_i) . The wavelength of the source, its polarization, and the polarization of the reflected radiance are important parameters.

The complete plane-polarized BRDF², $\rho'_{ai,ar}(\theta_i, \phi_i, \theta_r, \phi_r; \lambda)$ can be written as:

$$\rho'_{ai,ar}(\theta_i, \phi_i, \theta_r, \phi_r; \lambda) = \frac{dL'_{ar}(\theta_r, \phi_r; \lambda)}{dE_{ai}^i(\theta_i, \phi_i; \lambda)} \quad (10)$$

where:

- $dE_{ai}^i(\theta_i, \phi_i; \lambda)$ = the irradiance from the sample direction (θ_i, ϕ_i) ($dL_{ai}^i(\theta_i, \phi_i; \lambda) \cdot \cos(\theta_i) \cdot d\omega_i$)
- $dL'_{ar}(\theta_r, \phi_r; \lambda)$ = the radiance reflected in direction (θ_r, ϕ_r)
- $d\omega_i$ = the solid-angle element within which the incident radiance is confined
- λ = the wavelength of the incident irradiance
- ai = the azimuth angle of the polarizer on the source
- ar = the azimuth angle of the polarizer on the receiver

As subscripts, ai and ar represent, respectively, the plane-polarization state of the incident irradiance and the plane-polarized component of the reflected radiance selected by the analyzer on the receiver. The polarization specifier known as the polarization azimuth angle α , is the angle between the electric field polarization and the normal vector to the reference plane. Thus, $\alpha = 0$ corresponds to perpendicular polarization. The polarization azimuth angle is constrained to satisfy $-90^\circ \leq \alpha \leq 90^\circ$, with the sign determined by a viewer looking into the propagating radiation (i.e., looking "upstream"). If the angle from the reference-plane normal vector to the electric field polarization plane is counterclockwise for such a view, then the polarization azimuth angle is positive.

Polarization indicators \perp and \parallel may be used to indicate perpendicular or parallel, to the plane of incidence if referring to the source, or to the plane of reflection of referring to the receiver ($\alpha = 0$ and 90° , respectively). If the incident irradiance is unpolarized, the symbol ai in (10) is replaced with U . If the detector used in a ρ' measurement has no polarization preference and senses the total radiance at the receiver aperture, the symbol ar in (10) is replaced by T . Thus, for example, $\rho'_{\perp, \parallel}$ represents the results of a measurement under conditions of perpendicularly-polarized sample irradiance and a parallel-polarized analyzer on the receiver. The symbol $\rho'_{U,T}$ refers to conditions of unpolarized incident irradiance and no analyzer on the receiver.

3.1.3 Directional-Hemispherical Reflectance

The directional-hemispherical reflectance of a surface is the ratio of the total power reflected (into the entire hemisphere) by a sample to the power incident on the sample from a specified direction. It is usually measured as a function of the wavelength, λ . Although the angular effects are largely averaged out, these data are very important because of the spectral information they provide. For a measurement of directional-hemispherical reflectance, the incident power is usually unpolarized, spectrally filtered in a wavelength band $\Delta\lambda$

²In this document, the bidirectional reflectance distribution function is denoted formally by ρ' and given the name "rho prime". Other formal notations in common use are f_λ , BRDF, and f_λ .

centered at wavelength λ , collimated, and directed onto the sample at an angle of incidence (θ_i, ϕ_i) . The directional-hemispherical reflectance, $\rho_d(\theta_i, \phi_i; \lambda)$ is related to the BRDF as follows:

$$\rho_d(\theta_i, \phi_i; \lambda) = \frac{P'_r(2\pi; \lambda)}{P'_i(\theta_i, \phi_i; \lambda)} = \int_{2\pi} \rho'_{U,T}(\theta_i, \phi_i, \theta_r, \phi_r; \lambda) \cos(\theta_r) d\omega_r \quad (11)$$

with units of $\frac{\text{watts}}{\text{watts}}$ and $0 \leq \rho_d \leq 1$.

Directional reflectance data do not provide any information about the angular distribution of the radiance reflected by the surface and are completely adequate only for surfaces for which $\rho'(\theta_i, \phi_i, \theta_r, \phi_r; \lambda)$ is independent of θ_r and ϕ_r . Usually, $\rho_d(\theta_i, \phi_i; \lambda)$ is measured for one incidence angle only, typically $\theta_i = 0$ to 10° ; the dependence on θ_i and ϕ_i is generally ignored and $\rho_d(\theta_i, \phi_i; \lambda) = \rho_d(\lambda)$ is assumed. Surfaces for which $\rho' = \rho'(\lambda)$ only are diffuse reflectors, and for a diffuse reflector, $\rho'_{U,T}(\lambda) = \rho_d(\lambda)/\pi$ and $\rho'_{w,w}(\lambda) = \rho_d(\lambda)/2\pi$.

3.2 EMITTANCE PROPERTIES OF MATERIALS

Remote sensing in the thermal infrared may in some ways be more difficult than in the reflective portion of the spectrum. In the reflective region at a given instant in time, materials with different reflectance characteristics will produce differences in the reflected spectral radiance, albeit the nature of these differences varies with sun angle, view angle, atmospheric, etc. But in the thermal infrared, differences in spectral radiance characteristics may result either from differences in optical (reflectance/emittance properties), or differences in thermal (bulk) properties such as heat capacity and thermal conductivity, and temperatures.

Temperature variations are a source of noise when inferring emissivities from observed spectral radiances in the thermal infrared. Although there is no way to unambiguously determine both the temperature and the emissivity of a material from only a measurement of spectral radiance, if the spectral emissivities are sufficiently different from one material to the next, variations in the spectral radiances due to $\epsilon(\lambda)$ may be larger than those due to variations in T .

The emittance (or emissivity) of a material at wavelength λ , $\epsilon(\lambda)$, is the ratio of the radiation emitted at wavelength λ by the material at temperature T to that emitted at wavelength λ by a blackbody at temperature T . In principle, the emittance of a material is its emittance when it is in thermal equilibrium with the environment, also at temperature T . The emittance of a material may depend on the angle from which it is viewed, θ , and the emittance may exhibit some polarizing characteristics, $\epsilon = \epsilon(\theta, \lambda, P)$. The emission of a blackbody is given by (2), and is independent of angle and unpolarized.

The emittance of an opaque material is related, by Kirchhoff's Law, to its reflectance by the relationship:

$$\epsilon(\theta, \lambda) = 1 - \rho_d(\theta, \lambda) \quad (12)$$

Direct measurement techniques for emittance require accurate sample temperature measurements. This is difficult under the best of circumstances, and nearly impossible for many natural materials, e.g., vegetation and various soils. An alternate approach is to measure the reflectance and to infer the emittance of the samples.

4. BRDF MODELS AND MEASUREMENT

BRDF data may be obtained by estimation based upon measured spectra or other data, by modeling from first principles, by direct measurement, or by a combination of limited measurement and empirical modeling.

4.1 SOURCES OF BRDF DATA

Estimation procedures, although useful, suffer from obvious limitations, in that assumptions of purely Lambertian or specular behavior are necessary.

For some material types, first principles models have been developed which do not depend upon laboratory reflectance measurements. An example of such a model is the Coatings Reflectance Engineering Evaluation Program (CREEP) model for paints and coatings. This model is driven by physical inputs such as particle size and distribution, pigment constituents, etc., and produces a computed BRDF directly. Models such as these show great promise but are limited in their use because they have been generated only for specific material types. Further, ascertaining input parameters to drive such models can be difficult and time consuming.

Direct measurement of BRDF is clearly the most desirable for the user, but is seldom available. A few facilities have capabilities to perform such measurements, but typically carry out these characterizations only over limited spectral regions or for limited geometrical configurations. A full characterization is prohibitive in terms of data volume and measurement time. For example, characterizing a spectral BRDF across the optical region of the spectrum assuming 550 spectral sampling points sampled at 2° intervals results in about 10⁸ measurements, even after invoking reciprocity and symmetry. Although this is a very large data set, it is not beyond the storage capacity of current computers. However, even if a nominal 2 seconds per measurement is assumed, the measurement times are clearly prohibitive. Directly measured BRDF data are utilized, but usually in validation of models, and at limited spectral regions or geometric configurations, as discussed above.

4.2 THE BEARD/MAXWELL BRDF MODEL

The most common source of BRDF data are from empirical or semi-empirical models. These models allow calculation of BRDF from parameters determined from laboratory reflectance measurements at a limited number of wavelengths. We have used one such model, the Beard/Maxwell Model (Maxwell et al., 1974a, 1974b). This model assumes that specular scatter occurs from a rough dielectric surface composed of smooth but randomly oriented first surface elements, that diffuse scatter occurs via multiple reflection of first surface elements, and volumetric scatter occurs via scatter from scattering elements beneath the first surface. The volumetric scattering area is assumed to be thick enough that no other material interface is encountered. In addition, the model includes consideration of shadowing and obscuration that occurs for the first surface scatter. The B/M BRDF model is of the form:

$$BRDF_{U,T} = \frac{R(\beta)}{R(0)} \cdot \frac{BRDF_{FS}(\theta_N) \cos^2(\theta_N)}{\cos(\theta_i) \cos(\theta_r)} \cdot SO + BRDF_D + \frac{2 \cdot BRDF_V}{\cos(\theta_i) + \cos(\theta_r)} \quad (13)$$

where:

- $BRDF_{U,T}$ = total BRDF for an unpolarized receiver and source,
- $R(\beta)$ = Fresnel reflection coefficient for angle β ,
- β = specular angle relative to the normal to the first surface scattering element,
- $BRDF_{FS}$ = measurement-based first surface BRDF curve,
- θ_N = zenith angle of the scattering element relative to the surface normal of the material,
- θ_i = incidence direction zenith angle,
- θ_r = reflectance direction zenith angle,
- SO = shadowing and obscuration function (see below),
- $BRDF_D$ = diffuse BRDF value, and
- $BRDF_V$ = volumetric BRDF scattering value.

Model input parameters include six scalars:

- the complex index of refraction, $n - ik$
- $BRDF_D$
- $BRDF_V$
- two shadowing and obscuration parameters, Ω and τ , and

a vector of measurement-based first surface BRDF values, $BRDF_{FS}(\theta_N)$.

Special cases, identified by the model input parameters, select either purely specular (mirror or Fresnel) or purely diffuse (Lambertian) components of the model. In this model, the BRDF parameters are extracted only at discrete wavelengths (known as reference wavelengths) at which laboratory measurements were performed.

Thus some procedure for interpolating/extrapolating the modeled BRDF across spectral bands of interest is necessary.

5 SPECTRO-RADIOMETRIC PARAMETER MODELING

5.1 Effective Directional Reflectance

The value of ρ_A in (8) represents an effective directional reflectance. At a given wavelength, this effective value may be calculated as:

$$\rho_A(\theta_r, \phi_r) = \frac{\int_{2\pi} \rho'(\theta_i, \phi_i; \theta_r, \phi_r) L_i(\theta_i, \phi_i) d\Omega_i}{\int_{2\pi} L_i(\theta_i, \phi_i) d\Omega_i} \quad (14)$$

where $\rho'(\theta_i, \phi_i; \theta_r, \phi_r)$ represents the BRDF evaluated at $(\theta_i, \phi_i; \theta_r, \phi_r)$; $L_i(\theta_i, \phi_i)$ represents the directional distribution of the hemispherical illumination, $d\Omega_i = \cos(\theta_i) d\omega_i$, the projected solid angle of the source; and integration over the hemisphere is implied.

Figure 4 depicts a general reflection geometry. The values (θ_i, ϕ_i) define the incident direction, and (θ_r, ϕ_r) denote the direction to the receiver, or sensor. The θ directions are defined relative to a normal to the surface (z-axis). The ϕ directions are relative to a user-defined reference direction in the material plane. Usually, the reference direction is chosen along the projection of the receiver in the material plane. Thus ϕ_r is usually zero, and ϕ_i represents a direction relative to the receiver (sensor) direction.

For clarity, the dependence of ρ_A upon the sensor direction (θ_r, ϕ_r) is shown explicitly. The incident illumination distribution function, $L_i(\theta_i, \phi_i)$, assumes the role of a weighting function in (14).

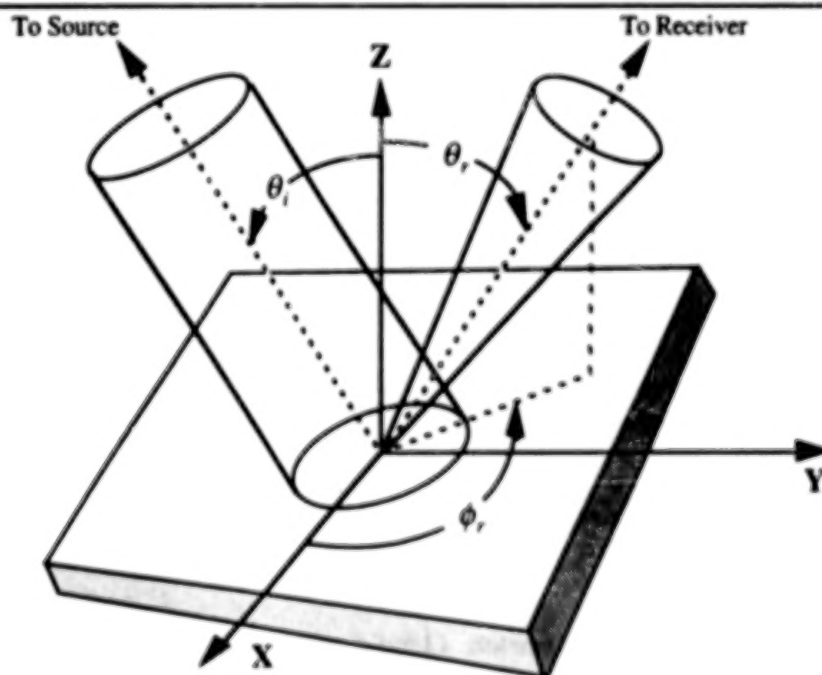


Figure 4. General Reflection Geometry

5.2 WEIGHTING FACTORS

For a horizontal surface, $L_i(\theta_i, \phi_i)$ represents the global hemispheric spectral irradiance from the sky, as shown on the left of Fig. 5. However, for an arbitrarily oriented surface $L_i(\theta_i, \phi_i)$ represents irradiance from a

hemisphere that is partially sky and partially ground, as shown on the right in Fig. 5. This concept is further illustrated in Fig. 6.

The $L_i(\theta, \phi)$ "inclined surface weighting factor" may be estimated in the following manner:

1. For each incident direction, the reflection angles relative to surface (θ, ϕ) are transformed to ground relative zenith angle and azimuth (γ, α) .

2. If $\gamma \leq 90^\circ$, then $L_i(\theta, \phi) = L_{sky}(\gamma, \alpha)$ (15)
the directional spectral sky radiance calculated, for example, from LOWTRAN

3. If $\gamma > 90^\circ$, then $L_i(\theta, \phi) = \epsilon_B L_{BB}(\lambda, T_G) + (1 - \epsilon_B) L_{SKY}$ (16)

where:

- ϵ_B = estimated average emissivity of background
- T_G = estimated temperature of background
- $L_{BB}(\lambda, T_G)$ = blackbody spectral radiance computed from Planck's Law
- $L_{sky}(\gamma, \alpha)$ = the directional spectral sky radiance
- L_{SKY} = total hemispheric atmospheric down-welling radiance (integrated over hemisphere).

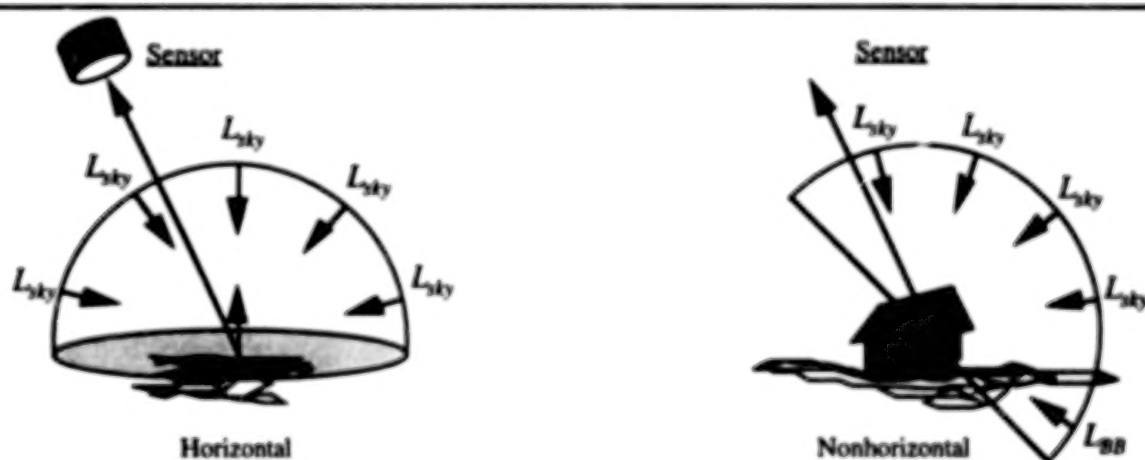


Figure 5. Hemispherical Illumination Sources

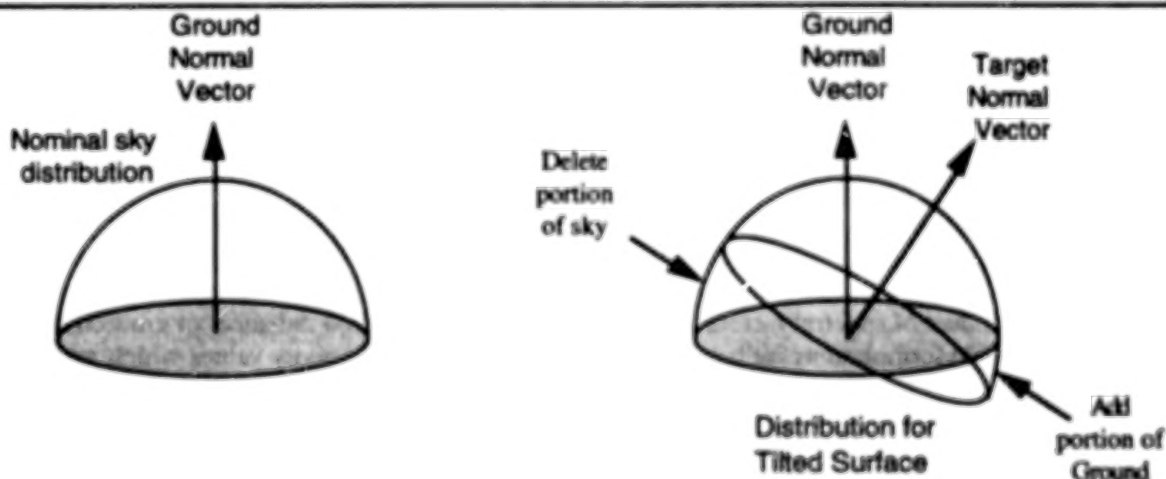


Figure 6. Creation of Illumination Function

With the above approach, it appears a value of $\rho_A(\theta_r, \phi_r)$ could be calculated via (14). Unfortunately, in many applications it would still be incorrect to use the value for anything but horizontal materials. This is because in a typical applications scenario, $\rho_A(\theta_r, \phi_r)$ is multiplied by the total hemispheric spectral radiance output, designated L_{SKY} , which still represents sky radiance only. Therefore, we can adjust the value of $\rho_A(\theta_r, \phi_r)$ so that the term $\rho_A(\theta_r, \phi_r) L_{SKY}$ is correct for an arbitrarily oriented surface by applying an appropriate weighting function in the numerator of Equation (14); i.e.,

$$\rho_A(\theta_r, \phi_r) = \frac{\int \rho'(\theta_i, \phi_i; \theta_r, \phi_r) L_i(\theta_i, \phi_i) d\Omega_i}{\int_G L_{sky}(\gamma, \alpha) d\Omega} \quad (17)$$

where:

- $L_{sky}(\gamma, \alpha)$ = sky radiance shape function
- $L_i(\theta_i, \phi_i)$ = hemispherical radiance shape function, given by (15) and (16)
- γ, α = zenith and azimuth angles, respectively, relative to the ground normal vector
- \int_M = integral over hemisphere above the Material
- \int_G = integral over hemisphere above the Ground
- $d\Omega_i$ = projected differential solid angle.

The numerator in (17) corresponds to the hemisphere actually seen by the material, while the denominator corresponds to the hemisphere represented by the integrated sky radiance L_{SKY} . Defined this way, the value of $\rho_A(\theta_r, \phi_r)$ loses its physical meaning as a reflectivity, since its value may become greater than unity. We may interpret $\rho_A(\theta_r, \phi_r)$ as the product of material reflectance and the ratio of energy received from the hemisphere above the material to the down-welling energy from the sky.

5.2 Bidirectional Solar Reflectance

The bidirectional reflectivity for insolation incident at the material surface in Equation 8 is given by

$$\rho_i = \rho'(\theta_{sun}, \phi_{sun}; \theta_{sensor}, \phi_{sensor}) \Omega_{sun} \cos(\theta_{sun}) \quad (18)$$

where $\theta_{sun}, \phi_{sun}; \theta_{sensor}, \phi_{sensor}$ are used to represent a specific realization of $\theta, \phi; \theta_r, \phi_r$ at the solar-sensor directions relative to the (possibly inclined) material surface, and Ω_{sun} is the solar solid angle subtended at the material surface. Note that ρ_i is a bidirectional quantity, as it depends on the positions of both the sun and the sensor. However, as defined, it is not a BRDF value, but a bidirectional reflectance, since it does not have units of inverse steradians.

6. BAND EFFECTIVE VALUES

In (9), the quantity L_{MEAS} is a band effective value, spectral integration inherent in recording this quantity via a sensor. In many instances, the quantities in square brackets, $[]$, in (9) are also estimated and supplied as band effective values. In this case, band effective values must be estimated for the sensor response, and for the material surface optical properties, ρ_D , ρ_A , and ϵ_A . A multiplication of band-averaged values will not be the same as the integral of the product of spectral factors yielding band effective reflected radiance (or emitted radiance). In this section, we provide formulations for band effective reflectivity and emissivity values which may be used when only band-integrated radiance and sensor response are available to the analyst.

Estimates for band equivalent Aperture Effective Values may be formulated for use in spectro-radiometric analysis of imaged remote sensor data. These involve integration of modeled BRDF values over spectral bands

of interest as well as over the hemisphere. Specifically, three aperture effective material parameters may be estimated for use in spectrometric/radiometric exploitation:

1. ρ_A = band-effective, effective directional diffuse reflectivity
2. ρ_s = band-effective bidirectional reflectivity at the solar angle
3. ϵ_A = band-effective directional emissivity.

The term "band-effective" refers to a weighted average value of a wavelength-dependent quantity over some spectral band. A "directional" quantity is one that depends on a single angular direction, in this case the direction pointing toward the sensor as seen at the material. The additional "effective" in the description of ρ_A and ρ_s indicates that the quantity is also a weighted average over the illumination hemisphere seen by the material, as discussed in Section 5. Recall also that ρ_s is a bidirectional quantity, as it depends on the positions of both the sun and the sensor, but not a BRDF value, since it does not have units of inverse steradians. Note also that in certain spectral regions, certain of the above terms are not useful (e.g. ϵ is not meaningful for $\lambda \leq 0.7\mu\text{m}$ except at extremely high temperatures).

6.1 BAND EFFECTIVE VALUES

The band-effective value \bar{x} of some spectral dependent quantity $x(\lambda)$ is given by:

$$\bar{x} = \frac{\int W(\lambda) x(\lambda) d\lambda}{\int W(\lambda) d\lambda} \quad (19)$$

where $W(\lambda)$ is the scene-atmosphere-sensor system weighting function. Note that if we normalize $W(\lambda)$ to some constant value W_0 , such that $W(\lambda) = W_0 w(\lambda)$, we may write:

$$\bar{x} = \frac{\int w(\lambda) x(\lambda) d\lambda}{\int w(\lambda) d\lambda} \quad (20)$$

This shows that the absolute values of the weighting function are unimportant; what is important is the spectral "shape" of the function.

To use (20) to compute band-effective values, we must apply the appropriate weighting functions. The appropriate functions are as follows:

$$(1) \text{ for } \rho_A, \quad W(\lambda) = r(\lambda) \tau_a(\lambda) L_i(\lambda) \quad (21)$$

$$(2) \text{ for } \rho_s, \quad W(\lambda) = r(\lambda) \tau_a(\lambda) \tau_s(\lambda) E_{\text{sun}}(\lambda) \quad (22)$$

$$(3) \text{ for } \epsilon_A, \quad W(\lambda) = r(\lambda) \tau_a(\lambda) L_{\text{BB}}(\lambda, T_M) \quad (23)$$

where:

$r(\lambda)$ = system-relative spectral response function, commonly called the "sensor response function";

$\tau_a(\lambda)$ = spectral transmission of the atmospheric path between the material and the sensor, estimated by "model environment" as discussed below;

$L_{\text{BB}}(\lambda, T_M)$ = blackbody spectral radiance computed by Planck's Law at material-apparent temperature, T_M , (estimated by the user; although this may seem circular, a rough estimate here is adequate to provide the appropriate "shape function");

$L_i(\lambda)$ = spectral distribution of the hemispherical illumination (discussed in Section 3);

$\tau_s(\lambda)$ = spectral atmospheric transmission of the path from the material to the sun, estimated by "model environment" as discussed below;

$E_{sun}(\lambda)$ = exo-atmospheric spectral irradiance of the sun.

Values of several of the above quantities, specifically, $\tau_a(\lambda)$, $L_i(\lambda)$, and $\tau_s(\lambda)$ may be computed using a model such as LOWTRAN. In this instance, however, they are not available in spectral form and are therefore not available to the user. Since these spectral values are to be used as parts of weighting functions, it is primarily their spectral shapes that are of interest. Thus, if these shapes can be reasonably approximated, the actual parameter values are of less importance. We have found that adequate approximations may be obtained by users, based upon scene-dependent "model environment" estimates, and LOWTRAN outputs based upon these.

A "model environment" defined by the user consists of a combination of

1. Standard atmosphere - tropical, mid-latitude summer, mid-latitude winter, sub-Arctic summer, sub-Arctic winter, 1962 US Standard, etc.,
2. Aerosol extinction code - urban, rural, maritime
3. Visibility - 1.5, 7.7, 17.7 km

6.2 APERTURE EFFECTIVE VALUES

The complete formal definitions of the three Aperture Effective Values (ϵ_A , ρ_A , and ρ_s) that can be calculated are summarized as follows. Values for ρ' are provided by a BRDF model (see Section 5).

$$\epsilon_A = 1 - \frac{\iiint \rho'(\theta_i, \phi_i; \theta_{sensor}, \phi_{sensor}; \lambda) r(\lambda) \tau_a(\theta_{sensor}, \lambda) L_{BB}(\lambda, T_M) \cos(\theta_i) \sin(\theta_i) d\theta_i d\phi_i d\lambda}{\int r(\lambda) \tau_a(\theta_{sensor}, \lambda) L_{BB}(\lambda, T_M) d\lambda} \quad (24)$$

$$\rho_A = \frac{\iiint \rho'(\theta_i, \phi_i; \theta_{sensor}, \phi_{sensor}; \lambda) r(\lambda) \tau_a(\theta_{sensor}, \lambda) L_i(\theta_i, \phi_i; \lambda) \cos(\theta_i) \sin(\theta_i) d\theta_i d\phi_i d\lambda}{2 \iint r(\lambda) \tau_a(\theta_{sensor}, \lambda) L_i(\gamma, \lambda) \cos(\gamma) \sin(\gamma) d\gamma d\lambda} \quad (25)$$

$$\rho_s = \rho'_s \Omega_{sun} \cos(\theta_{sun}) \quad (26)$$

where

$$\rho'_s = \frac{\int \rho'(\theta_{sun}, \phi_{sun}; \theta_{sensor}, \phi_{sensor}; \lambda) r(\lambda) \tau_a(\theta_{sensor}, \lambda) \tau_s(\theta_{sun}, \lambda) E_{sun}(\lambda) d\lambda}{\int r(\lambda) \tau_a(\theta_{sensor}, \lambda) \tau_s(\theta_{sun}, \lambda) E_{sun}(\lambda) d\lambda} \quad (27)$$

where $\theta_{sun}, \phi_{sun}; \theta_{sensor}, \phi_{sensor}$ are used to represent a specific realization of $\theta_i, \phi_i; \theta_s, \phi_s$ at the solar-sensor directions relative to the (possibly inclined) material surface. For the case of a horizontal surface, $\epsilon_A = 1 - \rho_A$.

7 SUMMARY AND CONCLUSIONS

As stated in the introduction, the purpose of this paper was to provide mathematical formulations useful to researchers and analysts of spectro-radiometric remote sensing data. We realize that the detail of the formulations presented may not be appropriate for many uses, and that in most current instances, approximations to these formulations may be more appropriate. However, as sensor technology and atmospheric modeling become more sophisticated, it will become necessary to have material optical properties which may match these technologies in their rigor.

The formulations presented are predicated upon the BRDF as the basis for emissivity and reflectivity calculations. We are studying further the measurement and modeling of BRDF, and the derived reflectivities and emissivities. Our interests are in validation and modification of the models, particularly the Maxwell/Beard BRDF model, and in ascertaining error estimates associated with spectra and modeled BRDF and derived directional reflectivities and emissivities.

REFERENCES

- Kneizys, F.X., et al, 1980: Atmospheric Transmittance/Radiance: Computer Code LOWTRAN 5. AFGL-TR-80-0067, Air Force Geophysics Laboratory, Hanscom AFB, Mass.
- Kneizys, F.X., et al., 1983: Atmospheric Transmittance/Radiance: Computer Code LOWTRAN 6. AFGL-TR-83-0187, Air Force Geophysics Laboratory, Hanscom AFB, Mass.
- Maxwell, J.R., and Weiner, S.F., 1974: Polarized Emittance Volume 1: Polarized Bidirectional Reflectance with Lambertian or Non-Lambertian Diffuse Components, BRL-CR-154, USA Ballistic Research Laboratories, Aberdeen Proving Ground, Maryland.
- Maxwell, J.R., Vincent, R., and Weiner, S.F., 1974: Polarized Radiance Volume 2: Polarized Spectral Emittance from 4 to 14 μm , BRL-CR-155, USA Ballistic Research Laboratories, Aberdeen Proving Ground, Maryland.
- Maxwell, J.R., and Weiner, S.F., 1974: Polarized Radiance Volume 3: Wavelength Dependence of Polarized Bidirectional Reflectance, BRL-CR-156, USA Ballistic Research Laboratories, Aberdeen Proving Ground, Maryland.
- Nicodemus, et al., 1977: Geometrical Considerations and Nomenclature for Reflectance. NBS Monograph 160, Washington, D.C.

SCENE/OBJECT CLASSIFICATION USING MULTISPECTRAL DATA FUSION ALGORITHMS

T.J. Kuzma, L.E. Lazofson, H.C. Choe, E.B. Preston and J.D. Chovan

Battelle
Columbus, OH 43201 USA

ABSTRACT

Near-simultaneous, multispectral, coregistered imagery of ground target and background signatures were collected over a full diurnal cycle in visible, infrared, and ultraviolet spectrally filtered wavebands using Battelle's portable sensor suite. The imagery data were processed using classical statistical algorithms, artificial neural networks and data clustering techniques to classify objects in the imaged scenes. Imagery collected at different times throughout the day were employed to verify algorithm robustness with respect to temporal variations of spectral signatures. In addition, several multispectral sensor fusion medical imaging applications were explored including imaging of subcutaneous vasculature, retinal angiography, and endoscopic cholecystectomy. Work is also being performed to advance the state of the art using differential absorption lidar as an active remote sensing technique for spectrally detecting, identifying, and tracking hazardous emissions. These investigations support a wide variety of multispectral signature discrimination applications including the concepts of automated target search, landing zone detection, enhanced medical imaging, and chemical/biological agent tracking.

1. INTRODUCTION

The spectral distribution of energy reflected and/or emitted from an object is a unique characteristic that may be exploited to discriminate the object of interest from the local background. Multispectral sensor fusion techniques can be used to solve a variety of classification and discrimination problems. Battelle's portable multispectral sensor suite has been used to collect simultaneous multispectral scene imagery in several data collection episodes. Implementing tailored data fusion algorithms, Battelle has processed some of the recorded imagery to solve classification problems including automatic detection of ground targets and location of aircraft landing zones. Upcoming investigations using active lidar technology include the detection and identification of gaseous emissions for environmental monitoring and chemical/biological weapons treaty verification. Also being studied are medical applications including imaging of subcutaneous vasculature, retinal angiography, and endoscopic cholecystectomy.

Algorithms implemented in the study included unsupervised maximum likelihood, Linde Buzo Gray, and "fuzzy" clustering algorithms along with Multilayer Perceptron and Learning Vector Quantization (LVQ) artificial neural networks. Supervised clustering of the data was also used. The algorithms were tailored to perform pixel-level classification of scene imagery using simultaneous multispectral measurements covering the UV, visible, near-IR, MWIR, and LWIR wavebands. Imaged outdoor scenes were comprised of tactical targets, buildings, roads, runways, and vegetation. Imagery were spatially co-registered with an RMS error on the order of 0.5 pixels. Outdoor scenes processed through the data fusion algorithms were displayed with artificial color to assess algorithm classification performance.

Waveband saliency analyses were performed to determine which spectral bands contained the bulk of the discriminating information for discerning objects in the scenes. Equally important, these analyses determine the optimum subset of wavebands for discriminating the problem phenomenology. Histograms and scatter plots of the multispectral data were used. For system implementation, the benefits of waveband

saliency analyses and judicious pruning are clear as a reduction in the number of system sensors minimizes cost, weight, complexity, and processing requirements.

To further verify classification robustness, algorithms were tested on outdoor scene imagery recorded over broad periods of time throughout the day. Results were excellent, indicating that scene classification is achievable despite temporal signature variations.

Results of the investigation are currently being implemented in a near-real-time hardware system. This system will implement a field-portable sensor suite feeding multispectral data through a fusion algorithm. The system output will provide an enhanced visualization on a flat-panel, color video display of objects classified within a scene.

2. MULTISPECTRAL IMAGERY DATA COLLECTION AND PROCESSING

Battelle's portable sensor suite consists of two high-resolution, high-sensitivity thermal imagers and four charge-coupled-device (CCD) cameras. A variety of spectral filters and telescopic lenses accompany the sensor suite to enable rapid system reconfiguration to support many unique imaging and data collection requirements. The attached photograph (Figure 1) of the multispectral sensor suite shows a sample system configuration using telescopic lenses on the thermal imagers for long distance, outdoor imaging. However, the sensor suite is easily reconfigured to support close-up multispectral imaging applications. With its collection of spectral filters, the Battelle sensor suite images over a large selection of wavebands in the visible, infrared, and ultraviolet regions of the spectrum. The CCD cameras generate 640 x 480 pixel images while the thermal imagers spatially sample a coarser resolution of 207 x 260 pixels in the MWIR and 207 x 344 pixels in the LWIR.

During two data collection episodes, Battelle's multispectral sensor suite was positioned looking downward from a 110-foot tower location. Imagery were then recorded over a period of several days. Feature-level sensor fusion was accomplished by feeding coregistered multispectral pixel intensity measurements into data fusion algorithms.

In the initial multispectral data collection episode conducted in June 1992 at Wright-Patterson AFB, Ohio, Battelle recorded scene imagery of a mobile missile launcher amidst roads, buildings, trees, and grass over a full diurnal cycle. Figure 2 depicts a 35 mm photograph of a scene containing the mobile missile launcher and ground clutter imaged simultaneously in six wavebands by the sensor suite. The multispectral imagery of this scene, processed through an artificial neural network, is displayed in Figure 3 with artificial color showing the different classes of objects (target, road, building, trees, and grass) identified by the network algorithm. To further verify robustness of the data fusion algorithm, it was tested on imagery recorded over broad periods of time throughout the day. Results were excellent, indicating that scene classification is achievable despite temporal signature variations.

Ground truth data covering a variety of meteorological parameters and site thermocouple measurements on targets and background were collected. This critical data, in conjunction with the multispectral imagery, provides a valuable record of weather and atmospheric conditions to support future modeling and analysis efforts using the imagery.

There are clear tactical advantages in implementing a data fusion algorithm to automatically perform multispectral data fusion for detecting potential targets. Chaotic and obscured operational environments pose a challenge for human observers looking for targets and threats. Even in more placid scenarios, system operators may become task and data saturated to the point where potential threats go unnoticed. Automatic target detection/cuing can leverage an operator's effectiveness by reducing workload and increasing probability of target detection. Battelle's investigation implementing sensor fusion of multispectral target and background signatures supports the concept of automated target search.

In conjunction with the Federal Aviation Administration's Runway Detection Program, Battelle collected additional multispectral imagery in a separate measurement episode and processed the data using analysis and fusion techniques to detect a runway at Wright-Patterson AFB, discriminating it from other objects in the area using spectral characteristics. Figure 4 shows a 35 mm photograph of a scene imaged in multiple wavebands consisting of a runway, roads, vegetation, and tactical targets at approximately 3 km. Figure 5 displays, in two colors, the binarized result of a data fusion algorithm merging the multispectral data to segment, or detect, the runway.

3. DATA CLUSTERING ALGORITHMS

As a baseline, the study began with an investigation using an unsupervised maximum likelihood statistical algorithm for clustering the multispectral data. Displaying the clustered pixel classes with artificial color indicated that fusion of data from all six wavebands successfully distinguished the classes of interest. Using only the visual and near-infrared bands, the camouflage-green mobile missile launcher was difficult to discriminate from background trees. Employing data from the two thermal bands, the clustering algorithm confused the mobile missile launcher with paved road, but successfully separated vegetation from man-made objects. Combining the data from all six wavebands successfully clustered the classes of interest, distinguishing target pixels from background pixels as well as differentiating between vegetation and man-made objects. Pruning combinations of sensor inputs indicated that the green-filtered visual band and the 8-12 micron thermal band together contained most of the key information for distinguishing the classes. Clustered classes were displayed with artificial color.

A version of the Linde Buzo Gray clustering algorithm was also used on the same multispectral scene imagery. (Linde, 1980) Results were satisfactory.

A fuzzy clustering algorithm was also applied to the multispectral scene imagery containing the mobile missile launcher target. Similar to other techniques, this algorithm carved different object regions within the multispectral feature space, except that it allowed for overlapping class possibilities among the data clusters. In other words, a specific point in the multidimensional pattern recognition feature space may have been simultaneously designated as belonging to more than one cluster or object class, with weighted possibility factors pertaining to the "degree of belonging" to each class. However, the user must ultimately select a defuzzifying threshold to apply when making a final classification decision.

4. NEURAL NETWORK ARCHITECTURES AND TRAINING RESULTS

The scene employed in the initial investigation consisted of a mobile missile launcher parked on a grassy area in front of a grove of trees (Figure 2). Additional objects within the scene consisted of paved areas and buildings. Imagery from all measured spectral bands were spatially coregistered, or aligned, with an RMS error on the order of 0.5 pixels. To assess classification robustness, the tailored neural networks were trained and tested on near-simultaneous data from scenes imaged at different times of day. Learning coefficients, number of computational nodes, and node transfer functions were varied to optimize performance of a Multilayer Perceptron network and a modified Learning Vector Quantization (LVQ) network employing "conscience" and adding training noise. Both architectures trained successfully, converging within several thousand training iterations to a 98% pixel classification accuracy on separate test data. As shown in Figure 3, trained network outputs of classified pixels from a full scene were displayed with artificial color to pictorially convey the near-perfect segmentation and classification of the five class regions (mobile missile launcher, buildings, paved road, trees, and grass). Network architectures were developed and tailored with the NeuralWorks Professional II/PLUS software package by NeuralWare, Inc. (NeuralWare, 1992) Image pixel data were processed with the Geographic Resources Analysis Support System (GRASS), a Geographical Information System (GIS) possessing some image processing capabilities. (GRASS, 1991)

The initial training data set consisted of 750 vectors (pixels) comprised of 150 for each of the five classes. The corresponding test data set contained 250 vectors including 50 pixels for each class. The trained neural networks were later used to classify all 233,000 pixels imaged in a full scene, of which approximately 5600 were target pixels. Results were excellent, indicating that the trained neural networks served as robust target/background classifiers. With only limited training, approximately 90% of the on-target pixels were correctly classified and over 99% of the background pixels were correctly classified as not being on target. The contiguity of the on-target pixels offers an advantage in that a few misclassified on-target pixels will not detract from the target segmentation decision. Also, image processing techniques, such as image convolution with a median filter, may serve to "clean up" many of the misclassified pixels.

5. SUPERVISED CLASSIFICATION

Another algorithm applied to the multispectral data set was a supervised classification algorithm. The supervised algorithm generated a pixel intensity histogram in each waveband for pixels sitting on a user-designated object (i.e. target) within an imaged scene. Thresholds were established near the tails of the histograms. Pixels were then classified as target pixels if the intensity values in each waveband fell within the established thresholds on the histograms.

6. CLASSIFICATION ROBUSTNESS FOR TEMPORAL SIGNATURE VARIATIONS

To further verify the classification robustness of the LVQ neural network for target detection, the network was trained and tested on imagery recorded over broad periods of time throughout the day. Results were excellent, indicating that automatic target detection is achievable despite target and background signature variations throughout the day.

7. WAVEBAND SALIENCY ANALYSIS

Waveband saliency analyses were performed to determine which spectral bands contained the bulk of the discriminating information for discerning targets amidst cluttered background. Equally important, these analyses investigated the waveband combinations providing complementary information for finding targets. Spectral inputs to the networks were ultimately pruned to include only the green, near-infrared, and LWIR wavebands. For system implementation, the benefits of this are clear as a reduction in the number of system sensors minimizes cost, weight, complexity, and processing requirements.

8. HARDWARE IMPLEMENTATION

Results of the investigation are currently being implemented in a near-real-time hardware system. This system will be a field-portable sensor suite feeding multispectral data through a tailored data fusion algorithm to provide an enhanced visualization output on a flat-panel, color video display. This field-portable hardware may be used to further develop and validate sensor fusion algorithms for different applications.

9. MEDICAL APPLICATIONS

The transfer of multispectral sensor fusion technology has been explored with respect to its application to medical problems. Medical images are typically interpreted by physicians with years of extensive training and experience. By adapting multispectral sensor fusion techniques to medical image processing, a new tool could be provided to physicians to decrease their workload and assist them in making better decisions. Quite

possibly, some of the more routine tasks of health professionals that make use of medical images could be fully automated using these techniques.

Three candidate medical imaging areas have been explored thus far. The first of these was the noninvasive recognition of human blood vessels. Human hands were imaged using infrared and visual spectra to characterize the subcutaneous vasculature. A second problem was image understanding during endoscopic cholecystectomy. In this procedure, a surgeon uses a camera that is inserted into a small incision in the patient to perform gall bladder surgery, viewing only a two-dimensional monitor of the internal image. This image, of course, does not contain all of the information that the surgeon would like to have in performing the surgery. The multispectral sensor fusion methodology was used to describe the various objects in these images, thus providing more information to the surgical team.

Retinal perfusion during angiography was also investigated. In retinal angiography, a dye is injected into a patient's arm, and then the perfusion of the dye through the vasculature in the retina is studied using a series of still images. Multispectral sensor fusion was explored to assist in describing how the dye moves through this vasculature over time.

10. SUMMARY

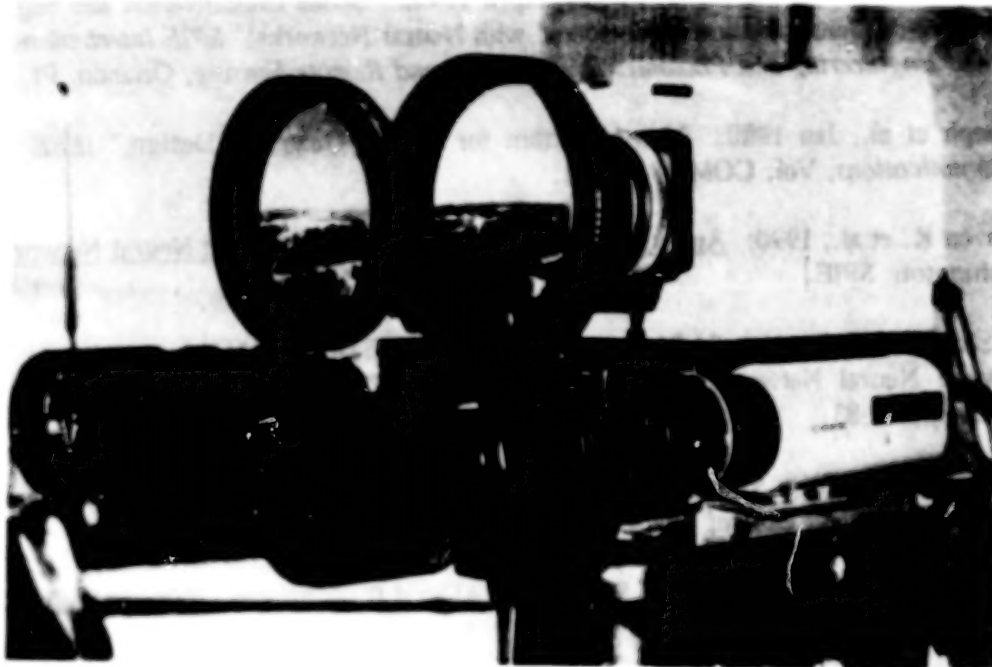
The spectral distribution of energy reflected and/or emitted from an object is a unique characteristic that may be exploited to discriminate the object of interest from the local background. Near-simultaneous, multispectral, coregistered imagery of ground target and background signatures were collected over a full diurnal cycle in visible, infrared, and ultraviolet spectrally filtered wavebands using Battelle's portable sensor suite. The imagery data were processed using classical statistical algorithms, artificial neural networks and data clustering techniques to classify objects in the imaged scenes. Imagery collected at different times throughout the day were employed to verify algorithm robustness with respect to temporal variations of spectral signatures. The investigation supports a wide variety of multispectral signature discrimination applications including the concepts of automated target search, landing zone detection, enhanced medical imaging, and chemical/biological agent tracking.

Results of the study were excellent and indicated that the chosen data fusion algorithm was not critical to solving the object classification problem. Rather, the system solution lies in choosing the best set of features (wavebands) for discriminating the object of interest (i.e. target, runway, etc.) from its background surroundings. With a set of wavebands judiciously chosen for discriminating the object of interest under established conditions, any of the mentioned algorithms can be tailored to use the multispectral information to effectively classify the imagery.

11. REFERENCES

- DeRouin, Ed and Joe Brown, 1992: "Hyperspectral Data Fusion for Target Detection and Segmentation Using the Intel ETANN," *1992 Digest of Papers, Government Microcircuit Applications Conference*, 39-42.
- Kuzma, Thomas J. and Laurence E. Lazofson, 24-27 May 1993: "Automated Target Detection Using Multispectral Sensor Fusion Implemented with Neural Networks," *1993 Automated Mission Planning Society Symposium*, San Antonio, TX.
- Kuzma, Thomas J. and Laurence E. Lazofson, March 1993: "Scene Classification and Segmentation Using Multispectral Sensor Fusion," *1993 Meeting of the IRIS Specialty Group on Passive Sensors*, Applied Physics Laboratory/Johns Hopkins University, Laurel, MD.

- Lazofson, Laurence E. and Thomas J. Kuzma, April 1993: "Scene Classification and Segmentation Using Multispectral Sensor Fusion Implemented with Neural Networks," *Sixth National Symposium on Sensor Fusion*, Orlando, FL.
- Lazofson, Laurence E. and Thomas J. Kuzma, April 1993: "Scene Classification and Segmentation Using Multispectral Sensor Fusion Implemented with Neural Networks," *SPIE International Symposium on Optical Engineering and Photonics in Aerospace and Remote Sensing*, Orlando, FL.
- Linde, Yoseph et al., Jan 1980: "An Algorithm for Vector Quantizer Design," *IEEE Transactions on Communications*, Vol. COM-28, No. 1.
- Rogers, Steven K. et al., 1990: An Introduction to Biological and Artificial Neural Networks. Bellingham Washington: SPIE.
- Seldin, J.H. and J.N Cederquist, 24-26 August 1992: "Classification of Multispectral Data: A Comparison Between Neural Network and Classical Techniques," *Government Neural Network Applications Workshop*, 79-83.
- Sims, S. Richard F. and Belur V. Dasarathy, December 1992: "Automatic Target Recognition Using a Passive Multisensor Suite," *Optical Engineering*, 31: 2584-2593.
- Geographic Resources Analysis Support System (GRASS) 4.0 (Software), 1991, U.S. Army Construction Engineering Research Laboratory.
- NeuralWorks Professional II/PLUS Software, 1992, NeuralWare, Inc., Pittsburgh, PA.



Battelle Imaging Sensor Suite Bands:

UV 0.2 - 0.4 μm

blue 0.42 - 0.49 μm

green 0.51 - 0.56 μm

red 0.61 - 0.66 μm

NIR 0.81 - 0.95 μm (vegetation)

Subband MWIR 3.5 - 4.1 μm

Subband MWIR 4.5 - 5.0 μm

Broadband MWIR 3.0 - 5.3 μm

Subband LWIR 7.81 - 9.8 μm (CW)

Subband LWIR 9.98 - 11.41 μm (CW)

Subband LWIR 9.14 - 9.68 μm (CW)

Subband LWIR 10.497 - 10.857 μm

(CO₂ laser/CW)

Broadband LWIR 8.0 - 13.0 μm

Fig. 1. Battelle multispectral sensor suite.

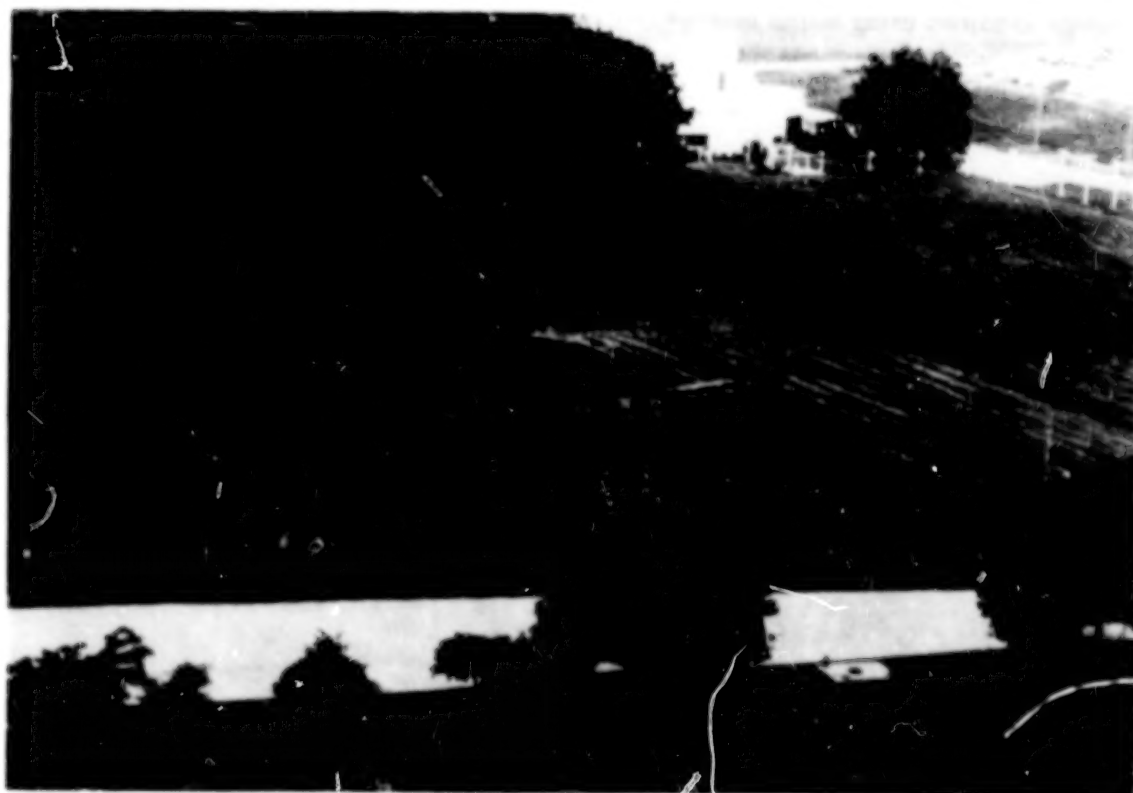


Fig. 2. Multispectral signature test - tower view.

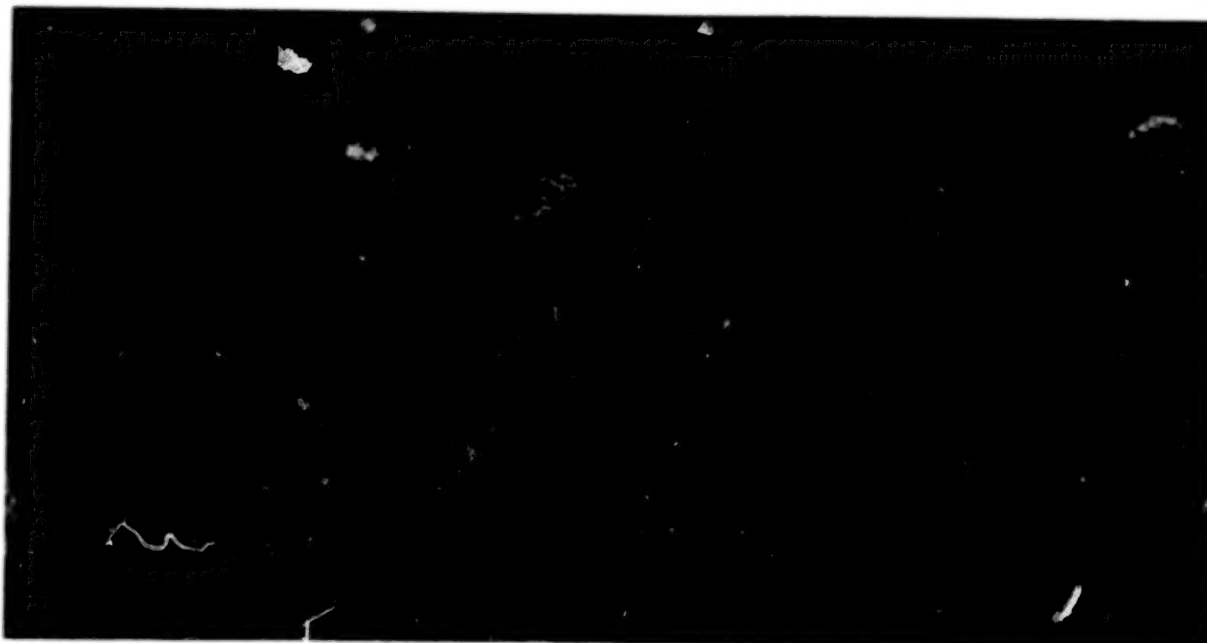


Fig. 3. Image classified using neural network.



Fig. 4. FAA landing program data collection - imaged scene.

BEST COPY AVAILABLE

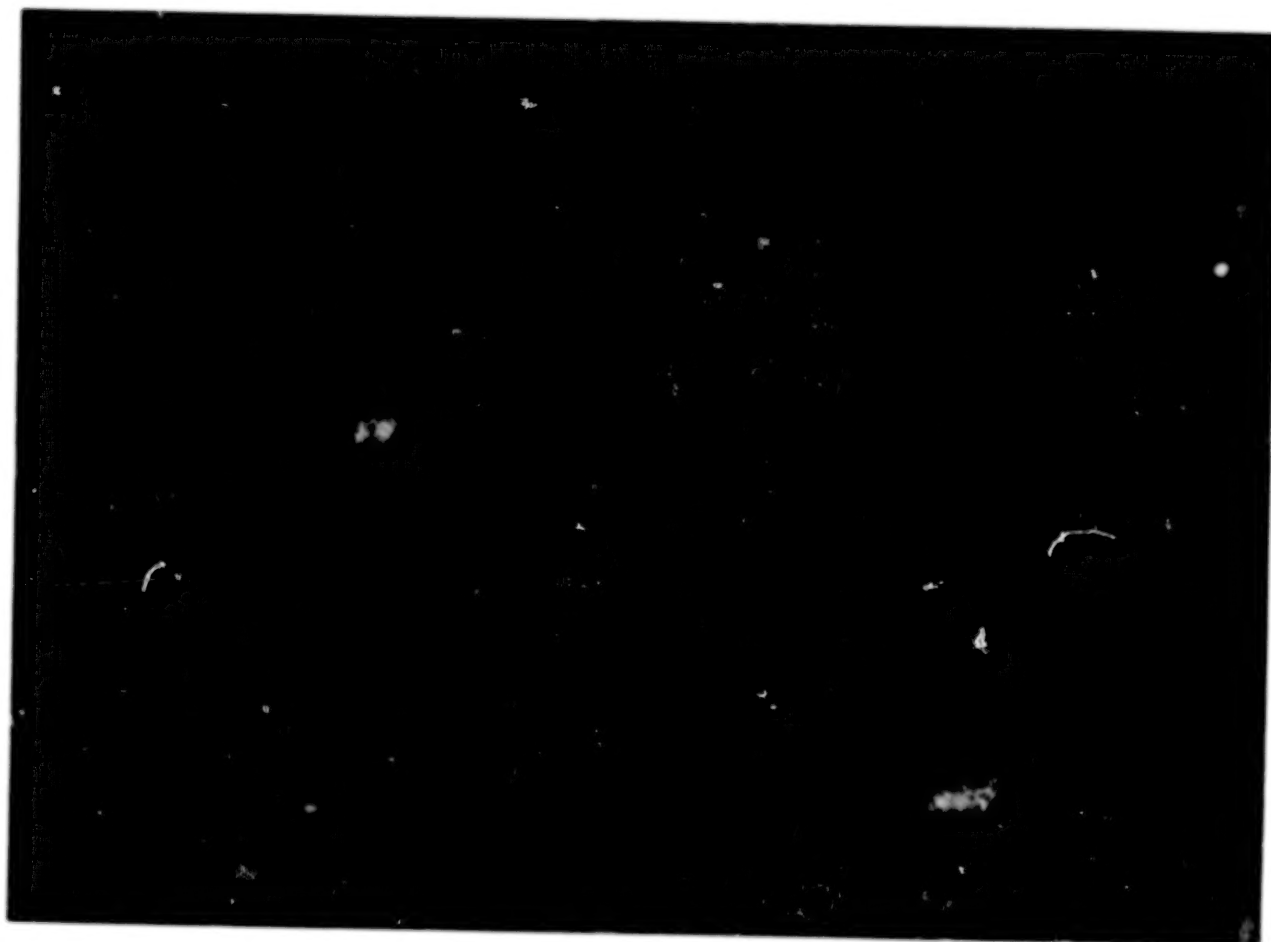


Fig. 5. Segmented runway using unsupervised classification - 1800 hours, 3km.

BEST COPY AVAILABLE

BLANK PAGE

AN ASSESSMENT OF THE EFFECTS OF DATA COMPRESSION ON MULTISPECTRAL IMAGERY

Ken Riehl Jr., Carey D. Erdman
Itek Optical Systems
10 Maguire Rd.
Lexington, MA 02173-3199, U.S.

ABSTRACT

The Defense Landsat Program Office (DLPO) has funded development of advanced multispectral data compression techniques because future multispectral land remote sensing satellite systems would likely be constrained in terms of cross-link and/or downlink communications bandwidth. In support of this initiative, a study was performed to characterize the effects of data compression on multispectral imagery¹. Results are presented on the development of different types of data compression utility measures (metrics) in support of advanced Landsat concepts, and on the relationship of those metrics to image characteristics, such as scene dynamic range and entropy. Fourteen data compression metrics were used to evaluate three different compression techniques using 23 multispectral images. The images consisted of up to 12 spectral bands each and ranged in spatial resolution from 2 to 10 meters.

1. INTRODUCTION

The Defense Landsat Program Office (DLPO) has sponsored studies to address the design of future remote sensing systems and to develop technologies which will enable such future systems. Among these efforts is the development of data compression algorithms specifically designed for multispectral imagery (Vaughn et al., 1993). The need for data compression results from a "requirements pull" to have better spatial quality, more spectral channels, and as much collected area as possible. Even improved future data links will operate at some finite rate and hence, data compression becomes a fundamental ingredient in system trade-off strategies.

The requirement for data compression is not unique to multispectral systems. Single-band panchromatic sensors employ data compression to increase the amount of collected area that can be transmitted to the ground. On the ground, data compression is used to reduce the number of bits per image pixel that must be stored. What is new for multispectral data compression however, is the means to quantify the impact of compression on multispectral data and its utility.

Even with single-band imagery, there is no single method for measuring the degradation (error) due to data compression. The most common measures of compression error are statistical, such as root mean square error. As multispectral data compression effects had not been previously measured in any standardized manner, a study was performed to develop candidate metrics and to use these to measure the performance of two multispectral compression algorithms which the DLPO was sponsoring. The algorithms were an adaptive differential pulse code modulation technique (Brower et al., 1994) and a transform-based procedure (Saghri et al., 1994).

¹The research reported here was funded by the Defense Landsat Program Office.

The relative goodness of the metric set was determined in three steps:

1. Apply each metric to the compressed imagery and assess the significance of results
2. Correlate the results of the metrics to ascertain redundancy
3. Correlate metric results with the uncompressed imagery characteristics to determine the extent to which compression effects can be predicted from scene characteristics.

The objective of this paper is to report on the metrics selected and developed for (the DLPO) this study. Illustrative results of measurements made on the output of the DLPO algorithms are presented to contrast the sensitivity, consistency, redundancy, and usefulness of the metrics. It is expressly not the intent to recommend or otherwise document preferred characteristics of the tested data compression algorithms.

This paper is organized into seven sections, including this introduction. The second section, Metric Development, describes the developed metrics and why they were selected for test. Section III, Study Parameters, provides an overview of the study, including: the test imagery, compression algorithms and tested bit rates. Illustrative results from selected metrics are presented in Section IV, Results and Analysis. Metric to metric correlations are presented and discussed in Section V; these were performed to assess metric redundancy. Highly correlated metrics are duplicative in their assessment of data compression effect, and should be considered for removal from a standard set. Section VI, Metric Relationships to Image Characteristics, shows relationships between metrics and uncompressed imagery characteristics, like scene dynamic range and entropy. These data begin to allow prediction of compression effect based on the original images' characteristics. Finally, the work is summarized and top-level conclusions are made in Section VII.

II. METRIC DEVELOPMENT

The developed/evaluated metrics are arranged in two basic categories: (1) statistical, and (2) multispectral machine applications. "Statistical metrics" are those which produce a statistical measure of the effect of compression. Although these measures may be difficult to relate directly to user application impacts, they provide a quantitative way to compare the relative performance of compression algorithms as a function of bit rate. Machine application metrics are those that measure the impacts of compression on multispectral imagery user applications. The metrics are listed below, and briefly described in the following sections.

Statistical

- Global (applied over whole image)
 - Maximum, Mean Absolute, RMSE
 - Signal Quantization Noise Ratio
 - Spectral Vector Difference
- Local (computed over local scene regions)
 - Edge/non-edge MAE and RMSE
 - Texture (mean, variance, edge gradient)
 - Likelihood ratio
 - Power spectrum

MS Machine Applications

- Classification error
 - Unsupervised
 - Supervised
- Principal component error
- Control point measurement
- Simultaneous diagonalization

2.1 STATISTICAL METRICS

Statistical metrics can be further categorized as global (full-scene) and localized measures. Global metrics yield a single number for the entire image, while localized metrics yield information on sub-scene areas. Traditional data compression metrics typically fall into the category of global measures, such as: maximum error, mean absolute error (MAE), and root mean square error (RMSE). Local area metrics are often more sensitive to compression error than global metrics since they evaluate specific portions or characteristics of a scene and are not diluted by averaging performance over the entire scene.

In this study, most of the statistical metrics were applied to each spectral band of an image independently and then the mean and variance were computed over bands. Confidence intervals were used to show the relative spread of the error over bands at each bit rate.

2.1.1 Global Statistical Metrics

Maximum Error is the maximum difference (error) between the uncompressed and compressed images. It shows the worst/most objectionable error, and is important since a data compression algorithm may produce low error over the entire scene, but objectionable error in isolated regions.

Mean Absolute Error is the average absolute difference between the uncompressed and compressed images. It provides the most straightforward measure of the average error over the entire scene and is useful for comparing the relative performance of one algorithm against another.

Root Mean Square Error is the average of the square root of the sum of squares of the difference between the uncompressed and compressed images. It is one of the most common estimates of compression error and as such is useful for comparing results to different studies.

Signal Quantization Noise Ratio is the ratio of the uncompressed image standard deviation to the RMS error between the uncompressed and compressed images. It provides a measure of compression error relative the uncompressed image.

Spectral Vector Difference is similar to RMSE, but is calculated through image spectral bands. It is a measure of the average spectral change between the uncompressed and compressed images.

2.1.2 Local Statistical Metrics

Edge/non-edge metric calculates MAE and RMSE on the edge and non-edge areas (inverse of edge) of the image. This is a particularly useful metric to assess compression artifacts because compression algorithms generally yield higher error on edges than on others portions of a scene. The metric uses a Laplacian filter to identify the edges for each spectral band. The filtered images are thresholded and binary edge and non-edge masks are made for each band. The masks are combined to create a multispectral edge mask and then grown by three pixels radially to capture the entire edge transition. MAE and RMSE are computed for pixels within the edge and non-edge masks, and the number of pixels in the uncompressed and compressed edge masks are recorded and compared.

Texture metric calculates MAE and RMSE on three types of image texture (mean, variance, edge gradient). The texture images are produced by sliding a 3x3 pixel window over the uncompressed and compressed images. The mean texture image is a simple box-car average over the sliding window, variance is simply the variance over the window, and edge gradient is the average of the

difference between the four pixels adjacent to the center pixel. These metrics are useful because image classification may use image texture to help classify a scene.

Likelihood ratio is a test of similarity between the uncompressed and compressed image's covariance matrices, derived from 25x25 pixel window areas. It uses a chi-square test to determine if the likelihood ratio statistics are different between the uncompressed and compressed images.

Power spectrum evaluates the spatial frequency differences between the uncompressed and compressed images. Power spectrums are calculated on 16 pixel block areas, and then RMSE is calculated between the compressed and uncompressed power spectrums.

2.2 MACHINE APPLICATION METRICS

Unsupervised classification is performed on the uncompressed and compressed images using training sets which are statistically derived as the most spectrally separable segmentation of the image. A confusion matrix is constructed to show the number and percentage of pixels for each class that changed classes from the uncompressed to the compressed image. Classification error (e.g., pixels that changed class) is summarized for each image using both a weighted (by the number of pixels in each class) and unweighted average of the correctly classified pixels of all the classes. Also, the class exhibiting the highest classification error is identified and its percentage correctly classified pixels recorded.

Supervised classification is similar to unsupervised; the main difference being that the 12 or more training sets were operator-derived, instead of derived by a computer. The information classes resulting from supervised classification may in fact be similar spectrally.

Principal component error is calculated between the 32 bit components resulting from the uncompressed and compressed imagery. Although compression error could be analyzed separately for each component, MAE and RMSE are averaged for the first three components. The rationale for this is that the first three components are often used as a way of representing most of the MS information contained in a multiband image. Measurement of principal component compression error is important not only because it is a commonly used processing technique for MS imagery, but also because examination of the higher order components is one of the most sensitive spectral assessments of change resulting from compression.

Control point location error locates 15 control points on a three-band color infrared composite of each uncompressed image, using both an experienced human operator and a machine-based autocorrelation procedure. Point identification error between the uncompressed and compressed image (to a precision of 1/5th of a pixel) is measured in x and y, and the mean error calculated over the 15 points. Control point selection is a basic requirement to establish geometric control of imagery in the production of orthophotos and image mosaics, as well as in data fusion and other MSI applications. The accuracy of how well control points are selected significantly effects the integrity of the final product.

Simultaneous diagonalization involves linearly transforming the uncompressed and compressed images based on operator-provided training set data to maximize spectral discrimination of specific features. This metric is used to assess compression impacts on feature spectral discrimination, an important component of automatic target recognition and image classification.

Normalized Difference Vegetation Index (NDVI) ratio (red-NIR/red+NIR) is computed on the uncompressed and compressed images. NDVI values are segmented into 16 bins and a confusion

matrix is used to show how many pixels changed bins between the uncompressed and compressed images. NDVI is a popular use of MS imagery to assess the relative presence and vigor of vegetation.

III. STUDY PARAMETERS

Twenty-three unique multispectral images were compressed to seven different bit rates by the two MSI-based compression algorithms, and eleven bit rates by JPEG. The fourteen compression metrics just described were developed and applied to the compressed imagery. Because of the large amount of test imagery and resulting metric output, not all metrics were applied to all images.

3.1 IMAGERY

Imagery for this study was selected to represent a variety of multispectral collection systems, scene content and acquisition conditions. Imagery from ERIM's M-7 sensor and NASA's Advanced Solid-State Array Spectroradiometer (ASAS) were utilized. The imagery scene content included urban, rural, forested, desert, water and snow, and the imagery ranged in spatial resolution from 2 - 10 meter Ground Sample Distance (GSD). The M-7 has up to 16 collection bandpasses, ranging from ultra-violet to long wave infrared. Twelve of the 16 available bands were utilized for this study, from visible through reflected IR (0.4 - 2.5 μm). About half the test images included all 12 bands; the others were composed of a sub-set of bands. This was done to test the sensitivity of the compression algorithms to band-to-band correlation (i.e., fewer bands implies less correlation). Most of the images were sub-sectioned to 512² pixels, but larger areas (up to 6,600 lines) were compressed to allow monitoring of compression rate over changing scene type.

3.2 COMPRESSION ALGORITHMS

Three compression techniques were evaluated as part of this study. Two of these took advantage of the redundant information between highly correlated spectral bands to reduce compression error. The third algorithm, JPEG, is an industry standard and was used to compare the performance of the two advanced algorithms with current capabilities. One of the "multispectral" algorithms, henceforth called "Algorithm 1" performed a Karhunen-Loève transform on all bands to take advantage of redundant spectral information and then used JPEG to compress the transformed images. The second algorithm used a 2D and 3D DPCM compression procedure. The images were compressed to seven bit rates, ranging from 0.15 bits per pixel (bpp) to 2.5 bpp.

IV. SAMPLE METRIC RESULTS AND ANALYSIS

4.1 STATISTICAL METRICS

4.1.1 Global Statistical Metrics

Figure 1, on the following page, shows typical output from the statistical metrics. Using Image 11 as an example, average MAE and maximum error are plotted with 95% confidence bands, for all three algorithms as a function of bit rate. Compared to mean absolute error, maximum error is higher in magnitude and the confidence intervals are wider indicating there is more band-to-band variability than for mean absolute error.

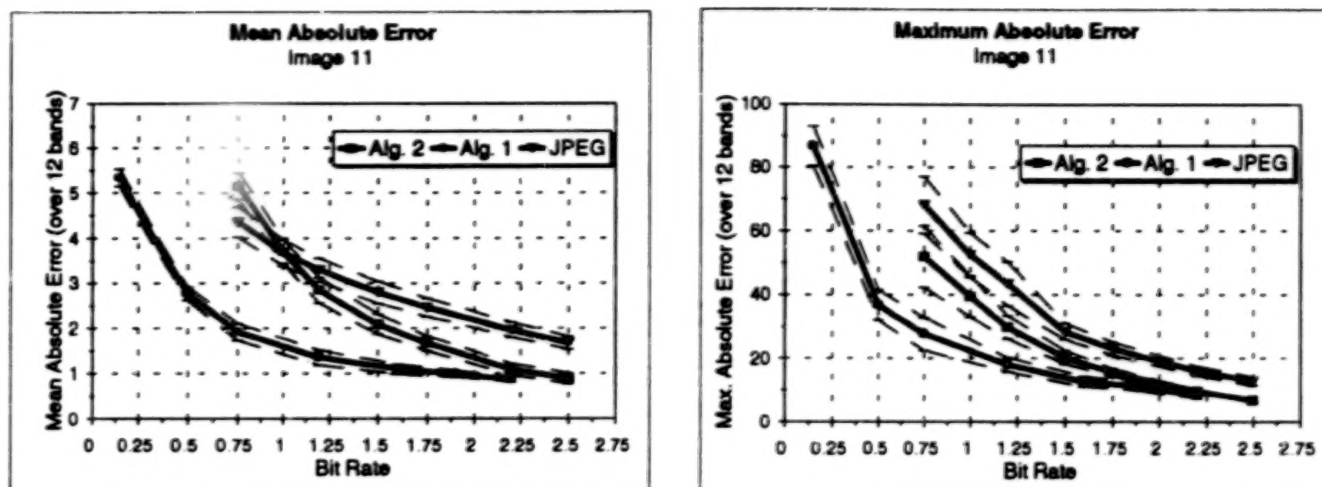


Figure 1. Mean Absolute Error and Maximum Absolute Error Applied to Image 11.

4.1.2 Local Statistical Metrics

Illustrative results are shown for both edge and non-edge areas of Image 11 in Fig. 2. It can be seen that all three algorithms have higher error in the edge regions than otherwise.

4.2 MACHINE APPLICATION METRICS

4.2.1 Principal Components

Illustrative findings are shown for Image 11 in Fig. 3 on the following page. Overall, there is little difference in compression error between Algorithms 1 and 2; compression error is relatively constant above 1 bit per pixel and the magnitude of the error is small. Visual evaluation of the first three components supported this finding. However, a marked difference was seen between the original and compressed components, and between the two algorithms themselves in the higher order components for higher compression rates. Components derived from Algorithm 1's output showed DCT blocks boundaries, while Algorithm 2's higher order components appeared noisy compared to the uncompressed components. Those users who do utilize higher order components would be impacted by these artifacts.

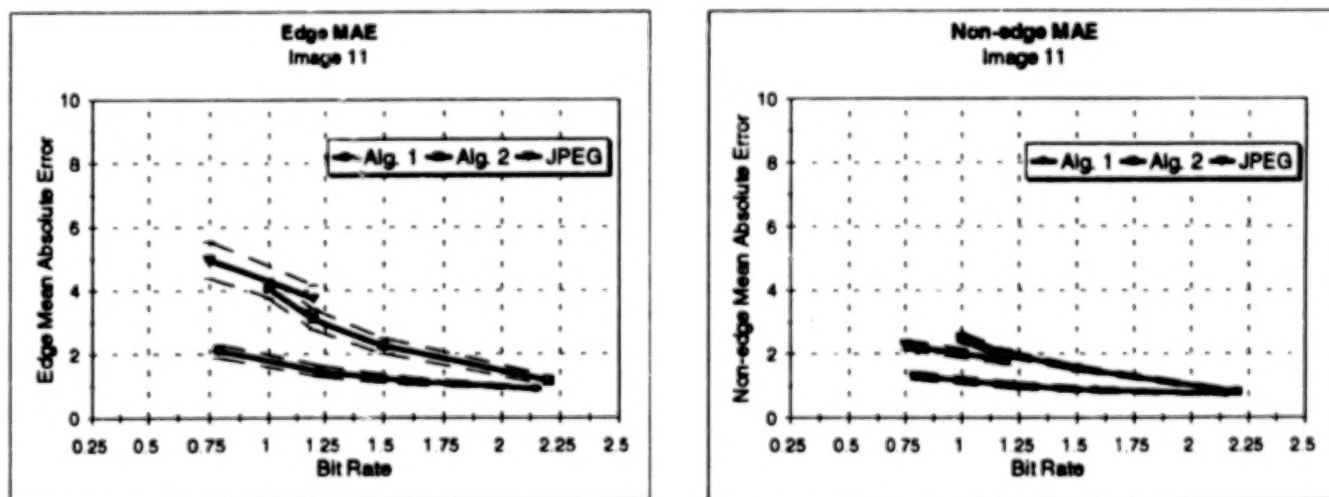


Figure 2. Edge/Non-edge Metric Applied to Image 11.

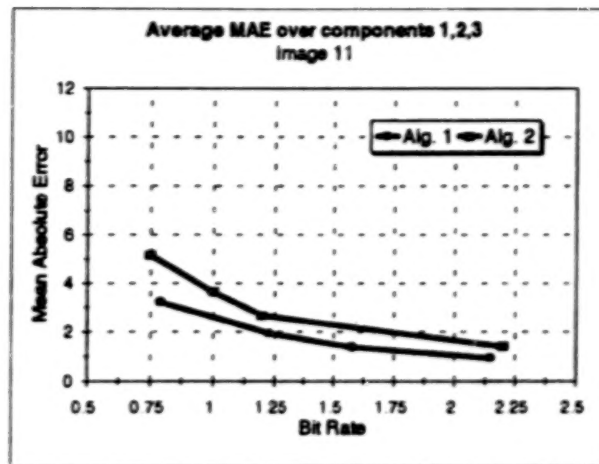


Figure 3. Average MAE over first three principal components for Image 11.

4.2.2 Classification

Figure 4 shows illustrative results from the unsupervised and supervised classification metrics. Overall, unsupervised classification yielded better than 90% unchanged pixels at 1 bit per pixel and over 95% at 1.5 bits per pixel for the two multispectral data compression algorithms, JPEG; was slightly worse. Supervised classification was more impacted by compression, with just over 80% of the total pixels unchanged from the uncompressed to the compressed images at 1.0 bits per pixel and about 85% pixels unchanged at 1.5 bits per pixel. The comparison between classification technique performance is somewhat misleading because supervised classification used more classes, on average, than were used for unsupervised classification. Image 11, for example, was segmented into 12 classes in the unsupervised classification and 14 classes for the supervised procedure. Findings appeared to indicate that compression error was dependent on the number of spectral classes into which the image had been segmented. The reason for this is as the number of feature classes is increased, the statistical difference between those classes decreases, so individual pixels are more likely to switch classes.

4.2.3 Control points

Figure 5 shows results using Image 11 illustrative of the control point metric. In summary, for the algorithms and compression rates tested, (1) control point location was insensitive to compression error, (2) there was no distinct difference between measurements in the x and y directions, and (3) control point positional error

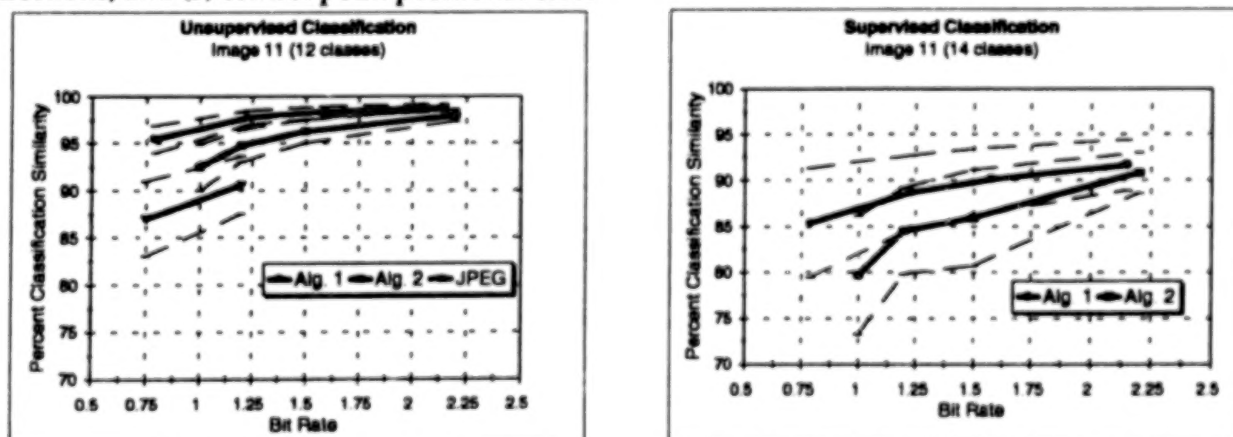


Figure 4. Unsupervised and Supervised Classification Error for Image 11.

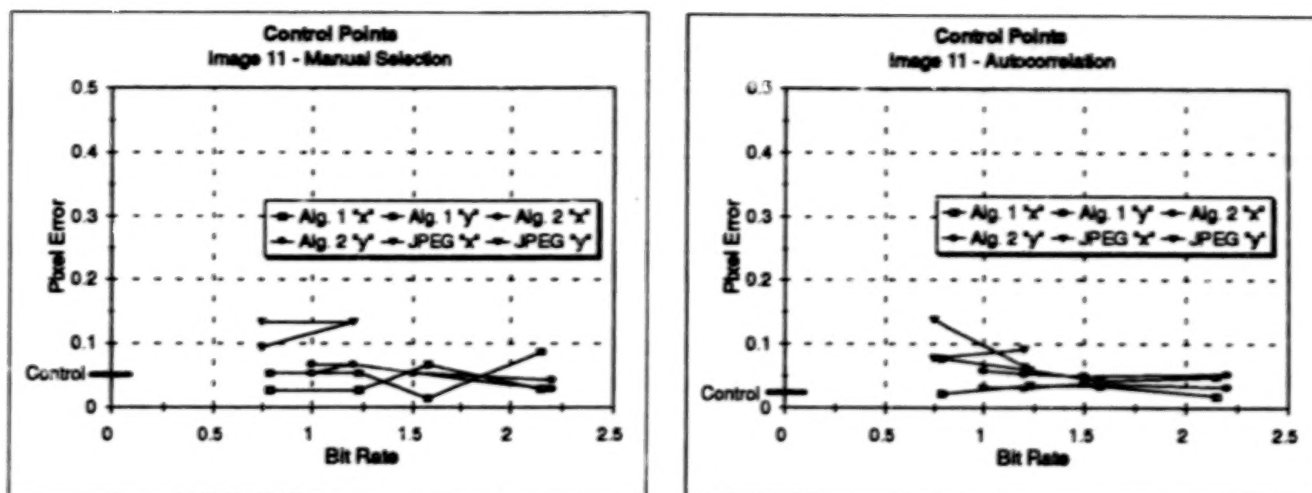


Figure 5. Control point selection error in x and y for manual and autocorrelation procedures using Image 11.

was within both the process measurement error and industry's acceptable level of 1/4 pixel average error. Process measurement error was determined by measuring the location of control points on two uncompressed images. Process measurement error was determined to be 1/20th pixel for the manual procedure and 1/40th pixel for autocorrelation.

V. METRIC-TO-METRIC CORRELATIONS

Correlations between metrics were determined to help identify a standard set of metrics unique in their quantification of data compression effects. Metrics found to be highly correlated with other metrics most likely yield redundant compression error information, and could subsequently be dropped from the set. Although only RMSE and maximum error with MAE are discussed here, qualitative assessment of other metrics' correlation showed that most appeared to be highly correlated. For example, RMSE with edge/non-edge error, RMSE with principal component error, and RMSE with both unsupervised and supervised classification.

5.1 RMSE VS. MAE

RMSE was regressed against MAE for each image/band combination, for Algorithms 1 and 2 separately and together for all 8, 10 and 12 bit images. Correlation between the two metrics was extremely high ($R^2 = 0.99$), and they were found to be the most correlated of the four tested. It was also found that there was no significant difference in the RMSE - MAE relationship between the two compression algorithms and that the metric relationships across 8, 10 and 12 bit original images were the same. As these two metrics are so highly correlated, it makes sense to drop one from a standard set of metrics.

5.2 MAXIMUM ERROR VS. MAE

Correlations between maximum error and MAE for the different types of images and algorithms were not as high (R^2 between 0.58 and 0.84) as found for RMSE and MAE. This is not unexpected due to the nature of the maximum error metric; it is a measure of the highest single pixel error over the whole image. Any one pixel with high error will determine the maximum error for the image, regardless of the magnitude of the error over the rest of the scene. Influencing the correlation of this particular relationship is "random noise" that was digitally added to some bands

of some images. Random noise drives up the maximum error, but leaves MAE largely unchanged (since it is averaged over the whole scene). Because this metric is valuable to users who need to know the magnitude of maximum compression errors to expect, and because it is not highly correlated with other metrics, we feel it is a good metric to include in a standard set.

VI. METRIC RELATIONSHIPS TO IMAGE CHARACTERISTICS

Relationships between data compression metrics and image characteristics were derived to determine which characteristics most influenced compression error. Relationships were developed for Algorithm 1 and 2 on three image characteristics; scene dynamic range, entropy and band-to-band correlation. Derived relationships could be used to predict compression effects on other images without having to re-run the compression algorithms. These predictions could be used by imaging system and compression algorithm designers to perform system optimization trades. Image characteristics, alone, serve another purpose; they allow for accurate comparison of this study's results to other studies.

6.1 ENTROPY AND RMSE

Two types of entropy were calculated, first order and vertical neighbor difference. Vertical neighbor difference is similar to first order, but operates on an image created from differences between vertical neighbor pixels. A summary of minimum, maximum, mean and 95% confidence interval for first order and vertical neighbor difference entropy are shown on the left side of Fig. 6. As expected, vertical neighbor difference results in lower entropy than first order, but the two are highly correlated. Images 4, 8 and 14 had the lowest of both entropies and they were also the lowest in scene dynamic range.

Log RMSE was regressed against both types of entropy. High correlation ($R^2 = 0.92$) was found between log RMSE and vertical entropy (right side of figure 6), moderate correlation ($R^2 = 0.80$) was found between log RMSE and first order entropy. This second relationship, in particular was driven by the 12 and 10 bit ASAS images (16 and 17). No difference was seen between algorithm 1 and 2 for either of the entropy - RMSE relationships.

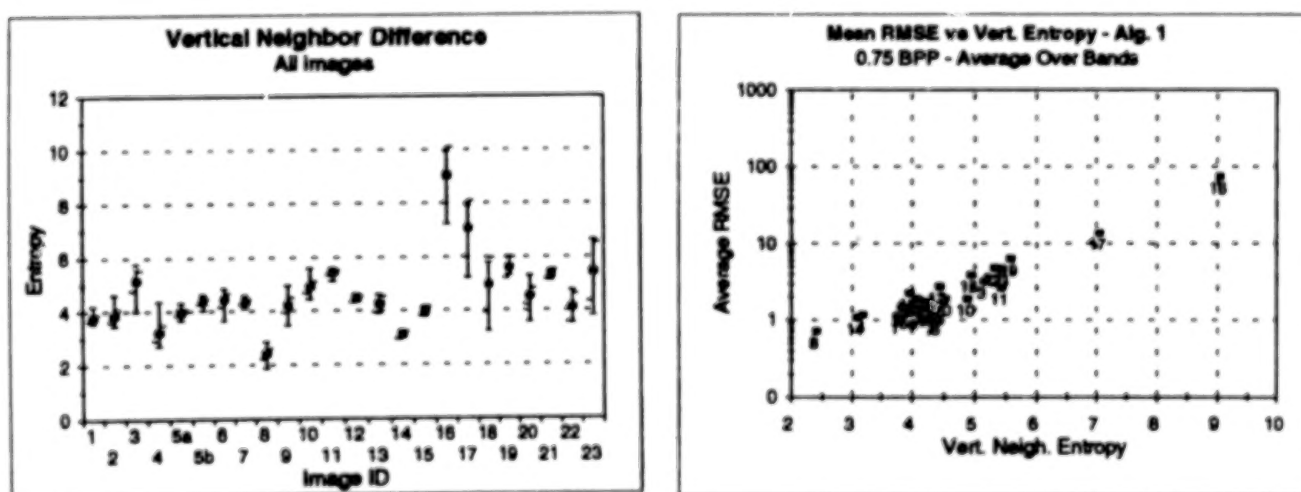


Figure 6. Left plot - Minimum, maximum, mean and 95% confidence interval of vertical neighbor difference entropy for all original test images. Right plot - Log RMSE vs. mean vertical neighbor difference entropy for Algorithm 1.

6.2 SCENE DYNAMIC RANGE AND RMSE

Scene dynamic range is known to be a main contributor to the magnitude of the error resulting from image compression. It was measured as the range in digital counts between the 5% and 95% points on the image histograms. To allow for relation to other image characteristic measures and data compression metrics, scene dynamic range was averaged over each images' spectral bands. Confidence intervals (at the 95% level) were used to show the relative spread of dynamic range across bands. Log RMSE was plotted against scene dynamic range. A qualitative assessment of the relationship showed it not to be as strong as even that of first order entropy and log RMSE.

6.3 BAND-TO-BAND CORRELATION AND RMSE

Band-to-band correlation was thought to be an important image characteristic as it related to algorithm performance because Algorithms 1 and 2 used redundant information across spectral bands to help in the compression. Two dimensional correlation matrices were calculated, from which the mean band-to-band correlation and variance were computed. Log RMSE was plotted against the mean band correlation for all test images. Although no correlation was observed, more work should be done to determine if a better summary measure (other than the mean) of band-to-band correlation can be developed to achieve higher correlation for the regression.

VII. SUMMARY AND CONCLUSIONS

A study was performed for the Defense Landsat Program Office as a first step toward the development of a set of metrics that would uniquely characterize the effects of data compression on multispectral imagery. Fourteen metrics were developed to assess the statistical nature of compression error and to characterize compression impacts on MS imagery user applications. Twenty-three MS images, ranging in spatial resolution from two to ten meter ground sampled distance and consisting of as many 12 spectral bands from 0.4 to 2.5 μm , were compressed by three algorithms to several bit rates. Statistical metrics included both global and local measures. Global metrics were found to be a good way to assess relative algorithm performance over the whole scene. Localized metrics (e.g., edges, image texture) helped to better allocate compression error to one or more scene characteristics. Machine application metrics showed compression impacts on user applications, such as: principal components, classification and control point location. It was found that: (1) higher order principal components exhibited compression artifacts that would affect utility, (2) supervised and unsupervised classification showed similar trends, but supervised classification appeared more sensitive to compression than unsupervised and (3) measurement of control points from compressed three band composite images was not significantly effected by any of the compression algorithms at the tested bit rates. Metric-to-metric correlations were run to determine the redundancy and predictability of the metrics. RMSE and MAE were most correlated ($R^2=0.99$) which suggests that one could be dropped from a standard metric set. Metric-to-image correlations were run to assess algorithm sensitivity and predictability with image characteristics. RMSE and vertical neighbor difference entropy were shown to be highly correlated.

ACKNOWLEDGMENTS

The authors would like to thank Larry Maver (Itek Optical Systems) for his insight and guidance, Val Vaughn and Linda Kalman (Aerospace Corp) for their help with image selection,

processing, and their technical consultation, and Capt. David Ehrhard for his leadership and management of this project.

REFERENCES

Brower, B. V., C. Couwenhoven, B. Gandhi, and C. Smith, 1994: An adaptive differential pulse code modulation compression algorithm for advanced multispectral downlink applications. *Proc. of an industry workshop: Image Compression - Applications and Innovations*. Held in Conjunction with the IEEE Data Compression Conference, Snowbird, Utah, 1 - 10.

Saghri, J. A., A. G. Tescher, and J. T. Reagan, 1994: Terrain-adaptive multispectral bandwidth compression. *Proc. of an industry workshop: Image Compression - Applications and Innovations*. Held in Conjunction with the IEEE Data Compression Conference, Snowbird, Utah, 1 - 6.

Vaughn, V. D., T. S. Wilkinson, and L. S. Kalman, 1993: Multispectral image compression for future LANDSAT remote sensing systems. *Proc. of Twenty Seventh Asilomar Conf. on Signals, Systems & Computers*, IEEE Computer Society Press, Los Alamitos, CA, 1330 -1334.

AUTOMATIC IDENTIFICATION OF SPECTRAL ENDMEMBERS IN HYPERSPECTRAL IMAGE SEQUENCES

Joseph C. Harsanyi
Applied Signal and Image Technology Company
Pasadena, MD 21122

William H. Farrand
Science Applications International Corporation
McLean, VA 22046

Joseph M. Hejl
Applied Signal and Image Technology Company
Pasadena, MD 21122

Chein-I Chang
Department of Electrical Engineering
University of Maryland, Baltimore County
Baltimore, MD 21228-5398

ABSTRACT

A primary goal of imaging spectrometry in earth remote sensing applications is to determine the identities and abundances of surface materials in a geographic area of interest. The problem of determining material abundances can often be reduced to a linear inverse problem where each pixel is modeled as a linear combination of the reflectances of several distinct materials. The distinct material reflectance spectra, modulated by illumination geometry and atmospheric effects, are commonly termed image endmembers. In order to formulate the linear inverse or spectral mixture analysis problem correctly, both the number of image endmembers, and their corresponding reflectance spectra must be determined. In this paper, a technique for determining the number and then automatically identifying the image endmembers is developed and demonstrated using simulated AVIRIS data.

The technique for determining the number of endmembers p is based on an information theoretic approach to model order determination. Once the number of endmembers required to describe an area of interest in the scene is known, the endmember spectra themselves are identified by projecting each element of a candidate endmember spectral library onto the subspace that is orthogonal to the principal eigenvectors of the data correlation matrix. Candidates which are present in the library are nulled by the orthogonal subspace projection operator. This technique provides an objective approach to endmember identification that is robust in the presence of subpixel mixtures and does not require testing of all possible combinations of p signatures within the candidate spectral library.

1.0 INTRODUCTION

A hyperspectral image sequence is made up of hundreds of spatially registered images, taken contiguously over a large wavelength region, with high (< 10 nm) spectral resolution [Vane and Goetz, 1988]. Each pixel in a hyperspectral image sequence is an observation vector which represents the reflected energy spectrum of the materials within the spatial area covered by the pixel. Generally, the spatial coverage of each pixel may encompass several different materials each with a unique spectral signature. In this case, the observation vector is affected by the individual spectral signatures of each material, and the pixel is termed mixed [Smith et al., 1985] [Gillespie et al., 1990].

Since all pixels in an image sequence are potentially mixed, standard statistical classification and spectral signature matching techniques do not provide reliable identification of the spectral endmembers present in the hyperspectral scene unless the locations of spectrally pure pixels are known *a priori*. This paper addresses the problem of identifying both the number and identity of the spectral signatures resident within the image sequence without the need for locating and extracting pure pixels from the scene. First, the approach takes advantage of the noise-whitened data covariance matrix eigenvalues to automatically and objectively determine the number of distinct spectral signatures based on an information theoretic criteria. Once the number, p , of distinct spectral signatures or image endmembers is known, the principal eigenvectors of the covariance matrix can be used to form a subspace which is orthogonal to all possible linear combinations of the spectral signatures within the scene. Knowledge of this subspace is used to form an orthogonal subspace projection (OSP) operator that is applied to each individual spectral signature in an appropriate spectral library. The spectra that are contained within the scene are nulled by the OSP operator.

2.0 PROBLEM FORMULATION

A mixed pixel of p endmembers, denoted by the $l \times 1$ reflectance vector $r(x, y)$, can be described by the linear model

$$r(x, y) = M\alpha(x, y) + n(x, y) \quad (1)$$

where

l is the number of spectral bands;

(x, y) is the spatial position of the pixel;

$M = (m_1 \cdots m_i \cdots m_p)$ is an $l \times p$ matrix where the $l \times 1$ column vector m_i is the reflectance spectrum of the i th distinct material;

$\alpha(x, y)$ is a $p \times 1$ vector where the i th element represents the fraction (abundance) of the i th distinct material present in the pixel;

$n(x, y)$ is an $l \times 1$ vector representing the combined noise which is assumed to be a wide sense stationary Gaussian process with zero mean and covariance matrix Σ_n .

In this model, it is assumed that the atmospheric effects have been removed by a radiative transfer code or other reliable method [Farrand, 1994]. Also, the elements of the abundance vector $\alpha(x, y)$ are constrained to be positive and sum to unity, thus reducing the dimensionality of the data to $p-1$.

The covariance matrix of r can be separated into independent signal and noise terms and is given by

$$\Sigma_r = M\Sigma_s M^T + \Sigma_n = \Sigma_s + \Sigma_n \quad (2)$$

where $\Sigma_s = M\Sigma_s M^T$ is the signal covariance matrix and Σ_n is the noise covariance matrix. The first term in Equation 2 has rank $p-1$. The noise covariance matrix is of full rank l . The problem at hand is to determine the data dimensionality, $p-1$, given a sample estimate of Σ_r which is also of full rank l .

3.0 DETERMINING THE NUMBER OF IMAGE ENDMEMBERS

To determine the number of distinct spectral signatures, p , given a sample estimate of Σ_r , the noise must be whitened. This is accomplished by transforming the second term in Equation 2 to the identity matrix.

Determining the whitening transformation requires estimation of the noise covariance matrix Σ_n . Methods for estimating Σ_n directly from the scene are described in [Green et. al., 1938] [Lee et. al., 1990]. Given the noise covariance estimate $\hat{\Sigma}_n$, the whitening transformation is derived from the eigendecomposition given by

$$\hat{\Sigma}_n = UDU^T \quad (3)$$

Here U is an $l \times l$ unitary matrix whose columns are the orthonormal eigenvectors and D is an $l \times l$ diagonal matrix containing the eigenvalues. By manipulation of Equation 3 we see that $\hat{\Sigma}_n$ is diagonalized by the transformation

$$U^T \hat{\Sigma}_n U = D \quad (4)$$

The overall whitening transformation is thus given by

$$W^T \hat{\Sigma}_n W = I \quad (5)$$

where

$$W = UD^{-1/2} \quad (6)$$

Application of the whitening transformation to the sample estimate of Σ_r results in

$$\hat{\Sigma}_w = W^T \hat{\Sigma}_r W = W^T \hat{\Sigma}_s W + I \quad (7)$$

The number of image endmembers can now be determined from the eigenstructure of $\hat{\Sigma}_w$ using the information theoretic criteria proposed by Schwartz and Rissanen known as the minimum description length (MDL). This criteria was first applied to the detection of the number of signals from the data covariance eigenstructure by [Wax and Kailath, 1985].

The MDL criteria is given by

$$MDL(k) = -\log \left(\frac{\prod_{j=k+1}^l \lambda_j^{x_j}}{\frac{1}{l-k} \sum_{j=k+1}^l \lambda_j} \right)^{(l-k)n} + \frac{\log(n)}{2} k \left(l - \frac{(k+1)}{2} \right) \quad (8)$$

where λ_j is the j th eigenvalue of $\hat{\Sigma}_w$ and n is the number of pixels in the scene. The value of $k \in (0, 1, \dots, p-1, \dots, l-1)$ which minimizes the MDL criteria is a strongly consistent estimate of the data dimensionality $p-1$. The number of distinct spectral signatures within the scene is derived by adding one to the data dimensionality.

4.0 ENDMEMBER DETERMINATION USING ORTHOGONAL SUBSPACE PROJECTION

The eigendecomposition of $\hat{\Sigma}_{xx}$ is given by

$$\hat{\Sigma}_{xx} = V\Lambda V^T \quad (9)$$

where $\Lambda = \text{diag}(\lambda_1 \dots \lambda_l)$ is the diagonal matrix containing the eigenvalues and $V = (v_1 \dots v_{p-1} \dots v_l)$ is the matrix containing the orthonormal eigenvectors.

In the previous section, the eigenvalues of $\hat{\Sigma}_{xx}$ were used to provide an objective determination of the number of endmembers p . The $p-1$ principal eigenvectors of $\hat{\Sigma}_{xx}$ can now be used to identify the endmembers themselves by application of a particular orthogonal subspace projection operator [Harsanyi, 1993] to an appropriate spectral library.

The eigenvectors of the covariance matrix $\hat{\Sigma}_{xx}$ represent all of the information contained within the scene. Based on the number of endmembers, these eigenvectors can be separated into two groups which span two distinct subspaces. The subspace spanned by the first $p-1$ eigenvectors is often called the signal subspace. The subspace spanned by the remaining $l-p+1$ eigenvectors is called the noise subspace. The terminology span means that the subspace is representative of all possible linear combinations of the particular set of vectors. For example, the signal subspace represents all possible linear combinations of the principal eigenvectors $\tilde{V} = (v_1 \dots v_{p-1})$.

Since all of the information regarding the endmembers is represented by the principal eigenvectors, any linear combination or mixture of the endmembers is also represented by some linear combination of these eigenvectors. This is stated mathematically as

$$W^T(M\alpha - \langle r \rangle_{xy}) = \tilde{V}\beta \quad (10)$$

where $W^T(M\alpha - \langle r \rangle_{xy})$ is a modification of the first term in Equation 1 where the mean value of the data denoted by $\langle r \rangle_{xy}$ has been removed and the result has been pre-multiplied by the transpose of the whitening operator given in Equation 6. On the right hand side of the equation, \tilde{V} is the $l \times (p-1)$ matrix whose columns are the principal eigenvectors, and β is a $(p-1) \times 1$ vector containing the fraction of each eigenvector required to achieve the above equality. Note that β does not represent the fractional abundances of the endmembers.

We now identify the subspace that is orthogonal to the signal subspace. This subspace is defined by the orthogonal subspace projection (OSP) operator

$$P = (I - \tilde{V}\tilde{V}^T) \quad (11)$$

where $\tilde{V}^\# = (\tilde{V}^T \tilde{V})^{-1} \tilde{V}^T$ is the Moore-Penrose pseudo-inverse. Applying this operator to both sides Equation 10 we have

$$PW^T(M\alpha - \langle r \rangle_{xy}) = P\tilde{V}\beta = 0 \quad \text{for all } \alpha \text{ and } \beta \quad (12)$$

Since this result is independent of the fractional abundances of the endmembers, we consider the case where one of the elements of the α vector is unity while the remaining elements are zero. This implies the following relation

$$PW^T(m_i - \langle r \rangle_{xy}) = 0 \quad \text{for } i = 1, \dots, p-1 \quad (13)$$

which shows that the combined OSP/whitening operator reduces the individual endmembers to the all zeros vector.

Since there is always some uncertainty in the principal eigenvector estimates due to noise and finite sample sizes, Equation 13 does not hold exactly, but application of the operator to a spectral library will identify the spectra that are closest to the endmember spectra.

To identify these spectra, we apply the following detection operator

$$S(u_i) = u_i^T W P W^T u_i \quad \text{for } i = 1 \dots n \quad (14)$$

where $u_i = m_i - \langle r \rangle_{xy}$ is the i th signature of the spectral library $U = (u_1, \dots, u_i, \dots, u_n)$ where the mean value of the data has been removed. The output of this detection operator $S(u_i)$ is a scalar. The elements in the spectral library for which this scalar is minimized are the spectral signatures which are closest to the endmembers in the scene. This operator is equivalent the Multiple Signal Classification (MUSIC) algorithm [Haykin, 1991] which is focused on the signal direction of arrival estimation problem.

5.0 SIMULATION RESULTS

In this section, we demonstrate the above results using linearly mixed reflectance spectra. These spectra are representative of materials that are found at the Lunar Crater Volcanic Field, Nye County, Nevada. This area has been studied extensively using both field measurements and remote sensing data [Farrand, 1991] [Scott and Trask, 1971] [Snyder, et. al., 1972]. Five hundred hyperspectral pixels were simulated using the playa, vegetation and cinders spectra shown in Figure 1. These spectra were taken from a small spectral library containing the signatures listed in Table 1. The spectra were convolved to AVIRIS band passes, and the 1.4 and 1.9 μm atmospheric water absorption bands have been removed.

The abundance of each material varied randomly from pixel to pixel, and Gaussian noise was added to each pixel to achieve a 200:1 signal- to-noise ratio. The signal-to-noise ratio is defined as 50% reflectance divided by the standard deviation of the noise.

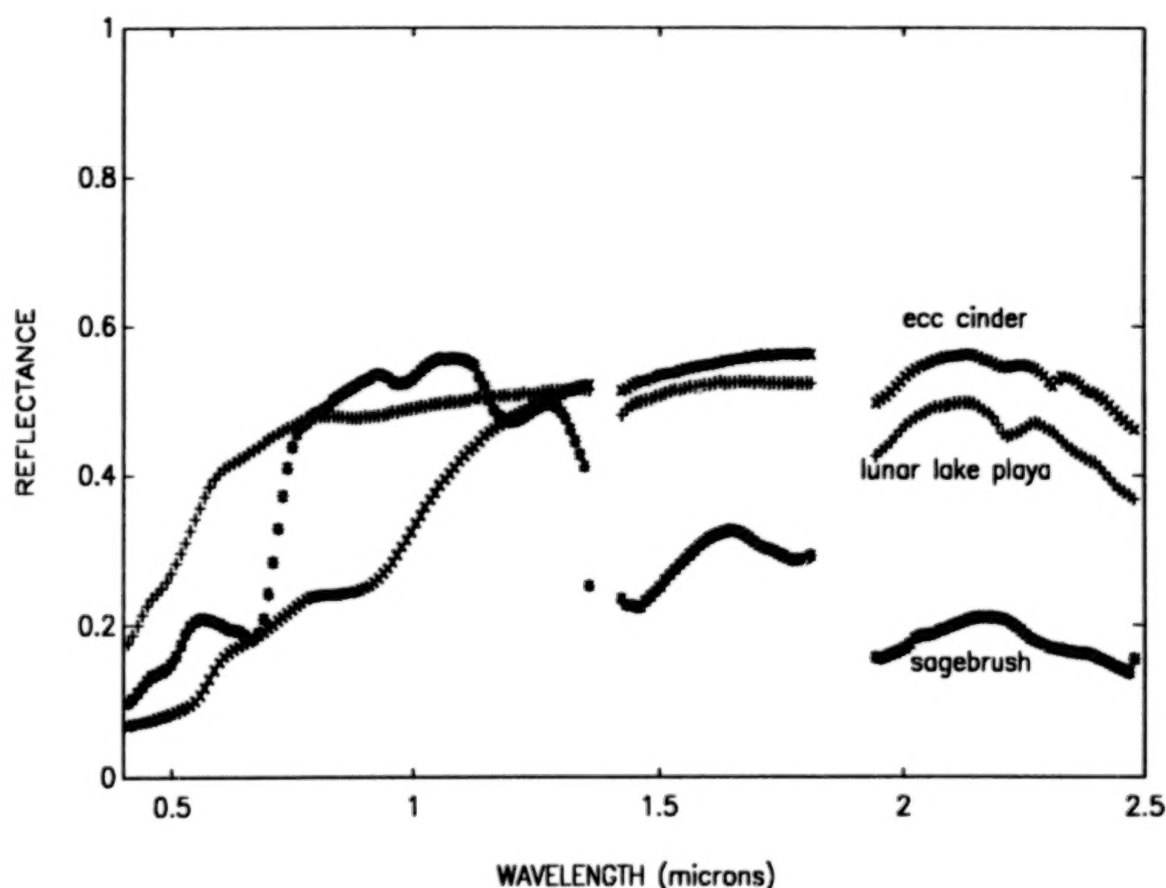


Figure 1: Simulation Spectra

Library Index	Material Description
1	Dry Long Grass
2	Avg. of sagebrush, atriplex and rabbit brush
3	Black Brush
4	Rabbit Brush
5	Red Soil
6	Lunar Lake Playa
7	unaltered cinder
8	Easy Chair Crater Cinder (ECC Cinder)
9	Orange Cinder
10	Bright Red Cinder
11	Yellow Coated Cinder

Table 1: Spectral Library

In the first part of the simulation, the data covariance matrix was computed and a noise whitening operator W was applied. In this case, the noise covariance matrix is assumed to be known, but as noted above there are techniques for estimating the noise covariance directly from the data.

The first twenty-five eigenvalues of the whitened data covariance matrix $\hat{\Sigma}_w$ are shown in Figure 2. Note that there are two prominent eigenvalues. The output of the MDL detector automatically indicates the correct dimensionality as two and thus the correct number of endmembers is determined.

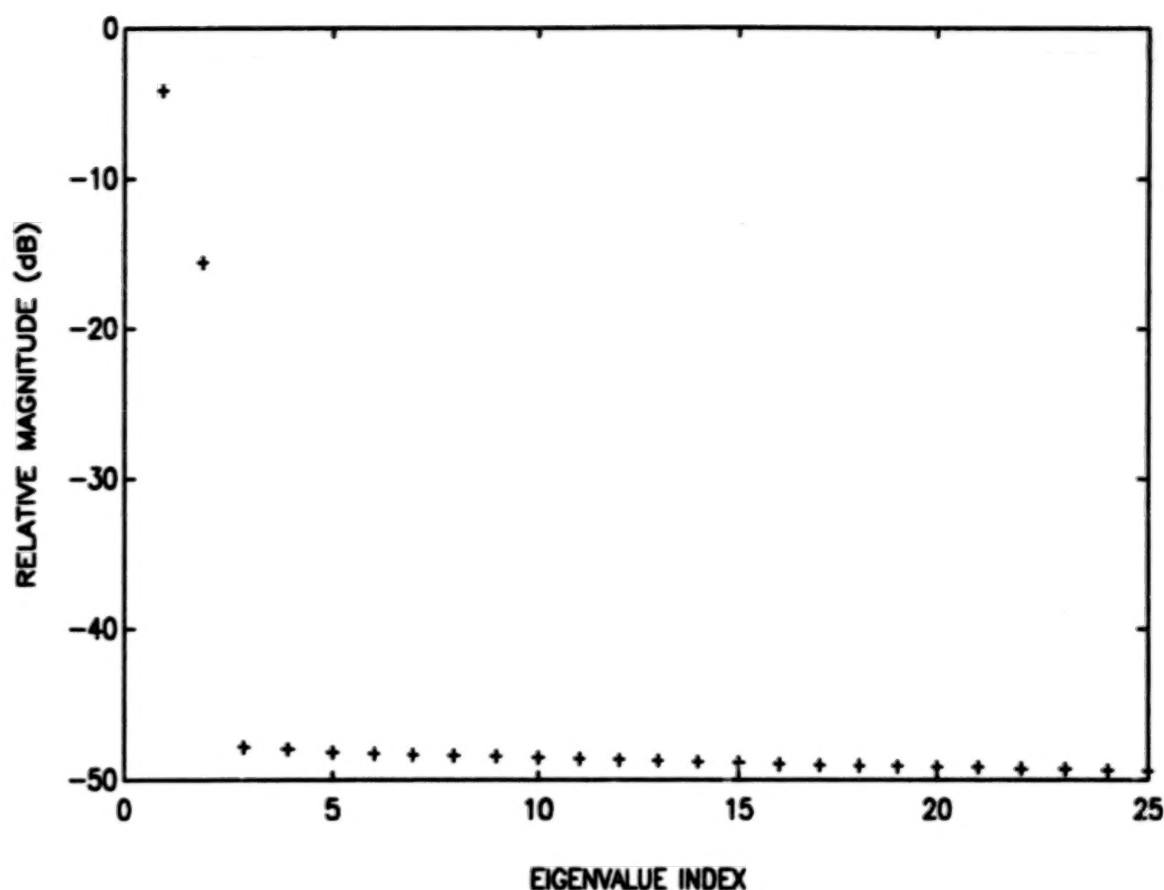


Figure 2: Whitened Covariance Matrix Eigenvalues

The dimensionality of the data is now used to identify the principal eigenvectors and formulate the OSP operator given in Equation 11. This operator along with the whitening operator is used to formulate the endmember detector given in Equation 14. As noted above, application of this detector to each element in the spectral library results in a scalar value. The output for the spectral library of Table 1 is shown in Figure 3. Note that the minima correspond to spectra 2, 6 and 8 from the library which are the spectra that were used in the simulation.

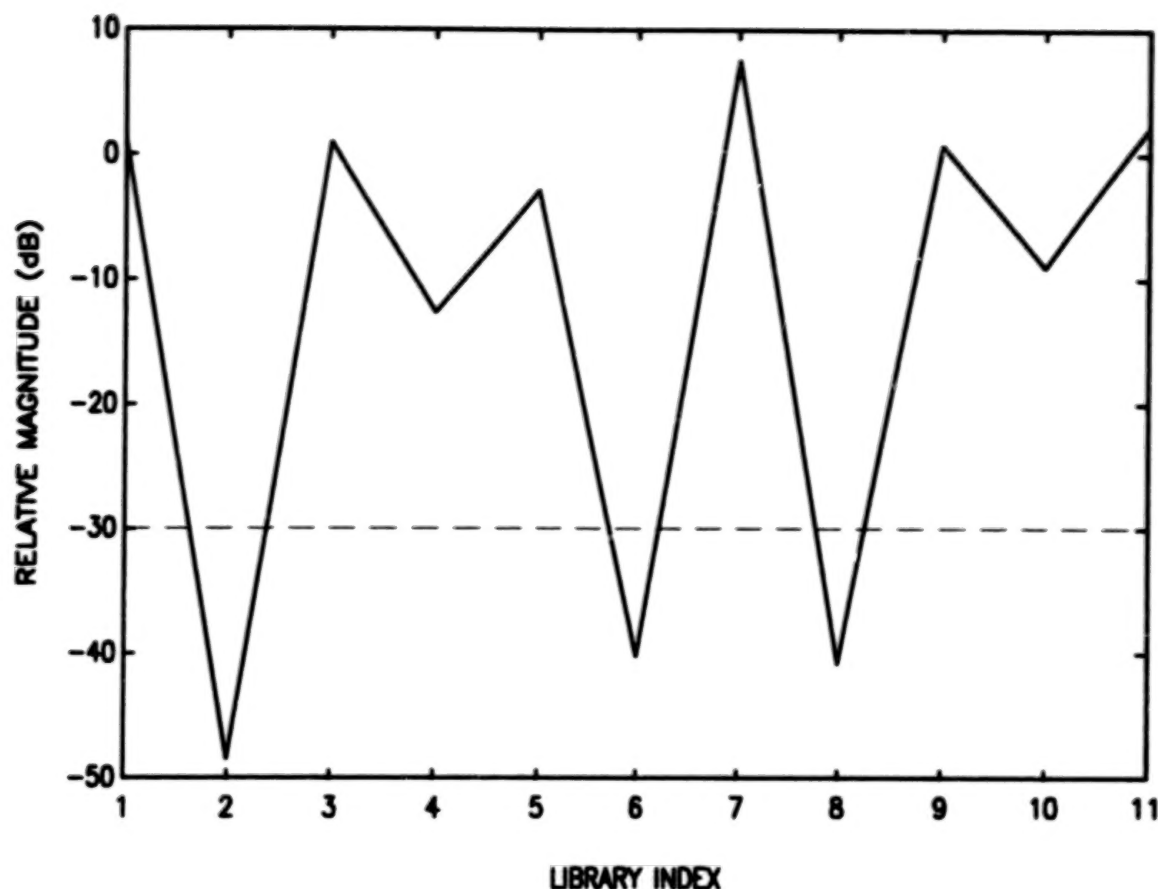


Figure 3: Endmember Detector Output

6.0 CONCLUSIONS

In this paper, an objective method for determining the number of image endmembers, and identifying their corresponding reflectance spectra from a spectral library has been developed and demonstrated against simulated AVIRIS data composed entirely of mixed pixels.

The technique for determining the number of endmembers p is based on Minimum Description Length, an information theoretic approach to model order determination. Once the number of endmembers required to describe the data is known, the endmember spectra themselves are identified by projecting each element of a candidate endmember spectral library onto the subspace that is orthogonal to the principal eigenvectors of the data correlation matrix. Candidates which are present in the library are nulled by the orthogonal subspace projection operator.

For the case of non-Gaussian noise, a whitening transformation is derived from the sample estimate of the covariance matrix and used to better separate the signal and noise subspaces and improve the determination of the number of endmembers. The whitening transformation must also be applied to the library spectra prior to applying orthogonal subspace projection operator.

This technique provides an objective approach to endmember identification that is robust in the presence of subpixel mixtures and does not require testing of all possible combinations of p signatures within the candidate spectral library.

REFERENCES

- Farrand, W. H., (1991) *"Visible and Near Infrared Reflectance of Tuff Rings and Tuff Cones,"* Ph.D. dissertation, University of Arizona, Tucson, Arizona.
- Farrand, W. H., R. B. Singer, E. Merenyi, (1993) "Retrieval of Apparent Surface Reflectance from AVIRIS Data: A Comparison of Empirical Line, Radiative Transfer and Spectral Mixture Methods," *Remote Sensing of the Environment*, vol. 47, no. 1, pp. 311-321.
- Gillespie, A. R., M. O. Smith, J. B. Adams, S. C. Willis, A. F. Fischer III, and D. E. Sabol, (1990), "Interpretation of Residual Images: Spectral Mixture Analysis of AVIRIS Images, Owens Valley", California, *Proceedings of the Second AVIRIS Workshop*, (R. O. Green ed.), JPL Publication 90-54, 243-270.
- Green, A. A., M. Berman, P. Switzer, and M. Craig, (1988) "A Transformation for Ordering Multispectral Data in Terms of Image Quality with Implications for Noise Removal," *IEEE Transactions on Geoscience and Remote Sensing*, vol. 26, no. 1, pp 65-74, Jan. 1988.
- Harsanyi, J. C., (1993), *Detection and Classification of Subpixel Spectral Signatures in Hyperspectral Image Sequences*, Ph.D. Dissertation, University of Maryland, Baltimore County, 116 pp.
- Haykin, S., (1991), *"Adaptive Filter Theory (2nd Edition),"* New Jersey: Prentice Hall.
- Lee, J. B., A. S. Woodyatt and M. Berman, (1990), "Enhancement of High Spectral Resolution Remote Sensing Data by a Noise-Adjusted Principal Components Transform," *IEEE Transactions on Geoscience and Remote Sensing*, vol. 28, no. 3, pp 295-304, May 1990.
- Scott, D. H. and N. J. Trask, (1971) "Geology of the Lunar Crater Volcanic Field, Nye County, Nevada," USGS Prof. Paper 599-I, .
- Smith, M.O., P. E. Johnson, J. B. Adams, (1985) "Quantitative Determination of Mineral Types and Abundances from Reflectance Spectra Using Principal Components Analysis," *Proceedings of the Fifteenth Lunar and Planetary Science Conference, Part 2, Journal of Geophysical Research*, vol. 90, Supplement , pp. C797-C804, Feb. 15, 1985.
- Snyder, R. P., E. B. Ekren, G. L. Dixon, (1972), "Geologic Map of the Lunar Crater Quadrangle, Nye County, Nevada," USGS Misc. Geol. Inv. Map I-700, scale 1:48000.
- Vane, G. and A. F. H. Goetz, (1988) "Terrestrial Imaging Spectroscopy," *Remote Sensing of the Environment*, vol. 24, no. 1, pp. 1-29.
- Wax, M. and T. Kailaith, "Detection of Signals by Information Theoretic Criteria," *IEEE Transactions on Acoustics, Speech, and Signal Processing*, vol. ASSP-33, no. 2, pp. 387-392, Apr. 1985.

SUBPIXEL DETECTION METHODS: SPECTRAL UNMIXING, CORRELATION PROCESSING, AND WHEN THEY ARE APPROPRIATE

Alan Schaum
Naval Research Laboratory
Washington, DC 20375-5320

Alan Stocker
Space Computer Corporation
Santa Monica, California 90404

ABSTRACT

Unmixing methods to detect specific minerals, gases, liquids, vegetation, or manmade objects have become popular analytical tools in multispectral imaging. Some aspects of these methods are often ad hoc and, by incorporating interactive techniques, they often implicitly exploit image spatial information as well as prior knowledge by an operator. This makes the effectiveness of these methods difficult to characterize quantitatively, and many reported results are anecdotal. Correlation methods of detection have a longer history and are well understood mathematically. Measures of performance can be predicted from signal statistics and target signatures.

The relationship between correlation methods and spectral unmixing is explained in this report. Image characteristics for which one method is the more appropriate are described. Related algorithms are explored, and the ideal conditions are explained for which particular techniques are theoretically optimal. Finally, hybrid methods are described that incorporate the better aspects of both approaches.

1. BACKGROUND

Maturing multispectral sensing technologies have raised the question of whether spatial methods of detecting localized targets might be supplanted by ones based purely on color. This report considers the most stressing case of *subpixel* targets, for which spatial processing can usually effect only a small gain. For this case the question of sensor optical resolution enters only through its effect on the fill factor of a target in a pixel. When combined with a signal processing technique, the fill factor is ultimately translatable into a detection range, which is one of the more important operational system parameters.

We first review statistical signal processing (SSP) methods of multispectral detection and then show their relationship to methods derived from an increasingly popular perspective called Linear Mixing Models (LMM). This leads to a proposal for how current applications of LMMs should be modified, in order that a direct comparison can be made between them and the more traditional SSP methods. It also leads to the development of hybrid detection methods, which exploit the best aspects of both approaches.

2. BACKGROUND REMOVAL

The SSP methods of target detection considered in this report can always be interpreted as algorithms for reducing an unwanted background clutter, while

simultaneously constraining some target feature, such as peak value, to be constant. Clutter is defined as the standard deviation of the background signal, and minimizing it with a target constraint is equivalent to maximizing the target to clutter ratio (T/C_l). Detection is usually accomplished after clutter reduction by setting a signal threshold and then declaring only exceedances to be targets.

LMM [Adams (1986)] methods provide image descriptions based on an assumed background phenomenology, and these can be applied to the problem of removing clutter. After an image is modeled with an LMM, any error can be interpreted as residual clutter; it can then be compared to a threshold and produce candidate targets, just as SSP methods do.

When the background statistics are multivariate Gaussian and the signature of a small target is known, an SSP method called the matched filter (MF), is optimal in the sense that thresholding its output produces the maximum detection probability for a fixed false alarm rate. The MF also maximizes the T/C_l gain. If, however, background statistics or the target signature are unknown, another SSP method called principal components analysis (PCA) is often used. In many cases PCA leads to nearly identical results to LMM methods *as currently devised*. However, for imagery that is fully faithful to an LMM, proper model exploitation can lead, in principle, to target detection performance *superior* to any possible with SSP methods. This is explained in more detail in the following Sections.

In practice, departures from ideal performance by LMM methods are usually expressed in ways (unphysical endmember fractions) not immediately comparable to similar measures (residual clutter) used for SSP methods. This difficulty is remedied in the following Sections. The results are used to define the conditions for which one can expect LMM methods to be superior tools for target detection.

3. STATISTICAL SIGNAL PROCESSING (SSP) METHODS: PCA AND THE MF

3.1 PRINCIPAL COMPONENTS ANALYSIS

A sensor designed to simultaneously resolve closely spaced spectral features and to cover a wide spectral band invariably collects redundant information. PCA is a method of transforming N spectral radiances L_i into a set of mutually statistically independent channels with known variances. The method (also called the Karhunen-Loève transformation) is commonly employed [Richards (1993)] in visual image processing (e.g., contrast stretching), and can be derived by diagonalizing a measured color covariance matrix.

The use of PCA for background removal involves the successive deletion of the higher-variance image components until only those corresponding to sensor noise remain. The method can enhance the contrast of a subpixel target that has a nonzero projection outside the space of deleted dimensions. However, it can also suppress or remove a target.

For example, Fig. 1 depicts a two-band background scatter plot, with the bounding ellipse representing points of constant probability density function. For simplicity, we generally assume in our discussion of SSP methods that all bands have been modified by gain and offset corrections so that the background variances are all equal (to one) and the means are zero. That is,

$$\begin{aligned}\langle L_i \rangle &= 0 \\ \sigma_i &= 1,\end{aligned}\tag{1}$$

in which $\langle \rangle$ denotes the expected value.

Deleting the first principal component of the background in Fig. 1 removes the variance associated with the $L_1 = L_2$ direction. This procedure eliminates most of the background clutter, but if the target described by the vector T happened to point parallel to the $L_1 = L_2$ direction, then the PCA method would annihilate it, because the only remaining principal component is proportional to $L_1 - L_2$. PCA in this case is equivalent to a projection onto the vector F , which lies along the $L_1 = -L_2$ direction.

3.2 MATCHED FILTERING

PCA is an example of a vector filter, which maps an input N -component signal into a lower-dimensional one. The MF is also a linear filter, but its output is always one dimensional and is appropriate for thresholding. The MF also differs from the PCA in its concern for balancing the amount of clutter removal with the amount of target reduction. For example, if T were parallel to the $L_1 = L_2$ line in Fig. 1, then the output of the MF would be proportional to $L_1 + L_2$ and would produce a small T/C/I gain. On the other hand PCA, which ignores target properties, destroys such a target.

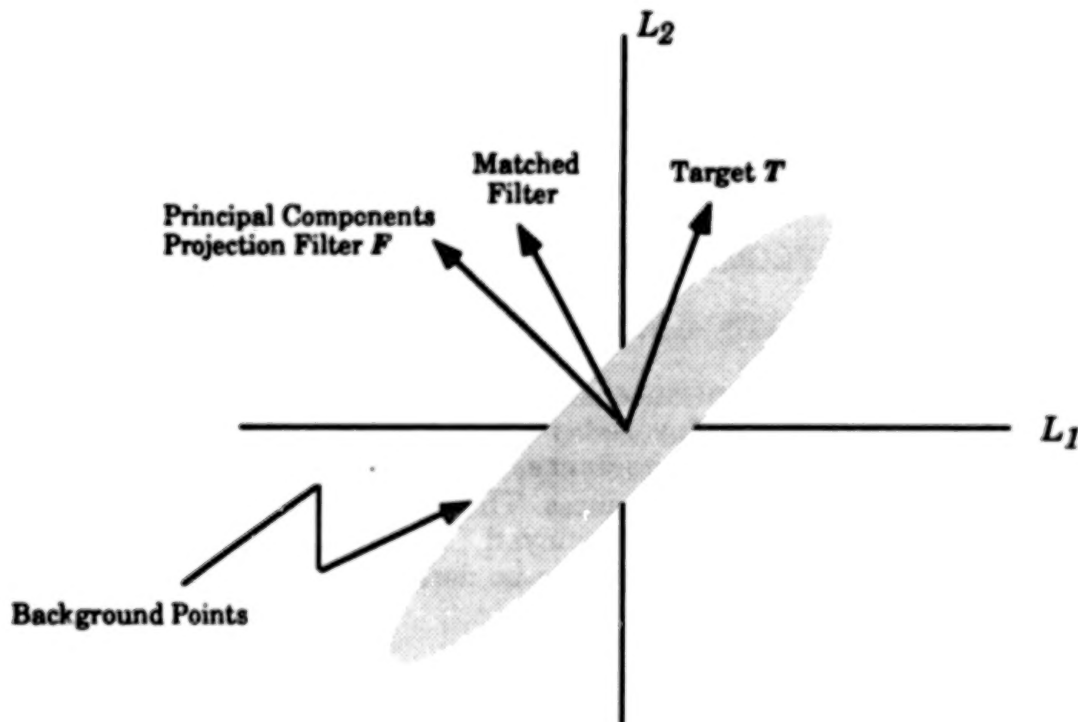


Figure 1. Distribution of background data in two bands, with vectors corresponding to target, PC filter, and matched filter.

With the variances all equalized, as in Eq. (1), second-order background statistical information is contained in the spectral cross correlation coefficients ρ_{ij} , where

$$\rho_{ij} = \langle L_i L_j \rangle. \quad (2)$$

Eq. (1) implies that $\rho_{kk} = 1$ for all k . If the backgrounds are identical in bands i and j , then also $\rho_{ij} = 1$, and perfect background removal can be achieved by subtraction, which is a special case of correlation processing. The decorrelation

$$\delta_{ij} = 1 - \rho_{ij}, \quad (3)$$

which measures the background residual after subtraction, has been measured for natural backgrounds at values less than 10^{-4} [Stocker (1993)].

Apart from an unimportant scale factor, any linear filter—including the MF—that maps N dimensions to one can be associated with a direction in spectral space. For example, the action of the filter associated with vector F in Fig. 1 amounts to projecting each data point onto F 's direction. A filter defined by the direction shown—along the minor axis of the ellipse—minimizes the output variance. It is just $L_1 - L_2$, in this case equivalent to the removal of the first principal component.

The filter that best preserves the target strength T in Fig. 1 is parallel to T , because for any other filter only a part of the target signal survives the projection process. The optimal filter—one that maximizes the T/Cl ratio—lies in a direction representing a compromise between F and T . It is the MF, also depicted in Fig. 1.

Figure 2 plots the gain G that is achievable with two-color MFs for various values of the correlation ρ_{12} . G is defined as the ratio of output T/Cl to input T/Cl. There are two bands to choose from in representing input T/Cl, and the graph ordinate represents the gain relative to the band in which the input T/Cl is higher. In this sense G represents a conservative estimate of the gain achievable with an MF. However, the large potential gains depend on the availability of the prior knowledge that is needed to construct an MF: (1) background covariances, and (2) target color ratio R (the abscissa in Fig. 2). The former, which are also necessary for PCA, can be estimated from image data. The color ratio, which is generally defined as the ratio of the T/Cl ratios in the two bands, is often known only in an average sense.

If the target spectrum were deterministic, then the optimal detection procedure would be trivial: Subtract the measured signal from the target spectrum and declare "target" if the difference is zero (or less than some noise-defined threshold). However, target signatures can vary for many reasons: time-dependence of illumination (in the visible) or of temperature (in the thermal infrared), or intrinsic reflectivity/emissivity variability. The MF is actually optimal only for deterministic targets that are seen as additions to the clutter. This corresponds to targets so small that their occlusion of the background can be ignored. Nevertheless, the MF is quite robust and usually serves as an excellent general purpose processor for extended, and even multi-pixel targets.

One interpretation of the MF/thresholding process is depicted in Fig. 3, in which the target is now represented as a variable object, with statistics inherited from a surrounding background. The decision boundary of Fig. 3 is a line perpendicular to

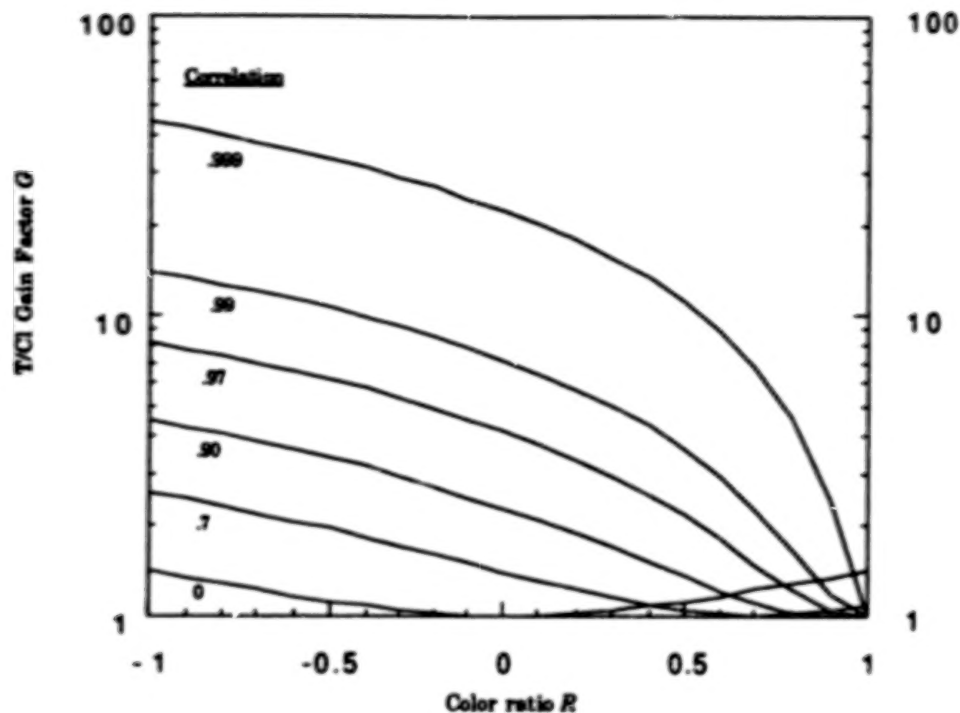


Figure 2. Two-color T/CI gain factors.

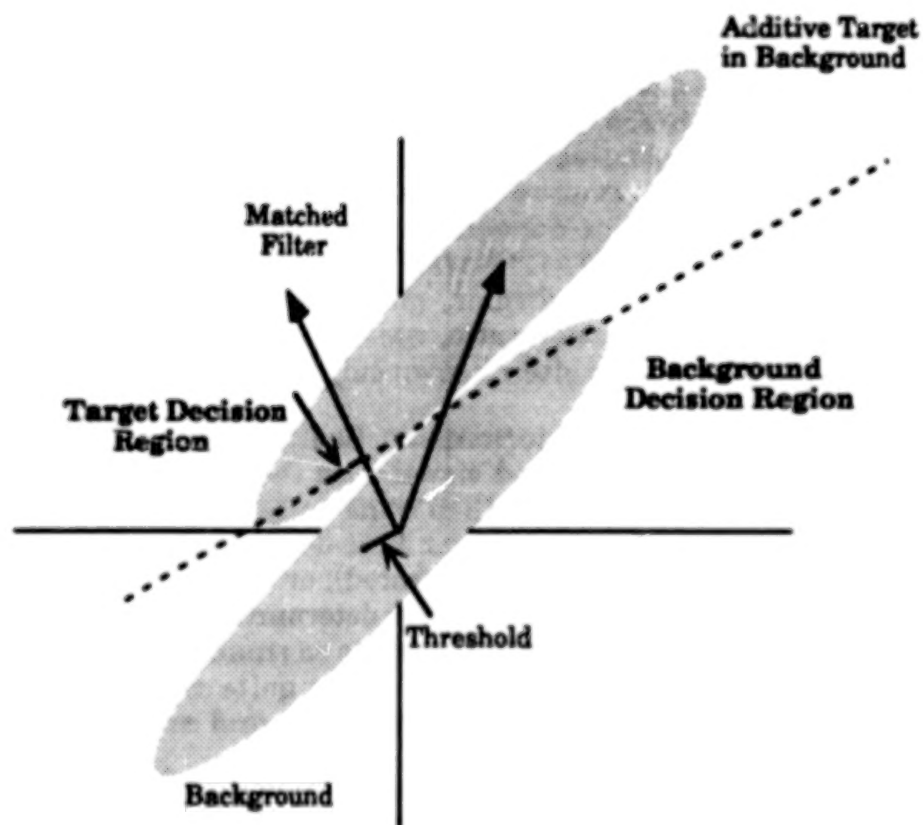


Figure 3. Matched filtering as pattern recognition. Thresholding separates color space into two regions: target or background.

the direction defined by the MF. The appropriate such line to choose depends on the value of the threshold, which arises in turn out of a selection of false alarm rate.

3.2 LINEAR MIXING MODELS

If the background statistics are Gaussian, then some points corresponding to targets always fall on the wrong side of the decision boundary, as do some clutter points. Figures 1 and 3 are meant to depict these missed detections and false alarms with "soft" edges around the scatter plots. By contrast, Fig. 4 shows the related kind of scatter plot expected when LMMs apply. In this case detection performance superior to that achievable even with a matched filter can be expected, especially if the target displaces the clutter points far enough. If the ensemble of target data points actually becomes disjoint from the background, then complete clutter removal might be achievable, in principle.

The prospect of performance exceeding that of the MF has motivated the study of an LMM's ability to confine background data [Resmini (1994)]. The radiance from each image pixel is assumed to arise from the linear superposition of individual spectra defining one or more elementary components called "endmembers" (EMs). Figure 4 represents an idealized configuration in the thermal IR. Two tangible EMs (1 and 2) are depicted, along with virtual cold (VC). VC is the point of convergence of linear projections of data points derived from a finite temperature range; it does not represent true absolute zero because of the nonlinearity of the Planck function.

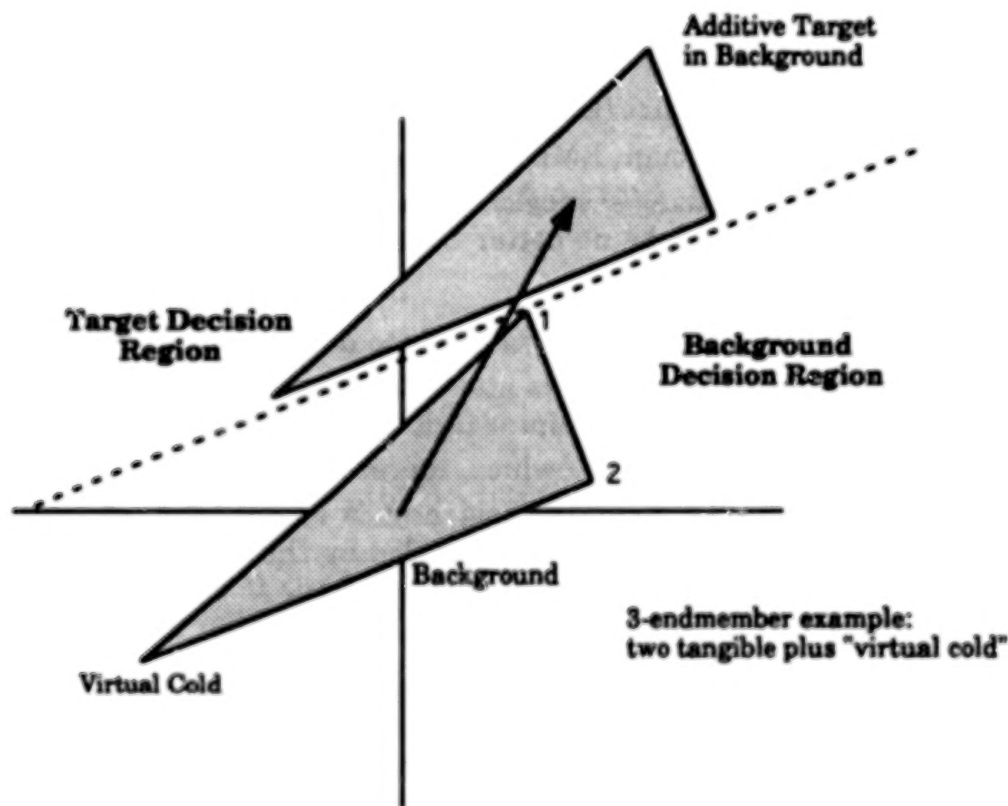


Figure 4. Potential separability of target and background using LMMs.

Given any set of EM spectra e_{in} (i =endmember, n =color), it is a straightforward exercise in linear algebra to find the fractions f_i that minimize the mean squared error

$$\epsilon^2 = \sum_n [L_n - \sum_i f_i e_{in}]^2 \quad (4)$$

between measurements and the LMM approximation. However, adhering to the full endmember model requires the imposition of two extra constraints. The first is the sum constraint on the fractions

$$\sum_i f_i = 1. \quad (5)$$

Equation (5) restricts the LMM's approximation $\sum_i f_i e_{in}$ to the measured radiance L_n to be among vectors lying in an $N_e - 1$ dimensional subspace, such as the two-dimensional one depicted in Fig. 4, where N_e is the number of EMs in the linear mixing model.

A second constraint

$$0 \leq f_i \leq 1 \quad (6)$$

further restricts the value of the LMM's approximation to the measured radiance to lie within the simplex defined by the EM spectra. In the example of Fig. 4, this means within the (background) triangle.

Most reported results that use an LMM impose only the equality constraint (Eq (5)), and not the inequality constraint (Eq (6)) in the minimization of ϵ^2 . However, if the LMM is a good model—i.e., if enough EMs are found so that ϵ^2 corresponds to noise (and not to clutter)—then minimizing ϵ^2 subject to Eq. (5) is nearly equivalent to a PCA. In fact, such a decomposition can be no better than a PCA, as measured by residual error.

The distinctive ability of LMM-based methods to detect targets beyond the limits imposed by linear filtering (PCA or MF) is measured by ϵ^2 only when the inequality constraint of Eq. (6) is included in the minimization calculation. If an LMM achieves true background confinement then ϵ^2 , which represents residual clutter, has the value zero. However, if only the equality constraint is required, ϵ^2 can become zero even for background points that are not well modeled by the LMM. For example, any data point in the plane of Fig. 4 corresponds to zero error if Eq. (6) is not imposed, although it may be located far from the "physical" interior region of the triangle.

The usual diagnostic indicating that background points do not fit an LMM model exactly is the presence of one or more unphysical values of the fractions f_i . These provide the basis of one of two general approaches to further analyzing imagery for target detection. One hybrid method replaces L_i with f_i as the background descriptor, and then applies standard detection techniques to these fractions. This method has been successfully applied to the detection of subpixel targets and is reported in a companion paper [Resmini (1994)].

A second approach, more easily compared to SPP techniques, involves solving the minimization problem with the full set of constraints, corresponding to both Eqs. (5) and (6). This can be accomplished, in principle, because Eq. (4) is a quadratic form,

and general solutions are known to the quadratic programming problem [Lawson (1974)]. Nevertheless, the translation of the endmember-defined constraints in Eqs. (5) and (6) into the language used in the standard quadratic programming solution is complicated, and this method has seldom (if ever) been implemented.

However, a recent algorithm developed by one of us (Schaum) bypasses the standard approach by exploiting the fact that the region of confinement is a simplex—a convex hull. This method provides a solution to the fully constrained problem using only the well-known solutions to the equality-constrained minimization problem. The algorithm is, therefore, easily implemented as a minor modification of software in common use. It is now being applied to multispectral images to compute contributions to ϵ^2 "in the subspace of endmembers," allowing a direct comparison of LMM- to SSP-based methods. Preliminary results [Resmini (1994)] have shown that at least one LMM achieves, at a minimum, clutter suppression comparable to that of a PCA. The more important question—whether or not LMMs can be used to surpass the performance of SSP methods—has not been answered at this writing.

Finally, it should be noted that the relative effectiveness of SPP and LMM methods depends on the spectrum of the target being sought. Usually the intrinsic dimensionality of multispectral images of natural backgrounds is smaller than the number of spectral channels. For such imagery it could happen that a predominant part of a target's spectral energy lies outside the space spanned by the endmembers or, in SPP language, outside the space spanned by the first few principal components. In this case the confinement advantage of the simplex structure is minimal, LMM and PCA methods become equivalent for target detection, and neither is as good as matched filtering.

4. FUTURE

The work described in this paper is part of the algorithm research effort of the Joint Multi-Spectral Program (JMSP), a cooperative research project among the US Navy, Air Force, and Army. The JMSP is a long-range effort incorporating sensor design, experiment planning, signal processing, and selection of communication architectures. All electro-optical wavelengths are considered, with special emphasis on the thermal infrared.

Algorithm research includes the evaluation of existing techniques and the development of specialized concepts. This work influences sensor design and experiment planning by defining the empirical background/target attributes that most influence detection performance. General theoretical problems are also being investigated, such as dimensionality reduction for hyperspectral applications.

A major program objective is to define the background and target types amenable to multispectral methods of detection and identification. Performance predictions for a wide range of military, environmental, and commercial applications are anticipated. General implementation requirements will be developed, applicable technologies will be identified, and areas requiring further development will be defined.

REFERENCES

- Adams, J.B. et al., 1986, Spectral mixture modeling: a new analysis of rock and soil types at the Viking Lander 1 site, *J. Geophys. Res.*, v. 91, no. B8, pp. 8098-8112.
- Lawson, L. L., and R.J. Hanson, 1974: *Solving Least Squares Problems*, Prentice-Hall, Inc., Englewood Cliffs, N.J., 334 pp.
- Resmini, R.G. et al., 1994: Assessment of the Linear Mixing Model for Subpixel Materials Detection in Thermal Infrared Multispectral Scanner Images, *This proceedings*.
- Richards, J.A., 1993: *Remote Sensing Digital Image Analysis*, 2nd edition, Springer-Verlag, New York, N.Y.
- Stocker, A. et al., 1994: Analysis of Infrared Multispectral Target/Background Field Measurements," *SPIE Proc. Aerospace Sensing Symp., Signal and Data Processing of Small Targets*.

PREDICTING SUB-PIXEL TARGET DETECTIBILITY

M. J. Duggin^{*1}, R. Richter⁺, W. N. Philpot² and J. Lamicela^{*}

^{*} Research Associates of Syracuse, Inc.
Hancock Army Complex, 510 Stewart Drive
N. Syracuse, NY 13212, USA

⁺ DLR, German Aerospace Research Establishment
Institute for Optoelectronics
Wessling, Germany

¹ 308 Bray Hall
CESF, SUNY
Syracuse, NY 13210, USA

² 453 Hollister Hall
Cornell University
Ithaca, NY 14853, USA

ABSTRACT

We describe the adaptation of an existing scene-target-sensor model to sub-pixel target detection in heterogeneous terrain. User-friendly front ends for this Fortran code have been written for Windows 3.1, and alternatively for MS-DOS, and have been implemented successfully on a 6 pound notebook computer. The effect of position of the target in the ground instantaneous field of view (GIFOV) on the probability of detection is considered. Up to six different terrain types may be considered to exist in the GIFOV. The target and the background may be spectrally dependent, and the sensor parameters may be readily altered. On-line help is provided, and there are examples given for the visible, for the near, mid-wave and thermal infrared parts of the spectrum.

1. INTRODUCTION

A major difficulty in detecting sub-pixel targets is to determine whether, in any bandpass, it is possible to discriminate the target from background. Whether or not this is possible will depend upon the contrast of the target to the background, and whether this changes the radiance from the ground instantaneous field of view (GIFOV) sufficiently to make the target-containing pixel contrast with those around it. This will depend upon several factors: the spectral response of the target, and of the background elements, the spectral response of the sensor across the bandpass under consideration, and the convolution of the rear-projection of the point-spread function (PSF) of the sensor with the upwelled radiance from within the GIFOV (from the target and from background). The presence of unresolved (sub-pixel) cloud within the sensor IFOV will clearly impede detection, and will not be taken into consideration by any of the standard atmospheric models.

We describe a model which permits the user to determine the theoretical limits on sub-pixel target detection imposed by environmental factors, such as view and illumination geometry, the atmosphere, ground cover content and heterogeneity, topography and optical bandpass. It also enables the user to predict the effect of the sensor to be used on detection capability, or to so select or design a sensor to optimize discriminability. We include a means of assessing the effect of the location of scene elements within the GIFOV in our model,

but do not calculate the probability of detection as a function of the distance of the target from the center of the GIFOV (we assume a Gaussian PSF with no sidelobes).

The equations and algorithms are all well known. The model used was designed for the mainframe by Dr. Rudolf Richter (1991) in Germany. We added a user-friendly front end for Windows 3.1, as well as an alternative MS-DOS based front end, with split screen help and plotting utilities. The model is available for distribution, and we point out the potential utility of extending such a model to operate in batch mode over a range of wavebands, so being of utility in hyperspectral applications, and providing some limits as to the anticipated likelihood of feature detection/quantification by means of spectral decomposition, taking into account the above environmental and instrumental variables.

2.0 MODEL DESCRIPTION

Here, we deal with a non-imaging sensor model. The purpose of this model is to determine the target-to-background contrast and the probability of detection of spatially unresolved targets. In this way, it is possible to predict whether, and under what circumstances a ground feature of pre-known characteristics can be discriminated from background as an anomalous (radiometrically different from background, but spatially undetectable) pixel. The model works in one bandpass. However, several successive runs can be made which will make it possible to say if discrimination is better using several bandpasses, if the radiometric contrast in each of the bandpasses between the target-containing pixel and the background is different.

We consider in an off-line routine the effect of the position of an unresolved target in the detector IFOV. A target which is radiometrically different from surrounding background within the sensor GIFOV, for the bandpass under consideration, will have a differing contrast with respect to background depending where in the sensor field of view the target resides. At the GIFOV center, the sensor response is a maximum, but this falls off in a (generally, although there is a shortage of data) Gaussian manner as one moves away from the GIFOV origin. In fact, the radiometric response from a single GIFOV (recorded as the brightness value for one pixel) will be the convolution of the radiance upwelled from the scene and the reverse point spread function of the sensor (Duggin and Philipson 1985, Duggin 1986, 1987). An early version of SENSAT (Richter 1987) contained a similar module, which was later removed, due to the complexity of input requirements. The purpose of considering the effect of where a spatially unresolved target is within the GIFOV is to place limits on the contrast between a target-containing pixel and surrounding background, which will give an estimate on the likely impact of this factor on the probability of target detection. However, the position of the target in the GIFOV does not at present directly modify probability of detection calculations, which assume that the target is somewhere within a point spread function which is of unit value to the edges of the GIFOV.

Our aim was to use available software, and modify it for use on a common platform, including a portable notebook computer.

This model is based on off-the-shelf technology. From studies of available models, there are some developed for use in the mid-wave infrared (MWIR; 3.5-4.2 micrometers) and in the thermal infrared (TIR; 8-14 micrometers) regions. Typical examples here are the Night Vision Laboratory Static Performance Model (NVLSPM) and the derivative Missile Command Infrared Static Performance Model (MI2SPM). A model which works in the visible region as well as in the MWIR and TIR regions is the Fire Control Sensor Simulator Model (FCSS) of Ball Systems Engineering (Davis, et al. 1990). In this model, a sensor mounted on a platform is allowed to trace a trajectory (fly an engagement) with respect to a target mounted in a clutter background. In this program, there is considerable flexibility in input. However, the background is considered homogeneous.

There are several other models available. However, in most cases, it was difficult to find out about such models, the learning curve is usually steep, and might pose difficulties to the image analyst who just

wants to determine the probability of detection for given environmental conditions, or for a given data set obtained under predetermined conditions, or who wants to configure a sensor and/or plan a mission with the idea of detecting sub-pixel targets. Further, little is reported about model validation, and our enquiries pointed out the difficulty of obtaining simultaneous ground reflectance, atmospheric and digital image data.

We wished to consider the case of a heterogeneous field of view containing several background cover types, as well as an unresolved target. We found a way to modify the front end to SENSAT to facilitate the inclusion of up to six background types with different spectral reflectance or emissivity characteristics, which may be included in different areal proportions within the GIFOV. One shortcoming of the program is that it is difficult at present to consider (statistically random) clutter in the visible region, while structured clutter (giving rise to a power spectrum) is not included. We plan to address this situation.

We wanted to make this model extendible (using multiple runs) to the multispectral, and the hyperspectral cases, so that we wanted to include the effect of combining different ground cover components to constitute the background. We wanted these features to be simply included by those inexperienced in scene-atmosphere-sensor models, who want only to use such models to determine feasibility for a specific task.

We also wanted to make this model a framework upon which further extension could be made, as needs become evident with use in the field. One of the major difficulties in using such models has been the implicit assumption that the end user has a great deal of knowledge about optics, the atmosphere, and the whole problem of target detection. Analysts, while expert in their specific fields do not have time to tackle the long learning curve to become adept at the use of such methods. It was therefore evident that even a very effective model would be of little use unless capable of being used by an analyst with little training. With this in mind, we have attempted to concentrate on the user interface, and on using a common platform and operating system. Higher-level languages, while a useful vehicle for the adept, can give rise to real problems in terms of software installation, use and maintenance. A simpler model which is more user friendly seems a safer starting point.

We have modified the original SENSAT 4 to run in a simplified way within Windows 3.1. In order to achieve this, we restricted the number of possible cases that could be included to those which are of interest to analysts performing feasibility studies for sub-resolution target detection prior to image selection, or data acquisition, whichever may be applicable. Thus, we consider only downlooking scenarios involving detectors working in the visible/near infrared (VNIR), mid-wave infrared (MWIR) and thermal infrared (TIR) regions.

For those users who are more adept in the use of modeling techniques, and more conversant with computers, we also have a MS-DOS version of the program which has the full functionality of SENSAT 4, but which requires more expertise in use than the Windows version. This version does have a split-screen help capability, where an explanation of each parameter appears on the lower screen.

Another important point was expandability. Two possibilities occurred to us. First, after use in the field, the evident needs of users could result in extensive modifications to the types of questions one might address with such a model. Clearly, it would make little sense if this resulted in the setting aside of all that we have done, and starting over from scratch. We therefore felt that concentration on a portable user interface, which could be fit to a new core at a subsequent stage makes good fiscal and logistical sense.

Further, we are aware of the growing importance of imaging spectrometry in detecting and quantifying component features on the earth's surface either because they are too small to resolve with a candidate sensor, or because they are part of a large (compared to the sensor GIFOV) but heterogeneous ground cover. This mode of operation would involve the inclusion of a third looping variable, so that many short, contiguous spectral scans may be made, so as to scan a spectral range. In the MS-DOS version of SENSAT, it is possible to perform a spectral scan with constant bandwidth (setting wavelength of the band center as variable 1), and to sequentially modify the values of one other variable. However, this cannot be done in the Windows-based

version. In future, we would like to consider the effects of more than one environmental variable on SNR and on the probability of target detection, as a function of wavelength.

The SENSAT (sensor-atmosphere-target) model was developed by Dr. Rudolf Richter at DLR, Wessling, Germany (Richter, 1987, 1991). This computer code predicts the static performance of a passive sensor in the 0.2 to 30 micrometer range, with a spectral resolution which depends on the atmospheric model used: either LOWTRAN-7 with a 20 cm^{-1} resolution or MODTRAN with a 2 cm^{-1} resolution. This model calculates basic (scene-dependent) radiometric quantities such as at-aperture radiance, radiometric temperature, signal-to-noise ratio. It also calculates the derived (post-sensor) quantities such as signal to noise ratio (SNR), etc. It calculates for several (presently up to three) components in the ground instantaneous field of view (GIFOV) contributing to upwelling radiance. Slope and aspect may be considered. There is an infrared clutter model, which allows the inclusion of background clutter in SNR calculations for selected clutter parameters. There is no MTF calculation except in rudimentary form, but this is not so much of a drawback, since we are interested only in anomalous (potentially target-bearing) pixel detection, not in macroscopic target recognition (according to Johnson criteria: Johnson, 1958). Thus MTF degradation will only cause some radiometric smoothing to occur, which may degrade target detectability.

The target is illuminated by direct and by scattered (sky) radiance in the VIS through the MWIR regions of the spectrum. Additionally, in the MWIR and the TIR, the target is illuminated by atmospheric radiance and solar radiance, but most of the upwelled radiance to the sensor is emitted. The radiance upwelled to the sensor is attenuated in part by the atmosphere, to an extent that depends on the spectral bandpass and the length of the atmospheric path to the sensor, and on atmospheric conditions (vertical gas profile, aerosol vertical and horizontal distributions).

For the wavelength region 0.2 to $1.0 \mu\text{m}$, the radiance in bandpass r at the aperture of the sensor is, for a given view angle

$$L_r = \frac{\int_{\lambda_1}^{\lambda_2} I(\lambda) \left\{ \int_0^\pi \int_{-\pi/2}^{\pi/2} E(\theta, \phi, \lambda) \left[\sum_{n=1}^{n=6} a_n \frac{\rho_n(\lambda)}{\pi} \right] d\phi d\theta \tau(\lambda) + L_{\text{path}}(\lambda) \right\} d\lambda}{\int_{\lambda_1}^{\lambda_2} I(\lambda) d\lambda} \quad (1)$$

where

- λ_1, λ_2 = the zero power limits to the bandpass
- λ = wavelength
- θ = zenith angle of element of irradiance
- ϕ = azimuth angle of element of irradiance
- $E(\theta, \phi, \lambda)$ = spectral global irradiance on ground resolution cell viewed by sensor instantaneous field of view (IFOV)
- $I(\lambda)$ = spectral response of sensor for bandpass
- $\rho_n(\lambda)$ = spectral reflectance factor for element or in IFOV. Our windows based model considers up to 6 elements
- a_n = fraction of IFOV covered by area n

$\tau(\lambda)$ = atmospheric spectral transmittance for path to sensor

$L_{\text{path}}(\lambda)$ = spectral path radiance

Here, we have ignored the variation of the sensor response across the IFOV. SENSAT does not consider the interaction of the PSF with the scene (see Duggin, 1985, 1987). However, we have added a capability for consideration of the system PSF in our package, although it does not yet permit the calculation of SNR and probability of detection as a function of the position of the target in the GIFOV. Here, we represent the target as an annulus of constant area, at various radial distances from the center of the GIFOV, and calculate the change in radiometric contrast between the target-containing GIFOV and its neighbors, which contain only background.

In the case of the TIR region, the radiance at the sensor is given for a particular view angle by

$$L_r = \frac{\int_{\lambda_1}^{\lambda_2} I(\lambda) \left\{ \left[\sum_{n=1}^{n=6} a_n \epsilon_n(\lambda) W(\lambda, T_n) + (1 - \epsilon_n(\lambda)) \cdot \frac{E_{\text{sky}}(\lambda)}{\pi} \right] \cdot \tau(\lambda) + L_{\text{self}}(\lambda) \right\} d\lambda}{\int_{\lambda_1}^{\lambda_2} I(\lambda) d\lambda} \quad (2)$$

where

$\epsilon_n(\lambda)$ = spectral emissivity for element n in GIFOV. The windows-based version of SENSAT considers up to 6 elements in the GIFOV at present.

$L_{\text{self}}(\lambda)$ = spectral atmospheric self-radiance

However, in the 1.0 to 4.5 μm region, the radiance at the sensor is given by a summation of the reflected and emitted radiance described by the previous two equations:

$$L_r = \frac{\left\{ \int_{\lambda_1}^{\lambda_2} I(\lambda) \left\{ \int_0^\pi \int_{-\pi/2}^{\pi/2} E(\theta, \phi, \lambda) \left[\sum_{n=1}^{n=6} a_n \frac{\rho_n(\lambda)}{\pi} \right] d\phi d\theta \cdot \tau(\lambda) + L_{\text{path}}(\lambda) \right. \right.}{\int_{\lambda_1}^{\lambda_2} I(\lambda) d\lambda} + \left. \left. + \left[\sum_{n=1}^{n=6} a_n \epsilon_n(\lambda) W(\lambda, T_n) + (1 - \epsilon_n(\lambda)) \cdot \frac{E_{\text{sky}}(\lambda)}{\pi} \right] \cdot \tau(\lambda) + L_{\text{self}}(\lambda) \right\} d\lambda \right\}}{\int_{\lambda_1}^{\lambda_2} I(\lambda) d\lambda} \quad (3)$$

In a more detailed consideration, the rear-projected spectral point spread function (PSF) of the sensor is convolved with the spectral upwelled radiance field to determine upwelled radiance at ground level.

2.1 NOISE IN THE SIGNAL AND IN THE DETECTOR

The radiance field at the sensor is subject to systematic and random fluctuations as discussed by (e.g.) Duggin, 1986. Such variations in upwelled photon flux provide the limit to detection with a background (photon noise) limited (BLIP) detector. Such detectors have low enough internal noise characteristics that the fluctuations (clutter) in upwelled photon flux at the sensor limit the performance of the detector, rather than sensor noise.

Detector characteristics of interest relate to the sensitivity of the detector, its inherent internal noise, and its variation in performance with wavelength and electrical bandpass.

2.1.1 Temporal and Spatial Fluctuations in Recorded Signal

Noise fluctuations considered below are temporal. However, there are other fluctuations across an imaged scene, which give rise to a spatial variability in signal at the sensor. The amount of spatial clutter in a background scene in which one is trying to detect a target is dependent on the size and the location, topography and constitution of the area examined. Clutter of a spatial nature is not considered at present, but is available in a later mainframe version of SENSAT (SENSAT5) and will later be included in this model. Both spatial and temporal variations in the sensor output, whether they are present in the upwelled radiance field, or whether they are partly introduced by temporally varying noise sources in the sensor will make it more difficult to detect an "anomalous" (potentially target-containing) pixel embedded in a clutter background. Thus the probability of detection will depend in part on sensor noise, shot noise and spatial background clutter.

2.1.2 Noise in Detectors Working in the Visible to Shortwave Infrared

Detectors operating in the visible and near infrared regions typically are limited by the fluctuations in photon flux. For quantum detectors operating in the 0.2 to 3.0 μm region noise is usually specified in terms "electrons". There are two contributions to the number of noise electrons for a quantum detector operating in this region:

$$N_{SH} = \sqrt{S_e} \quad \text{which is called photon noise, where } S_e \text{ is the number of signal electrons.}$$

Photon noise is due entirely to statistical fluctuations in signal level at the entrance to the sensor.

$$N_R = \quad \text{residual noise, which includes noise sources characteristic of the sensor, which are not related to fluctuations in the signal. Residual noise includes thermal (Johnson) noise, generation-recombination noise, noise due to fluctuation of detector temperature, detector dark current, 1/f noise (due to surface irregularities and contact noise), CCD readout noise for focal plane (staring) arrays, and quantization noise.}$$

The sources of noise in the signal and in the sensor are statistically independent, and the total number of noise electrons may be expressed

$$N_e = \sqrt{N_{SH}^2 + N_R^2} = \sqrt{S_e + N_R^2} \quad (4)$$

We need to use a different noise model in the shortwave infrared through thermal infrared region. In general, the emitted thermal radiation for ambient temperature emitters (about 290 K) may be neglected for wavelengths less than 2.5 μm . However, for hotter objects, we need to include emitted radiance at shorter wavelengths.

2.1.3 Noise in Detectors Working in the 2.0 to 14 μm Region

Here, there are two options

1. The user can specify the detectivity $D^*(\lambda)$ of the detector. In order to understand the meaning of detectivity, it is necessary to consider the noise equivalent power (NEP), which is the rms monochromatic flux which is necessary to produce an rms SNR of 1.0. The NEP should be specified

for the electrical bandwidth, wavelength, detector area, and (where applicable) chopping frequency. The spectral detectivity $D(\lambda)$ has the unit W^{-1} and is defined by

$$D(\lambda) = 1/NEP(\lambda) \quad (5)$$

The spectral D-star; $D^*(\lambda, f_o, \Delta f)$ is a normalization to take into account detector area, electrical bandwidth dependence, and chopping frequency where applicable.

$$D^*(\lambda, f_o, \Delta f) = D(\lambda) \sqrt{A \Delta f} \quad (6)$$

The detectivity of a sensor with an overall spectral response of $\Phi(\lambda)$ is given by

$$D^*(\lambda, f_o, \Delta f) = \Phi(\lambda) D_p(\lambda, f_o, \Delta f) \quad (7)$$

where $D_p(\lambda, f_o, \Delta f)$ is the peak detectivity for the detector. Wavelength is the principal determinant of where the detectivity (spectral D-star) peaks.

2. Some photovoltaic and intrinsic photoconductive quantum detectors can approach the theoretical limits of performance. Spectral D-double star is a normalization of D-star to take into account the detector field of view.

$$D^{**}(\lambda, f_o, \Delta f) = (\Omega/\pi)^{1/2} D^*(\lambda, f_o, \Delta f) \quad (8)$$

This model of noise can be used to simulate background limited (BLIP) performance. The calculation of D-star blip permits an assessment of whether photon noise for a given background scene is negligible or dominates. In optimizing sensor design, such calculations can facilitate a selection of band center and bandwidth to maximize detectivity.

2.1.4 Total Noise Used to Calculate System Spectral D-Star

The major sensor and photon (scene radiance fluctuation) noise components can be incorporated into an expression to compute the rms noise current

$$i_t = \sqrt{i_{pn}^2 + i_{th}^2 + i_{1/f}^2} \quad (9)$$

where

i_{pn} = photon noise

i_{th} = thermal noise

$i_{1/f}$ = rms 1/f noise current, where f is frequency at which noise is measured

The spectral system detectivity normalized for electrical bandwidth, detector area, and corrected for the field of view defined by the cold shield angle may be derived for a photovoltaic detector and has the form

$$D_{sys}^*(\lambda) = \frac{\eta(\lambda)\lambda}{hc} \cdot \left\{ 2Q_s \sin^2 \frac{\Theta}{2} + \frac{4kT_d}{q^2 R_s A_d} + \frac{B I^2}{q^2 A_d f} \right\}^{-1/2} \quad (10)$$

where

$\frac{\theta}{2}$	= cold shield half angle
$\eta(\lambda)$	= quantum efficiency of detector
Q_B	= total photon flux on the detector
h	= Plank constant
c	= speed of light
k	= Boltzmann's constant
T_d	= detector temperature
q	= electron charge
A_d	= detector area
R_0	= equivalent total resistance of detector
B	= constant
I	= direct current through detector
f	= frequency at which noise measured

The factor $\sin^2\theta/2$ accounts for a cooled cone of half-angle $\theta/2$ with a radiance contribution negligible in comparison to the scene radiance. In the event of a photoconductive detector (which we shall not consider here) an analogous expression may be derived.

In the case of a photoconductive, rather than a photovoltaic detector, this equation has a similar form, but includes consideration of generation-recombination noise and photoconductive gain.

2.1.5 Modeling the Atmosphere

SENSAT-4 has the option of using either a modified version (Richter, 1991) of LOWTRAN-7 or MODTRAN, which has a higher spectral resolution. This program accepts view and a modified version (Richter, 1991) illumination geometry inputs, solar declination data, aerosol and vertical gas profile data. Calculations are performed with a selected spectral resolution and bandpass. Spectral path radiance, transmission, reflected, emitted and total radiance are computed. Multiple scattering may be employed, and atmospheric refraction is taken into account for long atmospheric paths.

2.2 MIXED PIXELS

2.2.1 SNR for Target Smaller Than IFOV

In the case of the target being smaller than the IFOV, the SNR is given by the equation

$$SNR = \frac{|S_2 - S_1|}{N} \quad (11)$$

Where S_1 = signal with no target in IFOV (i.e., background signal), and S_2 = signal with target in IFOV. The noise consists of shot (photon) noise and residual (sensor system) noise, together with clutter noise in the infrared case.

2.3 CALCULATION OF PROBABILITY OF DETECTION

For imaging sensors, the probability of static detection is designated P_{∞} and relates to the probability that a target will be detected if environmental conditions persist for a very long period of time. For large targets the probability of static detection is based on the number of resolution elements across the target, as defined by Johnson (1958). In the case of unresolvable targets, it is better to use the well-known formula given by (e.g.) Davis, et al. (1990), for the infrared search and track (IRST) sensor. The assumption here is that noise sources are Gaussian in magnitude, and frequency-independent.

$$P_{\infty} = \frac{1}{\sqrt{2\pi} \sigma} \int_T^{\infty} \exp \left\{ -\frac{E_T - E}{2\sigma^2} \right\} dE \quad (12)$$

where

- E = irradiance
- E_T = target contrast irradiance (W/cm^2)
- T = threshold value for irradiance (W/cm^2)
= $S/N \times \sigma$
- S/N = specified signal-to-noise ratio for detection
- σ = total system noise (in terms of equivalent irradiance)

The probability of false alarms is given by

$$P_{FA} = \frac{1}{\sqrt{2\pi} \sigma} \int_T^{\infty} \exp \left\{ -\frac{E}{2\sigma^2} \right\} dE \quad (13)$$

and the false alarm rate is

$$FAR = 3600 T_F P_{FA} N_P (hr^{-1}) \quad (14)$$

where

- T_F = frame time (s)
- N_P = number of pixels per frame.

2.4 HELP FILES

Few users want to be bothered leafing back and forth to manuals, so we included extensive help files on-line. In the windows-based version these are easily brought up by use of the mouse or track ball. In the case of the MS-DOS-based version, there is a split screen help, advising of the options for each input parameter.

3. EXAMPLES

Several canned examples are on file to show how it is possible to model anticipated SNR, and so calculate the probability of detection as a function of changes in selected environmental variables. In this way, the probabilities of detecting anomalous pixels, potentially containing targets, for ranges of selected variables, such as range, altitude, atmospheric extinction for various sensors may be predicted, provided we know the anticipated background spectral characteristics. The menus are self-explanatory. Modifications may be made by using a given example, making changes, and saving the problem to a new sub-directory. An example, where a silicon detector views a stressed vegetation target 9 m² in diameter, embedded in a vigorous vegetation background is shown in Figs. 1 through 9. The inputs, target and background spectral responses, sensor spectral response, and other environmental parameters on the SNR and on the probability of detection of the stressed vegetation target are shown. Not surprisingly, detection is possible at a higher altitude when the solar elevation is higher. However, here, the vegetation target and background are both assumed to be Lambertian.

4. CONCLUSIONS

We have discussed methods and models to predict the change in detectability of anomalous (potentially target-bearing) pixels as a function of various environmental and sensor parameters. This permits the prediction of the limits beyond which the detection of anomalous pixels becomes unreliable, either as a result of environmental conditions, or as a result of sensor type and performance. Further, such models will aid in the selection of sensors, and in the definition of environmental conditions for which data may be collected with an anticipated high likelihood of success in detecting anomalous pixels.

REFERENCES

- Davis, J. S., S. L. Crawford, R. C. Allen, R. L. Grotbeck, L. N. Peckham and M. A. Wood, 1990: "IR Brassboard Design: Fire Control Sensor Simulator Analyst/User Manual", Ball Systems Engineering Division, SE&A-R-002-89-17, 267.
- Duggin, M. J., 1985: Comments on the intercalibration of multisensor, multitemporal, multichannel digital radiance data, *Appl. Optics*, 24, 2292-2294.
- Duggin, M. J., 1986: Variance in radiance recorded from heterogeneous targets in the optical-reflective, middle-infrared, and thermal-infrared regions, *Appl. Optics*, 25, 4246-4252.
- Duggin, M. J., 1987: Impact of radiance variations on satellite sensor calibration, *Appl. Optics*, 26, 1264-1271.
- Duggin, M. J., and W. R. Philipson, 1985: Relating ground, aircraft and satellite radiance measurements: spectral and spatial considerations, *Int. J. Remote Sensing*, 6, 1665-1670.
- Johnson, J., 1958: Analysis of image forming systems, *Proc. Image Intensifier Symposium*, 249-273.

Ratches, J. A., W. R. Lawson, L. P. Obert, R. J. Bergemann, T. W. Cassidy and J. M. Swenson: Night Vision Laboratory static performance model for thermal viewing systems, U.S. Army Electronics Command, Research and Development Technical Report ECOM-7043, 208.

Richter, R., 1987: Infrared simulation model SENSAT-2, *Applied Optics*, 26, 2376-2382.

Richter, R., 1991: Model SENSAT-3 sensor-atmosphere-target, DLR-IB 552-06/89, Institute for Optoelectronics, D-8031, Wessling, Germany, revised edition, 143.

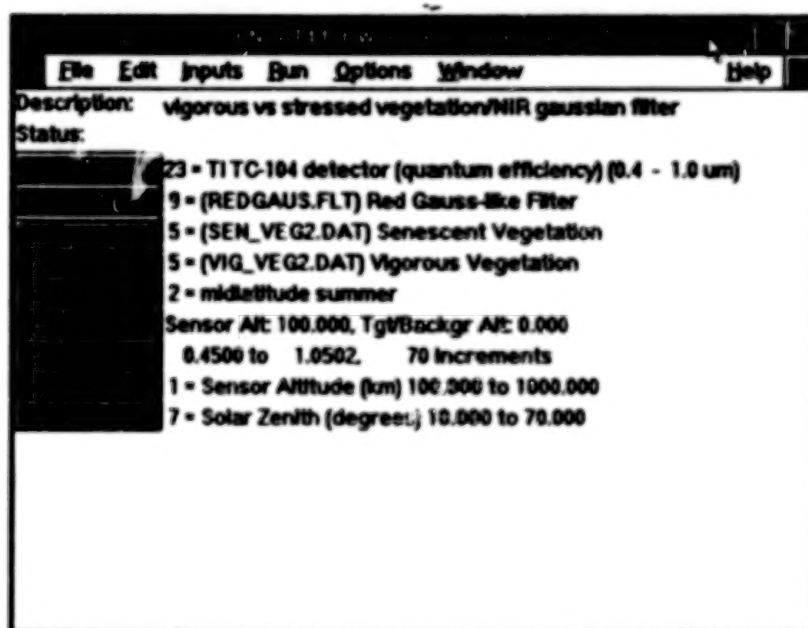


Figure 1. Inputs to example where a silicon sensor views a stressed vegetation canopy from various altitudes, and with various solar elevations. Note that any of the inputs, including those for MODTRAN, may be altered by accessing the appropriate window with the mouse.

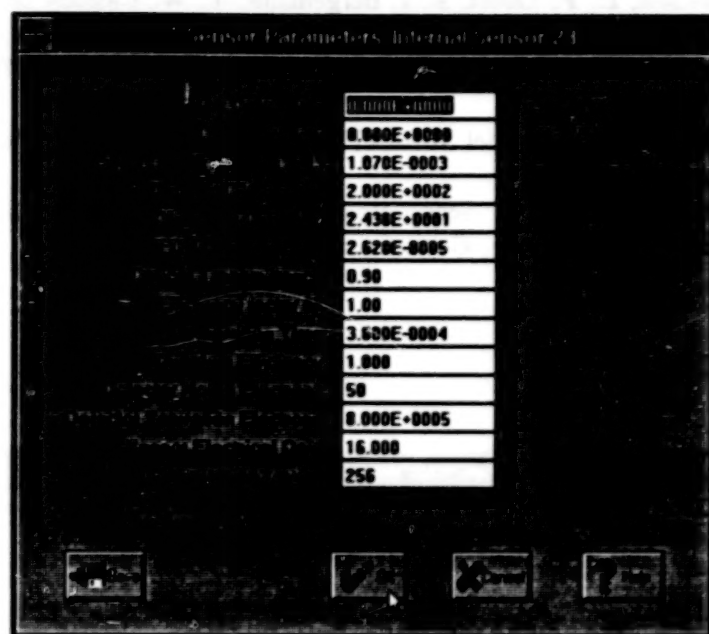


Figure 2. Sensor parameters for the sensor shown in Fig. 1. Any of these parameters may be altered, with consequent alteration of the calculated SNR and probability of detection of the target-containing pixel.

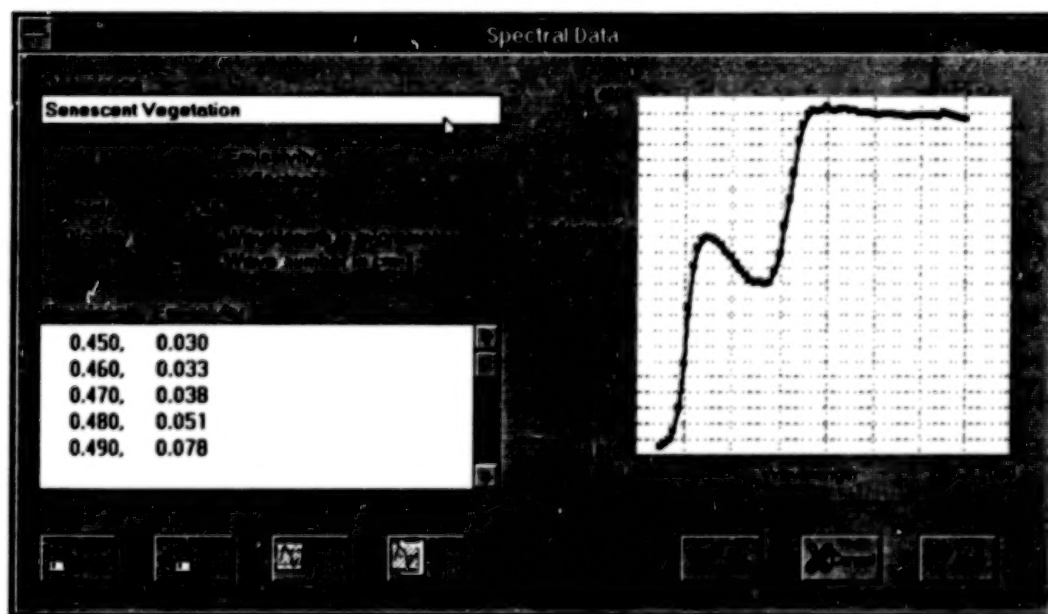


Figure 3. Target spectrum. In this example, the target is stressed vegetation. The spectrum may be input from an ASCII file and/or modified from the window.

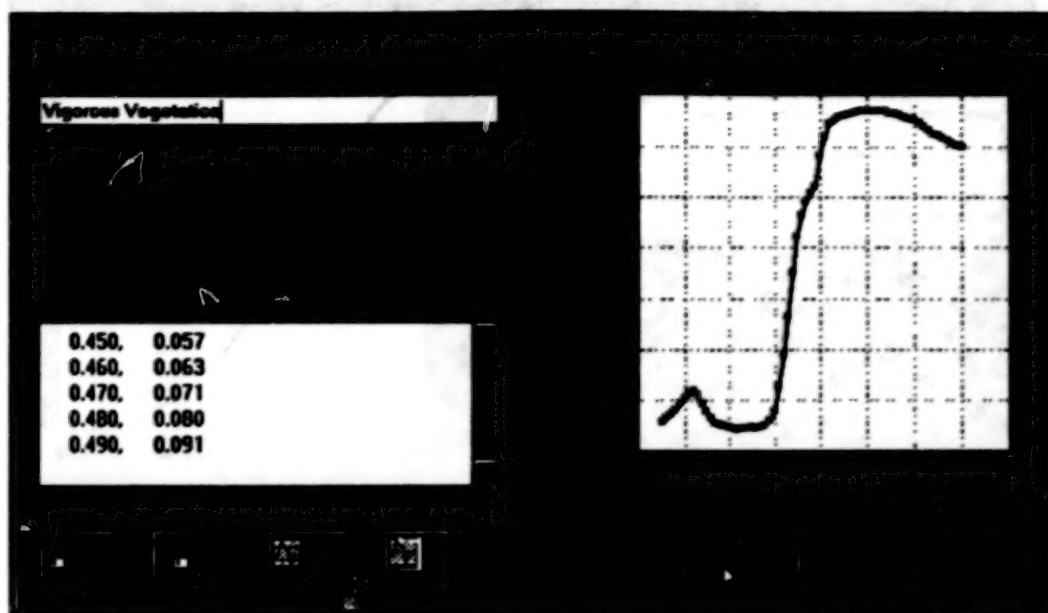


Figure 4. Background spectrum. In this case, the background is vigorous vegetation. The spectrum may, as in the case of the target, be input via an ASCII file and/or modified from the window.

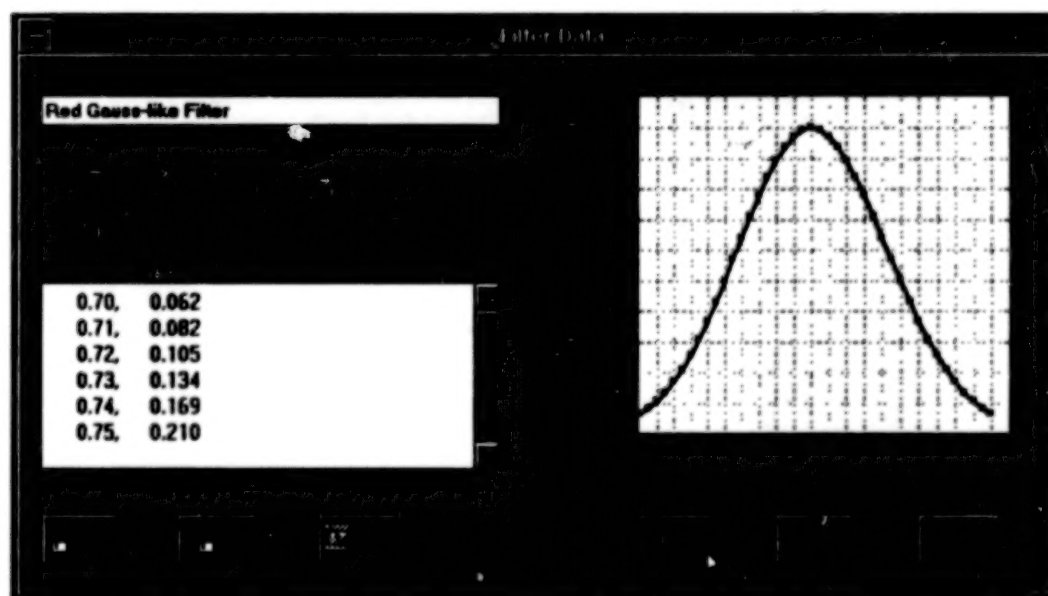


Figure 5. Input window for filter. In this case, a filter viewing the reflective IR region, of an approximately Gaussian shape, is used.

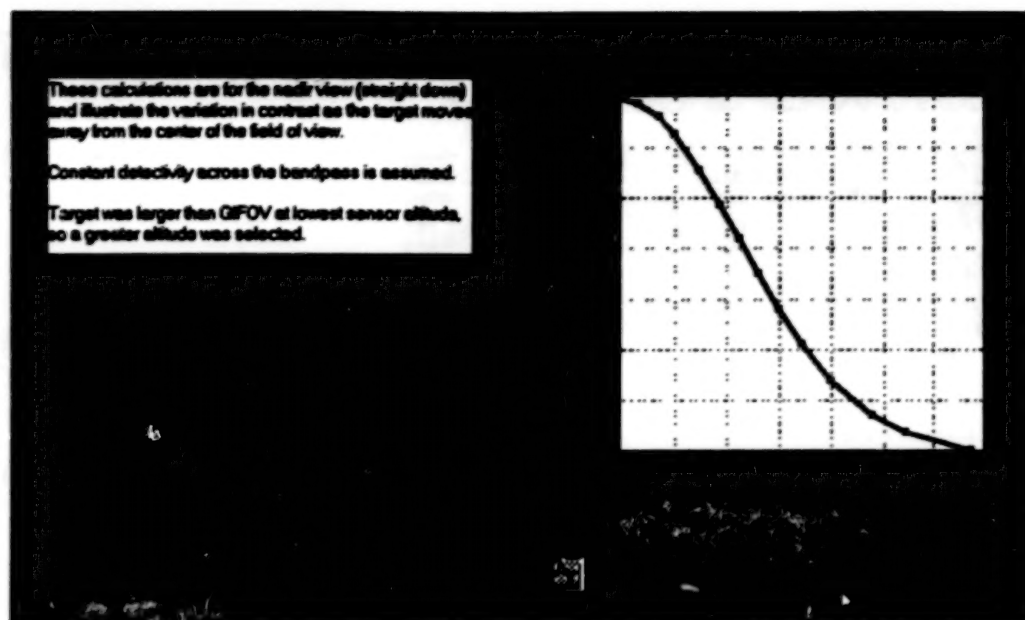


Figure 6. Effect of the distance of the unresolved target from the center of the GIFOV on the contrast between the target-containing pixel and its neighbors. A Gaussian PSF with no sidelobes is assumed here.

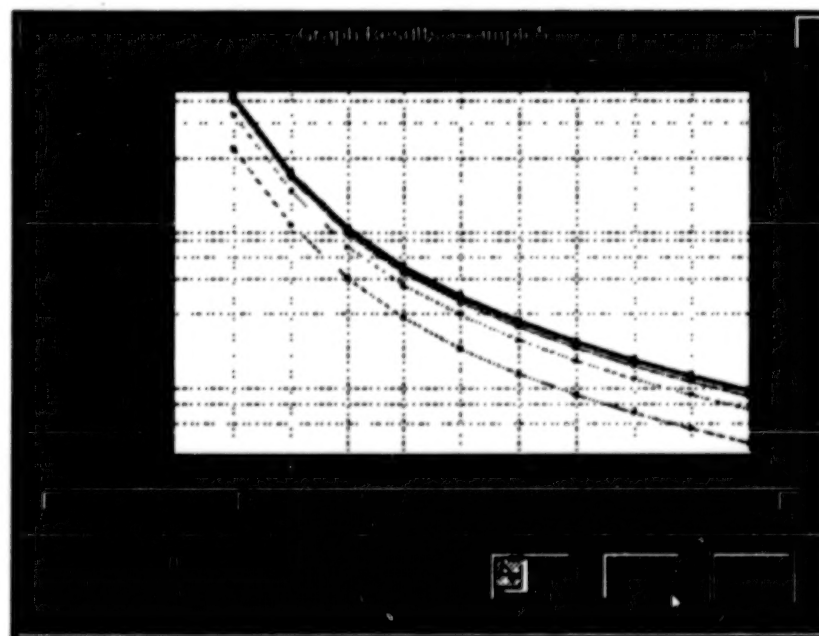


Figure 7. SNR calculations for the example shown in the figures above. Note that scientific notation, log scale, or dB scale may be selected for the ordinate. Variable 1 is the abscissa, while a separate graph (there may be up to 5) is plotted for each value of variable 2.

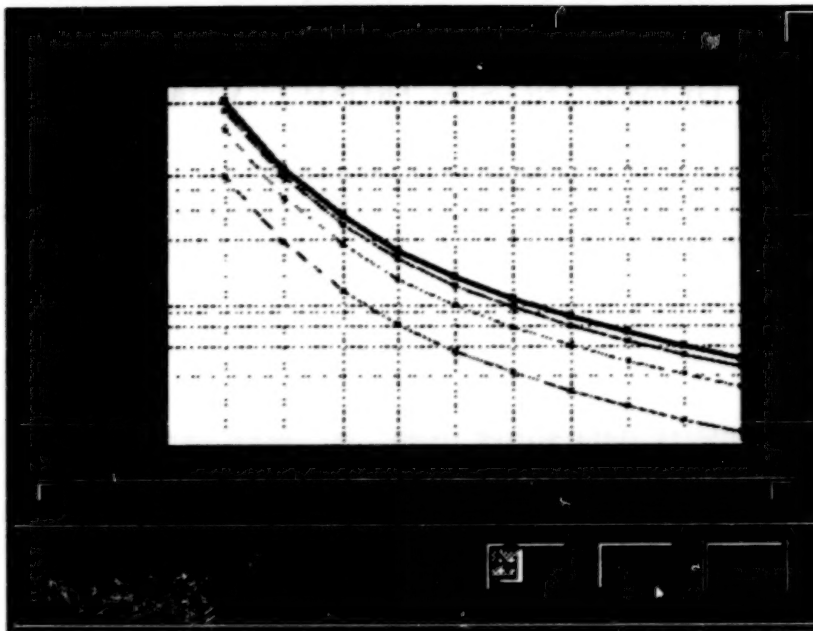


Figure 8. Gray scale contrast. The method of plotting this data is the same as in Fig. 7.

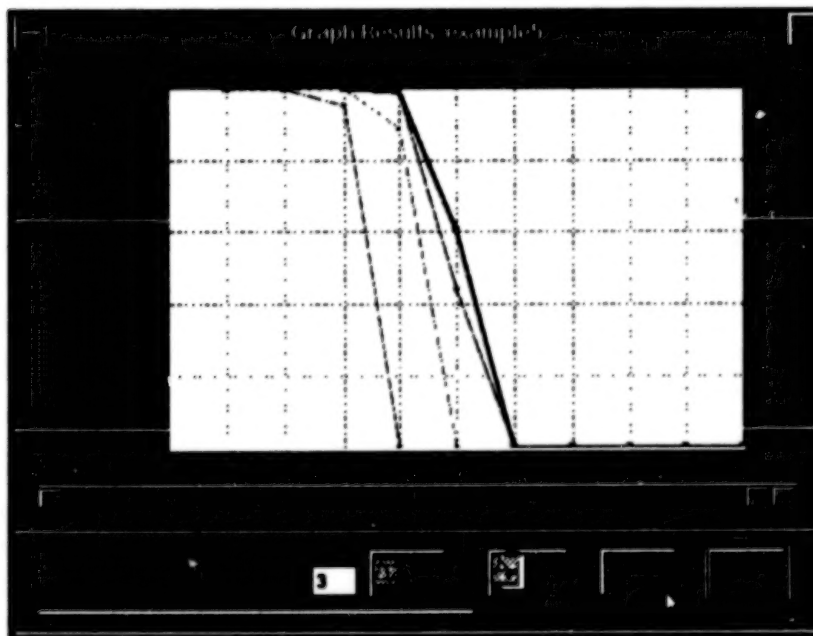


Figure 9. Probability of detecting the sub-pixel target, if it is at the center of the GIFOV for those cases shown in Fig. 1. Note that the method of displaying this data is the same as for Figs. 7 and 8.

AUTOMATING LINEAR MIXTURE ANALYSIS OF IMAGING SPECTROMETRY DATA

Joseph W. Boardman

Center for the Study of Earth from Space, CIRES, University of Colorado, Boulder
Campus Box 216, Boulder, Colorado, 80309, USA

ABSTRACT

Imaging spectrometry data suffer from two types of spectral mixing: linear and nonlinear. Linear mixing is a result of the spatial averaging inherent in all digital imagery. The nonlinear mixing is a natural effect common to all reflectance measurements. A solution to the linear mixing problem (estimation of the number of endmembers, their pure spectra and their spatial abundance patterns) can, in some cases, be derived using only the mixed data themselves. This data-driven automatic linear unmixing is based on an affine and convex geometry model.

1. INTRODUCTION

While imaging spectrometry combines the best features of laboratory spectroscopy and remote sensing (Goetz et al., 1985), permitting rapid and quantitative surface mapping of large areas, it also combines their worst features and limitations. Airborne and spaceborne digital imagery suffer from the resampling effects inherent in their sensor design and construction. The finite spatial resolutions of these remote sensing instruments strictly limit the image quality. Likewise, laboratory reflectance spectroscopy is hindered by the effects of variable transmission path lengths and multiple scattering. These limitations are inherited by imaging spectrometry from its two parent fields, digital imagery remote sensing and reflectance spectroscopy. The result is spectral mixing. The spatial resolution limitation introduces linear spectral mixing. The reflectance spectroscopy complications introduce nonlinear mixing.

Instrument-induced linear mixing can be modeled, and to some extent unravelled, using the concepts of affine and convex geometry. This paper presents a method for estimating the number of linearly mixing endmembers, estimates of their pure spectral signatures and spatial maps of their apparent surface distributions using no outside information. The mixed data themselves are used to derive the endmember estimates. The method only addresses linear mixing introduced by the digital sampling of the sensor. The underlying nonlinear reflectance systematics remain a difficult problem. The following sections discuss the linear and nonlinear spectral mixing inherent in imaging spectrometry data, the root causes of the two types of mixing, how linear mixing can be modeled as a geometry problem and how the mixed data themselves can be used to overcome this limitation.

2. INHERENT SPECTRAL MIXING

All imaging spectrometry data are spectrally mixed to some degree. Two fundamentally different types of mixing exist in imaging spectrometry data, caused by two very different processes. Linear mixing of spectral signatures is introduced by the interaction of finite instrument spatial resolution and the natural spatial heterogeneity of the imaged surface. This type of spectral mixing occurs inside the instrument, as the incoming radiance for a single pixel is integrated between detector readout cycles. Nonlinear spectral mixing occurs as a result of transmission and multiple scattering effects. This mixing occurs at the ground surface and is controlled by the geometry, spectral character and physical distribution of the surface materials. It is unrelated to the mixing that occurs within the instrument. The severity of each type of mixing, and the balance between them, varies among data sets. Both of the spectral mixing processes should be modeled and understood separately since they arise from separate causes.

2.1 LINEAR MIXING AT THE SENSOR

The concept of linear mixing of spectral signatures in digital imagery dates to the early days of airborne multi-spectral sensors (Horwitz et al., 1971). Digital imagers, by definition, resample the spatially-continuous and spectrally-continuous incoming radiance field by integration on an array of opto-electronic detectors. Linearity is assured if the detectors have a linear response function and the data are radiometrically calibrated. Accumulation of the integrated radiance signal for a single pixel is an additive process preserving the linear relationship. The degree of linear mixing present in a data set is a function of the spatial scales of surface heterogeneity and the size of the ground instantaneous field of view (GIFOV) of the instrument. Linear mixing is an instrument-induced effect. Decreasing the size of the GIFOV for a heterogeneous scene increases the variance in the data and makes purer pixels more likely. The particular dependence of the severity of linear mixing on instrument spatial resolution varies among scenes and even among the several different spectral endmembers that comprise a single scene.

2.2 NONLINEAR MIXING AT THE SURFACE

Nonlinear spectral mixing is the result of photons encountering more than one material before being reflected to the sensor. Intimate mixtures of minerals (Mustard and Pieters, 1987), vegetation (Roberts et al., 1993) and water (Hamilton et al., 1991) remote sensing typically have significant multiple scattering and transmission effects that introduce nonlinearities. The underlying common feature in nonlinear spectral mixing is the multiple scattering of photons among different surface materials. As opposed to the sensor-induced linear mixing, this nonlinear mixing is a naturally-occurring phenomenon that is present in the upwelling radiance field even if no instrument is present to measure it. Measurements in laboratory spectrometers seek to eliminate linear mixing, by measuring a homogenous field of view, but cannot escape the naturally-occurring nonlinear mixing. Airborne or spaceborne imaging spectrometry data, with their much larger GIFOV, inherently suffer from both types of mixing. The degree of transmission, multiple scattering and the spatial scales of compound mixing ultimately determine how the mixing is partitioned between the natural nonlinear process and the measurement-caused linear effect.

2.3 IMPLICATIONS FOR QUANTITATIVE ANALYSES

A full range of distributions between linear and nonlinear mixing is possible. If a homogeneous area fills the GIFOV of a pixel, or a laboratory spectrometer, then no linear mixing effects will be present in the recorded spectrum since the detector integrates a spatially constant signal. No variance is lost because of the digital sampling. Nevertheless, the signature for this homogeneous area may very well be a nonlinear composite of the signatures of the compounds that make up the sample being measured. On the other hand, a large pixel covered with many different cover types that have a minimal amount of intimate mixing and little multiple scattering between materials will approach purely linear mixing. In this case the bulk of the photons in the radiance field only encounter one material before being reflected to the sensor. Much of the variance in the upwelling radiance field will be lost in the digital sampling process. A real example of the nearly-nonlinear case is a homogeneous and closed forest canopy. A real example of the nearly-linear case is a desert environment with geological variations whose spatial scales are small compared to the pixels. Typical imaging spectrometry data sets are more complicated, with the degree of nonlinear and linear mixing varying both spatially across the scene and spectrally across the wavelength region imaged.

Ideally, both types of spectral mixing must be unravelled to get the full benefit of the quantitative remote sensing promised by imaging spectrometry. But they must be done separately using appropriate algorithms. The remainder of this paper deals with a data-driven method for modeling and inverting the instrument-caused linear mixing using affine and convex geometries. No attempt is made here to further decompose the underlying nonlinear reflectance spectroscopy problem. If the linear problem can be addressed and solved, requiring little or no outside information, then one of the major limitations of quantitative imaging spectrometry will be overcome. This will put imaging spectrometry on a similar footing with laboratory reflectance spectroscopy, removing the most compromising effect introduced by the remote measurement, the linear mixing caused by integration over a large GIFOV. However, even in this event, the nonlinear mixing eventually must be addressed. Unfortunately, crucial variables such as viewing geometry, transmission path lengths and illumination conditions, all used in laboratory spectroscopy to analyze the nonlinear mixing, are either unavailable or poorly determined in the remote sensing setting.

3. GEOMETRIC MIXTURE ANALYSIS

Linear spectral mixture analysis can be modeled as a geometry problem in n -dimensional Euclidean space. A geometric model provides both a basis for intuitive understanding of mixing systematics and an analytical framework for solving the mixing problem by inversion of the mixing process (Boardman, 1993). The method has three main steps, assuming the data have already been reduced from spectral radiance to apparent surface spectral reflectance (Gao et al., 1993). First, the number of mixing endmembers is determined by a dimensionality analysis of the apparent reflectance data. Second, the shape of the convex hull of the data is used to find estimates of the unknown spectral signatures of the pure endmember materials. Finally, the mixed data are transformed into maps of the apparent surface abundance of each endmember material, unmixing the data using data-derived endmembers. The goal of this processing is to model and remove the

deleterious effect of linear mixing caused by the digital sampling of the instrument and to provide a set of data-derived spectral endmembers that explain the bulk of the variance in the data. Excessive nonlinear mixing in the data can corrupt this processing, yielding unreliable and incorrect results. It is best applied to data sets dominated by linear mixing, where the nonlinear mixing effects are minimal or at least spatially constant. The method described here is a follow-on to one outlined by Craig (1990). Subsequent literature searches have uncovered similar geometric approaches to linear unmixing in several other fields (Full et al., 1981; Full et al., 1982; Renner, 1993).

3.1 N-DIMENSIONAL SPECTRAL SPACE

The concept of n -dimensional spectral space is crucial for the geometric modeling of linear mixing. If n is the number of bands in the data, then each spectrum in the scene corresponds to a point in this n -dimensional Euclidean space. Each band is assigned to one of the n orthogonal axes and the position of a single spectrum in n -space is determined by the reflectance value in each band of its spectrum. The many spectra in a scene map to an equal number of points in the n -dimensional scatterplot. The derivation of the number of endmembers and the estimates of their pure spectra are based on the covariance structure and exterior shape of this n -dimensional scatterplot.

3.2 AFFINE HULL DETERMINATION

The number of linearly-independent and spatially-variable endmembers is one more than the inherent dimensionality of the data. Just as two points span a 1-dimensional line and three points span a 2-dimensional plane, $m+1$ points, or endmembers, define an m -dimensional flat or subspace. This linear subspace is called the affine hull (Valentine, 1964) of the points it contains. All possible linear mixtures of these $m+1$ endmembers must lie in this m -dimensional affine hull. We use the covariance structure of the n -band data to determine the dimensionality and orientation of the m -dimensional affine hull that spans the data. The value of m is chosen to be as small as possible. It must be large enough to account for the real variance in the data, preserving the fidelity of the reflectance signal but not the noise component. A noise-whitening affine transform (Green et al., 1988; Boardman, 1993) is used to minimize the impact of noise on this estimation. The affine hull is defined as the subspace spanned by the mean of the data and the m eigenvectors associated with signal-carrying dimensions. In the case of imaging spectrometry data m is typically much less than n . The dimensionality of imaging spectrometry data is less than the number of bands. This is indicated by the degeneracy of the covariance matrix. The complementary $n-m$ -dimensional space spans only noise and is treated as a residual.

An accurate determination of the data dimensionality requires the number of bands to exceed the data dimensionality. If data that are inherently three dimensional, being linear mixtures of four endmembers, are imaged with only two spectral bands then their true dimensionality cannot be recovered. The undersampled data can be thought of as a shadow of the true data, projected onto a subspace spanned by the two bands. No amount of processing can uniquely determine the spectral shape of these data given only their projected shadow. If the covariance matrix of the data is not degenerate then not enough bands were used to image the scene. In other words, one must have too many spectral bands before one can be sure there are enough spectral bands. Hyperspectral data should spectrally oversample the observable radiance field, otherwise the number of endmembers

can not be determined. Once the dimensionality is determined, all the data are projected onto this subspace for further processing. This projection serves several useful functions: the number of endmembers is determined to be $m+1$; much of the noise is removed from the data; and the data are compressed by a factor of m/n , accelerating and stabilizing subsequent numerical processing (Boardman and Kruse, 1994).

3.3 CONVEX HULL MODELING

The definitions of linear spectral mixing and convex sets are identical. Both are linear combinations of some set of basis points, with positive coefficients that sum to unity for each sample. This direct correspondence of convexity and linear mixing permits the application of convex geometry methods (Lay, 1982) that can be used to estimate the pure spectral signatures of the unknown $m+1$ endmembers. The unknown endmembers make up the vertices of a mixing simplex that must contain all the observed spectra, if the mixing is linear. The goal of this part of the processing is to estimate this mixing simplex, defined by its vertices and faces, using the interior mixed points as guides and constraints.

Ideally all possible mixtures would be present in the scene, filling the mixing simplex and making its derivation an easy task. In this sense, spatially variable mixing is now an ally rather than an enemy. The more different mixtures that occur within the scene, the easier it is to estimate the unknown simplex from the mixed data. Any pixel that has a zero abundance of one or more of the endmembers must be on one of the faces of the desired simplex, mapping out its faces. An optimal method for simplex estimation is not currently known, but approximate methods for finding small-hypervolume, data-enclosing simplices have shown promise. Finding a small, enclosing simplex can be cast as a series of nonlinear optimization of dimension $m+1$ subject to a set of p linear inequality constraints, where p is the number of vertices of the convex hull of the data. The current method uses a logarithmic change of variables and a rotation of the parameter space to transform this problem into an unconstrained nonlinear optimization problem in dimension m . Practical cases have been treated up to dimension 6 with over 100,000 hull vertices, running in a few minutes on a typical UNIX workstation. Several examples will be demonstrated at the symposium, illustrating the potential of the method for recovering pure endmember spectra even when no pure pixels exist in the scene.

A mixing simplex that contains the convex hull of the dimension-reduced data must give feasible, positive and unit-sum, abundances for each pixel. This obviates the need for time-consuming and potentially-misleading non-negative least-squares programming. The problem is solved as even-determined, thus there is a unique and exact solution. The only part of the signal not explained by the data-derived endmembers is that part spanned by the neglected $n-m$ -dimension noise-carrying subspace. Constrained methods that force a solution to be positive and unit-sum, when the unconstrained solution is infeasible, are ignoring the message contained in the infeasible answer: the wrong endmembers have been selected. Processing degenerate data in the full n -dimensional space, as opposed to working in the dimension-reduced m -dimensional subspace, destabilizes the inversion solution and invites numerical roundoff problems.

3.4 UNMIXING AND INTERPRETATION

Once the $m+1$ endmember spectra have been estimated, the calculation of abundance is a simple transformation to barycentric coordinates (Valentine, 1964). This transformation can be cast as the inversion of an even-determined system of $m+1$ simultaneous linear equations, the m spectral dimensions provide m equations and the final equation is due to the unit-sum constraint. Thus the actual unmixing is trivial when the endmembers are known or derived. It is the estimation of the number of endmembers and their spectral signatures that is the real essence of mixture analysis. Geometrically, the transformation to abundance is a nonorthogonal change of basis, where the new axes are the inward-pointing normals of the mixing simplex facets. The hyperplanes of equal abundance of a certain endmember are parallel to the hyperplane that contains the $m-1$ -dimensional facet formed by the other m endmembers. Ironically, one must know the orientation of this opposite facet, determined by all but one endmember, to correctly unmix that endmember of interest.

Interpretation and validation of the results are done by inspection of the derived endmember spectra and their corresponding abundance images. Since there is an infinite set of possible simplices that contain the data the derived endmembers can be incorrect. Currently three methods are used to assess the success or failure of the endmember derivation. First, the m -dimension endmember spectra are back-transformed into their n -band counterparts. Inspection of these pure endmember estimates for feasibility and similarity to known Earth materials is used to judge the processing. Second, the spatial images depicting the apparent surface abundances of the endmembers are used, in conjunction with the spectra, to identify the endmembers and assess the derivation. For example, if significant topography is present a shade/black endmember should be identifiable, characterized by a very low amplitude spectrum and an abundance image that is the complement to an image of the cosine of the local solar incidence angle. Third, the fit of the simplex around the convex hull of the data can be used to qualitatively determine the uniqueness of the results. Obviously a hyperspherical scatterplot has no unambiguous best-fit simplex, while a scatterplot that is nearly simplicial in shape would give a high degree of confidence in the result.

3.5 PARTIAL AND DIRECTED UNMIXINGS

The computational complexity of geometric processing rises very rapidly with dimension, easily outpacing hardware capabilities. Complex scenes imaged with current sensors indicate that the dimensionality of natural scenes can exceed fifteen. This is far too high a dimension for the full unmixing method outlined above. A partial unmixing method is currently under development. In this partial unmixing approach the original n -band data space is partitioned into three subspaces. One k -dimension subspace spans only the noise in the data. The remaining $n-k$ -dimension subspace is then split into an m -dimension subspace and a p -dimension one, where $p+m+k$ equals n . With a suitable choice of this partitioning, the m -dimension space spans all m of the endmembers of interest and another virtual endmember representing the composite of the other p materials. Some rotation of the $m+p$ space will permit an orthogonal projection onto the m -dimension space where all $p+1$ of the other endmembers will project to the same point. In this way an intractable $m+p$ -dimension problem can be reduced to a manageable m -dimension one, especially if the number of endmembers of interest is relatively small.

4. CONCLUSIONS

Imaging spectrometry data are inherently spectrally mixed. This mixing results from two very different sources: the digital spatial sampling of the instrument and the multiple scattering and transmission of photons through multiple surface materials. The instrument-induced mixing is purely linear, since it is the result of an additive integration of photons on the detectors. The multiple scattering mixing is nonlinear because of the cascaded multiplications involved in transmission and scattering. The degree of linear mixing is much higher in imaging spectrometry data than laboratory spectral data because of the large GIFOV.

Much of the information needed to unravel the linear mixing in imaging spectrometry data is available, imbedded in the data. If a wide range of mixing occurs in the data and the number of spectral bands exceeds the number of dominant linear endmembers, then the data themselves can be used to deduce the number of endmembers and estimates of their pure spectra. This can be done successfully even if no pure pixels exist in the scene. This method is not effective on scenes dominated by spatially-variable nonlinear mixing and scenes where all materials co-occur in almost equal proportions in every pixel.

Convex and affine geometries provide a natural basis for understanding and analysis of the linear mixing in imaging spectrometry data. Determining the affine hull of the data fixes the number of endmembers. Fitting a simplex around the convex hull of the dimension-reduced data derives estimates of the pure endmember signatures. If the dimensionality is too high this full unmixing will not be possible, due to computational constraints. In these cases a possible solution is a partial unmixing, based upon these same geometric ideas.

ACKNOWLEDGMENTS

This work was supported at the University of Colorado by two funding sources: a grant from NASA and a contract from Texas Instruments as part of their MUSE Project. Their support and the support of the University are happily acknowledged. The author also benefited from discussions of spectral mixing with co-workers at CSES. Professor Victor Klee, of the University of Washington, has been a source of crucial advice on the application of convexity concepts.

REFERENCES

- Boardman, J.W., 1993, Automating spectral unmixing of AVIRIS data using convex geometry concepts, in: Summaries of the Fourth Annual JPL Airborne Geoscience Workshop, JPL Publication 93-26, pp 11-14.
- Boardman, J.W. and F.A. Kruse, 1994, Automated spectral analysis : a geological example using AVIRIS data, North Grapevine Mountains, Nevada, in: Proceedings of the

- Craig, M., 1990, "Unsupervised Unmixing of Remotely Sensed Images", in: Proceedings of the Fifth Australasian Remote Sensing Conference, Perth, Australia, pp. 324-330.
- Full, W.E., R. Ehrlich and J.E. Klovan, 1981, EXTENDED QMODEL - objective definition of external endmembers in the analysis of mixtures, Math. Geol., v. 13, pp. 331-344.
- Full, W.E., R. Ehrlich and J.C. Bezdek, 1982, Fuzzy QMODEL - a new approach for linear unmixing, Math. Geol., v. 14, pp. 259-270.
- Gao, B-C, K. B. Heidebrecht and A. F. H. Goetz, 1993, Derivation of scaled surface reflectances from AVIRIS data, Remote Sensing of Environment, v. 44, no. 2, pp. 165-178.
- Goetz, A. F. H., Vane, G., Solomon, J. E., and Rock, B. N., 1985, Imaging spectrometry for earth remote sensing, Science, v. 228, 1147-1153.
- Green, A. A., M. Berman, P. Switzer and M. D. Craig, 1988, A transformation for ordering multispectral data in terms of image quality with implications for noise removal, IEEE Transactions on Geoscience and Remote Sensing, v. 26, no. 1, pp. 65-74.
- Hamilton, M.K., C.O. Davis, S.H. Pilorz, W.J. Rhea and K.L. Carder, 1991, Examination of chlorophyll distribution in Lake Tahoe, using the Airborne Visible/Infrared Imaging Spectrometer (AVIRIS), in: Proceedings of the Third Airborne Visible/Infrared Imaging Spectrometer (AVIRIS) Workshop, Pasadena, CA, JPL Publication 91-28, pp. 289-301.
- Horwitz, H.M., Nalepka, R.F., Hyde P.D., and Morgenstern, J.P., 1971, Estimating the proportions of objects within a single resolution element of a multispectral scanner, in: Proceedings, 7th International Symposium on Remote Sensing of Environment, Ann Arbor, Michigan, pp. 1307-1320.
- Lay, S. R., 1982, Convex Sets and their Applications, John Wiley and Sons, New York.
- Mustard, J.F. and C.M. Pieters, 1987, Quantitative abundance estimates from bidirectional reflectance measurements, J. Geophys. Res., v. 92, p. E617-E626.
- Renner, R.M., 1993, The resolution of a compositional data set into mixtures of mixed source compositions, Applied Statistics, v. 42, pp. 615-631.
- Roberts, D.A., M. O. Smith and J.B. Adams, 1993, Green vegetation, nonphotosynthetic vegetation, and soils in AVIRIS data, Remote Sens. of Environ., v. 44, pp. 255-269.
- Valentine, F. A., 1964, Convex Sets, McGraw-Hill Book Company, New York.

FROM A NATURAL TO A BEHAVIORAL CLASSIFICATION

Jean Paul Rasson, F. Orban-Ferauge and V. Granville
Laboratory GEOSATEL, F.U.N.D.P. University
B5000, Namur
BELGIUM
33 81 72 4928

After the publication in 1977 of the solution for the estimation of the convex support of a uniform density, it has been suggested that this result could be useful for the classification problems. The first application, for clustering which used the Homogeneous Poisson Process, generating uniform conditional densities led to a very intuitive criterion: "Find the g groups of points such that the sum of the Lebesgue measures (i.e. areas in the plane) of their convex hulls is minimal". This led also to a natural criterion in the dual problem of discriminant analysis "Affect x to the class for which the Lebesgue measure, added by convexity to the convex hull of its training set, is minimal".

This algorithm was very expensive in terms of C.P.U. time. This problem was solved using, as estimations of the new convex sets including the point to classify, only the homothetic expansion of the initial convex hulls of the training sets. A second problem was that, with this model, we were unable to classify the points belonging to the intersection of several convex hulls. We then adopted an empirical rule in order to classify these points.

In order to avoid an heuristical part in the algorithm, we generalized the basic hypothesis, the Homogeneous Poisson Process into the hypothesis of Non-homogeneous Poisson Process. As a result, the same equation gave a rule for all the points to be classified, which was a direct generalization of the natural one. But, since the training sets were not, generally, sampled randomly, we adopted a different "behaviour", estimating the a-priori probabilities via an E.M.-like algorithm, keeping the nonparametric density estimators fixed; a way of estimating the bandwidth is given. Finally, in order to take into account the contextual point of view, we adapted the classical I.C.M. algorithm.

APPLICATION OF THE NATURAL AND THE BEHAVIORAL APPROACHES FOR SUPERVISED REMOTE SENSING CLASSIFICATION

F. Orban-Ferauge, Jean Paul Rasson and V. Granville
Laboratory GEOSATEL, F.U.N.D.P. University
B5000, Namur
BELGIUM
33 81 72 4928

Related to the paper "*From a Natural to a Behavioral Classification*"² that presents the theoretical aspects of our approach, we propose to illustrate the progressive steps of our research with classifications of SPOT, LANDSAT and RADAR images using only the spectral information. The results will be discussed in terms of C.P.U. time and well classified pixels rates, the confusion matrices will be commented, as well as the soil affectations will be interpreted. A connection will be established with the segmentation problematic.

Following the stages of the research, the interpretation of the images shows a progressive homogeneity of the parcels correctly affected. Consequently most of the scattered small groups of pixels have disappeared, the boundaries of the parcels are clearer delimited. Most of the small lines of wrong affected pixels along these boundaries are cancelled.

The results may of course be ameliorated by using a preliminar segmentation: if we classify only the pixels inside the segments and reallocate the boundary pixels by a fuzzy classification, the rates of well classified pixels reach the same rate of good classifications than pure pixels, which is more than the results obtained by neural networks and expert systems using ten additional parameters.

The Behavioral Classification ameliorates not only the global rates of well classified pixels, it produces a more homogeneous result in terms of parcellar. It also ameliorates the sharpness of the boundaries and could become in interaction with the segmentation problematics.

Manuscript not available at time of printing. Please contact authors for further information.

²Rasson, J.P., Orban-Ferauge, F., Granville V., *From a Natural to a Behavioral Classification*, ISSSR '94, San Diego, California, USA.

ASSESSMENT OF THE LINEAR MIXING MODEL FOR SUBPIXEL MATERIALS DETECTION IN THERMAL INFRARED MULTISPECTRAL SCANNER (TIMS) IMAGES

Ronald G. Resmini¹, Jessica M. Sunshine¹, Alan Schaum²,
Thomas B. McCord¹, Jennifer L. Forsythe¹ and Alan R. Gillespie³

¹SETS Technology, Inc.
300 Kahelu Avenue, Suite #10
Mililani, Hawaii 96789-3911, USA

²Naval Research Laboratory, Code 5620
4555 Overlook Avenue, SW
Washington, D.C., 20375-5326, USA

³Department of Geological Sciences, AJ-20
University of Washington
Seattle, Washington 98195, USA

ABSTRACT

The subpixel linear mixing model (LMM) has been successfully applied to visible and near infrared multi- and hyperspectral remote sensing imagery (MSI and HSI, respectively). Few studies have applied LMM to thermal infrared (TIR) imagery; results suggest that LMM is a powerful tool for extracting information from and classifying TIR images. Here, we report on results of LMM applied to images acquired with the Thermal Infrared Multispectral Scanner (TIMS; six channels between 8 and 12 μm). LMM was applied to images containing implanted targets in order to assess the ability of LMM to detect subpixel targets. The data were atmospherically corrected, calibrated to radiance, and temperature and emissivity were extracted. Target materials were then selected for their spectral similarities and contrasts with their intended host pixels and were implanted within background pixels with various small temperature contrasts and fractional proportions. LMM was subsequently applied. Note that target spectra were not selected as image endmembers. Total RMS error, band residual, and fraction images output by LMM are analyzed as are signal to clutter images of individual, summed band residual, and summed absolute fractional abundance images. LMM exposes the implanted targets for pixels containing $\geq 20\%$ of target. The actual detection threshold percentage is primarily a function of the spectral contrast between target and background. The image type in which the targets appear as anomalies varies and so analysis of the several images created by LMM is required. Mixing model-produced image post-processing enhances the target detection performance of LMM. Based on these results, LMM holds promise as a robust materials detection methodology for TIR MSI.

1. INTRODUCTION

The goals of the analysis of remote sensing imagery are the detection, identification and characterization of objects, materials and events within captured scene(s). Early remotely sensed data were panchromatic images in which, optimally, objects had to be multipixel in scale to be identifiable. Objects that are single pixel in dimension are detectable though difficult or impossible to identify; objects which comprise only a fraction of a pixel can be undetectable. Furthermore, with panchromatic imagery, object and material characterization, i.e., a determination of composition and/or temperature, is nearly impossible.

The next generation of remote sensing systems to be developed—multi- and hyperspectral imaging spectrometers—overcame these limitations. Imaging spectrometers simultaneously acquire many coregistered images of a single scene in many different regions of the electromagnetic spectrum.

These multiband or multi- and hyperspectral images (MSI and HSI, respectively) facilitate multipixel-scale object and material detection, identification, *and* characterization as well as the detection, tentative identification, and characterization of single and subpixel scale features.

Substances commonly present in terrestrial images (e.g., vegetation, rock, soil, etc.) have emission signatures in the mid- to thermal infrared (TIR) region. Emission spectra are controlled by the type, arrangement, and bonding between atoms and molecules, and as such contain features that are characteristic and diagnostic of measured substances. Thus, TIR MSI is useful for studying and modeling the terrestrial environment. It should be noted that the study presented here is designed to exploit the spectral properties of materials in the TIR to detect targets and not merely use TIR sensors to identify thermal anomalies.

In the present study, funded by and in collaboration with the Optical Sciences Division of the Naval Research Laboratory, U.S. Navy, we determined detection thresholds of implanted subpixel materials in TIR MSI using the subpixel linear mixing model (LMM; Adams et al., 1986) in order to assess and quantify the ability of LMM to detect subpixel materials and events. The images studied also generally contain other naturally occurring features of potential interest to military and civil planners (e.g., roads). LMM has been applied extensively to MSI and HSI acquired in the visible and near infrared regions of the electromagnetic spectrum with considerable success (e.g., Adams et al., 1986; Sabol et al., 1992; Bateson and Curtiss, 1993; Tompkins et al., 1993; Mustard, 1993). Relatively few studies, however, have applied LMM to TIR imagery (e.g., Gillespie, 1992a; Gillespie et al., 1990). Performance characteristics will facilitate comparisons of LMM with other subpixel material and event detection methodologies (e.g., Yu et al., 1993; Schaum and Stocker, 1994). Our results indicate that LMM is a powerful tool for extracting information from and classifying TIR images and has significant military and civil potential to be a robust subpixel *and* multipixel material and event detection methodology.

2. SUBPIXEL MIXING ANALYSIS WITH LMM

The LMM is an algorithm which performs subpixel mixture analysis using purely spectral characteristics (Adams et al., 1993). Under LMM, the radiance of a pixel in band i , R_i , is assumed to be a linear combination of endmember spectra:

$$R_i = \sum_{j=1}^n f_j M_{j,i} + r_i \quad (1)$$

where f_j is the fraction of the pixel consisting of the radiance of the j th endmember, $M_{j,i}$ is the unmodeled or residual radiance for the pixel in band i , and n is the number of endmembers. In this report, the sum of the fractions is constrained to equal one:

$$\sum_{j=1}^n f_j = 1 \quad (2)$$

With equation 2, the number of endmembers is less than or equal to one plus the number of image channels, k .

The endmembers, $M_{j,i}$, can either be reference endmembers chosen from a spectral library or, as in this analysis, endmembers are selected from within the scene. Each pixel is then represented by the fractional amount of each endmember required to best model the actual pixel spectrum. The number of endmembers is generally considered to be one plus the number of eigenvalues in a principal components analysis (PCA) greater than sensor noise. "Virtual" cold (and its analog, shade, in

visible/near images) is always an endmember but it is not a physical or tangible image component like vegetation. Information on the temperatures of the actual, tangible endmembers is accounted for by the fractional abundance of the cold endmember. Because of the virtual cold endmember, shaded regions in a TIR image are not likely to be incorrectly modeled as a combination of radiances from other cold image constituents (e.g. snow) that occur elsewhere within the scene (Gillespie, 1992a).

The end products of the LMM are a series of n images containing the fractional amount of each endmember in every pixel. These fraction images provide a quantitative characterization of the scene which is readily interpretable in terms of the materials that create the spectral signatures. The LMM thus performs image classification and provides quantitative abundance maps of image components. LMM also produces k band-residual images which display the goodness-of-fit, r_i , of the endmembers on a band-by-band basis and a total RMS image displaying a global goodness-of-fit:

$$\sqrt{\frac{\sum_{j=1}^k r_j^2}{k}} \quad (3)$$

3. METHOD

LMM was applied to two scenes acquired with the Thermal Infrared Multispectral Scanner (TIMS). TIMS is a six-channel (between 8 and 12 μm), airborne, cross-track scanner built by Daedalus Enterprises, Inc. and operated by NASA (Palluconi and Meeks, 1985). TIMS bandwidths and locations are given in Table 1. After applying Kirchhoff's Law, laboratory-measured reflectance spectra (hemispherical reflectance) of three military-related target substances (see below) were convolved with the TIMS spectral response functions (Palluconi and Meeks, 1985) to produce six emissivities corresponding to each of the six TIMS bands. Target materials were selected for their spectral similarities and low contrasts with their intended host pixels. The three target materials (0007UUUFAB = dark brown neoprene rubber fabric; 0033UUUCNT = green cloth camouflage net; and 0430UUUML = light gray paint on metal) were each, in turn, mixed in varying proportions (10%, 20%, 35%, 50%, 70%, 100%) with background and implanted into two TIMS scenes: 1) White Mountains, Calif., acquired on September 25, 1987 at (start/stop time) 21:44:16 to 21:48:48 (GMT) and from (lat., lon. to lat., lon.) 37° 41.0', -118° 20.0' to 37° 23.0, -118° 02.0' at an altitude of ~5029 m (pixel size is ~12.6 m); and 2) Cascade Head, Ore., acquired on June 19, 1990 at (start/stop time) 20:15:53.0 to 20:15:36.0 (GMT) and from (lat., lon. to lat., lon.) 45° 3' 36.2", -123° 53' 35.3" to 45° 1' 21.9", -123° 53' 11.6" at an altitude of ~4480 m (pixel size is ~11.2 m). (The Oregon data were acquired as part of the Oregon Transect Ecosystem Research Project (OTTER) of NASA/Ames Research Center.) Optical blurring of implanted pixels was not employed. Small temperature contrasts between the target pixels and the background were chosen (0K, +2.5K, and -2.5K). Background temperatures and emissivity spectra of the host pixels were determined by converting digital number (DN) to radiance after Palluconi and Meeks (1985), and applying a LOWTRAN-derived atmospheric correction (a midlatitude summer model atmosphere defined by LOWTRAN; Kneizys et al., 1983) and the channel 6 emissivity model (Kahle et al., 1980). Eight pixels in each scene contained implanted targets; targets were implanted within single, isolated pixels and in small (generally 2X2) pixel 'clumps'. Target and background emissivity spectra are given in Fig. 1. All image processing was performed using SETS Technology's HIPSTM (Hyperspectral Image Processing System) and STARSTM (Spectrometric Target Analysis and Recognition System) software; the STARSTM module performs the subpixel linear mixing analysis.

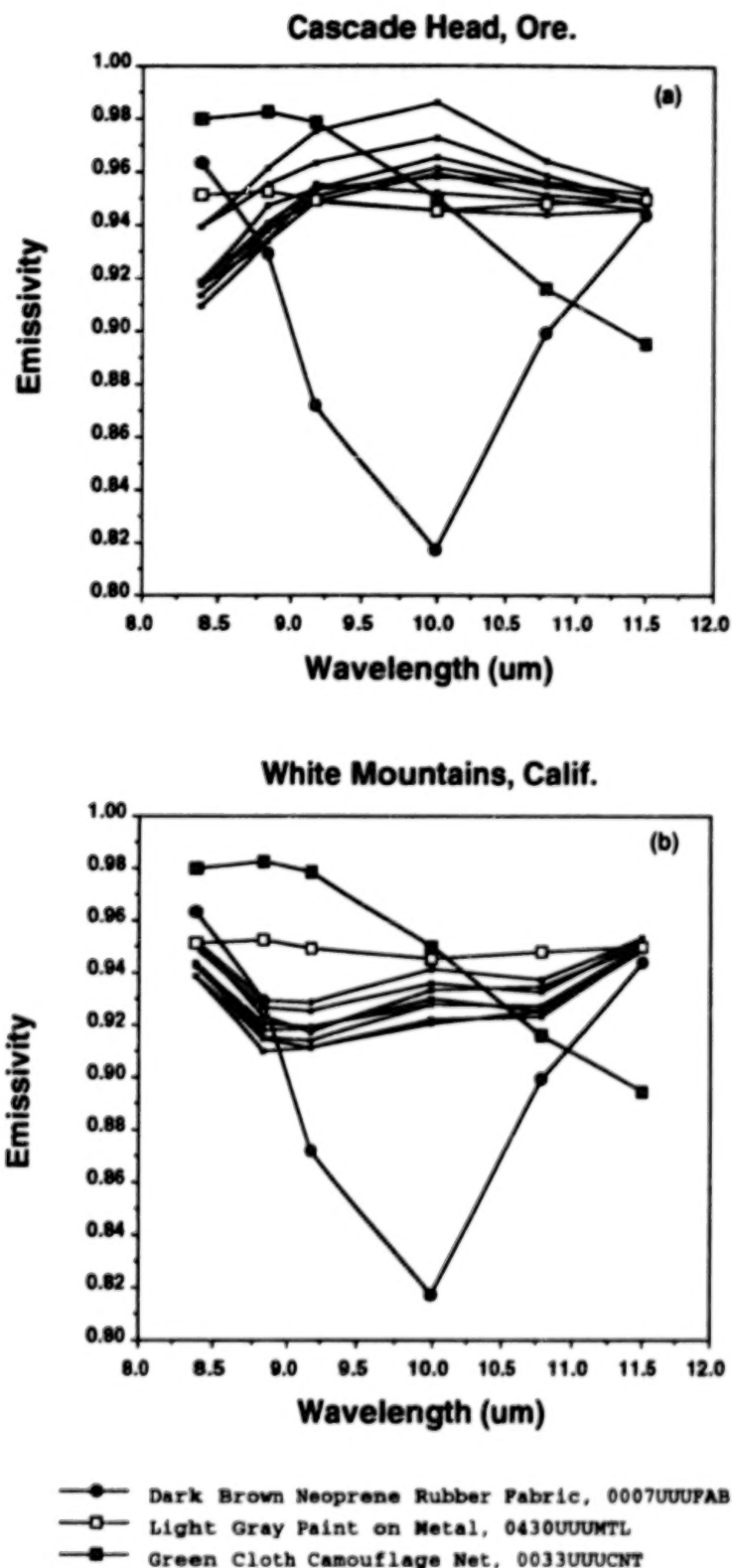


Figure 1: Target and background emissivity spectra for (a) Cascade Head, Ore., and (b) White Mountains, Calif. Target spectra, calculated by convolution with the TIMS spectral response functions, are indicated by the large symbols. Background spectra are indicated with the small, filled squares. The eight background emissivity spectra in each plot correspond to the eight pixels in each scene used for target implanting.

TABLE 1. TIMS BAND WIDTHS AND LOCATIONS

TIMS Band	Lower Bound μm	Band Center μm	Upper Bound μm
1	8.00	8.39	8.96
2	8.32	8.82	9.44
3	8.64	9.18	9.76
4	9.47	9.99	10.72
5	10.14	10.78	11.39
6	10.88	11.50	11.84

The image endmember selection process is assisted by analyzing PCA images and decorrelation contrast stretched images of the respective scenes (Soha and Schwartz, 1978; Gillespie et al., 1986; Gillespie, 1992b). Target spectra are not selected as image endmembers; i.e., we employ the residual threshold analysis of Sabol et al. (1992). The objects/materials which generally dominate terrestrial remotely sensed imagery (vegetation, soil, rocks, water, etc.) are characterized and essentially removed by LMM. The remainder are anomalies or features that were not well modeled by LMM—potential targets. Total RMS error, band residual, and fraction images produced by the LMM are analyzed as are summed fraction images and signal to clutter images of summed band residuals (see below).

3.1 SIGNAL TO CLUTTER

The goodness of fit, as measured by the residual images, can be used to search for anomalous pixels. To facilitate this, an image composed of the sum of the absolute values of the 6 band residual image DNs (on a pixel-by-pixel basis) is constructed. The standard deviation of the DNs of the entire summed band residual image is found. A 3X3 high-pass (mean removal) filter is passed over the summed band residual image. After mean removal, each pixel is divided by the standard deviation of the DNs of the entire summed band residual image. The resulting image is termed a signal-to-clutter of the summed band residuals (S/C). Below, we present several S/C images as well as plots of signal to clutter as a function of mixing proportion of target material and host pixel.

3.2 RESIDUAL GAIN

The gain resulting from LMM compared to standard image processing techniques is calculated by dividing the summed band residual S/C image by the signal to clutter image of the original TIMS band in which the implanted targets have the greatest contrast with the background (e.g., band 4 for 0007UUUFAB and band 6 for 0033UUUCNT; see Fig. 1). The signal to clutter of a single band image is constructed in a manner similar to that for the summed band residuals: after mean removal with a 3X3 high-pass filter, each pixel is divided by the standard deviation of the DNs of the entire (single band) scene. The result is termed a residual gain and provides a measure of the gain in signal to clutter of anomalous pixels due to post-processing of LMM-produced output. Because the denominator term is a maximum, the residual gain is a worst-case representation of signal to clutter gain. Below, residual gains are presented graphically as a function of mixing proportion of target material and host pixel.

3.3 SUM OF ABSOLUTE VALUES OF FRACTIONS

Typically, background pixels will have physically realistic fractional abundances (i.e., between 0% and 100%). Thus, in addition to high residual errors, target pixels may also be identified based on anomalous values in fraction images. Also, recall that under LMM, the fractional abundances are constrained to add to 100% (equation 2). As such, some anomalous pixels can be identified, as presented below, by constructing an image composed of the sum of the absolute values of each of the

fractions, and examining pixels which have absolute fractional abundances that sum to much greater than one.

4. RESULTS AND DISCUSSION

4.1 CASCADE HEAD, Ore.

Cascade Head, Ore. is a forested highland region located in SW Oregon. Fig. 2 shows an ~638X512-pixel band 4 raw TIMS image. Note, the contrast in TIR imagery of forested lands is low. There is evidence of development in the lower left portion of the image. Fig. 3 shows six 64X64 pixel subscenes (covering an actual area of ~0.5 km²) corresponding to each of the original six TIMS bands. The location of the subscene is indicated by the square in Fig. 2. With the exception of line striping that is hardly noticeable in the original TIMS images (Fig. 3), the data are relatively noise-free. The bright sinuous features running vertically through the left-center of the subscenes (and Fig. 2) are roads. The images of Fig. 3 contain eight pixels implanted with 70% 0033UUUCNT (green cloth camouflage net) and 30% host pixel. A PCA (of the whole scene without implanted targets) indicates, with only two eigenvalues greater than noise, that there are three endmembers. The spectra of the endmembers: vegetation, brush covered ground, and cold (shade analog) are chosen from the image and do not occur in the 64X64 pixel subscenes. The endmember selection process is based primarily on image analysis and interpretation. Endmember spectra are given in Fig. 4.

Using these three endmembers, LMM was applied to the images. Fig. 5 shows six S/C images as functions of mixing proportion of 0033UUUCNT (green cloth camouflage net) with host pixel. Target temperature is equal to the background temperature (~297.0 K). Note that the anomalous pixels (in the center of the subscene) are clearly visible down to ~20%. The dark band surrounding the light interiors—a "ringing effect"—is due to the application of the 3X3 high pass filter. The anomalous pixels are no longer discernible at ~20%. Graphically, however, S/C values are high as shown in Fig. 6. There are eight lines per target substance plot because there are eight target implanted pixels in the image. S/C values for 0033UUUCNT range from ~4.0 at 20% target to ~16.0 for 100% target. Note, from Fig. 1, that the maximum spectral contrast between the 0033UUUCNT and background is only ~7%; i.e., emissivity differences of ~0.06 in band 6 and 0.07 in band 1. S/C values for 0007UUUFAB range from ~7.5 at 20% target to ~35.0 for 100% target and, for 0430UUUMTL, ~1.5 at 20% target to ~8.0 for 100% target. Residual gain values are also high as shown in Fig. 7. Here, too, there are eight lines per target substance plot because there are eight target implanted pixels in the image. Recall that the residual gain is a worst-case scenario in S/C gain. The apparent decrease in residual gain with increasing mixing proportion evident in a number of plots is due to a low S/C value at low mixing proportions in the original TIMS image which composes the denominator of the residual gain term. As mixing proportion increases, so does the signal-to-clutter value and hence, the denominator term in the residual gain grows. Residual gain values—i.e., gains in S/C after LMM processing, range from virtually zero to ~150. Residual gains for targets with temperatures that are 2.5K greater than background temperature also range from virtually zero to ~140.

Figure 8 shows an example of target detection based on fractional abundances. Here, pixels with 50% 0033UUUCNT (green cloth net) and 50% background, with no temperature contrast, are clearly detectable in the image created by summing the absolute values of each of the three fraction images. As described above, physically realistic fractions should sum to 100%. In this case, implanted targets have values between 360-430%, whereas the scene average is 130%. Thus, the gain between the targets and the background is substantial. Note also that other targets, in this case a road, are also enhanced by this method, but have lower values (150-200%) than the implanted targets.



Figure 2: An approximately 640X512 pixel band 4 TIMS image of Cascade Head, Ore. Pixel size is ~11.2 m. The area within which the eight target implanted pixels are located is indicated by the box. Note the several roads throughout the scene.

BLANK PAGE

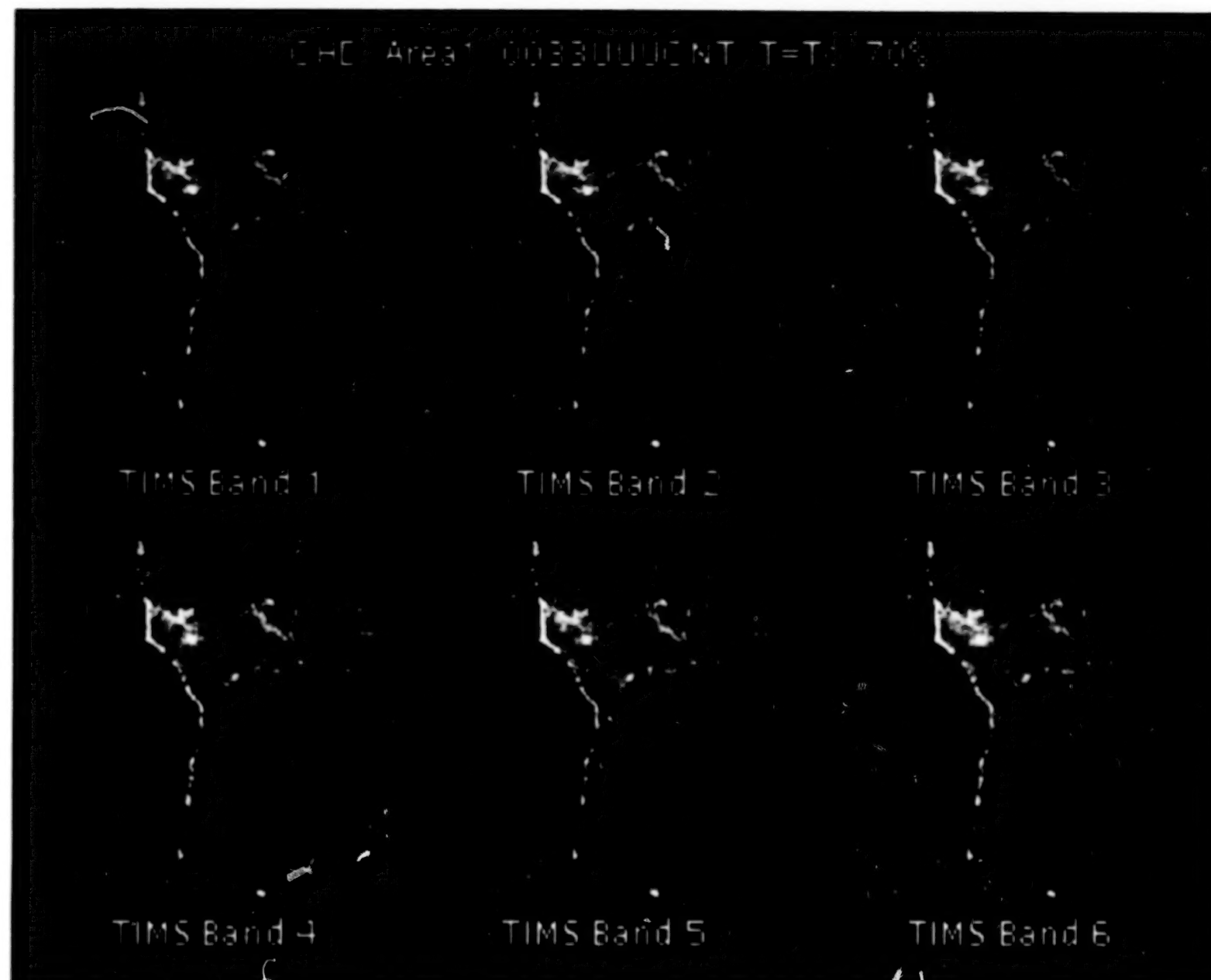


Figure 3: Six 64X64 pixel subscenes of the original 6 bands of the Cascade Head, Ore. TIMS data. These data have material 0033UUUCNT, green cloth camouflage netting, implanted at 70% target and 30% host pixel; target temperature equal to background temperature.

BEST COPY AVAILABLE

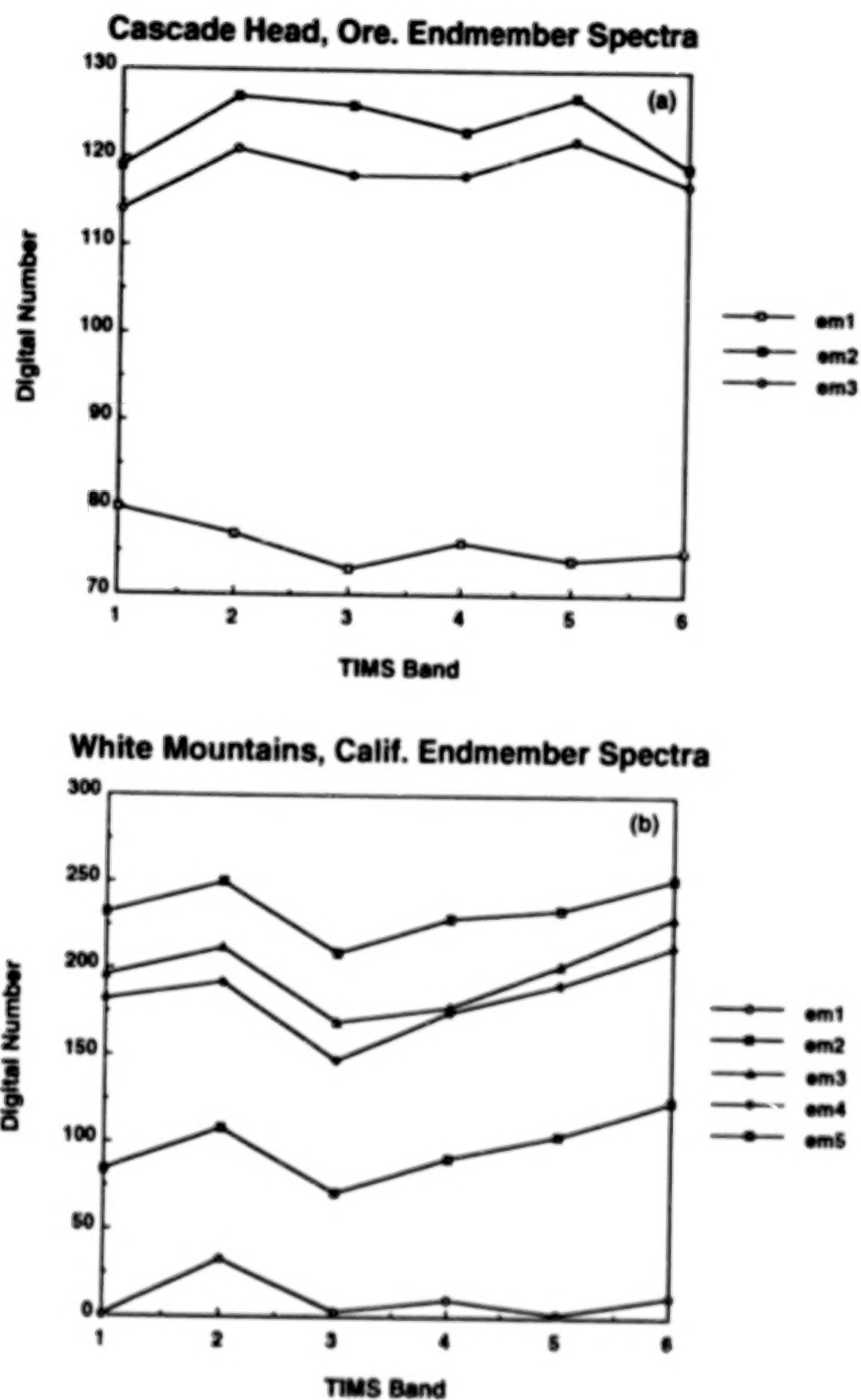


Figure 4: Endmember spectra input to LMM for (a) Cascade Head, Ore., and (b) White Mountains, Calif.

BLANK PAGE

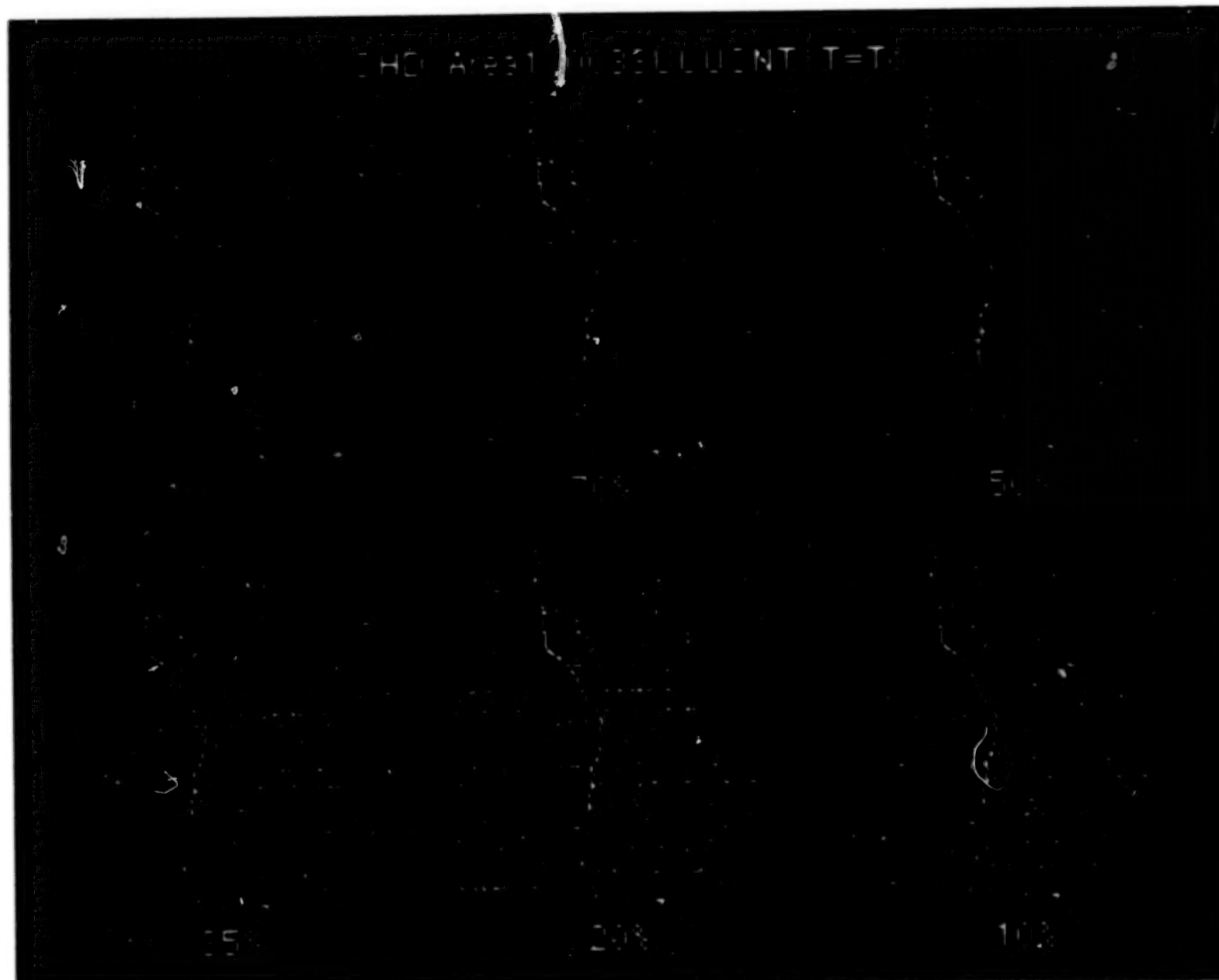
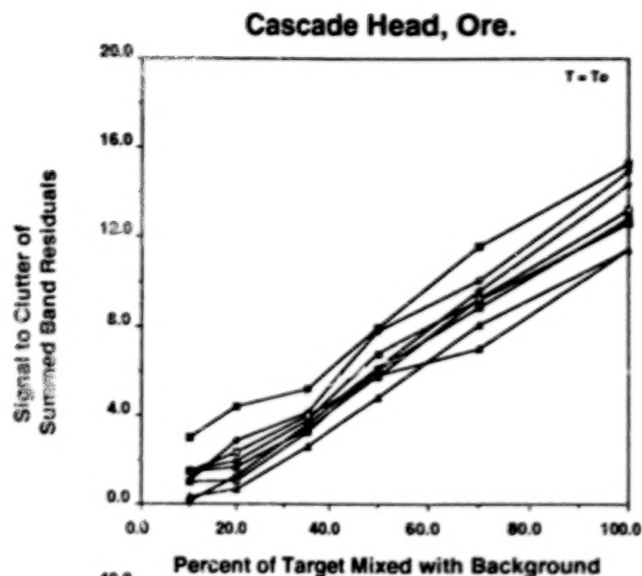


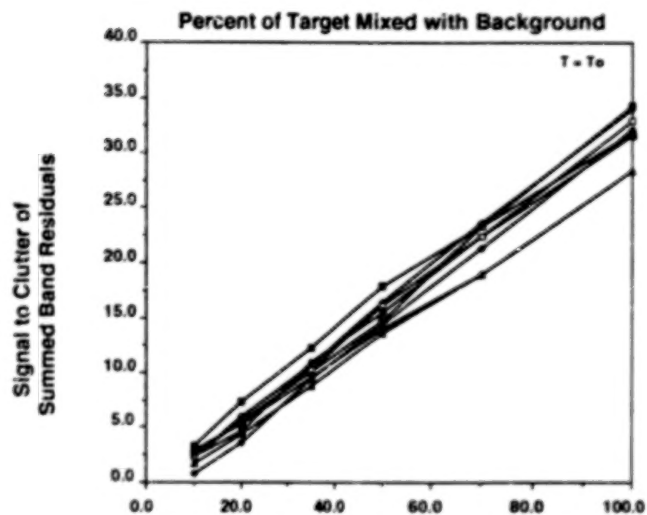
Figure 5: Six S/C images as functions of mixing proportion of target with host pixel. Results for 0033UUUCNT, green cloth camouflage netting. Target temperature equal to background temperature.

BEST COPY AVAILABLE

Green Cloth
Camouflage Net
0033UUUCNT



Dark Brown Neoprene
Rubber Fabric
0007UUUFAB



Light Gray Paint
on Metal
0430UUUMTL

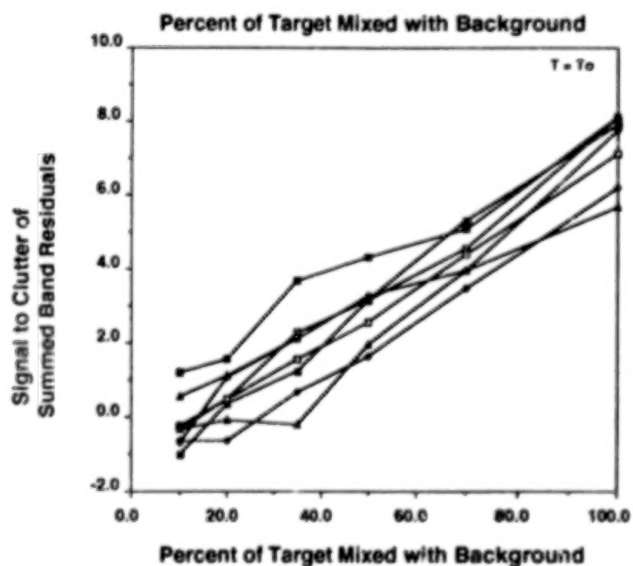
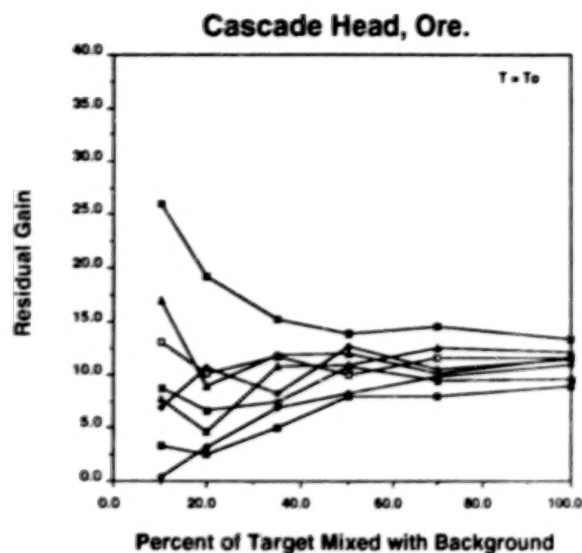
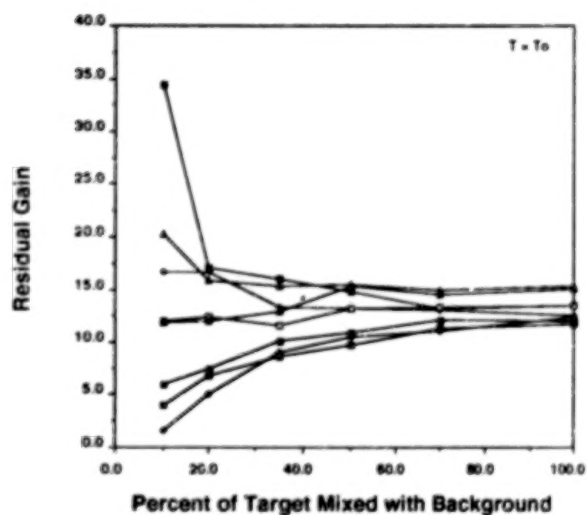


Figure 6: Plots of S/C values for all three target substances implanted into the Cascade Head, Ore. scene. Target temperature equal to background temperature. There are eight lines per target substance plot because there are eight target implanted pixels in the image.

Green Cloth
Camouflage Net
0033UUUCNT



Dark Brown Neoprene
Rubber Fabric
0007UUUFAB



Light Gray Paint
on Metal
0430UUUML

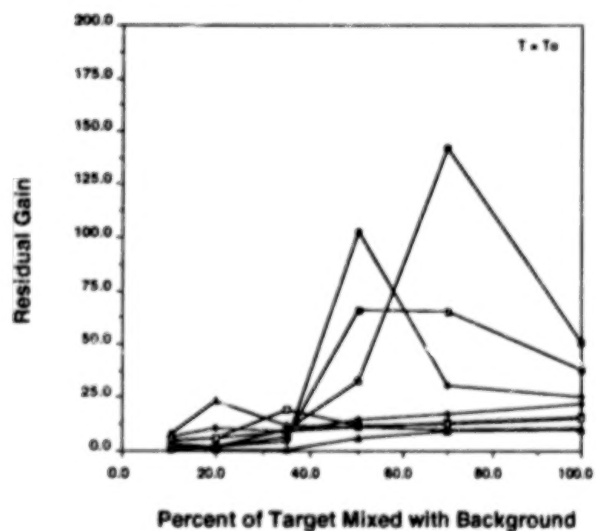
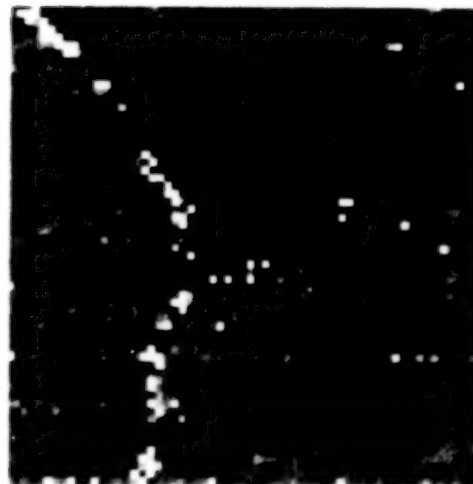
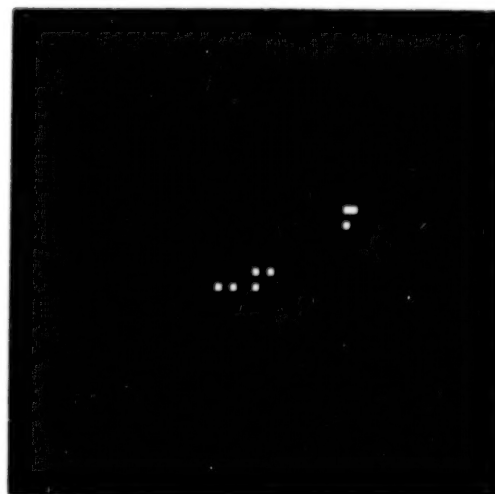


Figure 7: Plots of residual gain values for all three target substances implanted into the Cascade Head, Ore. scene. Target temperature equal to background temperature. There are eight lines per target substance plot because there are eight target implanted pixels in the image.



(a)



(b)

Figure 8: Sum of the absolute values of fractions—Cascade Head, Ore. (a) Pixels with 50% green cloth camouflage netting (0033UUUCNT) and 50% background (with no temperature contrast) are detectable. Values for the implanted targets are between 360-430%, well above the average value of 130% and significantly greater than physically realistic fractions which would ideally sum to 100%. Note also that other targets, in this case a road, are also enhanced by this method. (b) Same as (a) showing only the target-implemented pixels.

4.2 WHITE MOUNTAINS, CALIF.

White Mountains, Calif. is a sparsely vegetated desert region with considerable topographic relief. Fig. 9 shows an $\sim 638 \times 512$ -pixel band 4 raw TIMS image. Fig. 10 shows six 64×64 pixel subscenes (covering an actual area of $\sim 0.65 \text{ km}^2$) of the original 6 TIMS bands of the scene; these data contain $\sim 0.25\%$ to 1.0% noise pixels. The subscenes are centered on a lowlands region of the image indicated by the square in Fig. 9. Note the road running diagonally through the lower halves of the scenes. The contrast in this scene is high as evidenced by Fig. 9 and is due to the occurrence of several different rock types exposed in this region. The images of Fig. 10 contain eight implanted targets; 70% 0430UUUMTL (light gray paint on metal) and 30% host pixel. A PCA of the entire scene without implanted targets indicates that there are five endmembers. As for Cascade Head, Ore., the endmembers: 3 lithologies, 1 vegetation, and cold (shade) are chosen from the image and do not occur in the 64×64 pixel subscenes shown here. Using the endmember spectra given in Fig. 4, LMM was applied to the images.

Fig. 11 show six S/C images as functions of mixing proportion of target with host pixel. Target-implanted pixels are arranged in an "L" pattern and are indicated by the box in Fig. 11. Note the noise pixels in the right hand side of the subscenes. Target temperature is equal to the background temperature ($\sim 322.4 \text{ K}$). Standard deviations are higher in this image because of the high noise content; therefore, S/C and residual gains appear lower. Note that the target-implanted pixels are visible down to approximately 50%. Graphically, however, S/C values are high as shown in Fig. 12. S/C values for 0430UUUMTL range from ~ 1.0 at 55% target to ~ 3.5 for 100% target. From Fig. 1, however, it is evident that the maximum spectral contrast between 0430UUUMTL and background is a maximum of $\sim 4\%$ in band 2. S/C values for 0007UUUFAB range from ~ 1.0 at 25% target to ~ 6.0 for 100% target and, for 0033UUUCNT, ~ 1.0 at 30% target to ~ 5.5 for 100% target. Residual gain values are also high as shown in Fig. 13. Residual gains range from virtually zero to ~ 80 .

5. SUMMARY AND CONCLUSIONS

The subpixel linear mixing model (LMM) was applied to images acquired with the Thermal Infrared Multispectral Scanner (TIMS; six channels between 8 and $12 \mu\text{m}$). The images contain implanted targets in order to assess the ability of LMM to detect subpixel targets. Target materials were selected for their spectral similarities and contrasts with their intended host pixels and were implanted within pixels with varying temperatures and varying fractional proportions. Target spectra were not selected as image endmembers. Total RMS error, band residual, and fraction images output by LMM are analyzed as are signal to clutter images of individual, summed band residual images, and summed absolute fractional abundance images. LMM exposes the implanted targets for pixels containing $\geq 20\%$ of target. Actual detection threshold percentages are primarily a function of the spectral contrast between target and background. The image type in which the targets appear as anomalies varies and so analysis of the several images created by LMM is required. Mixing model-produced image post-processing enhances the target detection performance of LMM. Based on these results, LMM holds promise as a robust materials detection methodology for TIR MSI.

ACKNOWLEDGMENTS

This work was funded by Naval Research Laboratory contract no.: N00014-93-C-2244 to SETS Technology, Inc., Mililani, HI.



Figure 9: An approximately 640X512 pixel band 4 TIMS image of White Mountains, Calif. Pixel size is ~12.6 m. The area within which the eight target implanted pixels are located is indicated by the box.

BLANK PAGE

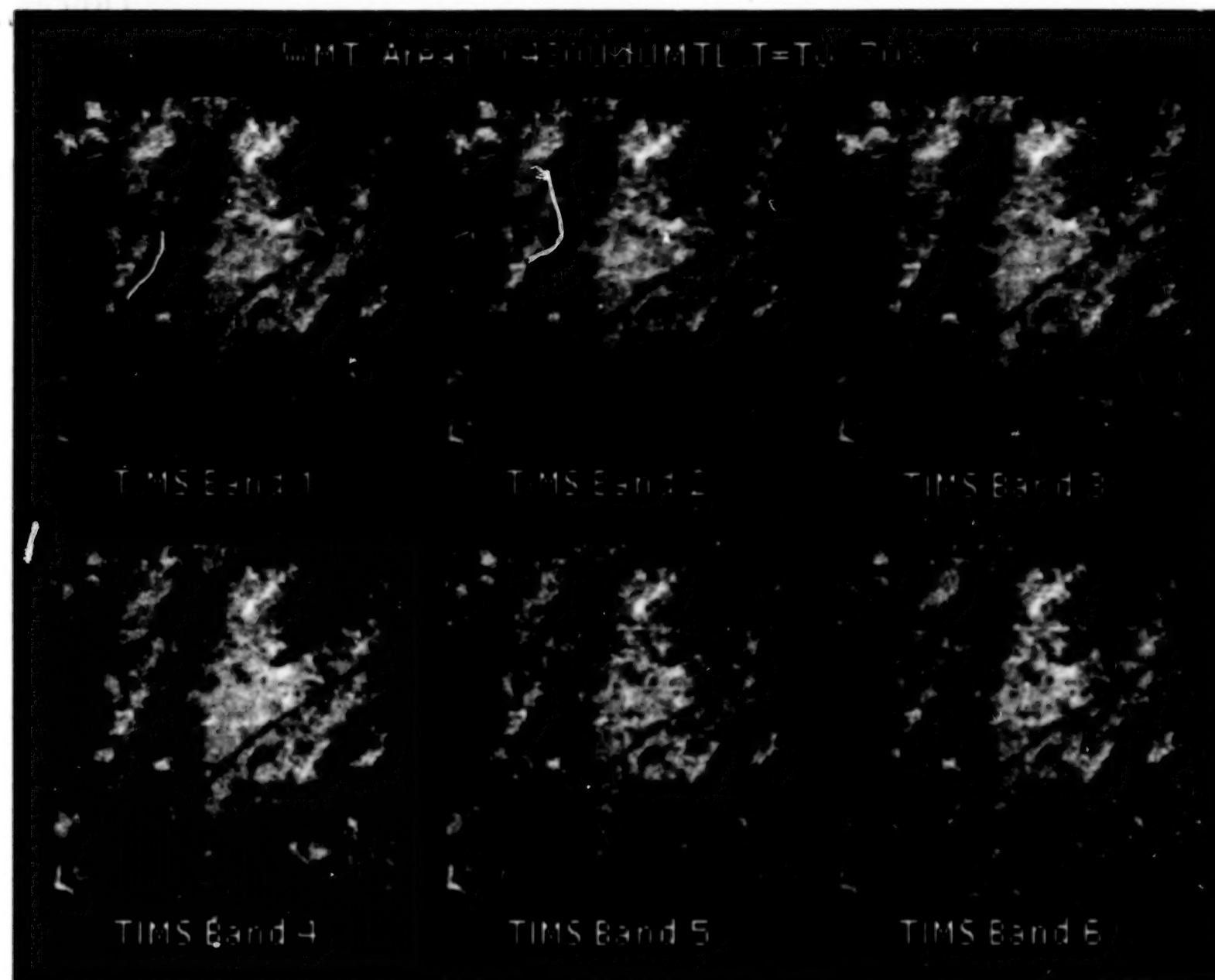


Figure 10: Six 64X64 pixel subscenes of the original 6 bands of the White Mountains, Calif. TMS data. These data have target material 0430UUUUMTL, light gray paint on metal, implanted at 70% target and 30% host pixel; target temperature equal to background temperature.

BEST COPY AVAILABLE

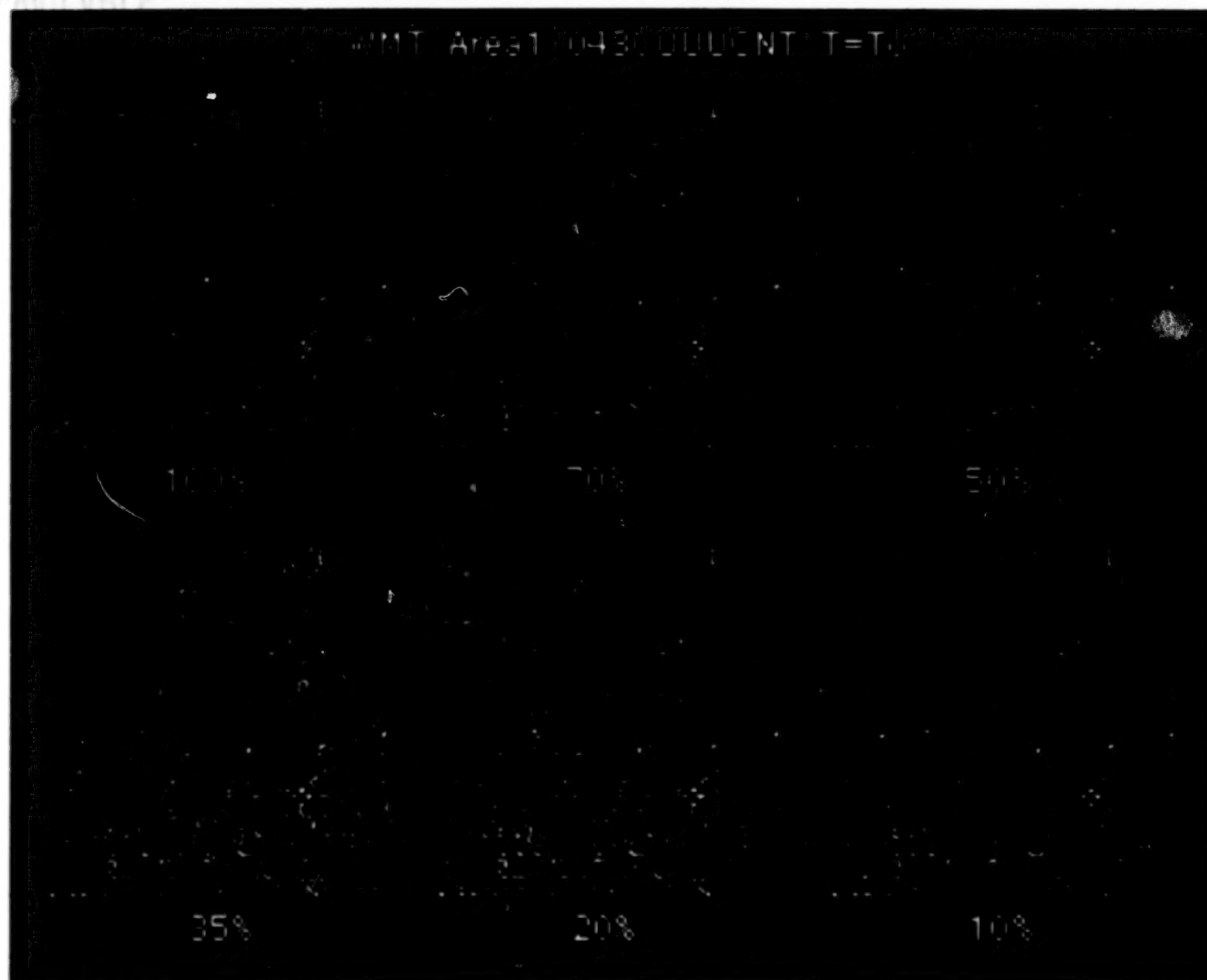


Figure 11: Six S/C images as functions of mixing proportion of target with host pixel. Results for 0430UUUMTL, light gray paint on metal. Target temperature equal to background temperature.

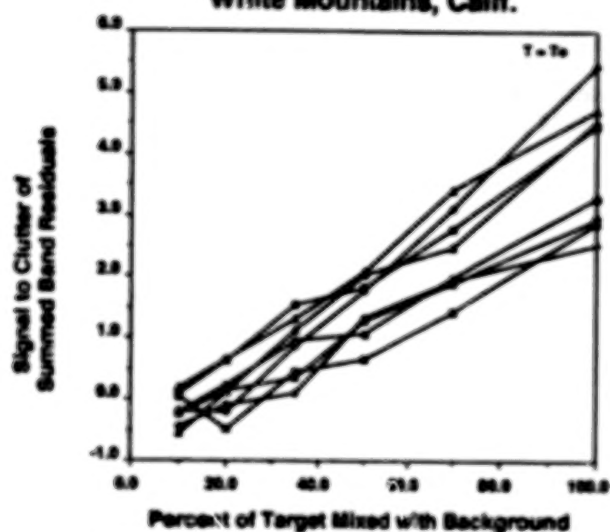
BEST COPY AVAILABLE

328

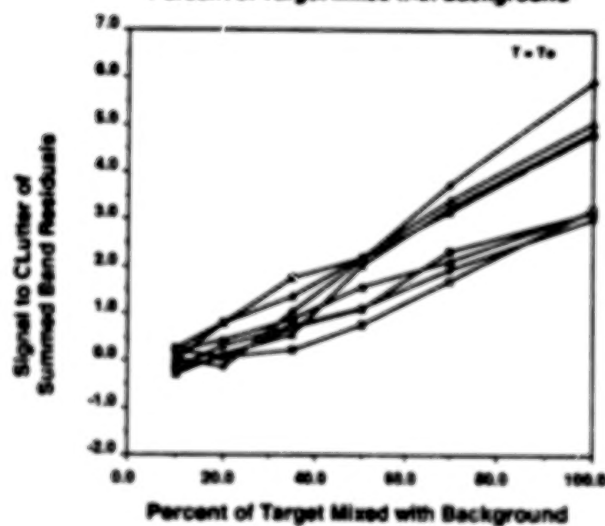
BLANK PAGE

Green Cloth
Camouflage Net
033UUUCNT

White Mountains, Calif.



Dark Brown Neoprene
Rubber Fabric
0007UUUFAB



Light Gray Paint
on Metal
0430UUUMTL

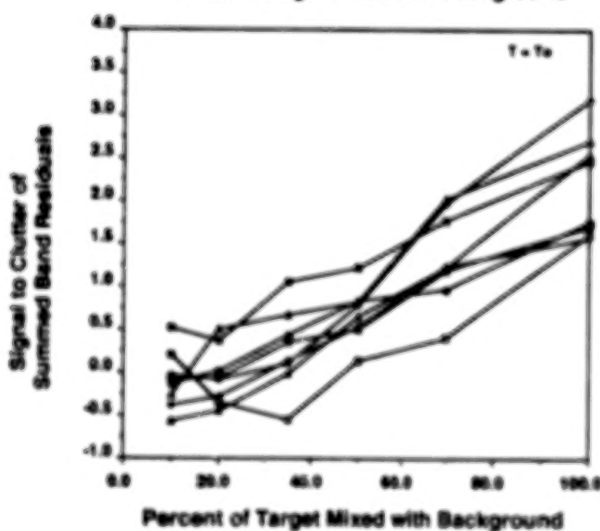
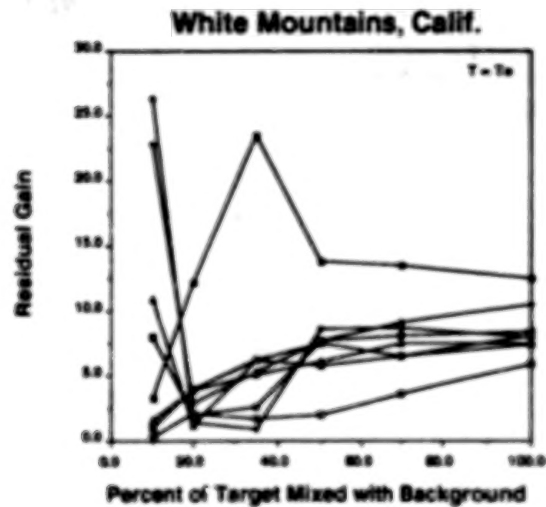
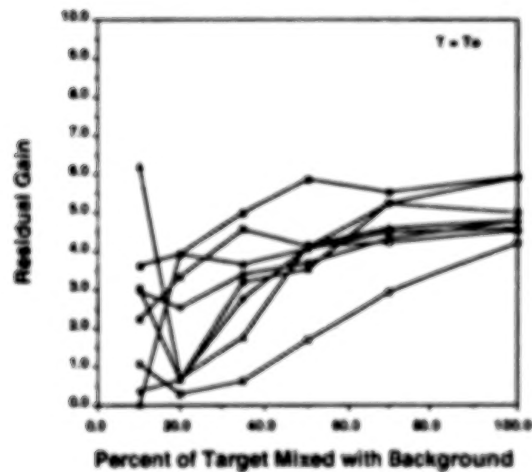


Figure 12: Plots of S/C values for all three target substances implanted into the White Mountains, Calif. scene. Target temperature equal to background temperature. There are eight lines per target substance plot because there are eight target implanted pixels in the image.

Green Cloth
Camouflage Net
0033UUUCNT



Dark Brown Neoprene
Rubber Fabric
0007UUUFAB



Light Gray Paint
on Metal
0430UUUMTL

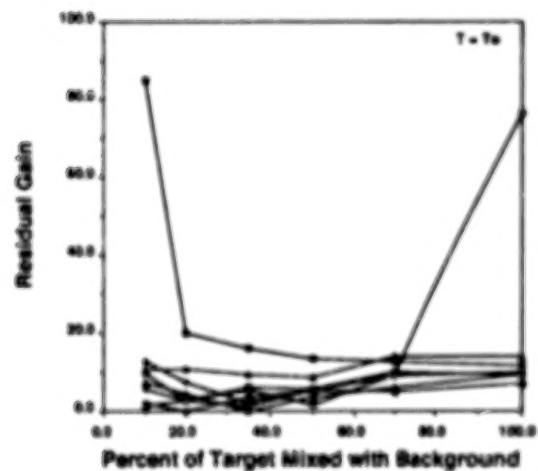


Figure 13: Plots of residual gain values for all three target substances implanted into the White Mountains, Calif. scene. Target temperature equal to background temperature. There are eight lines per target substance plot because there are eight target implanted pixels in the image.

REFERENCES

- Adams, J.F., Smith, M.O., and Gillespie, A.R. (1993), Imaging spectroscopy: interpretation based on spectral mixture analysis. In: *Remote Geochemical Analysis: Elemental and Mineralogical Composition*, C.M. Pieters and P.A.J. Englert, eds. Topics in Remote Sensing, #4, Cambridge University Press. pp. 145-166.
- Adams, J.B., Smith, M.O., and Johnson, P.E. (1986), Spectral mixture modeling: A new analysis of rock and soil types at the Viking Lander 1 site. *J. Geophys. Res.*, v. 91, no. B8, pp. 8098-8112.
- Bateson, C.A. and Curtiss, B. (1993), A tool for manual endmember selection and spectral unmixing. Proceedings of the 4th Annual JPL Airborne Geoscience Workshop, v. 1, AVIRIS Workshop, JPL Publ. #93-26, Jet Propulsion Laboratory, Pasadena, CA, pp. 3-6.
- Gillespie, A.R., Kahle, A.B., and Walker, R.E. (1986), Color enhancement of highly correlated images. I. Decorrelation and HSI contrast stretches. *Rem. Sen. Env.*, 20, pp. 209-235.
- Gillespie, A.R., Smith, M.O., Adams, J.B., and Willis, S.C. (1990), Spectral mixture analysis of multispectral thermal infrared images. Proceedings of the 2nd Thermal IR Multispectral Scanner (TIMS) Workshop, JPL Publ. #90-55, Jet Propulsion Laboratory, Pasadena, CA, pp. 57-74.
- Gillespie, A.R. (1992a), Spectral mixture analysis of multispectral thermal infrared images. *Rem. Sen. Env.*, v. 42, pp. 137-145.
- Gillespie, A.R. (1992b), Enhancement of multispectral thermal infrared images: Decorrelation contrast stretching. *Rem. Sen. Env.*, v. 42, pp. 147-155.
- Kahle, A.B., Madura, D.P., and Soha, J.M. (1980), Middle infrared multispectral aircraft scanner data: Analysis for geological applications. *Applied Optics*, v. 19, no. 14, pp. 2279-2290.
- Kneizys, F.X., Shettle, E.P., Gallery, W.O., Chetwynd, J.H., Jr., Abreu, L.W., Selby, J.E.A., Clough, S.A., and Fenn, R.W. (1983), Atmospheric transmittance/radiance: Computer code LOWTRAN 6. Environmental Research Paper #846, Technical Report AFGL-TR-83-0187, NTIS AD A137796, Air Force Geophysics Laboratory, Bedford, MA.
- Mustard, J.F. (1993), Relationships of soil, grass, and bedrock over the Kaweah serpentine melange through spectral mixture analysis of AVIRIS data. *Rem. Sen. Env.*, v. 44, pp. 293-308.
- Palluconi, F.D. and Meeks, G.R. (1985), Thermal Infrared Multispectral Scanner (TIMS): An investigator's guide to TIMS data. Jet Propulsion Laboratory Publication #85-32, Jet Propulsion Laboratory, Pasadena, CA.
- Sabol, D. E. Jr., Adams, J.B., and Smith, M.O. (1992), Quantitative subpixel spectral detection of targets in multispectral images. *J. Geophys. Res.*, v. 97, no. E2, pp. 2659-2672.
- Schaum, A. and Stocker, A.D. (1994), Subpixel detection methods: spectral unmixing, correlation processing, and when they are appropriate. Proceedings of the International Symposium on Spectral Sensing Research, 1994, this volume.
- Soha, J.M. and Schwartz, A.A. (1978), Multispectral histogram normalization contrast enhancement. Proceedings of the 5th Canadian Symposium on Remote Sensing, Victoria, B.C., Canada, pp. 86-93.
- Tompkins, S., Mustard, J.F., Pieters, C.M., and Forsyth, D.W. (1993), Objective determination of image end-members in spectral mixture analysis of AVIRIS data. Proceedings of the 4th Annual

JPL Airborne Geoscience Workshop, v. 1, AVIRIS Workshop, JPL Publ. #93-26, Jet Propulsion Laboratory, Pasadena, CA, pp. 177-180.

Yu, X., Reed, I.S., and Stocker, A.D. (1993), Comparative performance analysis of adaptive multispectral detectors. IEEE Transactions on Signal Processing, v. 41, no. 8, pp. 2639-2656.

LINEAR ESTIMATION OF HYPERSPECTRAL MIXED PIXEL COMPONENTS

Edmundo Simental and Elisa C. Gonzalez
U. S. Army Topographic Engineering Center
Alexandria, VA 22315-3864

ABSTRACT

This paper presents a method to determine end members along with their relative concentration in a hyperspectral mixed pixel. The method is modeled as a linear combination of the end members reflectance spectra and a library of spectral prototypes. This method was tested with 431-band, laboratory controlled, data sets. Indications are that this method can be extended to field data observations with a small number of end members and that at least some error source can be identified and data and results adjusted accordingly.

1. INTRODUCTION

Linear estimation is a viable method for analyzing mixed pixels under the simplified assumption of accurate reflectance calibration, accurate laboratory spectral prototypes, and dominant linear mixing.

1.1 OBJECTIVE

This paper addresses a method for estimating the concentration of materials in a mixed pixel using laboratory measured hyperspectral data, a library of spectral prototypes, and a linear model. A library of spectral prototypes is simply a collection of spectra of pure materials or objects which may be components of the mixed pixel. The model is based on least squares. A basic requirement is that the spectral prototypes be linearly independent. The library can contain several hundred prototypes and each prototype can contain several hundred bands.

1.2 HYPERSPECTRAL MIXED PIXEL CONCEPT

An imaging spectrometer measures percent reflectance or radiometric values of a pixel at various frequencies. A plot of the reflectance as a function of frequency represents the spectral response of the pixel. A pixel is said to be *mixed* if its measured reflectance is a result of imaging multiple object types or materials within the pixel's footprint. In such cases the measured response will be a combination of the individual responses of the objects or materials. If the number of materials in the pixel's footprint is less than or equal to the number of measurements, and if the combination of the responses within the measuring instrument is linear, then the most probable mix of components may be estimated by a linear model and a library of spectral prototypes of materials suspected in the mixed pixel.

1.3 LINEAR ESTIMATION THEORY CONCEPTS

Estimation is defined as the process of making a decision or judgement concerning the approximate value of parameters when the decision is weighted or influenced by all available information on those parameters. The estimation is linear when the estimation characteristics are *additive* and *homogeneous*.¹ In this particular case *additive* means that the spectral response combination is the sum of the product of the individual material component responses and a scalar quantity associated with the particular material. *Homogeneous* means that the scalar quantity is dependent on the material and independent of the frequency. The spectral response ' ω ' at frequency f_0 is composed of material 'a' and material 'b', then for any frequency 'f',

$$\omega_f = k_1(\text{spectral response of 'a' at frequency 'f'}) + k_2(\text{spectral response of 'b' at frequency 'f'})$$

where:

$$\begin{aligned}\omega_f &= \text{total reflectance at frequency 'f'} \\ k_1 &= \text{scalar constant associated with material 'a'} \\ k_2 &= \text{scalar constant associated with material 'b'}\end{aligned}$$

1.4 LINEAR MODEL

Assume that there are 'p' different objects in a spectrometer's footprint and that 'n' discrete frequencies are measured, then the output reflectance measured at any frequency 'k' is given by;

$$\omega_k = \sum_{i=1}^p r_{k,i} s_i$$

where:

$$\begin{aligned}\omega_k &= \text{total output reflectance at frequency 'k'}, \\ r_{k,i} &= \text{response of material 'i' at frequency 'k'} \\ s_i &= \text{coefficient of concentration of material 'i'}$$

The above equation in matrix form is given by;

¹ Ralph Deutsch, *Estimation Theory*, Prentice Hall

$$\omega = \begin{bmatrix} r_{1,1} & \dots & \dots & \dots & r_{1,p} \\ \dots & \dots & \dots & \dots & \dots \\ \dots & \dots & \dots & \dots & \dots \\ \dots & \dots & \dots & \dots & \dots \\ r_{n,1} & \dots & \dots & \dots & r_{n,p} \end{bmatrix} \begin{bmatrix} s_1 \\ . \\ . \\ . \\ s_p \end{bmatrix}$$

The above expression written in matrix notation is given by:

$$\Omega = RS \quad (1)$$

The above equation represents a linear statistical measurement model in which the 'R' matrix, (n x p) is a 'laboratory prototype' spectral library of reflectance values for materials that may occur in the pixel footprint. It is important to note that these values must be obtained separately from a mixed pixel solution. These values could be obtained from measurements in the laboratory or measurements in the field under the same conditions as those employed for the mixed pixel. They represent the spectrum of a pure material or object. The column matrix 'Ω' (n x 1) represents the 'n' response measured by the spectrometer. The column matrix 's' (p x 1) is the 'coefficient of concentration' of each material and is unknown. The problem is to estimate this parameter from the 'spectral library' and from the 'n' measurements. Once determined, these coefficients can be converted to represent the relative quantity of each material.

1.5 LINEAR MODEL SOLUTION

The number of measurements is normally expected to be much larger than the number of components in the mixed pixel to produce an over determined system of linear equations. Methods for the solution of an over determined system of linear equations are many and are well documented. A basic least square solution is presented here.

Let,

R^t = transpose matrix of R in equation (1) above and multiply on the left both sides of the equation by it to obtain,

$$R^t \Omega = R^t RS \quad (2)$$

The matrix product $[R^t R]$ produces a p x p symmetric matrix and the matrix product $R^t \Omega$ produces a p x 1 column matrix.

Let,

m = inverse of $[R^t R]$

Multiply on the left both sides of equation (2) by m to obtain,

$$m[R^t Q] = m[R^t R]s \quad (3)$$

By definition, the matrix product $m[R^t R]$ is the identity matrix and equation (3) becomes

$$m[R^t Q] = s \quad (4)$$

The matrix product $m[R^t Q]$ is $p \times 1$, a column matrix, and is the least square solution vector for 's'.

2. LABORATORY TEST

The development of an understanding of potential complications to simplified unmixing models and their ramifications may be best understood by working with laboratory controlled data.

2.1 EXPERIMENT DESIGN

A laboratory controlled experiment was designed to assess the validity of the developed model. The experiment consisted of obtaining a prototype 'spectral library' of materials and then imaging a target with a known mix of these materials. Three materials were selected for the experiment; red, green, and yellow dye. The targets were a known mix of red and green dye. Yellow was produced where the red and green overlapped in the targets. The overlap is slight but uncontrolled and the red/green interaction is not always in the same proportion. It is caused by saturation of the two dyes in the cardboard. The spectral library was obtained by imaging separately 'pure' red, green, and yellow dye on 10x10 inch cardboards and recording the spectra. These spectra constitute the library of 'spectral prototypes'.

2.2 TARGETS

A 10 x 10 inch cardboard was subdivided into 64 $1\frac{1}{4}$ x $1\frac{1}{4}$ inch squares, 8 across and 8 down. Each square was alternately dyed red and green so that the cardboard had an even mix of red and green dye, 32 red squares and 32 green squares. This constitutes a 50/50 percent red/green target. A second target was constructed like the first, except that every other green square was dyed red so that this target had a mix of 48 red squares and 16 green squares. This constitutes a 75/25 percent red/green target. A third target was constructed like the second one, except that the red and green dye are interchanged so that this target had 16 red squares and 48 green squares. This constitutes a 25/75 percent red/green target. This data set of targets was labeled 'large square' targets. A second data set was constructed just like the one above except that the cardboard was subdivided into 128 $\frac{1}{2}$ x $\frac{1}{2}$ inch squares, 16 across and 16 down.

This data set was labeled 'small square' targets. Fig. 1 shows the spectral library cardboards and the different targets.

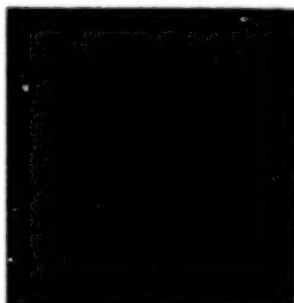
2.3 SPECTROMETER

The instrument used for this effort was a tripod mounted, factory calibrated, Geophysical Environmental Research (GER) IRIS MkIV dual field of view spectrometer. Fig. 2 shows the spectrometer in a field environment. Radiometric values for 431 discrete spectral bands, wavelengths from 350-2500 nanometers at 5 nanometer increments, were obtained for each of the spectral prototypes and the targets. The spectrometer's raw output values, 32-bit hexadecimal numbers, were downloaded to an IBM-compatible PC for conversion to floating point numbers and percent reflectance. A Halon reflectance standard was used as a reference for the conversion to percent reflectance. Table I shows a sample of the PC output data for three of the targets. The last column of Table I is a description of the data entries. The data were collected in a laboratory with constant temperature, pressure, and lighting conditions. It was collected over two consecutive days thereby minimizing the probability of any changes which could affect the spectral information.

2.4 IMAGING PROCEDURE

The spectrometer was set up on a tripod looking straight down, one meter from the floor. The checkerboard target was placed on the level floor directly below the spectrometer. The board was constructed so that it would be larger than the spectrometer's circular field of view. The board was positioned so that its geometric center was coincident with the spectrometer's field of view center so that whatever portion of the board was imaged by the spectrometer, the color dye proportion was retained. Fig. 3 shows how a 25/75 percent checkerboard was imaged. The field of view is represented by concentric circles. The portion of the board inside each circle has the same red/green ratio as the whole board. This is true as long as the targets are symmetric about the center, the centers of the field of view and targets are coincident, and the field of view is within the board boundaries. Even if the field of view is oval or rectangular, the red/green ratio is retained as long as the above three conditions hold. The '50/50 Red/Green Large Squares Target' was imaged three times. The second data set is labeled 'repeated' and the third data set is labeled 'repeated again'. Other targets were rotated 45° for a second image and are labeled 'rotated'.

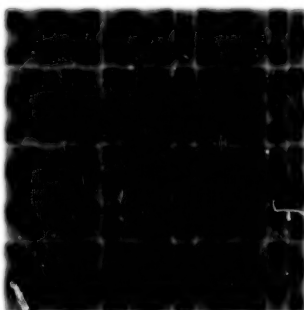
FIGURE 1. SPECTRAL PROTOTYPES AND TARGETS



SPECTRAL PROTOTYPES



TARGETS: LARGE SQUARES

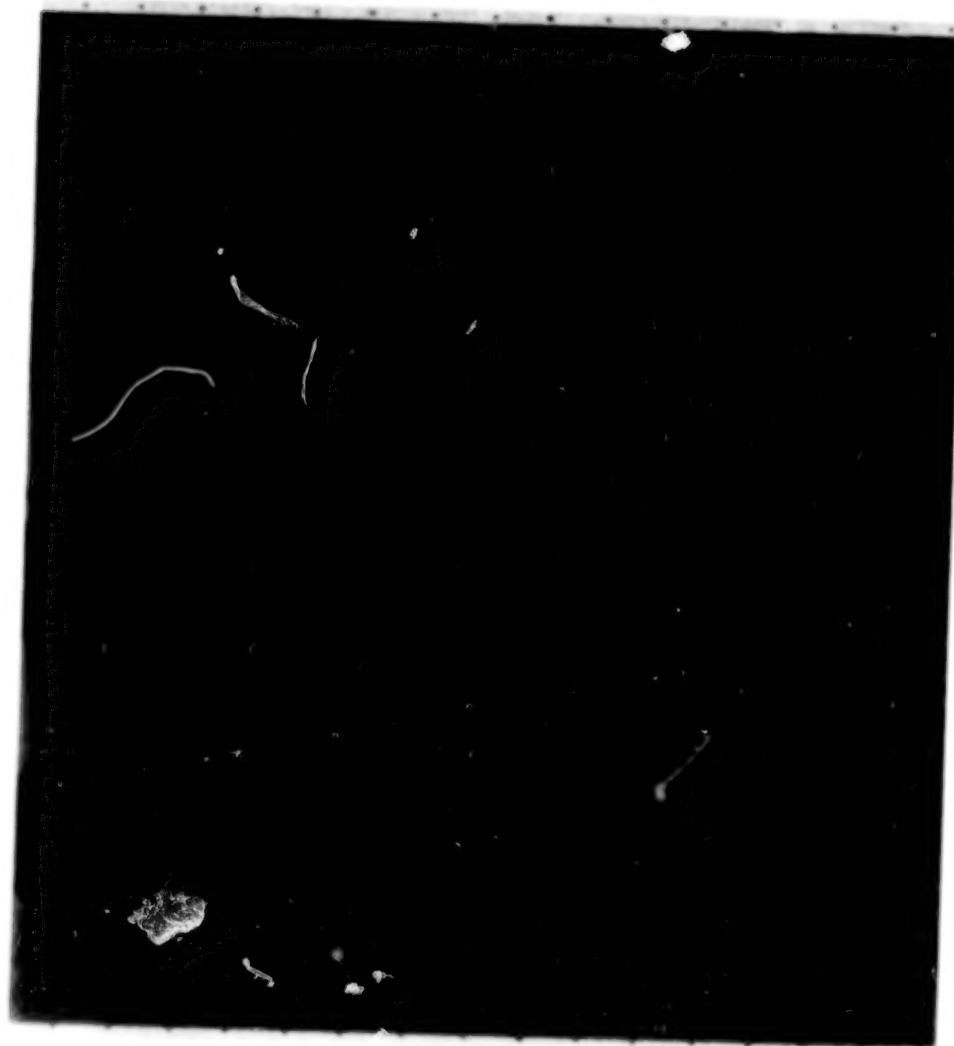


TARGETS: SMALL SQUARES

FIGURE 2. SPECTROMETER



FIGURE 3. TARGET INSTRUMENT FIELD OF VIEW DIAGRAM



Checkerboard = 25:75 Percent Red-Green Target
Concentric Circles = Spectrometer's Field of View

BEST COPY AVAILABLE

TABLE 1. PC OUTPUT DATA SAMPLE

8mar93tR.002	8mar93tR.003	8mar93tR.004	File Name
2	3	4	File Number
350	350	350	Start Wavelength
2500	2500	2500	End Wavelength
5	5	5	Increment
0	0	0	Separator
0	0	0	"
0	0	0	"
0	0	0	"
0	0	0	"
16.57344	13.20345	6.9677	Reflectance Data
23.66057	26.47618	37.70111	"
6.227723	4.790452	5.270441	"
18.11797	10.74448	21.21313	"
20.65312	11.15195	31.23604	"
23.36005	20.7199	34.12856	"
...	"
...	"
...	"

3. RESULTS

The results obtained embodied different factors, computer equipment, data, computations, and interpretation.

3.1 COMPUTER EQUIPMENT

The data sets were processed on a SUN SPARC workstation using the UNIX operating system and the X-Windows windowing system. Two commercial software packages, Interactive Data Language (IDL) and Mathematica, were used for the computations and analyses. 'IDL' is a computing environment for the interactive analysis and visualization of scientific and engineering data. It provides a broad range of high quality mathematical analysis and graphical display techniques. The graphical and statistical analyses were conducted with the aid of IDL. 'Mathematica' is a general software system and language intended for matrix operations, statistical analysis, and other mathematical applications. The matrix operations and mathematical computations were conducted with the aid of Mathematica.

3.2 DATA FILTERING

High priority was given to the data filtering process to minimize the probability of using false data. The data suspected of being contaminated was filtered out. As a consequence, a significant amount of data were not used. A plot of wavelength vs. percent reflectance was made of all the data sets to analyze the characteristics of the spectra and to detect any anomalies. Figs. 4-7 show the plots made. The first few data points, around 350-500 nanometers, of all sets are irregular spikes and seem to be an idiosyncrasy of the spectrometer when it first starts to record data. These data points are obvious misreadings since reflectance values greater than 100 percent were recorded. These data points were filtered from any processing. The region around 800-1100 nanometers of all data sets deviates from the smooth spectrum curve for no readily explanatory reason other than it is an 'instrument error'. Processing with or without these data points made very little difference in the computed solutions. This is an indication that the data were valid, however the results which will be presented later do not contain these data points. Data associated with wavelengths greater than 1500 nanometers seem to be the same regardless of the dye combination, probably because at these frequencies the spectrometer was responding to the cardboard material and not the dye. These data points were filtered from processing. Additional data points were filtered out from individual data sets which accounts for the different number of data points used in the various solutions.

3.3 COMPUTATIONS

A computer routine was prepared to process the collected data and compute 'coefficients of concentrations' according to equation (4) above and to compute simple statistics of the results. Each data set was processed for a 'two vector' solution where the assumption was that the mixed pixel consisted of red and green dye and for a 'three vector' solution where the assumption was that it consisted of red, green, and yellow dye.

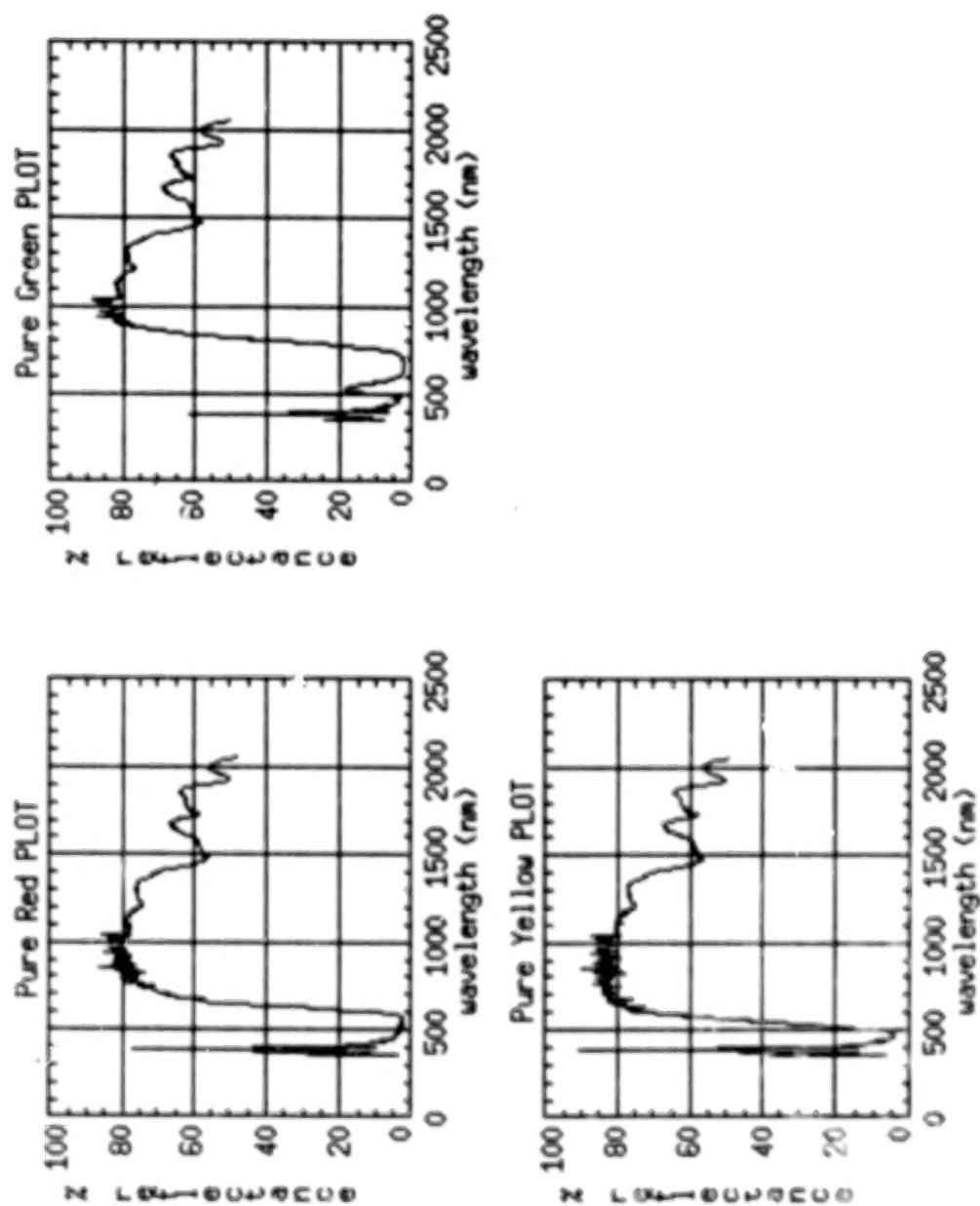
These coefficients were converted to percent concentration (pc) by,

$$pcc_i = [s_i / \sum_{k=1}^K s_k] 100$$

where:

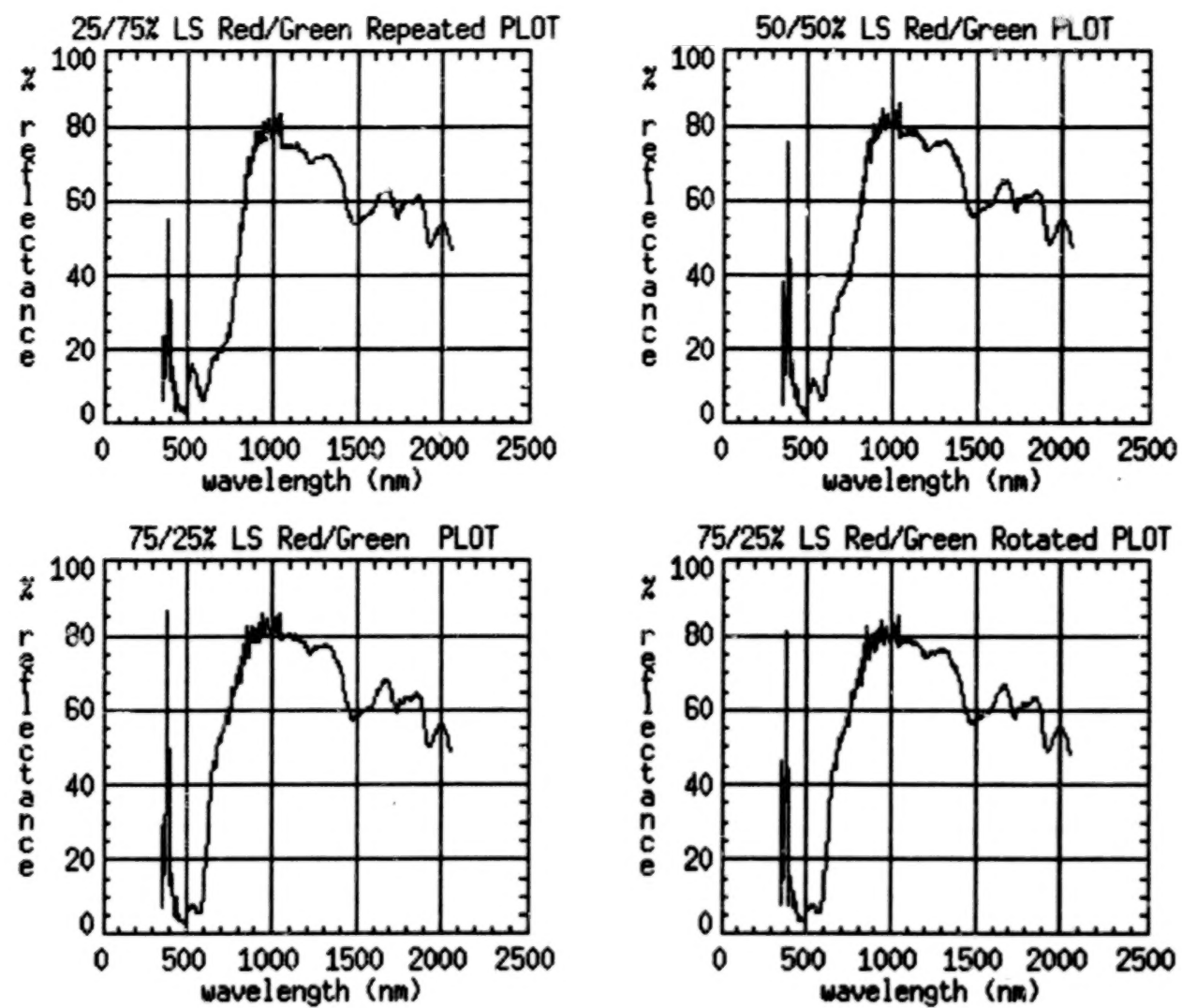
- pc_i = percent concentration for material i,
- s_i = computed coefficient for material i,
- s_k = computed coefficient for material k.

FIGURE 4. PLOTS OF SPECTRAL PROTOTYPES



BLANK PAGE

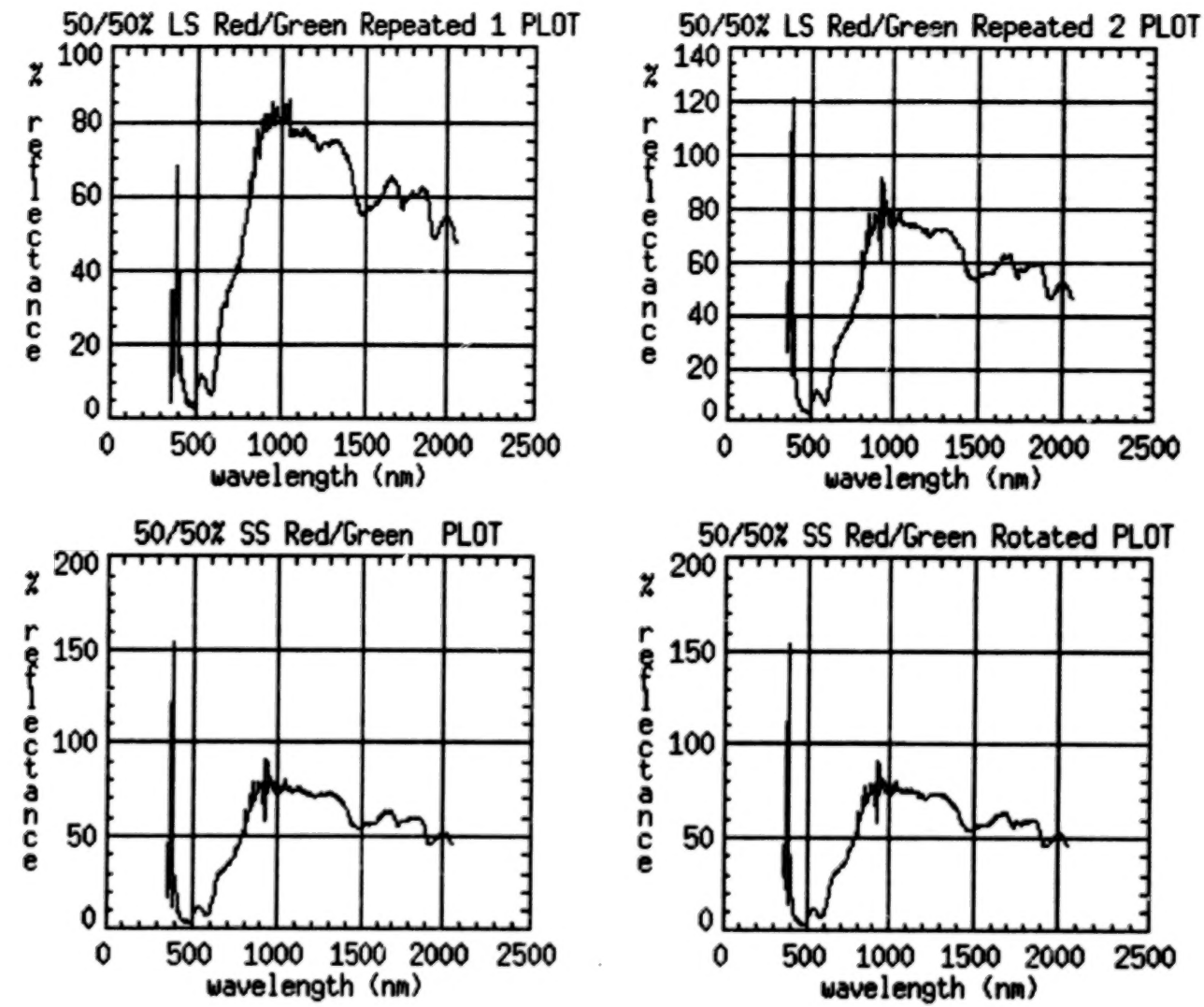
FIGURE 5. PLOTS OF TARGETS



344

344

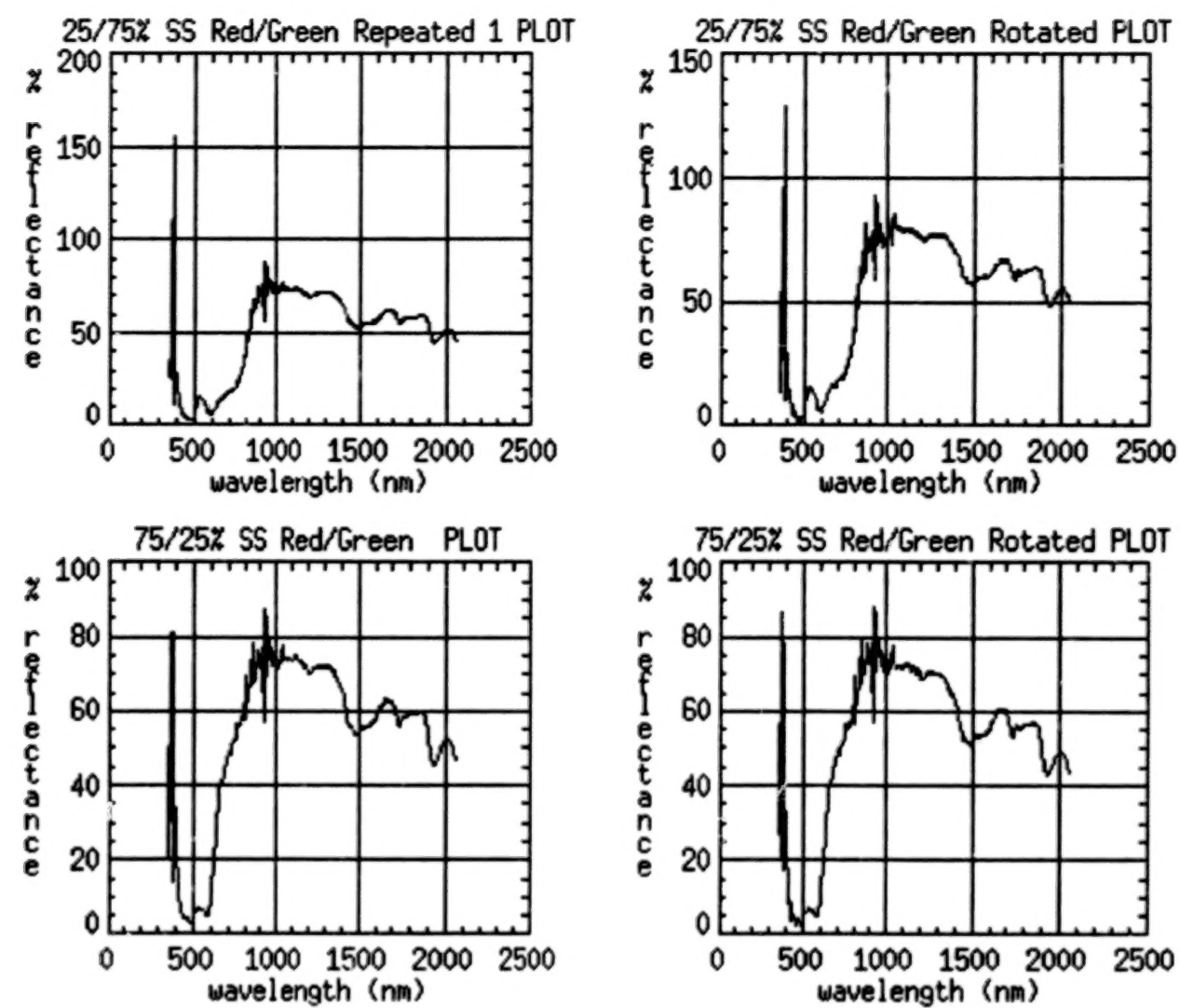
FIGURE 6. PLOTS OF TARGETS



345

345

FIGURE 7. PLOTS OF TARGETS



346

346

BLANK PAGE

Tables 2-7 show the results of the various tests. The tables show the percent red, green, and yellow, the statistics variance, standard deviation (std), mean, maximum and minimum residuals for the various targets. The percent concentration is the most fundamental test of the computed information because if this value is not close to the true concentration, the rest of the statistical information is meaningless. As can be seen from the tables, all the computed concentrations are very close to the known concentrations. It was pointed out earlier that yellow was produced in the targets where red and green came together. It is not possible to accurately determine the true concentration of yellow in the targets, but all the red/green targets have a little yellow. The small square targets should contain twice as much yellow as the corresponding large ones, but only if the red/green dyes overlap exactly in the same constant manner in the different targets. In the computations, the yellow dye in the targets varied from 1.56 to 5.16. Table 8 list-ranks the computed yellow in each of the targets. The higher values, except for one, belong to the 'small square' target group. This seems to confirm the fact that 'small square' targets contain more yellow than 'large square', but not in the expected proportion. The targets and spectral prototypes were computer generated and printed with a Kodak XL7700 color printer. Although the quality of the printer is excellent, small variations in paper quality and idiosyncrasies of the printer can account for some of the yellow differences in the targets. It was noted that hard copy prints of the generated spectral prototypes contained slight, but noticeable, color variations. Similar variation in the targets could exist, but in a much smaller scale which would be very hard to detect and correct. Also, yellow is defined as a homogenous mixture of equal amounts of pure red and pure green. The yellow spectral prototype was generated with this definition. In the targets equal amounts of red and green produced yellow, but any deviation in the red/green ratio would produce a shade of yellow whose spectra is different from pure yellow. The model then would not detect all of these shades as yellow. Residual vectors were computed for each data set by;

$$\text{residual vector} = \text{measured vector} - \text{computed vector}$$

The computed vector is the matrix product of the computed coefficients and the spectral library. A large residual variance or large residuals would indicate that the data does not fit the model, or in other words, that the model is not valid. As seen from the tables, the residual variances vary from 0.229514 to 2.07936 percent. These low values are indications of a valid model. The size and distribution of the residuals are shown in Fig. 8-13. The distribution is balance, but residuals at the higher frequencies seem to have a different pattern than those at the lower ones.

TABLE 2. PERCENT CONCENTRATION RESULTS

Large Squares 50/50 Red/Green Mix
62 Data Points Used

Red = 48.3615%
Green = 51.6385%
Residual Variance = 0.399593
Residual Standard = 0.632134
Residual Mean = 0.117161
Residual Max Value = 1.328410
Residual Min Value = -1.40322

Large Squares 50/50 Red/Green Mix
62 Data Points Used

Red = 47.6452%
Green = 50.7926%
Yellow = 1.56212%
Residual Variance = 0.229514
Residual Standard = 0.479076
Residual Mean = -0.0542426
Residual Max Value = 1.07
Residual Min Value = -1.30296

Large Squares 25/75 Red/Green Mix
71 Data Points Used

Red = 27.9018%
Green = 72.0982%
Residual Variance = 0.717481
Residual Standard = 0.847043
Residual Mean = 0.412358
Residual Max Value = 2.098570
Residual Min Value = -2.58418

Large Squares 25/75 Red/Green Mix
71 Data Points Used

Red = 24.9470%
Green = 72.3506%
Yellow = 2.70239%
Residual Variance = 0.349629
Residual Standard = 0.591294
Residual Mean = 0.042242
Residual Max Value = 1.204380
Residual Min Value = -2.17339

TABLE 3. PERCENT CONCENTRATION RESULTS

Large Squares 75/25 Red/Green Mix
73 Data Points Used

Red	= 75.3445%
Green	= 24.6555%
Residual Variance	= 0.546755
Residual Standard	= 0.739429
Residual Mean	= 0.326348
Residual Max Value	= 1.585870
Residual Min Value	= -2.00696

Large Squares 75/25 Red/Green Mix
73 Data Points Used

Red	= 73.1665%
Green	= 24.5850%
Yellow	= 2.24847%
Residual Variance	= 0.271439
Residual Standard	= 0.520998
Residual Mean	= 0.0251939
Residual Max Value	= 1.576690
Residual Min Value	= -1.59279

Large Squares 75/25 Red/Green Mix (Rotated)
72 Data Points Used

Red	= 75.4534%
Green	= 24.5466%
Residual Variance	= 0.614468
Residual Standard	= 0.783880
Residual Mean	= 0.325845
Residual Max Value	= 1.537690
Residual Min Value	= -1.51769

Large Squares 75/25 Red/Green Mix (Rotated)
73 Data Points Used

Red	= 73.1881%
Green	= 24.2567%
Yellow	= 2.55518%
Residual Variance	= 0.249141
Residual Standard	= 0.499140
Residual Mean	= -0.00771091
Residual Max Value	= 1.45873
Residual Min Value	= -1.16877

TABLE 4. PERCENT CONCENTRATION RESULTS

Large Squares 50/50 Red/Green Mix (Repeated)
84 Data Points Used

Red = 51.1206%
Green = 48.8794%
Residual Variance = 0.769353
Residual Standard = 0.877128
Residual Mean = 0.241784
Residual Max Value = 2.036880
Residual Min Value = -2.04926

Large Squares 50/50 Red/Green Mix (Repeated)
70 Data Points Used

Red = 48.5735%
Green = 49.0389%
Yellow = 2.38761%
Residual Variance = 0.442796
Residual Standard = 0.665429
Residual Mean = 0.0265032
Residual Max Value = 1.792760
Residual Min Value = -1.73661

Large Squares 50/50 Red/Green Mix (Repeated Again)
70 Data Points Used

Red = 48.5496%
Green = 51.4504%
Residual Variance = 1.396780
Residual Standard = 1.181850
Residual Mean = 0.309275
Residual Max Value = 2.828240
Residual Min Value = -2.46116

Large Squares 50/50 Red/Green Mix (Repeated Again)
71 Data Points Used

Red = 47.2529%
Green = 48.6534%
Yellow = 4.09364%
Residual Variance = 0.821457
Residual Standard = 0.906343
Residual Mean = 0.0171588
Residual Max Value = 3.294860
Residual Min Value = -2.66248

TABLE 5. PERCENT CONCENTRATION RESULTS

Small Squares 50/50 Red/Green Mix
64 Data Points Used

Red = 47.728%
 Green = 52.272%
 Residual Variance = 2.07936
 Residual Standard = 1.442
 Residual Mean = 0.488669
 Residual Max Value = 3.32402
 Residual Min Value = -2.92235

Small Squares 50/50 Red/Green Mix
65 Data Points Used

Red = 45.3574%
 Green = 49.5448%
 Yellow = 5.09777%
 Residual Variance = 0.697811
 Residual Standard = 0.835351
 Residual Mean = -0.0189529
 Residual Max Value = 2.80651
 Residual Min Value = -1.70586

Small Squares 50/50 Red/Green Mix (Rotated)
63 Data Points Used

Red = 46.4724%
 Green = 53.5276%
 Residual Variance = 1.60674
 Residual Standard = 1.26757
 Residual Mean = 0.295009
 Residual Max Value = 3.2525
 Residual Min Value = -2.16634

Small Squares 50/50 Red/Green Mix (Rotated)
60 Data Points Used

Red = 45.399%
 Green = 50.2944%
 Yellow = 4.30659%
 Residual Variance = 0.749072
 Residual Standard = 0.86549
 Residual Mean = 0.0065667
 Residual Max Value = 2.94102
 Residual Min Value = -1.56352

TABLE 6. PERCENT CONCENTRATION RESULTS

Small Squares 25/75 Red/Green Mix
63 Data Points Used

Red = 24.1692%
Green = 75.8308%
Residual Variance = 1.95059
Residual Standard = 1.39664
Residual Mean = 0.608475
Residual Max Value = 3.1749
Residual Min Value = -4.60226

Small Squares 25/75 Red/Green Mix
63 Data Points Used

Red = 19.8927%
Green = 74.9423%
Yellow = 5.16505%
Residual Variance = 0.80603
Residual Standard = 0.897791
Residual Mean = 0.0905302
Residual Max Value = 1.93587
Residual Min Value = -2.78372

Small Squares 25/75 Red/Green Mix (Rotated)
63 Data Points Used

Red = 24.724%
Green = 75.276%
Residual Variance = 1.93654
Residual Standard = 1.3916
Residual Mean = 0.523531
Residual Max Value = 3.11238
Residual Min Value = -3.996

Small Squares 25/75 Red/Green Mix (Rotated)
63 Data Points Used

Red = 21.0989%
Green = 74.4886%
Yellow = 4.41252%
Residual Variance = 1.08177
Residual Standard = 1.04008
Residual Mean = 0.0763604
Residual Max Value = 2.05594
Residual Min Value = -2.42596

TABLE 7. PERCENT CONCENTRATION RESULTS

Small Squares 75/25 Red/Green Mix
63 Data Points Used

Red = 75.964%
Green = 24.036%
Residual Variance = 1.90755
Residual Standard = 1.38114
Residual Mean = 0.399542
Residual Max Value = 3.64191
Residual Min Value = -3.37843

Small Squares 75/25 Red/Green Mix
63 Data Points Used

Red = 75.126%
Green = 21.1961%
Yellow = 3.67788%
Residual Variance = 1.31538
Residual Standard = 1.1469
Residual Mean = 0.0340338
Residual Max Value = 3.92794
Residual Min Value = -2.0951

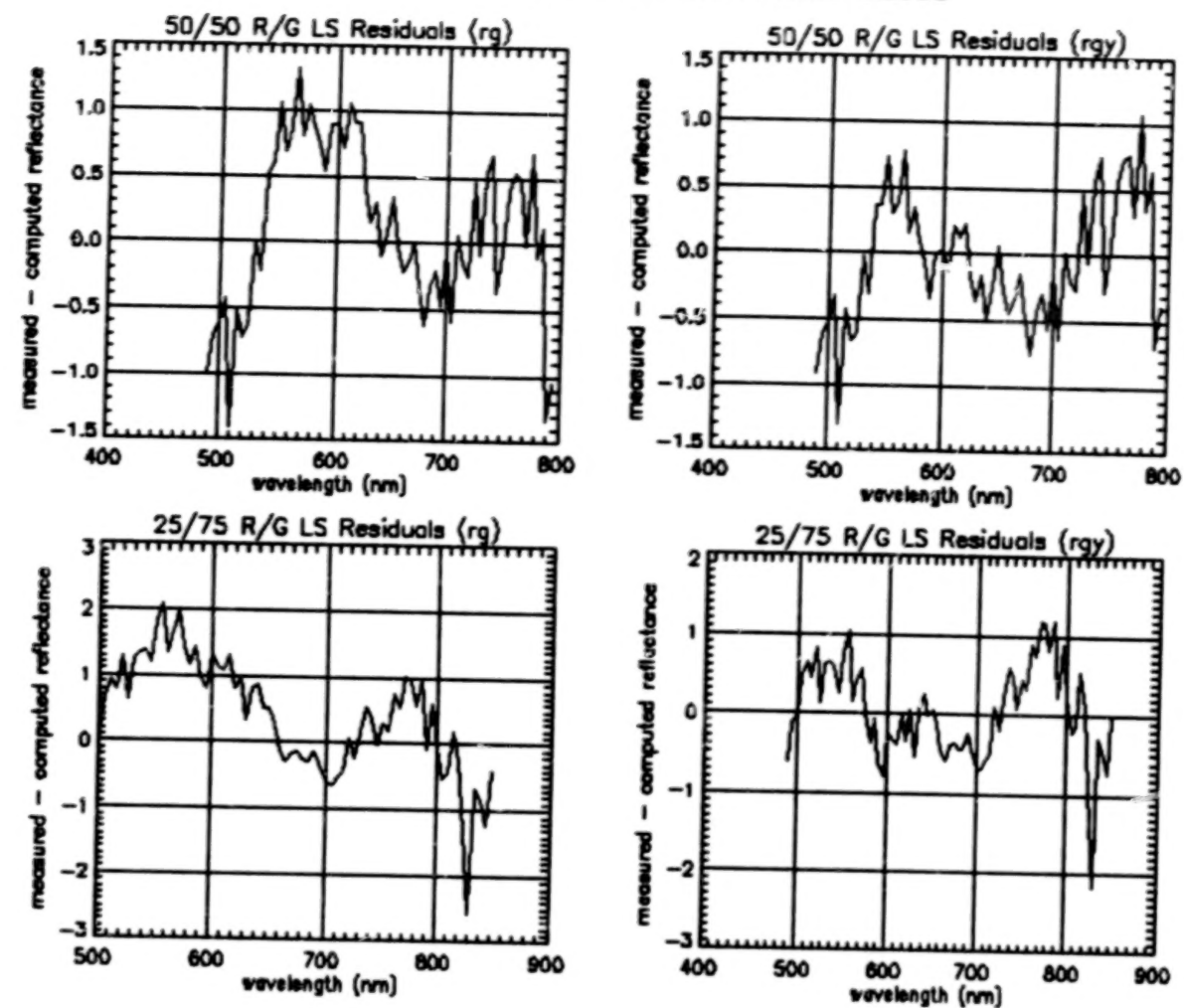
Small Squares 75/25 Red/Green Mix (Rotated)
63 Data Points Used

Red = 77.5492%
Green = 22.4508%
Residual Variance = 1.98097
Residual Standard = 1.40747
Residual Mean = 0.450635
Residual Max Value = 3.61223
Residual Min Value = -3.88359

Small Squares 75/25 Red/Green Mix (Rotated)
63 Data Points Used

Red = 76.6859%
Green = 19.1925%
Yellow = 4.12151%
Residual Variance = 1.28975
Residual Standard = 1.13567
Residual Mean = 0.0522504
Residual Max Value = 3.92398
Residual Min Value = -2.48484

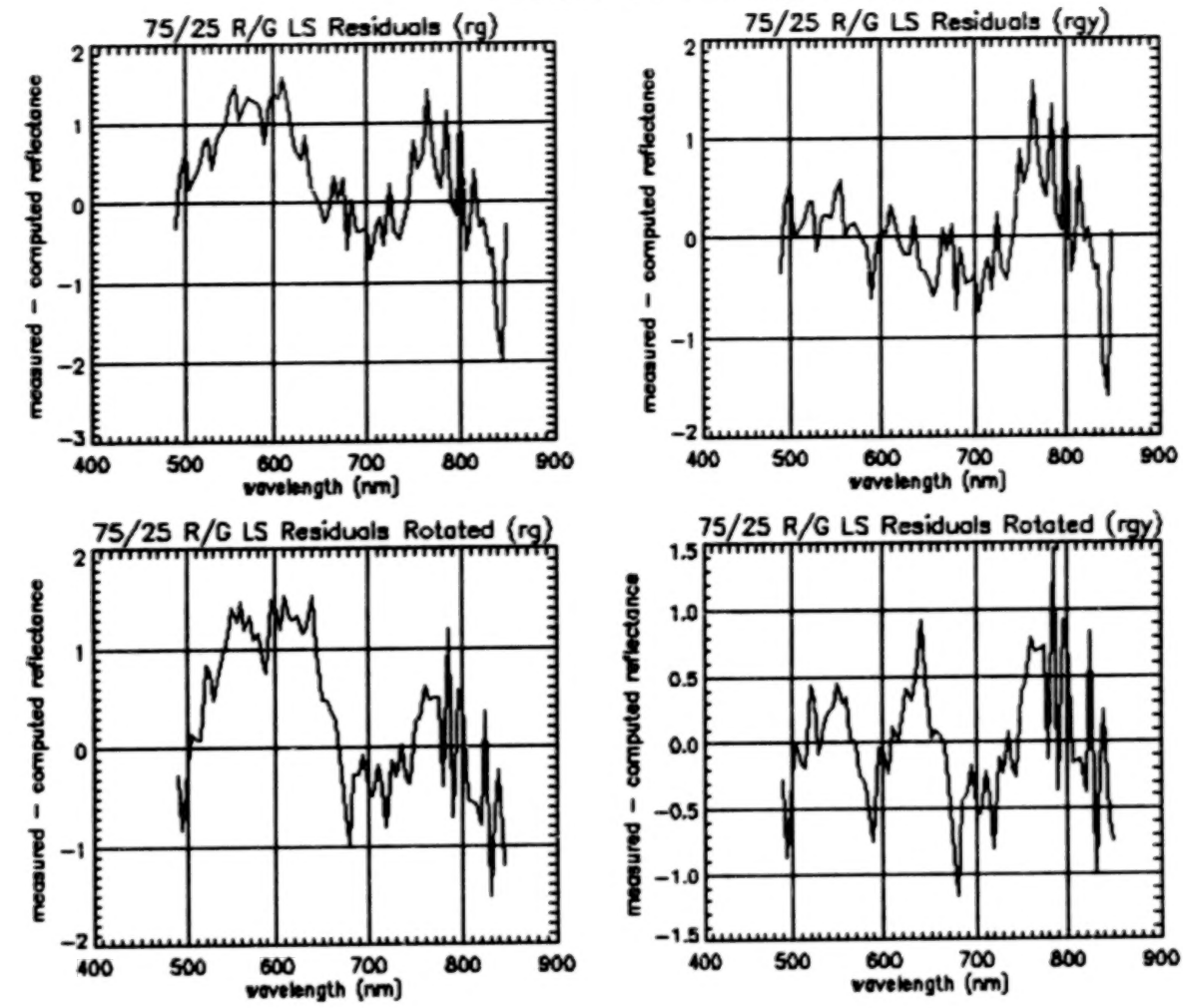
FIGURE 8. RESIDUAL PLOTS



354

354

FIGURE 9. RESIDUAL PLOTS



355

355

FIGURE 10. RESIDUAL PLOTS

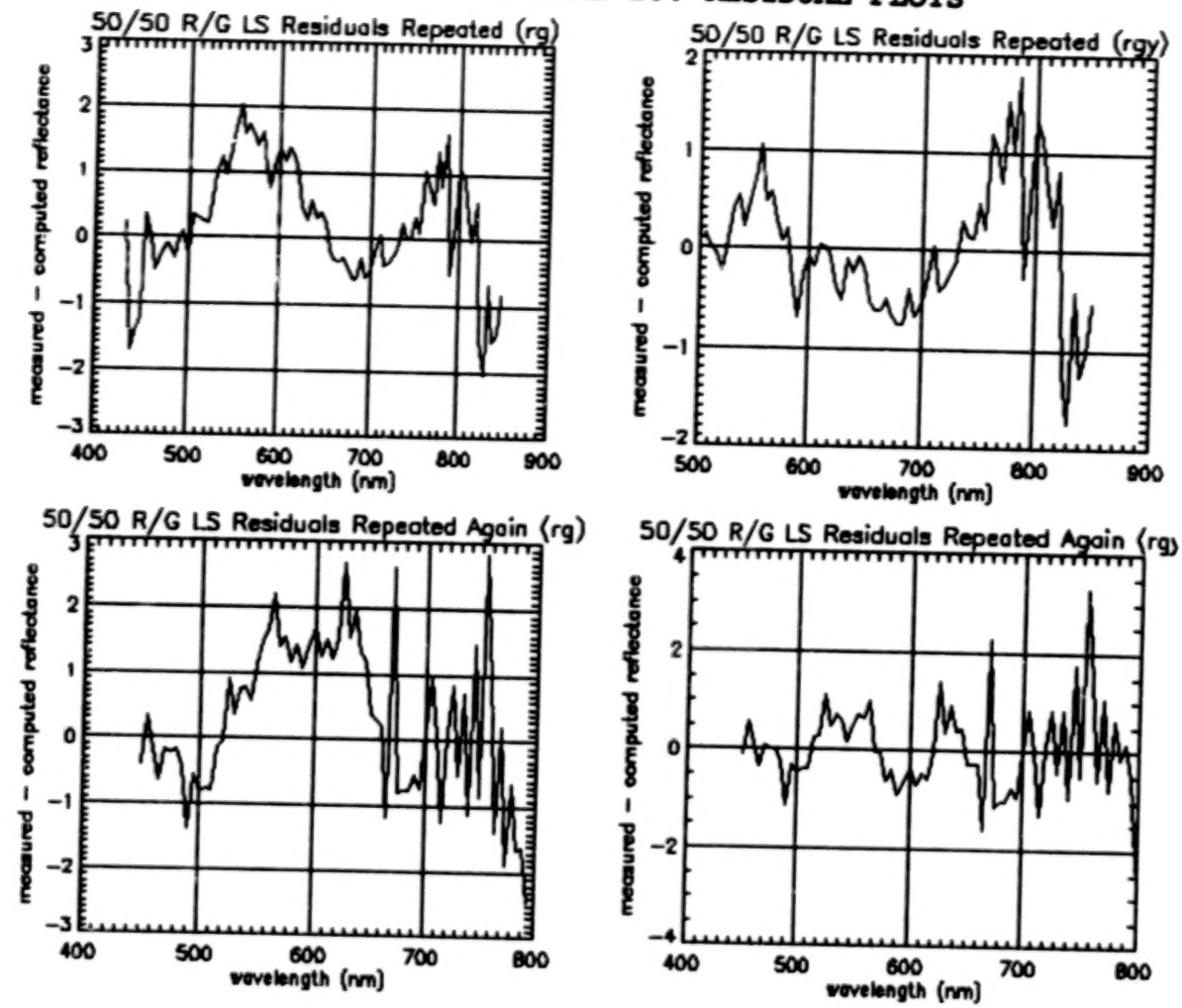
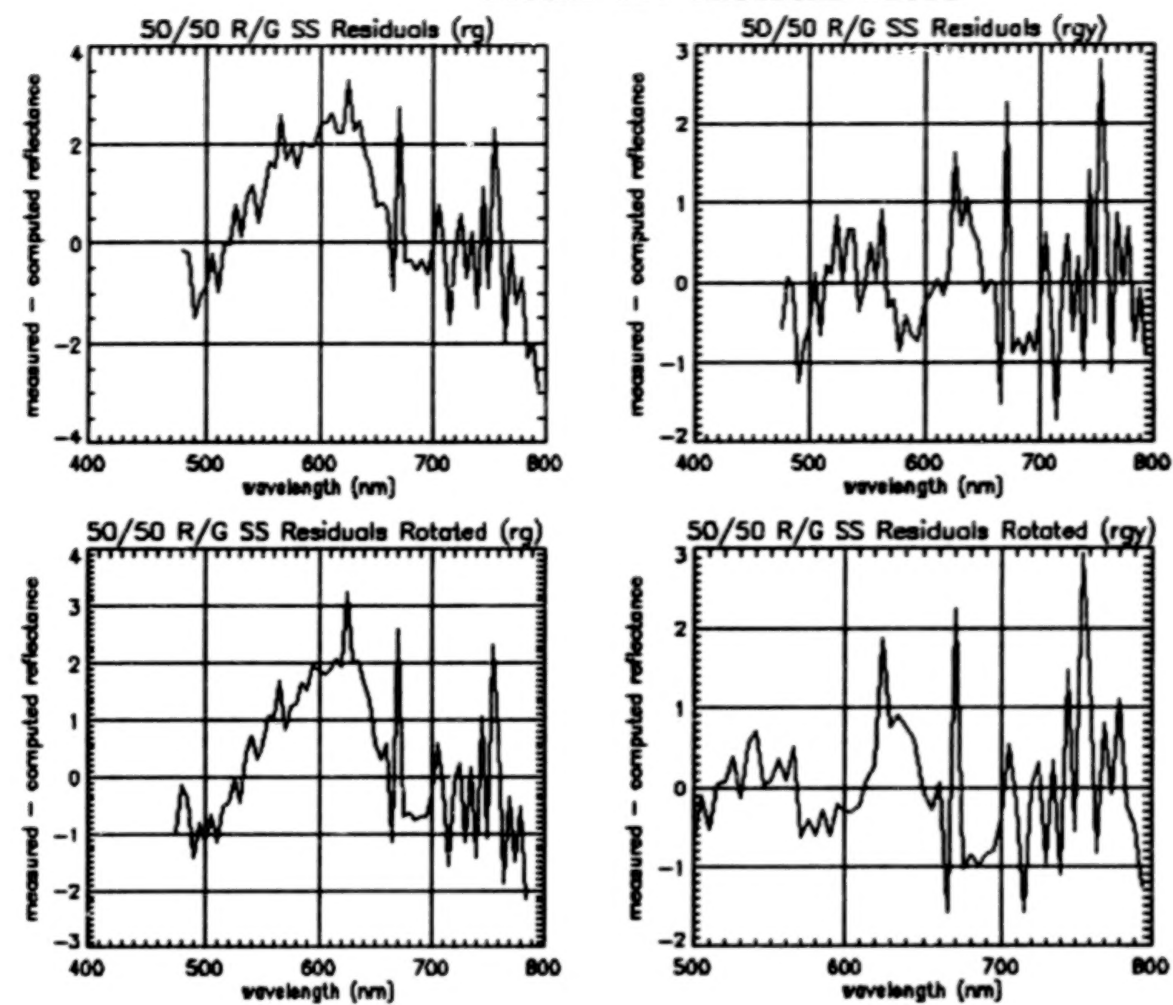


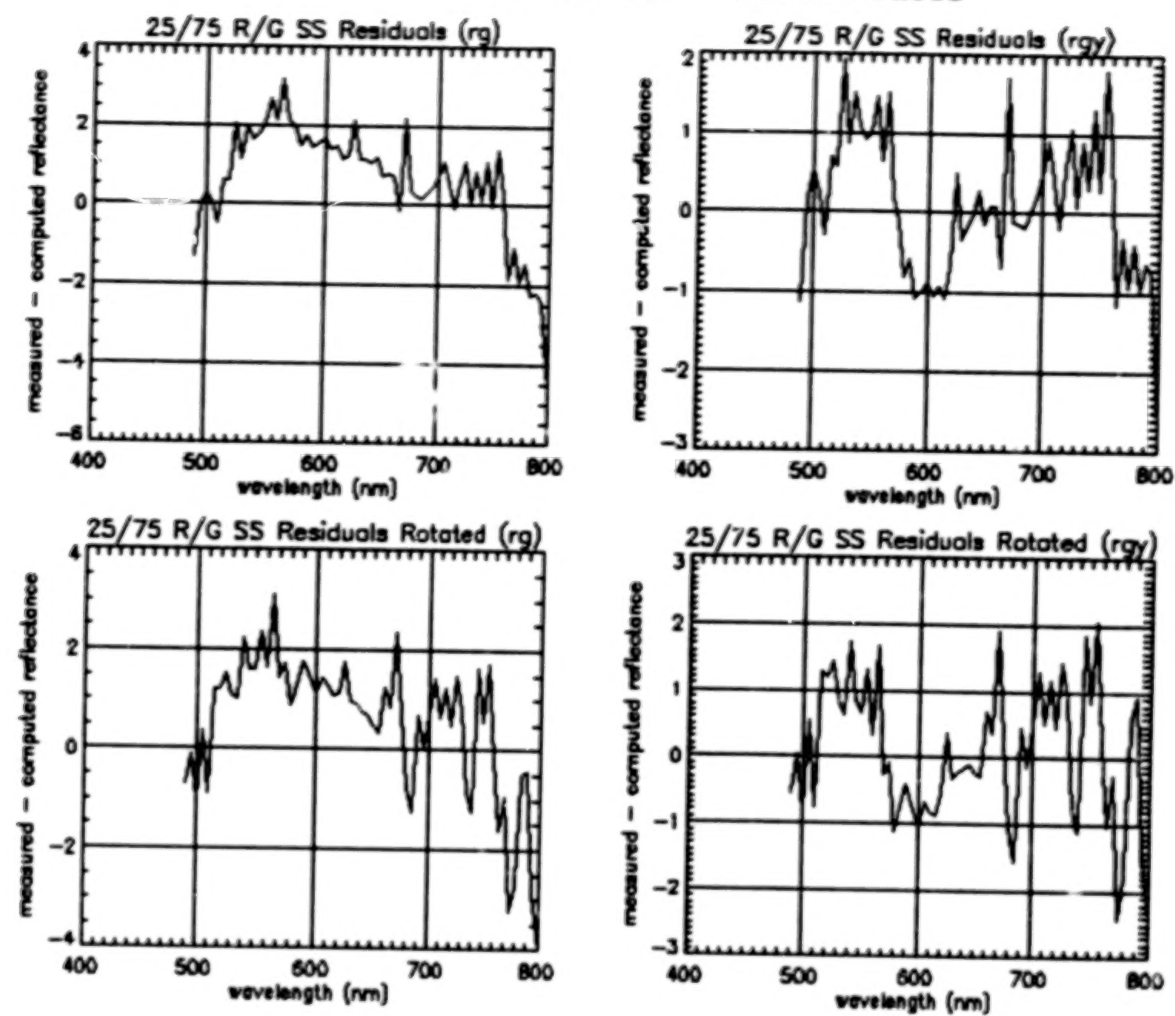
FIGURE 11. RESIDUAL PLOTS



357

357

FIGURE 12. RESIDUAL PLOTS



358

358

FIGURE 13. RESIDUAL PLOTS

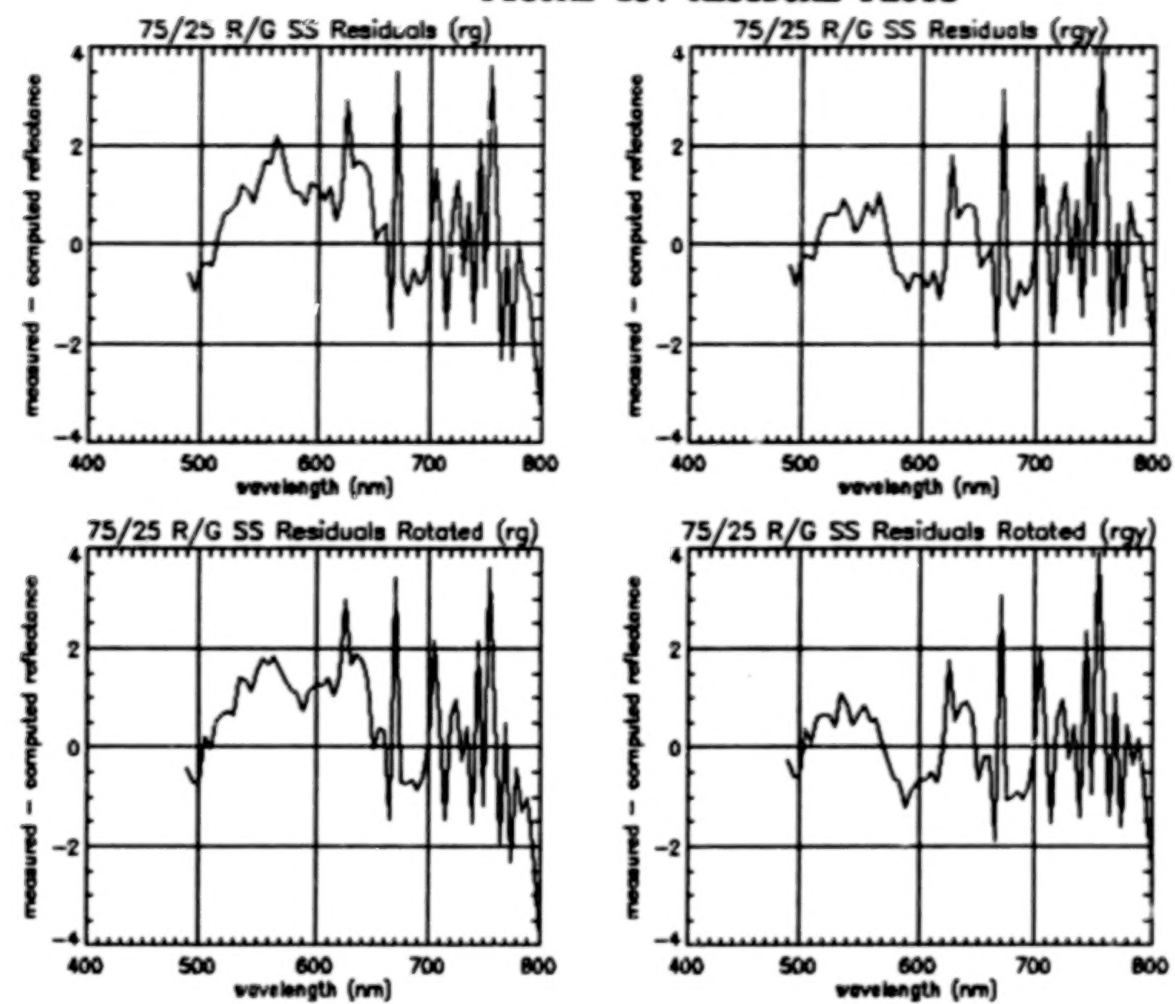


TABLE 8. PERCENT YELLOW IN TARGETS

Rank	Percent Yellow	Red/Green Combination	Size Square
1	5.15	25/75	Small
2	5.09	50/50	Small
3	4.09	50/50 (Repeated again)	Large
4	4.41	25/75 (Rotated)	Small
5	4.30	50/50 (Rotated)	Small
6	4.12	75/25 (Rotated)	Small
7	3.68	75/25	Small
8	2.56	75/25	Large
9	2.70	25/75	Large
10	2.39	50/50 (Repeated)	Large
11	2.25	75/25 (Rotated)	Large
12	1.56	50/50	Large

No effort was made to determine the various errors which may influence the results. Equation (4) above has an inherent error term, but was assumed to be zero for this effort. A misalignment, uneven dyes, uneven checkerboards and a number of other factors would cause errors, however in light of the analysis of the results and statistics, it appears that an error analysis at this point would not provide much information.

4. CONCLUSIONS

The results obtained show that a linear estimation model and a library of spectral prototypes are viable methods for de-mixing hyperspectral mixed pixel. The computed dye concentrations agree with the known concentrations to a small percent difference. The variance and standard deviation of the residuals are indicative of a valid model. The residuals themselves show no spectral bias. Fig. 8-13 show a plot of the residuals for the various tests. In the figures 'LS' means large squares, 'SS' small squares, 'rg' red/green vector, and 'rgy' red/green/yellow vector.

ACKNOWLEDGEMENTS

The authors are indebted to Dr. Woody Kober of Data Fusion Corporation who provided the initial topic and ideas for this work. The authors gratefully acknowledge the support of Tim Evans and Ponder Henley of the Spectral Research Division, U. S. Army Topographic Engineering Center (USATEC) for data aquisition and formatting and Peter Johnson, Chief Imagery Research Division (USATEC) for his intellectual support.

REFERENCES

- Boardman, J. W., "Inversion of imaging spectrometer data using singular value decomposition," Preprint, Center for the Study of Earth from Space (CSES), University of Colorado, Boulder, 1990.
- Fletcher, R., "A General Quadratic Programming Algorithm," J. Inst. Math. Appl., Volume 7, 1971.
- Kruse, F. A., et al., "Automated Extraction of Absorption Features from Airborne Visible/Infrared Spectrometer (AVIRIS) and Geophysical Environmental Research Imaging Spectrometer (GERIS) Data," JPL Publication #88-38, Pasadena, CA.
- Stocker, A., Jensen, P., "Algorithms and Architectures for Implementing Large Velocity Filter Banks," Proceedings SPIE, Volume 1481, Signal and Data Processing of Dim Targets.

BLANK PAGE

SESSION III

SPECTRAL ANALYSIS/PROCESSING SYSTEMS AND TOOLS

BLANK PAGE

EFFECTS OF SPECTRAL AND SPATIAL RESOLUTIONS ON NDVI

P.M. Teillet and K. Staenz
Canada Centre for Remote Sensing
Ottawa, Ontario, Canada

D.J. Williams
MacDonald Dettwiler and Associates Ltd.
Richmond, British Columbia, Canada

ABSTRACT

Vegetation indices derived from satellite image data have become one of the primary information sources for monitoring vegetation conditions and mapping land cover change. The most widely used vegetation index in this context is NDVI, the Normalized Difference Vegetation Index, which is a function of red and near-infrared spectral bands. Given that the spectral and spatial characteristics of imagery in the red and near-infrared vary from sensor to sensor, NDVI values based on data from different instruments will not be directly comparable. The present study demonstrates the impact of changes in spectral bandwidth and spatial scale on NDVI derived from Airborne Visible/Infrared Imaging Spectrometer (AVIRIS) data acquired at 20 m resolution over a forested region in Southeastern British Columbia. For this purpose, the 10 nm AVIRIS data were spectrally and spatially aggregated in the red and near-infrared to simulate bandwidths from 10 nm to 150 nm for ground resolutions varying from 20 m to 1100 m. Sensor-specific spectral bands and spatial resolutions such as those for SPOT HRV, Landsat TM, NOAA AVHRR, EOS MODIS and Envisat MERIS were also generated. NDVI values were then calculated using atmospherically corrected surface reflectances for forestry-related targets for the entire simulated bandset at the various scales. The results indicate that the NDVI is significantly affected by differences in spectral bandwidth, especially for the red band, and that changes in spatial resolution lead to less pervasive but more land cover specific effects on NDVI.

1. INTRODUCTION

Satellite image data have become an important source of information for monitoring vegetation and mapping land cover and land cover change on regional, continental, and global scales. In particular, sensors with spectral bands in the red (RED) and near-infrared (NIR) lend themselves well to vegetation monitoring since the difference between the red and near-infrared bands has been shown to be a strong indicator of the amount of photosynthetically active green biomass. As a result, widespread use is being made of the Normalized Difference Vegetation Index (NDVI), which is defined as $(\text{NIR} - \text{RED}) / (\text{NIR} + \text{RED})$.

The NDVI from remote sensing is increasingly being used as an indirect means of study for biophysical plant canopy properties (Pinty et al., 1993), including its relationship to biomass (Tucker, 1979; Elvidge and Lyon, 1985), leaf area index (Holben et al., 1980; Badhwar et al., 1986; Peterson et al., 1987; Clevers, 1988, 1989; Spanner et al., 1990; Baret and Guyot, 1991; Danson et al., 1994), photosynthetic activity (Asrar et al., 1984; Choudhury, 1987; Baret and Guyot, 1991; Goward and Huemmerich, 1992), carbon dioxide (Tucker et al., 1986; Cihlar et al., 1992), and ecological parameters (Cihlar et al., 1991), among others. Perhaps the most prevalent use of NDVI is in multi-temporal mapping of vegetation dynamics based on maximum-NDVI compositing (Townshend et al., 1985; Holben, 1986; Gutman, 1989; Wiegand et al., 1991; Viovy et al., 1992; Loudjani et al., 1994; Qi and Kerr, 1994).

NDVI values can vary significantly as a function of sensor calibration (Price, 1987; Goward et al., 1991), atmospheric conditions (Deering and Eck, 1987; Singh and Saull, 1988; Kaufman and Tanré, 1992; Myneni and

Asrar, 1994), directional surface reflectance effects (Kirchner et al., 1981; Holben et al., 1986; Lee and Kaufman, 1986; Paltridge and Mitchell, 1990; Koslowsky, 1993), and terrain relief (Teillet and Staenz, 1992; Burgess and Lewis, 1994). Special attention has also been paid to soil background effects (Huete, 1988; Baret et al., 1989; Major et al., 1990; Qi et al., 1994a, b). Alternative vegetation indices have been formulated or proposed to try to overcome some of these effects, but their discussion is beyond the realm of this paper. Aman et al. (1992) have examined the correspondence between spatial integration of NDVI as opposed to computing NDVI from spatially integrated reflectances.

Given that the characteristics of spectral bands in the red and near-infrared vary distinctly from sensor to sensor, NDVI values based on data from different instruments will not be directly comparable. The spatial resolution also varies significantly between sensors, as well as within a given scene in the case of wide-angle and oblique sensors. As a result, NDVI values will vary according to combinations of the heterogeneity and scale of terrestrial surfaces and pixel footprint sizes. Therefore, the question arises as to the impact of differences in spectral and spatial resolutions on vegetation indices like the NDVI. In order to address this question, Airborne Visible/Infrared Imaging Spectrometer (AVIRIS) data acquired over a forested region in Southeastern British Columbia were atmospherically corrected and used to generate NDVI values for a variety of spectral and spatial resolutions. The data set is well suited to this investigation since AVIRIS collects imagery at 20 m ground resolution in 224 spectral bands, each approximately 10 nm wide, in the 400 nm to 2450 nm region (Porter and Enmark, 1987; Green et al., 1990). Pixel averages for several forestry-related land cover types (conifers, mixed stands, clear-cuts, etc.) were extracted from the imagery for NDVI calculations.

Values of NDVI for a given vegetation target will not only differ because of the spectral and spatial characteristics of the sensor, but also as a function of the radiometric processing applied to the image data. The properties of NDVI space will vary considerably depending on whether NDVI is defined in terms of digital signal levels, top-of-the-atmosphere radiances, top-of-the-atmosphere reflectances, or atmospherically-corrected surface reflectances. The scope of the investigation reported in this paper is limited to NDVI defined in terms of atmospherically-corrected surface reflectances in the red and near-infrared spectral bands.

2. DATA SETS AND METHODOLOGY

The AVIRIS data used for this NDVI study were acquired over two forested areas in the Kootenay Valley near Invermere in Southeastern British Columbia on August 14, 1990. Available ground reference information includes a geographic information system (GIS) of the test sites on a 1:20,000 scale with digital elevation models, forest inventory maps, and forest attribute information.

Specific target types as listed in Table 1 were selected from the AVIRIS imagery on the basis of the forest inventory maps. For this purpose, it was necessary to register the forest cover maps to one of the AVIRIS scenes in order to definitely delineate the target areas (polygons) while the polygon boundaries in the other scene could be visually determined for the targets selected. This map-to-image registration resulted in a root-mean-square error of ± 1.50 pixels in the pixel direction and ± 0.95 pixels in the line direction using the nearest neighbour resampling technique. The selected target areas are located in flat terrain and vary in size between $0.3 \times 0.3 \text{ km}^2$ and $2.0 \times 3.0 \text{ km}^2$. This means that for ground instantaneous fields-of-view (GIFOVs) of 500 and 1100 m, the target area may consist of a mixture of different target types (Table 1).

Figure 1 summarizes the data processing flow. The AVIRIS data were spatially degraded to resolutions of 20, 60, 100, 260, 500, and 1100 m by averaging blocks of pixels within selected vegetated areas. This approach to spatial degradation was felt to be appropriate for examining the behaviour of NDVI as a function of varying scale and spectral bandwidth. Therefore, more sophisticated techniques such as those based on modulation transfer functions (Justice et al., 1989) were not used. The spectral resolution simulation was carried out by convolving the AVIRIS radiance data with gaussian-like spectral response profiles in the red and near-infrared to generate a series of generic bandwidths: 10, 30, 50, 100, and 150 nm FWHM (full width at half maximum). The red and near-infrared bands were centred at 660 nm and 850 nm, respectively. Sensor-specific bands such as those for SPOT HRV, Landsat TM, and NOAA AVHRR were generated using their actual spectral response profiles and

Table 1: Targets selected from the AVIRIS scenes. The simulated GIFOVs (Ground Instantaneous Field-of-View) that completely enclose the targeted polygons are indicated, where the set of GIFOVs includes 20, 60, 100, 260, 500 and 1100 metres

Target Type (Symbols)	GIFOV Cases		Target Characteristics			Remarks
	Within Polygon Boundaries	Outside Polygon Boundaries	Crown Closure (%) [*]	Age (years) [*]	Height (m)	
Spruce (S)	≤ 500 m	1100 m	80	130	11-20	
Yellow pine (YP)	≤ 260 m	500 m, 1100 m	30	130	11-20	
Douglas fir (F)	≤ 260 m	500 m, 1100 m	30	50	11-20	Minor species; yellow pine
Aspen/spruce (AS)	≤ 260 m	500 m, 1100 m	40	130	11-20	
Douglas fir/larch/ lodgepole pine (FLP)	≤ 1100 m	—	20	70	≤ 10	Immature stand
Clear cut (CC)	≤ 1100 m	—	—	—	—	Logged in 1981-83
Clear cut/ forested area (CF)	—	≤ 1100 m	50	50	20	Mixture between clear cut areas and pine stands (see target characteristics)

^{*} Averaged values

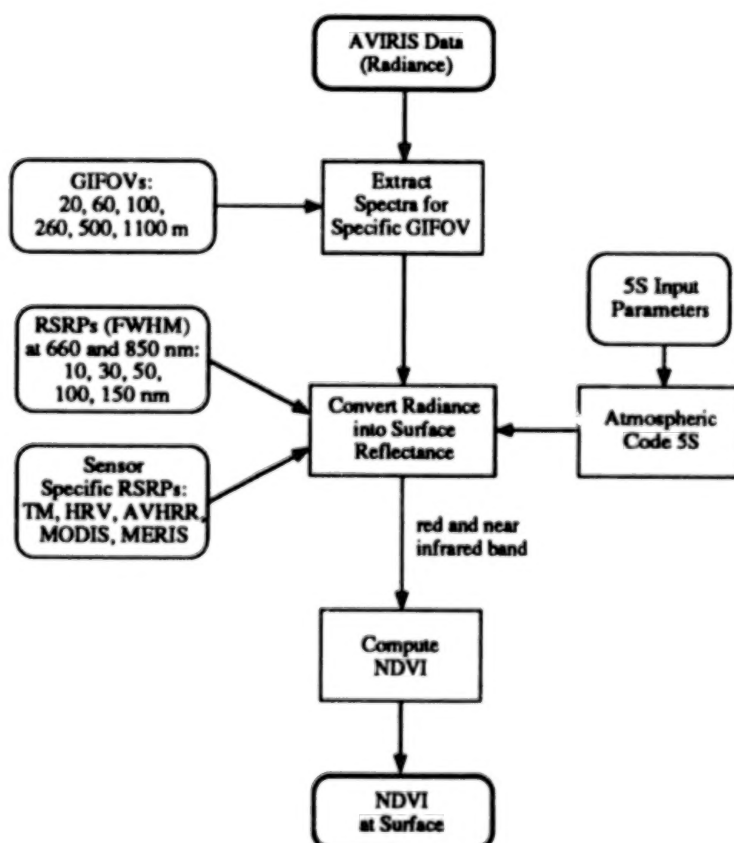


Figure 1. Processing data flow for the NDVI study, where RSRP = relative spectral response profile.

Table 2. Sensor Specific Band Characteristics Used for Calculation of the Surface Reflectance in the Red and Near-Infrared Bands

Sensor	Red Band			Near-Infrared Band		
	Band #	Centre Wavelength (nm)	Bandwidth (nm)	Band #	Centre Wavelength (nm)	Bandwidth (nm)
Landsat TM	3	661	66	4	838	121
SPOT HRV	2	653	64	3	840	101
NOAA AVHRR	1	633	113	2	847	229
EOS MODIS	1	645	50	2	858	35
Envisat MERIS	7	665	10	12	880	10

Table 3. 5S Input Parameters

Parameter	Area 1	Area 2
Atmospheric model	Mid-latitude summer	Mid-latitude summer
Aerosol model	Continental	Continental
Date of overflight	August 14, 1990	August 14, 1990
Solar zenith angle	35.87 degrees	35.69 degrees
Solar azimuth angle	179.49 degrees	182.73 degrees
Sensor zenith angle	Variable	Variable
Sensor azimuth angle	30.3 or 20.3 degrees	32.68 degrees
Ground elevation	Variable	0.900 km
Sensor altitude above sea level	19.850 km	19.844 km
Horizontal visibility	50 km	50 km

simulated bands were generated for EOS MODIS and Envisat MERIS using gaussian-like profiles (Table 2). These data were corrected for atmospheric effects using a modified version of the 5S atmospheric code (Tanré et al., 1990; Teillet, 1989; Teillet and Santer, 1991) and the input parameters given in Table 3. Finally, NDVI values were computed on the basis of the red and near-infrared bands for the simulated bandwidth set at the different spatial resolutions.

It is clear that most of the spatial resolution combinations for the known sensor types are fictitious. Nevertheless, these combinations are included in the results for completeness and because they provide useful information for the acquisition of validation data sets based on ground-based and aircraft sensor data. In the spectral dimension, the NDVI results were generated on the basis of both equal and differing bandwidth combinations for the red and near-infrared spectral bands.

3. RESULTS

Figure 2 illustrates the main results for three target types: spruce, yellow pine, and mixed coniferous forest (Douglas fir, larch, lodgepole pine), which are seen to have distinct NDVI amplitudes. In all three cases, varying

the spatial resolution from 20 metres up to 1100 metres has no effect on NDVI and the curves for the six spatial resolutions are almost superimposed. In the spectral domain, NDVI clearly decreases as the spectral bandwidth of the bands making up the vegetation index increases from 10 nanometres up to 150 nanometres. The decrease is relatively small from 10 nanometres to 50 nanometres, but is considerably steeper for bandwidths wider than 50 nanometres. The same decreasing NDVI behaviour is observed in the sequence of specific sensors from MERIS, to MODIS, to TM, to HRV, to AVHRR. Note that these specific sensor cases are individual ones and that connecting lines are used in Figures 2 and 3 for visualization purposes only.

Figure 3 shows the NDVI results for the other target types involved in this study. The spectral character of these results is much the same as that of the three target types already discussed, but changes in the spatial resolution do have an effect for the four classes shown in Figure 3. For the aspen/spruce stand and for the Douglas fir stand, the NDVI drops significantly for GIFOVs greater than 260 metres and 500 metres, respectively. For the heterogeneous target made up of clear cut and forested terrain, the NDVI decreases markedly when the spatial resolution gets too high, i.e., finer than 260 metres in this case. For the clear cut target type, the NDVI increases when the spatial resolution is degraded, with the exception of the 260-metre case which is indistinguishable from the 20- and 60-metre cases. This situation for the clear cut target area arises because of some scattered mixed vegetation near, but not at, the centre of the clear cut. All of these results are consistent with what one would expect as the GIFOV is varied relative to the size of land cover elements such as the forest stands.

For the forestry-related target categories in this investigation, Figure 4 emphasizes how changes in NDVI, whether up or down, tend to occur at scales on the order of 260 to 500 metres. The MERIS case is shown in Figure 4, but the other sensors and spectral resolutions all give similar results.

If the spectral resolutions in the visible, red spectral band and the near-infrared spectral band are varied separately, one finds that NDVI is considerably more sensitive to changes in the red spectral band. The contour plot in Figure 5 illustrates this point for the spruce stand at 260-metre spatial resolution. Contour plots for the other spatial resolutions and target types have very similar characteristics.

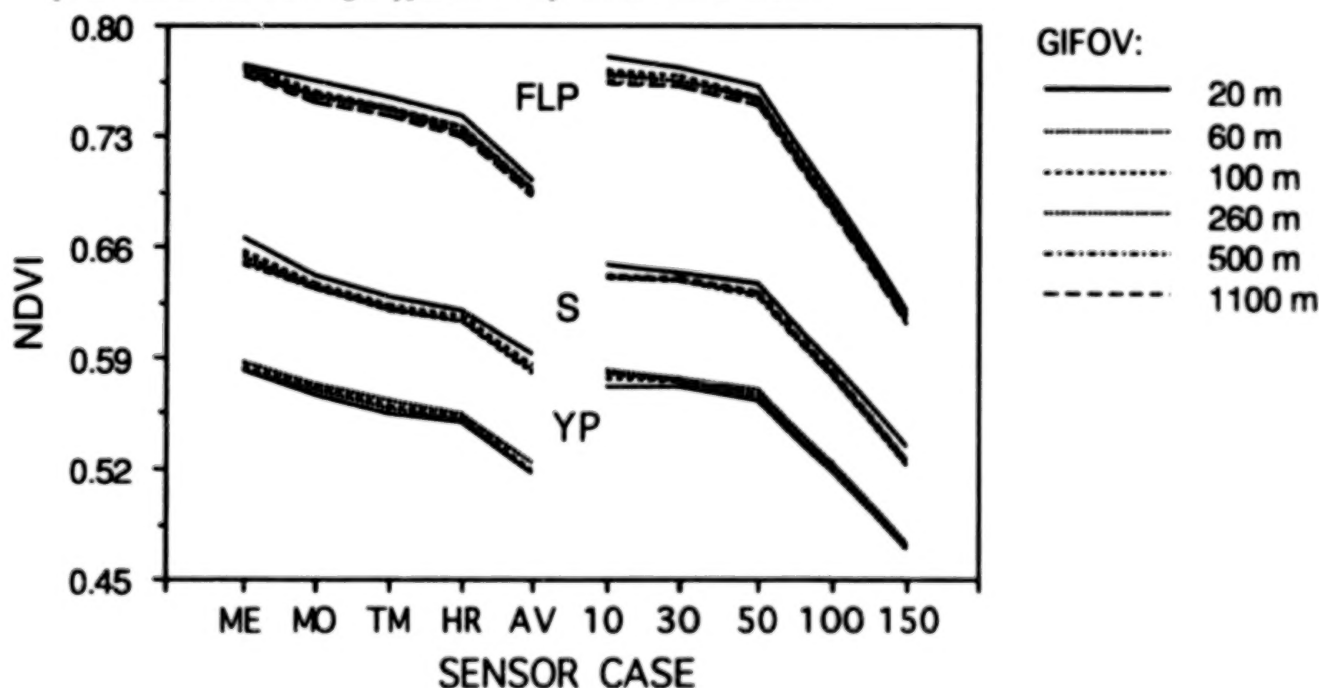


Figure 2. NDVI study results emphasizing the spectral domain for spruce (S), yellow pine (YP), and fir/larch/pine (FLP) stands for the indicated GIFOVs. The sensor cases are the generic spectral bands with full width at half-maximum of 10, 30, 50, 100, and 150 nanometres, and the specific sensors MERIS (ME), MODIS (MO), TM, HRV (HR), and AVHRR (AV).

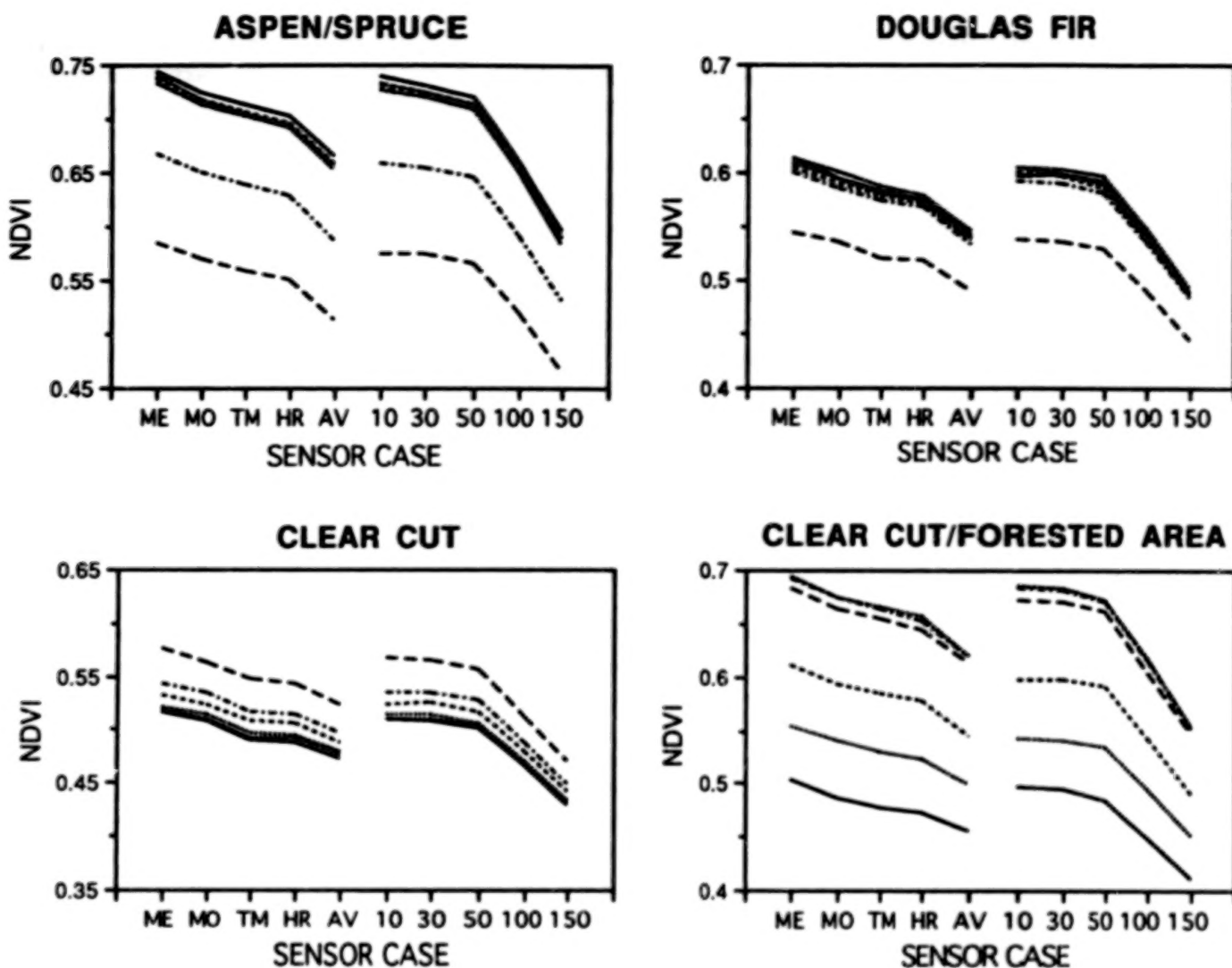


Figure 3. NDVI study results emphasizing the spectral domain for the indicated target categories, where the sensor cases and the different line types indicating GIFOV cases are as defined in Figure 2.

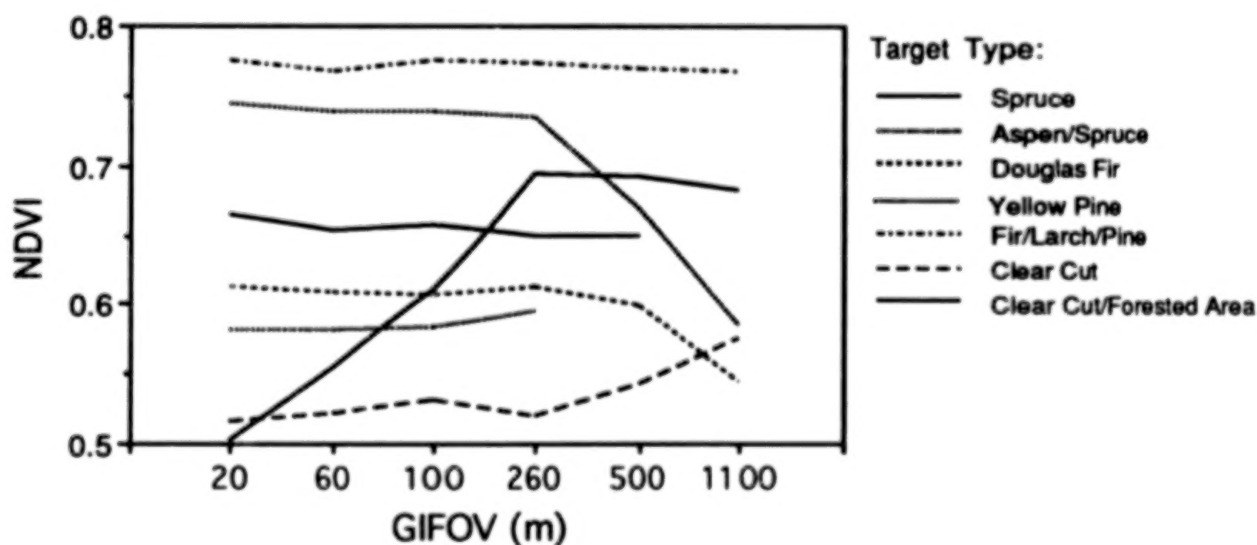


Figure 4. NDVI study results emphasizing the spatial domain, for the MERIS case as an example.

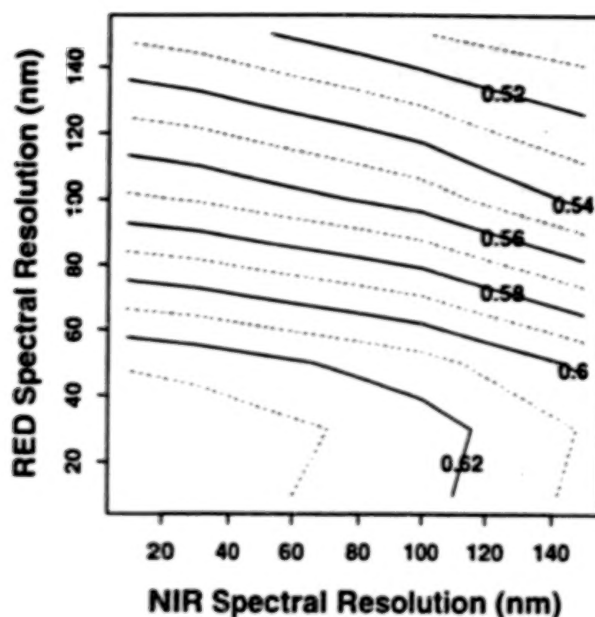


Figure 5. NDVI study results for independently varying spectral resolutions in the RED and near-infrared (NIR) spectral bands, for the spruce stand at 260-metre spatial resolution.

4. CONCLUSIONS

For the forestry-related targets examined in this study, an increase in the bandwidths of the red and near-infrared spectral bands used to form NDVI leads to a decrease in NDVI values, with most of the change attributable to the bandwidth of the red channel. This result is much as one would expect given the limited spectral width of the chlorophyll absorption well of vegetation at red wavelengths. The result emphasizes the point that, even if spectral data from different sensors are radiometrically calibrated and atmospherically corrected, the NDVI values derived from them are not directly comparable. Moreover, for an optimum NDVI definition, the red spectral band should be as narrow as possible and less than 50 nanometres wide (FWHM). Even the Landsat TM and SPOT HRV sensors are sub-optimum in this respect. Although MERIS and MODIS datasets will likely be used to generate new and improved vegetation indices, NDVI values derived from these forthcoming data sets would be close to being optimum spectrally.

Changes in NDVI due to differences in spatial resolution depend on the nature of the land cover, particularly the spatial extent of forest stands and clear cuts in this study. For the forested region in Southeastern British Columbia, distinct changes in NDVI occur at scales on the order of 260 to 500 metres, regardless of spectral band characteristics.

REFERENCES

- Aman, A., H.P. Randriamanantena, A. Podaire, and R. Frouin, 1992: Upscale Integration of Normalized Difference Vegetation Index: The Problem of Spatial Heterogeneity. *IEEE Transactions on Geoscience and Remote Sensing*, 30(2), 326-338.
- Asrar, G., M. Fuchs, E.T. Kanemasu, and J.L. Hatfield, 1984: Estimating Absorbed Photosynthetic Radiation and Leaf Area Index from Spectral Reflectance in Wheat. *Agronomy Journal*, 76, 300-306.
- Badhwar, G.D., R.B. MacDonald, and N.C. Mehta, 1986: Satellite-Derived Leaf-Area-Index and Vegetation Maps as Input to Global Carbon Cycle Models - A Hierarchical Approach. *International Journal of Remote Sensing*, 7(2), 265-281.

- Baret, F., and G. Guyot, 1991: Potentials and Limits of Vegetation Indices for LAI and APAR Assessment. *Remote Sensing of Environment*, 35, 161-173.
- Baret, F., G. Guyot, and D. Major, 1989: TSAVI: A Vegetation Index Which Minimizes Soil Brightness Effects on LAI or APAR Estimation. *Proceedings of the 1989 International Geoscience and Remote Sensing Symposium (IGARSS '89) and the Twelfth Canadian Symposium on Remote Sensing*, Vancouver, Canada, 1355-1358.
- Burgess, D.W., and P. Lewis, 1994: The Topographic Effects on NDVI Measurements Derived from AVHRR Data. *Proceedings of the Seventh Australasian Remote Sensing Conference*, Melbourne, Australia, 189-196.
- Choudhury, B.J., 1987: Relationships Between Vegetation Indices, Radiation Absorption, and Net Photosynthesis Evaluated by a Sensitivity Analysis. *Remote Sensing of Environment*, 22, 209-233.
- Cihlar, J., P.H. Caramori, P.H. Schuepp, R.L. Desjardins, and J.I. MacPherson, 1992: Relationship Between Satellite-Derived Vegetation Indices and Aircraft-Based CO₂ Measurements. *Journal of Geophysical Research*, 97(D17), 18515-18521.
- Cihlar, J., L. St-Laurent, and J.A. Dyer, 1991: Relation Between the Normalized Difference Vegetation Index and Ecological Variables. *Remote Sensing of Environment*, 35, 279-298.
- Clevers, J.G.P.W., 1988: The Derivation of a Simplified Reflectance Model for the Estimation of Leaf Area Index. *Remote Sensing of Environment*, 25, 53-70.
- Clevers, J.G.P.W., 1989: The Application of a Weighted Infrared-Red Vegetation Index for Estimating Leaf Area Index by Correcting for Soil Moisture. *Remote Sensing of Environment*, 29, 25-37.
- Danson, F.M., K.J. Winstanley, and A.M. Stocks, 1994: High-Spectral Resolution Indices for Forest Leaf Area Index. *Proceedings of the Sixth International Colloquium on Physical Measurements and Signatures in Remote Sensing*, Val d'Isère, France, 6 pages, in press.
- Deering, D.W., and T.F. Eck, 1987: Atmospheric Optical Depth Effects on Angular Anisotropy of Plant Canopy Reflectance. *International Journal of Remote Sensing*, 8(6), 893-916.
- Elvidge, C.D., and R.J.P. Lyon, 1985: Influence of Rock-Soil Spectral Variation on Assessment of Green Biomass. *Remote Sensing of Environment*, 17, 265-279.
- Goward, S.N., and K.F. Huemmerich, 1992: Vegetation Canopy PAR Absorptance and the Normalized Difference Vegetation Index: An Assessment Using the SAIL Model. *Remote Sensing of Environment*, 39, 119-140.
- Goward, S.N., B.L. Markham, D.G. Dye, W. Dulaney, and J. Yang, 1991: Normalized Difference Vegetation Index Measurements from the Advanced Very High Resolution Radiometer. *Remote Sensing of Environment*, 35, 257-277.
- Green, R.O., J.E. Conel, V. Carrere, C.J. Bruegge, J.S. Margolis, M. Rast, and G. Hoover, 1990: Determination of the In-Flight Spectral and Radiometric Characteristics of the Airborne Visible/Infrared Imaging Spectrometer (AVIRIS). *Proceedings of the Second Airborne Visible/Infrared Imaging Spectrometer (AVIRIS) Workshop*, JPL Publication 90-54, Pasadena, California, 15-34.
- Gutman, G., 1989: On the Relationship Between Monthly Mean and Maximum-Value Composite Normalized Vegetation Indices. *International Journal of Remote Sensing*, 10(8), 1317-1325.

- Holben, B.N., 1986: Characteristics of Maximum-Value Composite Images from Temporal AVHRR Data. *International Journal of Remote Sensing*, 7, 1417-1434.
- Holben, B.N., C.J. Tucker, and C.J. Fan, 1980: Spectral Assessment of Soybean Leaf Area and Leaf Biomass. *Photogrammetric Engineering and Remote Sensing*, 46, 651-656.
- Holben, B.N., D.S. Kimes, and R.S. Fraser, 1986: Directional Reflectance in AVHRR Red and Near-IR Bands for Three Cover Types and Varying Atmospheric Conditions. *Remote Sensing of Environment*, 19, 213-236.
- Huete, A.R., 1988: A Soil-Adjusted Vegetation Index (SAVI). *Remote Sensing of Environment*, 25, 295-309.
- Justice, C.O., B.L. Markham, J.R.G. Townshend, and R.L. Kennard, 1989: Spatial Degradation of Satellite Data. *International Journal of Remote Sensing*, 10(9), 1539-1561.
- Kaufman, Y.J., and D. Tanré, 1992: Atmospherically Resistant Vegetation Index (ARVI) for EOS-MODIS. *IEEE Transactions on Geoscience and Remote Sensing*, 30, 261-270.
- Kirchner, J.A., C.C. Schnetzler, and J.A. Smith, 1981: Simulated Directional Radiances of Vegetation from Satellite Platforms. *International Journal of Remote Sensing*, 2(3), 253-264.
- Koslowsky, D., 1993: The Influence of Viewing Geometry on Annual Variations of NDVI. *Proceedings of the 1993 International Geoscience and Remote Sensing Symposium (IGARSS '93)*, Tokyo, Japan, 1140-1142.
- Lee, T.Y., and Y.J. Kaufman, 1986: Non-Lambertian Effects on Remote Sensing of Surface Reflectance and Vegetation Index. *IEEE Transactions on Geoscience and Remote Sensing*, GE-24(5), 699-708.
- Loudjani, P., F. Cabot, V. Gond, and N. Viovy, 1994: Improving NDVI Time-Series Using Imposed Threshold on IRT, IR and Visible Values (INTUITIV): A Method for Reducing Cloud Contamination and Noise in NDVI Time-Series over Tropical and Sub-Tropical Regions. *Proceedings of the Sixth International Colloquium on Physical Measurements and Signatures in Remote Sensing*, Val d'Isère, France, 7 pages, in press.
- Major, D.J., F. Baret, and G. Guyot, 1990: A Ratio Vegetation Index Adjusted for Soil Brightness. *International Journal of Remote Sensing*, 11(5), 727-740.
- Myneni, R.B., and G. Asrar, 1994: Atmospheric Effects and Spectral Vegetation Indices. *Remote Sensing of Environment*, 47, 390-402.
- Paltridge, G.W., and R.M. Mitchell, 1990: Atmospheric and Viewing Angle Correction of Vegetation Indices and Grassland Fuel Moisture Content Derived from NOAA/AVHRR. *Remote Sensing of Environment*, 31, 121-135.
- Peterson, D.L., M.A. Spanner, S.W. Running, and K.B. Teuber, 1987: Relationship of Thematic Mapper Simulator Data to Leaf Area Index of Temperate Coniferous Forest. *Remote Sensing of Environment*, 22, 323-341.
- Pinty, B., C. Leprieux, and M.M. Verstraete, 1993: Towards a Quantitative Interpretation of Vegetation Indices - Part 1: Biophysical Canopy Properties and Classical Indices. *Remote Sensing Reviews*, 7, 127-150.
- Porter, W.M., and H.T. Enmark, 1987: A System Overview of the Airborne Visible/Infrared Imaging Spectrometer (AVIRIS). *Proceedings of SPIE Conference on Imaging Spectroscopy II*, Vol. 834, San Diego, California, 22-31.

- Price, J.C., 1987: Calibration of Satellite Radiometers and the Comparison of Vegetation Indices. *Remote Sensing of Environment*, 21, 15-27.
- Qi, J., and Y. Kerr, 1994: On Current Compositing Algorithms. *Proceedings of the Sixth International Colloquium on Physical Measurements and Signatures*, Val d'Isère, France, 8 pages, in press.
- Qi, J., Y. Kerr, and A. Chehbouni, 1994a: External Factor Consideration in Vegetation Index Development. *Proceedings of the Sixth International Colloquium on Physical Measurements and Signatures*, Val d'Isère, France, 8 pages, in press.
- Qi, J., A. Chehbouni, A.R. Huete, Y.H. Kerr, and S. Sorooshian, 1994b: A Modified Soil Adjusted Vegetation Index. *Remote Sensing of Environment*, 48, 119-126.
- Singh, S.M., and R.J. Saull, 1988: The Effect of Atmospheric Correction on the Interpretation of Multitemporal AVHRR-Derived Vegetation Index Dynamics. *Remote Sensing of Environment*, 25, 37-51.
- Spanner, M.A., L.L. Pierce, D.L. Peterson, and S.W. Running, 1990: Remote Sensing of Temperate Coniferous Forest Leaf Area Index: The Influence of Canopy Closure, Understorey Vegetation and Background Reflectance. *International Journal of Remote Sensing*, 11, 95-111.
- Tanré, D., C. Deroo, P. Duhaut, M. Herman, J.J. Morcrette, J. Perbos, and P.Y. Deschamps, 1990: Description of a Computer Code to Simulate the Satellite Signal in the Solar Spectrum: The 5S Code. *International Journal of Remote Sensing*, 11(4), 659-668.
- Teillet, P.M., 1989: Surface Reflectance Retrieval Using Atmospheric Correction Algorithms. *Proceedings of the 1989 International Geoscience and Remote Sensing Symposium (IGARSS '89) and the Twelfth Canadian Symposium on Remote Sensing*, Vancouver, British Columbia, 864-867.
- Teillet, P.M., and K. Staenz, 1992: Atmospheric Effects due to Topography on MODIS Vegetation Index Data Simulated from AVIRIS Imagery Over Mountainous Terrain. *Canadian Journal of Remote Sensing*, 18(4), 283-291.
- Teillet, P.M., and R. Santer, 1991: Terrain Elevation and Sensor Altitude Dependence in a Semi-Analytical Atmospheric Code. *Canadian Journal of Remote Sensing*, 17(1), 36-44.
- Townshend, J.R.G., T.E. Goff, and C.J. Tucker, 1985: Multitemporal Dimensionality of Images of Normalized Difference Vegetation Index at Continental Scales. *IEEE Transactions on Geoscience and Remote Sensing*, 23, 888-895.
- Tucker, C.J., 1979: Red and Photographic Infrared Linear Combinations for Monitoring Vegetation. *Remote Sensing of Environment*, 8, 127-150.
- Tucker, C.J., I.Y. Fung, C.D. Keeling, and R.H. Gammon, 1986: Relationship Between Atmospheric CO₂ Variations and a Satellite-Derived Vegetation Index. *Nature*, 319, 195-199.
- Viovy, N., O. Arino, and A.S. Belward, 1992: The Best Index Slope Extraction (BISE): A Method for Reducing Noise in NDVI Time-Series. *International Journal of Remote Sensing*, 13(8), 1585-1590.
- Wiegand, C.L., A.J. Richardson, D.E. Escobar, and A.H. Gerbermann, 1991: Vegetation Indices in Crop Assessments. *Remote Sensing of Environment*, 35, 105-119.

APPLICATION OF DARK OBJECT SUBTRACTION TO MULTISPECTRAL DATA

James B. Campbell and Xiangdong Liu
Virginia Polytechnic Institute & State University
Blacksburg, VA 24061-0115 USA

ABSTRACT

Dark-object subtraction has formed an old and widely used procedure for adjusting multispectral digital remote sensing data for effects of atmospheric scattering. The method's limited capabilities, relative to more sophisticated methods, are believed by some to be at least partially offset by its wide applicability, due to the requirement for minimal ancillary data. This study examines several facets of the procedure to assess its effects upon the transformed data, using chromaticity co-ordinates to compare the original data with the transformed data. Examples are drawn from several 512 by 512 sections of multispectral SPOT scenes, but the method of analysis is generally applicable to digital multispectral data. Here the success of an adjustment is evaluated by assessing the direction and magnitude of changes induced by the method, as examined in chromaticity space. Dark pixels, such as those representing shadows or open water, are especially sensitive to application of dark object subtraction. Subtraction of constant values from all values in the image means that, proportionately, dark pixels are altered much more than brighter pixels. Therefore, analysts that have a special interest in dark pixels (such as hydrologic investigations for example) should exercise special care in the application of this technique.

1. INTRODUCTION

Atmospheric effects pose some of the most serious obstacles to the practice of remote sensing using radiation in and near the visible portion of the spectrum. Impacts of atmospheric effects vary in severity from subtle to obvious. The most noticeable effects include shifts in colors, changes in overall brightness, and losses in contrast and resolution (Kaufman, 1984, 1989; Rees, 1990). Atmospheric effects do not influence all spectral regions equally, so interrelationships between spectral channels are altered, creating obstacles for application of vegetation indices and band ratios (Kowalick, Lyon, and Switzer, 1983). Atmospheric scattering also inhibits application of techniques to normalize data to reduce variations in brightness caused by irregular surface topography (Eliason, Soderblom, and Chavez, 1981; Colby, 1991). Further, atmospheric effects form obstacles to standardization of data collected at differing sun angles to permit construction of mosaics and to analyze multi-temporal data.

For the visible and near infrared regions, wavelength-dependent scattering is usually considered to be the dominant atmospheric influence (e.g., Turner et al, 1971) (Figure 1). Observed radiance at the sensor, I , is the sum of I_S , radiance reflected from the earth's surface, conveying information about surface reflectance, I_0 , radiation scattered from the solar beam directly to the sensor without reaching the earth's surface, and I_D , the brightness of radiation, directed to the ground, then to the atmosphere before reaching the sensor. Effects of these components are additive within a given spectral band (Kaufman, 1984):

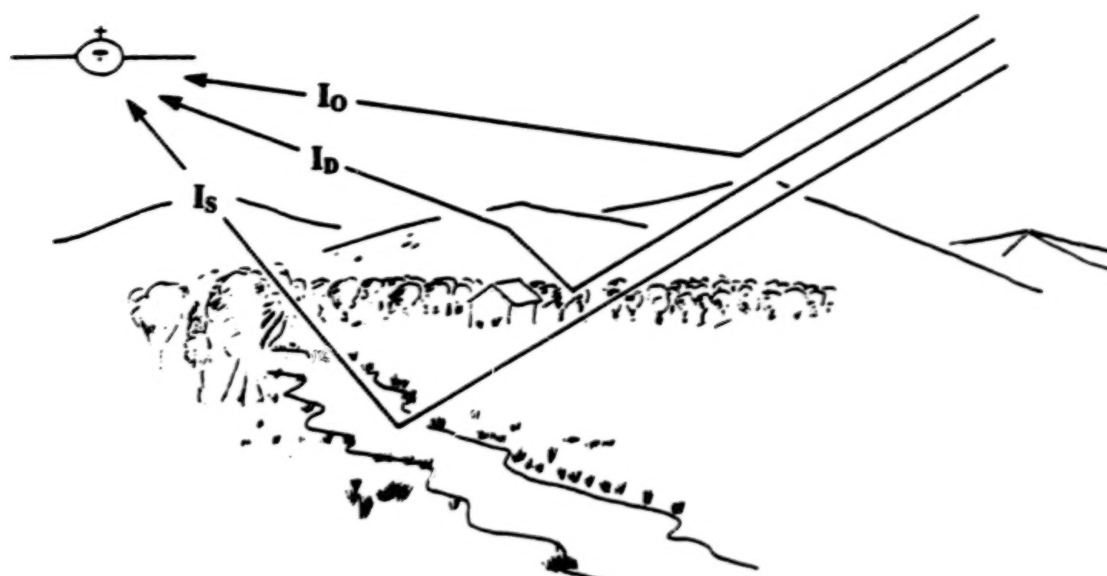


Figure 1. Schematic diagram illustrating principal components of atmospheric scattering (based on Kaufman, 1984). I_S represents radiation reflected from the ground surface, I_0 is energy scattered by the atmosphere directly to the sensor, and I_D represents diffuse light, directed to the ground, then to the atmosphere before reaching the sensor.

$$I = I_S + I_0 + I_D \quad (1)$$

I_S varies with differing surface materials, topographic slope and orientation, and angles of illumination and observation. I_0 is often assumed to be more or less constant over large areas, although most satellite images represent areas large enough to encompass atmospheric differences sufficient to create variations in I_0 . I_D , diffuse radiation, is expected to be small relative to other factors, but varies from one land surface type to another, so in practice would be difficult to estimate. We should note the special case presented by shadows, in which $I_S = 0$, because the surface receives no direct solar radiation. However, shadows have their own brightness, derived from I_D , and their own spectral patterns, derived from the influence of local land cover upon diffuse radiation.

Remote sensing is devoted to the examination of I_S at different wavelengths to derive information about the earth's surface. Therefore, methods that permit isolation of I_S from other components of I are of interest to a wide range of practitioners of remote sensing. The most rigorous efforts to account for atmospheric effects attempt to model behavior of radiation, sometimes using site-specific data describing atmospheric conditions, sensor orientation, topographic slope, and the nature of the illumination (Lambeck and Potter, 1979; Rogers et al, 1973, Kawata et al, 1988). Atmospheric conditions are known to vary within areas represented by typical satellite images, so the expense and inconvenience of acquiring scene-specific data simultaneously with image data are likely to remove such methods from the repertoires of most analysts, especially for analysis of data of remote regions, or of archived data. Another approach is to attempt a less precise, but more widely applicable, correction based upon a few estimates of atmospheric conditions, information derived within the image itself, and assumptions concerning the nature of the scattering. Others (e.g., Potter, 1984; Switzer, Kowalick, and Lyon, 1981; Kowalick, Lyon, and Switzer, 1983) developed transformations based upon observed interrelationships between spectral channels to compensate for estimated atmospheric effects in each spectral channel. Simple adjustments have also been based upon a general knowledge of the behavior of multispectral radiation in the atmosphere and observation of specific features of known identity as examined in a given image (Chavez, 1988).

2. THE BASIC DARK OBJECT SUBTRACTION TECHNIQUE

Perhaps the most widely known of simple approximation methods is the dark object subtraction technique, also known as the "histogram minimum method" (HMM). The technique is based on the premise that it is possible to approximate I_0 by finding examples of features dark enough that I_s is at or near 0, so that its observed brightness estimates I_0 in each spectral channel observed. Estimates of I_0 in each band are then subtracted from values in the image in the hope of bringing their values closer to I_s , adjusting each band to account for effects of atmospheric path brightness. Even though the adjustment is applied globally, the use of individual values for each band may assist in restoring the balance between spectral channels. It should be emphasized that the technique attempts only to address problems introduced by wavelength-dependent scattering; it does not have the capability to adjust for effects of atmospheric absorption or other multiplicative effects. Chavez (1988) proposed a modification to the basic technique, by which one of the visible bands is selected as the standard for estimation of subtraction values for other bands, using one of five alternative models for atmospheric clarity. The modified technique has been discussed by Campbell (1993). Although the results of the present study apply to the modified technique, for the sake of conciseness, the modified technique is not discussed separately here.

The method is clearly a rough approximation, and is generally recognized as such. Its chief advantage is that it relies only on information available with each scene, and requires no ancillary data. Therefore it is applicable to a large body of data for which few other adjustments might be attempted. Despite the wide use of this technique, its effects have not been evaluated in detail. Therefore, the analyst has little basis for assessing its usefulness or judging the conditions under which it might be useful, or perhaps inappropriate. Furthermore, dark objects can form important elements of more sophisticated models (e.g., Holben et al, 1992), so some aspects of this method may have significance in the context of more elaborate models for adjusting multispectral data.

3. THE CHROMATICITY DIAGRAM

An effort to apply the dark object subtraction technique, or similar methods, is faced with a companion problem of equal difficulty-- that of evaluating the success of the attempt. Those who attempt to use evidence internal to an image as a means of correcting for atmospheric effects are likely to also lack data to assess the success of the results. Evaluation of results, in the absence of on-site measurements, can only be suggestive rather than definitive. But it may be possible to examine the image itself for evidence of the success or failure of an attempted correction.

General effects of the atmosphere upon multispectral data are well known. Atmospheric effects shift brightnesses, reduce contrast, alter relationships between multispectral bands, and degrade spatial resolution. Some of these effects manifest themselves through recognizable characteristics, such as average brightnesses, variability in brightness, and interrelationships between multispectral bands. Likewise, such characteristics are likely to suggest the success or failure of efforts to correct for atmospheric effects. Because the principal effects of atmospheric scattering (the major atmospheric influence in the visible and near-visible regions) are wavelength-dependent, examination of relationships between multispectral bands offers one of the most fruitful approaches for examining atmospheric effects and efforts to adjust for atmospheric effects.

One vehicle for assessing internal characteristics of multispectral imagery is the chromaticity diagram, developed originally for the visible spectrum, then modified for multispectral remote sensing data by Alföldi and Munday (1977) (Figure 2). Their diagram is a variation of the well-known CIE (*Commission Internationale de L'Eclairage*) diagram that depicts colors in the visible spectrum using three axes (usually designated by x, y, and z), one for each primary (Stimson, 1974; IES, 1992). Each axis represents the proportion of total brightness accounted for by a single primary, so the diagram shows chromaticity only-- brightnesses are removed when the proportions are calculated. Thus, two objects of the same color but differing brightness will have identical positions within the diagram. The diagram itself is formed from two perpendicular axes; because the three proportions always sum to 1.0, two of the three co-ordinates (usually x and y) are sufficient to convey all of the information concerning the color of a given object.

The focus of the diagram, where each primary has a value of 0.333, forms the equal radiance point. Objects with co-ordinates at or near this point are without a dominant color. Lateral differences (parallel to the axes) produce changes in hue (color), while changes in position from the center outwards towards the periphery signify increasing significance of a single primary. Atmospheric effects are likely to reduce the dominance of a single primary-- i.e., in comparison with similar objects observed through a clear atmosphere, objects viewed through a turbid atmosphere can be expected to display chromaticities displaced towards the equal radiance point, as atmospheric scattering tends to reduce the effect of a dominant primary

Alföldi and Munday (1977) modified the CIE diagram for applications to remote sensing by discarding the blue primary and adding the near infrared region for calculation of the co-ordinates. Thus, they used MSS4 (green), MSS5 (red), and MSS6 (near infrared) values as the three axes to form the "Landsat chromaticity diagram." Implementation of the technique requires conversion of DNs to the radiances upon which they are based. Chavez (1988) describes the procedure for converting digital counts to radiances, and (together with others such as Nelson, 1985) gives calibration values for each of the Landsat sensors. The SPOT Handbook (SPOT Image Corporation, 1988) and Price (1987) give comparable data for SPOT sensors. In addition, descriptor records that accompany digital remote sensing data typically provide calibration data applicable to each scene.

Munday and Alföldi (1975) examined several characteristics of the chromaticity diagram, with the objective of creating isoluminous ("equal radiance") images. Their objective was to define a transformation such that a raw image, with variations in both brightness and chromaticity, might be transformed into an isoluminous image, such that variations in total brightness might be removed to leave only chromaticity information. Their work was based on the premise that variations in image brightness create perceptual interference with efforts to interpret differences in chromaticity, so an isoluminous image would facilitate visual interpretation of multispectral images.

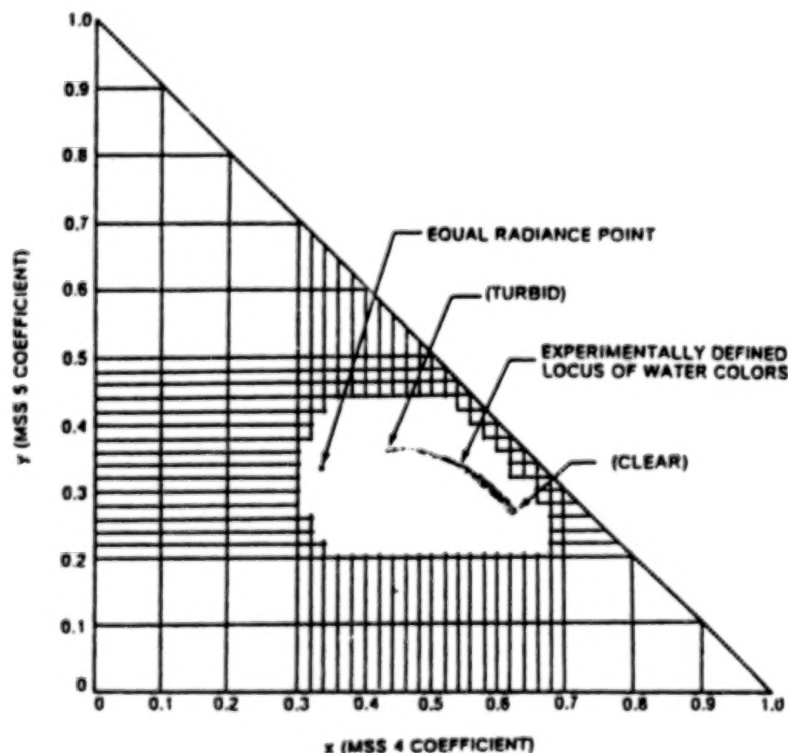


Figure 2. The CIE chromaticity diagram as applied to Landsat MSS data. (Based upon Alföldi and Munday (1977), as revised in Campbell, 1987).

Although others (e.g., Yost and Wenderoth, 1970) had examined this topic in the analogue domain (photographic processing), Munday and Alföldi (1975) attempted to define algebraic expressions to provide a general analytical solution. Although they were unable to define a concise, general, algebraic solution, they did describe characteristics of several special cases through computational examples. Although our interest differs from that of these earlier studies, we share with them a general interest in understanding the nature of the chromaticity diagram.

Our interpretation of the results reported by Alföldi and Munday (1977), and our own experiments with both actual and contrived data lead to a general understanding of the effects of additive and subtractive operations upon chromaticities. Although carefully contrived additive effects could, in principle, preserve the chromaticity of a given pixel, in practice, additive effects of the character produced by atmospheric effects (i.e., unevenly allocated to wavelengths) will tend to displace points towards the equal radiance point, and to compress the range of chromaticities. Likewise, subtractive effects of the character produced by dark object subtraction (also unequally weighted by wavelength) tend to disperse chromaticities, and to move them away from the equal radiance point.

The Landsat chromaticity diagram is not a direct application of the CIE diagram, in the sense that it cannot convey information about colors of the visible spectrum, because one of the visible primaries has been discarded and replaced by a non-visible channel. However, it can serve as a framework for examining spectral properties of features before and after application of atmospheric correction techniques. Alföldi and Munday (1977) developed their technique for application to examination of turbidity of water bodies. Their locus (Figure 2) defines the colors of water bodies as developed for their specific research; although other water bodies will exhibit different chromaticities, these differences are likely to be small in the context of present purposes.

In the instance of water bodies, positions of pixels (within the chromaticity diagram) relative to the locus defined by Alföldi and Munday provides evidence of a satisfactory correction-- i.e., atmospheric effects have distorted original spectra, moving them away from the locus, so a satisfactory correction should move them back to the locus. From chromaticity evidence alone, we cannot be absolutely confident that a pixel value has been moved to its correct position on the locus, but evidence suggests that the correction is reasonable relative to another correction more distant from the locus.

For other classes of features, spectral qualities are much more broadly defined, and seldom can we know beforehand the correct locus, as is possible in a general way with water bodies. However, it is possible to look for general indications of a successful correction. In general, atmospheric scattering tends to reduce the dominance of a given primary, and shift chromaticities from edges of the diagram towards the equal radiance point. Therefore, we might expect (in general) a successful adjustment to reverse this process, to shift chromaticities from the center of the diagram towards the edge.

4. EXPECTED ATMOSPHERIC EFFECTS

This study is based upon the premise that atmospheric effects influence the observed chromaticities of pixels, and that efforts to correct for atmospheric effects can be evaluated, in at least a general way, using the chromaticity diagram. It extends earlier work (Campbell, 1993; Campbell and Ran, 1993) that examined displacements of individual pixels). Here we apply this general approach to examine chromaticities of substantial segments of images-- these larger areas offer the advantage of providing a broader context for interpretation of the individual changes noted in earlier studies. The examples described here are based on subimages of 512 by 512 pixels in size, although we have examined larger segments as well. These subimages are selected from a multispectral SPOT scene of southwestern Virginia (K= 616, J= 275, 14 August 1988). This scene is useful for our purposes because it includes a variety of land cover classes, areas of open water, irregular topography, as well as clouds and cloud shadows. These varied features provide contrasting spectral patterns for our analysis. We have also examined data from numerous other multispectral images of varied geographic settings; the results we report here are typical of those observed in other data from other regions.

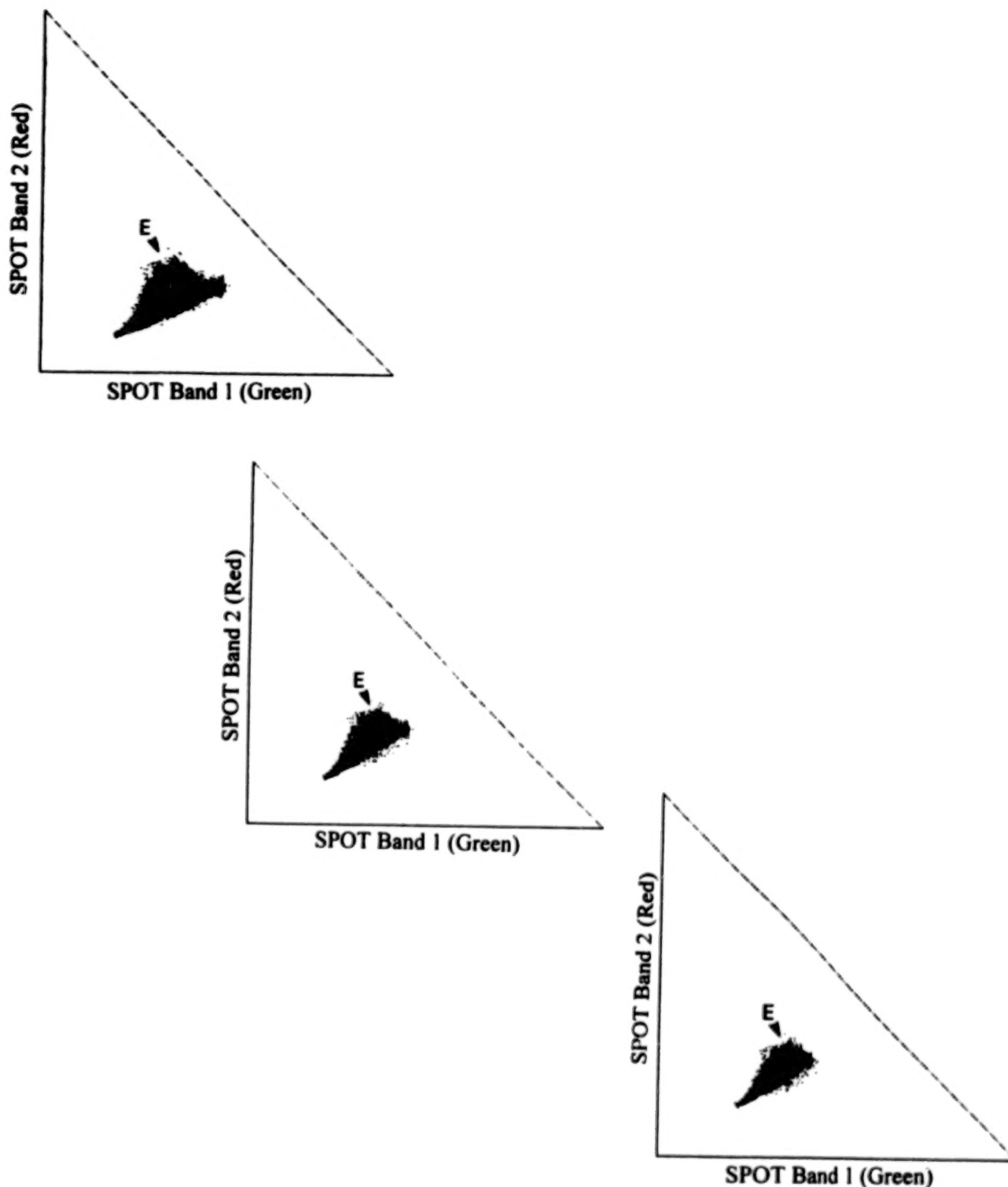


Figure 3. Atmospheric Effects on Chromaticity. The atmospheric scattering model proposed by Chavez (1988) was applied to multispectral data to simulate what is impossible, or very difficult, to observe in nature-- the same scene recorded under differing atmospheric effects. The diagrams show the same data (from a 512 by 512 region of a SPOT image) under clear (top), moderate (center), and hazy (bottom) conditions, as defined by Chavez (1988). E designates the equal radiance point. For this, and for subsequent diagrams, the vertical axis represents SPOT band 2 (red), and the horizontal axis represents SPOT band 1 (green). Each point in diagram represents the chromaticities of many pixels in the original image (i.e., the diagram does not depict frequencies at each chromaticity). Atmospheric effects displace the swarm, and reduce the range of chromaticities observed.

To approximate atmospheric effects upon chromaticity, a scattering model was applied to a multispectral image. Multispectral values from a SPOT scene were taken, for purposes of illustration, to form ground level spectra, without atmospheric effects. Then the effects of atmospheric scattering were simulated by adding values to digital numbers in each band using Chavez's (1988) scattering model. These values were then added to the SPOT data to provide three different versions (for clear, moderate, and hazy atmospheres) of the same scene, each influenced by differing levels of additive atmospheric effects. The results simulate what is impossible, or very difficult, to observe in nature-- the same scene recorded under differing atmospheric effects.

For Figure 3, and subsequent diagrams, the horizontal axis represents SPOT band 1 (green), and the vertical axis represents SPOT band 2 (red) (following the practice employed for Figure 2). The dots represent chromaticities observed within a specific image, but do not (to best preserve legibility) show frequencies at each chromaticity. Generally speaking, frequencies are greatest near the lower left of each swarm, then decline near the edges. Figure 3 represents a single scene portrayed under very clear (top), moderate (center), and very hazy (bottom) conditions. Increasingly severe atmospheric effects shift the swarm of points from the periphery of the diagram towards the equal radiance point. When a scene examined for such analysis includes a water body, positions of water pixels slide along the locus defined by Alföldi and Munday (1977) (Figure 2).

The shape and orientation of the swarm change slightly under differing atmospheric conditions. The swarm slides from the periphery towards the equal radiance point with increasing atmospheric effects, as anticipated from a strictly quantitative examination of the chromaticity diagram. Further, the range in chromaticities decreases with increasing atmospheric effects. Under clear atmospheric conditions the cluster of chromaticities corresponding to open water is partially recognizable at the right edge of the swarm, near the position predicted by Alföldi and Munday (1977) and labeled in Figure 2. With increasing atmospheric effects, these pixels become less distinct, and move away from the locus defined by Alföldi and Munday (1977).

5. ANALYSIS

Chromaticity space permits examination of effects of dark object subtraction (Figure 4). Dark object subtraction does **not** restore chromaticities of hazy and moderate conditions to those of clearer conditions. Typically, as shown in Figure 4, dark object subtraction enlarges the size of the swarm, creating a larger range in chromaticities relative to the unadjusted data. Although in a general sense this effect might be desirable, in that it tends to reverse the effect of the atmosphere to compress the range of chromaticities, the practical impact for our data is to over-compensate, greatly increasing the range of chromaticities, and creating the linear voids and outliers easily visible in Figure 4. Although the general dispersion of chromaticities was anticipated by Munday and Alföldi (1975), the distinctive character of the pattern was unexpected.

In every instance examined here dark object subtraction produces linear outliers of the form visible in Figure 4. Figure 4 is annotated to identify some of the linear patterns. Investigation of groups 1, 2, 3, and 6 reveals that they represent water pixels in the original image. Dark object subtraction has shifted chromaticities, spreading the range of chromaticities relative to those expected in clearer atmospheres. Although some pixels can be said to acquire reasonable chromaticities, most of these pixels are aligned in an unrealistic pattern, so the attempted correction can be judged to be unsuccessful.

This effect appears to be caused by the darkness of the water pixels. The set of dark object values is applied to the entire image, but has proportionately greater effects for those pixels with the lowest values. The attempted correction is known to be imperfect; for relatively bright pixels, the imperfections create insignificant errors in the new chromaticities. However, for dark pixels, such as water pixels, the imperfections can create large and unrealistic shifts, as reported in Campbell (1993).

The linear forms in the lower left, labeled 4 and 5 in Figure 4, display substantial shift to a new region of the diagram, and a modest spread in chromaticity. These pixels are found to correspond to regions of shadowed forest. In this instance, dark object subtraction has produced substantial changes in the raw pixels

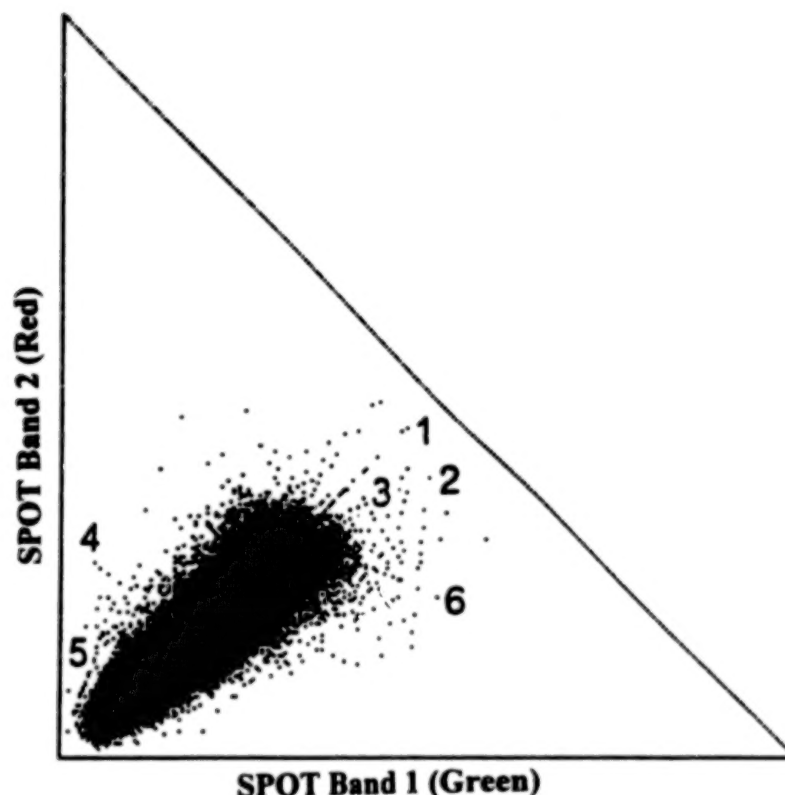


Figure 4. Effects of dark object subtraction upon chromaticities. The original pattern of chromaticities in this scene resembled those shown in Figure 3. The subtraction has dispersed the chromaticities, as discussed in the text. Numbers annotate regions mentioned in the text.

values, creating chromaticity changes that do not appear to be realistic. The problem appears to be related to their identities as shadows. Shadows are regions of diffuse light (the quantity $[I_D + I_O]$ in Equation 1). Dark object subtraction is based on the assumption that a pixel has a value approximated by the quantity $(I_S + I_O + I_D)$; after subtraction of the dark object-- an estimate of I_O -- the pixel has a value of $(I_S + I_D)$. Because I_D is believed to be small relative to I_S , the value is taken as an approximation of I_S . However, shadowed pixels have the brightness of diffuse light only, so they have brightnesses approximated by the quantity $(I_D + I_O)$. Subtraction of the dark object (I_O) leaves only I_D . Although I_D has a spectral pattern that has been influenced by I_S , it is, in our experience, usually unlike I_S . Therefore, shadowed pixels adjusted by dark object subtraction acquire chromaticities unlike those of unshadowed pixels. This attempt to correct these values is therefore unsuccessful, and in general it seems unlikely that dark object subtraction could be effective for shadowed pixels. Because I_O accounts for a substantial portion of the quantity $(I_O + I_D)$ for shadowed pixels, the dark object subtraction will create inappropriately large chromaticity shifts.

Further, although dark regions can often be recognized as shadowed pixels, and possibly excluded from a dark object transformation, there are, in areas of uneven terrain many other pixels influenced by partial shadowing or microshadowing that cannot be so easily identified. Such effects might contribute to the noticeable dispersion of chromaticities created by dark object subtraction.

6. ALTERNATIVE DARK OBJECTS

Dark object subtraction can be implemented in several ways. Ideally, the analyst can identify a true "dark object"-- a clearly identifiable feature with low brightnesses in all spectral bands. Perhaps the ideal would be a clear, calm, deep water body large enough to be recorded by a large number of homogeneous

pixels. Such a feature would be dark in all of the normally used channels in or near the visible spectrum, would be imaged by pure pixels, and have the additional characteristic of forming a flat, horizontal, surface.

However, it is not always possible to identify such features. In such situations, practitioners of dark object subtraction often select other features (such as topographic shadows, cloud shadows, or minimum values from each spectral band, following the reasoning that somewhere within a large image there is likely to be at least one pixel that is dark enough to provide a basis for the atmospheric adjustment. These values form the "histogram minimum" (HMM) values sometimes used as estimates of atmospheric path brightness (e.g., Chavez, 1988). However, such features are not all equivalent to the ideal mentioned above.

Many of these dark objects, as recorded on the imagery, are not absolutely black. Shadows, for example, are dark in appearance on most photographs and computer displays, but have their own brightness caused by diffuse light reflected from the ground surface to the atmosphere, and then to the sensor (I_d in Figure 1). Dark object subtraction is based on the premise that the analyst has identified a pixel that is dark enough that the brightness of ($I_s + I_d$) is very small, so that the observed brightness at that pixel forms a reasonable estimate of I_0 .

Further, dark object subtraction is based on the premise that the spectral pattern of I_0 is revealed by the observed brightness of the dark object in several bands. However, the spectral distribution of diffuse light in shadows depends in part on the land cover within the shadow. Therefore, the spectral distribution of radiation in shadowed pixels is unlikely to form a reasonable estimate of I_0 because it carries information not only about atmospheric path brightness, but also about the reflectivity of land surfaces near the pixel. However, for shadows, ($I_s + I_d$) is formed mainly of I_d , and is typically much brighter than a true dark object-- certainly much brighter than might be expected from visual appearance alone-- so the magnitude of ($I_0 + I_d$) under these circumstances does not form an accurate estimate of I_0 .

The situation is further complicated when histogram minimum values (i.e., the lowest value observed in each spectral channel) are used as dark objects, because the values in each band may each originate from different objects, and therefore may not reveal the spectral distribution of I_0 , but simply the character of the objects that have influenced the spectra of these separate dark pixels. In this context, the modified method proposed by Chavez (1988) may provide an advantage, as it estimates likely values, given a value from a single band.

Objects other than the true minima create practical problems in the application of dark object subtraction. From a computational perspective, each image can have only one dark object, because objects brighter than the true minima create negative values when used as the basis for dark object subtraction. For purposes of illustration, the examples for Figure 5 were prepared by resetting negative values to avoid generating negative values in the chromaticity diagram. Figure 11 shows that the choice of dark object will influence the nature of the chromaticities in the output image.

7. CONCLUSIONS

Results of this investigation form a cautionary note for users of the dark object subtraction technique. This study presents evidence that dark object subtraction introduces artifacts in at least some scenes. Effects observed in these scenes (which do not seem to be atypical) include the following:

- dispersal of chromaticities, relative to the unadjusted data;
- observed shifts in chromaticity do not always restore chromaticities to those expected for clearer atmospheres;
- the choice of dark object is likely to influence the nature of the results; shadows will not produce accurate adjustments.

Such conclusions present the analyst with a dilemma-- these results constitute evidence that dark object subtraction, under what appear to be typical conditions, creates artifacts in the corrected data. However, it is not clear what forms the context for interpreting this evidence. In other situations, such as destriping, or

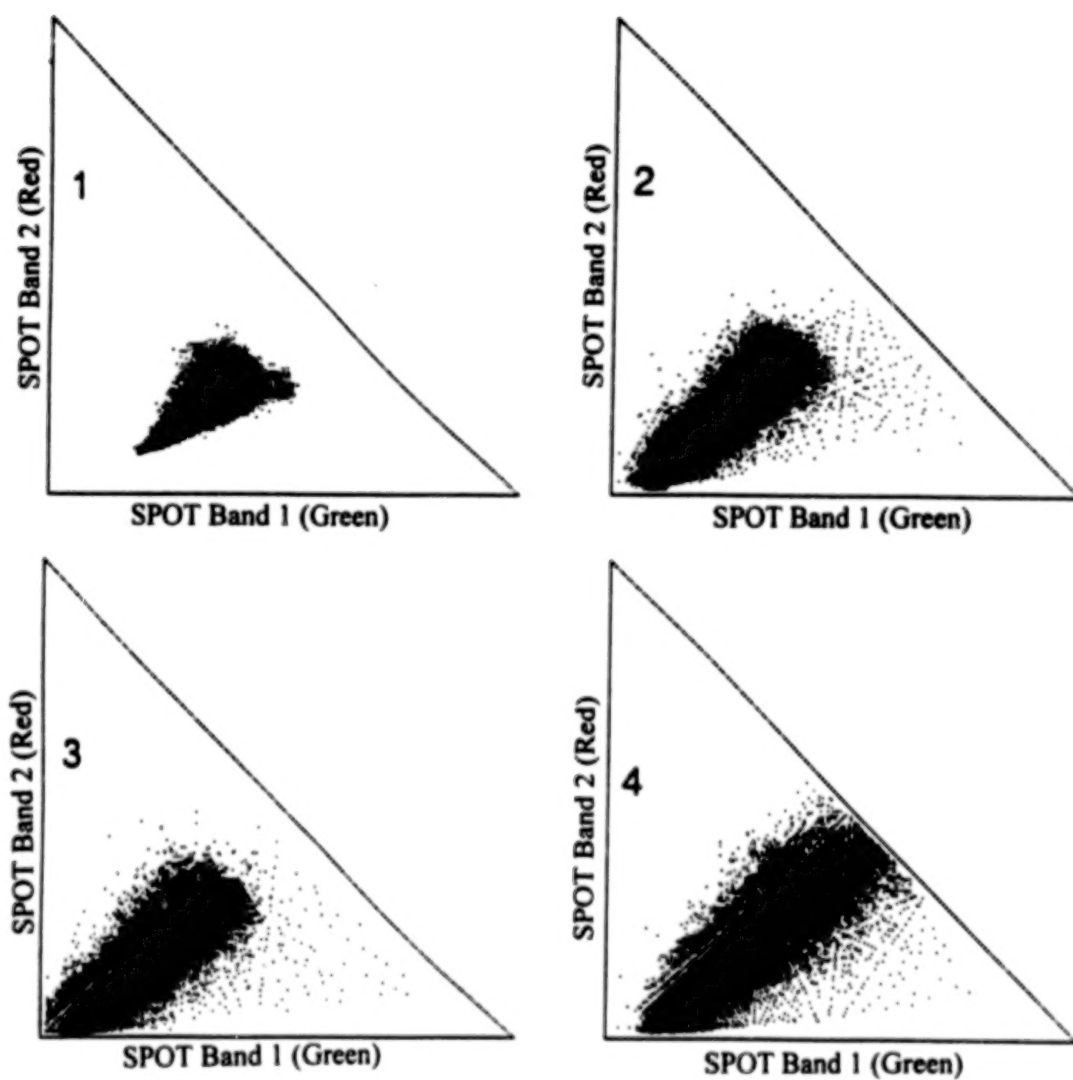


Figure 5. Effects of selection of dark objects. Diagram 1 shows chromaticities of the original data; 2, 3, and 4, show chromaticities resulting from differing choices of features for use as dark objects. Results differ with respect to the dispersion of chromaticities in the adjusted data.

image registration and resampling, analysts routinely accept results that have altered image characteristics, often in ways and to degrees that are not understood. In these examples, the results are usually not visually obvious— examination of photographic prints and computer displays of the images examined here do not reveal dramatic differences in the overall appearance of the image. Yet the results are real, in the sense that spectral patterns of pixels are noticeably altered, most especially dark pixels. Analysts who must focus their efforts on examination of dark pixels, such as might be typical of hydrologic or water quality studies, should be especially cautious in their application of dark object subtraction.

REFERENCES

- Alföldi, T.T., and Munday, J.C., 1977: Progress towards a LANDSAT Water Quality Monitoring System, *Proceedings of the Fourth Canadian Symposium on Remote Sensing*. Ottawa: Canadian Aeronautics and Space Institute. pp. 325-340.
- Campbell, J.B. and Ran, L., 1993: CHROM: A C Program to Evaluate the Application of the Dark Object Subtraction Technique to Digital Remote Sensing Data, *Computers and Geosciences*, **19**, 1475-1499.
- Campbell, J.B., 1993: Evaluation of the Dark Object Subtraction Technique for Adjustment of Multispectral Remote Sensing Data, *SPIE Proceedings 1819* (M.J. Carlotto, Ed), 176-188.
- Campbell, J.B., 1987:, *Introduction to Remote Sensing*. Guilford: New York, 551 pp.
- Chavez, P.S., 1988: An Improved Dark-Object Subtraction Technique for Atmospheric Scattering Correction of Multispectral Data, *Remote Sensing of Environment*. **24**: 450-479.
- Colby, J.D., 1991: Topographic Normalization in Rugged Terrain, *Photogrammetric Engineering and Remote Sensing*. **57**: 531-537.
- DeMarsh, LeRoy E., and Giorianni, E.J., 1989: Color Science for Imaging Systems, *Physics Today*. **42**: 9, 44-52.
- Eliason, P.T., Soderblom, L.A., and Chavez, P.S., 1981: Extraction of Topographic and Spectral Albedo Information from Multispectral Images, *Photogrammetric Engineering and Remote Sensing*. **48**: 1571-1579.
- Holben, B., Vermote, E., Kaufman, Y.J. Tanré, D., and Kalb, Virginia, 1992: Aerosol Retrieval over Land from AVHRR Data— Application for Atmospheric Correction. *IEEE transactions on Geoscience and Remote Sensing*. **30**: 212-221
- IES Color Committee (Illuminating Engineering Society of North America), 1992: *Color and Illumination*. New York: Illuminating Engineering Society of North America, 44 pp.
- Kaufman, Y. J., 1984: Atmospheric Effects on Remote Sensing of Surface Reflectance, *Remote Sensing. Proceedings SPIE 475* (P.N. Slater, Ed.), 20-33.
- Kaufman, Y. J., 1989: The Atmospheric Effect on Remote Sensing and Its Correction, In *Theory and Applications of Optical Remote Sensing*. (Ghassam Asrar, Ed.) New York: John Wiley, 336-428.
- Kawata, Y, Ueno, S., and Kusaka, T., 1988: Radiometric Correction for Atmospheric and Topographic Effects on Landsat Images, *International Journal of Remote Sensing*. **9**: 729-748.

- King, D., 1991: Determination and Reduction of Cover Type Brightness Variations with View Angle in Airborne Multispectral Video Imagery, *Photogrammetric Engineering and Remote Sensing*. **57**: 1571-1577.
- Kowalick, W.S., Lyon, R. J. P., and Switzer, P., 1983: The Effects of Additive Radiance Terms on Ratios of Landsat Data, *Photogrammetric Engineering and Remote Sensing*. **49**: 659-669.
- Lambeck, P.F., and Potter, J.F., 1979: Compensation for atmospheric effects in Landsat data. *The LACIE Symposium: Proceedings of Technical Sessions*. Houston, TX: NASA LBJ Space Center. Vol II, 723-754.
- Munday, J.C., and Alföldi, T.T., 1975: Chromaticity Changes From Isoluminous Techniques Used to Enhance Multispectral Remote Sensing Data, *Remote Sensing of Environment*. **4**: 221-236.
- Nelson, R., 1985: Reducing MSS Scene Variability, *Photogrammetric Engineering and Remote Sensing*. **54**: 583-593.
- Potter, J.F., 1984: The Channel Correlation Method for Estimating Aerosol Levels From Multispectral Scanner Data. *Photogrammetric Engineering and Remote Sensing*. Vol **50**: 43-52.
- Price, J.C., 1987: Calibration of Satellite Radiometers and the Comparison of Vegetation Indices, *Remote Sensing of Environment*. **21**: 15-21.
- Rogers, R.H., Peacock, K., and Shah, N. J., 1973: A Technique for Correcting ERTS Data for Solar and Atmospheric Effects, *Third Earth Resources Technology Satellite-1 Symposium. (NASA SP-351)*. 1787-1804.
- Rees, W.G., 1990: *Physical Principles of Remote Sensing*. Cambridge University Press: Cambridge. 247 pp.
- SPOT Image Corporation, 1988: *SPOT User's Handbook*. SPOT Image Corporation: Reston, VA. 2 Vols.
- Stimson, A., 1974: *Photometry and Radiometry for Engineers*. Wiley: New York. 446 pp.
- Switzer, P., Kowalick, W.S., and Lyon, R.J., 1981: Estimation of Atmospheric Path Radiance by the Covariance Matrix Method, *Photogrammetric Engineering and Remote Sensing*. **47**: 1469-1476.
- Turner, R.E., Malila, W.A., and Nalepka, R.F., 1971: Importance of Atmospheric Scattering in Remote Sensing, *Proceedings of the 7th International Symposium on Remote Sensing of Environment*, 1651-1697.
- Yost, E., and S. Wenderoth, 1970: Remote sensing of coastal waters using multispectral photographic techniques, Long Island University Science Engineering Research Group Technical Report SERG-TR-10, C.W. Post Research Center, Long Island University, Greenville, N.Y., 170-170.

TEMPORAL MEASUREMENTS OF HIGH RESOLUTION SPECTRAL SIGNATURES OF PLANTS AND RELATIONSHIPS INDICATING WATER STATUS

C. Bostater, C. Hall¹, D. Vieglais², J. Rebbman, and M. Provancha¹

Marine and Environmental Remote Sensing Center
Marine and Environmental Systems Division
Florida Institute of Technology
150 West University Blvd.
Melbourne, Fl. 32937

ABSTRACT

Measurements of near nadir viewing spectral reflectance, as a function of 252 channels between 368 and 1115 nm, were made to evaluate temporal changes in reflectance signatures as a function of growing season for sand live oak (*Quercus geminata*), myrtle oak (*Quercus myrtifolia*) and saw palmetto (*Serenoa repens*). Laboratory based spectral measurements were related to Scholander pressure bomb measures of leaf water potential (bar) and to percent moisture to determine applicability of optimal passive ambient correlation spectroscopy (OPACS) techniques to the analysis of remote sensing data of vegetation. Field measurements of reflectance, at the canopy level, indicate that leaf water potential can be estimated for the selected species throughout senescence, leaf drop, sprouting, and maturation during the spring growing season (March-May). Objective analytical data processing techniques were used to determine optimal bands for estimating leaf water potential and percent moisture. These techniques were based on utilization of inflection or second derivative spectra followed by an optical cleanup procedure that computes the double inflection ratio (DIR) spectra for all possible combinations of three bands normalized to previously computed optimal bands. These results demonstrate how high spectral resolution reflectance signatures can be collected and analyzed for detecting the leaf water potential or water status of plants.

1. INTRODUCTION

Remote sensing represents the ultimate tool for non-destructive determination of many environmental parameters making it ideally suited for a variety of monitoring and research applications. The utility of remote sensing techniques is currently limited by many factors that include hardware constraints, spatial and spectral limitations, empirical and numerical model limitations, data processing and analysis approaches, cost constraints and lack of experience under the full range of variability that exists in the natural environments we wish to sense. Researchers at the Florida Institute of Technology in collaboration with researchers at John F. Kennedy Space Center, Florida, (KSC) are currently involved in development of non-destructive remote sensing technologies for the purpose of

¹The Bionetics Corporation, John F. Kennedy Space Center, Fl. 32899

²Biomedical Operations and Research Office, John F. Kennedy Space Center, Fl. 32899

monitoring vegetation and plant community responses to a variety of environmental variables. The eventual goal is to develop scientifically based techniques and associated data suitable for use in local and regional ecosystem management activities.

One area of special ecological interest is the definition of relationships between elevated CO₂ levels, soil and plant moisture conditions, stomatal conductance, and photosynthesis. Specifically, leaf moisture status, as defined by Scholander pressure bomb readings (Tyree and Hammel, 1972) are, in part, being utilized to assess treatment effects on scrub vegetation within open top growth chambers. This measurement technique is destructive and greatly limits the ability to collect adequate amounts of replicated data from the growth chambers. One possible solution to this problem may be the application of high resolution spectral remote sensing to define changes in water status and other parameters at the leaf and canopy level. Wessman (1989) states that subtle changes in ecosystem functioning may be expressed in plant canopy biochemistry as a result of altered metabolic processes, carbon allocation patterns, and nutrient availability. Also, the potential to remotely estimate canopy constituents depends partly on the influence of the parameter on the reflectance signature. The purpose of this paper is to report on techniques developed at FIT for the collection and analysis of spectral reflectance signatures collected at KSC as part of continuing research on effects of elevated CO₂ on subtropical plant communities.

1. BACKGROUND

Remote sensing for plant water stress or status has been the focus of research utilizing a variety of instruments under many environmental conditions (Hunt et al., 1987; Hunt and Rock, 1989; Bowman, 1989; Penuelas et al., 1993; Gao and Goetz, 1994). Previous studies focused on development of empirical relationships between infrared reflectance signatures and measured estimates of leaf or canopy water status. Light in the visible and near-infrared region incident on a leaf is reflected at the leaf surface or transmitted into the leaf, where it is then absorbed or scattered. In addition, the incident light is known to cause fluorescence responses in the leaf. The mechanisms for determining the magnitude of these optical processes is dependent on many factors, including the incident angle and geometric characteristics of the leaf surface. For example, surface reflected light generally results from two primary mechanisms at the air-leaf interface (Grant, 1987). When the size of the leaf surface features are large, compared to the incident wavelength, the surface is considered optically smooth yet rolling or undulating. In this case specular incident light will be reflected in many directions. In nature, many surfaces contain a variety of roughness scales relative to the incident wavelengths. In this case the large-scale roughness dominates scattering in the specular direction and small scale roughness controls scattering away from the specular direction. Surface reflectance from leaves is not generally diffuse or lambertian in character but instead contains some specular characteristics making it intermediate to true diffuse and specular reflection. Based on this discussion, changes in leaf surface features in response to changes in leaf water status (i.e. turgid vs. wilting) may produce differences in the spectral signature at the leaf and canopy level.

Light transmitted into the leaf is subject to multiple scattering and absorption with the relative magnitude of each being dependent on wavelength and biophysical characteristics of the internal leaf structure and chemistry. Reflectance and transmittance of leaves is relatively low in the visible portion of the spectrum (400-700 nm). The primary controlling factor in this region is light absorption by leaf

pigments which may be directly related to nutrient availability (Wessman, 1989). In the near- (700-1300 nm) and middle- (1300-3000 nm) infrared regions leaf pigments are virtually transparent and internal cell structure controls the larger amount of reflectance observed. This phenomena is responsible for the classic red edge characteristic in leaf spectra. Biophysical structures identified as being responsible for internal leaf reflectance include primarily the interfaces between the cell walls, palisade cells, air spaces, protoplasm, and chloroplast. These interfaces represent refractive discontinuities and reflection occurs when the angle of incidence is less than the critical angle (Grant, 1987). This phenomena of multiple reflection produces the diffuse lambertian distribution of both the internal reflected and transmitted light fields as they exit the leaf.

Two regions of the infrared reflectance spectra, the near- (700-1300 nm) and middle- (1300-3000 nm), have been identified as being especially useful for the detection of vegetation water stress or water content (Hunt, 1989; Penuelas, 1993; Rock, 1987; Bowman, 1989; Gao and Goetz, 1994, and others). Water absorption bands occur at 760, 970, 1450, 1940, and 2950 nm in response to the OH bond. This absorption becomes progressively stronger going from short wavelengths to long wavelengths (Valley, 1965). As stated previously, the near-infrared is characterized by high reflectance produced primarily from multiple scattering at the cell level. Changes in leaf water content have been observed to influence the leaf turgor pressure and the relative shape and arrangement of the leaf structures and interfaces responsible for reflectance. Thus, it is possible that changes in water content may be correlated to changes in the reflectance characteristics in the near-infrared (Grant, 1987; Bowman, 1989; Hunt, 1989; Hunt and Running, 1990; and Penuelas et al., 1993). Riggs and Running (1991) reported significant increases of approximately 20% in Norway Spruce reflectance in the 1000-1300 nm region during a controlled study of water stress effects on spectral signatures of their select species.

The objectives of this study were to evaluate at the bench top (leaf) and field (canopy) scale the potential for utilizing high resolution spectral reflection signatures to monitor the water status of three dominant species present in subtropical scrub communities. The three species were sand live oak (*Quercus geminata*), myrtle oak (*Quercus myrtifolia*) and saw palmetto (*Serenoa repens*). These species are dominant members of the evergreen scrub community at KSC and are of vital importance to the survival of several federally listed threatened and endangered species of wildlife in Florida (Bostater et al., 1992).

Measurements were made at the canopy level throughout the spring period of leaf senescence, drop, sprouting and maturation to document the change in reflectance as a function of wavelength (λ) that may occur for the species of oaks during this period of phenological transition. Gates (1980); Sinclair et al. (1971); Gausman et al. (1974) and Boyer et al. (1988) report that changes in leaf reflectance signatures during these transition periods can be attributed to changes in chlorophyll, other pigment concentrations and changes in the relative abundance and distribution of refractive interfaces within the leaf as the leaf changes shape. In addition, Deering (1989) indicates that changing green biomass will alter the spectral signature. Thus, as part of this report, we have attempted to analyze the reflectance spectra and relate them to water status or water potential in order to select spectral regions that are not overly influenced by normal phenological transitions but reflect plant water status only.

3. METHODS

All high resolution spectral signatures were collected at KSC using two SE590 high sensitivity solid state spectrographs with 252 channel linear diode arrays. Each channel samples approximately 3 nm producing a signal that extends from 386 to 1115 nm. An environmental optics chamber system with a barium sulfate reflectance coating was designed and constructed at FIT to measure leaf transmittance and reflectance utilizing a halogen light source. Each end of the optical chamber system was outfitted with SE590 spectrographs allowing for the simultaneous determination of leaf reflection and transmission. For each of four sample periods in March 1994 duplicate leaf samples were collected at KSC from two areas in the plant canopy of both *Q. geminata* and *Q. myrtifolia*. One pair was extracted from an area exposed to full sunlight and one pair was from full shade. The leaves were excised from the stems of individual plants with a scalpel to ensure a clean cut of the petiole for observation of response to application of a Scholander pressure bomb (Kramer, 1983). After collection, one leaf was immediately placed in an optical environmental test chamber where reflected and transmitted light were measured. The leaf was then cut in half, thickness was measured and it was placed in liquid nitrogen and stored frozen for future biochemical analyses. The second leaf was placed in the Scholander pressure bomb for measurement of water potential. Pressure values for this study are presented in bars. Thus, for each of the sample periods data were generated on water potential, spectral reflectance, transmittance and calculated absorptance signatures. These data were then subjected to optimal passive ambient correlation spectroscopy (OPACS) analysis (Bostater, 1992a and 1992b) to develop empirical relationships between optimal wavelengths and simple estimates of water status as defined by pressure bomb readings.

In the field phase of the study, canopy level spectral reflectance signatures for sand live oak, myrtle oak and saw palmetto at two locations were collected every 10-14 days for five sample periods between March and May 1994. All spectral signatures were collected in a random near nadir fashion from a distance of approximately 1-1.5 m above the targets, providing individual samples from an area of about 8-12 cm². For each collection, fifteen replicate readings were obtained and the average spectral reflectance signature was computed for comparison with indicators of plant water status. Upwelling light from the canopy was normalized to spectral signatures obtained from a Spectralon calibration panel. Measurements were made at the same instrument gain setting and integration time.

All field samples were collected during full sunlight in morning hours at a time that corresponded to a solar angle above the horizon of 55-60 degrees minimizing the influence of changing incidence angle on estimates of spectral signatures and changing water status in the plants as a result of diurnal cycles (Kramer, 1983; Riggs and Running, 1991). For each of the oak species, leaf samples were collected for triplicate determination of water status as indicated by Scholander pressure bomb estimates of the balance point (Tyree and Hammel, 1972) and measurement of percent moisture by low temperature drying in an oven at 80 C° for a minimum of 48 hours.

Natural scrub communities at KSC occur on an undulating topography that is described as a ridge and swale system created as relict sand dunes associated with the historic rise and fall in sea level (Schmalzer and Hinkle, 1990). One field canopy sample site was established adjacent to a wetland in an area where depth to the water table was approximately 0.5 m. The second sample site was located on a sand ridge system where depth to the water table was about 1.5 m. Soils in the upland area are

classified as Pomello sand. Soils adjacent to the wetland are classified as Immokalee sand. Both types are well drained (Huckle et al., 1974). Selection of the two sites was made to represent variability in soil moisture available to the plants, a possible contributing factor to leaf water potential (Kramer, 1983). Depth to water table at each site was monitored throughout the study period through the use of shallow groundwater wells. Rainfall frequency and volume were also noted throughout the study.

4. DATA ANALYSIS PROCEDURE

Data analysis consisted of selection of optimal bands or channels from reflectance signatures and relating these channels to the plant water potential measurements through a simple linear model. For this study, the relative water status of plants was defined as either percent moisture ((wet weight - dry weight)/(wet weight)) \times 100 or estimates of the water potential balance pressure (-bar) required to bring moisture to the cut cross sectional surface of the leaf petiole as determined by application of a Scholander pressure bomb.

Inflection signatures were computed from average reflectance signatures to develop three band optimum correlation estimates. Inflection was computed as a form of a second derivative (Bostater, 1992a; Grew, 1980). The inflection estimator was defined as :

$$I_{(\lambda) m, i, n} = R^2_{(\lambda)i} / [R_{(\lambda)i-n} \times R_{(\lambda)i+m}] \quad (1)$$

where $I_{(\lambda)}$ is the inflection or second derivative estimator centered at band i calculated from the reflectance signature. M and n are forward and backward operators, respectively. The optimal channel located at m, i, n is determined by computing all combinations of m, i, n ranging from $i = 2-251$, $m = 2-252$, and $n = 1-250$. For each combination of m, i, n , for a given set of reflectance signatures and water status estimators a linear regression was performed. Three band wavelength combinations providing the maximum correlation coefficient are defined as the optimum bands. To further optimize the band selection procedure, an "optical clean up" of the spectrum was performed by developing a ratio between the optimal bands for one biophysical feature and then selecting a second set of optimal bands. One example of this procedure is to compute this double inflection ratio (DIR):

$$DIR_{(\lambda)} = [R^2_{(\lambda)i} / (R_{(\lambda)i-n} \times R_{(\lambda)i+m})] / [R'^2_{(\lambda)i} / (R'_{(\lambda)i-n} \times R'_{(\lambda)i+m})] \quad (2)$$

where $R'_{(\lambda)}$ represent the first set of optimized inflection channels and $R_{(\lambda)}$ represents the second set of optimized inflection channels. This approach to optical clean up has been shown to be useful in aquatic remote sensing application related to separation of chlorophyll and suspended sediment signatures (Bostater, 1992a). The technique is based upon an objective differential spectroscopy method whereby relative absorption and backscatter spectral regions are detected utilizing second derivatives of the reflectance signatures.

5. RESULTS AND DISCUSSION

The primary objective of this study was to evaluate the potential for utilizing the OPACS procedure (Bostater, 1992a; 1992b) for the selection of optimal bands or combination of bands that could prove useful in developing non-destructive estimates of the water status or water potential of plants in field experiments being conducted at KSC. Results of preliminary laboratory measurements are shown in Figs. 1 and 2. Figure 1 presents the reflectance signatures of leaves measured in the laboratory environmental optics chamber system that derives data simultaneously on reflected and transmitted light. In Fig. 1 the computed reflectances from the underside of seven representative leaf samples are presented as examples of the signals that were obtained. Note that the signal becomes very noisy at the upper and lower wavelength regions of the measurement range. This is attributed to the lower output of the halogen light source at these wavelengths. The seven leaves shown in this figure were collected in the middle of March and represented a range of senescence stages that produced distinctively different leaf and canopy signatures. All of the leaves sampled were green in color. These oak species are virtual evergreens and they are never without some green leaf material in their canopies. Some leaves, late in the senescence process were stiff and brittle with age, while some were flexible and pliable at the time of sampling.

The degree of senescence is apparent in the reflectance signatures shown in Fig. 1 for the leaf level measurements. Leaves in the early stages of senescence displayed distinct reflectance maxima at 560-570 nm in a region that indicates the presence of chlorophyll and carotenoid pigments. For these leaves there is a distinct reflectance minima at the base of the red shoulder near 680 nm in the vicinity of the second absorption maxima for chlorophyll a and b (Boyer et al., 1988). For all samples there is a dramatic increase in reflectance in the 590- 740 nm region that is the result of enhanced light scattering within the leaf structure. Leaves further along in the senescence process display an increased reflectance in the 650 nm region possibly as a result of increased anthocyanin development and reduced moisture altering leaf structure (Boyer et al., 1988). In the near-infrared portion of the spectrum there appear to be slight absorption bands at about 775, 825 and 950 nm that correspond to identified water status correlation regions (Bowman, 1989; Penuelas et al., 1993).

Figure 2 presents results of the OPACS derived linear relationship between the leaf water potential (bar) estimate and the laboratory reflectance signatures as computed by the DIR algorithm. The coefficient of correlation was $r = -0.91$ for the relation between water potential and a six channel double inflection ratio. The six optimal bands were 953, 969 and 978 nm in the denominator and 798, 807 and 820 nm in the numerator. The bands defined as optimal, based upon the OPACS technique and on the laboratory measurements of reflectance, correspond closely to the known water absorption regions in the near-infrared region suggesting a biophysical basis for the spectral bands selected.

Results of the canopy level measurements of reflectance signatures for the three species dominant in the KSC scrub vegetation are shown in Figs. 3 through 5. During this period of sampling, between March 21 and May 6, 1994, the oak species were passing through a phenological transition where senescing leaves were falling to the ground as litter and new leaf material was being added rapidly to the canopy. Saw palmetto displayed no obvious changes in leaf characteristics during this period. Examination of the canopy level spectral signatures for sand live oak, myrtle oak and saw palmetto show that the major changes in reflectance signatures are expressed in the near-infrared with a

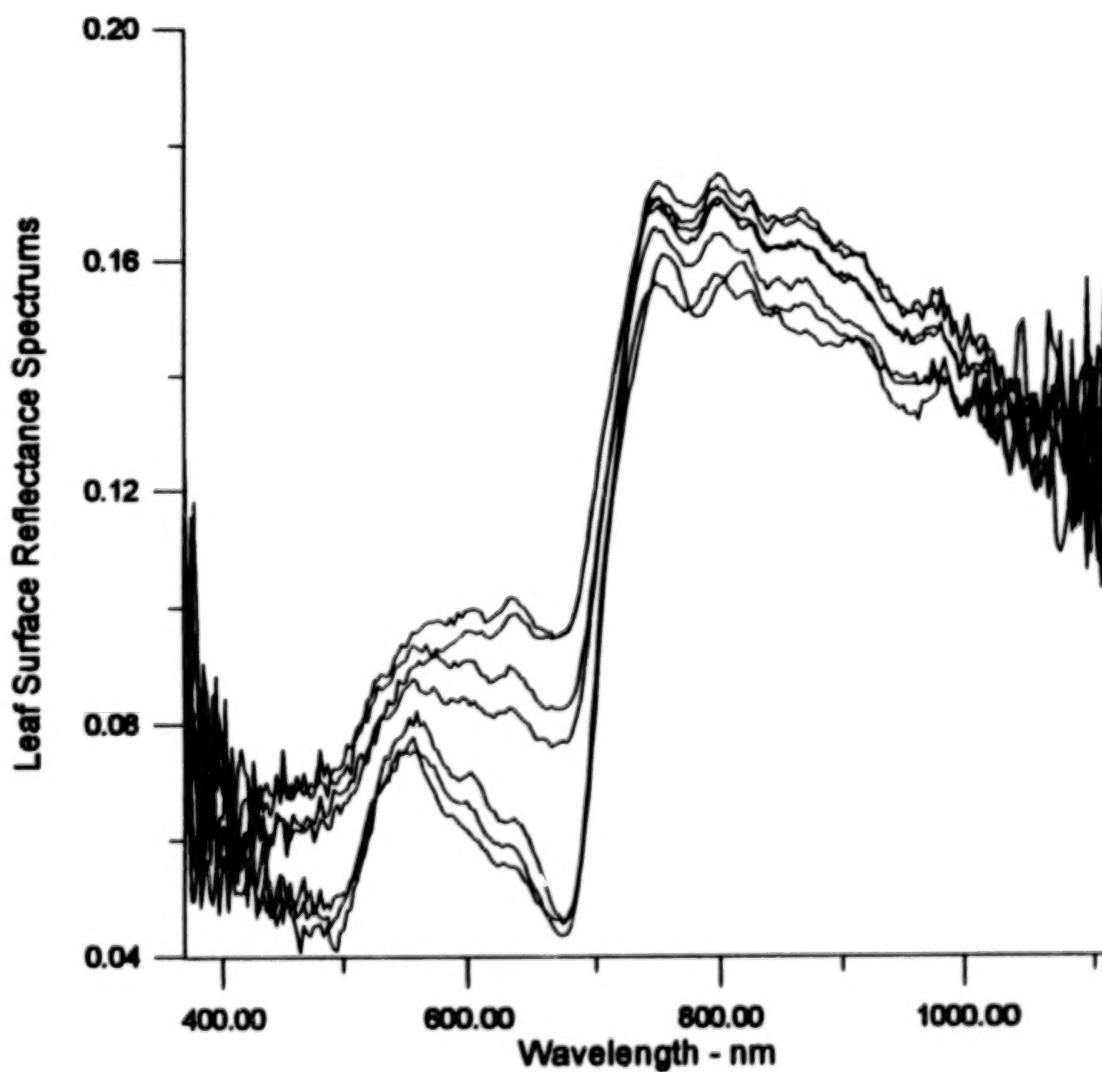


Figure 1. Mean ($n=5$) reflectance signatures for sand live oak (*Quercus geminata*) and myrtle oak (*Q. myrtifolia*) leaves subjected to analysis in the environmental optics chamber. Samples were collected to represent the range in variability of leaf senescence from full sunlight and full shade on March 14, 1994.

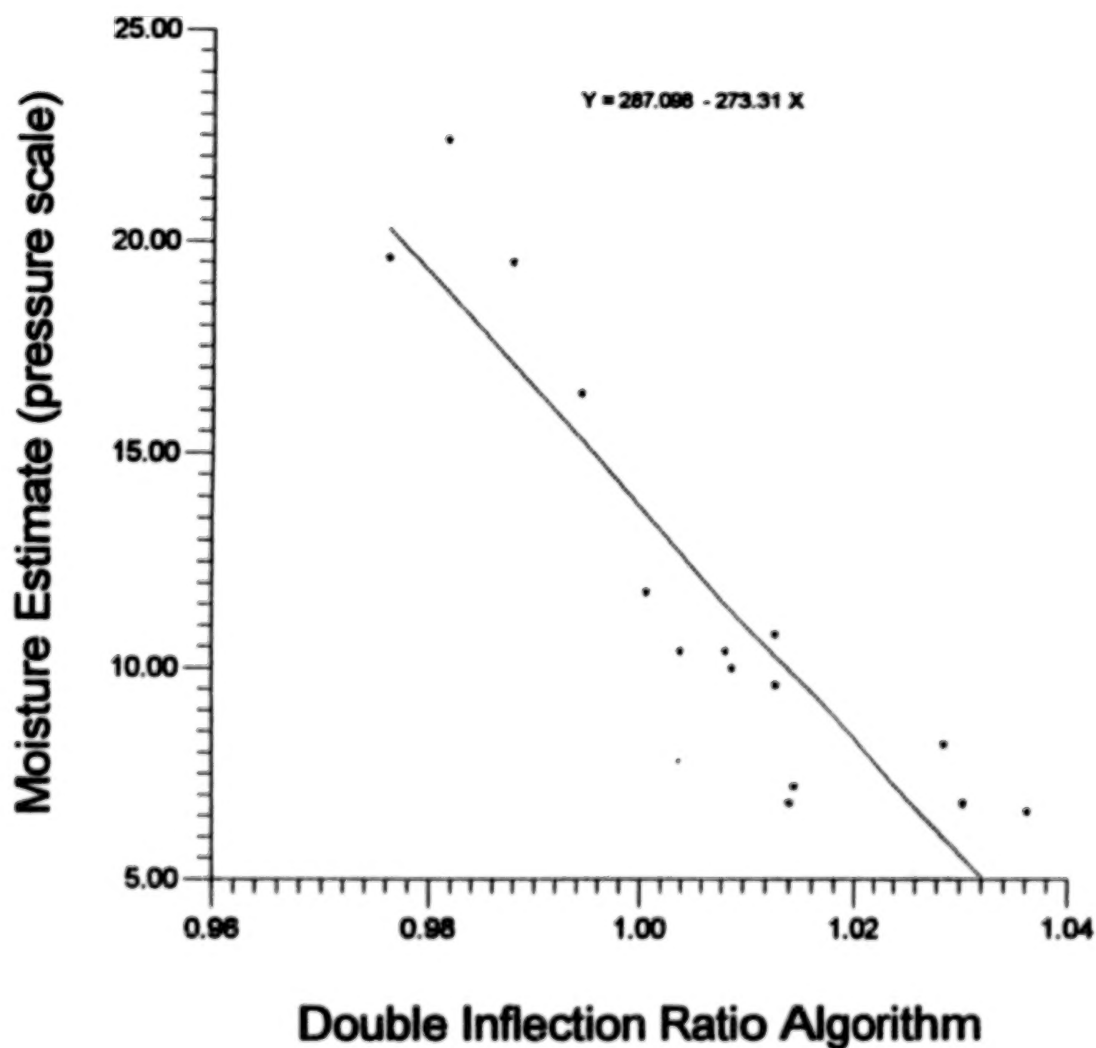


Figure 2. Linear relation ($r = 0.91$) between leaf water potential ($\bar{\psi}$) for sand live oak (*Quercus geminata*) and myrtle oak (*Q. Myrtifolia*) subjected to analysis in the environmental optics chamber and a six channel double inflection ratio ($n=15$). Optimal wavelengths were 953, 969, 978 (denominator) and 798, 807, 820 nm (numerator). Samples were collected to represent the range in variability of leaf senescence from full sunlight and full shade on March 14, 1994.

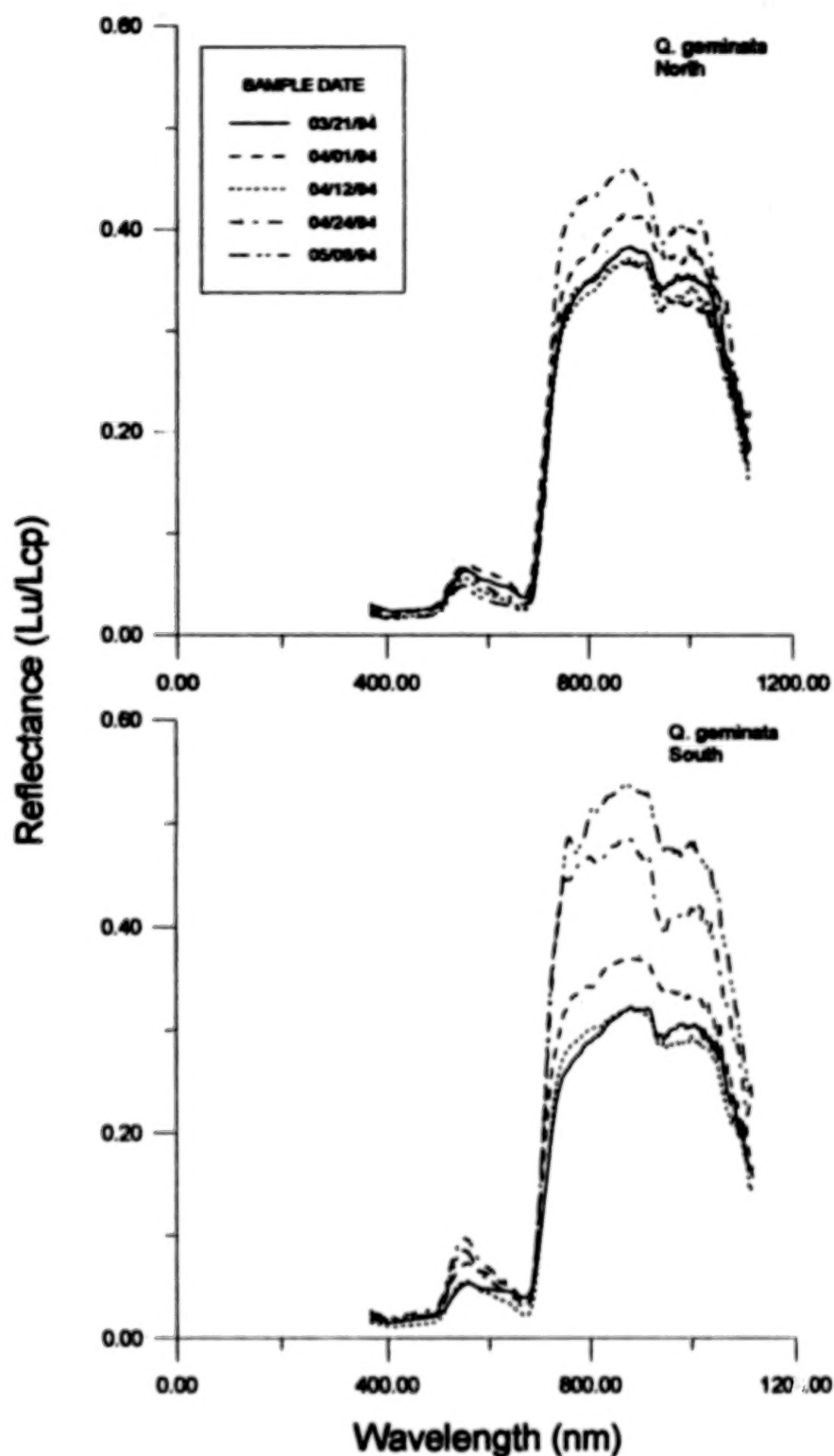


Figure 3. Canopy level mean ($n=15$) temporal spectral reflectance signatures for sand live oak (*Quercus geminata*) collected between March and May 1994 from two different field sites with different depths to water table and soil types. The north site was adjacent to a wetland and the south site was on a sand ridge. Spectral measurements were collected with near nadir viewing from a height of approximately 1 m above the canopy with a solar zenith angle of 30-35 degrees.

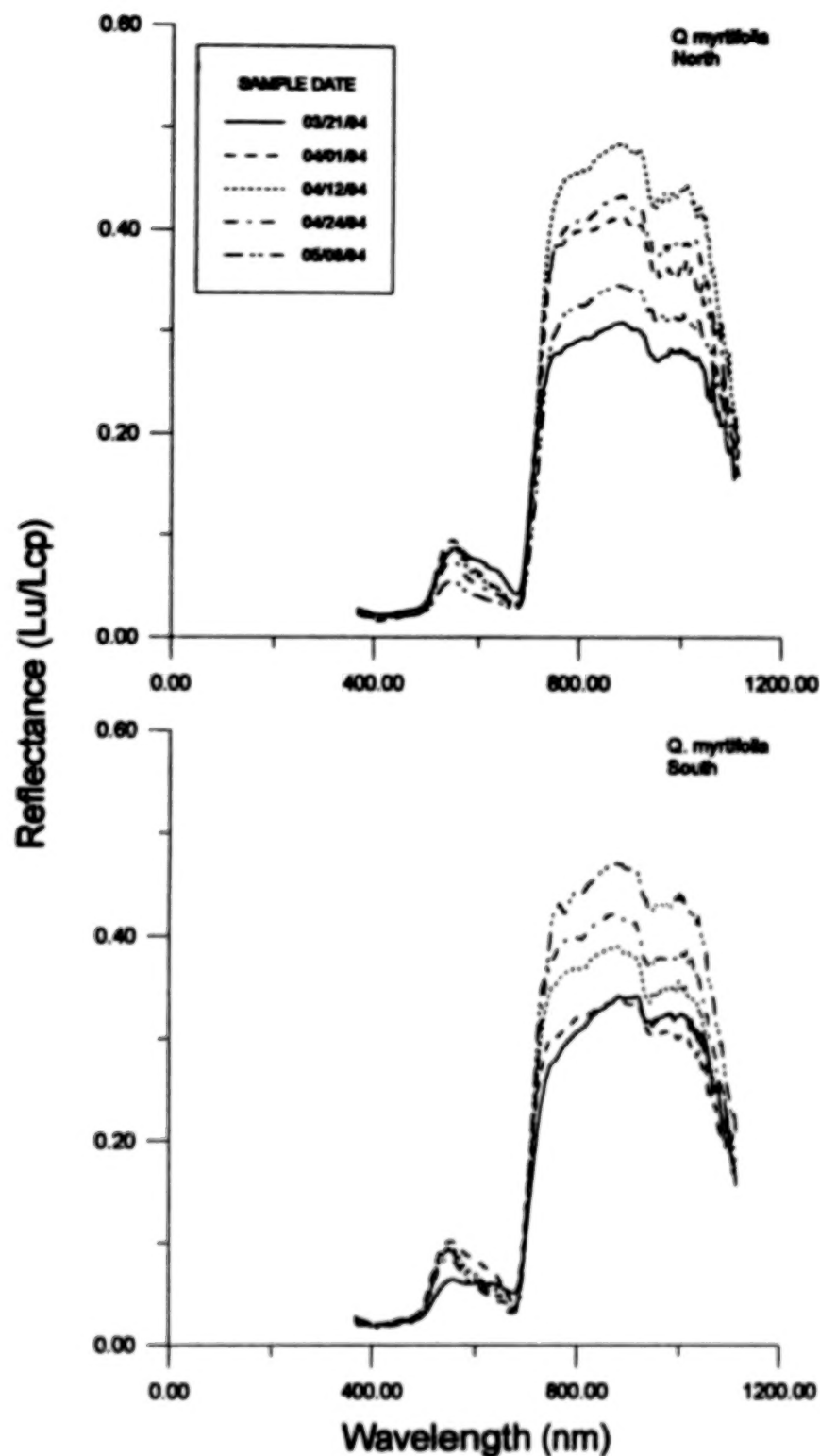


Figure 4. Canopy level mean ($n=15$) temporal spectral reflectance signatures for myrtle oak (*Quercus myrtifolia*) collected between March and May 1994 from two different field sites with different depths to water table and soil types. The north site was adjacent to a wetland and the south site was on a sand ridge. Spectral measurements were collected with near nadir viewing from a height of approximately 1 m above the canopy with a solar zenith angle of 30-35 degrees.

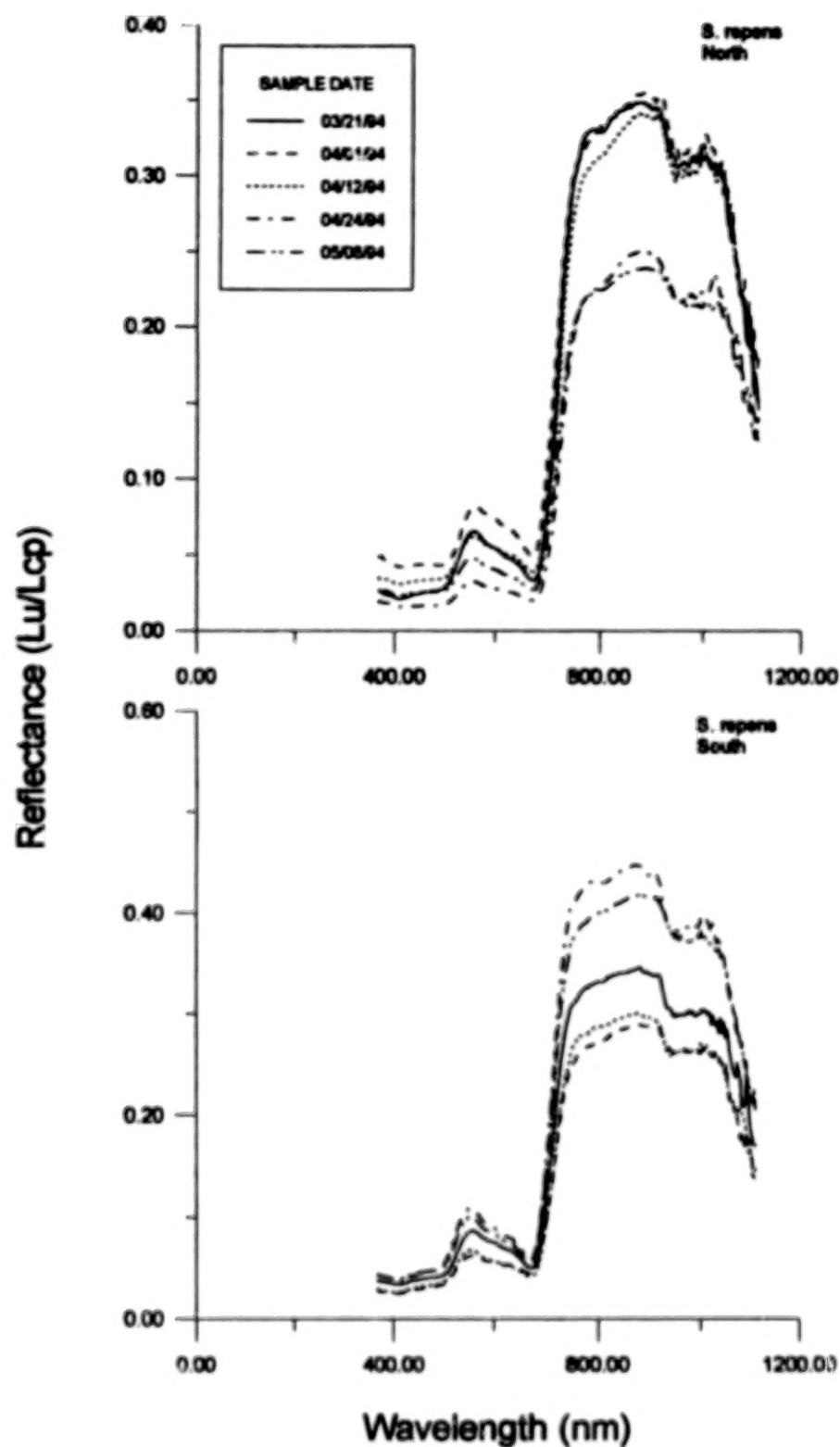


Figure 5. Canopy level mean ($n=15$) temporal spectral reflectance signatures for saw palmetto (*Serenoa repens*) collected between March and May 1994 from two different field sites with different depths to water table and soil types. The north site was adjacent to a wetland and the south site was on a sand ridge. Spectral measurements were collected with near nadir viewing from a height of approximately 1 m above the canopy with a solar zenith angle of 30-35 degrees.

general trend of increasing reflectance over time. This general increase results from a combination of factors including effects of leaf level structural changes and increases in reflecting surfaces within new mature leaves (Gates, 1980; Grant, 1987) and the changing leaf area index and canopy biomass as the growing season progresses with a corresponding decrease in the proportion of soil and litter reflectance. In the visible portion of the spectrum there are temporal changes in the reflectance signatures that are associated with the changing ratios and amounts of chlorophyll, carotenoid and anthocyanin pigments in the leaves. These signals are also influenced the soil and leaf litter reflectance in sparse canopy situations.

Results from the OPACS analysis between leaf water status indicators (percent moisture and water potential readings) for canopy level measurements are presented in Figs. 6 and 7. Figure 6 shows the results of the band selection analysis between leaf balance pressure (bar) and the reflectance spectra based on the single inflection three channel algorithm. The correlation coefficient was $r = 0.88$ with a residual error of 2.4 bar. The three optimum bands were 893, 816, and 762 nm. Bowman, (1989) found a high correlation between leaf water status and changes in reflectance in the 825 nm region for cotton (*Gossypium hirsutum*) leaves.

Figure 7 describes the linear relationship between the percent moisture of leaves and the spectral signature as defined by application of the OPACS derived six channel double inflection ratio algorithm. The correlation coefficient was $r = -0.95$ with a residual error estimated at less than 5%. For this six band double inflection ratio the three bands in the denominator were 943, 931, and 842 nm. The three bands in the numerator were 906, 848, and 810 nm. It is interesting to note that for each analysis the OPACS procedure produced optimal band selections in the near-infrared region of the spectra and no spurious optimal correlations were generated in the visible region where water and changing leaf structure have a negligible role in absorption and reflection.

6. SUMMARY AND CONCLUSIONS

For each of the regression analyses it appears that the optimum bands selected are defining the inflection or spectral curvature that is occurring in association with known water absorption regions centered around 760 and 970 nm. Other biophysical features such as changing internal leaf structure as a result of changing turgor pressures may also be contributing to the relative importance of the optimal bands and their strong linear relationships with the water moisture estimates utilized in this study. Based on these results, it would appear that the OPACS analysis procedure described by Bostater (1992a; 1992b) has potential in terrestrial remote sensing and environmental monitoring applications which utilize high spectral resolution reflectance signatures or hyperspectral imaging data.

Further testing and development in a larger variety of landscape types and situations, including application to high spectral resolution data derived from aircraft and satellites is needed to continue refining and testing the applicability of the procedure and the bands and spectral regions identified in this study for estimating water potential. Influences of spatial scale and pixel heterogeneity are additional sources of variability that need investigation and quantification. Use of optical cleanup techniques such as the double inflection ratio may also prove useful in estimating leaf biochemical constituents and in normalizing influences of competing sources of variation when attempting to detect specific biophysical parameters.

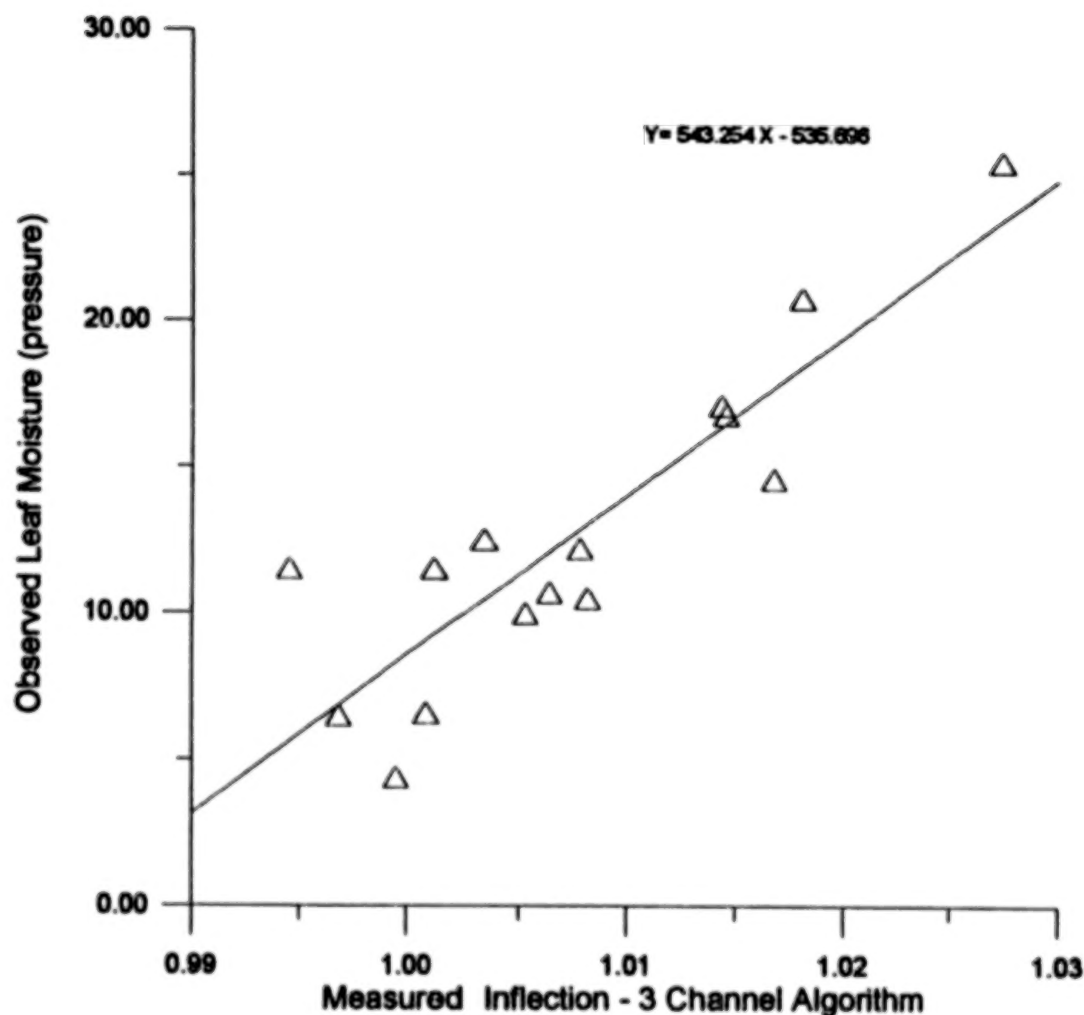


Figure 6. Linear relation ($r = 0.88$) between leaf water potential ($\bar{\psi}$) for sand live oak (*Quercus geminata*) and myrtle oak (*Q. myrtifolia*) and the canopy level inflection spectra estimated using three channels ($n=20$). Wavelengths used were 893, 816, and 762 nm. Spectral measurements were collected with near nadir viewing from a height of approximately 1 m above the canopy with a solar zenith angle of 30-35 degrees.

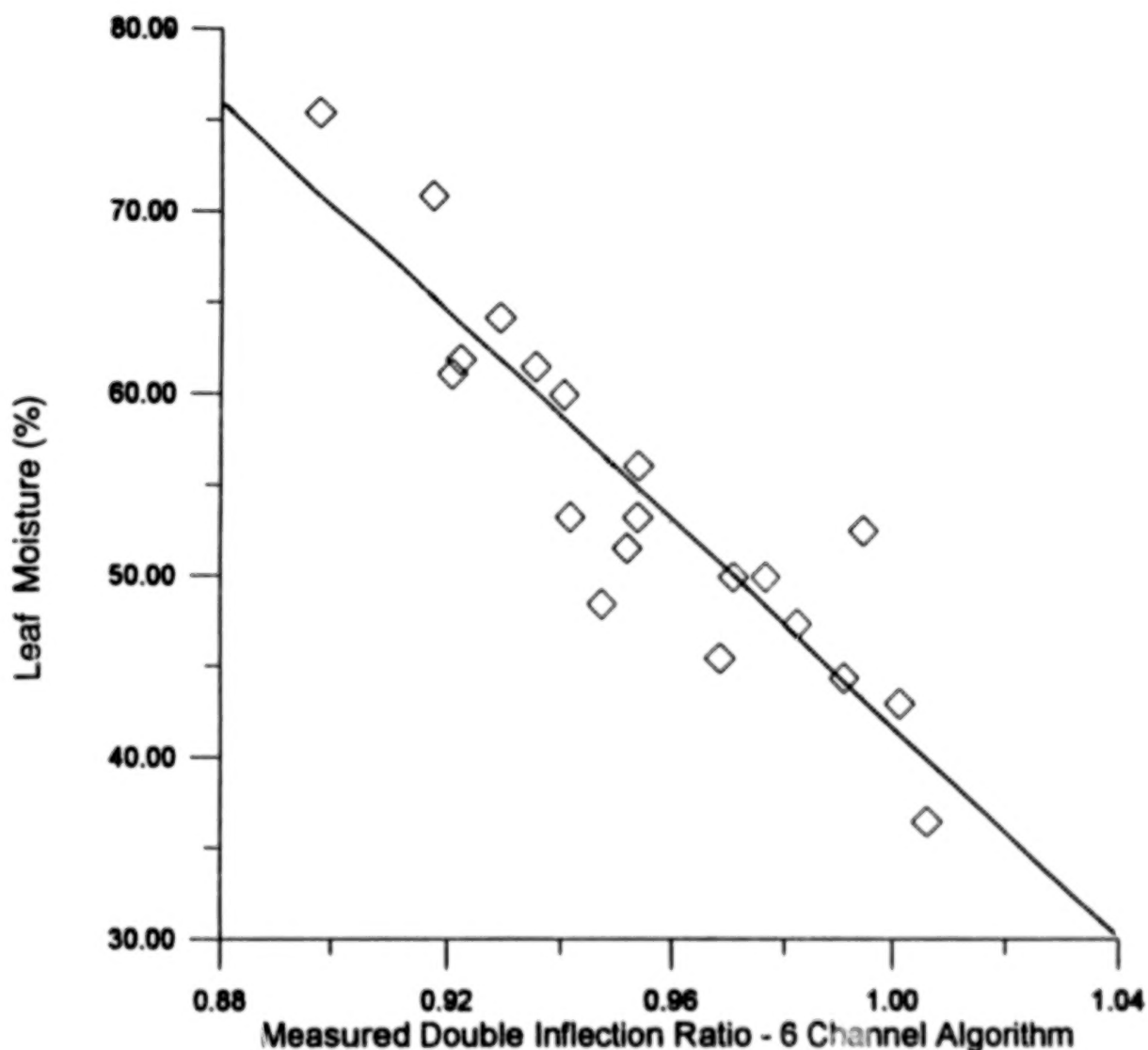


Figure 7. Linear relation ($r = -0.95$) between percent leaf moisture for sand live oak (*Quercus geminata*) and myrtle oak (*Q. myrtifolia*) and a double inflection ratio estimated using six channels ($n=20$). Wavelengths used were 943, 931, 842, nm and 906, 848, 810 nm. Spectral measurements were collected with near nadir viewing from a height of approximately 1 m above the canopy with a solar zenith angle of 30-35 degrees.

ACKNOWLEDGMENTS

This work was conducted under NASA Contract NAS10-11624 as part of the Biomedical Operations and Research Office Ecological Program for the John F. Kennedy Space Center. We thank William Knott III, and Burt Summerfield for providing the opportunity to conduct this study. Florida Institute of Technology and R&D Sciences provided most of the instrumentation and field equipment. Paul Schmalzer and Ross Hinkle provided critical reviews and comments on the manuscript. Opal Tilley provided manuscript preparation support.

REFERENCES

- Bostater, C. R., 1992a: Remote sensing methods using aircraft and ships for estimating optimal bands and coefficients related to ecosystem responses, Proceedings of the First Thematic Conference on Remote Sensing for Maine and Coastal Environments. New Orleans, La.
- Bostater, C. R., 1992b: Mathematical techniques for spectral discrimination between corals, seagrasses, bottom and water types using high spectral resolution reflectance signatures, Proceedings of the International Symposium on Spectral Sensing Research. Maui, Hawaii.
- Bostater, C. R., Hall, C. R., and D. R. Breininger, 1992: High resolution optical signatures and band selection techniques for endangered species habitat management, Proceedings of the International Symposium on Spectral Sensing Research. Maui, Hawaii.
- Bowman, W. D., 1989: The relationship between leaf water status, gas exchange and spectral reflectance in cotton leaves, *Remote Sensing of the Environment*, 30:249-255.
- Boyer, M., Miller, J., Belanger, M., and E. Hare, 1988: Senescence and spectral reflectance in leaves of northern pin oak (*Quercus palustris*, Muenchh.), *Remote Sensing of the Environment*, 25:71-87.
- Deering, D. W., 1989: Field measurements of bi-directional reflectance. In: Asrar, G. (Ed) (1989), Theory and applications of optical remote sensing, John Wiley and Son, New York, 14-65.
- Gao, Bo-Cai and A. F. H. Goetz, 1994: Extraction of dry leaf spectral features from reflectance spectra of green vegetation, *Remote Sensing of the Environment*, 47:369-374.
- Gates, D. M., 1980: *Biophysical Ecology*, Springer-Verlag, New York. 611 pp.
- Gausman, H. W., Allen, W. A., Cardenas, R., and A. J. Richards, 1970: Relationships of light reflectances to histological and physical evaluations of cotton maturity (*Gossypium hirsutum*, L.), *Applied Optics*, 9:545-552.
- Grant, L., 1987: Diffuse and specular characteristics of leaf reflectance, *Remote Sensing of The Environment*, 22:309-322.

- Grew, G., 1980: Real-time test of MOCS algorithm during superflux 1980. In: Chesapeake Bay Plume Study, Superflux 1980, NASA Pub. 2188, Washington, D. C., 301-322.
- Hunt, R. E. Jr., and B. N. Rock, 1989: Detection of changes in leaf water content using near- and middle- infrared reflectances, *Remote Sensing of the Environment*, 30:43-54.
- Hunt, R. E. Jr., Rock, B. N., and P. S. Nobel, 1987: Measurement of leaf relative water content by infrared reflectance, *Remote Sensing of The Environment*, 22:429-435.
- Hunt, R. E. Jr., and S. W. Running, 1990: Problems with scaling leaf water relations to regional scales. In: *Proceedings IGARSS '90*.
- Kramer, P. J., 1983: *Water relations of plants*, Academic Press, New York, 489 pp.
- Penuelas, J., Filella, I., Biel, C., Serrano, L., and R. Save, 1993: The reflectance at the 950-970 nm region as an indicator of plant water status, *International Journal of Remote Sensing*, 14:1887-1905.
- Riggs, G. A., and S. W. Running, 1991: Detection of canopy water stress in conifers using the airborne imaging spectrometer, *Remote Sensing of The Environment*, 35:51-68.
- Schmalzer, P. A., and C. R. Hinkle, 1990: *Geology, geohydrology and soils of Kennedy Space Center: a review*. NASA Technical Memorandum 103813. John F. Kennedy Space Center, Fl.
- Sinclair, T. R., Scriber, M. M., and R. M. Hoffer, 1971: Reflectance and internal structure of leaves from several crops during a growing season, *Agronomy Journal*, 63:864-868.
- Tyree, M. T. and H. T. Hammel, 1972: The measurement of the turgor pressure and the water relations of plants by the pressure-bomb technique, *Journal of Experimental Botany*, 23:267-282.
- Valley, S. L., 1965: *Handbook of geophysical and space environments*, Air Force Cambridge research Lab., Bedford. Mass.
- Vogelman, J. E., Rock, B. N., and D. M. Moss, 1993: Red edge spectral measurement from sugar maple leaves, *International Journal of Remote Sensing*, 14:1563-1575.
- Wessman, C. A., 1989: Evaluation of canopy biochemistry. In: Hobbs, J. H., and Mooney, H. A. (Eds), 1989: *Remote sensing of biosphere functioning*. Springer-Verlag, New York, 135-156.

SPECTRAL MANIPULATION FOR THE DETECTION OF MAN-MADE AND SMALL OBJECTS IN MULTISPECTRAL IMAGES

Vittala K. Shettigara
Gordon M. Sumerling
Defence Science and Technology Organisation
PO Box 1500 Salisbury SA 5108 Australia
Ph: 08 259 7176
fax: 08 259 5619

ABSTRACT

A new image processing technique - Background Discriminant Transformation - for the separation of artificial (man-made) objects from natural objects in multi-band (color) images is presented in this paper. It is demonstrated that the technique can be used for synthesising image bands, from a set of similar or dissimilar images, in which the required type of objects, such as artificial objects, are enhanced in a prominent color. It is shown that dissimilar images like SPOT and SAR can be fused to delineate artificial objects. It is further demonstrated that the enhanced objects can be semi-automatically segmented for easy storage in raster GIS data base.

1 INTRODUCTION

Environmental monitoring, defence mapping, surveillance and terrain analysis often require separation and detection of artificial (man-made) objects from natural surroundings in images. In the case of surveillance or reconnaissance it may be necessary to separate artificial objects from natural objects in real or near real time. It may be also required to fuse data from dissimilar sensors such as optical and synthetic aperture radar (SAR) images and display an appropriate image that highlights the artificial objects.

There are many research papers and reports that have endeavoured to separate artificial and natural objects. McKeown (1988) has developed a knowledge based system for detecting and analysing man-made structures in remotely sensed images. Their procedure requires the integration of spatial knowledge with image analysis. Moran and Korvin (1994) have developed mathematical procedures to detect man-made objects in SAR images using the model that such objects can be represented by chains of straight lines or circular arcs. Ormsby (1992) has used statistical measures of separation (divergence) between natural and artificial objects to recommend different Landsat TM bands to use for separating different objects. All of the above procedures require extensive prior knowledge of the area being investigated and require extensive computation. The above methods are more suitable for post-mission analyses, whereas there is a demand to process and display images in real time. Therefore there is a need to have a simple procedure that would separate and enhance artificial objects in remotely sensed images in near-real time and it would be beneficial if the procedure required little or no prior knowledge of the area.

This paper presents a technique based on Background Discriminant Transformation (BDT, Shettigara, 1991) to separate artificial objects from the natural objects. The process is simple and it can be used for real time requirements. The terms 'artificial' or 'man-made' refer to objects artificially created using synthetic or natural materials. For example sealed or unsealed roads, asbestos or tile roofed buildings, concrete materials and metallic objects are all artificial objects.

The procedure is only applicable to multispectral data such as SPOT and Landsat-TM images. It can be shown mathematically that the BDT technique is suitable for fusing dissimilar images such as SPOT and SAR images. The BDT technique has the ability to significantly enhance small objects for detection purposes in both defence and civilian tasks.

1.1 The objectives

The BDT procedure is developed to have the following abilities:

- a. Synthesize three useful bands out of the original multispectral bands, which when displayed in the red, green and blue guns, highlight man-made objects in distinctly different colors from the natural objects (vegetation). Further, constrain artificial objects to fixed hues of colors to assist in monitoring tasks that involve the scanning of large number of images.
- b. Fuse dissimilar data sets, such as optical and synthetic aperture radar images.
- c. Facilitate easy segmentation of the image set to separate artificial objects.

2 SPECTRAL CHARACTERISTICS OF ARTIFICIAL AND NATURAL OBJECTS

The BDT technique is based on the spectral characteristics of objects. As will be shown later in the report, the artificial objects are generally separable from the natural objects. Common natural objects are vegetation. If we consider the SPOT spectral bands: green, red, and near infrared, we note the following characteristics. A typical profile of vegetation displays a slight decline from the green to the red band followed by a sharp rise from the red to the near infrared (Figure 1). The sharp rise is due to the chlorophyll pigment in green vegetation. Chlorophyll absorbs the red portion of the spectrum and reflects the green and near-infrared bands in low and high proportions respectively. In contrast, the spectral profile of an artificial object displays a steady decrease in reflectance as the wavelength increases (Wharton 1987). Wheeler (1986) shows a series of profiles contrasting man-made and natural objects in an urban environment. Most man-made objects portray similar profiles but display a distinctly different shape to that of the vegetation profiles. In practice, however, the image pixels are rarely due to pure objects. Backgrounds generally dominate the image, making it difficult to enhance artificial objects in relation to natural objects.

Goward and Wharton (1984) found that iron oxides typically absorb the ultraviolet and the visible portion of the spectra. Many artificial objects are iron based so they will display absorption in the shorter wavelengths because of the iron content. The amount of absorption will depend on the proportion of iron oxide in the material. For example bitumen displays low reflectance through all the TM bands. These materials are dominated by hydrocarbons which are strong absorbers throughout the TM spectrum (Goward and Wharton, 1984). Thus, they appear dark in all bands.

Crist and Cicone (1984) developed the Tasseled Cap transformation for the Landsat TM images. The Tasseled Cap transformation, in mathematical terms, is a procedure to rotate the data reference axes such that the different physical properties of the terrain are highlighted. The original application of this transformation was for crop monitoring. Crist and Cicone (1984) provided six Tasseled Cap axes for Landsat TM images. Only the first four axes: brightness, greenness, wetness and haze are physically meaningful, and these contain 95% or more of the total data variability. The usefulness of brightness-greenness space in portraying the physical nature of the terrain is demonstrated in Figure 2. Notice that in this space the man-

made materials consistently fall below the line of soils (Goward and Wharton, 1984). There is no known equivalent to the Tasseled Cap transformation for SPOT images. However, the sketch in Figure 2 demonstrates that artificial objects are quite separable in spectral domains if the data are properly processed.

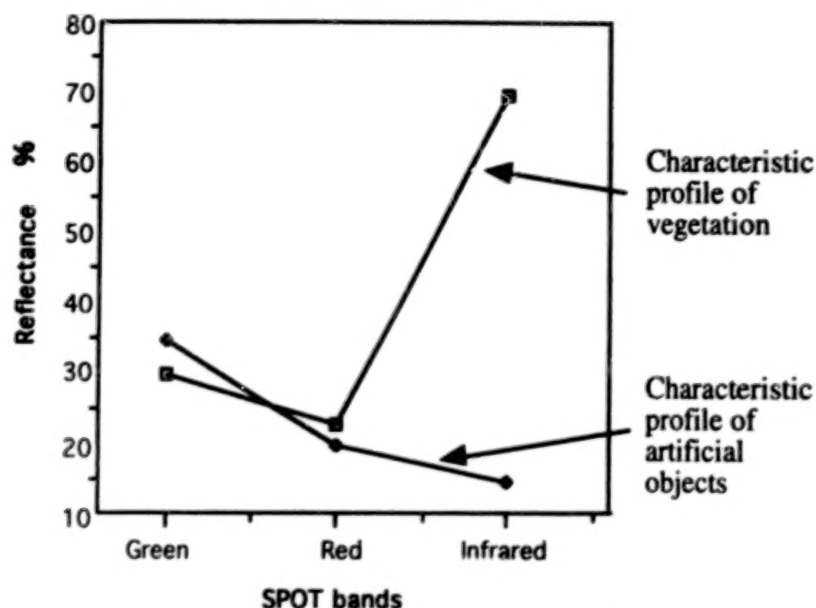


Figure 1 Typical profiles of vegetation and artificial objects

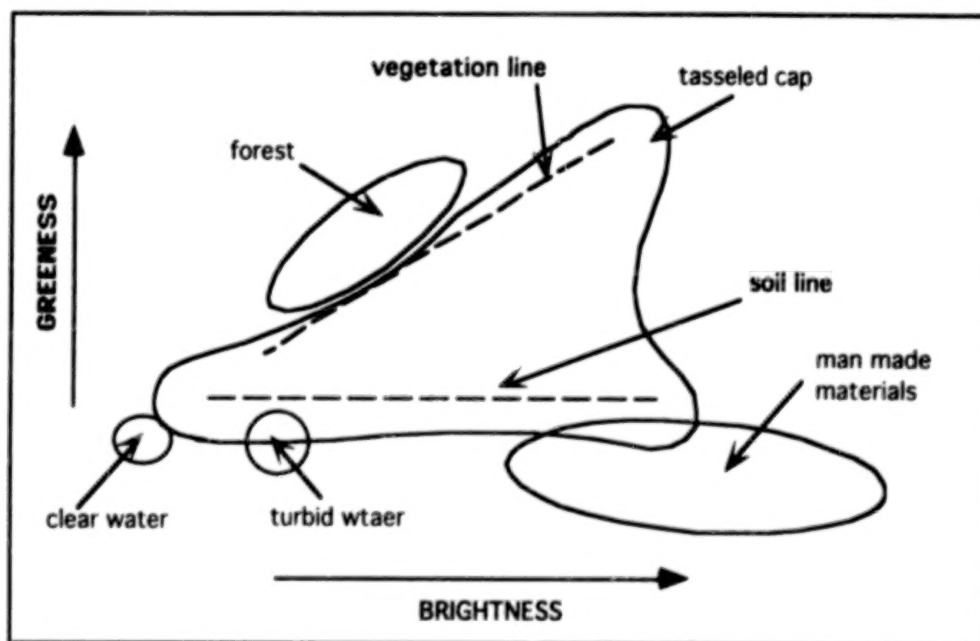


Figure 2 Sketch of distribution of commonly occurring ground covers in brightness-greenness plane of Tasseled Cap transformation (after Crist and Cicone 1984)

3 BAND DIFFERENCING TO SEPARATE ARTIFICIAL AND NATURAL OBJECTS

From the above discussion it is clear that in general natural objects are good reflectors and artificial objects are good absorbers in the infrared band. This characteristic may be used to differentiate artificial and natural objects. The difference between the infrared and red bands and the difference between the infrared

and green bands in a SPOT image was studied to assess their ability in differentiating artificial and natural objects. The following equations were used for computing the difference images.

$$(\text{infrared} - \text{red}) + 128 \quad (1)$$

$$(\text{infrared} - \text{green}) + 128 \quad (2)$$

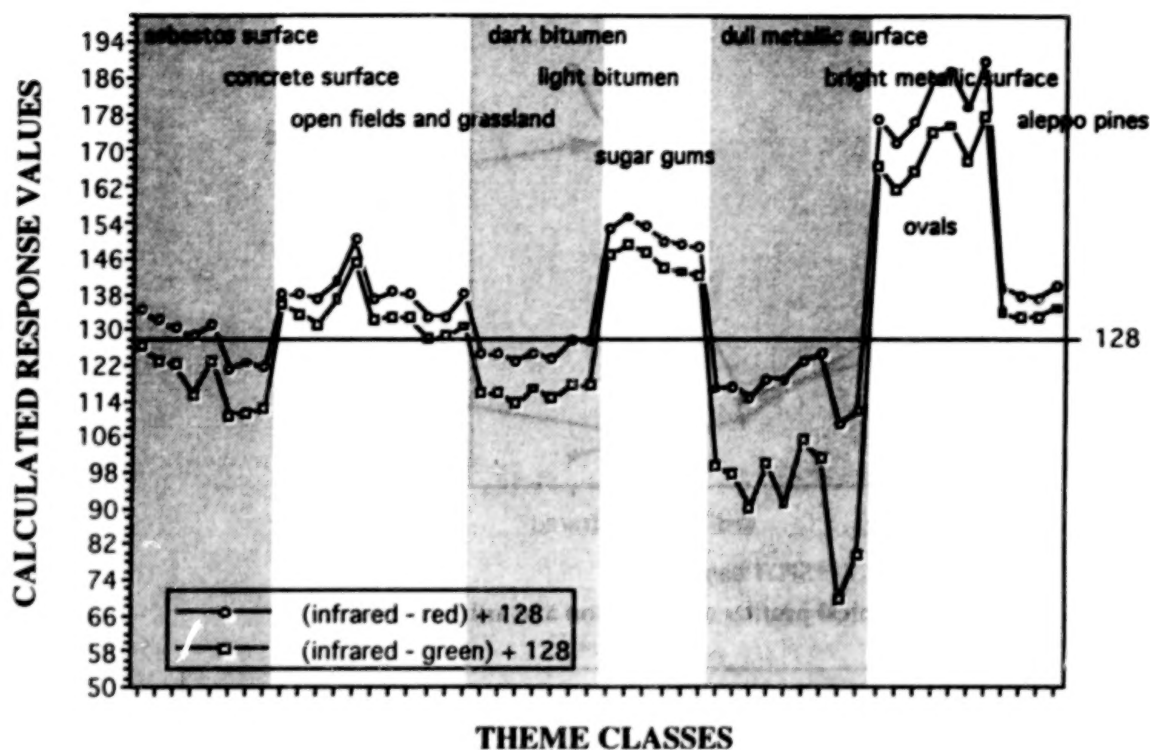


Figure 3 Mean spectral differences of natural and artificial objects. Unshaded parts of the graph are due to natural objects which display a value above 128 (variance not shown). The graph illustrates the possibility of simple differences as a means to separate the two types of objects

The results are summarised in Figure 3. The figure indicates that simple differencing of bands can lead to the separation of natural and artificial objects. In the example presented, a digital value of 128 forms the boundary between the natural and artificial objects and they may be displayed in contrasting colors by density slicing.

It is important to note that this process is not entirely satisfactory. The method is empirical and it does not exploit the multi-dimensional image data in its entirety. Difference images also tend to be bland in terms of textural and color information, making the terrain understanding difficult. For these reasons it was decided to explore the following possibility.

4 BACKGROUND DISCRIMINANT TRANSFORMATION

4.1 The procedure

The detection of small objects in images is often dependent on the suppression of the background. For example, it is difficult to detect small objects in the presence of background clutter. Numerous filters have been devised to suppress the background in single band images. Boulter (1983) has tested various spatial filters to enhance point targets by reducing background clutter. The Background Discriminant Transformation (BDT) is also a technique to suppress the dominance of the background, but in a multispectral space.

In the BDT technique, the multispectral images are linearly transformed, much like in the principal component transformation. The linear transformation coefficients are computed to maximise the variance (information content) of the non-background objects relative to the background objects (Shettigara, 1991). The technique assumes that an image has two major classes: background and non-background.

The method requires the user to identify the background class that needs to be suppressed in order to enhance the useful information. The background class is visually chosen by identifying a few training areas. The method requires mean vectors and covariance matrices of the background class and of the whole image. The procedure then automatically computes the mean vector and covariance matrix for the non-background class. The theoretical basis of the technique and the algorithm are presented in Shettigara (1991).

The procedure computes the same number of new transformed bands (axes) as the original bands in the multispectral image. In the first band, the ratio of variances of the non-background class and background class is the maximum, indicating the dominance of the non-background over the background. In the last band, the ratio is the minimum, indicating the dominance of the background over the non-background. In other bands, the ratio of variances will have intermediate values. For example, the second band will have the second best ratio of variances of the non-background and background classes.

For an effective color separation of the non-background and background objects the first, the last and the second transformed bands (BDT bands) are displayed in red, green and blue color guns of the monitor. By this arrangement it is possible to display non-background objects in reddish/pinkish hues and background objects in greenish-blue hues. Some times it may be necessary to invert one or more bands, depending on the polarity of the transformation vector.

4.2 Advantages of Background Discriminant Transformation

There are many advantages with BDT. The background is chosen by the user depending on the application. This provides control on the type of enhancement the user requires. The other attraction of the technique is that it is scale invariant. This is a very useful property because the gain and offset of the sensor system will not affect the quality of the transformed image. The implication is that images of the same area taken by different instruments or taken at different times can be merged without significantly affecting the analysis. The same property also enables one to integrate data from dissimilar sensors. For example, as will be shown later, SPOT and SAR (synthetic aperture radar) images may be merged to obtain good results.

It has been also observed that the transformation coefficients derived for one area for a given multispectral image can be used for other similar areas and similar images. For example the coefficients derived for a SPOT multispectral image of an area in South Australia were used for discriminating artificial objects from an equivalent Landsat TM image (bands 4, 3 and 2) of Weipa area in the northern tip of Australia. The results were surprisingly good. The successful adaptation of the transformation coefficients derived for a totally separate area indicates the robustness of the technique. The coefficients once derived can be used for a large area, which is a useful property for activities like wide area surveillance or environmental monitoring of a large area.

5 SEPARATION OF NATURAL AND ARTIFICIAL OBJECTS

Barring urban or industrial areas, more than 80 % of the land cover in satellite images consists of spectrally dominant natural objects such as tree and grass covers or in desert areas, barren soil cover. For this reason, any

procedure which separates natural objects greatly enhances the probability of detecting small and inconspicuous artificial objects.

The tool used in this study for separating artificial objects from natural land cover is the background discriminant transformation described above. The procedure provides a much better result than the commonly known techniques such as band differencing described in section 3, image segmentation or principal component analysis.

5.1 EXAMPLE 1 - LAND AREA MONITORING

The BDT technique was applied to a SPOT image of an area in South Australia. The area comprises an industrial complex, an air base, open fields, rows of pine and eucalypt trees and residential areas. For better clarity and for the purpose of discussion a small segment from the large image of the study area was extracted and is shown in figures 4a. This figure is a black and white photocopy of the standard false color SPOT image. Training areas consisting of trees, grass and crop fields and green ovals were chosen as the background. In Table 1 the transformation coefficients for the new bands (BDT 1, 2 and 3) derived from the background discriminant transformation technique are presented. In Figures 4b black and white photocopy of the color composites of BDT 1, BDT 3 and BDT 2, displayed in red, green and blue guns respectively, is shown.

In the color image the artificial objects appear in bright pink colors compared to the natural objects which appear in greenish colors. Land covers which are sparsely vegetated, and where soil is exposed, appear in bluish colors. This display not only highlights the artificial objects but also enables easy color differentiation between natural and artificial objects. In figure 4b the artificial objects appear as bright pixels and the natural objects appear as dark pixels.

Table 1 Background transformation coefficients for SPOT XS image

Background discriminant transformation coefficients			
	BDT 1	BDT 2	BDT 3
SPOT Green	0.876	-0.476	0.524
SPOT red	-0.481	-0.126	0.828
SPOT IR	-0.016	0.870	-0.200
Color guns in Figures 4b and 4d	RED	BLUE	GREEN
Objects highlighted	artificial	both	natural

5.2 EXAMPLE 2 - SEA SURVEILLANCE

Figure 5a is a black and white photocopy of the standard false color SPOT XS image of the Singapore Harbour. In this image, objects such as the main harbor, a number of islands and some ships outside the harbor in the ocean can be seen. The presence of small ships is difficult to notice as the light blue signature of the ships in the image tends to merge with the ocean.

In order to enhance the presence of the ships BDT was applied. For this process, the background class was selected to be a part of the ocean devoid of any ships. Only ocean is used to generate the statistics for the total image. The land area was masked because the intention was to exclusively enhance the ocean area. A black and white copy of the BDT enhanced color image is presented in Figure 5b. The ships in the ocean are



a

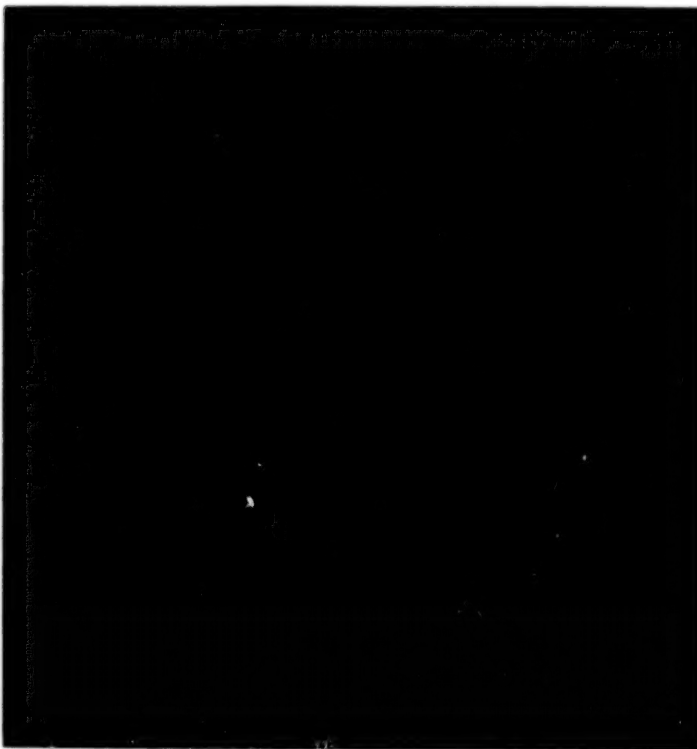
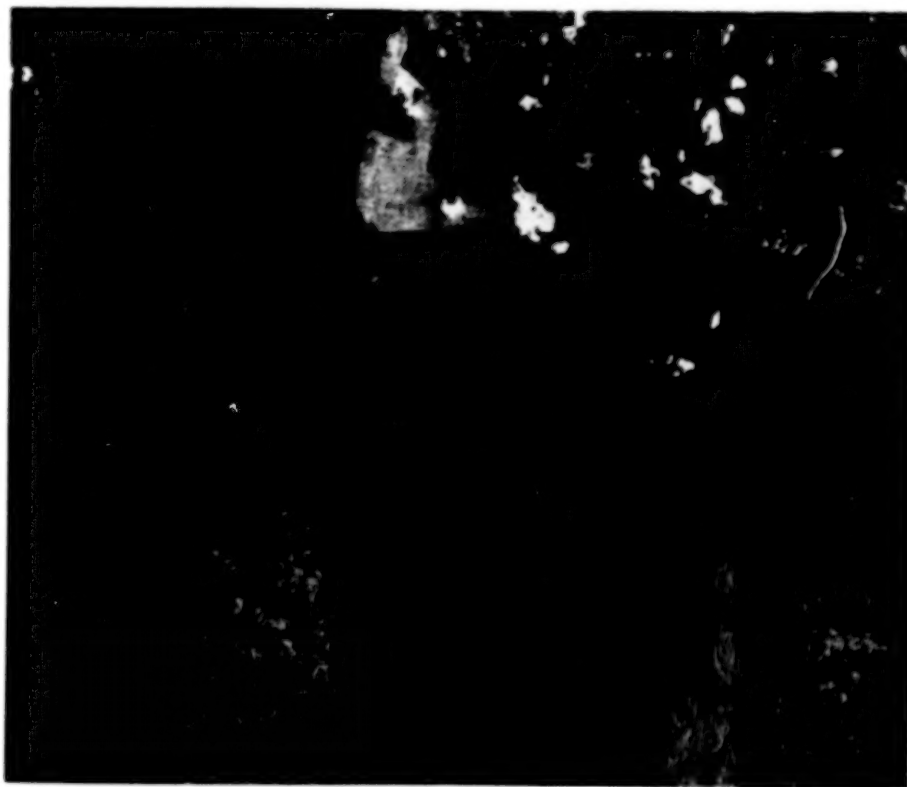
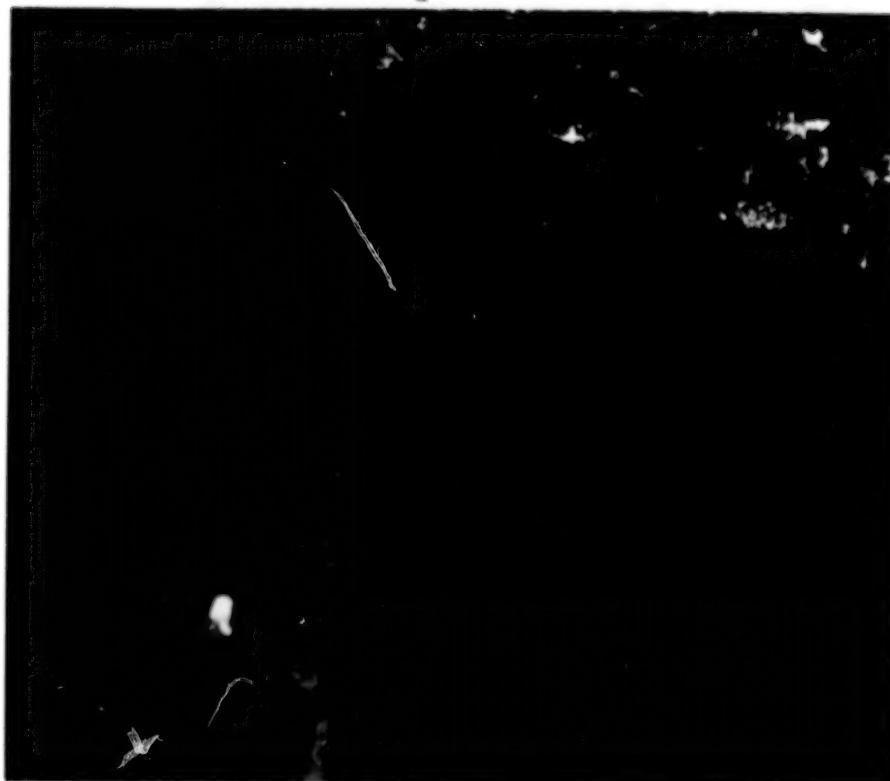


Figure 4 a) A SPOT XS image . Label A is on an asphalt surface where aircraft are parked. At the time of imaging , four aircraft were present just left of A. B is a residential area and C is an industrial area
 b) BDT enhanced image of a. Notice that the aircraft to the left of A are clearly visible as bright pixels on the dark background. As can be seen, the civilian and industrial structures around B and C are clearly visible as bright pixels in a dark background.



a



b

Figure 5

a) A SPOT XS image of Singapore Harbour

b) BDT enhanced image of Singapore Harbour.

Note the improved detection of ships waiting to enter the harbour

now detected as larger objects in red color. The number of ships present is significantly more than the number that could be detected in the un-enhanced image of figure 5a. Also enhanced in the transformed image are pontoons that extend into the ocean from the harbour and associated islands.

6 FUSION OF SAR AND SPOT IMAGE

Synthetic aperture radar (SAR) images and optical images such as SPOT behave quite differently. The scales of measurement and noise distribution in the two types of images are quite different. Due to these factors enhancing images to bring out objects of interest using conventional techniques is difficult.

An airborne synthetic aperture radar (AUSAR) image of the area of study was recently acquired. The ground resolution of the image is 3.00 m. The spatial resolution of the AUSAR image is approximately seven times better than that of the SPOT multispectral images shown partly in Figure 4. However, this does not make the discrimination of natural and artificial objects any easier in the AUSAR image. In the AUSAR image the natural objects such as trees and artificial objects such as buildings appear brighter than the surroundings and the artificial objects such as buildings appear brighter than the trees. However, when the buildings are surrounded by trees it becomes difficult to locate them. Locating objects is often made difficult due to the speckle noise.

In order to facilitate the better discrimination of artificial and natural objects in the AUSAR image it was decided to merge it with the SPOT multispectral image. A co-registered image set of the AUSAR and the SPOT image was created. The results of the conventional techniques were compared with that of the BDT procedure.

In Table 2 the covariance matrix of the combined data set is presented. As can be seen, the variance term of the AUSAR band is significantly different from the variances of other bands. This suggests that the variation of the AUSAR pixel intensities is significantly higher than the pixel intensity variation in other bands. The other possibility is that the scale of measurement is significantly different in the AUSAR image. The combined image set presents a typical problem associated with the fusion of dissimilar data sets.

Table 2 Covariance matrix of the AUSAR-SPOT XS image set

	AUSAR	SPOT Green	SPOT Red	SPOT IR
AUSAR	332.8			
SPOT Green	-27.3	15.1		
SPOT Red	-8.6	14.4	18.0	
SPOT IR	-109.4	2.7	-13.4	90.8

The combined image set was analysed using both conventional and BDT procedures. A simple overlaying of AUSAR and SPOT images did not help the discrimination of artificial and natural objects in terms of color characteristics.

Principal components were also determined for the combined set. Principal components 1, 2 and 3 of the merged data set, displayed in red, green and blue colors, did improve the look of the image. The artificial objects, in general, appeared in pink color. However, there was a lot of smearing of the pink color. The edges of the objects were not very sharply defined.

The coefficients of the principal components and the variance along each component are presented in Table 3.

Table 3 Principal components of the AUSAR-SPOT XS image set

	PC 1	PC 2	PC 3	PC 4
AUSAR	-0.996	-0.068	0.053	-0.112
SPOT Green	-0.067	0.664	-0.269	0.694
SPOT Red	-0.050	0.625	-0.298	-0.719
SPOT IR	0.021	0.404	0.914	-0.030
% VARIANCE	83.3	10.9	5.1	0.7

The AUSAR image was then fused with the SPOT image using the BDT procedure. Background discriminant bands 1, 2 and 4 were displayed in red, green and blue guns. In so doing all the cultural artefacts appeared in bright pink colors. The image had not only highlighted the major industrial complexes but also the small asbestos-cement roofed buildings in the study area. The artificial objects stand out quite clearly, both in terms of color contrast and edge sharpness.

In the BDT enhanced image all the major stands of trees appear in bright green colors. The greenness fades into bluish hues as the soil content in the image increases and the vegetation content decreases.

The addition of the higher resolution radar image has also increased the ability to detect small objects. Objects such as dirt roads, mounds, fence lines and river channels have become evident in the AUSAR BDT image that were not seen in the original SPOT XS BDT image.

In Table 4 the coefficients of the BDT are listed. The ratios of variances of non-background and background along each vector also appear. Ratios indicate the relative content of the non-background and background information in the transformed bands. The results are further discussed in the next section.

Table 4 Background discriminant transformation coefficients of the-SPOT XS image set

	BDT 1	BDT 2	BDT 3	BDT 4
AUSAR	0.074	0.210	0.105	0.024
SPOT Green	-0.504	-0.727	-0.516	0.767
SPOT Red	0.675	-0.628	0.800	-0.636
SPOT IR	-0.534	0.183	-0.288	-0.083
Ratio of variances of non-background and background classes	1.98	0.75	0.18	0.002

7 SEMI-AUTOMATIC EXTRACTION OF ARTIFICIAL OBJECTS

In many terrain monitoring operations it is desirable to detect man-made objects or man-made changes in real or near real time. A fundamental requirement to achieve this goal would be to quickly delineate all man-made objects in the current image being collected from a data acquisition platform. Then, if it is necessary, the current image may be compared with previously acquired images for change detection purposes. By automatically separating artificial objects in all the images, the process of change detection can be focussed on artificial objects. This would make the process more efficient. Delineation of artificial objects in an image presents opportunities to vectorise such geographical information for easy storage and retrieval purposes.

In this section, the advantage of background discriminant transformation (BDT) in semi-automatic extraction of artificial objects will be demonstrated. As discussed above, the color separation of artificial objects and natural objects can be made distinct using BDT. Using this property, both artificial and natural objects were automatically extracted from the BDT images of the AUSAR and SPOT set.

The semi-automatic extraction of objects was done using the K-Means clustering algorithm. It was specified that the whole image be clustered into four classes. Four classes were specified because in the BDT image four distinct shades of colors were noticeable. They were pink (artificial objects), green (vegetation), bluish (sparse grass cover or bare soil) and black (shadow of trees and buildings). Clustering has provided remarkably good result by classifying the pixels into objects as one would do manually along the color clues described above (Figure 6a).

The same clustering process was applied to the first three principal components (see section 6) of the SPOT XS and AUSAR image set. The result is shown in Figure 6b. As seen in the figure the classification is noisy. A lot of pixels belonging to the natural class are mis-classified as artificial objects. Within the natural class also there are significant mis-classifications. For example large areas are clustered as tree covered areas while they are actually open fields. Figure 6 clearly demonstrates the effectiveness of BDT in separating objects in to broad classes.

8 CONCLUSIONS

This study has demonstrated the applications of Background Discriminant Transformation (BDT) in the:

- separation of natural and artificial objects
- detection of small objects
- fusion of dissimilar types of images (SAR and Optical)
- detection of ships in oceans

There are theoretical advantages in BDT over other known techniques of image enhancement such as principal component transformation and image differencing. They are:

- BDT is scale invariant, which enables fusion of different types of data.
- the enhancement is tunable to user requirements by choosing an appropriate background.

It has been demonstrated that artificial objects can be automatically extracted very efficiently after transforming the data using BDT.



a



b

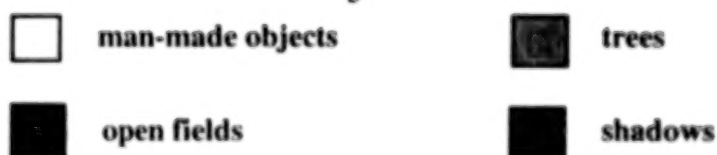


Figure 6 a) K-Means clustering of the BDT enhanced image of the AUSAR and SPOT XS set. Clustering was initiated by providing seed pixels for each of the four classes indicated by their distinct colors.
 b) K-Means clustering of the PC image of the AUSAR and SPOT XS set. Only the first three PCs were used. Clustering procedure was the same as in a.
 The BDT enhanced image facilitates much better and more accurate clustering than the PC image.

ADDITIONAL NOTE

The BDT procedure was developed for processing color (multispectral) images and only color images convey the potential of the technique fully. This paper is an extraction from a report on BDT by the authors (Shettigara and Sumerling, 1994), which contains color pictures to demonstrate the power of BDT.

Some aspects of this study are the subject of patent applications.

BIBLIOGRAPHY

- Boulter, J.F., 1983, Spatial Filtering for Enhancing Point Targets in Images from a Space-Based Mosaic IR Detector, Unclassified No. 4287/83, Research and Development Branch, Department of National Defence Canada.
- Crist E.P. and Ciccone, R.C., 1984, A physically based transformation of thematic mapper data-the TM Tasseled Cap, IEEE Transactions on Geoscience and Remote Sensing, GE22, pp. 256-263.
- Goward, S.N., and Wharton, S.W., 1984, Use of the TM Tasseled Cap transform for interpretation of spectral contrasts in an urban scene, 1984 Machine Processing of Remotely Sensed Data Symposium, pp. 84 - 91
- McKeown Jr, D. M., 1988, Building knowledge-based systems for detecting man-made structures from remotely sensed imagery, Philosophical Transactions of the Royal Society of London, 324, pp 423-435
- Moran, W., 1993, Detection of Man-Made Objects on Synthetic Aperture Radar (SAR) images, Personal communication.
- Ormsby, J. P., 1992, Evaluation of natural and man-made features using Landsat TM data, International Journal of Remote Sensing, 13, pp. 303-318.
- Rankin, J.R., 1989, Computer Graphics Software Construction using the Pascal Language, Prentice Hall, New York.
- Shettigara, V.K. and Sumerling, G.M., 1994, Separation of artificial and natural objects and small objects of defence significance in civilian satellite images, Report ERL-0821-RR, Electronics & Surveillance Research Laboratory, Defence Science and Technology Organisation, Australia, 50p.
- Shettigara, V.K., 1991, Image enhancement using background discriminant transformation, International Journal of Remote Sensing, 12, pp. 2153-2167.
- Wharton, S.W., 1987, A spectral knowledge based approach for urban land cover discrimination. IEEE Transactions on Geoscience and Remote Sensing, GE25, pp. 272-282
- Wheeler, D.J., 1986, Spectral characterisation of urban land covers for Thematic Mapper data, Symposium on Remote Sensing for Resources Development and Environmental Management, pp. 893 - 898

OPTIMAL ROUTING TECHNIQUES FOR FEEDFORWARD NEURAL NETWORKS AND PARALLEL DISTRIBUTED PROCESSORS

Perry J. LaPotin

Remote Sensing/GIS Center, U.S. Army Cold Regions Research and Engineering Laboratory
72 Lyme Road, Hanover, New Hampshire 03755, USA

and

School of Natural Resources, University of Vermont
Burlington, Vermont 05405, USA

and

Harlan L. McKim

Remote Sensing/GIS Center, U.S. Army Cold Regions Research and Engineering Laboratory
72 Lyme Road, Hanover, New Hampshire 03755, USA

ABSTRACT

In this paper optimal routing algorithms are provided for the design and implementation of feedforward neural networks (NN) and feedforward parallel distributed processors (PDP). The feedforward architectures are the focus of the analysis since their organization separates sequential processes from parallel processes, and optimal algorithms can be applied to the larger class of recurrent designs. Within the optimal routing algorithms, adaptation methods are used to govern the introduction and distribution of individual processors in the design. The purpose of the adaptation sequence is to produce PDP and NN architectures that are capable of recognizing portrayed test patterns in $k \geq 2$ multispectral or hyperspectral bands. Architectures that fulfill the derived recognition criteria are referred to as "candidate" designs since they are capable of recognizing the portrayed multispectral/hyperspectral test pattern, but may not be the final optimal network design for pattern recognition and analysis. Within the adaptation sequence, numerous candidate designs are generated that satisfy the criteria required for recognition. At the end of the adaptation sequence, candidate designs are evaluated, and a single optimal architecture is selected. The optimal architecture is the single design that minimizes the Bayes recognition error within prescribed tolerance limits for pattern recognition and/or pattern classification.

1.0 INTRODUCTION

Since the advent of parallel distributed processing (PDP)¹ and neural networks (NN)², various architectures have been proposed to model and recognize a diverse family of imagery³. The original work of Hebb (1949), the pioneering architectures of Rosenblatt (1958a, b), and the classic Perceptron modeling of Minsky and Papert (1972) have each shown that relatively simple parallel processing designs are capable of extremely complex adaptive learning. This complexity originates in the ability of each model to apply numerous parallel operators for the discrimination of often subtle patterns and features in test imagery. This style of adaptive learning

¹ A parallel processor is any machine design that allows for the parallel processing of information. Hence, any architecture that contains at least one layer of parallel elements can be characterized as a machine that is capable of parallel processing. A PDP is a design that is capable of distributing the parallel information across other elements in the design.

² A NN is a particular style of parallel processor whose parallel elements mimic the synaptic behavior of the brain. Therefore, these parallel elements are typically designed as purely Boolean processors and can be considered for modeling the axons and dendritic thresholds.

³ An image is any piece of input information that can be seen, displayed, scanned, or digitized. For example, an image can be any printed text such as the letter "P" or even the phrase: "the cows come home to be milked." An image can also be an analog film product such as a photograph or a lithographic print. Another example of an image is a digital product that is produced by image scanning or sensor input as exemplified by satellite imagery. Typically, this information is in the form of sequential pieces or bytes of data that comprise the colors within the image.

is important in the sense that the network is capable of learning by its mistakes and is capable of rewarding its own behavior in the event that it encounters a successful event.

A traditional computer architecture system executes statements in a sequential form. These systems are capable of sequential learning but are unable to adapt to changes in input stimuli. As an example, simple executable computer code is organized into procedures and functions that are executed from top to bottom with the capability of branching to other procedures and subroutines. While specific logic statements can be introduced into these programs, the actual computer code is set a priori and does not adapt to changes in input information of prior decisions within the system.

Conversely, parallel processing is non-queue oriented and may or may not contain sequential steps. In the design of a parallel architecture, each atom⁴ is capable of varying degrees of performance. In the case of a NN, each atom may be a simple Boolean detector. For example, the atom equals unity if it detects a certain condition within the image (e.g., a pixel is turned on) and equals zero otherwise. Conversely, an atom can perform more complicated tasks such as threshold detection or the processing of particular data as in the case of a standard language procedure or function. In all cases, however, the important distinction is in the fact that parallel processors operate independently of one another, whereas sequential processors require information from prior processors and are thus queue processors.

The design of a pattern recognition system can include both sequential and parallel operators. In the case of sequential operation, one processing step is directly dependent upon its predecessor, and the remainder of the operation cannot proceed without the information gained from the previous step. This is analogous to the traditional queuing problems or Markov chain modeling whereby current states are directly dependent (or autocorrelated with) the prior state. In the case of parallel operation, each processor acts as an independent entity and, therefore, is capable of unique behavior independent of prior states or adjacent operations. In the design of a parallel pattern recognition architecture, the system traditionally contains both sequential and parallel operators. The sequential operators typically handle the "management of information," such as summing prior states or performing decisions in "if-then-else" structures. Alternatively, the parallel operators handle information gathering and information "pipeline" tasks such as feature extraction and information transfer between system layers.

Within PDP and NN architectures statistical classification methods are employed to measure differences between scalar features and as a method to describe specific patterns. These methods are often criticized because they do not explicitly use the structural information that is contained within a scene, and summarize pattern boundaries using too few measures. These criticisms led to proposals for a linguistic model for pattern description whereby patterns are viewed as sentences in a language defined by a formal grammar (Hall 1988). The linguistic or syntactic model for pattern recognition uses a "primitive extractor," which transforms the input data into a string of symbols. The primitive extractor may itself be a feature extraction algorithm or an image classification process. A structural pattern analyzer then uses a formal grammar to parse the string and thus constructs a description of the pattern. In the past, much has been made of the apparent difference between the two models (i.e., statistical classification versus linguistic parsing). The stress on the distinction between the two models hides many similarities. In the syntactic model, the extraction of primitives can involve statistical classification procedures, and the association of patterns with generative grammars is equivalent to the classification of patterns into categories. The definition of the formal linguistic model can be enlarged to include other familiar generative mechanisms, such as differential models, functional equations, and finite-state Markov chains common in statistical analysis. Stochastic-syntactic models introduce probabilistic aspects into the linguistic model by specifying a discrete probability distribution over productions of a base grammar. For example, in the case of a n -class problem (a pattern containing n distinct classes), one could develop n stochastic grammars. Each parse provides a structure along with a probability that the structure represents the input pattern; the input is associated with the grammar giving the most probable parse (Fu and Swain, 1971; Fu, 1972; Batcher, 1980).

⁴The term "atom" is used to refer to a single primary processor within the PDP architecture. Each atom processes information and produces a product that is then routed to other elements (or atoms) in the design.

An outline of a formalism that attempts to combine the linguistic and statistical aspects of patterns has been presented in some thought provoking papers by Rumelhart and Zipser (1985). The major outlines of the designs are fairly easy to follow, but the details of the model are quite ambiguous and much interpretation must be provided by the reader (e.g. initial and boundary conditions). The statistical-linguistic model assumes we are given a set of primitive structural objects called signs, which together with known grammars or other known generative mechanisms, produce a set ζ of "pure images." Subsets of ζ satisfying certain similarity properties called "pure patterns." The pure images are subjected to probabilistic deformations to give a set ζ^D of deformed images. Recognition algorithms would then have to define the inverse mappings from the set of deformed images to the pure patterns. The formalism requires that there exists a method of analysis leading to a unique history of formation for any given image. In practice, however, most interesting problems contain deformed patterns corrupted by noise, and the deformations and generative mechanism must be discovered from a limited set of samples. Because there will rarely be a unique definition of primitives and generative mechanisms, there will rarely be a unique analysis as required by the model (Tank and Hopfield, 1986).

2.0 WEIGHT ADJUSTMENT

Parallel architectures employ weight adjustment methods to reinforce (dampen) the magnitude of specific atoms (processors) within the design. Reinforcement occurs when atoms receive information that aids in the pattern recognition and feature extraction process. Conversely, the signal strength may be modulated downward when atoms begin to process information that cannot be readily used within the feature extraction process. The form of the weight adjustment algorithm varies widely with the design of the architecture. For the general class of Multiple Layer Feedforward (MLF) architectures, the predominant weight adjustment technique is the delta rule (Forsyth and Rada, 1986).⁵ The delta rule is a gradient descent technique that is commonly employed in feedforward architectures (Anderson and Rosenfeld, 1989). The motivation for using this weight adjustment technique is as follows:

- (1) The delta rule can be equally applied to both single layer and multiple layer architectures, and is adapted to both feedforward and non-feedforward designs using information that is available within a single feedback step (Rumelhart and McClelland (1987)).
- (2) The delta rule is known to converge on an optimal set of weightings when two pattern classes are linearly separable. The approach has also been shown to be optimal for a wide variety of patterns that are not linearly separable such as mosaics and odd shaped regions (Sklansky and Wassel, 1981).
- (3) The delta rule and the general class of gradient descent techniques are both efficient and numerically robust. If random initial conditions are selected that significantly differ from the goal conditions, locally optimal solutions can be avoided (Rumelhart and McClelland, 1987).

The algorithm for applying the delta rule is provided in Equation (1.0). For the purpose of this discussion, a third subscript (c) has been added to the notation for each weight (α), atom (ϕ), and delta ordinate (δ). The third subscript is the cycle index c , that aids in our discussion of exactly *when* atom weights are updated within the PDP. As shown in Equation (1.0), each new weight in iteration $c + 1$ is calculated as a function of the old weight $\alpha_{i,j,c}$ minus the product of the delta ordinate, $\delta_{i,c}$, and the previous atom response $\phi_{i,j,c}$. Using this equation, the current iteration c of the PDP produces a new weight that will appear in the next subsequent iteration $c+1$, and the sequence of weight adjustment is repeated for each iteration c .

$$\alpha_{i,j,c+1} = \frac{1}{2} (\alpha_{i,j,c} - \delta_{i,c} \phi_{i,j,c}); \quad i = 1, \dots, L; j = 1, \dots, \omega_i \quad (1.0)$$

where

$\alpha_{i,j,c+1}$ is the new weight for atom $\phi_{i,j}$ in the next iteration $c+1$,

⁵The delta rule is commonly referred to as the *proportional increment training strategy* (Sklansky and Wassel, 1981). The method is based upon the original algorithm proposed by Rosenblatt (1958a,b), and Minsky and Selfridge (1961).

$\alpha_{i,j,c}$ is the weight for atom $\phi_{i,j}$ in the current iteration c ,

$\phi_{i,j,c}$ is the current Boolean atom response using the minimum modal rule,

$\delta_{i,c}$ is the ordinal value of the delta function in iteration c .

In Equation (1.0), the factor of $\frac{1}{2}$ is used to ensure that the new atom weight $\alpha_{i,j,c+1}$, is also bounded $[-1,+1]$ as required⁶. Also in Equation (1.0), the delta rule begins with a random initial weight for iteration $c = 0$. The initial weight is randomly selected within the interval $[-0.01, +0.01]$ for three important reasons:

- (1) A zero weight neither penalizes nor rewards the current atom for the signal that it received from the grafpot (Minsky and Papert, 1972). Each new atom is assigned an initial weight that is approximately neutral.
- (2) The initial weight assignment is randomly selected from within the small interval $[-0.01, +0.01]$ to minimize the likelihood of symmetric routing of the seekers in each layer (Rumelhart et al., 1986). A random value nearly equal to zero is used to maintain an approximately neutral weight assignment.
- (3) The initial weight assignment significantly differs from the goal weight. The assignment reduces the likelihood of locally optimal solutions within the delta rule (Rumelhart and McClelland, 1987).

In Equation (1.0), the delta ordinate $\delta_{i,c}$ is separately calculated for each layer i using the pivotal quantity $\frac{(\beta_{i+1} - \mu_0)}{s_{\beta_{i+1}} \sqrt{w_{i+1}}}$ as an index for the delta function:

$$\mathfrak{Z}_{i+1,c} = \frac{\beta_{i+1,c} - \mu_0}{s_{\beta_{i+1,c}} \sqrt{w_{i+1}}} \quad ; i = 1, \dots \quad (1.1)$$

where

$\beta_{i+1,c}$ is the mean seeker response in iteration c calculated using the w_{i+1} seekers that route information from layer i to layer $i+1$,

μ_0 is the critical value for the test equal to 0.95,

$s_{\beta_{i+1,c}}$ is the seeker standard deviation in iteration c calculated using the w_{i+1} seekers that route information from layer i to layer $i+1$,

$w_{i+1} = \omega_i \omega_{i+1}$, and

$\mathfrak{Z}_{i+1,c}$ is the index for the delta function $f_{\delta}(\mathfrak{Z}_{i+1,c})$ in iteration c .

The delta rule uses output responses to adjust the weights of all atoms in the architecture. For this reason, the pivotal quantity $\mathfrak{Z}_{i+1,c}$ in Equation (1.1) is calculated using information that is routed from layer i to layer $i+1$: $\beta_{i+1,c}$, $s_{\beta_{i+1,c}}$, and w_{i+1} . For each iteration c , the quantity $\mathfrak{Z}_{i+1,c}$ is used to index a delta function that scales the result to the required $[-1,+1]$ bound.

For the majority of feedforward PDP architectures, a Cauchy delta function is used to modulate the magnitude of $\mathfrak{Z}_{i+1,c}$. The Cauchy function is of the form:

⁶This may be seen by noting that: $\max\{\alpha_{i,j,c} - \delta\phi_{i,j,c}\} = +2$ when $\alpha_{i,j,c} = +1$, $\delta = -1$, and $\phi_{i,j,c} = 1$ (or $\alpha_{i,j,c} = +1$, $\delta = +1$, and $\phi_{i,j,c} = -1$). Similarly, the $\min\{\alpha_{i,j,c} - \delta\phi_{i,j,c}\} = -2$ when $\alpha_{i,j,c} = -1$, $\delta = +1$, and $\phi_{i,j,c} = 1$.

$$\delta_{i,c} = f_{\delta}(\mathfrak{Z}_{i+1,c}) = \frac{2}{\pi} \tan^{-1}(\mathfrak{Z}_{i+1,c}) ; i = 1, \dots, L ; -1 \leq f_{\delta}(\mathfrak{Z}_{i+1,c}) \leq +1 \quad (1.2)$$

The delta value $\delta_{i,c}$ is written using the subscript i (as opposed to $i + 1$) since the value is used to adjust the weights α_{ij} in layer i . Note that the delta function $f_{\delta}(\mathfrak{Z}_{i+1,c})$ is indexed by information that is routed from layer i to layer $i + 1$. For this reason, the pivotal quantity $\mathfrak{Z}_{ii+1,c}$ shown in Equation (1.1) is expressed using the subscript $i + 1$.

The motivation for using a Cauchy delta function is as follows:

- (1) The Cauchy function is bounded in the interval $[-1, +1]$ and crosses the origin when the quantity $\mathfrak{Z}_{i+1,c} = 0$. In traditional PDP architectures, the function is commonly applied as a weight adjustment strategy (e.g. Sejnowski and Rosenberg, 1986; Gibbons and Rytter, 1990).
- (2) The function is derived as a direct representation of the ratio of two Normally distributed random variables (Johnson and Kotz, 1970). The cumulative distribution function for Equation (1.2) may be interpreted probabilistically. Namely, the weighting of an atom is equal to the probability of the atom achieving its value or one value greater from the underlying Cauchy distribution⁷.
- (3) The Cauchy function is a standard distribution function. Cauchy indices are efficiently tabulated using high level calls to a standard C library.

By combining Equations (1.1) and Equation (1.2), the ordinal value for the delta function in iteration c is given as:

$$\delta_{i,c} = \frac{2}{\pi} \tan^{-1} \left\{ \frac{\beta_{i+1,c} - \mu_0}{s_{\beta_{i+1,c}} / \sqrt{w_{i+1}}} \right\} ; \quad i = 1, \dots, L \quad (1.3)$$

Substituting Equation (1.3) into Equation (1.0), each weight is assigned the value:

$$\alpha_{i,j,c+1} = \frac{\alpha_{ijc}}{2} - \frac{\phi_{ijc}}{\pi} \tan^{-1} \left\{ \frac{\beta_{i+1,c} - \mu_0}{s_{\beta_{i+1,c}} / \sqrt{w_{i+1}}} \right\} ; \quad i = 1, \dots, L \quad (1.4)$$

in iteration $c+1$ based upon the prior state of the weight $\alpha_{i,j,c}$, the prior state of the atom $\phi_{i,j,c}$, and the mean and standard deviation $\beta_{i+1,c}$ and $s_{\beta_{i+1,c}}$. In Equation (1.4), the weight adjustment increases with the number of seekers $w_{i+1} = \omega_i \omega_{i+1}$ routing information to the next successive layer, but decreases with the seeker dispersion as measured by $s_{\beta_{i+1,c}}$. The weight assigned to each atom in iteration $c+1$ is based upon one half the magnitude of the weight in the previous iteration c , minus a function of the previous Boolean response for the atom in iteration c . If the previous atom response $\phi_{i,j,c} = 0$, then $\alpha_{i,j,c+1} = \frac{\alpha_{ijc}}{2}$, and the weight declines by one-half (in a

⁷The Cauchy distribution can be derived as the transform of the quotient of two independent Normal random variables. In its general form, the Cauchy distribution is denoted as: $f(x; a, b) = \frac{1}{\pi b \{ 1 + [(x-a)/b]^2 \}}$; $-\infty < a < +\infty$, $b > 0$. For the special case when $a=0$ and $b=1$,

the distribution is written as: $f(x; 0, 1) = \frac{1}{\pi \{ 1 + x^2 \}}$ with a corresponding cumulative distribution function equal to: $F(x) = \int_{-\infty}^x \frac{du}{\pi \{ 1 + u^2 \}}$

$= \frac{1}{2} + \frac{1}{\pi} \tan^{-1}(x)$; $0 \leq F(x) \leq 1$. The Cauchy function shown in Equation (5.41) can then be calculated by re-normalizing the cumulative distribution function to match the required bound of $[-1, +1]$. This is accomplished by first subtracting $1/2$ from the cumulative distribution function and then multiplying that result by two since: $-1 \leq 2F(x) - 1 \leq +1$ for all cumulative distribution functions $F(x)$.

geometric progression) from iteration c to iteration $c+1$. Conversely, if $\phi_{i,j,c} = 1$, then the weight increases or decreases (from the base level of $\frac{\alpha_{ijc}}{2}$) by a factor of:

$$\frac{1}{\pi} \tan^{-1} \left\{ \frac{\beta_{i+1,c} - \mu_0}{s_{\beta_{i+1,c}} / \sqrt{w_{i+1}}} \right\}. \quad (1.5)$$

For the conditions when $\beta_{i+1,c} < 0.95$, the quantity $\beta_{i+1,c} - \mu_0 < 0$, and the value of the delta ordinate is negative. However, since the quantity shown in Expression (1.5) is actually subtracted from the initial adjustment of $\frac{\alpha_{ijc}}{2}$ in Equation (1.4), the net influence is positive, and the weight adjustment increases from iteration c to iteration $c+1$. Conversely, when the mean seeker response exceeds the critical value μ_0 , the expression shown in Equation (1.5) is greater than zero, and the weights for layer i are adjusted downward from the initial adjustment of $\frac{\alpha_{ijc}}{2}$ in Equation (1.4). In short, the PDP performs weight adjustment in a monotonically increasing fashion provided that $\beta_{i+1,c} < \mu_0$. However, once the critical level is exceeded, the weight adjustment declines until the mean seeker response for the layer once again drops below the critical level of μ_0 . In this regard, weights oscillate near the μ_0 critical level depending on the mean seeker response in iteration c . Note that the behavior of the seekers in layer $i+1$ may be independent of the oscillatory behavior for the weights in the same layer, since their assignment depends upon a propagation term routed from the previous layer i .

3.0 OPTIMAL BEHAVIOR

Weights are adjusted within *each* iteration of the architecture. The weight adjustment is applied to atoms in all layers of the design ($i = 1$ to L) using a delta ordinate δ_c as shown in Equation (1.3). For a given iteration c , the delta ordinate is such that:

$$\delta_c = f_{\delta}(\mathfrak{Z}_c) = (2/\pi) \tan^{-1}(\mathfrak{Z}_c),$$

and the test statistic is such that:

$$\mathfrak{Z}_c = (\beta_c - \mu_0) / (s_{\beta_c} / \sqrt{\omega_L}).$$

Hence, the weights in a given layer are adjusted based upon the mean β_c and the standard deviation s_{β_c} of the final layer seekers ($\beta_{\mathfrak{Z},1,1,c}, \beta_{\mathfrak{Z},2,1,c}, \dots, \beta_{\mathfrak{Z},\omega_L,1,c}$), where ω_L is the width of the final layer.

Within a sequence of $c = 1$ to c'' iterations, the weights are recursively adjusted, and the behavior of the weight adjustment algorithm shown in Equation (1.3) varies depending on the value of: $\alpha_{i,j,c}$, $\phi_{i,j,c}$ and δ_c . In the following discussion, we will focus our attention on four specific cases that describe the optimal behavior of the weight adjustment algorithm. These cases are summarized in Table 1. The four cases are labeled from 1 to 4 along the left edge of the table, and the conditions that describe each case are presented in the second column. In the third column, the requirements for each condition are labeled, and the recursive behavior of the weight adjustment algorithm is presented in the fourth column. In the final column, examples are presented to show when the respective conditions apply to the PDP design. Since the PDP begins adaptation as a single layer single atom architecture, case 3 and case 4 apply to the PDP at the beginning of the adaptation period (while initializing the architecture). Case 2 applies if the single atom single layer architecture does not recognize the test pattern, and Case 1 applies when the single layer multiple atom architecture does not recognize the test pattern. Hence, the Case 1 recursive equation describes the general behavior of the PDP weight adjustment algorithm, and the remaining cases indicate early weight adjustment forms that are used as the architecture moves from a single atom single layer design to a multiple atom, multiple layer architecture.

TABLE 1: SUMMARY TABLE FOR THE BEHAVIOR OF THE
PDP WEIGHT ADJUSTMENT ALGORITHM.

In Case 1, the general form of the PDP weight adjustment algorithm is presented for iteration n . This equation describes the behavior of the recursive Equation (1.3), for a particular weight $\alpha_{i,j,\epsilon}$ located in Layer $i \geq 2$, given that $\alpha_{i,j,\epsilon}$, $\phi_{i,j,\epsilon}$ and δ_ϵ are not constant. In Case 2, the Boolean response of the atom $\phi_{i,j,\epsilon}$ is assumed to be constant, and in Case 3, the ordinal value of the delta function δ_ϵ is assumed to be constant. In the final case, both $\phi_{i,j,\epsilon}$ and $\alpha_{i,j,\epsilon}$ are assumed to be constant. As a result, the recursive behavior of the weight adjustment algorithm is greatly simplified.

Case	Condition	Requirements for the Condition	Weight Adjustment Equation for Iteration n	Example Architecture
1	nonconstant $\alpha_{i,j,\epsilon}$, $\phi_{i,j,\epsilon}$, δ_ϵ	Layer $i \geq 2$	$\alpha_{i,j,\epsilon+n} = \kappa^n \{ \alpha_{i,j,\epsilon} - \delta_\epsilon \phi_{i,j,\epsilon} \} - \kappa^{n-1} \delta_{\epsilon+1} \phi_{i,j,\epsilon+1}$ - ... - $\kappa^2 \delta_{\epsilon+n-2} \phi_{i,j,\epsilon+n-2} - \kappa \delta_{\epsilon+n-1} \phi_{i,j,\epsilon+n-1}$	Multi-Atom Multi-Layer
2	constant $\phi_{i,j,\epsilon}$	$\phi_{i,j,\epsilon}$ is located in Layer 1 or $m(\beta_{i,j,1,\epsilon}, \beta_{i,j,2,\epsilon}, \dots, \beta_{i,j,k,\epsilon})$ = ... = $m(\beta_{i,j,1,\epsilon+n}, \beta_{i,j,2,\epsilon+n}, \dots, \beta_{i,j,k,\epsilon+n})$	$\alpha_{i,j,\epsilon+n} = \kappa^n \{ \alpha_{i,j,\epsilon} - \delta_\epsilon \phi_0 \} - \kappa^{n-1} \delta_{\epsilon+1} \phi_0$ - ... - $\kappa^2 \delta_{\epsilon+n-2} \phi_0 - \kappa \delta_{\epsilon+n-1} \phi_0$	Multi-Atom Single Layer
3	constant δ_ϵ	β_ϵ or s_{β_ϵ} are constant	$\alpha_{i,j,\epsilon+n} = \kappa^n \alpha_{i,j,\epsilon} - \kappa^n \delta_0 \phi_{i,j,\epsilon} - \kappa^{n-1} \delta_0 \phi_{i,j,\epsilon+1}$ - ... - $\kappa^2 \delta_0 \phi_{i,j,\epsilon+n-2} - \kappa \delta_0 \phi_{i,j,\epsilon+n-1}$	Single Atom Single Layer
4	constant $\phi_{i,j,\epsilon}$ and δ_ϵ	Requirements 2 and 3 above	$\alpha_{i,j,\epsilon+n} = \kappa^n \alpha_{i,j,\epsilon} - \delta_0 \phi_0 \sum_{c=1}^n \kappa^c$	Single Atom Single Layer

3.1 CASE 1: NONCONSTANT $\alpha_{i,j,\epsilon}$, $\phi_{i,j,\epsilon}$, and δ_ϵ

In a multiple layer architecture with multiple atoms per layer, the values of: $\alpha_{i,j,\epsilon}$, $\phi_{i,j,\epsilon}$ and δ_ϵ are not restricted to constant values. For this case, the following recursive weight adjustment sequence is generated using Equation (1.3):

Iteration (1):

$$\alpha_{i,j,\epsilon+1} = \kappa \{ \alpha_{i,j,\epsilon} - \delta_\epsilon \phi_{i,j,\epsilon} \} \quad (1.6a)$$

Iteration (2):

$$\begin{aligned} \alpha_{i,j,\epsilon+2} &= \kappa \{ \alpha_{i,j,\epsilon+1} - \delta_{\epsilon+1} \phi_{i,j,\epsilon+1} \} \\ &= \kappa \{ \kappa \{ \alpha_{i,j,\epsilon} - \delta_\epsilon \phi_{i,j,\epsilon} \} - \delta_{\epsilon+1} \phi_{i,j,\epsilon+1} \} \\ &= \kappa^2 \{ \alpha_{i,j,\epsilon} - \delta_\epsilon \phi_{i,j,\epsilon} \} - \kappa \delta_{\epsilon+1} \phi_{i,j,\epsilon+1} \end{aligned} \quad (1.6b)$$

Iteration (3):

$$\begin{aligned}
 \alpha_{i,j,\epsilon+3} &= \kappa \{ \alpha_{i,j,\epsilon+2} - \delta_{\epsilon+2} \varphi_{i,j,\epsilon+2} \} \\
 &= \kappa \{ \kappa \{ \alpha_{i,j,\epsilon+1} - \delta_{\epsilon+1} \varphi_{i,j,\epsilon+1} \} - \delta_{\epsilon+2} \varphi_{i,j,\epsilon+2} \} \\
 &= \kappa \{ \kappa \{ \kappa \{ \alpha_{i,j,\epsilon} - \delta_{\epsilon} \varphi_{i,j,\epsilon} \} - \delta_{\epsilon+1} \varphi_{i,j,\epsilon+1} \} - \delta_{\epsilon+2} \varphi_{i,j,\epsilon+2} \} \\
 &= \kappa^3 \{ \alpha_{i,j,\epsilon} - \delta_{\epsilon} \varphi_{i,j,\epsilon} \} - \kappa^2 \delta_{\epsilon+1} \varphi_{i,j,\epsilon+1} - \kappa \delta_{\epsilon+2} \varphi_{i,j,\epsilon+2}
 \end{aligned} \tag{1.6c}$$

Iteration (4):

$$\begin{aligned}
 \alpha_{i,j,\epsilon+4} &= \kappa \{ \alpha_{i,j,\epsilon+3} - \delta_{\epsilon+3} \varphi_{i,j,\epsilon+3} \} \\
 &= \kappa \{ \kappa \{ \alpha_{i,j,\epsilon+2} - \delta_{\epsilon+2} \varphi_{i,j,\epsilon+2} \} - \delta_{\epsilon+3} \varphi_{i,j,\epsilon+3} \} \\
 &= \kappa \{ \kappa \{ \kappa \{ \alpha_{i,j,\epsilon+1} - \delta_{\epsilon+1} \varphi_{i,j,\epsilon+1} \} - \delta_{\epsilon+2} \varphi_{i,j,\epsilon+2} \} - \delta_{\epsilon+3} \varphi_{i,j,\epsilon+3} \} \\
 &= \kappa \{ \kappa \{ \kappa \{ \kappa \{ \alpha_{i,j,\epsilon} - \delta_{\epsilon} \varphi_{i,j,\epsilon} \} - \delta_{\epsilon+1} \varphi_{i,j,\epsilon+1} \} - \delta_{\epsilon+2} \varphi_{i,j,\epsilon+2} \} - \delta_{\epsilon+3} \varphi_{i,j,\epsilon+3} \} \\
 &= \kappa^4 \{ \alpha_{i,j,\epsilon} - \delta_{\epsilon} \varphi_{i,j,\epsilon} \} - \kappa^3 \delta_{\epsilon+1} \varphi_{i,j,\epsilon+1} - \kappa^2 \delta_{\epsilon+2} \varphi_{i,j,\epsilon+2} - \kappa \delta_{\epsilon+3} \varphi_{i,j,\epsilon+3} \\
 &\quad : \quad : \quad : \quad : \quad : \quad : \quad : \quad : \quad :
 \end{aligned} \tag{1.6d}$$

Iteration (n):

$$\begin{aligned}
 \alpha_{i,j,\epsilon+n} &= \kappa \{ \alpha_{i,j,\epsilon+n-1} - \delta_{\epsilon+n-1} \varphi_{i,j,\epsilon+n-1} \} \\
 &= \kappa^n \{ \alpha_{i,j,\epsilon} - \delta_{\epsilon} \varphi_{i,j,\epsilon} \} - \kappa^{n-1} \delta_{\epsilon+1} \varphi_{i,j,\epsilon+1} - \dots - \\
 &\quad \kappa^2 \delta_{\epsilon+n-2} \varphi_{i,j,\epsilon+n-2} - \kappa \delta_{\epsilon+n-1} \varphi_{i,j,\epsilon+n-1}
 \end{aligned} \tag{1.6e}$$

where $n \leq \epsilon$.

The recursive weighting sequence shown in Equation (1.6a-e) places less emphasis on later cycles⁸ than it does on early iterations since κ^n approaches zero for $\kappa = 1/2$. In addition, the general form shown in Equation (1.6e) can be significantly reduced if either $\varphi_{i,j,\epsilon}$ or δ_{ϵ} are constant for $\epsilon = 1$ to n iterations. Cases when either $\varphi_{i,j,\epsilon}$ or δ_{ϵ} are constant are presented in the following discussion.

3.2 CASE 2: CONSTANT $\varphi_{i,j,\epsilon}$

The Boolean response from atom $\varphi_{i,j,\epsilon}$ is constant for $\epsilon = 1$ to n iterations if:

- (a) the atom $\varphi_{i,j,\epsilon}$ is located in the first layer of the architecture, or
- (b) the weighted Boolean response from the previous layer does not vary sufficiently so as to change the minimum mode of the seekers that connect the two layers.

In case (a), the Boolean values of each atom in the first layer are constant because the architecture does not alter the seeker sample ($\beta_{1,j,k,\epsilon}$). Since the $\beta_{1,j,k,\epsilon}$'s do not vary, the *min mode* ($\beta_{1,j,k,\epsilon}$) also remains fixed for $j = 1$ to ω_1 atoms in layer one, and $\epsilon = 1$ to n iterations. As a result, the Boolean output from the atoms in first layer: $\varphi_{1,1,\epsilon}, \varphi_{1,2,\epsilon}, \dots, \varphi_{1,\omega_1,\epsilon}$ does not vary.

⁸For example, if $n=10$ then $\kappa^n = 0.00097$.

In case (b), the minimum modal value of the weighted Boolean responses from the previous layer does not significantly change between iterations. Hence, for a single atom $\phi_{i,j,c}$, the minimum modes are equal across all iterations for $c = 1$ to n :

$$\begin{aligned} m(\beta_{i,j,1,c}, \beta_{i,j,2,c}, \dots, \beta_{i,j,k,c}) = \\ m(\beta_{i,j,1,c+1}, \beta_{i,j,2,c+1}, \dots, \beta_{i,j,k,c+1}) = \dots = \\ m(\beta_{i,j,1,c+n}, \beta_{i,j,2,c+n}, \dots, \beta_{i,j,k,c+n}), \end{aligned} \quad (1.7)$$

where the function $m()$ is the minimum mode of the enclosed arguments.

For layer two and above, information routed into an atom via a seeker $\beta_{i,j,k,c}$ contains only weighted data ($\alpha_{i-1,k,c}\phi_{i-1,k,c}$). In this regard,

$$\beta_{i,j,k,c} = \alpha_{i-1,k,c}\phi_{i-1,k,c} \text{ for each atom } j = 1 \text{ to } \omega_i \text{ in layer } i \geq 2 \quad (1.8)$$

where

$\alpha_{i-1,k,c}\phi_{i-1,k,c}$ is the weighted Boolean response from the previous layer $i-1$.

In Equation (1.8), the subscript k on $\beta_{i,j,k,c}$ replaces the subscript j in both $\alpha_{i,j,c}$ and $\phi_{i,j,c}$. This is due to the fact that for full connection designs:

$$\beta_{i,j,1,c} = \alpha_{i-1,1,c}\phi_{i-1,1,c}, \beta_{i,j,2,c} = \alpha_{i-1,2,c}\phi_{i-1,2,c}, \dots, \beta_{i,j,k,c} = \alpha_{i-1,k,c}\phi_{i-1,k,c}$$

Substituting Equation (1.8) into Equation (1.7) yields the following expanded form:

$$\begin{aligned} m(\alpha_{i-1,1,c}\phi_{i-1,1,c}, \alpha_{i-1,2,c}\phi_{i-1,2,c}, \dots, \alpha_{i-1,\omega_{i-1},c}\phi_{i-1,\omega_{i-1},c}) = \\ m(\alpha_{i-1,1,c+1}\phi_{i-1,1,c+1}, \alpha_{i-1,2,c+1}\phi_{i-1,2,c+1}, \dots, \alpha_{i-1,\omega_{i-1},c+1}\phi_{i-1,\omega_{i-1},c+1}) = \dots = \\ m(\alpha_{i-1,1,c+n}\phi_{i-1,1,c+n}, \alpha_{i-1,2,c+n}\phi_{i-1,2,c+n}, \dots, \alpha_{i-1,\omega_{i-1},c+n}\phi_{i-1,\omega_{i-1},c+n}) \end{aligned} \quad (1.9)$$

Now, since $\phi_{i-1,j,c} = m(\beta_{i-1,j,1,c}, \beta_{i-1,j,2,c}, \dots, \beta_{i-1,j,\omega_{i-1},c})$ for $i = 2$ to L and $j = 1$ to ω_i , Equation (1.9) becomes:

$$\begin{aligned} m(\alpha_{i-1,1,c} m(\beta_{i-1,1,1,c}, \beta_{i-1,1,2,c}, \dots, \beta_{i-1,1,\omega_{i-1},c}), \\ \alpha_{i-1,2,c} m(\beta_{i-1,2,1,c}, \beta_{i-1,2,2,c}, \dots, \beta_{i-1,2,\omega_{i-1},c}), \dots \\ \alpha_{i-1,\omega_{i-1},c} m(\beta_{i-1,\omega_{i-1},1,c}, \beta_{i-1,\omega_{i-1},2,c}, \dots, \beta_{i-1,\omega_{i-1},\omega_{i-1},c})) = \dots = \\ m(\alpha_{i-1,1,c+n} m(\beta_{i-1,1,1,c+n}, \beta_{i-1,1,2,c+n}, \dots, \beta_{i-1,1,\omega_{i-1},c+n}), \\ \alpha_{i-1,2,c+n} m(\beta_{i-1,2,1,c+n}, \beta_{i-1,2,2,c+n}, \dots, \beta_{i-1,2,\omega_{i-1},c+n}), \dots \\ \alpha_{i-1,\omega_{i-1},c+n} m(\beta_{i-1,\omega_{i-1},1,c+n}, \beta_{i-1,\omega_{i-1},2,c+n}, \dots, \beta_{i-1,\omega_{i-1},\omega_{i-1},c+n})). \end{aligned} \quad (1.10)$$

Contrasting Equation (1.9-1.10), the minimum modal values from the previous layer $i-1$ are equal across iterations if:

- (i) the previous layer's weight $\alpha_{i-1,j,c}$ or the minimum modal response from the previous layer's seekers $m(\beta_{i-1,j,1,c}, \beta_{i-1,j,2,c}, \dots, \beta_{i-1,j,\omega_{i-1},c})$ are equal to zero for $c = 1$ to n , or

- (ii) the minimum mode of the product of the previous layer's weight $\alpha_{i-1,j,\epsilon}$ and the minimum modal response from the previous layer's seekers $m(\beta_{i-1,1,1,\epsilon}, \beta_{i-1,1,2,\epsilon}, \dots, \beta_{i-1,1,\omega_{i-1},\epsilon})$ are constant across all iterations.

In Case (i), the weights are all equal to zero if $\delta_\epsilon \varphi_{i,j,\epsilon} = 0$ in Equation (1.6a). As a result, either $\delta_\epsilon = 0$ or $\varphi_{i,j,\epsilon} = 0$ for $\epsilon = 1$ to n . In Case (ii), the weights $\alpha_{i,j,\epsilon}$ and the atoms $\varphi_{i,j,\epsilon}$ can vary with each iteration cycle and still produce a constant minimum modal value of the weighted Boolean responses from the previous layer; however, the variation must be sufficiently small so as not to change the minimum modal response from the previous layer.

The expression shown in Equation (1.10) can be significantly reduced for the specific case of a multilayer architecture, where *each layer contains only one atom*. In the following derivation, we examine the behavior of the weight adjustment algorithm in $L \geq 2$ layers.

For an architecture with only one atom in each layer, the minimum modal response $m(\beta_{i,j,1,\epsilon}, \beta_{i,j,2,\epsilon}, \dots, \beta_{i,j,k,\epsilon})$ reduces to $\beta_{i,1,1,\epsilon}$ for $i = 2$ to L . However, in the first layer, the minimum modal response is still required since the seeker sample from the grafport may be larger than one. In this simple architecture, the value of $\varphi_{i,j,\epsilon}$ can be shown for each layer $i = 1$ to L :

$$\text{layer 1: } \varphi_{1,1,\epsilon} = m(\beta_{1,1,1,\epsilon}, \beta_{1,1,2,\epsilon}, \dots, \beta_{1,1,\omega_1,\epsilon}) = m_{1,1}$$

$$\text{layer 2: } \varphi_{2,1,\epsilon} = m(\beta_{2,1,1,\epsilon}) = \alpha_{1,1,\epsilon} \varphi_{1,1,\epsilon} = \alpha_{1,1,\epsilon} m_{1,1}$$

$$\text{layer 3: } \varphi_{3,1,\epsilon} = m(\beta_{3,1,1,\epsilon}) = \alpha_{2,1,\epsilon} \varphi_{2,1,\epsilon} = \alpha_{2,1,\epsilon} \alpha_{1,1,\epsilon} m_{1,1}$$

$$\text{layer 4: } \varphi_{4,1,\epsilon} = m(\beta_{4,1,1,\epsilon}) = \alpha_{3,1,\epsilon} \varphi_{3,1,\epsilon} = \alpha_{3,1,\epsilon} \alpha_{2,1,\epsilon} \alpha_{1,1,\epsilon} m_{1,1}$$

$$\vdots \quad \vdots \quad \vdots \quad \vdots \quad \vdots \quad \vdots \quad \vdots \quad \vdots$$

$$\text{layer } L: \varphi_{L,1,\epsilon} = m(\beta_{L,1,1,\epsilon}) = \alpha_{L-1,1,\epsilon} \varphi_{L-1,1,\epsilon}$$

$$= \alpha_{L-1,1,\epsilon} \alpha_{L-2,1,\epsilon} \dots \alpha_{1,1,\epsilon} m_{1,1} = m_{1,1} \prod_{i=1}^{L-1} \alpha_{i,1,\epsilon} \quad (1.11)$$

where $m_{1,1}$ is the minimum modal value of the seeker sample from the grafport to the first layer atom $\varphi_{1,1}$.

As presented in Equation (1.11), the minimum mode $m_{1,1}$, is constant for each iteration. As a result, the Boolean response from the first layer is also constant for each iteration. Conversely, each subsequent layer 2 to L shows a constant value for $\varphi_{i,j,\epsilon}$ only when either $m_{1,1} = 0$ or when $\prod_{i=1}^{L-1} \alpha_{i,1,\epsilon} = 0$. In this example, the product of the weights equals zero if any of the prior layer weights are equal to zero, and the minimum mode $m_{1,1}$ equals zero only when $m(\beta_{1,1,1,\epsilon}, \beta_{1,1,2,\epsilon}, \dots, \beta_{1,1,\omega_1,\epsilon}) = 0$.

If $\varphi_{i,j,\epsilon}$ is constant across iterations, then the recursive relationship shown in Equation (1.6a-e) can be significantly reduced. For example, suppose the PDP is a *single layer architecture*. For this case, the subscript i is always equal to one, and

$$\varphi_{1,j,\epsilon} = \varphi_{1,j,\epsilon+1} = \dots = \varphi_{1,j,\epsilon+n} = \varphi_0; j = 1 \text{ to } \omega_1 \text{ atoms in layer one}$$

where φ_0 is a constant that is Boolean valued.

As a result, the expression for iteration $n \leq \epsilon''$ in Equation (1.6e) can be simplified to the following form:

Iteration (n):

$$\alpha_{1,j,t+n} = \kappa (\alpha_{1,j,t+n-1} - \delta_{t+n-1} \varphi_0) \quad (1.12a)$$

$$\begin{aligned} &= \kappa^n (\alpha_{1,j,\epsilon} - \delta_{\epsilon} \varphi_0) - \kappa^{n-1} \delta_{\epsilon+1} \varphi_0 - \dots - \kappa^2 \delta_{\epsilon+n-2} \varphi_0 - \kappa \delta_{\epsilon+n-1} \varphi_0 \\ &= \kappa^n (\alpha_{1,j,\epsilon}) \text{ if } \varphi_0 = 0 \text{ and} \end{aligned} \quad (1.12b)$$

$$= \kappa^n (\alpha_{1+\epsilon} - \delta_\epsilon) - \kappa^{n-1} \delta_{\epsilon+1} - \dots - \kappa^2 \delta_{\epsilon+n-2} - \kappa \delta_{\epsilon+n-1} \text{ if } \varphi_0 = 1 \quad (1.12c)$$

In Equation (1.12a), the weight $\alpha_{1,j,\kappa}$ varies within the first layer depending upon the constant φ_0 . Since φ_0 is calculated using the minimum modal value of the first layer seekers, the weight adjustment varies by the factor κ^n if the minimum modal value of the first layer seekers $(\beta_{1,j,1,\kappa}, \beta_{1,j,2,\kappa}, \dots, \beta_{1,j,k,\kappa}) = 0$ (as in Equation 1.12b), and varies by the more complex polynomial expression shown in Equation (1.12c) if the minimum mode $(\beta_{1,j,1,\kappa}, \beta_{1,j,2,\kappa}, \dots, \beta_{1,j,k,\kappa}) > 0$. Also, note that for a large number of iterations, κ^n becomes very small, and the influence of δ_κ is reduced in each subsequent iteration.

3.3 CASE 3: CONSTANT δ_c

The delta ordinate is constant within a sequence of n iterations if: $\delta_c = \delta_{c+1} = \dots = \delta_{c+n}$. This condition occurs only when $\Im_c = \Im_{c+1} = \dots = \Im_{c+n}$, since $\delta_c = (2/\pi) \tan^{-1}(\Im_c)$.

The statistic \mathfrak{I}_c is constant if *both* the mean β_c and the standard deviation S_{β_c} for the final layer seekers is constant for each iteration cycle of the PDP (i.e., *both* $\beta_c = \beta_{c+1} = \dots = \beta_{c+n}$ and $S_{\beta_c} = S_{\beta_{c+1}} = \dots = S_{\beta_{c+n}}$).

Cases when: (a) β_x is constant, and/or (b) S_{β_x} is constant are presented in the following discussion:

3.4 WHEN β_c IS CONSTANT

The mean weighted Boolean response β_e from the final layer seekers is constant if the sum: $\sum_{k=1}^{w_L} \beta_{3,1,k,x}$ is constant for each iteration sequence. Hence,

$$\sum_{k=1}^{m_1} \beta_{3,1,k,\varepsilon} = \sum_{k=1}^{m_1} \beta_{3,1,k,\varepsilon+1} = \dots = \sum_{k=1}^{m_1} \beta_{3,1,k,\varepsilon+n}. \quad (1.13)$$

As shown in Equation (1.18), $\beta_{i,j,k,r} = \alpha_{i-1,k,r} \varphi_{i-1,k,r}$ for each atom $j = 1$ to ω_i in layer $i \geq 2$. As a result, the equality shown in Equation (1.13) is true only when the sum of the product $\sum_{i=1}^{\omega_L} \alpha_{L,j,r} \varphi_{L,j,r}$ is such that:

$$\sum_{j=1}^{m_1} \alpha_{l,j,x} \varphi_{l,j,x} = \sum_{j=1}^{m_1} \alpha_{l,j,x+1} \varphi_{l,j,x+1} = \dots = \sum_{j=1}^{m_1} \alpha_{l,j,x+n} \varphi_{l,j,x+n} \quad (1.14)$$

If we assume that the sum shown in Equation (1.14) is not equal across all iterations by happenstance (i.e., the positive weights and the negative weights do not somehow cancel one another out so as to produce the exact same sum for each iteration from $c = 1$ to n), then the products within the sum must be equal across all iterations. As a result,

$$\begin{aligned} \alpha_{L,1,\varepsilon} \varphi_{L,1,\varepsilon} &= \alpha_{L,1,\varepsilon+1} \varphi_{L,1,\varepsilon+1} = \dots = \alpha_{L,1,\varepsilon+n} \varphi_{L,1,\varepsilon+n} \\ \alpha_{L,2,\varepsilon} \varphi_{L,2,\varepsilon} &= \alpha_{L,2,\varepsilon+1} \varphi_{L,2,\varepsilon+1} = \dots = \alpha_{L,2,\varepsilon+n} \varphi_{L,2,\varepsilon+n} \\ &\vdots \\ \alpha_{L,\omega,\varepsilon} \varphi_{L,\omega,\varepsilon} &= \alpha_{L,\omega,\varepsilon+1} \varphi_{L,\omega,\varepsilon+1} = \dots = \alpha_{L,\omega,\varepsilon+n} \varphi_{L,\omega,\varepsilon+n} \end{aligned} \quad (1.15)$$

The condition shown in Equation (1.15) occurs in very restricted cases when the minimum modal response of the prior layer (L-1) does not alter each $\phi_{L,j,\epsilon}$ in the final layer L, and when the weight adjustment is such that the final layer weights are unchanged through $\epsilon = 1$ to n iterations in a given sequence.

As an example, consider the case when each $\phi_{L,j,\epsilon}$ is constant for each iteration in a sequence (i.e. $\phi_{L,j,\epsilon} = \phi_{L,j,\epsilon+1} = \dots = \phi_{L,j,\epsilon+n}$). As stated in the discussion preceding Equation (1.12a-c), this condition occurs in a *single layer PDP architecture* where $L=1$. Since the architecture contains no additional layers, the Boolean values $\phi_{1,j,\epsilon}$; $j=1$ to ω_1 are constant since the *min mode* ($\beta_{1,j,1,\epsilon}, \beta_{1,j,2,\epsilon}, \dots, \beta_{1,j,k,\epsilon}$) does not change for a given sequence. For constant values of $\phi_{1,j,\epsilon} \neq 0$, Equation (1.15) holds true only when the weights are such that: $\alpha_{1,j,\epsilon} = \alpha_{1,j,\epsilon+1} = \dots = \alpha_{1,j,\epsilon+n}$ for $j = 1$ to ω_1 . In addition, the first layer weights are constant across all cycles if, in the recursive Equation (1.0), $\alpha_{1,j,\epsilon+1} = \alpha_{1,j,\epsilon}$ for $j = 1$ to ω_1 . However, if $\alpha_{1,j,\epsilon+1} = \alpha_{1,j,\epsilon}$, then $\delta_\epsilon \phi_{1,j,\epsilon} = 0$ in Equation (1.0) and no weight adjustment occurs within the PDP architecture for $\epsilon=1$ to n iterations in a sequence.

Therefore, the mean final layer seeker response β_ϵ is constant only when there is no weight adjustment in the first layer of the PDP for each of the $\epsilon = 1$ to n iterations (given that $\phi_{1,j,\epsilon} \neq 0$ for $j = 1$ to ω_1).

3.5 CASE 4: CONSTANT $\phi_{1,j,\epsilon}$ AND δ_ϵ

If both $\phi_{1,j,\epsilon}$ and δ_ϵ are constant for $\epsilon = 1$ to n iterations, then the recursive relationship shown in Equation (1.12a-c) can be further reduced. Although this case is very restrictive, it adequately describes the weight adjustment behavior of a single atom single layer design. For the single atom single layer design, $\phi_{1,j,\epsilon} = \phi_{1,j,\epsilon+1} = \dots = \phi_{1,j,\epsilon+n} = \phi_0$ and $\delta_\epsilon = \delta_{\epsilon+1} = \dots = \delta_{\epsilon+n} = \delta_0$, where ϕ_0 is a Boolean valued constant, and δ_0 is a real valued constant such that $-1 \leq \delta_0 \leq 1$. For this particular architecture, Equation (1.12a-c) can be written as:

Iteration (n):

$$\begin{aligned} \alpha_{1,j,\epsilon+n} &= \kappa [\alpha_{1,j,\epsilon+n-1} - \delta_0 \phi_0] \\ &= \kappa^n [\alpha_{1,j,\epsilon} - \delta_0 \phi_0] - \kappa^{n-1} \delta_0 \phi_0 - \dots - \kappa^2 \delta_0 \phi_0 - \kappa \delta_0 \phi_0 \\ &= \kappa^n \alpha_{1,j,\epsilon} - \delta_0 \phi_0 (\kappa^n + \kappa^{n-1} + \dots + \kappa^2 + \kappa) \\ &= \kappa^n \alpha_{1,j,\epsilon} - \delta_0 \phi_0 \sum_{\epsilon=1}^n \kappa^\epsilon \end{aligned} \quad (1.16a)$$

$$\begin{aligned} &= \kappa^n [\alpha_{1,j,\epsilon}] \text{ if } \phi_0 = 0 \\ &= \kappa^n \alpha_{1,j,\epsilon} - \delta_0 \sum_{\epsilon=1}^n \kappa^\epsilon \text{ if } \phi_0 = 1 \end{aligned} \quad (1.16b)$$

Also for the single atom single layer architecture, $S_{\beta_\epsilon} = 0$ and $\delta_\epsilon = 1$ for each iteration sequence. As a result, Equation (1.16b) reduces to:

$$\alpha_{1,j,\epsilon+n} = \kappa^n \alpha_{1,j,\epsilon} - \phi_0 \sum_{\epsilon=1}^n \kappa^\epsilon \quad (1.16c)$$

The expressions shown in Equation (1.16b-c) applies only to the case of an architecture with constant $\phi_{1,j,\epsilon}$ and constant δ_ϵ for $\epsilon = 1$ to n iterations.

4.0 CONCLUSION

If weights are applied prior to atom processing, then the seeker information is weighted before an atom begins to process the signal. Hence, the atom can still employ the minimum modal rule (or some competing Boolean or non-Boolean threshold rule); however, the input signal always contains previously weighted data. The PDP routing algorithms represent a specific implementation of this case since information coming from a previous layer is weighted information (for $i = 2$ to L). For the special case of atoms in layer 1, the input information is not weighted since each seeker samples pattern data directly from the image plane (multispectral/hyperspectral data volume). For layer two and above, information routed into an atom via a seeker $\beta_{i,j,k,\epsilon}$ contains only weighted data ($\alpha_{i-1,j,k,\epsilon} \phi_{i-1,j,k,\epsilon}$) as shown in Equation (1.8). In addition to receiving only weighted information for layer $i \geq 2$, each atom in the architecture produces a Boolean response that is weighted before it is routed to the next successive layer. This output weight is applied within the design, where the Boolean response from the atom $\phi_{i,j,\epsilon}$ is combined with the atom weight $\alpha_{i,j,\epsilon}$ to produce a new weighted Boolean response: $\alpha_{i,j,\epsilon} \phi_{i,j,\epsilon}$. This new response is then routed to the next layer using a seeker $\beta_{i+1,j,k,\epsilon}$. This routing method produces four major advantages:

- (a) The approach can be generalized to $L \geq 2$ layers, so that each new layer applies the same rules for receiving weighted information and each new layer applies the same rules for generating new weighted information.
- (b) The minimum modal rule combined with the proportional increment training strategy produces solutions to a wide array of pattern recognition problems that are not restricted to vector polygonal data.

"Although our learning results do not *guarantee* that we can find a solution for all solvable problems, our analyses and results have shown that as a practical matter, the error propagation scheme (the general multi-layer application of the proportional increment training strategy shown in Equation 5.3) leads to solutions in virtually every case."

Rumelhart and McClelland (1987, page 361)

- (c) The approach clearly separates the processing that is performed within the atom, from the processing that is performed outside the atom. The processing that is performed inside the atom is the minimum modal rule applied to the weighted Boolean responses from the previous layer ($i \geq 2$). The processing outside the atom includes the linking of the weight with the Boolean response of the atom.

Since each layer in the architecture represents a distinct processing path, separate multispectral/hyperspectral bands can be assigned to each architectural layer within the PDP structure. Tracing the routing path through the architecture yields an optimal propagation strategy, where initial conditions can be assigned based upon a priori defined test patterns. The routing paths are optimal for each of the four cases described in this manuscript since they represent the most efficient propagation strategy for both single layer and multiple layer MFF architectures.

REFERENCES

- Anderson, J.A. and E. Rosenfeld, (Eds.), 1989: *Neurocomputing: Foundations of Research*, MIT Press, Cambridge, Massachusetts.
- Batcher, K.E., 1980: "Sorting Networks and Their Applications," Proceedings of the AFIPS, Spring Joint Computer Conference.
- Forsyth, R. and R. Rada, 1986: *Machine Learning: Applications in Expert Systems and Information Retrieval*, Ellis Horwood Limited, Chichester.
- Fu, K.S., 1972: "On Syntactic Pattern Recognition and Stochastic Languages," in *Frontiers of Pattern Recognition*, Academic Press, New York.
- Fu, K.S. and P.H. Swain, 1971: "On Syntactic Pattern Recognition," in *Software Engineering*, vol. 2, J.T. Tou, Ed., Academic Press, New York.
- Gibbons, A. and W. Rytter, 1990: *Efficient Parallel Algorithms*, Cambridge University Press, Cambridge.

- Hall, P., 1988: *Introduction to the Theory of Coverage Processes*, John Wiley & Sons, New York.
- Hebb, D.O., 1949: *The Organization of Behavior*, New York: Wiley.
- Johnson, N.L. and S. Kotz, 1970: *Continuous Univariate Distributions*, Houghton-Mifflin, New York.
- Minsky, M. and S. Papert, 1972: *Perceptrons: An Introduction to Computational Geometry*, 2nd Ed., MIT Press, Cambridge and London.
- Minsky, M. and O. G. Selfridge, 1961: "Learning in Random Nets," *Fourth London Symposium on Information Theory*, Collin Cherry (Ed.), Butterworth Inc., Washington D.C.
- Rosenblatt, F., 1958a: "The Perceptron: A Theory of Statistical Separability in Cognitive Systems," Cornell Aeronautical Laboratory Report No. VG-1196-G-1.
- Rosenblatt, F., 1958b: "The Perceptron: A Probabilistic Model for Information Storage and Organization in the Brain," *Psych. Rev.*, vol. 65.
- Rumelhart, D.E. and J.L. McClelland, 1987: *Parallel Distributed Processing Vol. 1—Foundations*, MIT Press, Cambridge, Massachusetts.
- Rumelhart, D.E. and D. Zipser, 1985: "Feature Discovery by Competitive Learning," *Cognitive Science*, vol. 9, p75-112.
- Rumelhart, D.E., G.E. Hinton and R.J. Williams, 1986: "Learning Internal Representations by Error Propagation," in *Parallel Distributed Processing: Explorations in the Microstructures of Cognition*, MIT Press, Cambridge, Massachusetts, vol. 1.
- Sejnowski, T.J. and C.R. Rosenberg, 1986: "NETalk: A Parallel Network that Learns to Read Aloud," The Johns Hopkins University Electrical Engineering and Computer Science Technical Report, JHU/EECS-86/01, 32 pp.
- Sklansky, J. and G. Wassel, 1981: *Pattern Classifiers and Trainable Machines*, Springer-Verlag, New York.
- Tank, D.W. and J.J. Hopfield, 1986: "Simple 'Neural' Optimization Networks: An A/D Converter, Signal Decision Circuit, and a Linear Programming Circuit," *IEEE Trans. on Circuits and Systems*, vol. CAS-33, no. 5, p. 533-451, May.

BLANK PAGE

APPLICATION OF AVIRIS DATA TO ESTIMATE
DYNAMIC RANGE DEMANDS ON HYDICE

William S. Aldrich and William H. Farrand
SAIC
McLean, VA 22102, USA

William W. Stoner
SAIC
Billerica, MA 01821, USA

Robert W. Basedow
Hughes Danbury Optical Systems, Inc.
Danbury, CT 06810, USA

ABSTRACT

The match between the HYDICE (Hyperspectral Digital Imagery Collection Experiment) system dynamic range and scene radiance levels is illustrated for seven representative AVIRIS (Airborne Visible/Infrared Imaging Spectrometer) scenes. Since the HYDICE system is not yet flying, its saturation radiance curve and signal-to-noise ratio at the design spectral radiance are modeled. For comparison with AVIRIS radiance data, the HYDICE saturation and design radiance curves are scaled for the difference in atmospheric path between the HYDICE collection altitude and the AVIRIS collection altitude. The HYDICE radiance curves are plotted with the 99.99-th and 1.0-th or 0.1-th radiance percentiles for each AVIRIS scene.

1. INTRODUCTION

HYDICE is a spectral imaging research program funded under the FY91 U. S. Congressional Dual-Use Initiative. Under the program, the Government is acquiring the HYDICE sensor, an airborne imaging spectrometer. The sensor is under construction at Hughes Danbury Optical Systems; it is scheduled to begin characterization flights in 1994 and collections in 1995.

One of the goals of HYDICE is to advance deep ocean and coastal water applications of imaging spectrometry (Rickard et al., 1993). Deep water is dark, and to reduce sunglint it is desirable to make observations when the sun is low in the sky. Consequently, the HYDICE signal-to-noise specification was stated for a design radiance corresponding to a 5% Lambertian reflectance and a 60 degree solar zenith angle. At the same sensor settings, a non-saturating range of operation was stated up to a maximum radiance corresponding to an 85% Lambertian reflectance and a 60 degree solar zenith angle. Since the cosine of 60 degrees is equal to

0.5, the HYDICE maximum radiance specification is about half the radiance that might be encountered over snow covered slopes. The design and maximum spectral radiances were modeled with MODTRAN (Berk et al., 1989) and are plotted in Fig. 1.

To obtain the best match between HYDICE and the spectral radiance variation over a collection area, the investigator has the option of setting the integration time shorter or longer than the design time of 12.79 ms. Generally, the integration time is set to maximize the signal-to-noise ratio (SNR) while avoiding saturation in the spectra of interest. To prevent instrument saturation in collections over bright scenes, the integration time may be set as low as 1 ms. At low detector irradiance levels, the sensor noise is dominated by noise sources other than photon noise. Hence, close to the design radiance level, the SNR is nearly proportional to the detector irradiance. To increase the SNR, it may be desirable to increase the integration time. An integration time of 31 ms is achievable.

We estimated the spectral radiance demands on HYDICE with AVIRIS data for a variety of surface types: water, snow, vegetated, and sparsely vegetated. Ocean scenes at Los Angeles (White's Point) CA and the Florida Keys provide water radiance data. A Mammoth Mountain CA scene provides sunlit snow and shaded forest radiance data. A scene covering the Jasper Ridge Biological Preserve at Stanford CA provides radiance data on vegetated terrain. Radiance data for sparsely vegetated surfaces is provided by three Nevada scenes: Cuprite Mining District, Lunar Crater Volcanic Field, and Fallon Naval Air Station.

2. HYDICE SYSTEM DESCRIPTION

The HYDICE system consists of the sensor, stable mount, onboard radiometric calibrator, environmental controls, data recording system, and operator station, all integrated onto an aircraft. The ground segment includes a transportable data processing system.

The HYDICE system incorporates a variety of measures to achieve the sensitivity and dynamic range required for water and land applications. The focal plane array has three partitioned gains to match the variations in spectral irradiance from 400 to 2500 nm; the integration time is selectable; the data quality is monitored in real time by an operator; and the airborne platform permits collections over a range of altitude and air speed.

The HYDICE sensor is a pushbroom imaging spectrometer. The nadir-looking fore-optics images the scene on the entrance slit of the prism spectrometer. The entrance slit passes a strip image of the scene into the spectrometer, where the strip image is dispersed by a prism and focused onto a 320 by 210 indium antimonide (InSb) focal plane array detector. All 210 spectral samples for each of 312 ground samples on the ground swath are detected simultaneously. (312 rather than 320 as 8 detector columns are reserved to monitor

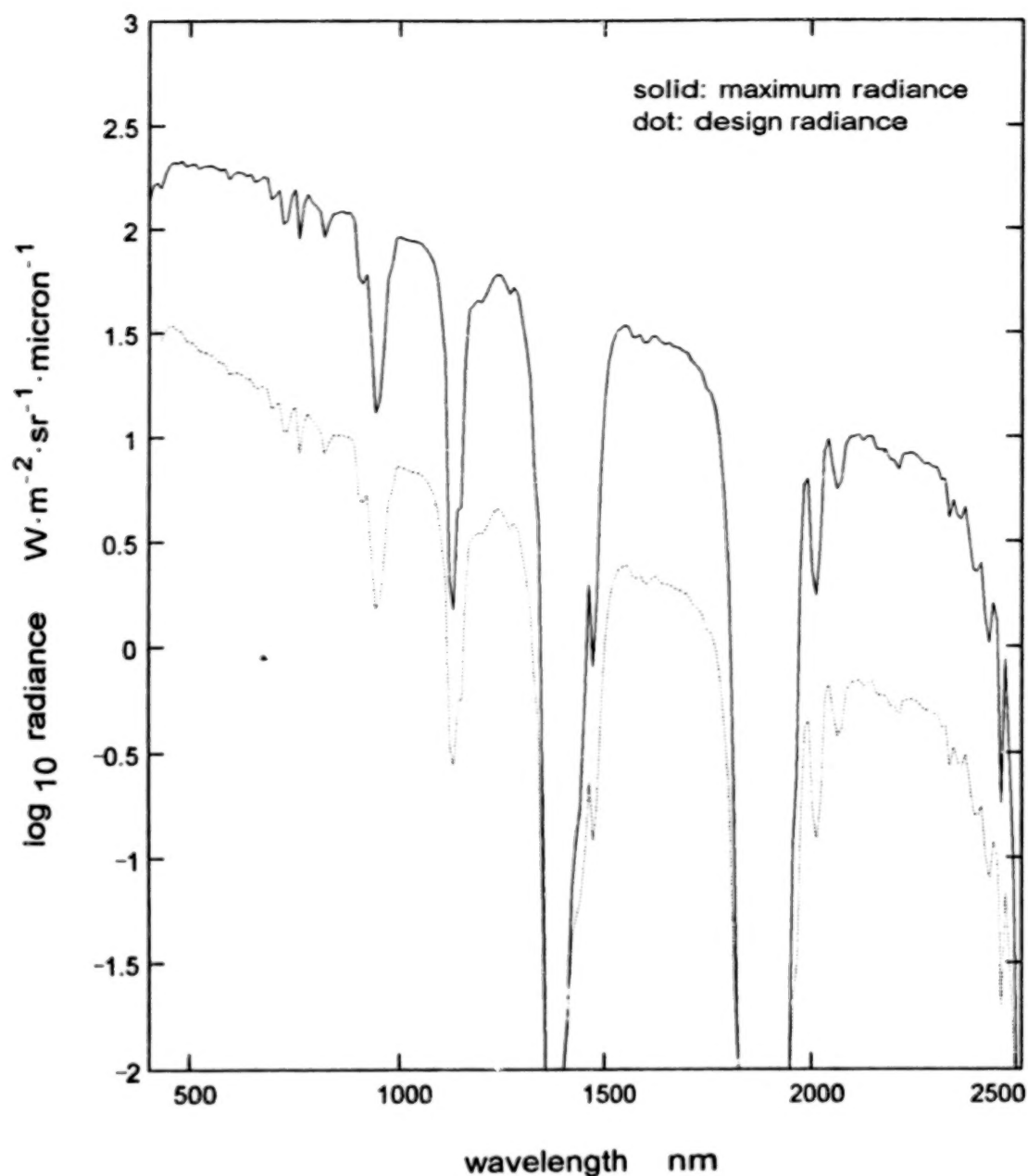


Figure 1. Plots of the design and maximum spectral radiances used in HYDICE specifications. The MODTRAN inputs for the design radiance were: midlatitude summer, multiple scattering, 23 km visibility maritime aerosol model for spring-summer, Mie model, 6 km sensor elevation, 0.05 reflectance, and a 60 degree solar zenith angle. For the maximum spectral radiance, the 23 km visibility rural aerosol model and a reflectance of 0.85 were used. The radiances were computed at 5 inverse cm resolution and averaged over 10 nm bands with centers at intervals of 10 nm from 400 to 2500 nm.

the thermal background radiation.) As the aircraft moves forward, the detector goes through a repetitive framing sequence of integration followed by electronic shuttering during the 7.3 ms readout of the entire array. Successive frames build up the image cube, which for HYDICE is nominally a 320 by 320 spatial array for each of 210 spectral samples.

As shown in Fig. 1, there is a large radiance variation over the HYDICE spectral range. To meet the HYDICE SNR requirements at the design radiance level, the noise floor must be small in the shortwave infrared, where the design radiance is smallest. To avoid saturation at the specified maximum radiance, the detector well depth must be large in the region around 1000 nm, where the sensor has the widest spectral bands. Since the image on the focal plane is spectrally dispersed, these constraints are satisfied by matching the spectral irradiance in three well depth and gain partitions. These and other key aspects of the focal plane design are illustrated in Fig. 2 (Rappoport et al., 1994).

The sensor instantaneous field-of-view (IFOV) is 0.5 milliradian, providing a 3 m ground spot diameter for a sensor elevation of 6 km. In the first year of operations, HYDICE will fly in the Environmental Research Institute of Michigan (ERIM) Convair CV-580. The altitude versus air speed collection envelope for the CV-580 is shown in Fig. 3 (data provided by William L. Gray of ERIM). The CV-580 is suited for collections from 2 km (6563 ft) above the ground up to an altitude of 7.62 km (25,000 ft). For collections of sea level targets, this range of altitudes corresponds to a ground spot diameter range of 1.0 to 3.8 m. To avoid out-flying the instantaneous field-of-view (IFOV), the 1 m ground spot requires a short integration time of about 7 ms. Even shorter integration times resulting in poor SNR performance would be required for collections at less than 2 km above the ground.

Generally, the CV-580 ground speed will be adjusted so that the forward motion during one frame time equals the IFOV; for a constant value of integration time the ground speed is directly proportional to the elevation above the ground. The three lines overlaid on the CV-580 envelope in Fig. 3 correspond to integration times of 30.70, 12.79, and 9.59 ms (2.4x, 1x, and 0.75x the design integration time). The line for 30.70 ms intersects the CV-580 envelope near its highest, slowest corner. Hence, the integration time cannot be increased much unless there is a strong head wind.

3. ESTMATING DYNAMIC RANGE DEMANDS ON HYDICE WITH AVIRIS DATA

AVIRIS data covers nearly the same 400 to 2500 nm spectral range as HYDICE, and is radiometrically calibrated to within an error of 5-7% across this spectral range (Green et al., 1993). If AVIRIS and HYDICE were nearly identical systems, the HYDICE dynamic range demands could be derived from the AVIRIS data after minor editing. However, significant differences do exist, and these need to be considered from the standpoint of radiometry. The

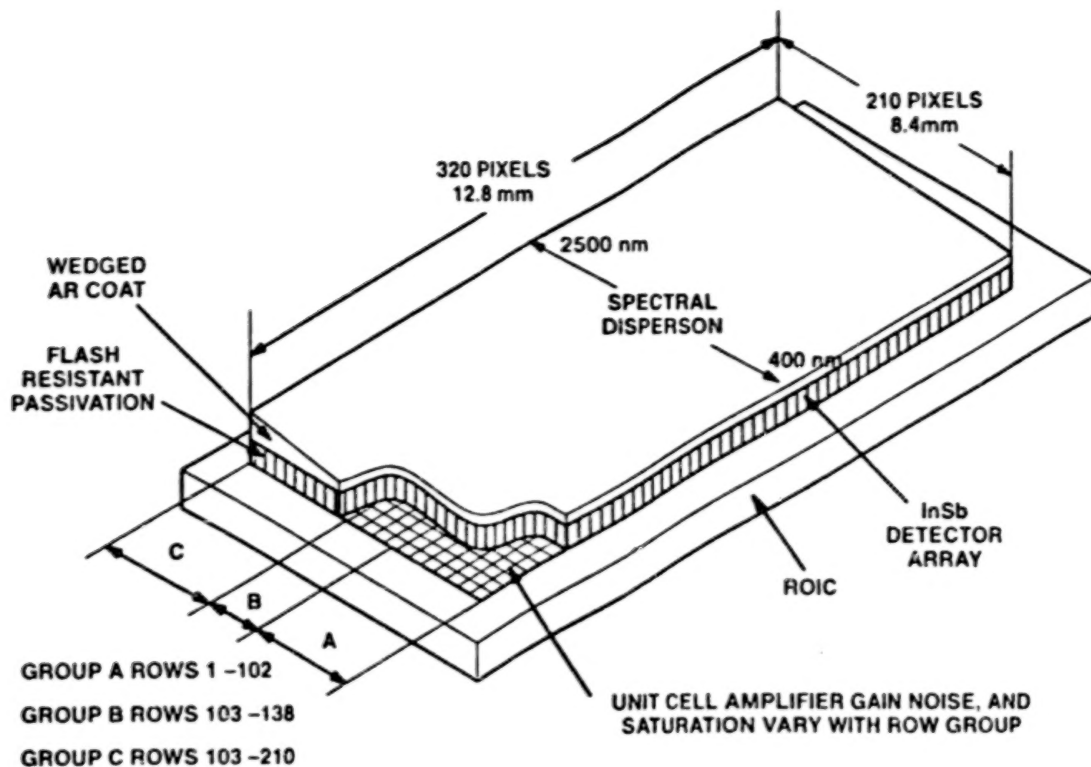


Figure 2. The HYDICE focal plane array structure (Rappoport et. al., 1994).

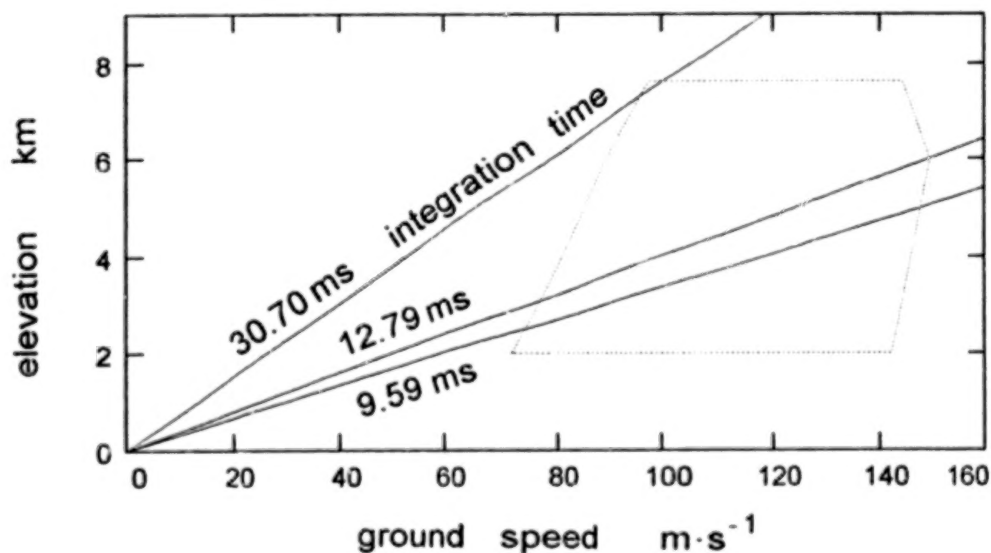


Figure 3. The ERIM CV-580 altitude versus air speed collection envelope is the dotted perimeter on this elevation and ground speed plot. (The plot applies to a target at sea level and no wind.) Pushbroom imaging (advancing one IFOV per frame period) is represented by straight lines of constant integration time. The overlap of a line with the CV-580 envelope shows the operation range for that integration time.

differences are the higher collection altitude, the larger ground spot diameter, and the larger noise equivalent delta radiance of AVIRIS compared with HYDICE.

AVIRIS operates from an ER-2 at an altitude of approximately 20 km (Chrien et al., 1991). Between the nominal HYDICE altitude of 6 km and the 20 km altitude where AVIRIS radiance data is collected, there is additional atmospheric scattering and absorption. To compare AVIRIS spectral radiances with the expected HYDICE performance, MODTRAN was used to scale the HYDICE design and saturation radiances to an altitude of 20 km.

HYDICE will resolve brighter and darker spots that are averaged within the AVIRIS ground spot. The ideal way to assess the increase in scene contrast that HYDICE will resolve is with spectral radiance data collected at 3 m resolution. Lacking this data, we can only make a rough estimate of the increase. In Section 4, we extrapolate AVIRIS radiances to a 3 m ground spot to predict an increase in contrast of about 4-10%. This extrapolation over a factor of 7 in spatial scale would be very interesting if it turns out to be accurate. Since the prediction is small and the extrapolation is unsubstantiated, we state the prediction but do not incorporate it in the rest of the analysis.

Noise in the AVIRIS data introduces an upward bias to the highest radiance percentiles and a downward bias to the lowest radiance percentiles. H. A. David's book, Order Statistics (David, 1981) contains expressions for estimating these biases. Consider a spatially uniform scene with 314,368 pixels (the same number of pixels as in an AVIRIS scene). In the complete absence of noise, all of the pixels will have the same spectral radiance curve. However, if noise is added to the measurements, the 99.99-th radiance percentile is defined by the 314,337-th highest ranked noise sample in each band. If the noise is Gaussian with a standard deviation of sigma, the upward bias is $3.718 \times \sigma$. In the more realistic case of a non-uniform scene, the bias will be less. If only 1% of the scene (3,144 pixels) is responsible for the highest radiance level, the 3,113-th highest ranked noise sample of the 3,144 will rank 314,337-th for the whole scene, so it will define the 99.99-th radiance percentile. This noise sample is biased upward by $2.325 \times \sigma$. The bias error is partially offset by the same type of biases within HYDICE. If extreme values of noise are more frequent than for Gaussian noise, the biases will increase. We expect that the biases will be negligible, since the noise equivalent delta radiance of both sensors is small compared to typical scene contrast. Accordingly, we ignore this effect in the rest of our analysis.

3.1 EDITING OF THE DATA

The spectral radiance variation within seven scenes was studied with the radiometrically calibrated AVIRIS data identified in Table 1. AVIRIS data for a single scene fills an image cube with nominal dimensions of 614 x 512 x 224. The number of valid

TABLE 1. THE AVIRIS DATA USED IN THE DYNAMIC RANGE STUDY

AVIRIS Scene	Scene Size	Year
Cuprite Mining District, NV	614 x 512	1992
Jasper Ridge Biological Preserve, Stanford, CA	614 x 512	1992
Lunar Crater Volcanic Field, NV	614 x 512	1989
Fallon Naval Air Station, NV	614 x 512	1993
Mammoth Mountain, CA	614 x 512	1993
White's Point, Los Angeles, CA	614 x 614	1991
Florida Keys	614 x 512	1992

spectral samples is actually 220, not 224, because AVIRIS's A, B, C, and D spectrometers output zeros in their first band (bands 1, 33, 97, and 161). Instead of using all 220 valid spectral bands, we used only 74 bands. The 74 bands provide adequate spectral resolution to assess the dynamic range of HYDICE. Since bands 1 and 161 are always zero, we used every 3rd band from 2 to 224, skipping band 161. One data set contained zeros in band 32 (1989 data for the Lunar Crater Volcanic Field), and in this instance, band 32 was also skipped.

In any band, the brightest 3 pixels in an AVIRIS scene have higher radiances than 99.999 percent of the scene (3 out of a total of $314368 = 614 \times 512$). It is not unusual for such very bright pixels to have twice the radiance of slightly lower percentiles. An effective way to weed out extremely bright pixels containing man-made structures like metal roofs is to accept a slightly lower percentile as the upper envelope of the natural background radiance. Therefore, we defined the upper envelope of spectral radiance using the radiance value of the 99.99-th percentile at each of the 74 spectral bands.

3.2 COMPARISON OF HYDICE DYNAMIC RANGE WITH SCENE RADIANCES

In addition to the AVIRIS radiance data, two analysis tools were needed to conduct the study:

- 1) the sensor radiometric model developed by Hughes Danbury Optical Systems, and
- 2) the MODTRAN atmospheric propagation code.

The sensor radiometric model was needed to predict the saturation spectral radiance as a function of the integration time. MODTRAN was needed to scale radiances at the HYDICE altitude to the 20 km altitude of the AVIRIS measurements.

Since we did not have radiance data collected at the altitudes HYDICE will fly, we could not directly compare the AVIRIS radiance data with the sensor radiometric model to find an integration time that avoids saturation. We circumvented this problem by using MODTRAN to create an analog saturation radiance curve that is directly comparable with AVIRIS radiance curves. If the AVIRIS radiance data falls below the analog saturation curve, then HYDICE will not saturate.

We also used MODTRAN to create an analog to the design radiance curve that is directly comparable with the AVIRIS data. If the AVIRIS radiances lie above (below) this analog design radiance curve, then the radiances at the actual HYDICE collection altitude will be above (below) the design radiance curve.

Since the AVIRIS radiance data was measured at 20 km, the analog design and maximum radiances that apply at 20 km were computed with the same MODTRAN inputs as for Fig. 1, except for the altitude change from 6 km to 20 km. To create the analog saturation radiance curve for 20 km, we multiplied the saturation radiance curve from the sensor model by the ratio of the maximum radiance for 20 km to the maximum radiance for 6 km. Scaling from 6 km to 20 km makes very little difference for most of the spectrum. Because of scattering in the longer air column, the design radiance for 20 km is larger in the blue. Also, the deep absorption regions at 1400 and 1900 nm are not as deep at 20 km as at 6 km. Most of the atmospheric water is at lower altitudes, and sunlight scattered at high altitudes partially fills in the spectrum in these bands. After scaling to 20 km, the saturation radiance curve has peaks at 1400 and 1900 nm. This change is consistent with the higher radiances in these absorption bands at 20 km than at 6 km.

The appropriate HYDICE collection altitude for three of the scenes is the CV-580 ceiling of 7.62 km (Mammoth Mountain, White's Point, and the Florida Keys). For these scenes we used MODTRAN to create analogs to the saturation curve and the design radiance curve that are directly comparable to the AVIRIS data if HYDICE is flying at 7.62 km. To create the analog saturation radiance curve for HYDICE at 7.62 km, we multiplied the saturation curve from the radiometric model by the ratio of the maximum radiance for 20 km to the maximum radiance for 7.62 km (same MODTRAN inputs as for Fig. 1, except for the altitude input values of 20 km and 7.62 km). To create the analog design radiance curve for HYDICE at 7.62 km, we formed the ratio of design radiance values modeled with MODTRAN for

altitudes 20 km and 7.62 km. The ratio of these values was used to scale the design radiance modeled at an altitude of 6 km.

Using these analogs, the HYDICE dynamic range relative to the radiance variation within a scene can be judged by a three-step process. First, pick a compatible collection altitude and integration time that avoids saturating spectra at some selected radiance percentile, for instance the 99.99-th percentile. This involves scaling the 99.99-th percentile radiance curve by the ratio of the integration time to the design time. We used integration time scale factors of 2.4x, 1.0x, and 0.75x. Second, find the spectral radiance for a low radiance percentile of the scene, for instance the 1.0-th percentile. Third, using the ratio of the integration time to the design time, scale the radiance curve for this low percentile so that it can be compared with the design radiance. Since the modeled SNR changes nearly linearly with irradiance near the design radiance, HYDICE will deliver a proportionately higher (lower) SNR where the scaled AVIRIS radiance percentile falls above (below) the design radiance. The SNR expected at the design radiance is plotted in Fig. 4.

The results for the seven scenes are represented with graphs of four radiance curves as a function of wavelength. The top curve in each graph is the saturation radiance. Lying just underneath is the curve for a high radiance percentile, typically the 99.99-th percentile. Under the high radiance percentile curve is the low radiance percentile curve, typically the 1.0-th percentile. This curve typically crosses the design radiance curve at various points in the spectrum.

Each of the graphs (Figs. 5-15) pertains to a single AVIRIS scene. The following quirks are apparent in each graph. The saturation radiance curve has three steps corresponding to the three gain and well depth partitions of the focal plane array. As mentioned above, scaling of the saturation radiance curve to 20 km introduced peaks at 1400 and 1900 nm. All the curves have been interpolated to AVIRIS wavelengths, and since there is an overlap in the AVIRIS wavelengths between spectrometers, the curves back-track on themselves at three wavelengths.

The following scenes did not saturate (at the 99.99-th radiance percentile) for the design integration time of 12.79 ms:

- Fallon
- Lunar Crater Volcanic Field
- White's Point
- Florida Keys.

Good data quality is expected for Fallon and Lunar Crater Volcanic Field, since the 0.1-th radiance percentile in the AVIRIS data for these scenes lies well above the design radiance over nearly the entire spectral range for the scenes. See Figs. 5 and 6.

For the ocean scenes, the 1.0-th radiance percentile is close to the design radiance in the blue-green portion of the spectrum.

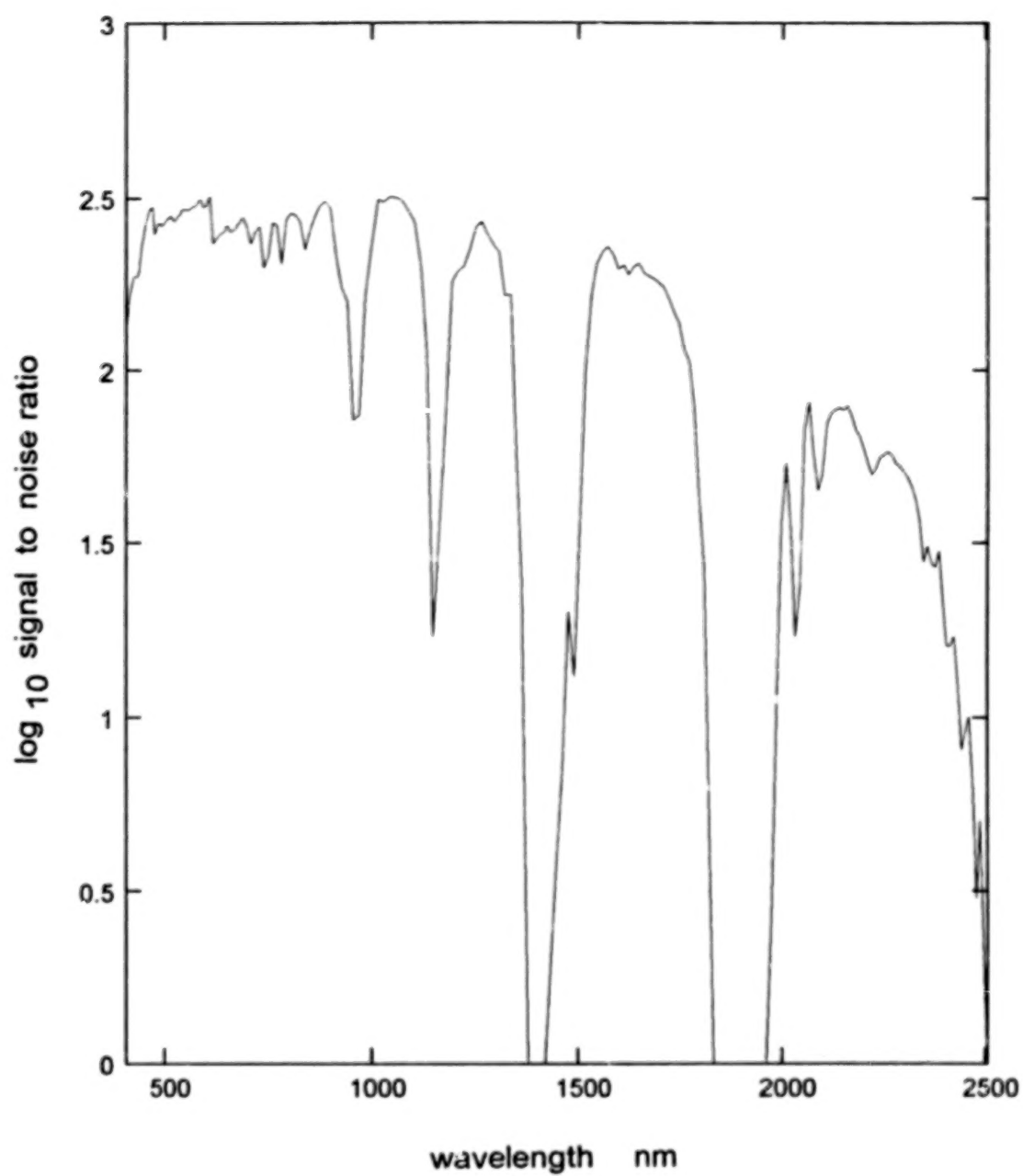


Figure 4. The HYDICE signal-to-noise ratio (SNR) is a function of the input spectral radiance. The SNR plotted above is modeled for the design spectral radiance.

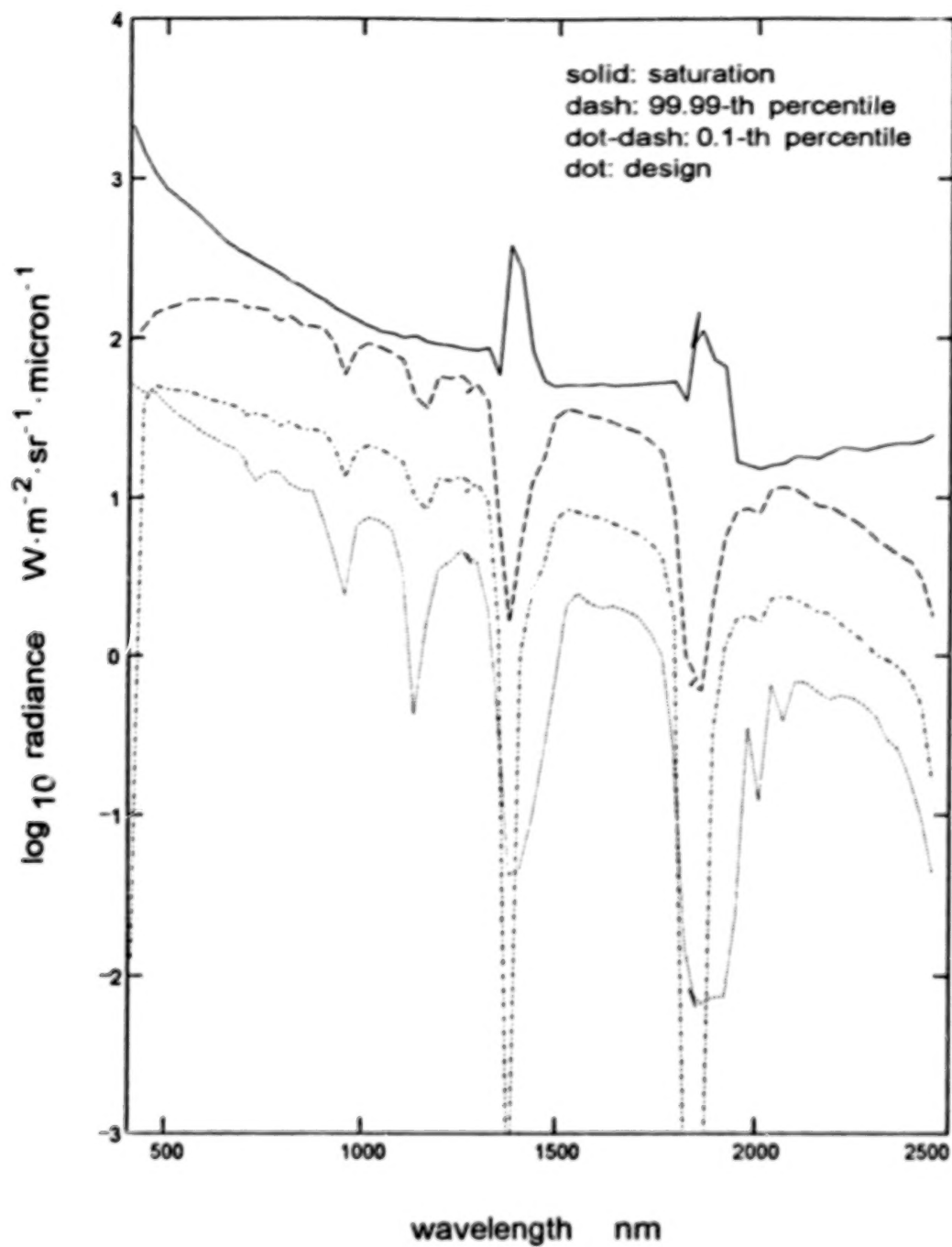


Figure 5. The Fallon scene at the design integration time of 12.79 ms: the 99.99-th and 0.1-th radiance percentiles are plotted with the saturation and design radiances.

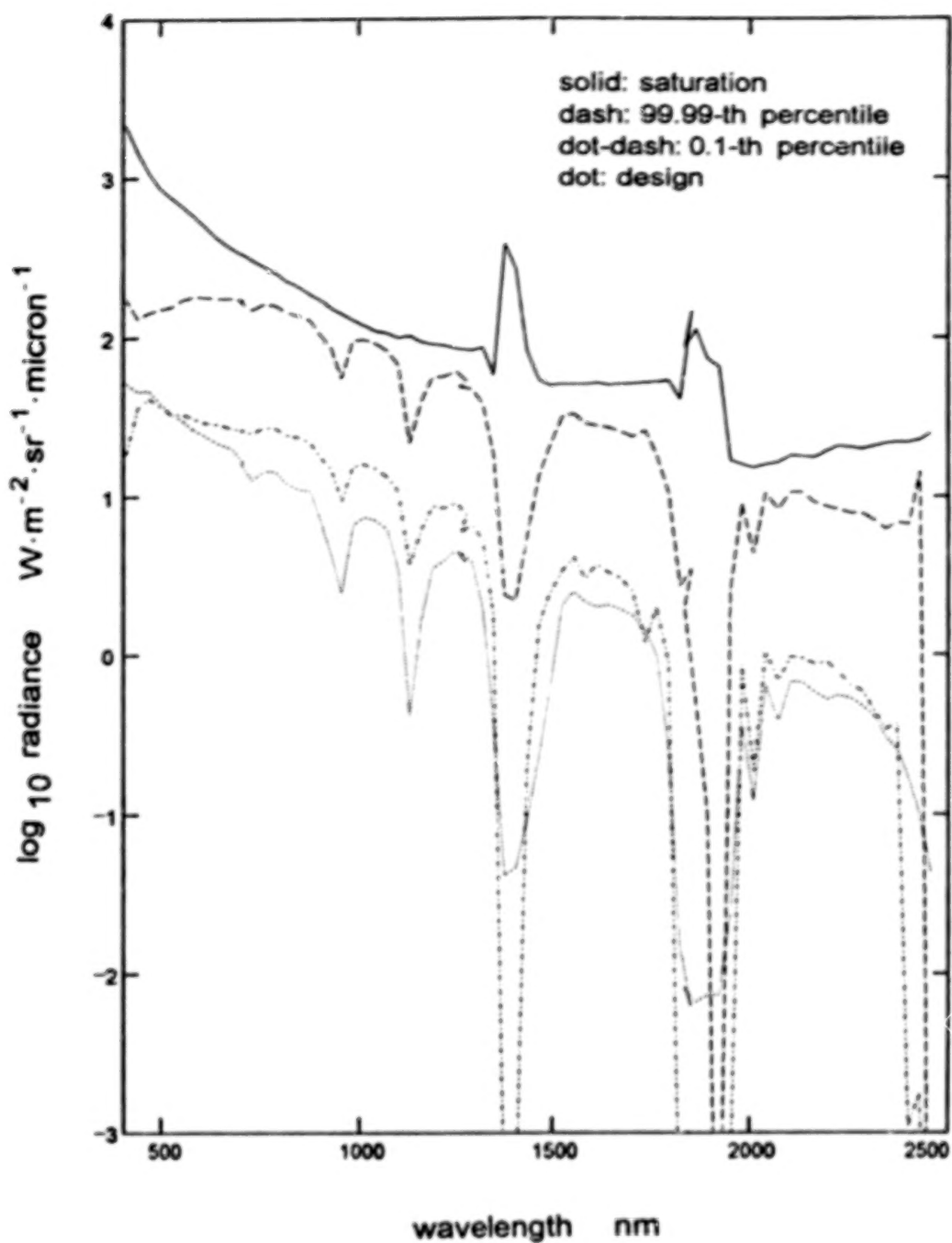


Figure 6. The Lunar Crater Volcanic Field scene at the design integration time of 12.79 ms: the 99.99-th and 0.1-th radiance percentiles are plotted with the saturation and design radiances.

See Figs. 7 and 8. The water pixels are far below saturation, so the integration time may be increased to improve the SNR of the water spectra. An increase by a factor of about 2.4x the design integration time is possible. (See Fig. 3, the collection envelope for the CV-580). Three things happen if the integration time is multiplied by 2.4. First, the spectral irradiance corresponding to the 1.0-th percentile is scaled by 2.4x, effectively raising this percentile above the design radiance from 400 to 660 nm for White's Point and from 400 to 760 nm for the Florida Keys. Second, the thermal background irradiance on the detectors is also multiplied by 2.4, and so the saturation threshold changes. Third, portions of the shore pixel spectra go into saturation. The saturation radiance is just above the 98.5-th percentile for White's Point and just above 98.9-th percentile for the Florida Keys scene. Since the primary interest in these collections is the water-leaving radiance, some saturation in spectra of shore pixels is a reasonable tradeoff. See Figs. 9 and 10 for high and low percentile data for these scenes compared with the saturation radiance and the design radiance at the 30.70 ms integration time (2.4x the design integration time). Since the CV-580 must fly near its 7.62 km ceiling to stretch out the integration time by a factor of 2.4, the saturation and design radiance curves in Figs. 9 and 10 are scaled for the AVIRIS altitude of 20 km and a HYDICE altitude of 7.62 km.

Since the 99.99-th radiance percentile for the three remaining scenes in our study saturated at the design integration time, an integration time of 9.59 ms (0.75x the design integration time) was used for the following scenes:

- Cuprite
- Jasper Ridge
- Mammoth Mountain.

To make a comparison between the saturation radiance and the 99.99-th radiance percentile at 0.75x the design integration, we recalculated the saturation radiance to account for the reduction by a factor of 0.75 in the thermal background irradiance, and we also scaled the 99.99-th radiance percentile by 0.75. See Fig. 11 for Cuprite, and Fig. 12 for Jasper Ridge. For Cuprite, the 0.1-th radiance percentile, after scaling by the factor of 0.75, lies well above the design radiance over most of the spectral range from 400 to 2500 nm. For Jasper Ridge, the scaled 1.0-th percentile lies above the design radiance over most of the spectral range from 500 to 1800 nm, but falls at or below the design radiance in the chlorophyll absorption region and from 2000 to 2500 nm.

The Mammoth Mountain scene demands a high dynamic range, since it contains both sunlit snow and shaded forest. The peak of the mountain is around 3.35 km (11,000 ft), and so HYDICE would probably be flown at the CV-580 ceiling of 7.62 km for this scene. Hence, the saturation radiance and design radiance curves were scaled for the AVIRIS altitude of 20 km and a HYDICE altitude of 7.62 km. Figure 13 shows the scaled 1.0-th radiance percentile against the design radiance, and the scaled 99.99-th percentile

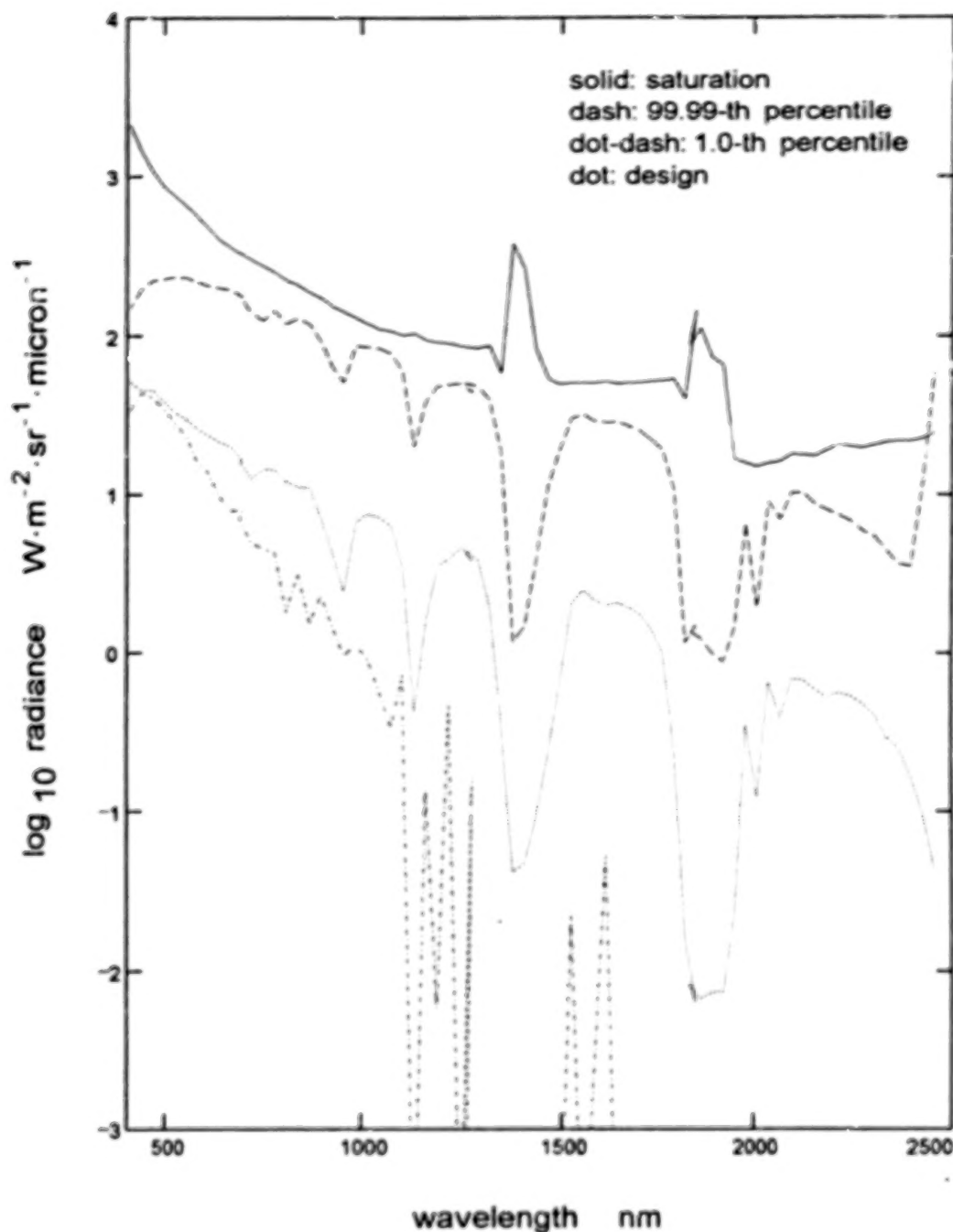


Figure 7. The White's Point scene at the design integration time of 12.79 ms: the 99.99-th and 1.0-th radiance percentiles are plotted with the saturation and design radiances. Since the scene is mostly water, the 1.0-th percentile closely corresponds to water; so at this percentile the water spectrum lies just below the design radiance in the blue-green. Figure 9 shows the situation for the same scene at a longer integration time.

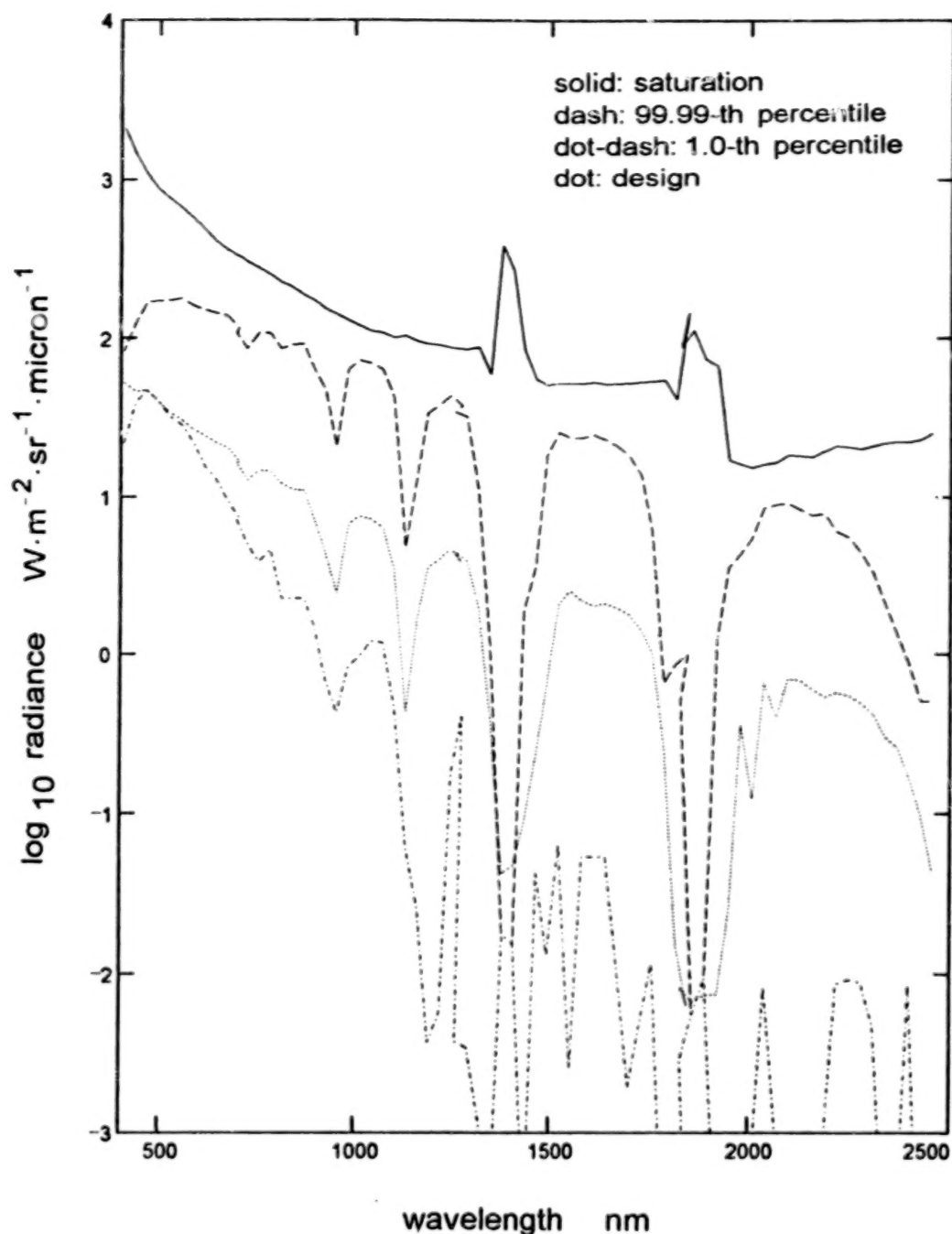


Figure 8. The Florida Keys scene at the design integration time of 12.79 ms: the 99.99-th and 1.0-th radiance percentiles are plotted with the saturation and design radiances. Since the scene is mostly water, the 1.0-th percentile closely corresponds to water; so at this percentile the water spectrum lies just at the design radiance in the blue-green. Figure 10 shows the situation for the same scene at a longer integration time.

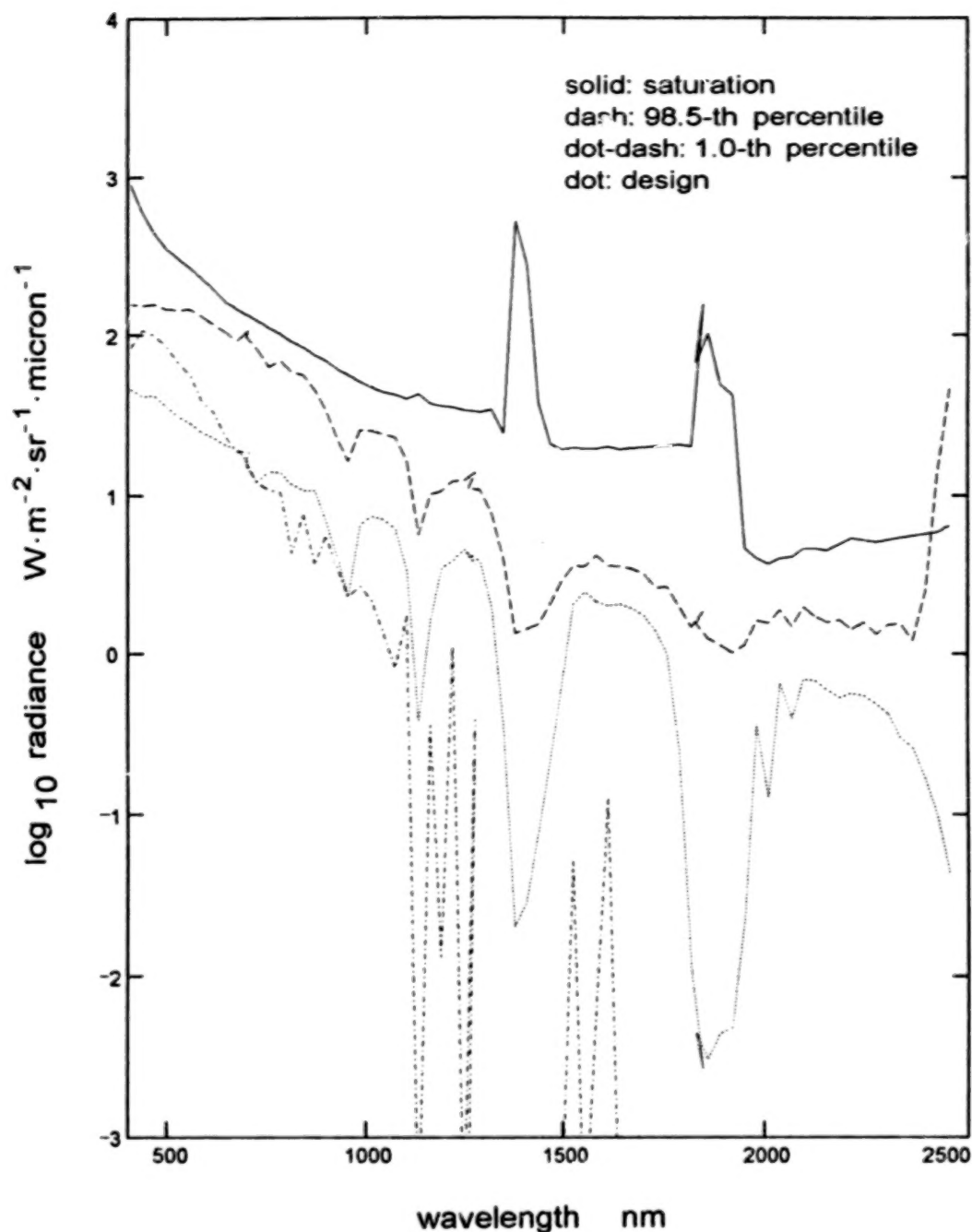


Figure 9. The White's Point scene at an integration time of 30.70 ms (2.4x design time): the 98.5-th and 1.0-th radiance percentiles have been scaled by a factor of (2.4) for comparison with the saturation and design radiances. Since the scene is mostly water, the 1.0-th percentile closely corresponds to water; so at this percentile the water spectrum lies above the design radiance from 400 to 660 nm.

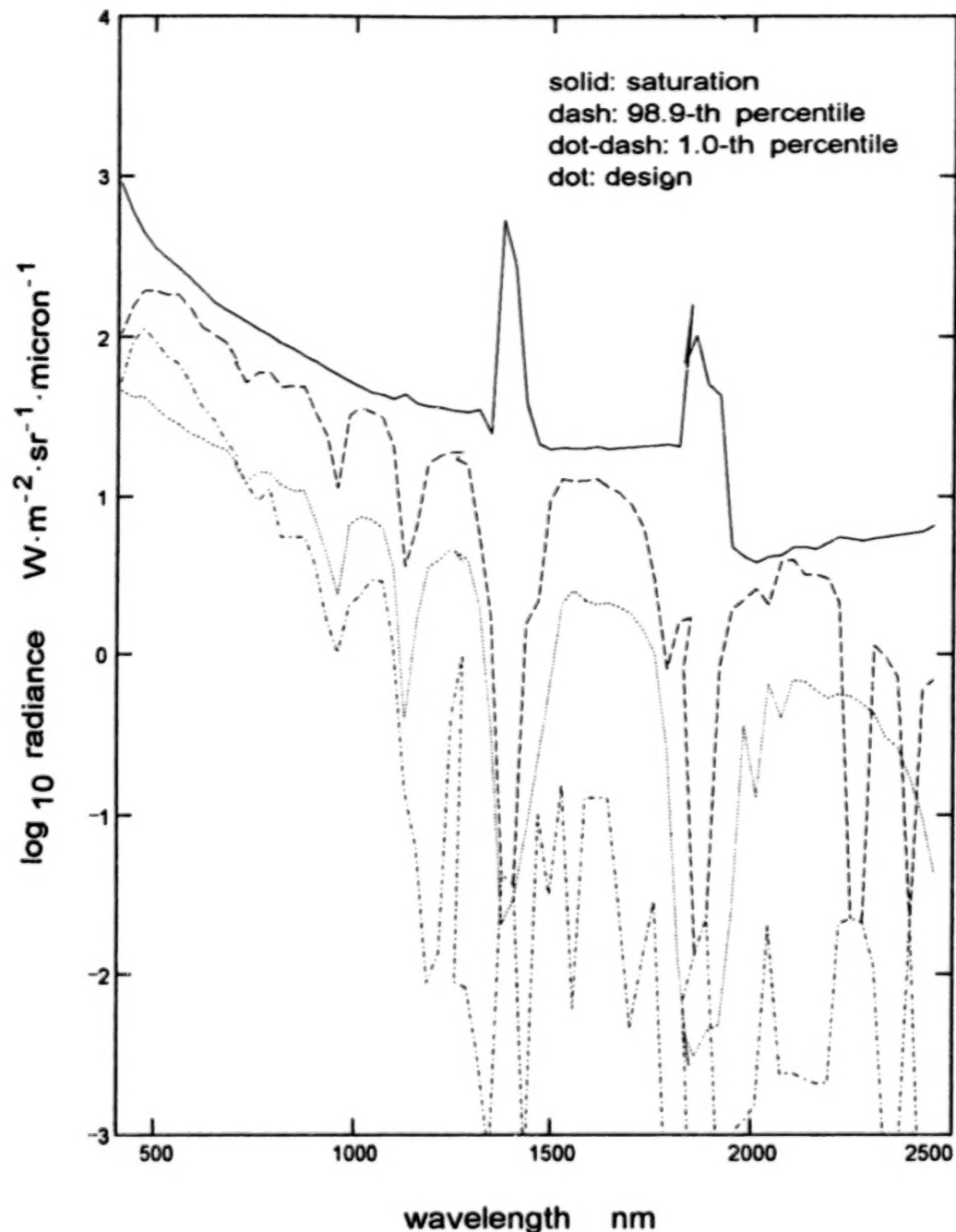


Figure 10. The Florida Keys scene at an integration time of 30.70 ms (2.4x design time): the 98.9-th and 1.0-th radiance percentiles have been scaled by a factor of (2.4) for comparison with the saturation and design radiances. Since the scene is mostly water, the 1.0-th percentile closely corresponds to water; so at this percentile the water spectrum lies above the design radiance from 400 to 700 nm.

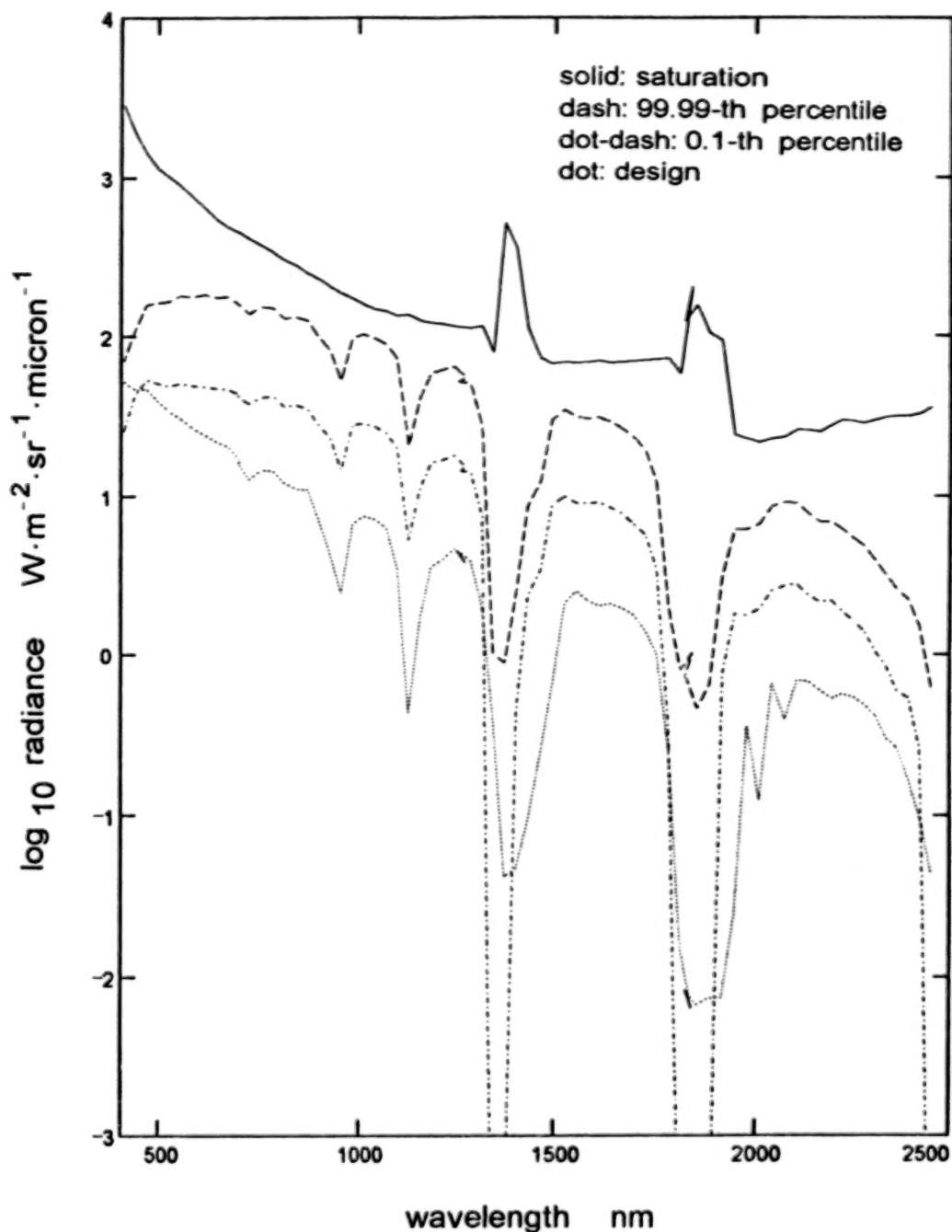


Figure 11. The Cuprite Mining District scene at an integration time of 9.59 ms (0.75x design time): the 99.99-th and 0.1-th radiance percentiles have been scaled by a factor of (0.75) for comparison with the saturation and design radiances. The gap between the saturation radiance and the 99.99-th percentile shows that a slightly longer integration time could have been used without saturating any spectra at this percentile.

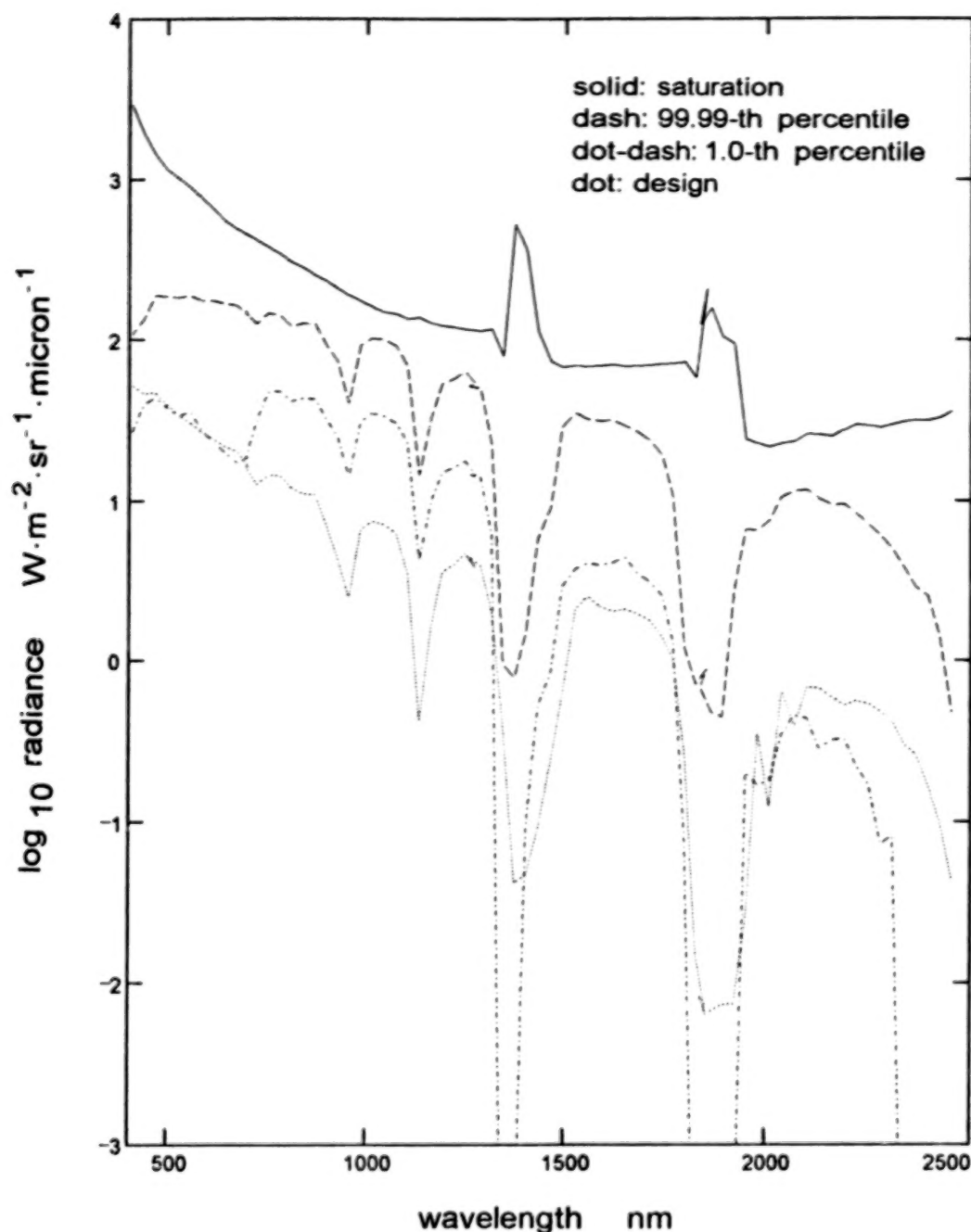


Figure 12. The Jasper Ridge scene at an integration time of 9.59 ms (0.75x design time): the 99.99-th and 1.0-th radiance percentiles have been scaled by a factor of (0.75) for comparison with the saturation and design radiances. The 1.0-th percentile dips below the design radiance from 400 to 700 nm and from 2000 to 2500 nm. The gap between the saturation radiance and the 99.99-th percentile shows that a slightly longer integration time could have been used without saturating any spectra at this percentile.

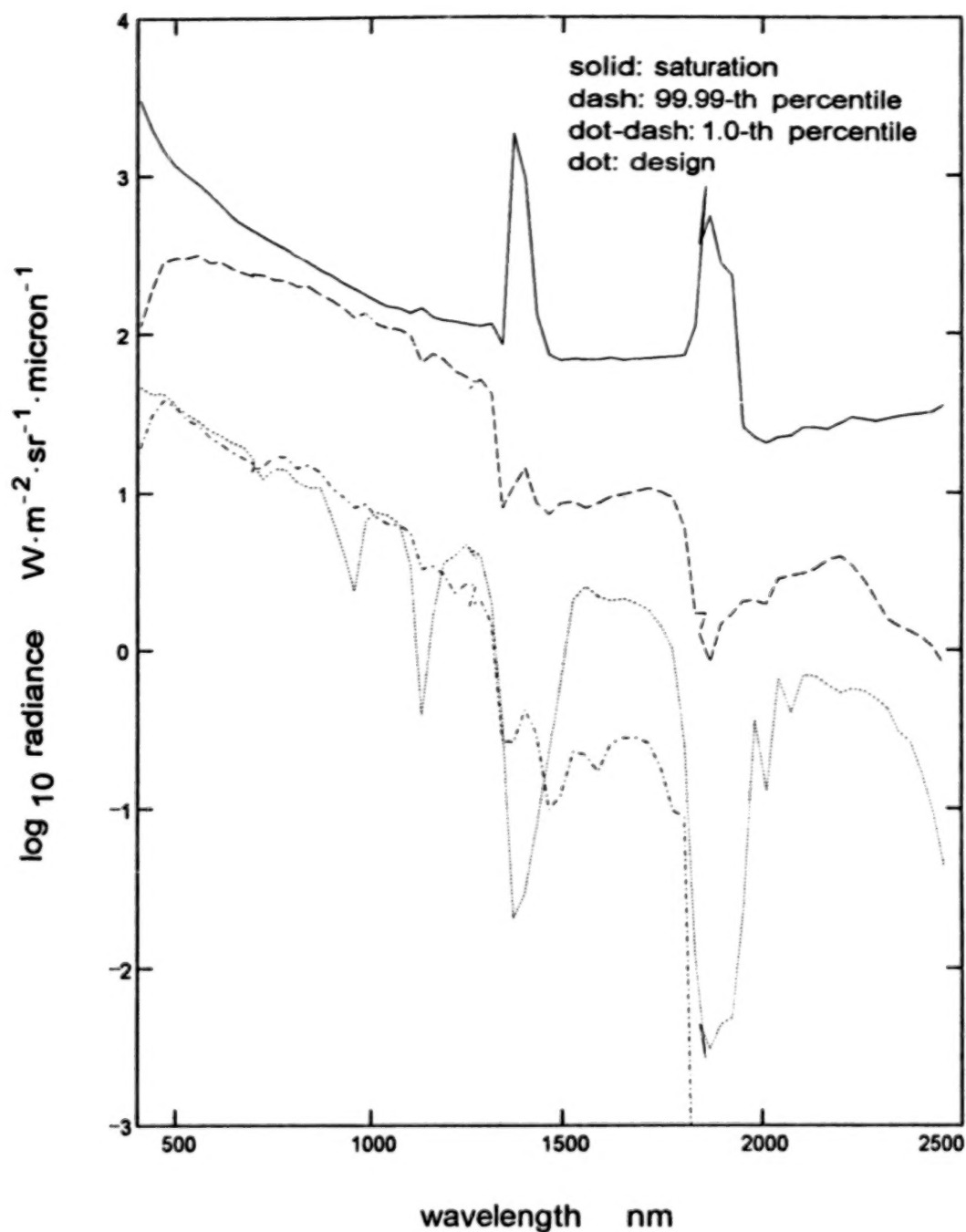


Figure 13. The Mammoth Mountain scene at an integration time of 9.59 ms (0.75x design time): the 99.99-th and 1.0-th radiance percentiles have been scaled by a factor of (0.75) for comparison with the saturation and design radiances. The 1.0-th percentile dips below the design radiance from 400 to 700 nm, rises above from 700 to 1000 nm, and is well below the design radiance for wavelengths greater than 1300 nm.

against the saturation radiance for the 9.59 ms integration time. The 1.0-th radiance percentile hugs the design radiance from 400 to 1100 nm, and falls well below the design radiance at longer wavelengths. Somewhat higher percentiles behave similarly. See Figs. 14 and 15 for plots of the 5.0-th and 20.0-th percentiles with the design radiance. These figures show that HYDICE can be used to collect spectra of sunlit snow and shaded forest spectra in the same scene. The spectra of the shaded forest will be comparable to the SNR at the design radiance in the spectral range from 400 to 1200 nm, and the SNR will fall below that level at longer wavelengths.

3.3 SOURCES OF ERROR IN THE ANALYSIS

Ideally, the uncertainty in the dynamic range graphs (Figs. 5-15) would be shown with error bars. However, several error sources enter into the results, making the error analysis difficult. In addition, error estimates are unavailable for some of the error sources.

AVIRIS radiometric accuracy is 5-7% (Green et al., 1993). However, in nearly every case, the part of the spectrum that lies closest to saturation is near 1000 nm; consequently, the AVIRIS accuracy in this spectral region is most important.

Current HYDICE performance estimates are modeled with component level measurements; the sensor is now entering a characterization phase to quantify the actual performance.

HYDICE will resolve brighter and darker spots that are averaged within the AVIRIS ground spot. A prediction of the increase in scene contrast is given in Section 4. This prediction is based on an extrapolation and we do not have any data to test it.

To draw conclusions from AVIRIS radiance data about HYDICE performance at altitudes of 6 km and 7.62 km, we used MODTRAN to create analogs to the saturation radiance and design radiance that are scaled for the 20 km altitude of AVIRIS. This scaling method takes into account the typical (not the actual) atmospheric absorption and scattering in the atmosphere between HYDICE and AVIRIS.

The sampling error introduced by studying only seven scenes is hard to quantify. We tried to minimize sampling error by selecting scenes containing deep water, sunlit snow, and other common surface types.

4. RADIOMETRIC CHANGES WITH GROUND SPOT SIZE

As mentioned in Section 3, HYDICE will resolve brighter and darker spots that are averaged within the AVIRIS ground spot. We explored the relationship between radiance and ground spot size

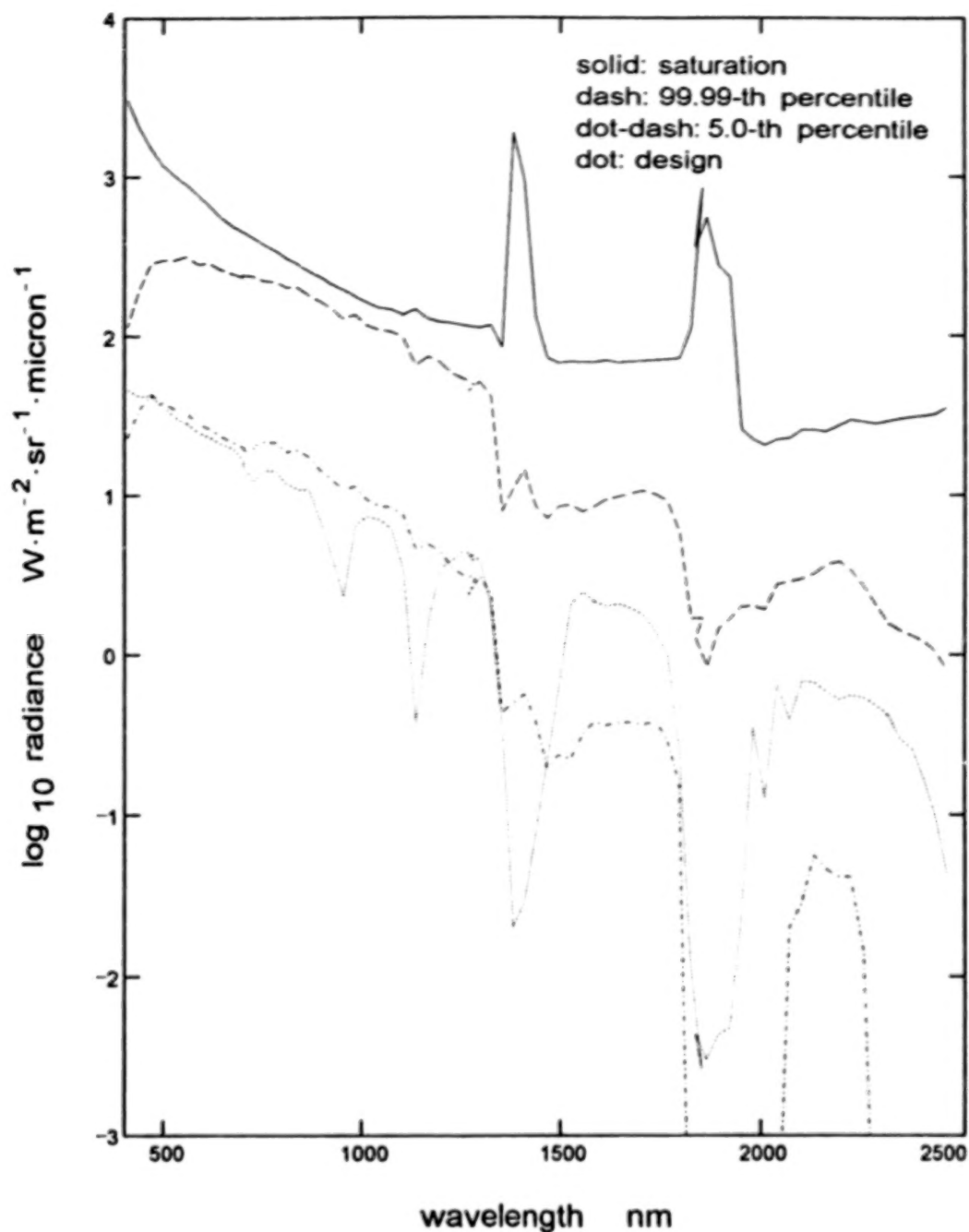


Figure 14. The Mammoth Mountain scene at an integration time of 9.59 ms (0.75x design time): the 99.99-th and 5.0-th radiance percentiles have been scaled by a factor of (0.75) for comparison with the saturation and design radiances. The 5.0-th percentile dips below the design radiance from 400 to about 500 nm and drops below the design radiance at wavelengths longer than 1200 nm.

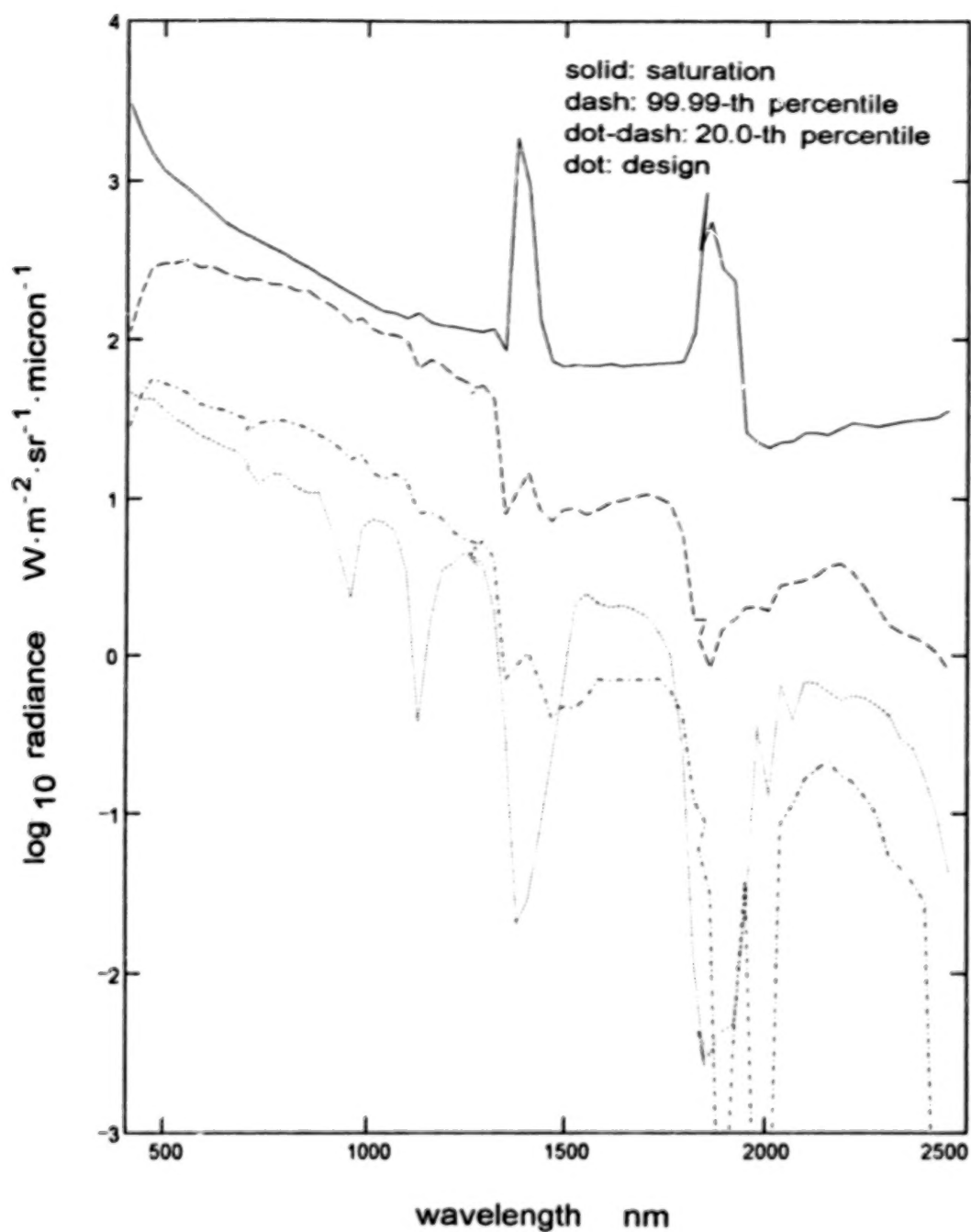


Figure 15. The Mammoth Mountain scene at an integration time of 9.59 ms (0.75x design time): the 99.99-th and 20.0-th radiance percentiles have been scaled by a factor of (0.75) for comparison with the saturation and design radiances. The 20.0-th percentile dips below the design radiance from 400 to about 450 nm and at wavelengths greater than 1250 nm.

with AVIRIS data for each of the seven scenes by computing radiance percentiles for blocks of pixels sized up to 7x7. For a given percentile, the linear trend in radiance versus spatial scale was estimated with weighted least squares. Extrapolation of these trends to the HYDICE ground spot indicates that the increase in spectral radiance range will be small.

Consider the difference in the effective ground spots of the two systems. The AVIRIS ground spot profile is accurately modeled by a Gaussian with a full width at half maximum (FWHM) of 22.4 m (Chrien and Green, 1993). If one assumes for the moment that a Gaussian model will be appropriate for the HYDICE ground spot profile, the ratio of surface area sampled by AVIRIS to the surface area sampled by HYDICE will be:

$$\text{ratio of AVIRIS area to HYDICE area} = (22.4/d)^2, \quad (1)$$

where "d" is HYDICE ground spot FWHM in meters. At the nominal 6 km HYDICE collection altitude, d is 3 m. In this representative case, (1) shows that AVIRIS samples a ground spot 55.8x the area of the HYDICE ground spot. The effective ground spot area for radiometrically calibrated AVIRIS data is actually slightly larger than a Gaussian spot with a FWHM diameter of 22.4 m. As part of the radiometric calibration, the data is re-sampled by taking a weighted average of successive samples in each spectral band (Green et al., 1991). The re-sampling introduces additional averaging of ground contrast. The resultant increase in effective ground spot area is determined by finding the increase in area that introduces the same amount of averaging as the re-sampling. The effects of re-sampling are largest in bands 65, 129, and 192. For these bands, the increase in effective AVIRIS spot area is a factor of 1.38. However, the effects of re-sampling are negligible near band 2 in spectrometer A, near bands 34 and 96 (spectrometer B), near bands 98 and 160 (spectrometer C), and near bands 162 and 224 (spectrometer D). Rather than explicitly accounting for the effect of re-sampling on the effective AVIRIS ground spot area, we relied on these relatively unaffected portions of the spectrum.

We studied the changes in spectral radiance over a range of ground spot diameters by binning AVIRIS data to simulate larger ground spots. In addition to the unbinned AVIRIS radiances, we averaged AVIRIS radiances over pixel blocks dimensioned 2x2, 3x3, 4x4, 5x5, 6x6, and 7x7. For each of these 7 spatial scales, the following radiance percentiles were computed: 99.99, 99.95, 99.9, 99.0, 97.5, 95.0, 90.0, 10.0, 5.0, 2.5, 1.0, 0.1, 0.05, and 0.01.

A roughly linear trend of radiance versus spatial scale was found over the range from 1 AVIRIS pixel width to 7 AVIRIS pixel widths. For the higher percentiles, the radiance increases as the spatial scale decreases; the lower percentiles show the opposite trend, i. e. decreasing radiance as the spatial scale decreases. Since the trends are roughly linear, we fit the data with straight lines, using weighted least squares. To emphasize the data for the smallest available spatial scales, the weights were inversely proportional to the spatial scale; i. e. a weight of 1 for the

single pixel data, $1/2$ for the 2×2 data, $1/3$ for the 3×3 data, and so forth. These weights can also be justified by the number of samples available at each of the 7 scales. Since we tiled the AVIRIS scene with non-overlapping blocks, the relative number of samples at each scale decreases in approximately the progression: 1, $1/4$, $1/9$, $1/16$, $1/25$, $1/36$, $1/49$. The statistical uncertainty in the radiance percentiles scales as the square root of the number of samples; this gives weights of: 1, $1/2$, $1/3$, $1/4$, $1/5$, $1/6$, and $1/7$.

The linear trends estimated with the weighted least square procedure were extrapolated to a 3 m spot size to predict the increase in radiance range that will be resolved by HYDICE. Changes of 2% to 5% are typical for the high percentiles and -2% to -5% for the low percentiles. These numbers imply the increase in radiance range resolved by HYDICE is in the range of 4% to 10%. This predicted increase in dynamic range requirements is small on the scale of the dynamic range plots.

ACKNOWLEDGMENTS

We are indebted to the Jet Propulsion Laboratory (JPL) Pasadena, California, and to the individuals listed below for the AVIRIS data used in our study. Michael Hamilton of JPL gave us the data set for the ocean at Los Angeles, California (White's Point). He also provided help in using the data. The data for Cuprite and Jasper Ridge was provided directly by the JPL AVIRIS Data Center. The AVIRIS ocean data for the Florida Keys was provided by Richard Burgett of Planning Systems Inc., Slidell, Louisiana. The AVIRIS snow scene at Mammoth Mountain, California was provided by Anne W. Nolin of the Center for the Study of Earth from Space (CSSE), University of Colorado, Boulder, Colorado. We thank John Colwell and Mary Kappus of SAIC for commenting on the draft paper.

REFERENCES

- Berk, Alexander, Lawrence S. Bernstein, David C. Robertson, 1989: MODTRAN: A Moderate Resolution Model for LOWTRAN 7, Final Report, GL-TR-89-0122, USAF Phillips Laboratory, Geophysical Directorate, Hanscom AFB, Massachusetts, 42 pp.
- Chrien, Thomas G., Michael L. Eastwood, Charles M. Sarture, Robert O. Green, Wallace M. Porter, 1991: Current Instrument Status of the Airborne Visible/Infrared Imaging Spectrometer (AVIRIS). Proceedings of the Third Airborne Visible/Infrared Imaging Spectrometer (AVIRIS) Workshop, May 20-21, 1991, Robert O. Green, (Ed.), Jet Propulsion Laboratory publication 91-28, Pasadena, California, 302.
- Chrien, Thomas G. and Robert O. Green, 1993: Instantaneous Field of View and Spatial Sampling of the Airborne Visible/Infrared Imaging Spectrometer (AVIRIS). Summaries of the Fourth Annual JPL Airborne Geoscience Workshop, October 25-29, 1993, Vol.

1., AVIRIS Workshop, Robert O. Green, (Ed.), Jet Propulsion Laboratory publication 93-26, Pasadena, California, 23-26.

David, H. A., 1981: Order Statistics, 2nd edition, pages 8-10. John Wiley & Sons, Inc., New York, New York, 360 pp.

Green, R. O., James E. Conel, Mark Helmlinger, Jeanette van den Bosch, Chris Chovit, Tom Chrien, 1993: Inflight Calibration of AVIRIS In 1992 and 1993. Summaries of the Fourth Annual JPL Airborne Geoscience Workshop, October 25-29, 1993, Vol. 1., AVIRIS Workshop, Robert O. Green, (Ed.), Jet Propulsion Laboratory publication 93-26, Pasadena, California, 69-70.

Green, R. O., Steven A. Larson, H. Ian Novack, 1991: Calibration of AVIRIS Digitized Data. Proceedings of the Third Airborne Visible/Infrared Imaging Spectrometer (AVIRIS) Workshop, May 20-21, 1991, Robert O. Green, (Ed.), Jet Propulsion Laboratory publication 91-28, Pasadena, California, 109-118.

Rappoport, W., R. Basedow, P. Silvergate, E. Zalewski, D. Gulbransen, C. Peterson, J. Rosbeck, L. Ruzicka, D. Murphy, R. Wyles, 1994: HYDICE FOCAL PLANE DESIGN AND PERFORMANCE. Proc. IRIS Passive Sensors Meeting, March 14-18, 1994, The Infrared Information Analysis Center, ERIM, Ann Arbor, Michigan.

Rickard, Lee J, Robert Basedow, Ed Zalewski, Peter Silvergate, Mark Landers, 1993: HYDICE: An airborne system for hyperspectral imaging. SPIE Proc. Vol. 1937, Gregg Vane (Ed.), Bellingham, Washington, 173-179.

TARGET DETECTION IN MULTISPECTRAL IMAGES USING RELATIVE ENTROPY THRESHOLDING

Mark L.G. Althouse
U.S. Army Edgewood Research Development & Engineering Center
Aberdeen Proving Ground, MD 21010

Chein-I Chang
University of Maryland
Baltimore, MD 21228

Joe Harsanyi
Applied Signal and Image Technology
Pasadena, MD 21122

ABSTRACT

A relative entropy thresholding technique is proposed for detection of spectrally active targets such as chemical vapor clouds in multispectral or hyperspectral imagery. The concept of relative entropy arises from information theory and has been widely used in source coding as a criterion to measure the discrepancy between two sources. The idea to use relative entropy for detection is to cast a detection problem as a thresholding problem where an object can be detected by sectioning an image set both spectrally and spatially into bilevel sub-images containing objects of interest. The information content of an image is generally characterized by its entropy and we can view the image as a source. As a result, the original and thresholded binary images can be considered as two sources. Consequently, the relative entropy becomes a natural measure to describe the mismatch between these two images. The smaller the relative entropy, the better the match between the two images. A potential target containing frame is chosen by selecting the frame with the highest relative entropy compared to the rest of the frames. Since the scene is highly structured, most of the background can be removed by taking the difference between the target frame and a well matched but spectrally independent frame. In this way the spectral dimensionality of the image set can be reduced. The target can then be segmented from the differential image using spatial entropy techniques. This method is applied to a multispectral image set containing a vapor cloud.

1. INTRODUCTION

Considerable use is being made of multispectral and hyperspectral data for many applications. As the imaging spectrometer sensors become more available and collect larger image cubes, the task of processing the data can become time consuming and complex. In this paper we present techniques to reduce the dimensionality of large spectral data sets when searching for unspecified or spectrally unidentified targets and then segment targets from the resulting difference images. The techniques are based upon the principles of information theory. Spatial transition probabilities are measured for the image set and various entropy measures are computed. The entropies are used to select spectral bands most different from the norm and also to select thresholds in difference images to segment the target from the residual noise. The multispectral data which will be used here is collected by an imaging system designed to detect and map multiple organic vapor compounds. Normally, the target vapor may have one or more spectral features appearing in one or more of the imager's spectral bands. Likelihood ratio testing methods of detection have been developed for this type of data and have worked well, but require considerable computing power. The search for less complex and possibly less robust methods has led to this work.

2. THE CO-OCCURRENCE MATRIX

Given a digital image of dimension $M \times N$ with L grey levels $G=\{1,2,\dots,L\}$, let the grey level of the pixel at the spatial location (x,y) be denoted by $I(x,y) \in G$. The image may then be represented by the matrix or two dimensional array $I=[I(x,y)]_{M \times N}$. A spatial co-occurrence matrix of I is an $L \times L$ matrix, $W=[f_{ij}]_{L \times L}$, which contains the frequency of spatial transitions from one grey level to another within I . For any pair of grey levels (i,j) , the (i,j) th entry of the co-occurrence matrix W is denoted by f_{ij} which is defined as follows:

$$f_{i,j} = \sum_{m=1}^M \sum_{n=1}^N \delta(m,n) \quad (1)$$

where

$$\delta(m,n) = 1, \text{ if } \begin{cases} I(m,n)=i, I(m,n+1)=j & \text{or} \\ I(m,n)=i, I(m-1,n)=j & \text{or} \\ I(m,n)=i, I(m,n-1)=j & \text{or} \\ I(m,n)=i, I(m+1,n)=j \end{cases} \quad (2)$$

$$\delta(m,n) = 0, \text{ otherwise}$$

Normalizing the total number of transitions in the co-occurrence matrix, we obtain the desired transition probability from grey level i to j as

$$p(i,j) = \frac{f_{i,j}}{\sum_{i=1}^L \sum_{j=1}^L f_{i,j}} \quad (3)$$

The preceding formulation looks at grey level transitions to the left, right, top, and bottom of $I(m,n)$. Most realizations of the co-occurrence matrix use only the right and bottom transitions. Use of the four closest neighbors has some redundancy which adds no additional information, but makes the co-occurrence matrix more symmetric.

3. SPECTRAL FRAME SELECTION

To determine where the vapor cloud might be, that is, which pair of images is most probable to resolve the cloud and should be used to generate a threshold, we look at the relative entropy between scenes based upon the spatial transition statistics. If the spatial co-occurrence matrix W_k is generated for each spectral band image k , then for the transition probabilities $p_k(i,j)$ computed from W_k , the relative entropy relating images k_1 and k_2 is

$$H(p_{k_1}; p_{k_2}) = \sum_{i=1}^L \sum_{j=1}^L p_{k_1}(i,j) \log \frac{p_{k_1}(i,j)}{p_{k_2}(i,j)} \quad (4)$$

A lower value of $H(p_{k_1}; p_{k_2})$ indicates that images k_1 and k_2 are better matched in a spatial transition probability sense.

Shown in Figure 3 are the six frames taken for one scene by the modified FSI imager. There is quite a range of image quality in these frames. The scene is looking across a field, with a tree about 100 yards distant in the center of the frame. The tree is clearly visible in bands 1, 2, and 5 and somewhat visible in band 6. Band 3 contains mostly vapor, but the top of the tree is visible. Band 4 has no

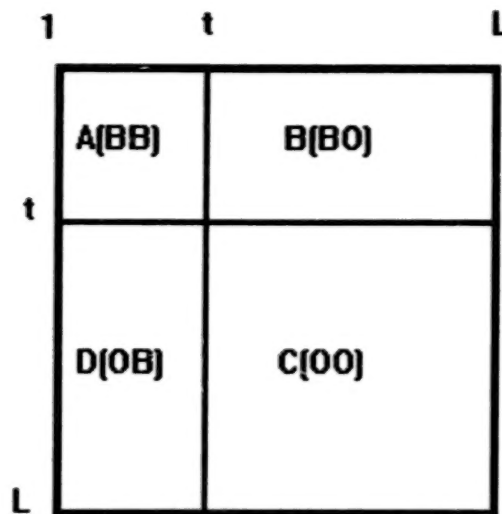


Figure 1 Quadrants of a co-occurrence matrix.

identifiable features; this is due to a severely degraded optical filter. Given that the frames are fairly well matched or normalized for background scene brightness, the one or ones containing the cloud should have some differences in the pixel greylevels which exhibit a spatial character. In practice, the differences are very subtle and not visible to the operator in the scene unless the vapor concentration is very high. In Table 1 the relative entropy values for this six images set are given. The horizontal axis of the table indicates the first argument in $H(p_{k1};p_{k2})$ and the vertical axis the second argument.

	1	2	3	4	5	6
1	0.0	.1855	.5239	1.232	.1906	.7712
2	.1573	0.0	.6582	1.490	.1020	.9975
3	.2349	.1359	0.0	.8906	.2561	.3500
4	.1424	.06497	.2924	0.0	.08132	.6332
5	.1637	.09869	.6038	1.408	0.0	.9490
6	.3289	.1631	.4366	.5148	.3265	0.0

Table 1. Values of relative entropy between spectral frames.

As can be seen from the data, there is no pattern in these values which would be of used in determining the best pair of images to use to detect the vapor cloud. A visual inspection of the images themselves would lead one to expect that image 4 would be the most different from the others, but it has some of the lowest values as well as the highest. The magnitude of $H(p_k;p_l)$ or $H(p_l;p_k)$ depends very much on the order of the arguments. Related to relative entropy is the function divergence, which is the symmetric relative entropy or discrimination function, and is often used when forming bounds on the probability of error in hypothesis testing problems. The divergence, $J(p_{k1};p_{k2})$, is the sum of the two relative entropy values generated by exchanging the order of the arguments.

$$J(P_{k_1}; P_{k_2}) = H(P_{k_1}; P_{k_2}) + H(P_{k_2}; P_{k_1}) \quad (5)$$

As with relative entropy, the smaller divergence value indicates a closer match. Thus one would select the image with the largest divergence values relative to the other images in the set and generate a segmentation threshold based upon that image and the one which most closely matches it. The closest matching image is chosen as the second of the pair because it will not have the cloud and have the best match for the background. Cases of vapors with more than one spectral feature can be accommodated by including some decision logic in the analysis of the divergence results. The divergence values for the above data are in the following table, Table 2.

	1	2	3	4	5	6
1						
2	.3428					
3	.7588	.7941				
4	1.3744	1.5550	1.1830			
5	.3543	.2007	.8599	1.4893		
6	1.1001	1.1606	.7866	1.1480	1.2755	

Table 2. Values of divergence for the six spectral bands.

As can be seen, these values have a very stable pattern since the dependence on argument order which relative entropy has is removed. On the basis of these figures, band 4 is a poor match with every other band and would be chosen as the band with the target. Prior knowledge, however, is that band 4 is a very poor filter and the image has almost no spatial detail, hence the mismatch. Excluding band 4, band 6 has the next highest divergence values. Again the imagery is poor, but better than band 4. One would process by the chosen method band 3 with band 6 since it has the best match with band 6. Visual assessment of the data leads to the conclusion that band 4 is of terrible quality; bands 3 and 6 are poor, but matched in quality; and bands 1, 2, and 5 are good and also well matched in quality. Thus the band 3 and 6 pairing is supported by the divergence function. Looking at only bands 1, 2, and 5, band 1 has the highest divergence, but is best matched with band 2. This also agrees with the visual assessment of the data and in fact with the absorption frequency of the vapor used. With some prior knowledge of the general data quality, bands 1 and 2 would be paired for processing.

4. ENTROPY BASED SEGMENTATION

Once a pair of bands have been chosen, a difference image is produced and is then segmented to separate the target from rest of the image, which should only be noise. Based upon the cell probabilities defined above, N.R. Pal and S.K. Pal (1989) defined what they call the local entropy and joint entropy as follows.

Let $t \in G$ be the desired threshold which separates two groups in an image; the object/s and the background. The co-occurrence matrix W is also partitioned by t into the four quadrants shown in Figure 1. We assume that pixels with grey levels equal to and greater than the threshold belong to the object and those below the threshold belong to the background. This assignment is for the convenience of discussion and does not limit the target to being brighter than the background. Quadrants or cells A, B, C, and D represent transitions within the background (BB), from background to object (BO), within the object (OO), and from object to background (OB) respectively.

The probabilities associated with each quadrant or cell are then defined by

$$\begin{aligned}
 P_A^t &= \sum_{i=1}^{t-1} \sum_{j=1}^{t-1} p(i, j) \\
 P_B^t &= \sum_{i=1}^{t-1} \sum_{j=t}^L p(i, j) \\
 P_C^t &= \sum_{i=t}^L \sum_{j=t}^L p(i, j) \\
 P_D^t &= \sum_{i=t}^L \sum_{j=1}^{t-1} p(i, j)
 \end{aligned} \tag{6}$$

Probabilities for elements within each of the cells can be further defined by

$$\begin{aligned}
 p_A^t(i, j) &= \frac{p(i, j)}{P_A^t} = \frac{f_{ij} / \left(\sum_{i=1}^L \sum_{j=1}^L f_{ij} \right)}{\sum_{i=1}^{t-1} \sum_{j=1}^{t-1} \left(f_{ij} / \left(\sum_{i=1}^L \sum_{j=1}^L f_{ij} \right) \right)} \\
 &= \frac{f_{ij}}{\sum_{i=1}^{t-1} \sum_{j=1}^{t-1} f_{ij}} \quad ; \quad \text{for } 1 \leq i \leq t-1, \quad 0 \leq j \leq t-1
 \end{aligned} \tag{7}$$

The probabilities $p_B^t(i, j)$, $p_C^t(i, j)$, and $p_D^t(i, j)$ are calculated similarly with summation indices as in (6).

4.1 Entropy Methods

Since quadrant or cell A and cell C reflect local transitions within the background or within the object, that is object greylevel to object greylevel, the entropy of the background denoted $H_A(t)$ and the entropy of the object denoted $H_C(t)$ are defined as

$$\begin{aligned}
 H_A(t) &= - \sum_{i=1}^{t-1} \sum_{j=1}^{t-1} p_A^t(i, j) \log p_A^t(i, j) \\
 H_C(t) &= - \sum_{i=t}^L \sum_{j=t}^L p_C^t(i, j) \log p_C^t(i, j)
 \end{aligned} \tag{8}$$

Combining the two terms in (8) we obtain the local entropy

$$H_{LE}(t) = \frac{H_A(t) + H_C(t)}{2} \tag{9}$$

The local entropy threshold is defined as the value t_{LE} which maximizes $H_{LE}(t)$. Maximum entropy means that the underlying probability distribution, the $p_A^t(i, j)$ and $p_C^t(i, j)$, are most uniform or equal in value. The

maximum local entropy threshold is that which best balances the distribution between the two cells.

Similar to the development of the local entropy is the joint entropy. Quadrants B and D contain transitions from the background to the object and vice versa. These transition quadrant entropies, $H_B(t)$ and $H_D(t)$ are defined as in (8) with the correct indices for the quadrant. Then, as with the local entropy, by combining the two terms we obtain the joint entropy $H_{JE}(t)$ as

$$H_{JE}(t) = \frac{H_B(t) + H_D(t)}{2} \quad (10)$$

and the joint entropy threshold, t_{JE} , is that which maximizes $H_{JE}(t)$.

The criterion global entropy, Chang et al. (1994), is based upon the local and joint entropies. Simply, the global entropy, $H_{GE}(t)$, is defined as

$$H_{GE}(t) = \frac{H_{LE}(t) + H_{JE}(t)}{2} \quad (11)$$

and the global entropy threshold, t_{GE} , is that which maximizes $H_{GE}(t)$. The global entropy threshold will generally fall between the local and joint entropy thresholds, but this feature is not guaranteed.

4.2 Relative Entropy Methods

This set of methods can be found in Chang et al. (1994) as well. Relative entropy is the measure of the discrepancy between two probability distributions on the same event space. Here the event space is formed of ordered pairs, (i,j) , from the set of greylevel values $G = \{1, 2, \dots, L\}$, which form f_{ij} , the elements of the co-occurrence matrix W . The element f_{ij} represents the frequency of spatial transitions from greylevel i to greylevel j within the image. From these frequencies is then derived the probability distribution p_{ij} . A second probability distribution, q_{ij} , based upon spatial transitions within the image would be that measured on the thresholded binary image. In this case the set of greylevels, G' , reduces to two, $G' = \{1, L\}$. The levels 1 and L are used since they represent the endpoints of the greyscale and are generally used to produce the best binary images in a greyscale representation. Using p_{ij} and q_{ij} , the relative entropy is defined as

$$H(p; p^*) = \sum_{i=1}^L \sum_{j=1}^L p_{ij} \log \frac{p_{ij}}{q_{ij}} \quad (12)$$

Minimizing $H(p; q)$ will yield a more closely matched pair of probability distributions. Since transition probability distributions of the co-occurrence matrix contain the spatial information which reflects homogeneity within groups (quadrants A and C), and changes across boundaries between groups (quadrants B and D), one can envision that a better result can be obtained if the thresholded bilevel image is chosen to be the one which has the best transition match to that of the original image in the sense that the relative entropy between the two images is minimized.

If t is the selected threshold, then all greylevels less than the threshold are assigned the value 1, while all those equal to or above the threshold are assigned the value L . We can obtain the probability distribution for the binary image as follows

$$\begin{aligned}
q^t_A(i, j) &= Q^t_A = \frac{P^t_A}{(t-1)^2} ; \quad \text{for } 1 \leq i \leq t-1, \quad 1 \leq j \leq t-1 \\
q^t_B(i, j) &= Q^t_B = \frac{P^t_B}{(t-1)(L-t)} ; \quad \text{for } 1 \leq i \leq t-1, \quad t \leq j \leq L \\
q^t_C(i, j) &= Q^t_C = \frac{P^t_C}{(L-t)(L-t)} ; \quad \text{for } t \leq i \leq L, \quad t \leq j \leq L \\
q^t_D(i, j) &= Q^t_D = \frac{P^t_D}{(L-t)(t-1)} ; \quad \text{for } t \leq i \leq L, \quad 1 \leq j \leq t-1
\end{aligned} \tag{13}$$

where P^t_A , P^t_B , P^t_C , and P^t_D are as defined in (6). For each selected t , $q^t_A(i, j)$, $q^t_B(i, j)$, $q^t_C(i, j)$, and $q^t_D(i, j)$ are constants and depend only upon the quadrant to which they belong. Therefore they can be represented as Q^t_A , Q^t_B , Q^t_C , and Q^t_D respectively and the relative entropy can be written as

$$\begin{aligned}
H(p; q) &= \sum_{i=1}^L \sum_{j=1}^L p_{ij} \log \frac{p_{ij}}{q_{ij}} \\
&= \sum_{i=1}^L \sum_{j=1}^L p_{ij} \log p_{ij} - \sum_{i=1}^L \sum_{j=1}^L p_{ij} \log q_{ij}
\end{aligned} \tag{14}$$

Because the first term in equation (14) is independent of threshold t , minimizing (12) is equivalent to maximizing the second term of (14). This term to be maximized can be further simplified as follows

$$\begin{aligned}
\sum_{i=1}^L \sum_{j=1}^L p_{ij} \log q_{ij} &= \sum_A p_{ij} \log Q^t_A + \sum_B p_{ij} \log Q^t_B + \\
&\quad \sum_C p_{ij} \log Q^t_C + \sum_D p_{ij} \log Q^t_D \\
&= P^t_A \log Q^t_A + P^t_B \log Q^t_B + \\
&\quad P^t_C \log Q^t_C + P^t_D \log Q^t_D
\end{aligned} \tag{15}$$

Thus we can obtain the desired threshold to segment objects from the background by maximizing the last expression in (15). As with the entropy methods, there are three relative entropy thresholds which can be computed for an image. Each has a particular character as will be seen in the nature as a function of t .

Following the method of Pal and Pal's local entropy, the local relative entropy (LRE) is

$$H_{LRE}(t) = P^t_A \log Q^t_A + P^t_C \log Q^t_C \tag{16}$$

and the local relative entropy threshold, t_{LRE} , is that for which $H_{LRE}(t)$ is minimized. The minimization is over the within object and within background transitions and maximizes object and background region probability distribution agreement.

The joint relative entropy (JRE) is based upon the object to background and background to object transitions and is defined as

$$H_{JRE}(t) = P^t_B \log Q^t_B + P^t_D \log Q^t_D \quad (17)$$

and the joint relative entropy threshold, t_{JRE} , is that which minimizes $H_{JRE}(t)$. This minimization maximizes the probability distribution agreement of the edges between the object and background.

Combining the local and joint relative entropy terms yields the global relative entropy

$$H_{GRE}(t) = H_{LRE}(t) + H_{JRE}(t) \quad (18)$$

and minimizing $H_{GRE}(t)$ over t will produce t_{GRE} , the threshold which will create the binary image with the best agreement with the original image in the spatial co-occurrence probability distribution sense.

The six entropy based thresholding methods described above are applied to the image lenna in Figure 4. One can see that for this particular image, the relative entropy methods provide better definition of the facial features, the primary subjective observer based image quality measure for a portrait type image. As a comparison, Figure 5 shows the six methods applied to band 5 of the multispectral image. The vapor cloud is not segmented, but rather varying degrees of the middle ground, which was the warmest part of the scene. Of greater interest is the data in Figure 6. This is the result of the six entropy methods applied to the band 1,2 difference image. Here the cloud is well resolved, as would be expected since the majority of the background is removed. The local and global entropy methods offer the best definition of the vapor cloud. Joint entropy selects a higher value and thus picks up only more concentrated areas of the vapor. The relative entropy methods have too low a threshold and pick up foreground clutter in addition to the cloud, obscuring the cloud outline.

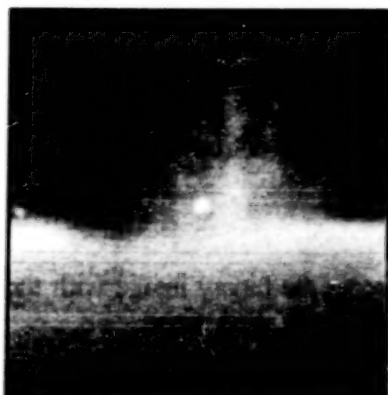
SUMMARY

We have presented a technique to reduce the dimensionality of a multispectral image when looking for a spectrally active, but unknown target. This method may be quite useful in systems where there is very high spectral resolution and many bands such as AVIRIS. We have also demonstrated several entropy based image segmentation methods useful in resolving a target outline once probable spectral band pairs have been selected. Choice of which segmentation method is best rests with the user since our experience is that the determination is linked closely to the image type and scene.

REFERENCES

- Chang, C-I., K. Chen, J. Wang, M.L.G. Althouse, 1994: A relative entropy-based approach to image thresholding, *Pattern Recognition*, accepted for publication.
- Pal, N.K., and S.K. Pal, 1989: Entropic Thresholding, *Signal Processing*, **16**, 97-108.

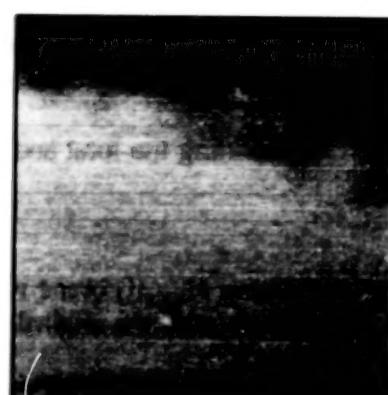
Figure 3. Image set with six spectral bands.



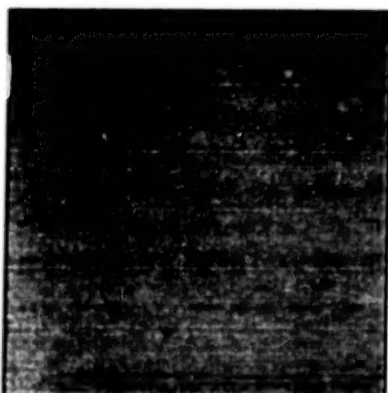
band 1



band 2



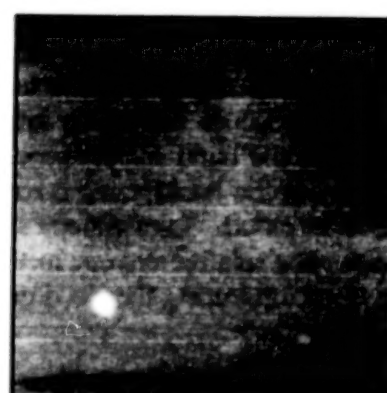
band 3



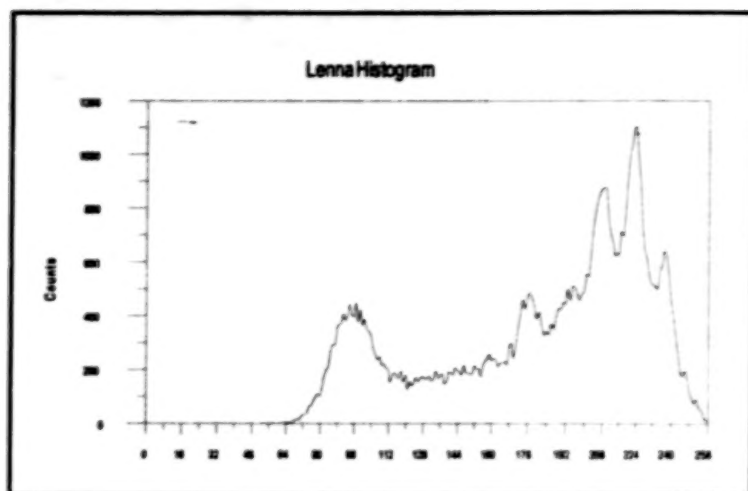
band 4



band 5



band 6



Original Image



Local Entropy, 160



Joint Entropy, 125



Global Entropy, 137



Local Relative Entropy, 191

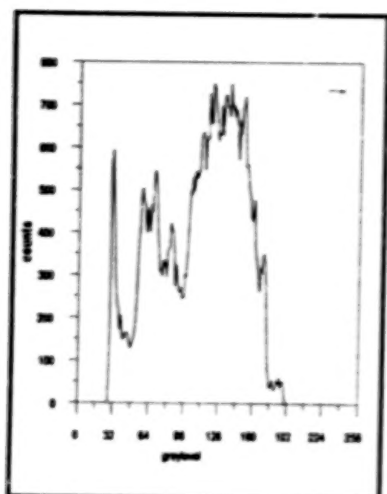


Joint Relative Entropy, 204



Global Relative Entropy, 193

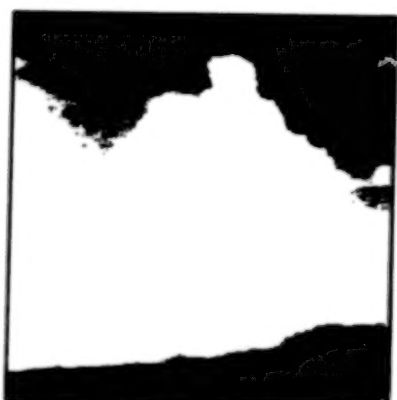
Figure 4. Entropy thresholding of image lenna.



histogram



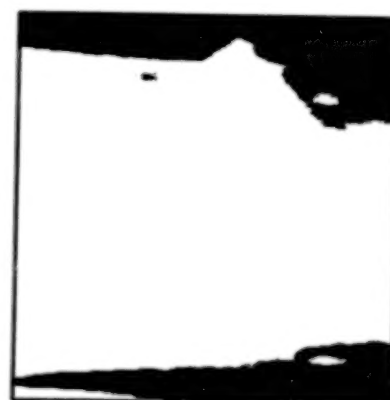
original image



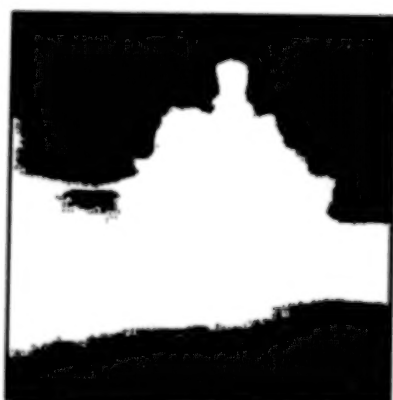
local, 103



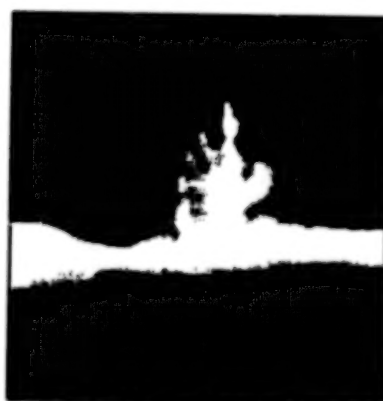
joint, 51



global, 74

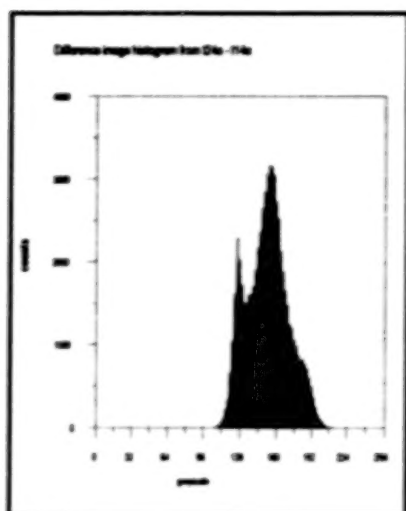


local relative, 122

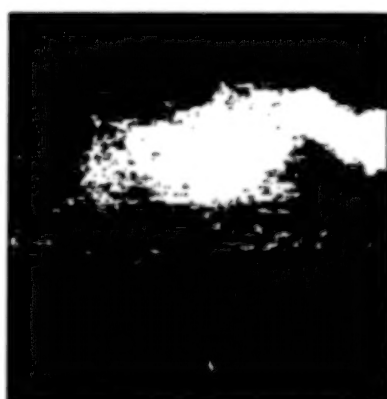


joint relative and global relative, 150

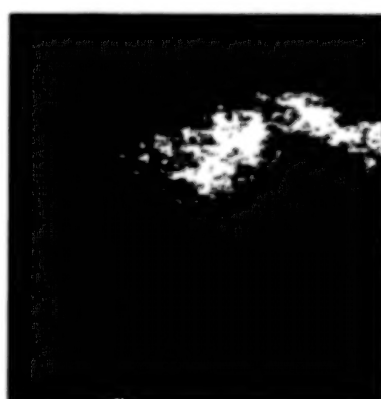
Figure 5. Entropy threshold results for t54a.img (image 1).



original difference image, t24a-t14a



local, 166



joint, 180



global, 166



local relative, 153



joint relative, 154



global relative, 155

Figure 6. Entropy threshold results for bands 1 and 2 difference image.

QUANTIFYING MULTISPECTRAL IMAGERY INTERPRETABILITY

C. Erdman, K. Riehl Jr., and L. Maver
Itek Optical Systems
Lexington, MA 02173-3199, USA

J. Leachtenauer, E. Mohr, J. Irvine, and J. Odenweller
ERIM
Ann Arbor, MI 48113-4001, USA

R. Simmons
Eastman Kodak Company
Rochester, NY 14653-7022, USA

D. Hothem
Booz-Allen & Hamilton
Vienna, VA 22182-3934, USA

ABSTRACT

An effort is underway to provide a metric for quantifying the interpretability of multispectral imagery. The goal is to produce a scale similar in concept and function to the National Imagery Interpretability Rating Scale (NIIRS). The NIIRS is used to numerically quantify the potential interpretability of single-band panchromatic imagery and thus provides a standard for imaging requirements specification, tasking and collection, exploitation, intelligence reporting, and engineering performance specification and evaluation. The methodology and experience used to develop the NIIRS has been applied to develop a Multispectral Imagery Interpretability Rating Scale (MS IIRS). This scale has been produced using imagery analyst evaluations of 200 images, ranging from 0.3 to 80 meter ground sample distance (GSD), and 550 exploitation tasks. Following a final validation, these results will be documented and published in an MS IIRS Reference Guide.

1. INTRODUCTION

An image interpretability scale is a tool used by people to make and communicate quantitative judgments about the potential interpretability of an image. The National Imagery Interpretability Rating Scale (NIIRS) is such a scale and is used by imagery analysts (IAs) to assign a number which indicates the interpretability of a given image. This process is referred to as "rating" an image.

The purpose of the NIIRS is to ensure responsiveness of imagery collection and exploitation processes to information needs. NIIRS provides a common scale which can be used with different imaging systems. Studies and experience have shown that ratings by trained IAs are accurate and precise. Because the NIIRS directly relates to interpretation tasks that can be accomplished with an image, it has become a standard means of communication to:

Define imaging requirements

- Select and task imaging systems
- Indicate the credibility of imagery-derived information
- Provide quality control feedback to operational systems
- Specify performance of new imaging systems
- Design imaging systems and perform engineering tradeoffs
- Measure performance of overall systems and subsystems

Due to the increasing use of multispectral imagery in military and intelligence problems, as well as the "dual use" application of reconnaissance assets, a study was initiated to evaluate the feasibility of developing a Multispectral Imagery Interpretability Rating Scale, or MS IIRS, analogous to the NIIRS. Before describing the MS IIRS development, a brief introduction of the format and application of the NIIRS is presented.

The NIIRS is a task-based scale consisting of ten graduated levels. At each level, representative intelligence tasks (termed criteria) indicate the degree of exploitation that can be accomplished with an image of that given interpretability. For example, with a NIIRS 2 image, an IA should be able to "Detect large hangers at an airfield," while with a NIIRS 8 image, they could "Identify the rivet lines on bomber aircraft." Thus at a higher NIIRS, more detailed information can be gathered from the image.

The NIIRS measures the *potential* interpretability of an image. This means that specific objects listed in the criteria need not be present, but the physical attributes of the image are such that the image would have the specified intelligence value if the necessary content were present. The NIIRS relies on the experience of IAs to be able to extrapolate, or imagine, how well criteria would be rendered if those features were present in the image to be rated.

The NIIRS accounts for all factors that effect image interpretability. Image scale, measured as photographic scale or ground sample distance (GSD), has a significant effect on interpretability. Edge sharpness, noise, and contrast can also impact the NIIRS rating of an image and may be due to system parameters (e.g., optical quality, focal plane characteristics), acquisition conditions (e.g., sun angle, atmospheric haze), and exploitation conditions (e.g., duplicate film quality, softcopy monitor quality). By design, the NIIRS is independent of any particular imaging system and provides an unbiased measure of image interpretability.

Because the NIIRS format is well established and has been successfully used by a broad community, it was adopted as the framework for this effort. The additional dimensionality of multispectral imagery and exploitation was recognized as a factor which could complicate the development of an MS IIRS. As described in the following sections, scale development and validation plans have attempted to address unique factors imposed by multispectral data while still developing a useful tool to quantitatively judge multispectral imagery interpretability.

2. APPROACH

This effort utilized the basic methodology established in developing the NIIRS. It consists of a series of three successive IA evaluations — image scaling, criteria scaling, and validation. Briefly, this methodology is as follows:

- In image scaling, IAs subjectively scale a large variety of images according to perceived interpretability using a "0 to 100" subjective quality scale (SQS) as the measurement mechanism. This evaluation establishes a relative interpretability level for each image.
- In criteria scaling, IAs subjectively scale numerous exploitation tasks (criteria) in terms of perceived difficulty using a similar SQS and a handful of "marker images" as interpretability tie points. This evaluation determines an interpretability level for each criterion.
- A draft interpretability metric is formulated by selecting equally spaced points along the SQS and then identifying commonly understood criteria rated at or very near those SQS aim-points. The scale is reviewed by users for consistency and content.
- In the validation evaluation, IAs rate the interpretability of images used in the image scaling evaluation using the textual interpretability metric. Success is measured statistically by the agreement between imagery ratings derived in this evaluation versus the effective ratings established by the image scaling evaluation.

Each of these evaluations is described in more detail in the following sections after some initial constraints to the problem are discussed.

2.1 Problem Constraints

The prospect of developing a NIIRS-like scale for MSI raised many concerns about multispectral-unique factors: multiple sensor types covering a wide range of spatial resolutions, virtually unlimited spectral band combinations, the possibility of increasing the level of interpretability through automated machine processing, and the display medium of the imagery. A pragmatic approach was developed to address these concerns while still satisfying the need for a metric to define and quantify multispectral image interpretability.

It was quickly apparent that the meaning of the term "multispectral" varied by user, and that some definition implications were too inclusive for this initial effort. For the purposes of this study, "multispectral" is defined to be several bands of co-registered imagery acquired in the reflective portion of the electromagnetic spectrum (0.4 - 2.5 μm). Therefore, this effort does not consider multiple band images including thermal or radar data.

It was also decided that this effort would focus on the feasibility of creating an interpretability metric for manual exploitation of minimally enhanced MSI. The fact that derived imagery products or machine exploitation algorithms may allow the extraction of additional information is not viewed as altering the inherent interpretability of the imagery. This added information may not be available to the typical analyst. The scale may be used with these derived products to measure the delta-interpretability improvement afforded by the additional processing. For similar reasons, the scale development effort does not attempt to address hyperspectral imagery, as this data is normally exploited by machine.

Another definition made to facilitate the development of a multispectral imagery interpretability metric regards the concept of an image. Operationally, most MSI users do not order their spectral bands individually. They generally acquire all bands available from an imaging sensor and then combine the bands to best suit their purpose. This composite-forming process may be

iterative as an IA's attention moves from one area to another, or from task to task. Rather than attempting to assign an interpretability rating to each of the thousands of possible band combinations from one image, this study characterizes MSI as a package of data (multiple bands) with a single inherent quality.

The interpretability scale under development assumes user familiarity with MSI exploitation. While the scale and accompanying Reference Guide are designed to be informative, the scale does not attempt to tell users which bands or band combinations to use. The authors felt the scale should not impose these constraints on the IAs, the exploitation experts, especially as these decisions are subjective and very site and task specific. The objective of the scale is to provide a knowledgeable multispectral user the means to communicate interpretability needs and observations.

2.2 Image Scaling Evaluation

The primary objective of the image scaling evaluation is to determine the relative interpretability of a wide range of MSI. A secondary objective is to relate interpretability to physical parameters, such that an understanding can be developed later to support, for example, system tasking. While these relationships are of operational interest, the immediate application of this scaling evaluation is to determine the relative interpretability of all images to (1) select marker chips at incremental levels for the criteria scaling evaluation and (2) provide an interpretability "truth" per image for the validation evaluation.

A diverse assortment of over 200 images was selected for use in the evaluation, representing a range of currently available orbital and airborne sensors. Imagery was included from three orbital sensors — Landsat Multispectral Scanner (MSS), Landsat Thematic Mapper (TM), and SPOT — and from five airborne imaging systems — NASA's Thematic Mapper Simulator (TMS), Daedalus AADS1268, ERIM's M7, MTL's Airborne Spectroradiometric Imaging Spectrometer (ASIS), and TRW's Imaging Spectrometer (TRWIS). The latter two systems are hyperspectral systems, but this effort made use of only a limited number of their bands. The spatial resolution of the imagery from all sources ranges from 0.3 to 80 meter ground sample distance (GSD).

The image scaling evaluation was administered using hardcopy image samples (film transparencies), primarily for logistical purposes. Experience with the NIIRS indicates this does not preclude the scale's use with softcopy, although hardcopy and softcopy representations of the same image will likely not rate quite the same. A softcopy rating would be applicable only to a softcopy image. Imagery was written to color film with a 25 μ m spot size using a Light Valve Technology (LVT) Saturn 1010 color writer, and mounted in antinewton glass slides. These were designed for viewing using calibrated zoom optics on a light table. The LVT writes all colors simultaneously, so there is no misregistration by the write-out device. The spot size allows an image area on the slide of 1,500 x 1,500 pixels.

The question of how to represent multiple bands of imagery on a single slide was given much attention. There are five major spectral regions in the reflective portion of the spectrum for which this scale is designed: blue, green, red, near-infrared (NIR), and short-wave infrared (SWIR). These can be represented in two commonly used three-band combinations. A natural color rendition composed of blue, green, and red bands provides a familiar literal representation of the scene and is good for water penetration tasks. A false color composite including SWIR, NIR, and red bands illustrates the information available from the reflective spectrum that the human eye cannot see. This composite is useful for such tasks as vegetation discrimination, identifying land/water interfaces, and

observing soil moisture content. A majority of the image chips were formatted so the slides were divided in half, allowing these two composites to be displayed side by side.

In some instances, a different composite was included, either because bands were not available to create the two standard composites or because it enhanced the interpretability. This composite was presented in the lower left quadrant of the slides. All images were contrast/brightness enhanced, and a conservative sharpening filter was applied. No other image processing was performed.

The image scaling evaluation is conducted at a light table with zoom optics. A "0 to 100" subjective quality scale (SQS) is defined at its nominal endpoints by an image of low interpretability (0 marker) and of high interpretability (100 marker). IAs assess the interpretability of each test image through the scope and then physically place it at the appropriate place along the SQS axis (on the light table) in terms of that image's interpretability with respect to the "0" and "100" endpoints. Many observers accomplish this in two passes, by first coarsely binning images within 10 unit increments, and then reviewing the images a second time for final scale placement. The test administrator records the SQS value to the nearest integer.

IAs are selected based on their experience with the imagery type and scene content under test. They are asked to judge interpretability with respect to how they use this imagery in their normal work experience. By using observers' operational experience as a basis, the resultant SQS values are representative of an operational context.

Typical IAs may scale scenes and exploitation tasks with many cultural features differently than scenes and tasks predominated by natural features. Consequently, the image selection and evaluation was designed to support two categories of criteria scaling: cultural and natural. The same marker images were used for both categories so they could be compared. One hundred twenty five images were included in the cultural image set and 102 images were part of the natural image set. Thirty seven images were used as tie points and included in both sets. Ten multispectrally experienced IAs participated in the image scaling evaluation, assessing the interpretability of 227 images. The results indicated that IAs could consistently scale the interpretability of MSI, but they had more difficulty doing this with the natural image set than with the cultural set. This may be because IAs are simply more experienced at exploiting cultural features, but it may also be true that natural features are less easily "sized" and discriminated.

The SQS data were first analyzed to identify images or observers significantly different than the population. If warranted, individual data points or observers were removed from the data set. The mean SQS value of each image indicates its interpretability relative to the endpoints. Images closest to the 25, 50, and 75 positions on the SQS axis were selected from both the cultural and natural image sets to be used in conjunction with the 0 and 100 markers to better define the SQS in the criteria scaling evaluation. Candidate marker images must also exhibit low rater variance and good scene content.

2.3 Criteria Scaling Evaluation

The objective of this second evaluation was to determine the relative difficulty of multispectral interpretation tasks for use in defining the interpretability scale. Interpretability criteria, or exploitation tasks, were primarily derived from the DoD MSI Requirements Survey. The original

requirements were entirely reworked in developing criteria, as existing requirements often combined multiple tasks which would have required various image interpretabilities to satisfy.

A number of guidelines used in developing criteria for this effort are listed below.

1. Criteria should be based only on imagery observables and not require inferences based on other equipment or image context.
2. Features listed in the candidate criteria should be current and familiar to most multispectral IAs.
3. The referenced features should be common enough so that most IAs can infer how well such features would have been rendered when they are not in a particular image.
4. The criteria should allow a rating to be assigned with confidence. There should be no cases where a criterion could be satisfied with an image of lower interpretability than indicated by the criterion.
5. The statement of each criterion should be sufficiently precise that its meaning is the same to IAs of diverse backgrounds.
6. Each criterion statement should reference features or characteristics important to the exploiters of MSI.
7. The rendering of specific features referenced in the criteria should be reasonably insensitive to feature orientation effects.
8. The criteria should be able to be satisfied with a single image (i.e., information derived from comparison of two images collected at different points in time or perspective is not acceptable for criteria).
9. Following the precedent established by the NIIRS, a relatively short list of well understood verbs should be used in describing tasks including "detect," "delineate," "determine," "distinguish between," and "identify."

In developing criteria, a special effort was made to represent spectrally derived information. Criteria were grouped into five categories: military, urban/industrial/lines of communication, vegetation, terrain, and water resources. The first two groups were combined to include 165 criteria in a cultural criteria set, and the remaining three groups contributed 145 criteria to a natural criteria set. Eighteen criteria appeared in both sets. These criteria groupings represent a departure from those used in the NIIRS (air, naval, ground, missile, and electronic order-of-battle). The primary applications and task groupings for MSI are different, and the new categories should be more relevant to the spectral nature of the scale.

Ten IAs participated in the criteria scaling evaluation. In a manner similar to subjective image scaling, the 300+ criteria were ranked and scaled along a "0 to 100" SQS established by five marker images at the 0, 25, 50, 75, and 100 points of the scale. At this stage of scale development, all positions along the SQS are considered to have a full complement of spectral data. As such, the scale attempts to account for both the spatial and spectral characteristics of the imagery. For

example, one of the spectrally focused criteria might be "detect swimming pools." If only the spatial characteristics of an image are considered, this criteria would be placed fairly high on the interpretability scale. The analyst would have to not only resolve the size and shape of the pool, but would require other details such as lane markings, diving boards, or swimmers to distinguish a pool from other similarly shaped features. When considering all the characteristics of the image, including spectral, the analyst only needs to resolve the pool and note the characteristic aqua color in the visible spectrum coupled with the lack of response in the reflective infrared (water absorbs all this energy, reflecting none of it to the camera) to be reasonably sure there is a pool there. This can be done on multispectral imagery of fairly poor spatial resolution.

The results of the criteria scaling SQS data analysis indicated that the levels of image interpretability required to satisfy most of the criteria were similarly perceived by the analysts and were discernible to the extent that an interpretability scale could be constructed. The average spread of responses for the criteria was such that seven interpretability levels could be differentiated within the range of image interpretability evaluated. Scaling of criteria common to both the cultural and natural sets indicated the scales established by the respective marker images were equivalent. The spread of responses for natural criteria, on average, was greater than for cultural criteria.

Having determined that the criteria scaling SQS data supported a seven-level interpretability scale, seven equally spaced SQS aim points were established. In selecting criteria to populate the seven levels, a number of factors were considered. First, it was desired to represent each of the five criteria sub-categories at each level. The desire to choose a criterion closest to the aim point was traded off with a desire to select criteria with the lowest rating variance among IAs and with the fewest negative comments by participants. Since the scale was being created for a wide variety of users, the "general purpose" appeal of the criteria was also a selection factor. If ratings indicated two criteria were nearly equivalent, preference was given to the criterion most benefited by spectral data. Criteria highly impacted by sun angle or the look angle of the imaging system were avoided. Finally, the relationship to other criteria in the scale was considered so that the individual criteria selected for the scale combined to form a cohesive interpretability metric.

Criteria selection for the interpretability metric highlighted the fact that none of the five sub-categories had an even criteria distribution across the full interpretability range. In an attempt to more fully populate all levels of the scale, additional criteria were developed for inclusion in a supplementary criteria scaling evaluation. Many additional criteria came from interviews with MSI users from organizations outside the intelligence community, such as the U.S. Forest Service, the Environmental Protection Agency, the U.S. Geological Survey, and the National Oceanographic and Atmospheric Administration. Other criteria were developed from remote sensing keys and texts. IA comments from the original criteria scaling evaluation were reviewed to see if particular criteria could be modified to improve their ability to convey a specific image interpretability. Criteria were reworded for better clarity, more examples were included, and exploitation tasks were further dissected to isolate single observables. In total, 280 criteria were evaluated in the supplementary criteria scaling evaluation. These were added to the original pool of over 300 criteria, and a seven-level scale was selected as shown in Fig. 1.

Level 1

Distinguish between urban and rural areas.

Identify a large wetland (greater than 100 acres).

Detect meander flood plains (characterized by features such as channel scars, ox bow lakes, meander scrolls).

Delineate coastal shoreline.

Detect major highway and rail bridges over water (e.g., Golden Gate, Chesapeake Bay).

Delineate extent of snow or ice cover.

Level 2

Detect multi-lane highways.

Detect strip mining.

Determine water current direction as indicated by color differences (e.g., tributary entering larger water feature, chlorophyll or sediment patterns).

Detect timber clear-cutting.

Delineate extent of cultivated land.
Identify riverine flood plains.

Level 3

Detect vegetation/soil moisture differences along a linear feature (suggesting the presence of a fence line).

Identify major street patterns in urban areas.

Identify golf courses.

Identify shoreline indications of predominant water currents.

Distinguish among residential, commercial and industrial areas within an urban area.

Detect reservoir depletion.

Level 4

Detect recently constructed weapon positions (e.g., tank, artillery, self-propelled gun) based on the presence of revetments, berms and ground scarring in vegetated areas.

Distinguish between two-lane improved and unimproved roads.

Detect indications of natural surface airstrip maintenance or improvements (e.g., runway extension, grading, resurfacing, bush removal, vegetation cutting).

Detect landslide or rockslide large enough to obstruct a single lane road.

Detect small boats (15-20' in length) in open water.

Identify areas suitable for use as light fixed-wing aircraft (e.g., Cessna, Piper Cub, Beechcraft) landing strips.

Level 5

Detect automobile in a parking lot.

Identify beach terrain suitable for amphibious landing operation.

Detect ditch irrigation beet fields.

Detect disruptive or deceptive use of paints or coatings on buildings/structures at a ground forces installation.

Detect raw construction materials in ground forces deployment areas (e.g., timber, sand, gravel).

Level 6

Detect summer woodland camouflage netting large enough to cover a tank against a scattered tree background.

Detect foot trail through tall grass.

Detect navigational channel markers and mooring buoys in water.

Detect livestock in open but fenced areas.

Detect recently installed minefields in ground forces deployment area based on a regular pattern of disturbed earth or vegetation.

Count individual dwellings in subsistence housing areas (e.g., squatter settlements, refugee camps).

Level 7

Distinguish between tanks and three dimensional tank decoys.

Identify individual 55 gallon drums.

Detect small marine mammals (e.g. harbor seals) on sand/gravel beaches.

Detect underwater pier footings.

Detect foxholes by ring of spoil outlining hole.

Distinguish individual rows of truck crops.

Figure 1. Draft Multispectral Imagery Interpretability Rating Scale

2.4 Interpretability Scale Validation Evaluation

The objective of the final evaluation is to validate whether IAs can use the textual MS IIRS to successfully rate imagery. Their ability to use the criteria scale will be compared against image interpretability values derived in the image scaling evaluation. In that earlier test, IAs determined interpretability based on a visual comparison of all images. Using an imagery interpretability rating scale is effectively a replacement to conducting an image comparison evaluation each time a rating is needed.

The preparation of the validation evaluation is currently in process (July 1994). Between 100 and 150 hardcopy images previously SQS-rated in the image scaling evaluation will be selected for use in the validation. The existing SQS ratings can be converted to MS IIRS scores by binning responses between the SQS aim points used to establish the MS IIRS. The IAs will rate these images using the textual MS IIRS. The correlation of SQS-derived MS IIRS and MS IIRS ratings from the new criteria-based scale is one indicator of the degree to which analysts can use the scale to convey image interpretability.

A preliminary validation, similar in format to that just described but using a limited set of 40 image chips, was conducted earlier using a draft MSI interpretability scale assembled before the supplementary criteria became available. The results indicated IAs were able to successfully rate the interpretability of MSI using a textual scale. There was a high correlation between the predicted interpretability derived from the image-based SQS ratings and the text-based ratings assigned with the MS IIRS. The current draft MS IIRS was designed to be more spectrally oriented than the original draft, and should better cover the intended interpretability range. It is hoped that with the current scale, IAs will be even more successful at consistently rating MSI.

3.0 PLANNED PRODUCTS AND REMAINING ACTIVITIES

The primary product to come from this effort is the MS IIRS and accompanying Reference Guide. The guide will give a brief description of the scale, its origin, and its intended use. The main attraction will be the scale itself. While it will not be possible to illustrate all of the criteria, photographic prints of two images will be included for each of the MS IIRS levels. In addition, the guide will feature an appendix listing many of the 500+ evaluated criteria with an associated decimal MS IIRS value. These criteria may lend a better understanding of tasks accomplishable with imagery at each interpretability level.

Although the scale is designed for experienced users of MSI, and the selection of critical spectral regions and preferred band composites is left to the analyst, the guide will feature several reference tables that may assist in using the scale operationally. One table will list operational multispectral imaging systems and the spectral regions they collect. Another will list features or phenomenology and the spectral regions generally thought to be most useful in the exploitation of that feature. These tables are currently being developed.

With "dual use" in mind, nearly every aspect of the MS IIRS has been maintained at an unclassified level, including the images, the criteria, the scale itself, and the supporting documentation. Individuals or organizations wishing to be considered for inclusion on the distribution list of the Reference Guide should contact the Scales Development Team at (703) 799-3467. Publication is anticipated to be late 1994.

Hyperspectral Image Processing

**Samuel Barr
U. S. Army Topographic Engineering Center
Alexandria, VA 22310-3864
U. S. A.**

Abstract

Hyperspectral remote sensing, also known as imaging spectroscopy, is a relatively new technology that is currently being investigated by the U. S. Army with regard to the detection and identification of military targets and backgrounds.

This technology involves data sets and processing methods that will permit the intelligence analyst to remotely identify target materials by means of spectral matching of a target's spectrum with that of a library of spectral signatures collected using laboratory and field spectrometers. Hyperspectral data sets are generally composed of hundreds of bands of relatively narrow bandwidths as opposed to multispectral data sets of about 10 bands with relatively wide bandwidths. Initially in our research, the spectral range of interest of these data sets encompassed that portion of the spectrum dealing with reflected energy from the visible to the mid-infrared (0.4 to 2.5mm). However, recent research regarding the detection and identification of chemical warfare agents and their precursors, as well as fuel vapor clouds, has caused this range of interest to be extended to the far infrared bands (3 to 5mm and 8 to 12mm).

An important aspect of this research involves data set calibration. This not only includes the sensor hardware calibration, but also methods relating to the elimination of the atmospheric effects from the remotely sensed data. The latter involves the application of atmospheric modeling software, such as LOWTRAN, as well as flat field correction and self-calibration with verification of these methods by means of field spectrometer measurements.

This technology, which can provide the direct identification of target materials, has applications to military background analysis, drug enforcement, pollution monitoring and geological exploration.

Introduction

Hyperspectral remote sensing combines imaging and spectroscopy in a single system which includes data sets and processing methods. Hyperspectral data sets are generally composed of about 100 to 200 spectral bands of relatively narrow bandwidths (5-10 nm); however, under certain circumstances multispectral data sets are also usable. Multispectral data sets are usually composed of about 10 bands of relatively large bandwidths (50-100 nm). In this paper, both types of data sets will be discussed and will involve three different airborne remote sensing systems. Hyperspectral processing provides for the remote identification of target materials without any need for ground truth. In order to provide a frame of reference in this discussion, only data sets of aircraft targets will be analyzed. Hyperspectral data set calibration will also be discussed.

The Hyperspectral Image Cube

Hyperspectral airborne sensors have the ability of imaging ground targets in many bands of relatively high-spectral resolution in a digital mode. Figure 1 illustrates this as applied to the Jet Propulsion Laboratory's (JPL) Airborne Visible Infrared Imaging Spectrometer (AVIRIS) sensor. If a stack of picture elements (pixels) of a single target were extracted from the data set and plotted out as a function of wavelength (see Figures 1 and 2), an average spectrum of all the materials in the pixel would result. Because of the three-dimensional nature (spatial-spatial-spectral) of these data sets, they are generally referred to as image cubes (depicted in Figure 3).

Image Calibration

Presently hyperspectral sensors are designed to respond to reflected solar energy in the visible to mid-infrared bands (0.4 to 2.5 μm) of the spectrum. In order to remotely identify a target's material, the sensor's output spectrum is compared to a data base of spectra which were measured and recorded using field and laboratory spectrometers. These spectrometers produce spectral recordings in reflectance values; however, the output spectrum of the sensor is in raw data numbers or DN values. In order to search the spectral data base, the DN values of the output spectrum must first be converted to reflectance values. The first step involves the hardware calibration of the sensor using a calibrated light source and an integrating sphere. This procedure results in a spectrum whose units are in radiance (energy) values (see top of Figure 4). In order to convert from radiance values to reflectance values, it will be necessary to remove or "back out" the effects of the solar response and atmospheric absorption bands as illustrated in Figure 5. Several methods are available for this, four of which are indicated in Figure 4. LOWTRAN (low resolution transmittance) is an atmospheric modeling program developed by the U. S. Air Force. The flat field correction and self-calibration methods use actual spectra extracted from the image cube for this correction, while the field spectrometer method uses a direct atmospheric measurement.

Spectral Search and Identification

Once the sensor's data set has been converted to reflectance values, it is possible to perform a library search in order to identify target materials. Prior to this, a sensor library was set up by

AVIRIS DATA COLLECTION

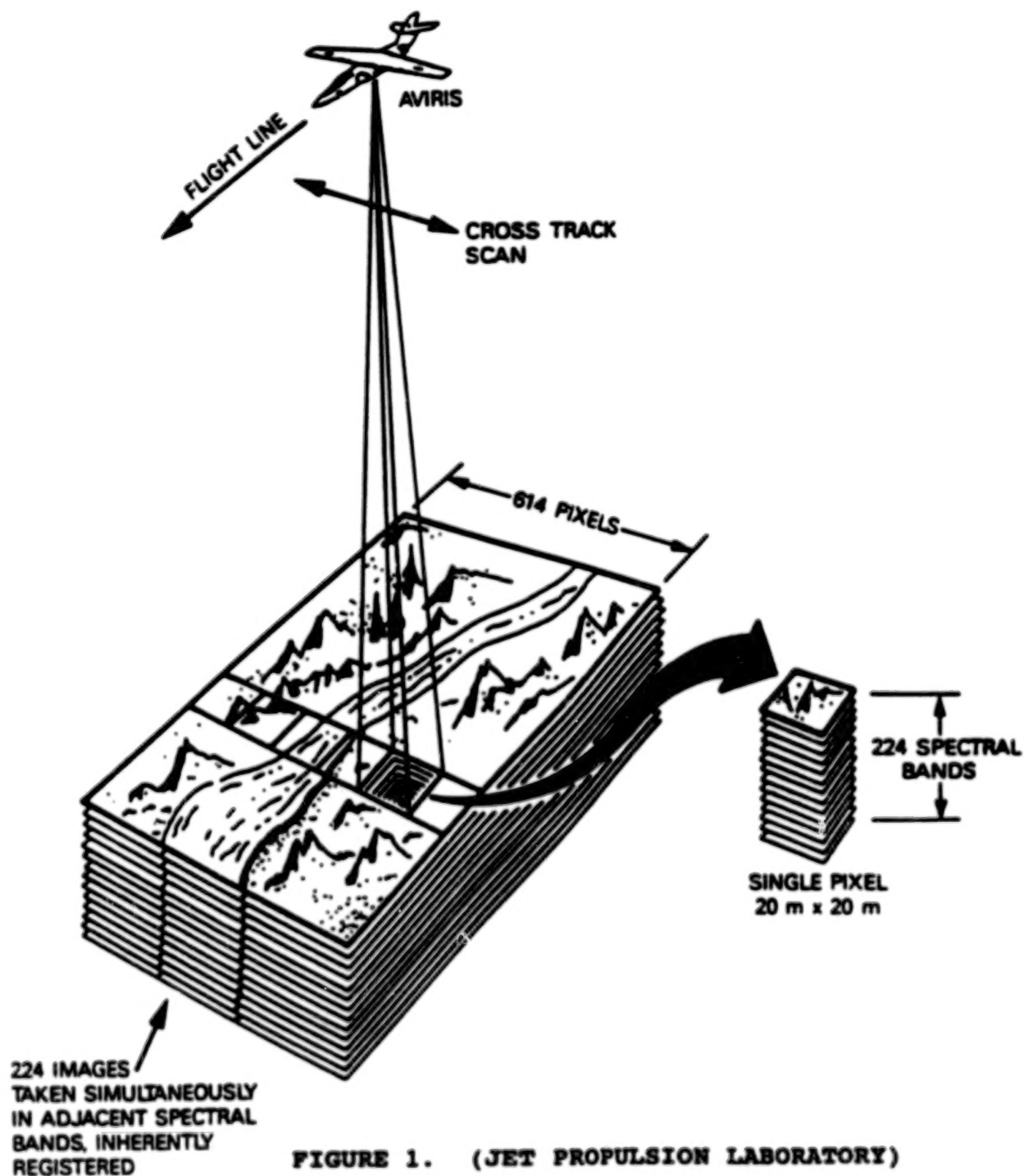


FIGURE 1. (JET PROPULSION LABORATORY)

SPECTRUM FROM SINGLE PIXEL

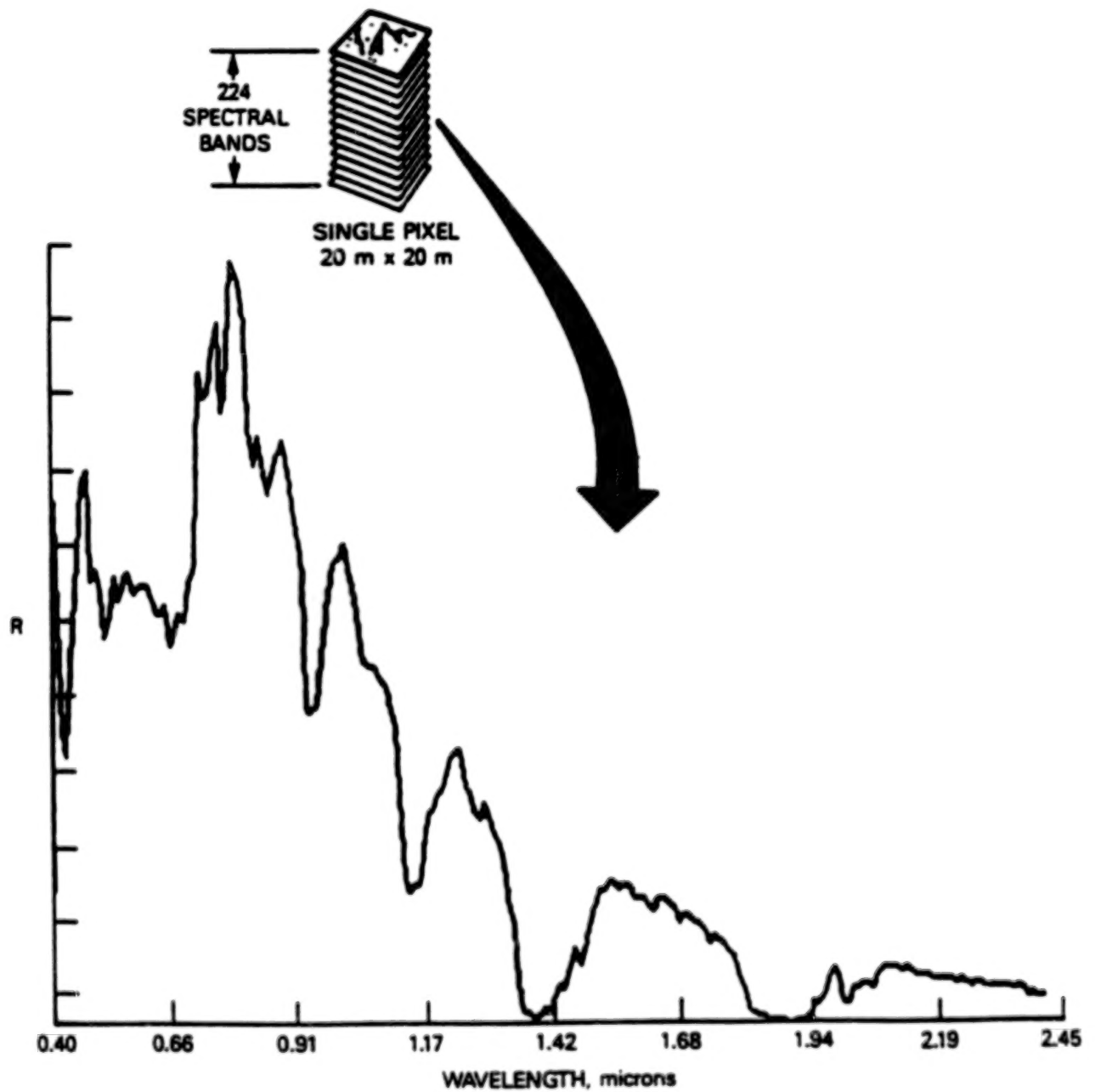


FIGURE 2. (JET PROPULSION LABORATORY)

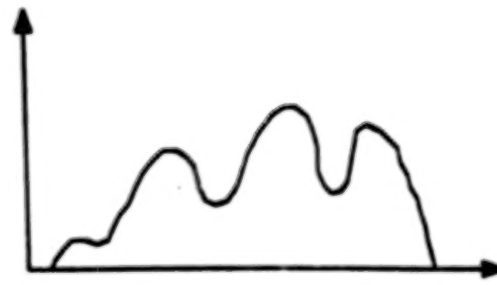
BASIC HYPERSPECTRAL DATA SET

**IMAGES OF THE SAME SCENE
AT DIFFERENT SPECTRAL
CHANNELS**

**SPECTRUM FOR ONE SPATIAL
ELEMENT (PIXEL)**



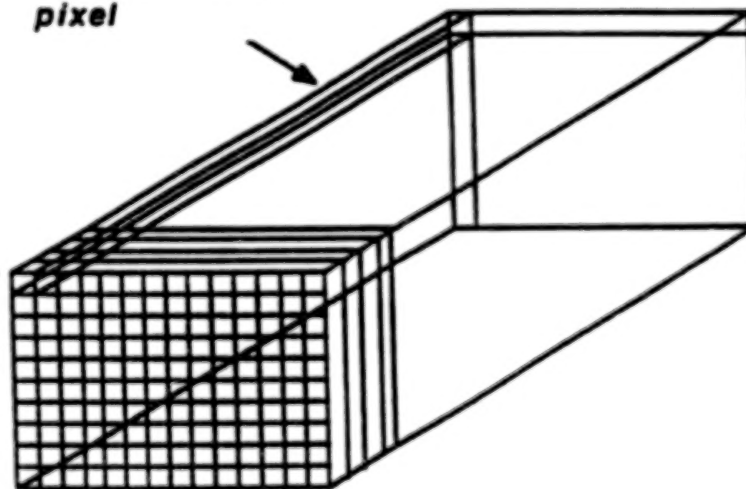
Reflectance or Emittance



Wavelength (Spectral Channel)

*Spectrum at one
pixel*

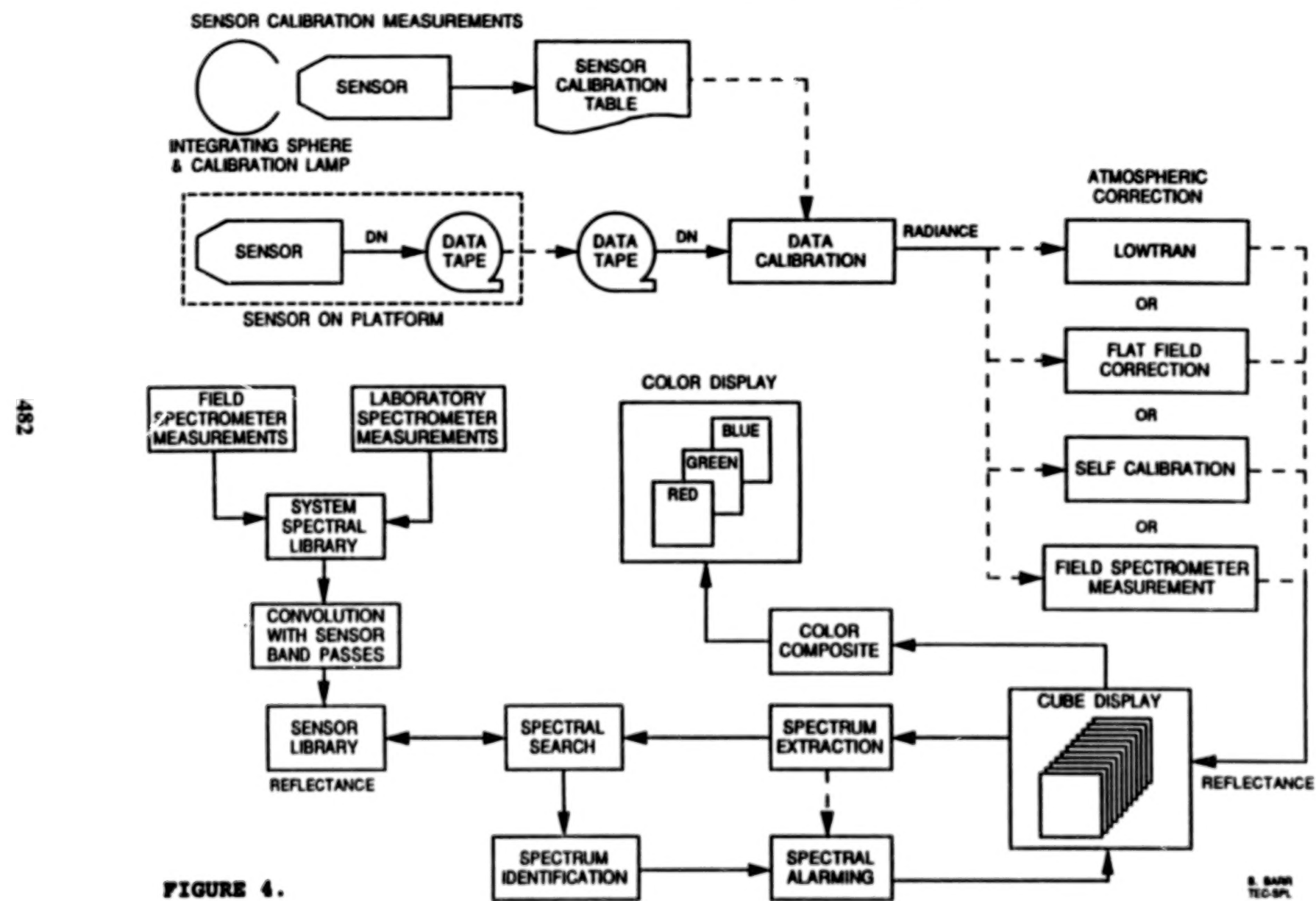
*Single
Pixel*



The basic hyperspectral data set can be visualized as a stack of images at different spectral channels (wavelengths) or as a stack of spectra, like square logs in a neat pile, one for each pixel.

FIGURE 3. (JET PROPULSION LABORATORY)

HYPERSPECTRAL DATA PROCESSING



482

BLANK PAGE

SOLAR SPECTRUM WITH ATMOSPHERIC ABSORPTIONS

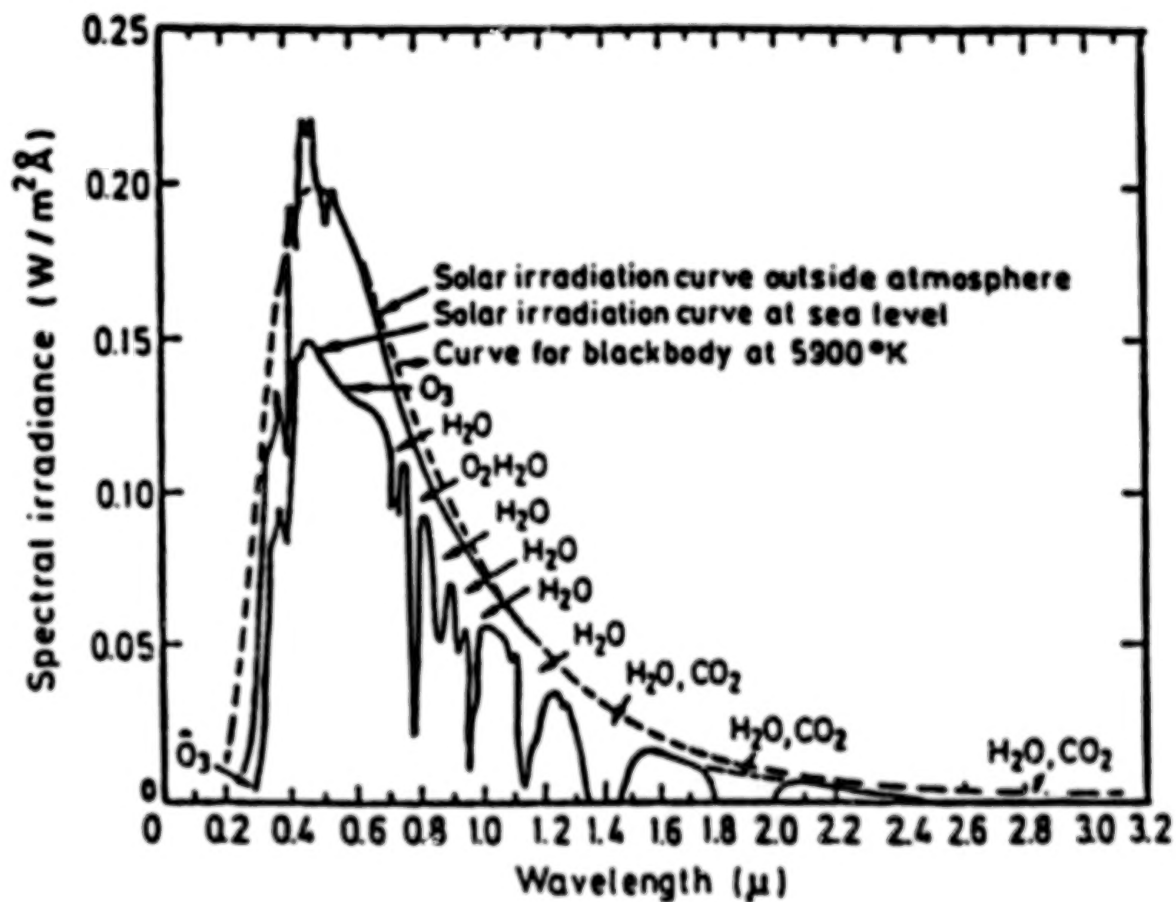


FIGURE 5.

convolving the spectrometer measurements with the sensor band passes so that searches can be performed along those portions of the spectrum of which the sensor responds.

Spectral searches can be performed in one of three ways: from the image cube against the library, from the library against the image cube and from the image cube against itself. In this paper, all three methods will be illustrated.

Once a spectrum has been identified, it is then possible to perform a spectral alarming on the image cube. This is accomplished by pseudo coloring every pixel in the image whose spectrum matches the identified one. Therefore, once a target of interest is located, it is possible to spectrally locate all other similar targets. This procedure is illustrated in the bottom portion of the flow chart in Figure 4.

Analysis of Data Sets

The data set in Figure 6 was produced using a Daedalus ADDS 1268 sensor, which was flown at 500 feet in a helicopter. Its ground sample distance (GSD) is 0.4 meter and it possesses only nine bands. In order to achieve a high-spatial resolution with a reasonable signal to noise ratio, it is necessary to use relatively fewer bands with wider bandwidths.

Due to the high-spatial resolution, the aircraft in the scene can be identified as an F-15E Strike Eagle. In the expanded image window, the cursor position is located at the upper portion of the right wing and appears as a small dark square. The spectrum that was extracted from this cursor position appears in the plot below the window. By performing a spectral search against a library (using Euclidean distance) the aircraft skin was identified as being composed of gray paint on metal as indicated in the two windows in the lower right corner of Figure 6.

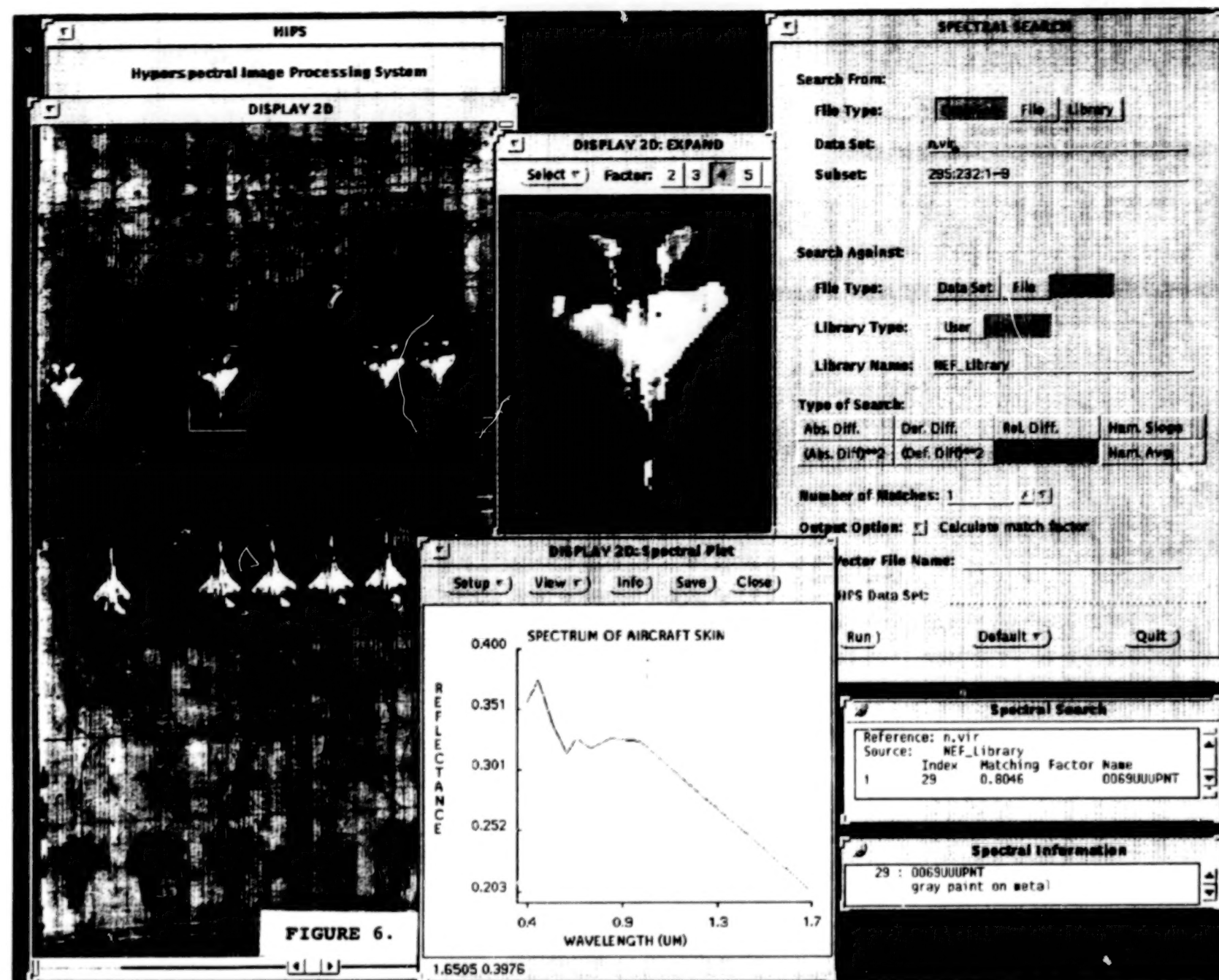
Figure 7 is the result of a spectral alarming operation using the identified spectrum. The shading that appears on the aircraft is a result of performing the spectral alarming for all match factors between 50 and 100 percent.

The data set in Figure 8 was produced using the Airborne Spectroradiometric Imaging Sensor (ASIS), which was flown at 10,000 feet. Its GSD is 10 meters and it possesses 63 bands; however, due to a system malfunction, only the first 23 bands (0.46 to 1.05 μm) were used.

The full-resolution image appears in the window labeled Display 2D. It is an image of Washington National Airport and the white box outlines the main terminal buildings. An enlargement of this area appears in the "expand" window. The white section in the lower part of the expand window is a carousel-type terminal building around which aircraft are usually clustered. However, at a 10-meter GSD, the aircraft would only appear as bright pixels without any distinguishing features that could be used for identification. The cursor was placed on one of these bright pixels to the left of the carousel building and appears as a dark square in the center of the black indicator ring. The spectrum of this target appears in the plot window. Performing a spectral search produces two possible material identifications; gray paint on metal and aluminum.

In Figure 9 the "expand" window shows the result of a spectral alarming operation using the

BLANK PAGE



BEST COPY AVAILABLE

485

486

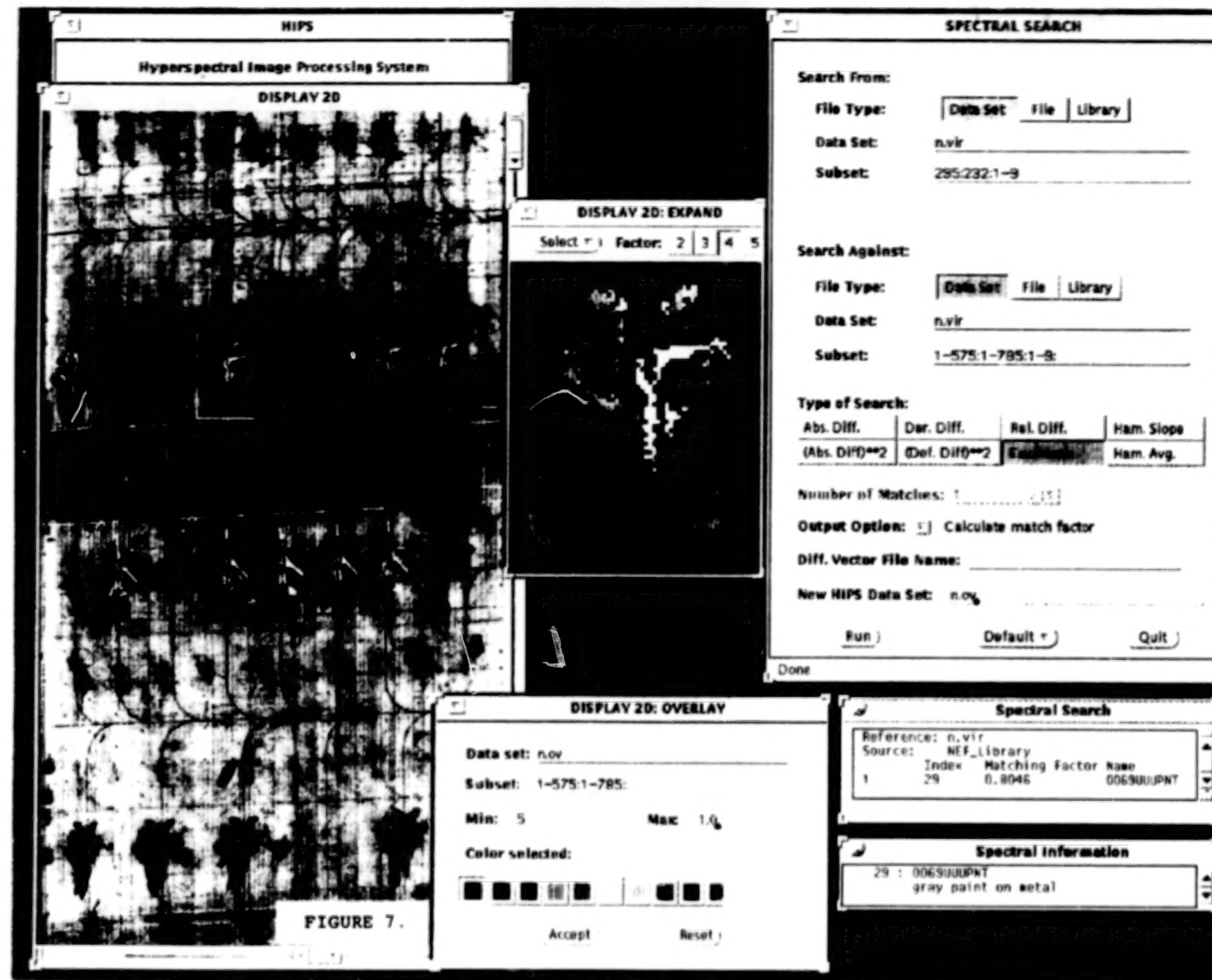


FIGURE 7.

BEST COPY AVAILABLE

486

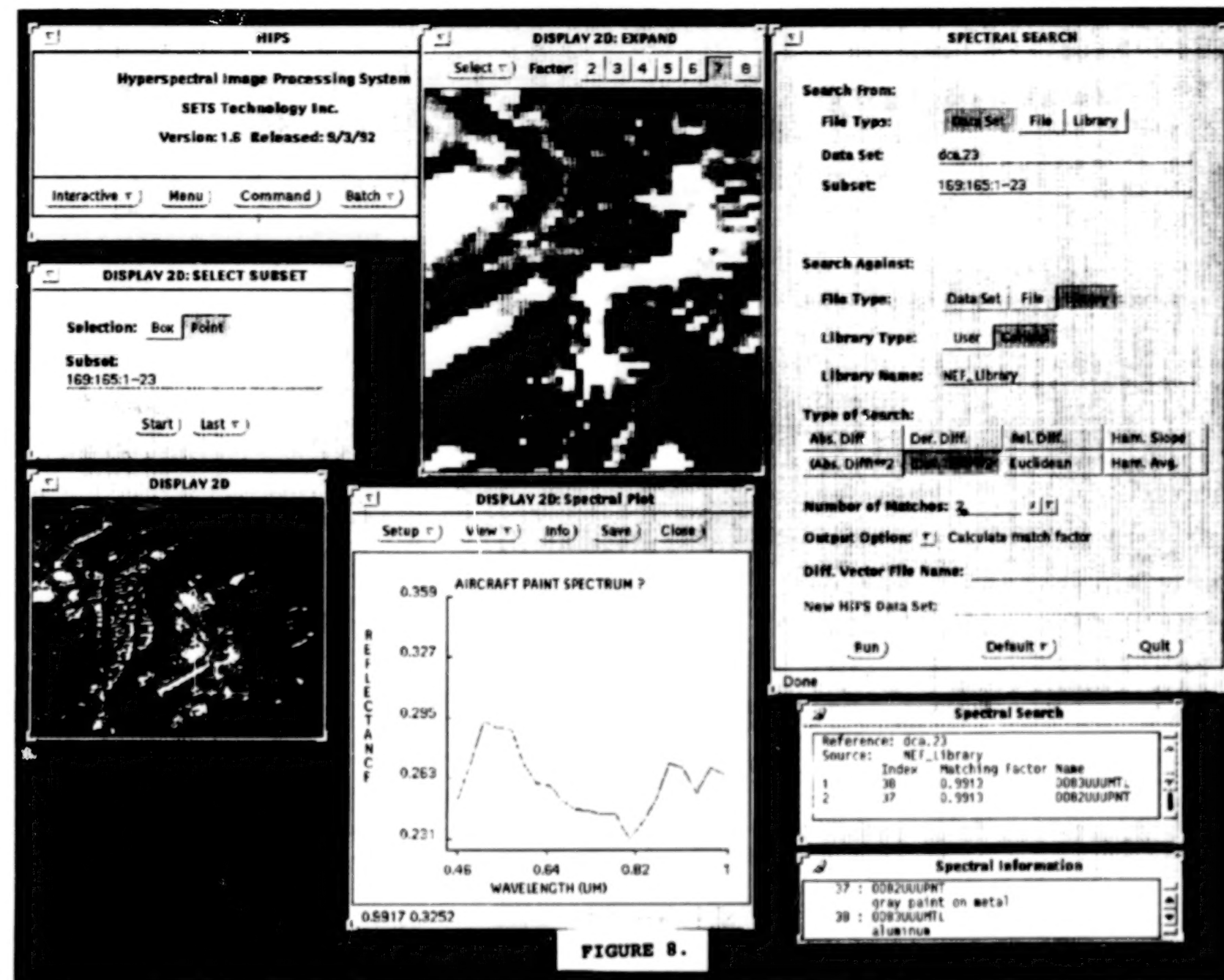
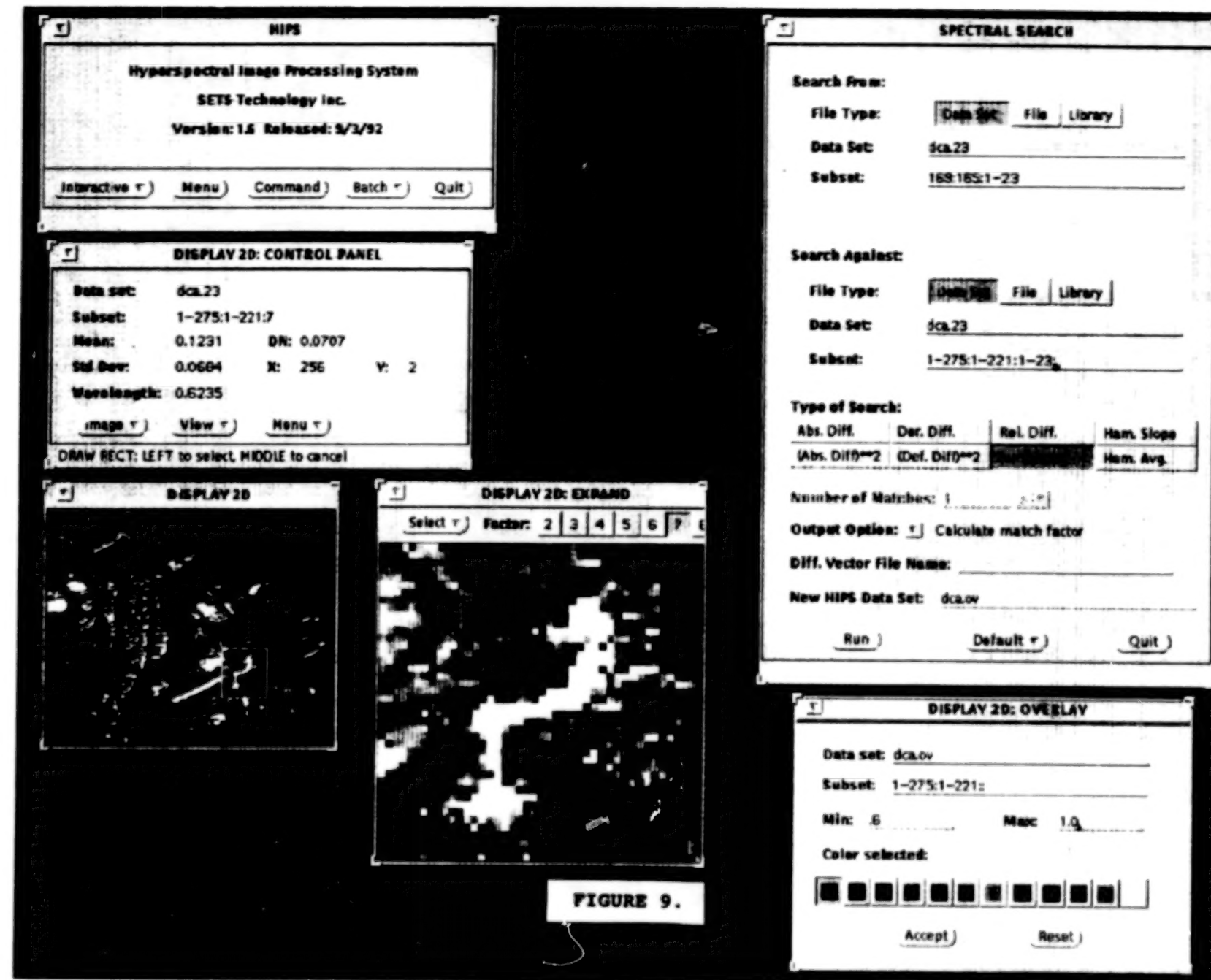


FIGURE 8.

488



BEST COPY AVAILABLE

488

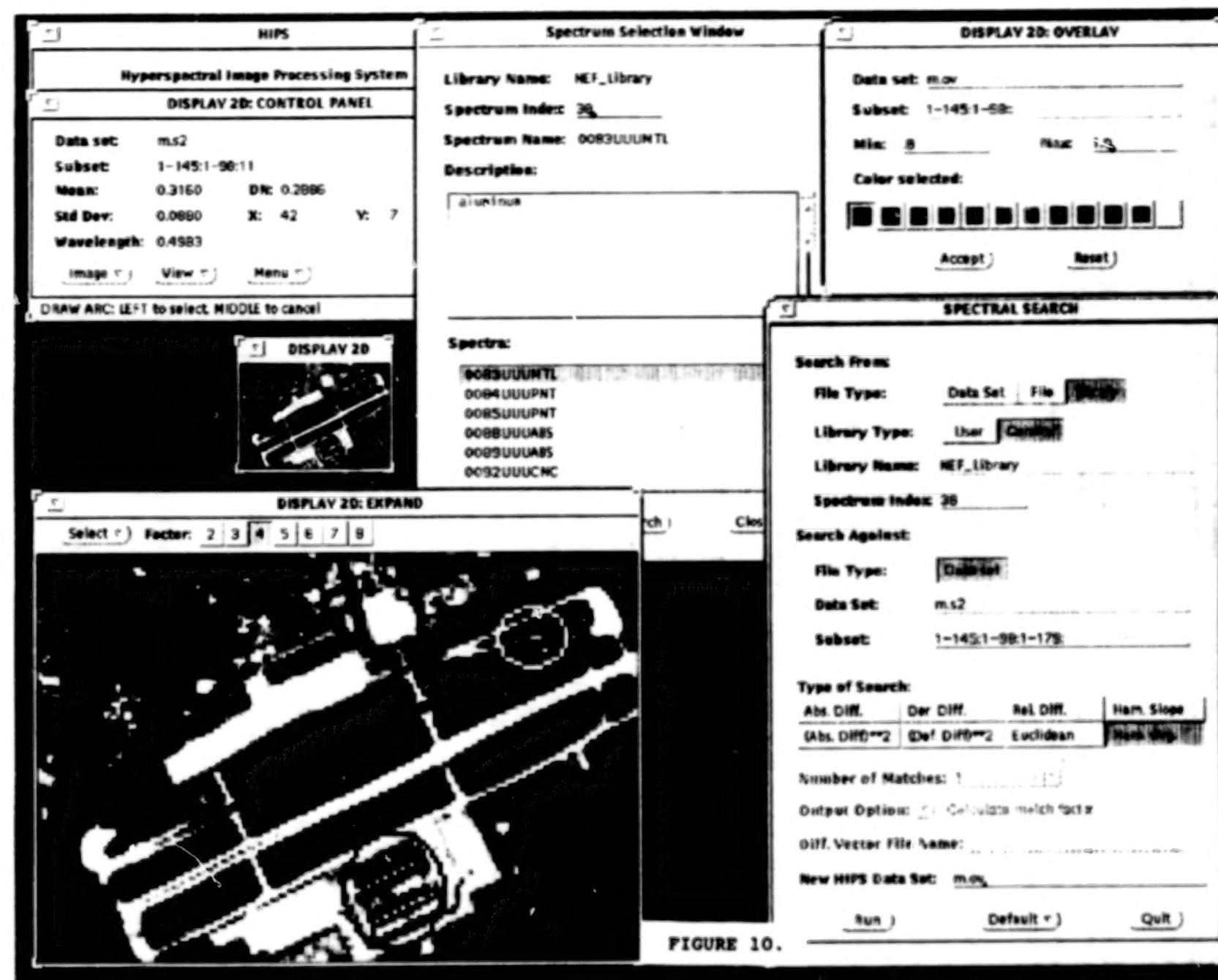


FIGURE 10.

aluminum spectra. In the large black indicator ring are twelve alarmed pixels that have responded to a match factor between 60 and 100 percent as compared to the original spectrum. They all appear as a light gray shade. In the original colored image, they all appear in red.

The last data set is Moffett Field, near San Francisco, Calif. (see Figure 10) It was produced by JPL's AVIRIS sensor, flown at about 60,000 feet and with a GSD of 20 meters. This relatively low spatial resolution permits the high-spectral resolution of about 200 bands while still maintaining a good signal to noise ratio.

However, at a 20-meter GSD, the only things that are obvious are the gross features of the runways and some of the larger buildings. Since there are no noticeable pixels that might represent aircraft from which a spectrum could be extracted, a search was performed from the library against the data set. The spectrum selected for the search was the same spectrum for aluminum that was extracted during the analysis of Washington National Airport. A spectral alarming for match factors between 80 and 100 percent produced eight alarmed pixels in the white indicator ring in the "expand" window. These would represent very large aircraft. One type of aircraft found at this field is the Lockheed P-3 Orion, whose fuselage and wing span are about 100 feet. This would be enough of a target area to provide for a few alarmed pixels. Another alarmed image is found in the black indicator ring. These are two large metal hangers used for dirigibles.

Summary

Hyperspectral remote sensing combines digital imagery with spectroscopy. This new technology can provide for the remote identification of target materials by means of library searches and spectral alarming. Spectral libraries of anticipated target spectra must first be compiled using field and laboratory spectrometers. Data set calibration also must be performed in order to achieve compatibility between the image cube and the spectral libraries prior to searching. A great advantage of this technology is the ability to spectrally identify targets whose dimensions are beyond the spatial resolution of the sensor.

References

- Chen, H. S. "Space Remote Sensing Systems." New York, NY: Academic Press, 1985.
- Elachi, C. "Introduction to the Physics and Techniques of Remote Sensing." New York, NY: John Wiley & Sons, 1987.
- Vane, G. "Imaging Spectroscopy II," Proceedings of SPIE-The International Society for Optical Engineers, Vol. 834, 20-21 August 1987: San Diego, CA.
- Vane, G. "Airborne Visible/Infrared Imaging Spectrometer (AVIRIS)," JPL Pub. 87-38, Jet Propulsion Laboratory, Pasadena, CA, 1987.

REAL -TIME ANALYSIS OF SPECTRAL AND SPATIAL DATA FROM HYPERSPECTRAL IMAGING SENSORS

**Wally T. Jansen
WTJ Software Services
San Mateo, California 94401, USA**

ABSTRACT

Since the early days of remote sensing, data has been accumulating faster than the ability to analyze it. Warehouses are being filled with various types of media in an attempt to save most of the record. The global Landsat data base has great historical value as record of changes in the environment, climate and land use. The analysis of such a data base can be performed at a rate commensurate with its' collection period. Basically, long term trends can be analyzed in the long term. Whereas in the past, remotely sensed spectral data was gathered to be stored for a subsequent, time-consuming analysis process, our goal has been to move from the experimental to a real-time operational stage with hyperspectral data. The recent proliferation of airborne imaging spectrometers has made it possible to respond much more rapidly to evolving or emergency situations. Under these circumstances these instruments produce detailed data which is most useful if it can be interpreted immediately. The time-value of the contained information is much shorter. Dual-Use applications such as oil spills and fires come to mind. With well defined, specific objectives, the aircraft actively participating in the containment effort could simultaneously gather, interpret, and then act on the derived information. The system to be demonstrated has been developed to ingest hyperspectral data, interpret it both spatially and spectrally and to present the results at real-time rates on readily available, portable computer hardware.

1. INTRODUCTION

Most imaging spectrometers produce data sets that are relatively long narrow strips. Typically under 1000 pixels wide they can easily extend to tens of thousands of lines in length. To display and analyze such images becomes cumbersome if it is done on a frame by frame basis. The approach within the developed system is to emulate the way in which the data is collected on a line by line basis. The system displays the data as a continuously scrolling screen display showing a composite color image of the terrain. As the data is read off the disk it is analyzed and the results are superimposed on the RGB image as multiple overlays identifying different surface characteristics. The analysis consists of a series of discrimination functions including spatial and spectral constraints. The functions determine the assignment of target identifiers (colors) to pixels in the moving image. The mix of functions and their constraint limits are defined by the operator interactively. The effect of the change in control parameters becomes visible immediately allowing the user to adapt to changing conditions during each flight. A built in spectral library enables on line calibration of the incoming data prior to classification.

2.ON-LINE ANALYSIS.

2.1 THE DISPLAY

At start-up of the system, the combined RGB image of the user-selected channels and stretch type is scrolled onto the entire screen. When analysis is activated, the scrolling screen is split into an upper and lower half. Both halves now show the same section of the RGB image as the upper image may become obscured by overlays the lower image can still show the original spatial information. Up to four distinct color overlays may be superimposed on the image in the upper half of the screen. These overlays are generated one line at a time by analyzing the spectrum associated with each pixel and assigning a new, primary color to the pixel if the pixel belongs to a certain category or class. The colors of the pixels that do not fall into a defined class remains unchanged. The line of analyzed pixels is written onto the lower edge of the upper image as it moves up the screen.

Often the objective of an analysis is to locate areas in the image whose spectral signature indicates the presence of a certain target material. In the example shown in Fig. 1, spectra from a training set from several points within a selected field were averaged and a "standard target spectrum" was calculated. During analysis this spectrum is matched against the spectrum associated with each image pixel generating a Similarity Index \sim for that pixel (GenIsis User's Manual, 1989). If the Similarity Index is within a user definable threshold the pixel is assigned a white overlay color. The soil of and/or vegetation in the white fields in the image are likely to be very similar to the one used as the training set. When the Similarity Index is within a second cutoff level, the pixel is assigned a different overlay color based on one of two parameters calculated from the spectrum for that pixel. The first parameter is just the relative value of a specific channel for the pixel and for the standard spectrum. If, for example, a thermal channel is chosen as the discriminator, (potentially suggesting a relative temperature,) and the pixel's thermal channel value is greater than that of the standard spectrum, then the pixel is assigned a red overlay, otherwise it is assigned a green overlay. The second discriminating parameter is a test of the relative value of a vegetation index (i.e. NDVI) that would be a rough guide to the vegetation canopy coverage. A greater value would show more coverage and generate a green pixel, a smaller index would suggest more soil is present and the pixel is colored red. Trends of vegetation coverage within fields or relative values between fields are easily discerned from the locations of the generated overlays.

Other functions are used to categorize pixels prior to and after spectral matching. A test for detector saturation or data dropout excludes affected pixels from consideration. A vegetation index, computed from channels across the vegetation red edge pre-qualifies pixels for further processing. Spatial-spectral variance is used to characterize the uniformity of the environment around each pixel. If the variance for a given channel in the spectra of the pixels surrounding the pixel being analyzed exceeds the user-defined cut-off level, the pixel can be included or excluded from the subsequent processing and its color remains unchanged. Boolean operators, based on the various test functions are controlled by the operator 'on-the-fly'.

2.2 ACTIVE OPERATOR CONTROL

Since the screen is continuously moving the mouse or a similar pointing device cannot be used to control the system. The "Function Keys" and several other keys on the keyboard control the system directly. The status of the functions is shown on the screen at frequent intervals. In addition to direct control over the functions being applied to identify the nature of the pixels in the image the operator can manipulate the image in several ways.

At any point during the analysis the screen colors can be adjusted for brightness, contrast and



Figure 1. ERIM M7 Airborne Imaging Spectrometer Data

This data set, courtesy of ERIM, Ann Arbor MI, was collected using the M7 multispectral scanner on 7 May 1993 at 2:06 P.M. over Peach Mountain in Michigan. The image contains 16 bands, 2640 rows, and 512 columns. The original data was resampled to 2.5 meters and was corrected geometrically.

This histogram stretched image was produced by combining three channels, 10 (1230–1290nm), 6 (520–570nm), and 3 (440–460), for red, green, and blue respectively. The 16 channels range in wavelength from 350 nm to 12 microns, most being in the visible to near-infra-red range. The overlays are the vegetation being sought (white); similar vegetation but more soil showing through (red); and, similar vegetation but with a more complete canopy (green).

saturation (independently from the overlays). The analysis can be halted and the image can be scrolled back to show over 3250 image lines (on a 2 Mbyte SVGA board). Both the color modification and the image scrolling are performed under mouse control.

2.3 DISPLAYING ANALYTICAL RESULTS

The system reports the progress, function status, and the numerical results of the analysis adjacent to the scrolling image. The number of image lines analyzed per second is shown. This number, with the knowledge of the pixel size (specifically line spacing) allows the operator to determine maximum ground speed for a certain computational load. The status of the functions operating on the data is shown along with a count of the pixels covered by each of the colored overlays.

Other optional displays in the upper half of the screen are the Similarity Index Map, showing the Similarity Index of each pixel in the image, and the spatial variance function, and the effect of the active Boolean operators.

2.4 HARD-COPY OUTPUT

Although the system normally scrolls through the data continuously, starting back at the beginning of the file when the end is found, the operator can force a restart which also provides the option to specify an output filename into which the upper image is written. This output image is a 24-bit RGB file unless a Similarity Index Map or Spatial Variance image is requested in which case a monochrome 8-bit plane is written. Another output option is a standard color-mapped 'TGA'-format file which can be scanned much faster than the hyperspectral image. The 8-bit image saved from the example 2640 line data set scrolls by in under 10 seconds (corresponding to 2640 km/h!). Scrolling speed can be reduced to a comfortable level by the operator or by the program when it detects the presence of many pixels covered by the white, red, or green overlays, i.e. targets of interest. The standard Targa file can be imported into most Windows based imaging tools for annotation and printing.

3. RESULTS

The example data set used to demonstrate the system comes courtesy of ERIM, Ann Arbor MI. It was collected using the M7 multispectral scanner on 7 May 1993 at 2:06 P.M. over Peach Mountain in Michigan. The image contains 16 bands, 2640 rows, and 512 columns. The original data was resampled to 2.5 meters and was corrected geometrically.

The image shown in Fig. 1 was produced by combining three channels, 10 (1230-1290nm), 6 (520-570nm), and 3 (440-460), for red, green, and blue respectively. Only the top 880 lines of the image are shown. This false color image is scrolled on the computer screen simulating the view from the aircraft. The PC notebook computer used for the demonstration takes approximately 90 seconds to cycle through the complete data set once. Since the pixel width and the line spacing was approximately 2.5 meters, an apparent ground speed may be calculated:

$$\text{'analysis speed'} = 2.5\text{m/line} \times 2650\text{lines} / 90\text{sec} \times 3600\text{s/hr} / 1000\text{m/km} = 265 \text{ km/hr.}$$

This speed is actually greater than that of the aircraft collecting the original data. The analysis rate is largely controlled by the speed at which the hard disk is able to transmit the file to the CPU, although the more complex spectral and spatial screening functions also have an impact on throughput. It should be noted that AVIRIS data with 224 channels is acquired at approximately 11 lines per second. SCANNER can analyze and display AVIRIS data at 16 lines/second. If SCANNER were to avoid the significant disk I/O bottleneck but was to be connected directly to an instrument through a SCSI port it will be able to process data much faster. The results from SCANNER may be saved to a file which can be displayed at ten times the real-time analysis speed

including an ability to slow down automatically when targets of interest appear.

4. CONCLUSION

The 1 1/2 year old notebook PC used to demonstrate this system is a 66MHz 486 with a reasonably fast IDE hard disk (11ms). Today PCs and even notebooks are available with much faster data busses and processors which would significantly increase data interpretation rate. Such a new computer connected directly to the spectrometer could improve performance even more. Then, by writing only the 24-bit image to the disk, more terrain can be covered and the results can be examined quickly. As the measured times to analyze this relatively simple image indicate, it is feasible to analyze hyperspectral data in a timeframe comparable to that taken to collect it. The vast increase in the amount of data that hyperspectral scanners provide can be used operationally.

A HYPERSPECTRAL IMAGE PROCESSING SYSTEM—HIPS™

Nicholas J. Susner, Juliana T. Lo and Thomas B. McCord
SETS Technology, Inc.
300 Kahelu Avenue, Suite #10
Mililani, HI 96789-3911, USA
(808) 625-5262

A hyperspectral image processing system, HIPS™, has been developed and is being distributed commercially. HIPS was designed and developed specifically to handle hyperspectral image cubes and to emphasize the spectral processing. Although there are many image processing systems, and some of these have been modified to handle multispectral analysis, there are very few hyperspectral image processing systems. HIPS is structured to handle large image cubes of any number of dimensions. The entire cube is treated and spectra and image planes are extracted for more traditional spectrum or image analysis. Spectral libraries are integrated into HIPS and are an integral part of the analysis process. Modules available on HIPS include subpixel mixing analysis of several types and automated material and target detection algorithms. HIPS is currently being extended to include ultraspectral analysis such as analysis of gases in an image format. HIPS runs under the UNIX operating environment and is coded in C. HIPS will soon be ported to the IBM massively parallel processing environment for treatment of very large data sets.

HIPS is a fully supported and documented system. Service and updates are provided on a continuing basis under annual maintenance contracts.

Manuscript not available at time of printing. Please contact authors for further information.

SPECTRAL CHARACTERISTICS (0.4 μm - 2.5 μm) AND THE DETECTION OF CAMOUFLAGE MATERIALS

**Timothy D. Evans and Ponder Henley
U.S. Army Topographic Engineering Center
Alexandria, Virginia 22310**

ABSTRACT

The spectral matching of camouflage materials (equipment nets and personnel uniforms) to natural backgrounds in the 0.4 μm to 0.9 μm region is well established. However, matching the materials spectral characteristics to backgrounds in the 1.0 μm to 2.5 μm region has not been a high priority effort due to the previous limitations of spectral imaging systems used for detection. Some classes of camouflage materials show easily detectable spectral differences in the reflected infrared region (0.7 μm - 2.5 μm). Presented are the spectral characteristics of camouflage materials and uniform fabrics measured as pure samples and with natural backgrounds. Detectable differences in spectra are shown and these are applied to airborne multispectral imagery for the discrimination and identification of camouflage materials against natural backgrounds.

1. INTRODUCTION

The development of camouflage materials includes careful matching of the dyes with likely background materials against which the camouflage is to be deployed. A variety of camouflage materials, including nets and fabrics, have been measured spectrally by the Topographic Engineering Center (TEC) both in the laboratory and in the field. Spectral signatures are presented which show that these materials are indeed good camouflage in the visible and near infrared portions of the spectrum (0.4 μm to 0.9 μm). However, above 0.9 μm , there are detectable differences between camouflage materials and natural backgrounds which can be exploited to locate camouflaged objects in a remote scene. The results of experiments using airborne multispectral instruments will be presented illustrating the application of these techniques to locating camouflaged objects in remotely acquired imagery.

1.1 LABORATORY AND FIELD SPECTRAL MEASUREMENTS

Spectral reflectance was measured by the authors both in the laboratory and in the field using Geophysical Environmental Research (GER) spectroradiometers. The spectral range covered was 400 nanometers (nm) to 2500 nm with a spectral resolution of 1.5 nm to 4.5 nm. The output from the spectroradiometer was downloaded to an IBM-compatible PC for data reduction. A data reduction program was used to convert the data to percent reflectance (compared to a Halon reflectance standard) and output the results in 5 nm increments.

Laboratory measurements were made using 500 watt tungsten halogen photolamps. Field measurements were taken in natural sunlight.

1.2 SPECTRAL CHARACTERISTICS OF CAMOUFLAGE MATERIALS AND BACKGROUNDS

The spectral characteristics of military paints (Figs. 1 to 4), camouflage nets (Figs. 5 to 10) and camouflage fabrics (Figs. 11 to 16) match closely those of natural backgrounds (Figs. 17 to 24) in the visible and near infrared regions (400-800 nm).

The purpose of camouflage is to break up the characteristic outline of an object and to make it indistinguishable from the background or environment in which it is located. Military camouflage may consist of painting an object to match the colors of the background, or covering an object with various materials to hide the shape and match the background color. Some camouflage methods and materials mask or hide the invisible but detectable thermal signatures of military equipment.

The camouflage materials and paints considered for this study were produced to match the reflectivity of natural vegetation and soil backgrounds in temperate and arid climates. All camouflage materials measured for this study share certain spectral characteristics. All show visible reflectance spectra which closely match the backgrounds of the intended areas of deployment and while no camouflage net or fabric spectra is identical to a natural soil or vegetation spectra, the camouflage spectra are good representations of an average spectra of the range of naturally occurring vegetation or soil surfaces. Camouflage materials such as the Woodland BDU (Battle Dress Uniform) which are designed for temperate or tropical regions with green vegetation backgrounds, have a reflectance spectra showing a reflectance peak in the green region (520-560 nm), a low absorption in the red region (600-690 nm) and a reflectance maximum in the near infrared region (800-900 nm). All of these spectral features are characteristic for healthy green vegetation (Figs. 21, 22 and 23). Likewise, camouflage materials designed for arid or desert regions show spectral characteristics of dry soils with some sparse brownish green vegetation (Figs. 17, 18 and 24).

Most camouflage materials do not show characteristic spectra of natural backgrounds in the near-infrared (NIR) to the short wave infrared (SWIR) region of the reflected spectra, and because of this, they should be detectable using remote sensing systems which operate over the NIR-SWIR range. Specific examples of the differences between natural background spectra and camouflage material spectra are shown in Figs. 18 and 13.

The materials shown are camouflage fabrics used for military uniforms, military paints used to create camouflage patterns on vehicles and equipment, and camouflage nets used for draping and hiding of equipment and personnel. A range of background materials is also shown. The reflectance spectra of all of these materials and backgrounds were collected by the authors using GER field spectroradiometers under solar illumination and using a Spectralon reflectance standard. No attempt is made to identify the camouflage nets other than by a generic description of the type, i.e. woodland or desert.

2. REMOTE DETECTION OF CAMOUFLAGE

Comparison of the spectral signatures of camouflage materials with the signatures of background materials above shows that it should be possible to detect camouflage remotely. Two experiments were performed in which the same camouflage materials were placed against different background materials and in different environments. Imagery was acquired using an airborne multispectral scanner. The results of the experiment show that it is indeed rather easy to locate the camouflage in the imagery.

2.1 REMOTE IMAGERY ACQUISITION

Two experiments were performed in which remote imagery of camouflage materials was acquired: one at the Marine Corps Air Ground Combat Center (MCAGCC), Twentynine Palms, California; and the other at the Maryland National Guard site at Olney, Maryland. The imagery at MCAGCC was acquired in September 1991 and was taken against a desert background. The imagery at Olney, Maryland was acquired in December 1992, and was taken against a grass background. In both experiments, the imagery was taken using a Daedalus 1268 multispectral scanner. The bands collected are given in Table 1. The scanner was flown by the EG&G Corporation on board a Cessna Citation II, a small business jet aircraft.

2.2 EXPERIMENTAL PROCEDURES

The camouflage materials used in both experiments were fabric panels made from camouflage uniform fabric. The panels were constructed by laying two three meter lengths of 52 inch wide fabric side by side. The panels were placed directly on the sand (California experiment) or grass (Maryland experiment). No attempt was made to level the surface under the fabric panels. The Maryland experiment also included two camouflage nets. One was a desert camouflage net which was draped over two vent pipes against a grass background. The other was a woodland camouflage net draped over an M-114 armored personnel carrier, also against a grass background.

In the California experiment, the airborne imagery was acquired between 1200 hrs and 1300 hrs PDT. Field spectra of the panels were acquired immediately before and immediately after the flights. In the Maryland experiment, the imagery was acquired at approximately 1430 hours EST. Field measurements of the panels were taken at the same time as the overflight.

2.3 DETECTION OF CAMOUFLAGE THROUGH IMAGE EXPLOITATION

In order to illustrate the detection of camouflage materials using spectral remote sensing, two imagery examples are shown in Figs. 25 and 26. In both cases, the imagery was collected under poor lighting conditions and show less than optimal discrimination. The imagery was collected using a Daedalus 1268 multispectral scanner; the spectral range and band characteristics of the scanner are shown in Table 1.

The first image is of camouflage materials arrayed on a bare dry desert surface. Both woodland and desert materials are placed on the surface to show spectral contrasts in the visible region. Figure 25 is an RGB composite image using Daedalus bands 5, 3 and 2 (see Table 1) on the red, green and blue guns of the RGB monitor. Two of the desert fabric panels are not easily detected, whereas the green or woodland materials are easily seen. Figure 26 is an RGB composite of three infrared bands, 7, 8 and 9. All of the fabric panels are easily seen in this image due to the reflectance contrasts between the desert soil and the camouflage materials in the NIR and SWIR spectral regions. To further illustrate the spectral contrasts between backgrounds and camouflage materials, Fig. 27 shows an RGB composite image using bands 7, 5 and 8. In this image, one material is separated from all the others due to its unique spectral signature. The material is a dark green tenting fabric whose spectral signature is shown in Fig. 15. If the spectral signature of a material is known and it is sufficiently different from other materials, then spectral bands can be selected for the image in which this material can be separated from all others.

The second example is of similar materials to the first, but in a built-up area in a temperate climate. In this case, the desert materials are readily seen in Fig. 28. This image is a composite of bands 5, 3 and 2 RGB. Poor illumination conditions during the image collection results in lessened contrasts in the image and makes separation of individual materials more difficult. However, the camouflage materials are readily separated from the backgrounds in Fig. 29, which is a composite of the infrared bands 7, 8, and 9 RGB.

3. CONCLUSIONS

While most camouflage materials mimic soil and vegetation background spectral characteristics in the visible to near infrared regions, sufficient differences in spectral reflectance are present in the near infrared and shortwave infrared spectral regions to allow separation of these materials from the natural backgrounds.

TABLE 1. CONFIGURATION OF DAEDALUS 1268 MULTISPECTRAL SCANNER

<u>CHANNEL</u>	<u>WAVELENGTH (NM)</u>	<u>PEAK (NM)</u>	<u>COLOR SPECTRUM</u>
1	425 - 450	440	violet/blue
2	460 - 520	505	blue/green
3	525 - 600	575	green/yellow
4	595 - 640	610	orange
5	625 - 690	660	red
6	685 - 760	730	near infrared
7	750 - 875	810	near infrared
8	865 - 1000	920	near infrared
9	1595 - 1790	1730	near infrared
10	not used		short wave infrared
11	3000 - 5000		mid wave infrared
12	8500 - 14000		long wave infrared



Figure 1. Reflectance signature of tan paint used on military vehicles.



Figure 2. Reflectance signature of dark green paint used on military vehicles.



Figure 3. Reflectance signature of black paint used on military vehicles.

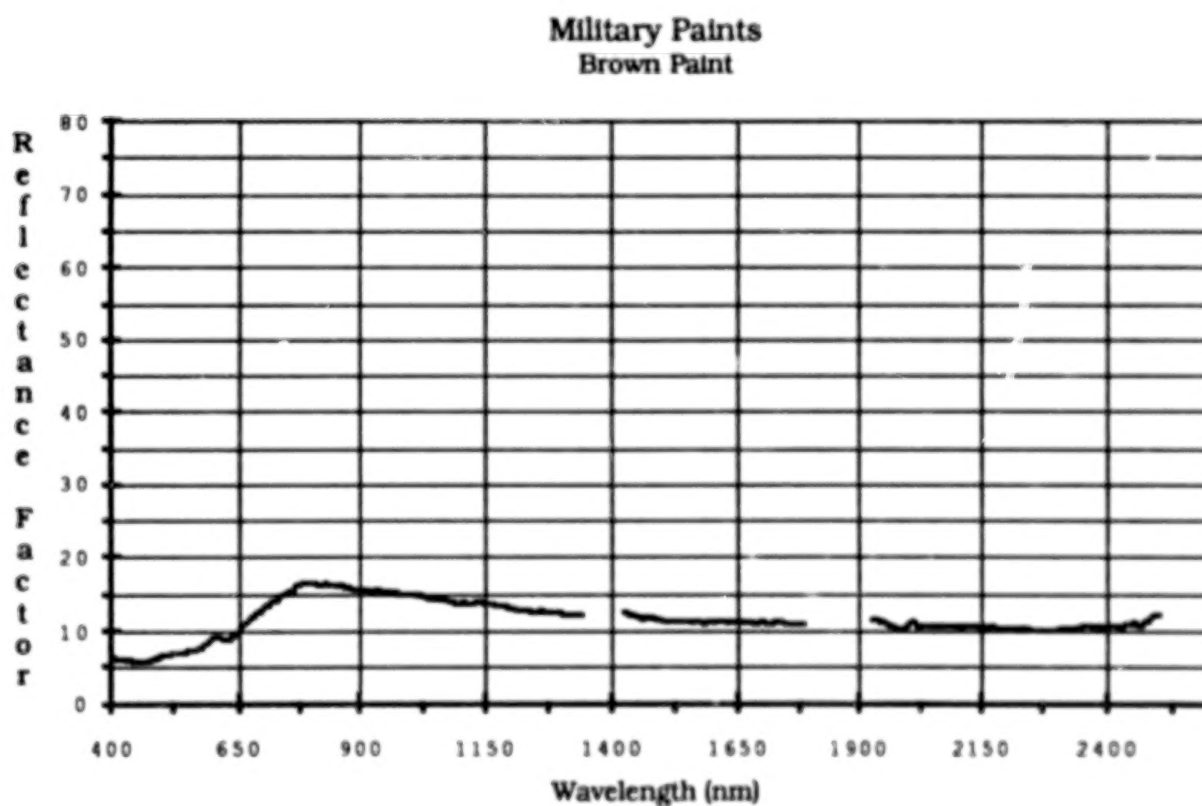


Figure 4. Reflectance signature of brown paint used on military vehicles.

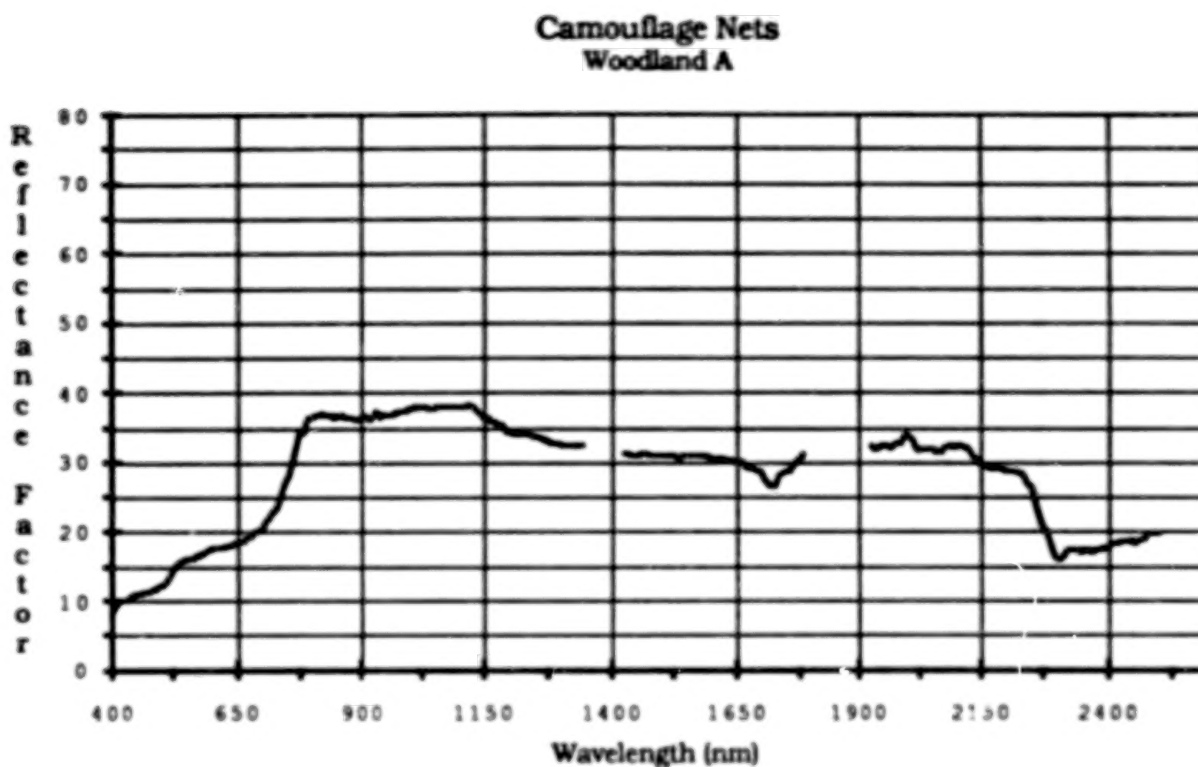


Figure 5. Reflectance signature of a woodland camouflage net with four color garnish.

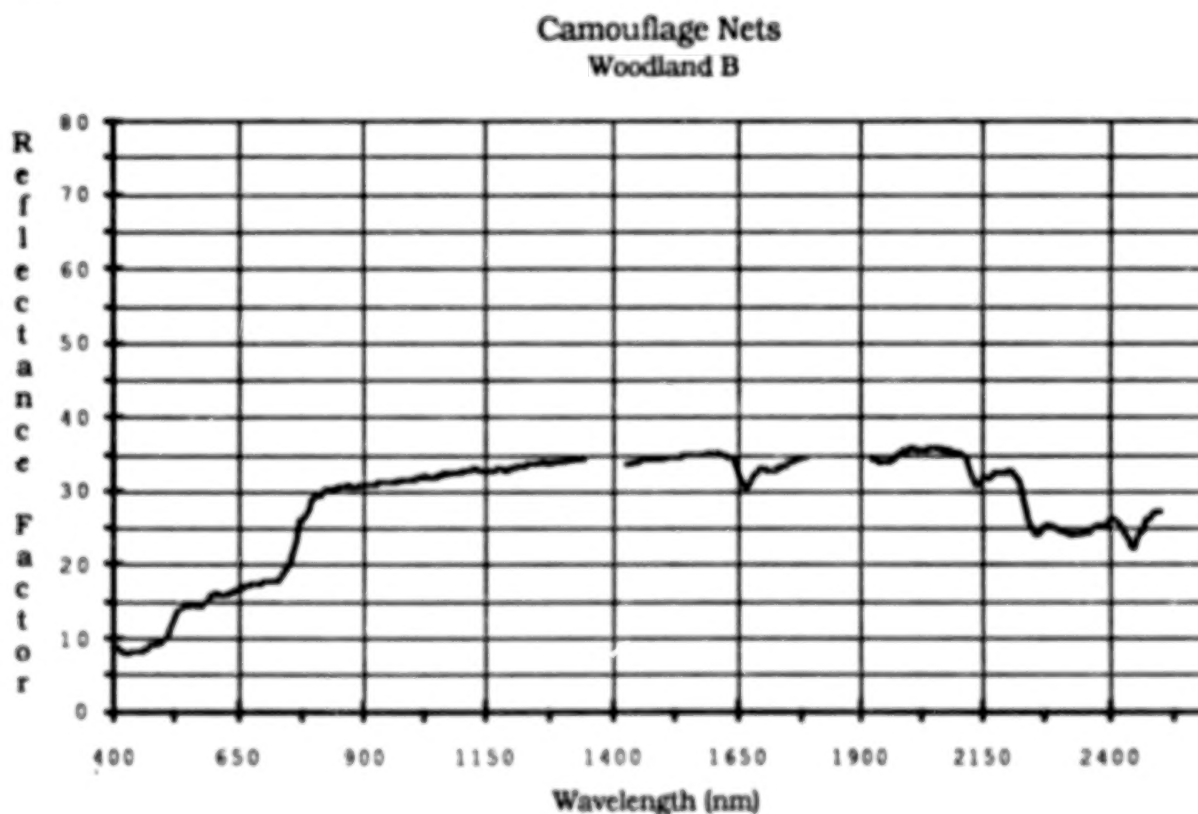


Figure 6. Reflectance signature of a painted woodland camouflage net without garnish.

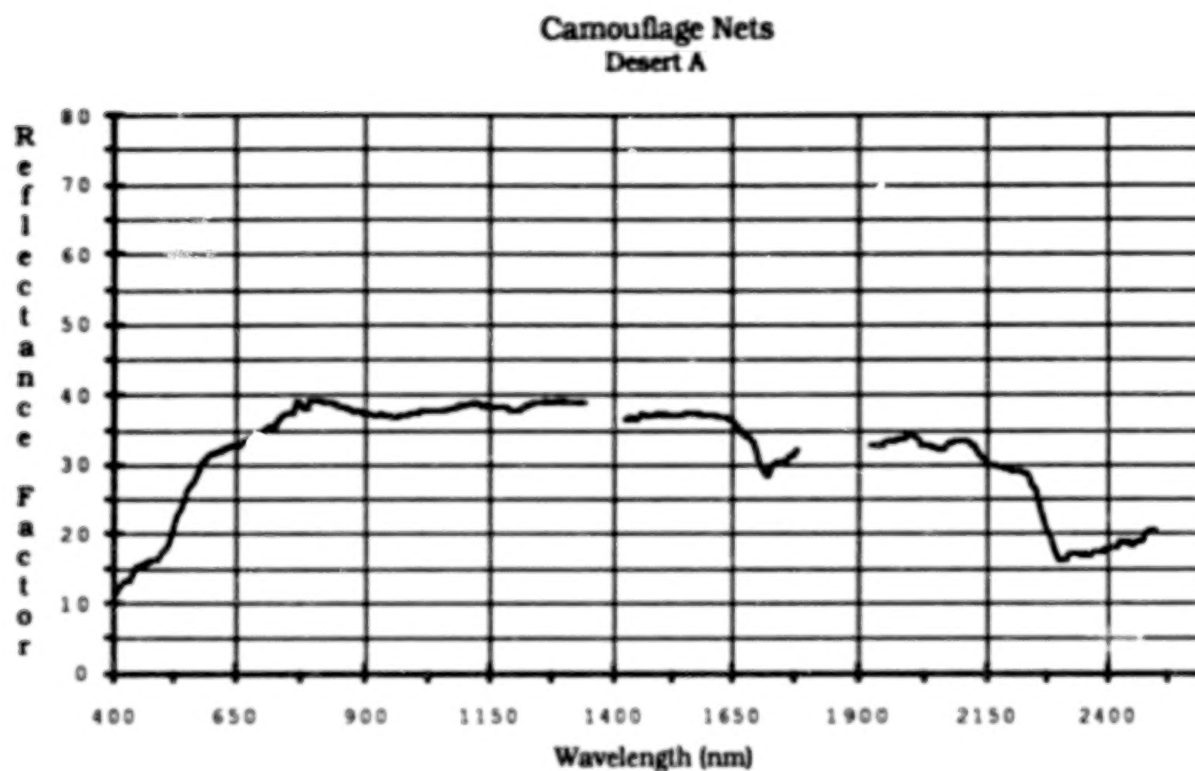


Figure 7. Reflectance signature of a desert camouflage net with seven color garnish.

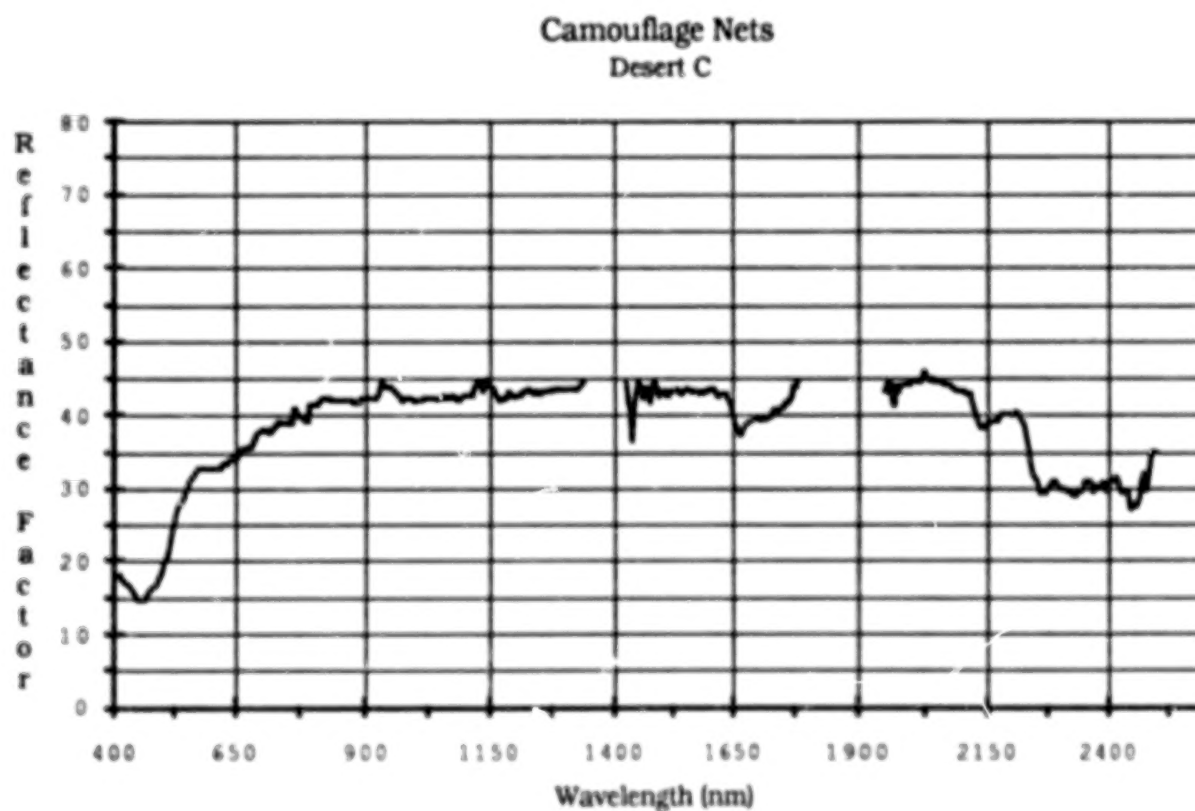


Figure 8. Reflectance signature of a single color desert camouflage net.

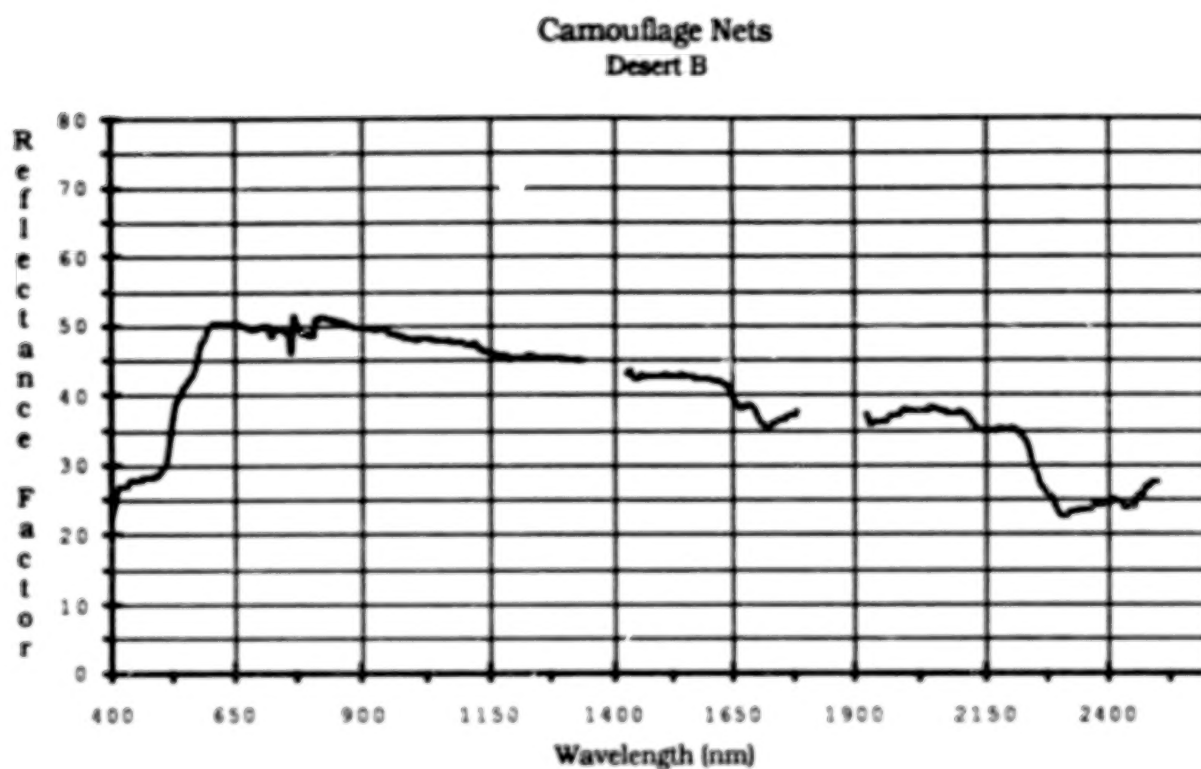


Figure 9. Reflectance signature of a light-toned single color camouflage net with garnish.

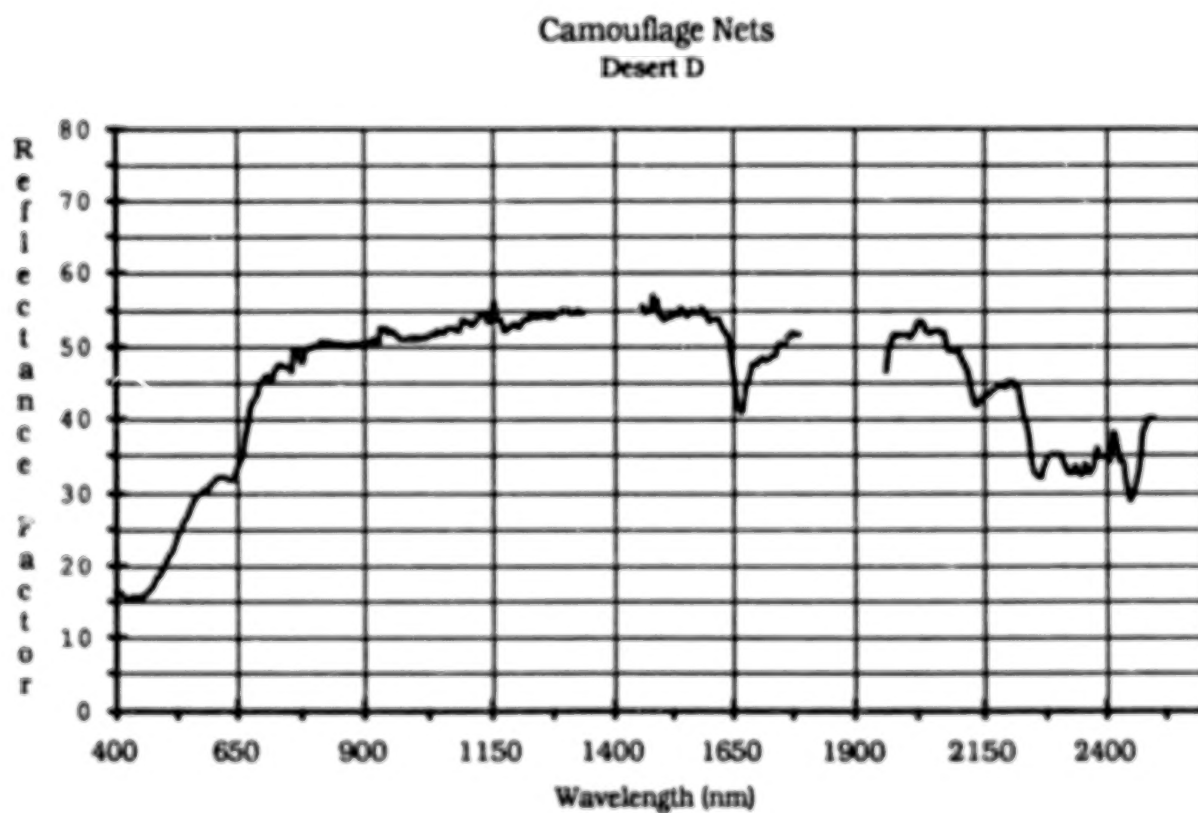


Figure 10. Reflectance signature of another single color desert camouflage net

Military Fabrics
Clothing--BDU Woodland

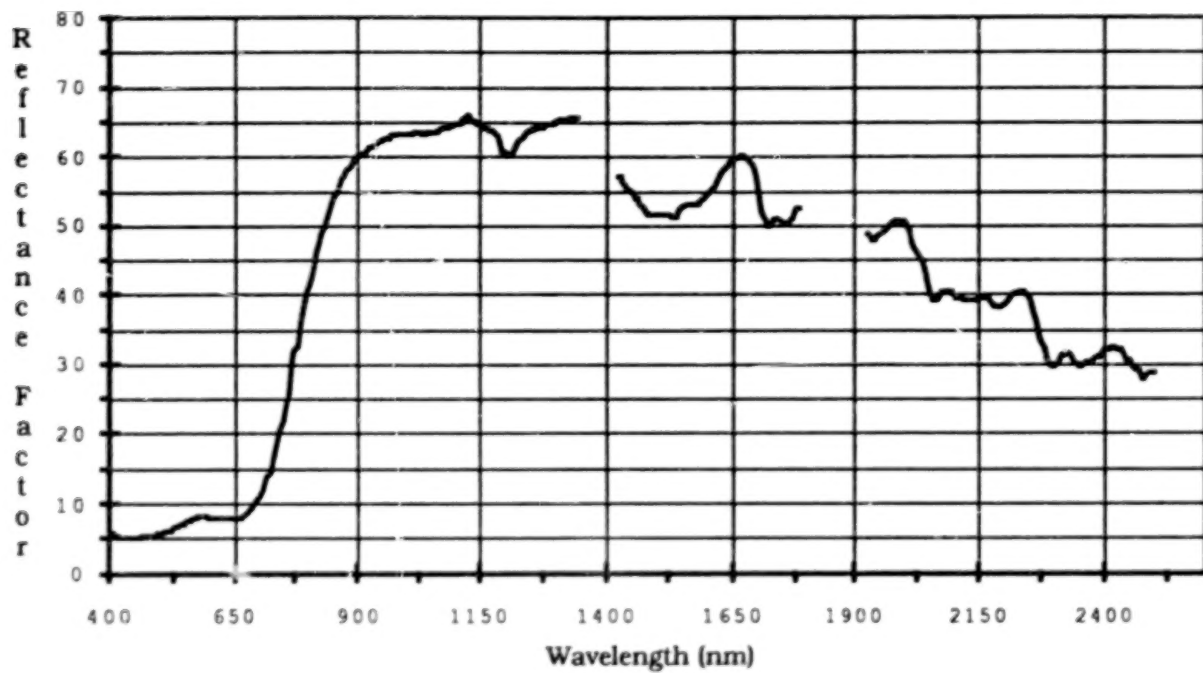


Figure 11. Reflectance signature of four-color poly/cotton battle dress uniform.

Military Fabrics
Clothing--Poncho Woodland

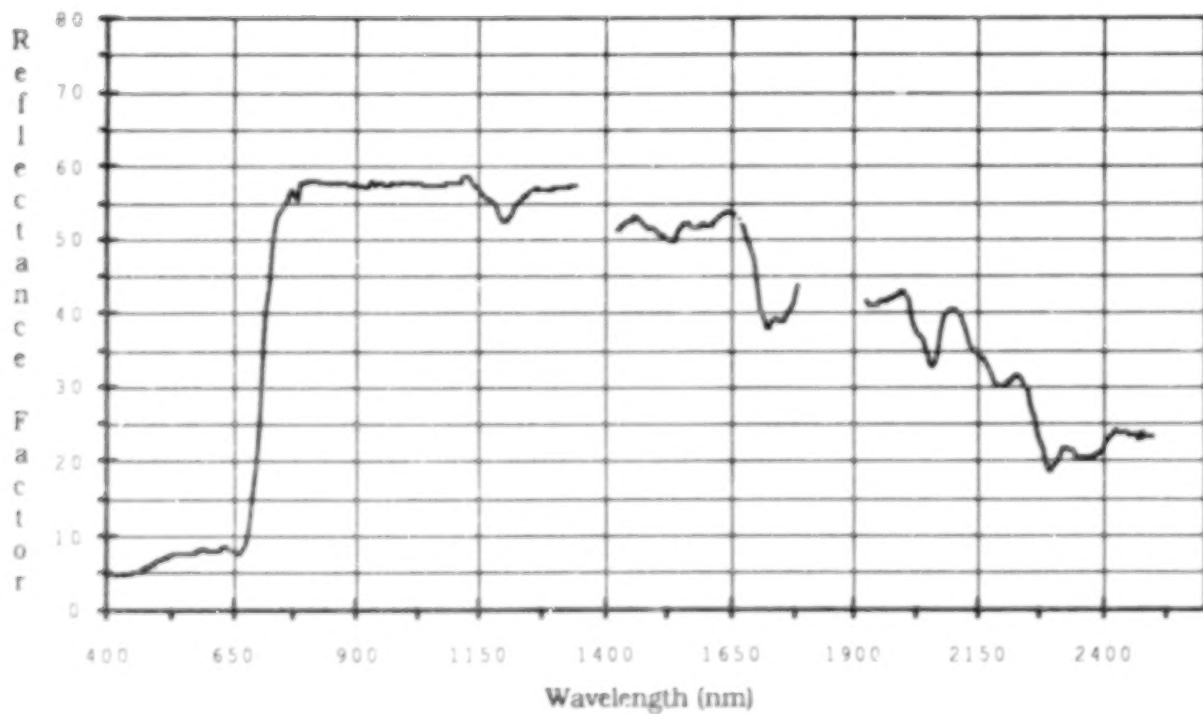


Figure 12. Reflectance signature of coated nylon four-color woodland fabric.



Figure 13. Reflectance signature of a three-color desert cotton fabric.



Figure 14. Reflectance signature of a single color cotton twill fabric.

Military Fabrics
Tenting materials--Green Tenting

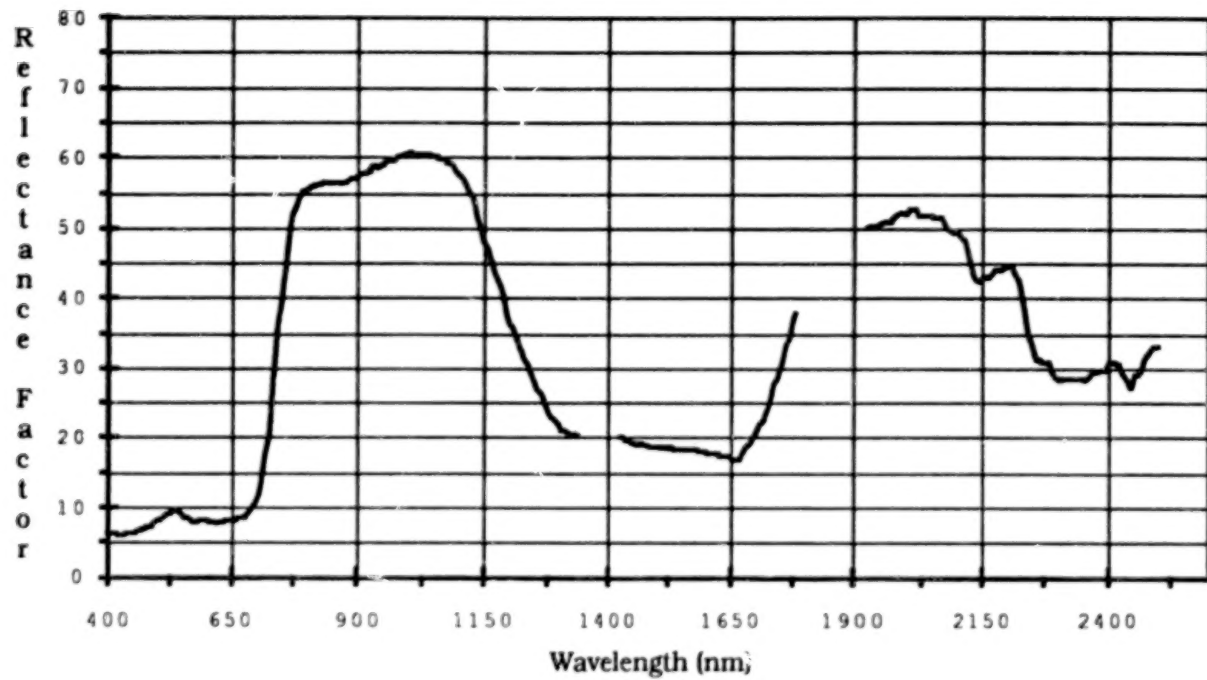


Figure 15. Reflectance signature of dark green coated poly/cotton tent fabric.

Military Fabrics
Tenting Material--Tan Tenting

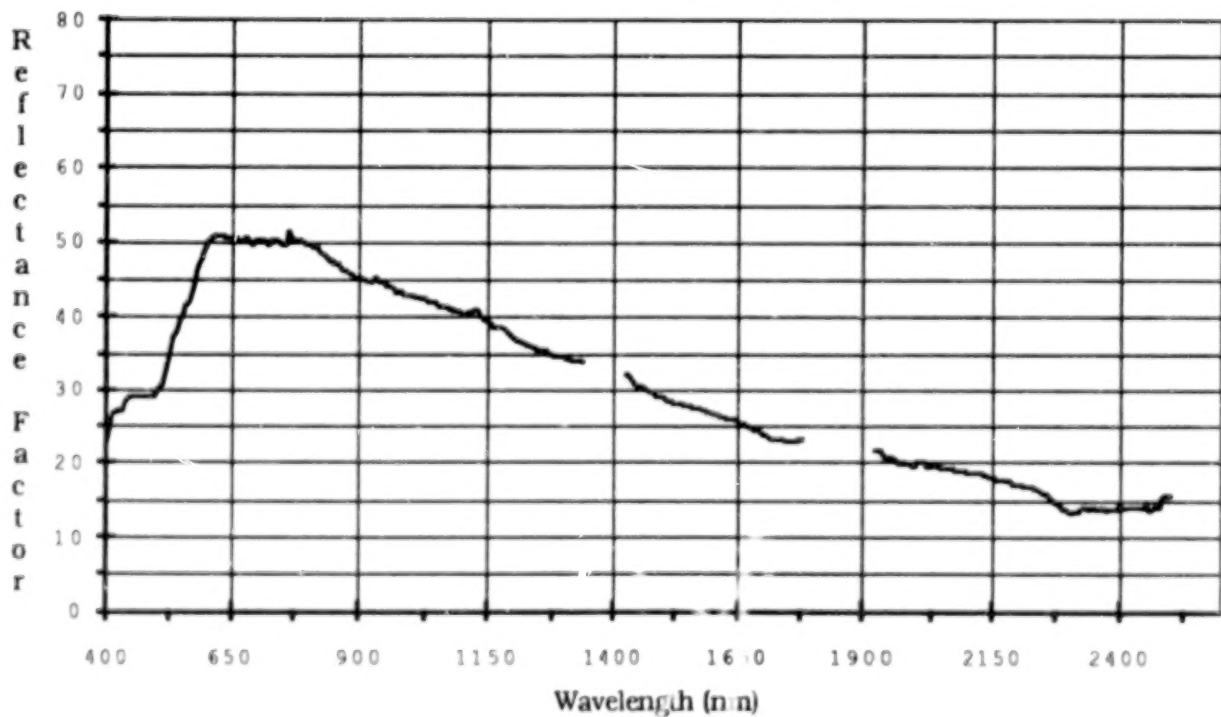


Figure 16. Reflectance signature of a coated tan poly/cotton tent fabric.

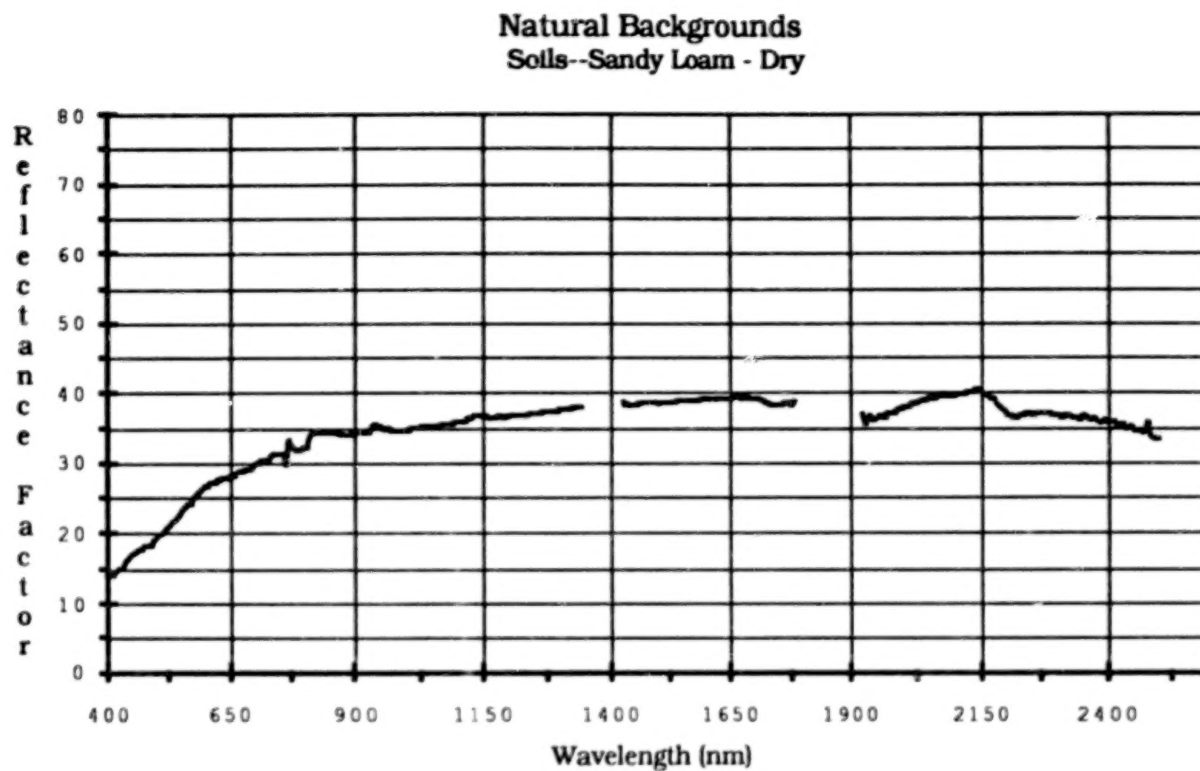


Figure 17. Reflectance signature of a dry sandy loam desert soil.

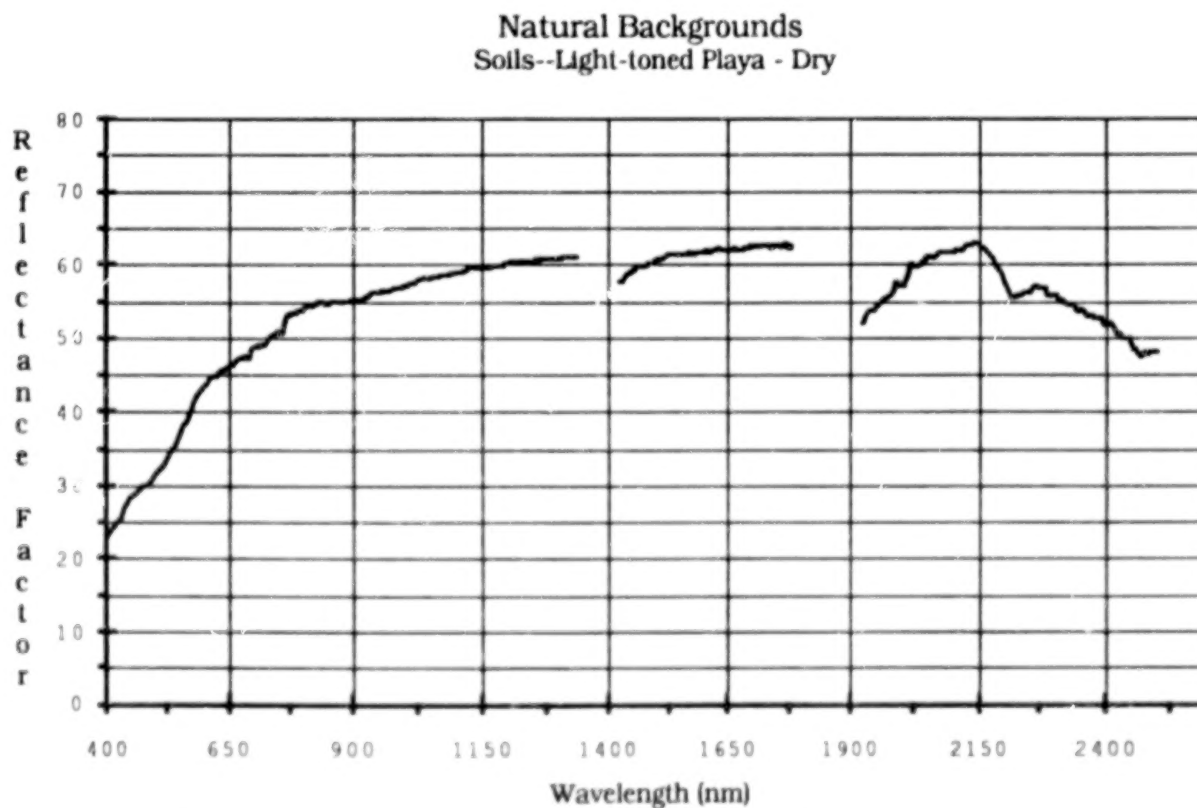


Figure 18. Reflectance signature of a light-toned dry silty clay surface.

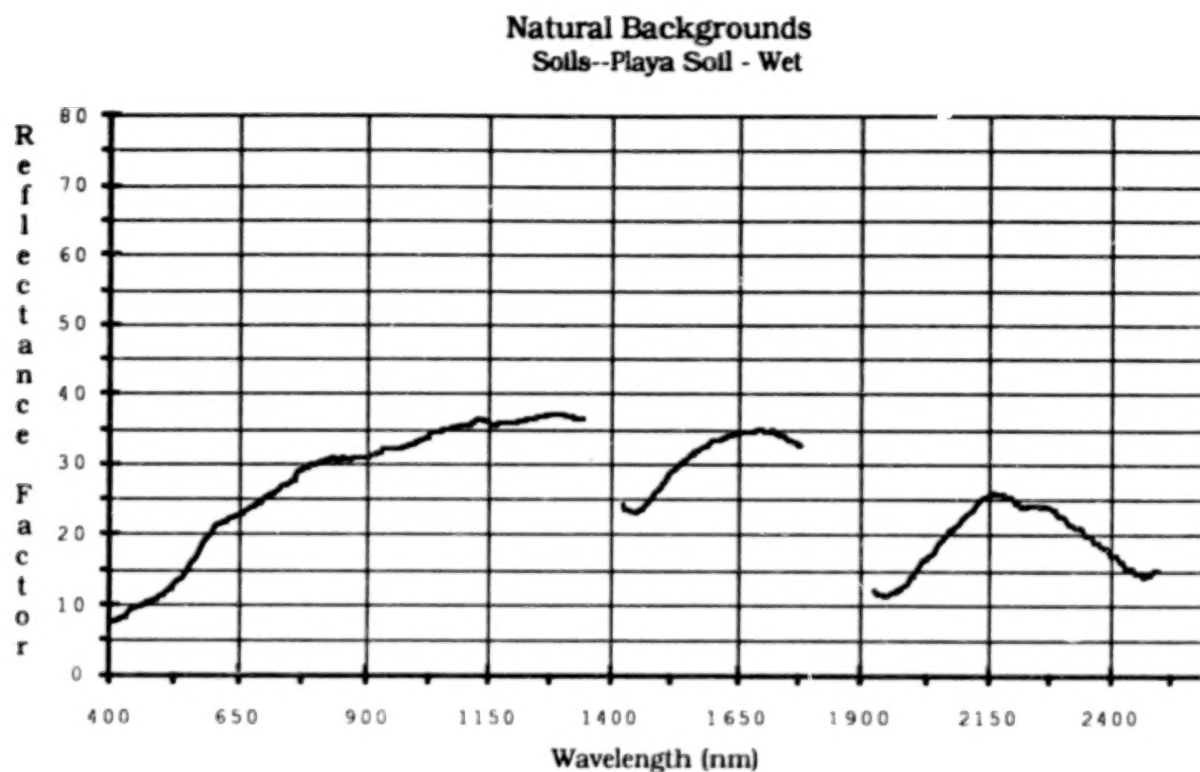


Figure 19. Reflectance signature of a wet light-toned silty clay surface.

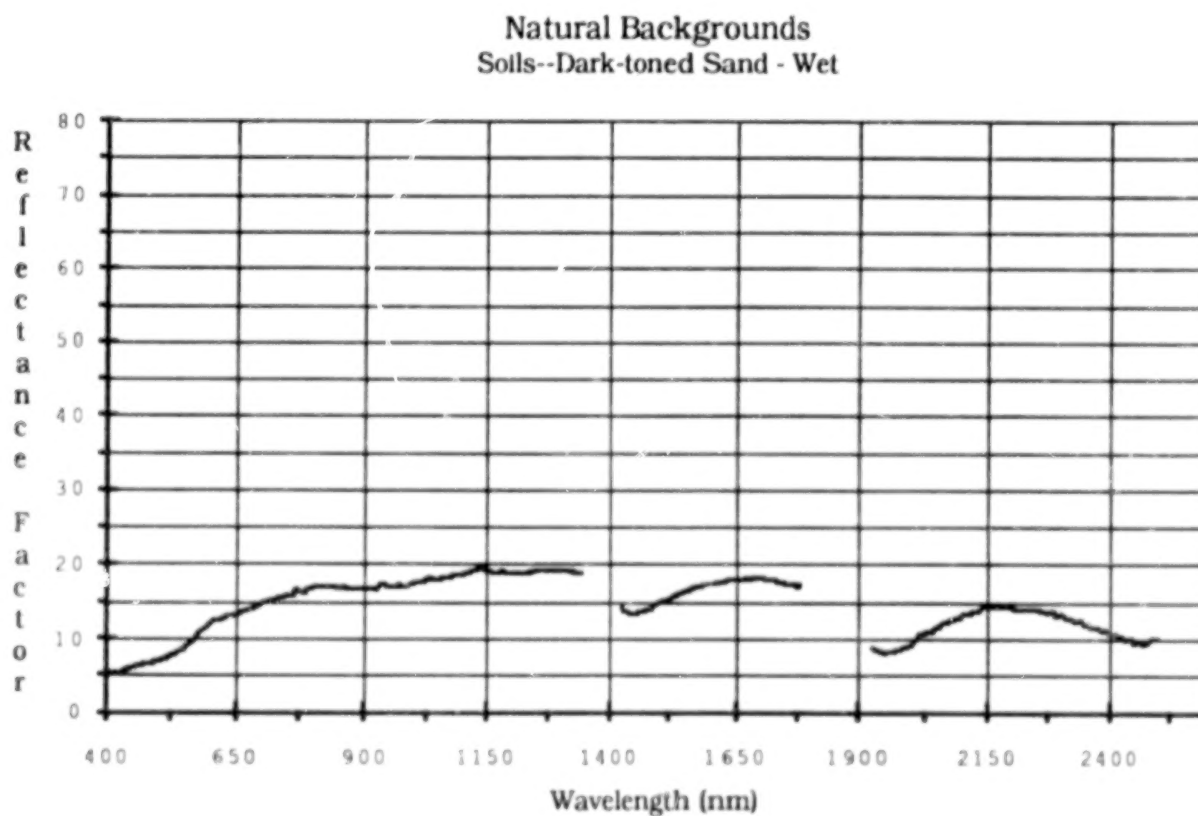


Figure 20. Reflectance signature of a dark-toned dry silty clay surface.

Natural Backgrounds
Vegetation--Greasewood - dark green

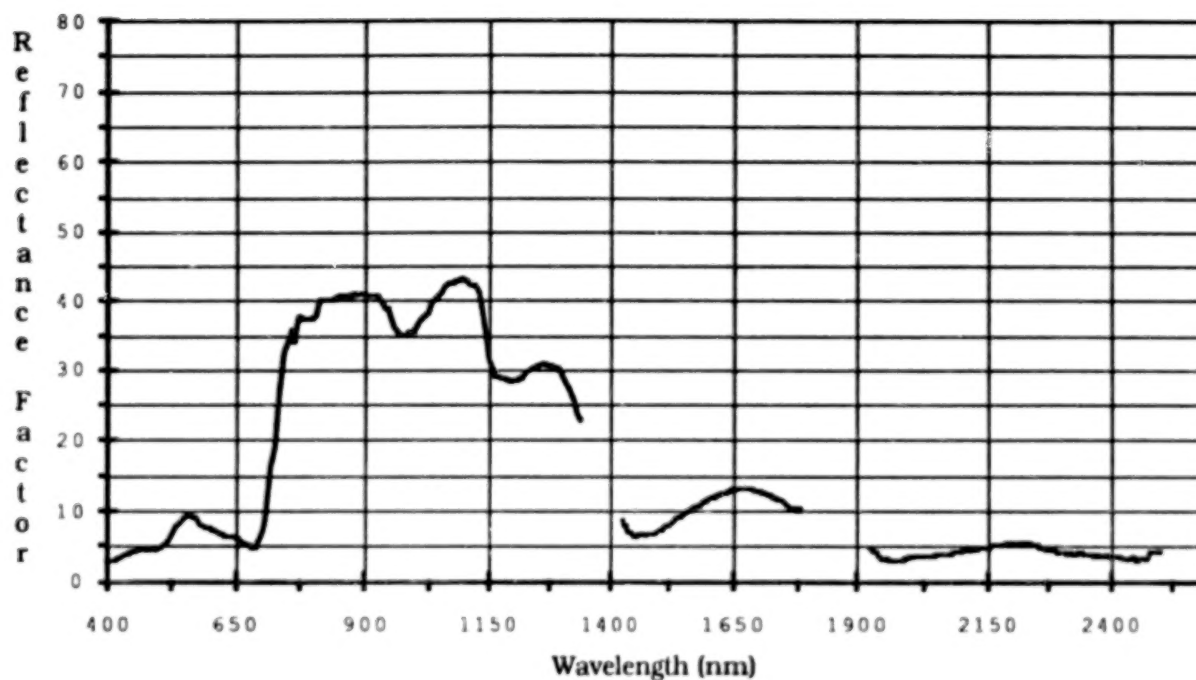


Figure 21. Reflectance signature of dark green desert shrub.

Natural Backgrounds
Vegetation--Shadscale - light green

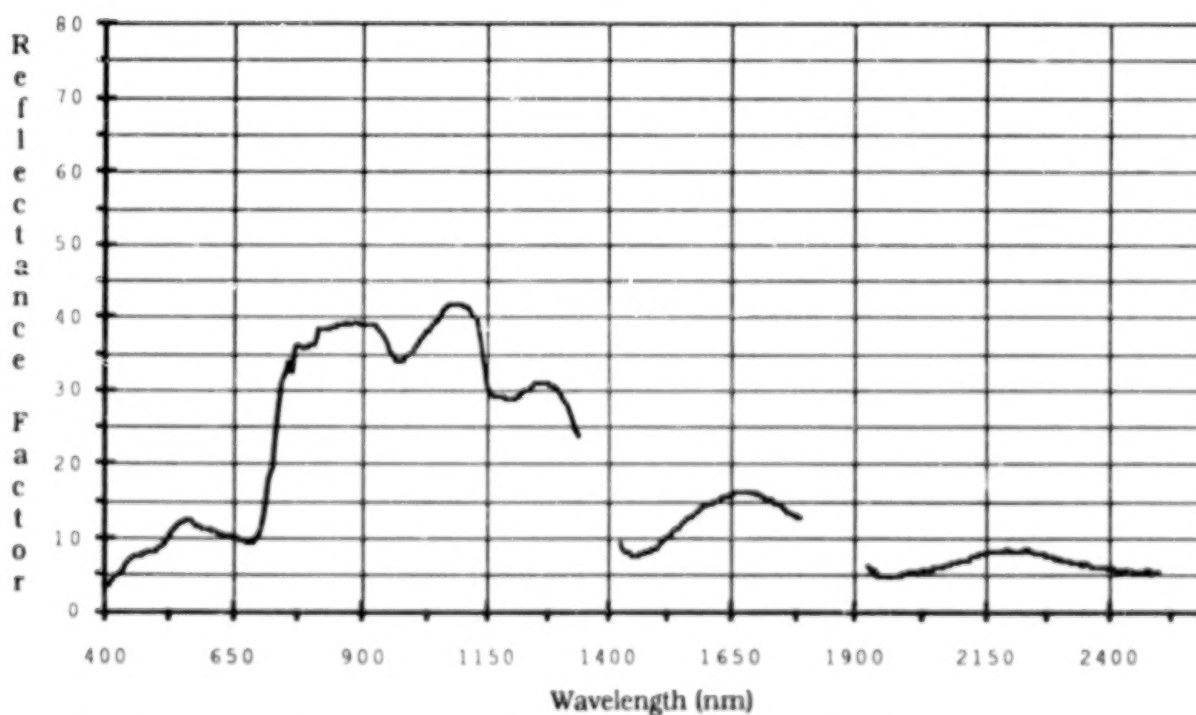


Figure 22. Reflectance signature of a light green desert shrub.

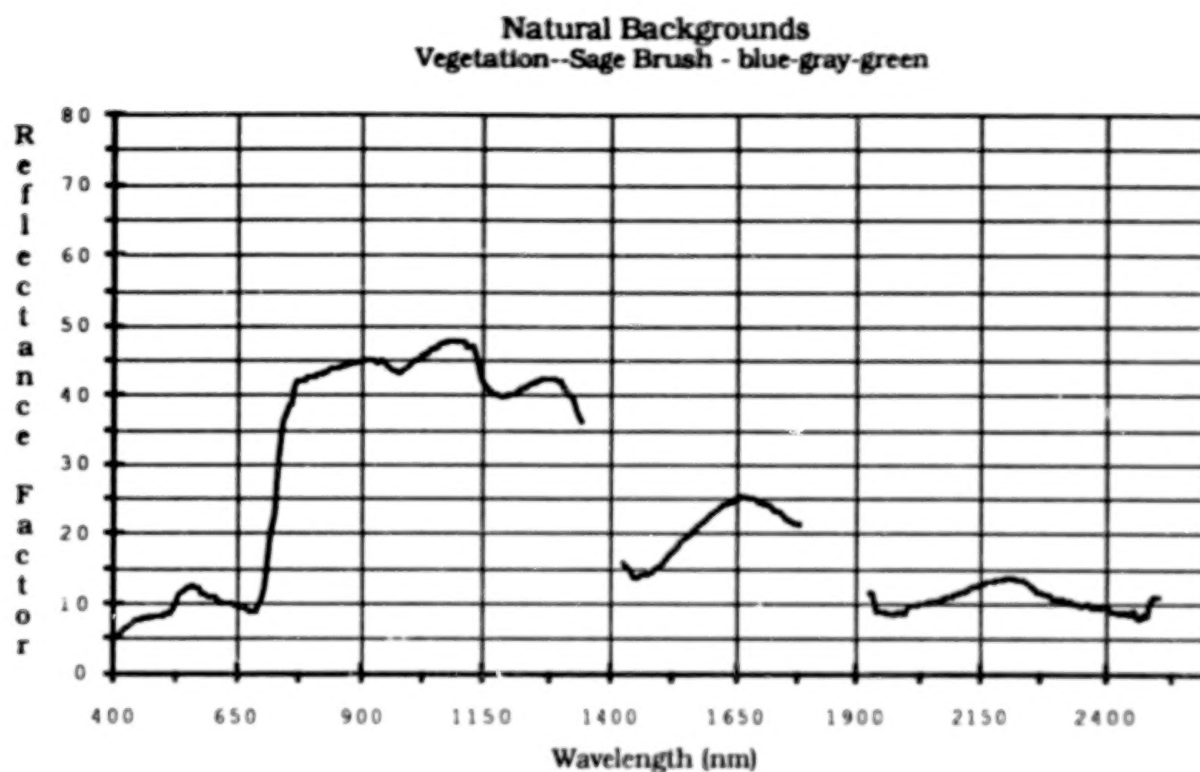


Figure 23. Reflectance signature of a grayish-green desert shrub.

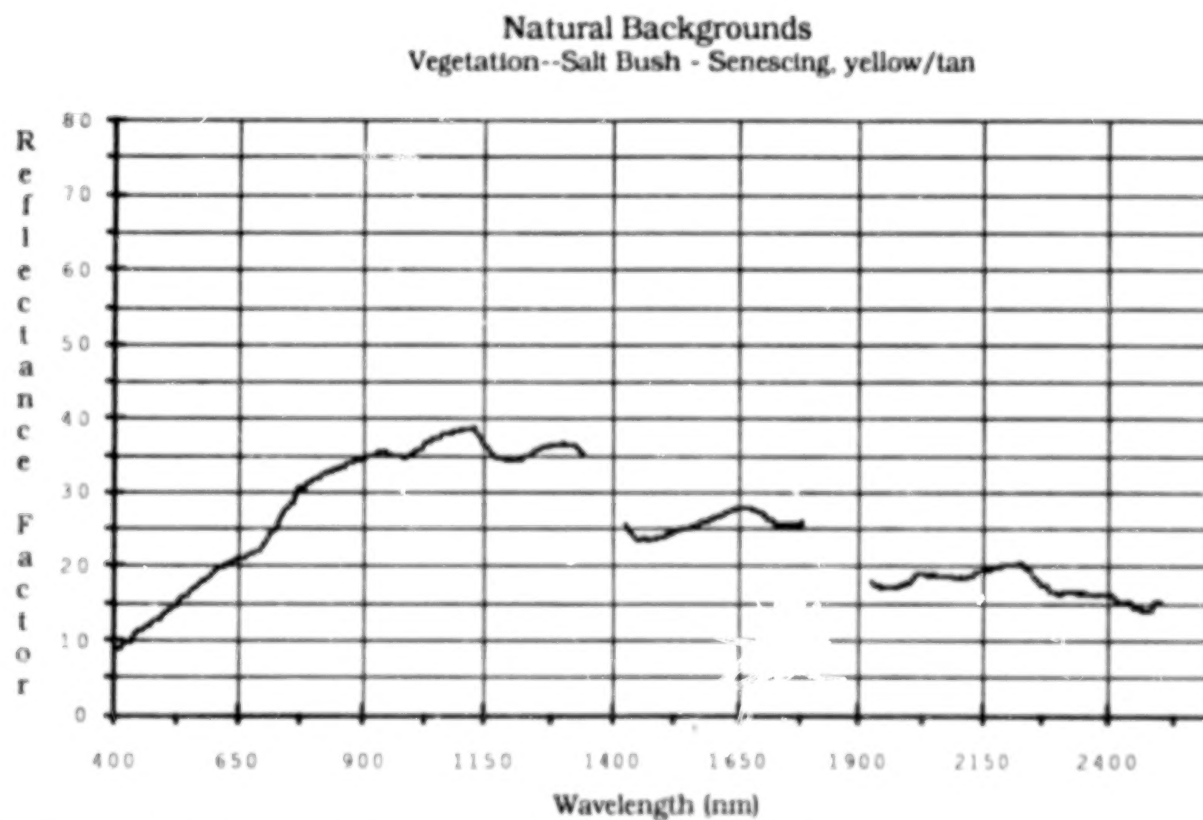


Figure 24. Reflectance signature of a senescing desert shrub.



FIGURE 25. Visible bands image of camo materials on a bare desert soil background. The desert BDU fabrics are not readily detectable.



FIGURE 26. Infrared bands image of camo materials on a bare desert soil background. All fabrics are easily detected.

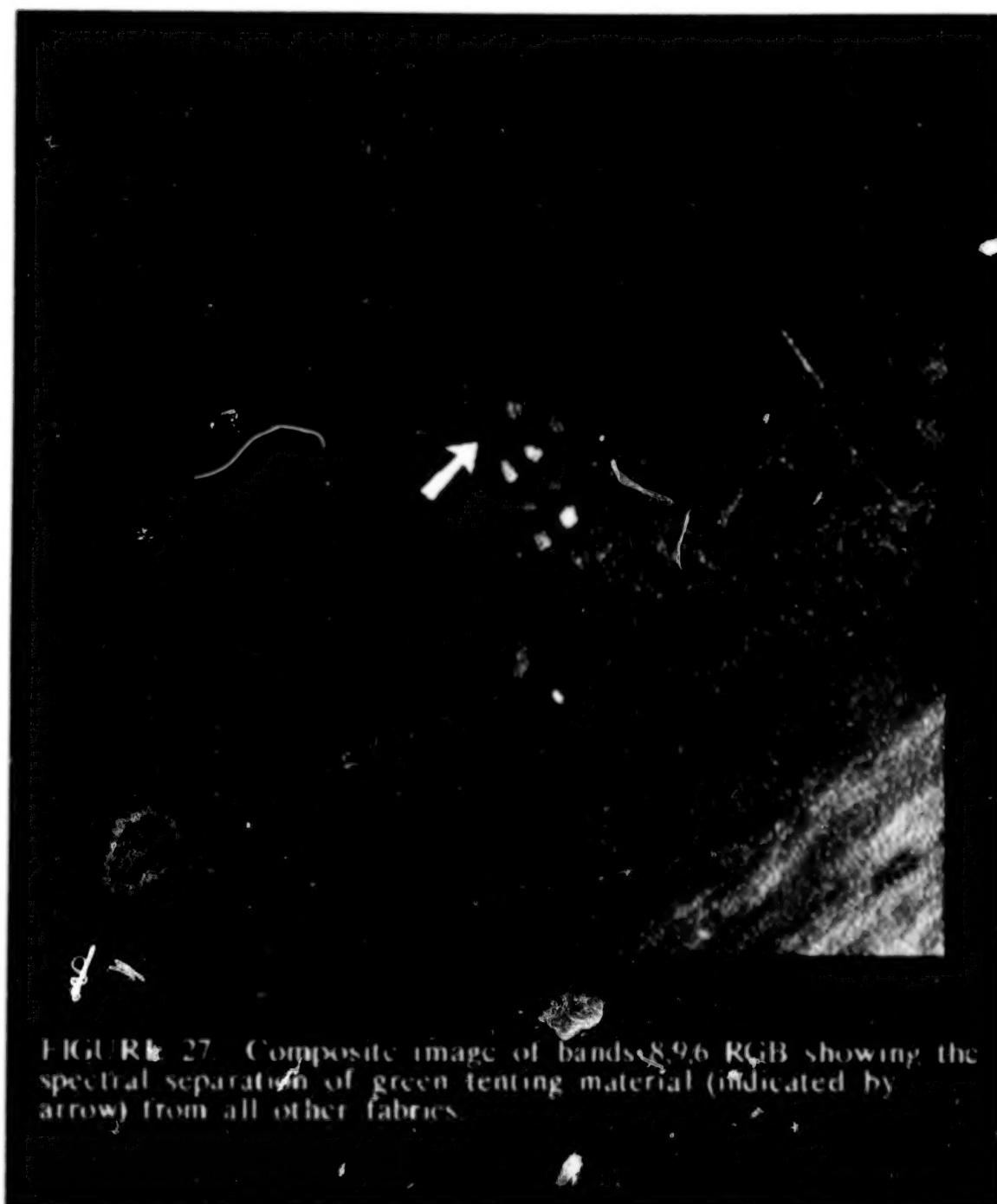


FIGURE 27. Composite image of bands 8, 9, 6 RGB showing the spectral separation of green tenting material (indicated by arrow) from all other fabrics.

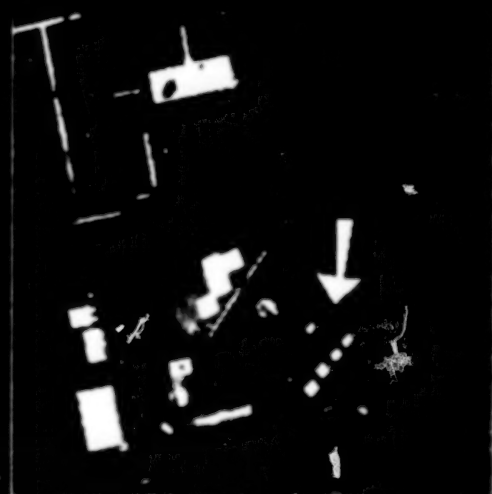


FIGURE 28. Visible bands image of camo materials (shown by arrow) on a temperate region thin grass background. The light toned desert fabrics are easily separated but the woodland fabrics blend into the background.



FIGURE 29. Infrared bands image of camo materials (shown by arrow) on a temperate region thin grass background. All of the fabrics can be separated from the background.

**A RATIONALE FOR PIXEL COLORATIONS
OF EVAPORITE MINERAL DEPOSITS IN THERMAL IMAGERY
OF DEATH VALLEY, CALIFORNIA**

John W. Eastes
U. S. Army Topographic Engineering Center
Alexandria, VA 22310-3864

False color thermal infrared multispectral scanner (TIMS) imagery relating terrain composition/conditions to pixel colorations is constructed with spectral emittance data in the 8-12 μ m wavelength region. Use of a specific combination of primary colors with three spectral data channels of the TIMS sensor allows qualitative predictions of hue to be expected in a color display on the basis of diagnostic emissivity features of terrain surface materials. Kahle and Goetz (1983) produced TIMS imagery of Death Valley, California constructed with emittance data in channels 1, 3 and 5 displayed as blue, green and red, respectively. This image depicts silica-rich, non-saline alluvial fans in red, carbonates in cyan and volcanic rocks in magenta, colors expected on the basis of laboratory spectral measurements with field samples of these materials. However, a consideration of the particular spectral properties of halite-rich mineral mixtures may help explain certain of the blue, green, cyan and yellow pixels associated with the saline deposits in the central basin of the Valley.

The central basin consists mainly of evaporite mineral deposits, chiefly halite, in which are suspended trace to large amounts of a variety of particulate mineral matter introduced by wind and water. Such mineral mixtures may exhibit distinctly different emissivity properties from either those of halite itself or of the suspended minerals when in more massive form. These differences stem from fine particle size of the suspended material together with transmission and refractive index properties of halite. An example of this type of spectral behavior is illustrated in Fig. 1 where a spectrum of a massive quartz surface is compared with one of finely divided quartz suspended in halite. In these spectra the emissivity of massive quartz is a minimum at the same wavelengths that the emissivity of finely particulate quartz in halite is a maximum. These spectra suggest that data processing used for the Death Valley scene would render massive non-saline quartzite features in red, however, some quartz/halite surfaces could appear cyan. Spectral behavior observed for other halite/mineral mixtures could account for various pixel colorations associated with the central basin of the Valley.

This poster describes a spectroscopic rationale for color renditions of highly saline terrain in TIMS imagery on the basis of data from laboratory and natural halite mineral mixtures. A knowledge of these distinct spectral effects may serve to avoid confusion and ambivalence in the interpretation of certain imagery.

A. B. Kahle and A. F. H. Goetz, *Science*, 222, 24-27, (1983).

BLANK PAGE

BLANK PAGE

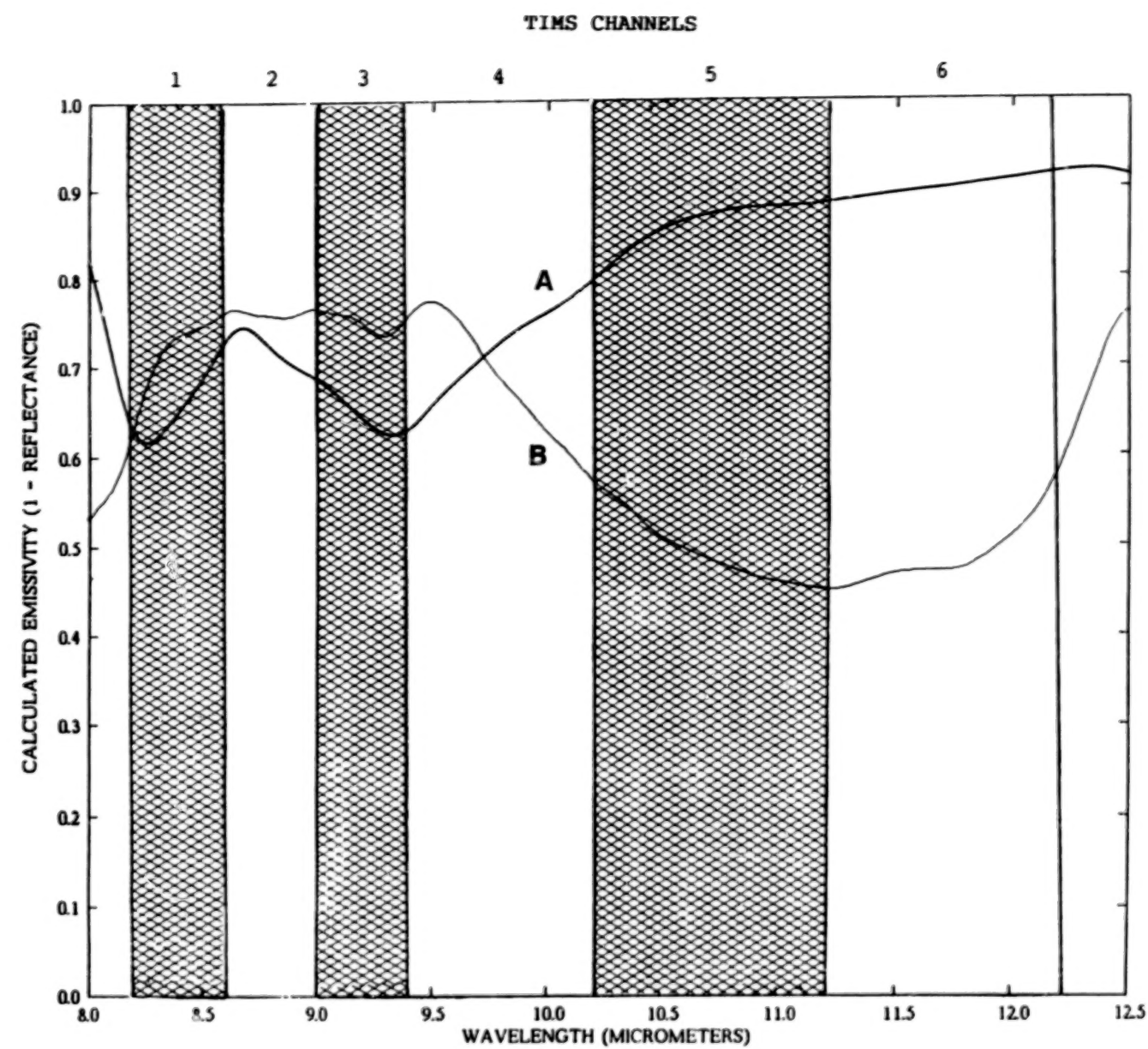


Fig. 1 Calculated emissivity of large surface quartzite (trace A) and finely particulate quartzite in NaCl (trace B). Surfaces corresponding to trace A should appear red in TIMS imagery. Surfaces corresponding to trace B would appear blue-green or cyan.

THE IMPACT OF SYSTEM MTF ON SUB-PIXEL TARGET DETECTION, AND ON SPECTRAL DEMIXING FOR SUB-PIXEL DISCRIMINATION

M. J. Duggin
308 Bray Hall, CESF
SUNY
Syracuse, NY 13210

and

Research Associates of Syracuse, Inc.
Hancock Army Complex, 510 Stewart Drive
N. Syracuse, NY 13212

ABSTRACT

Most scene-atmosphere-sensor models and image analytical procedures consider one ground instantaneous field of view (GIFOV) containing target (and background in the case of sub-pixel targets) and calculate the contrast of the resulting pixel relative to one or more pixels arising from adjacent background-filled GIFOVs. Some models consider the effect of system MTF on recognition of large targets, in terms of how many cycles are resolvable across a target (in each dimension) according to the Johnson criteria. However, little attention appears to have been paid to the impact of the location of unresolved scene elements in the GIFOV on their contribution to pixel radiance. If a target is not resolved, and if in a single bandpass the target material contrasts radiometrically to its surroundings, then the position of the target in the GIFOV will determine the contrast of the pixel radiance to the radiance recorded from surrounding (background) pixels. The theory is presented, together with examples. The impact of sampling rate, PSF shape, definition of the GIFOV and side-lobes on contrast degradation will be discussed. Such factors will degrade the probability of detection and the probability of false alarm. The interaction of spectral response and spatial response, especially in the case of spectral demixing, using hyperspectral data will be discussed, as will the impact of structure (and its resulting power spectrum) in the clutter background. Suggestions are made for the design of sensors intended for sub-pixel detection or surface discrimination on the basis of spectral demixing. The importance of calibration is discussed.

1. INTRODUCTION

Little information appears to exist on the variation of the sensitivity of response of a remote sensing device across the ground instantaneous field of view (GIFOV) of sensors. It is well known, however, that the sensitivity of a sensor does vary across the GIFOV in a manner described by the inverse Fourier transform of the cascaded modulation transfer functions of the atmosphere and sensor optics. This has been discussed by Duggin and Philipson (1985), Duggin (1987), Park, Schowengerdt and Kaczynski (1984) and by Schowengerdt, Archwamety and Wrigley (1985). In each bandpass of a sensing system, there is a spectral variation of the sensor response, as well as a spatial variation of the sensor response. In the latter case, the variation of the sensor response of the sensor across the GIFOV is described. This will be a two-dimensional variation which may, or may not have axial symmetry about the center of the GIFOV. The variation of the sensor response with spatial distribution across the GIFOV is described by the reverse-projected point spread function (PSF). The output from a given GIFOV, which is recorded as a digital radiance number for a single pixel, is the convolution of the spatial distribution of the upwelled radiance distribution at ground level with the rear-projected PSF, multiplied by atmospheric transmission, and with atmospheric backscatter and self-radiance added. In addition, there is a second convolution of the spectral response of the sensor with the

spectral responses of each of the components of the GIFOV. The spatial convolution may best be understood by reference to Fig. 1. In fact, for a diffraction-limited system, the PSF has an amplitude distribution such that 86 percent of the energy is recorded by the main lobe, while the remaining 14 percent is recorded by the side-lobes. We have considered an axially symmetric case, looking at nadir. However, some systems, such as the Landsat MSS were reported as having a rectangular GIFOV. In the case shown in Fig. 1, the radiance recorded by the sensor will depend upon the relative location of each of the different (radiometrically contrasting) elements within the GIFOV.

The situation is further complicated by the general lack of information on system MTF (reverse projected PSF). The GIFOV appears to be generally understood as the boundary defined by where the reverse PSF falls to -3 dB. Energy recorded from beyond the -3 dB limits of the rear-projected PSF, which defines the nominal GIFOV (otherwise known as a ground resolution cell; GRC) will serve to reduce the contrast of a potentially target-containing pixel relative to its neighbors, because it will worsen the oversampling problem. In the case of heterogeneous ground cover, or where there are unresolved features of interest to be detected, and/or quantified by means of anomalous pixel detection, or perhaps linear demixing, in the case of hyperspectral data, the contrast between pixels, or between the "target-containing" pixel and its surroundings will depend upon the location of the feature(s) of interest within the sensor GIFOV. This will be important for both image analysts looking at single-band or three band image data, as well as for automated analysis based upon multiband or hyperspectral digital image data, as in both cases contrast is the means by which detection and quantification are performed.

Formally, the sensor output for the GIFOV (object plane coordinates (X,Y); recorded as pixel (x,y)) for sensor p, bandpass q is described by the following equation (Duggin 1987).

$$(V_{p,q})_{x,y} = \left\{ \frac{\frac{A}{b_{p,q}} \int_{\lambda_{p,q}} I_{p,q}(\lambda) \left\{ \int_0^{\pi} \int_{-\pi/2}^{\pi/2} \left[E(\theta, \phi, \lambda) \int_0^X \int_0^Y \sum_{l=1}^{l_{\max}} c_{p,q}(X, Y; x, y, \lambda) g_f(X, Y) \cdot \rho_f(\theta, \phi; \theta', \phi', \lambda) dY dX \right] d\theta d\phi \cdot \tau(\theta', \phi', \lambda) \right. \right.}{\int_{\lambda_{p,q}} I_{p,q}(\lambda) d\lambda} + \left. \int_0^{\pi} \int_{-\pi/2}^{\pi/2} L_{\text{path}}(\theta_1, \phi_1; \theta'_1, \phi'_1, \lambda) d\theta_1 d\phi_1 \right\} d\lambda$$

$$+ \left\{ \frac{\frac{B}{b_{p,q}} \int_{\lambda_{p,q}} I_{p,q}(\lambda) \left[\int_0^X \int_0^Y \sum_{l=1}^{l_{\max}} c_{p,q}(X, Y; x, y, \lambda) g_f(X, Y) e_f(\theta', \phi', \lambda) dY dX \cdot W(T_1, \lambda) \cdot \tau(\theta', \phi', \lambda) + L_{\text{refl}}(\theta', \phi', \lambda) \right] d\lambda}{\int_{\lambda_{p,q}} I_{p,q}(\lambda) d\lambda} \right\}$$

$$- \left[\frac{a_{p,q} \cdot A}{b_{p,q}} + \frac{a_{p,q} \cdot B}{b_{p,q}} \right]$$

where A and B are factors describing the relative proportion of reflected and emitted radiance recorded by the SENSAT, depending upon bandpass.

Here $I(\lambda)_{p,q}$ = the spectral response of sensor p in bandpass q.

$E(\theta, \phi; \lambda)$ = spectral global irradiance on the GIFOV

$\zeta_{p,q}(X,Y;x,y,\lambda)$	=	reverse projected spectral point spread function of the sensor and atmosphere in bandpass p of sensor q. (X,Y) are the object plane coordinates, and (x,y) are the image plane, or pixel coordinates
θ	=	zenith angle of element of irradiance
ϕ	=	azimuth angle of element of irradiance
θ'	=	sensor view zenith angle
ϕ'	=	sensor view azimuth angle
λ	=	wavelength
$\rho_\ell(\theta,\phi;\theta',\phi',\lambda)$	=	hemispherical-conical spectral reflectance factor for sub-resolution scene element ℓ , where ℓ is one of the assemblage of n GIFOV components (recorded in pixel (x,y))
$\tau(\theta',\phi',\lambda)$	=	atmospheric spectral transmission coefficient along path to sensor (θ' , ϕ')
$\lambda_{p,q}, \lambda'_{p,q}$	=	upper and lower zero-power spectral bandpass limits for bandpass q of sensor p
$g_\ell(X,Y)$	=	delta function which = 1.0 if element ℓ is present at (X,Y) but otherwise zero
$L_{\text{path}}(\theta_1,\phi_1;\theta'_1,\phi'_1,\lambda)$	=	path radiance scattered from path (θ_1,ϕ_1) along path (θ'_1,ϕ'_1) into sensor
$\frac{1}{b_{p,q}}$	=	gain of sensor p in bandpass q
$a_{p,q}$	=	offset of sensor p in bandpass q
$\epsilon_\ell(\theta',\phi',\lambda)$	=	spectral directional emissivity of sub-resolution element ℓ
$L_{\text{self}}(\theta',\phi',\lambda)$	=	spectral atmospheric self radiance recorded by sensor
$W(T_\ell,\lambda)$	=	spectral black body exitance from body at absolute temperature T_ℓ from scene element ℓ

The motion of the scan mirror for an optical-mechanical whisk-broom scanner, as well as along track motion (also present for a push broom scanner) will cause blur. The blur will alter the contrast between the target-containing pixel and its neighbors. Depending upon the shape and size of the reverse-projected point spread function, the presence of a sub-pixel scene element can affect nearest, and next-nearest neighbors, reducing the contrast of the GIFOV containing the sub-resolution target relative to its neighbors and next-nearest neighbors.

Further, the reverse-projected PSF will vary in shape with view angle, atmospheric path, and with wavelength. It is suggested that some elementary laboratory measurements could provide valuable insights into the magnitude of this problem.

2. DISCUSSION

In order to demonstrate the impact of the size of the PSF and the method by which the boundaries of the PSF are defined, we have synthesized circularly symmetric, Gaussian-shaped PSFs of two different sizes. In each case, we ignored sidelobes (assuming that they were minimized by apodization) and we considered the cases where the rear-projected PSF (GIFOV) radius was defined either as the zero power radius, or the -3 dB radius. The four cases of nominal 5 m radius, and 10 m radius GIFOVs, where the GIFOV boundary is taken to be either where sensitivity falls to -3 dB or where it falls to zero are shown in Figs. 2-5. We synthesized a 39 pixel by 39 pixel panchromatic image of a scene containing an F4 Phantom on a taxiway, shown in Fig. 6, and stepped the PSF, in each case, across the scene in 5 m increments. We started 15 m left of image center, and finished at 15 m to the right of image center. The results are shown in Figs. 7-13 for the 10 m -3 dB radius GIFOV, Figs. 14-20 for the 10 m zero-power radius case, Figs. 21-27 for the 5 m -3 dB radius GIFOV, and Figs. 28-34 for the 5 m zero power radius case. The relative outputs of the GIFOV in each of the above cases, as a function of GIFOV position relative to the simulated scene center is shown in Fig. 35. The different outputs for the four different reverse-projected PSFs, each located over the center of the simulated image are shown both visually and numerically in Figs. 36-39. Clearly, the recorded digital radiance values depend on the shape and size of the sensor reverse-projected PSF, and upon the relative positions of scene elements in the GIFOV.

In the case of oversampled data, an unresolved target will appear in adjacent pixels, reducing the contrast of the target-containing pixel relative to its neighbors. This will reduce the probability of detection. The severity of this situation will depend upon the shape of the reverse-projected PSF (thus on the sensor and atmospheric MTFs), upon the existence of sidelobes, and upon the degree of oversampling. The Landsat MSS was reported to have a 33 percent GIFOV overlap along the scan line.

In the case of spectral demixing, it is suggested that the linear combination of scene elements which are deduced as occurring within a GIFOV, using hyperspectral data, may depend to some as yet unknown degree upon the shape and size of the rear-projected PSF, and upon the heterogeneity and composition of the ground cover.

Radiometric correction of an image for atmospheric effects, and correction for the atmospheric and sensor MTFs will aid in optimizing image contrast and resolution. A publication discussing these factors is in preparation.

3. THE EFFECT OF BACKGROUND CLUTTER

The detection of a sub-pixel target or the identification and quantification of scene components by means of spectral demixing techniques depend upon target-to-background contrast, as recorded by gray scale contrast and signal-to-noise ratio (SNR). The noise component consists of both system noise and clutter noise. Part of the latter is structured, and gives rise to a spatial frequency power spectrum which is characteristic of geography, topography, spatial resolution, bandpass, view and (visible-near IR region) illumination geometry. Conley (1993) suggested a signal-to-clutter ratio which takes account of the power spectrum of the background. The magnitude of the clutter will impact the degree of permissible oversampling which may be allowed before SNR degradation occurs. This matter needs further examination, as it will impact sensor design and the allowable parametric envelope for the environmental conditions which may exist during image acquisition.

4. CONCLUSIONS AND RECOMMENDATIONS

It is important to know how the reverse-projected PSF of a sensing system is defined, and to know the possible variation in the relative locations of scene elements in the GIFOV for heterogeneous ground cover.

It has been shown that the sensor output varies substantially with small movements of the GIFOV over a heterogeneous scene for four different sensor spatial response functions. Standardization in describing the GIFOV diameter is recommended. Both -3 dB radius and zero-power radius are recommended, together with the sidelobe/main lobe power ratio.

It is suggested that the system MTF and thus the reverse-projected PSF be measured for each sensing system used. The interaction of the system spatial response characteristics and the upwelled radiance field from heterogeneous terrain will impact the detection of sub-pixel (unresolved) targets, and might interfere with scene element identification and quantification by means of spectral demixing. It is recommended that these matters be further examined, as they are poorly understood at present.

The impact of clutter and the spatial structure of clutter, together with its spectral variation on SNR and on allowable oversampling without degradation of SNR needs to be further studied.

REFERENCES

- T. Conley, T., 1980: reported by J. S. Accetta, Chapter 4, Vol 5, The Infrared and Electro-Optical Systems Handbook, J. S. Accetta and D. L. Shumaker, executive editors, Environmental Research Institute of Michigan and SPIE, 1993, 302, et. seq.
- Duggin, M. J., 1987: Impact of Radiance Variations on Satellite Sensor Calibration, *Appl. Optics*, 26, 1264-1271.
- Duggin, M. J. and W. R. Philipson, 1985: Relating Ground, Aircraft and Satellite Radiance Measurements: Spectral and Spatial Considerations, *International Jol. Remote Sensing*, 6, 1665-1670.
- Park, S. K., R. A. Schowengerdt, and M. Kaczynski, 1984: Modulation Transfer Function Analysis for Sampled Image Systems, *Appl. Optics*, 23, 2572-2581.
- Schowengerdt, R.A., C. Archwamety, and R. C. Wrigley, 1985: Landsat Thematic Mapper image-derived MTF", *Photogramm. Eng. Remote Sensing*, 51, 1407.

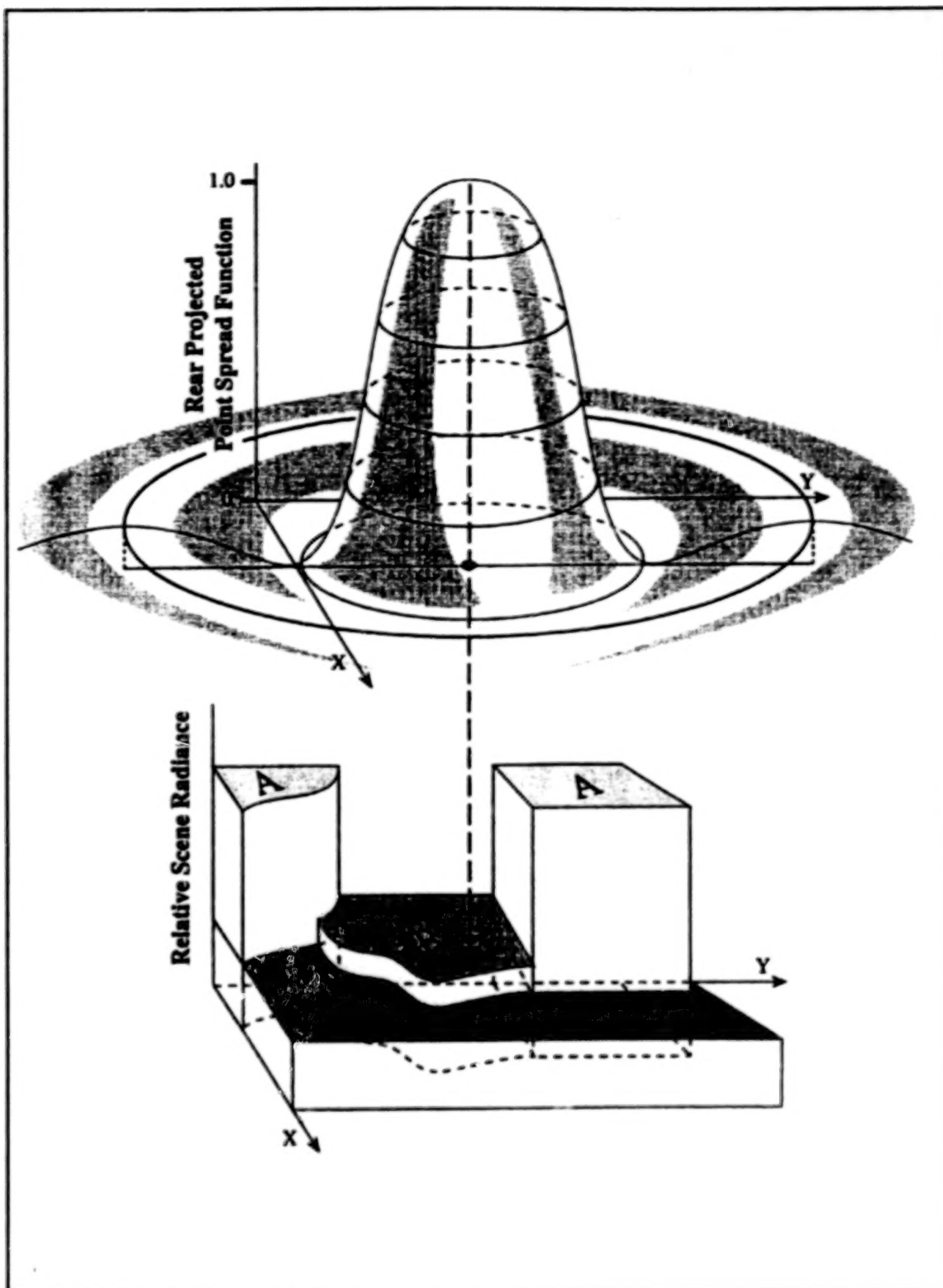


Figure 1. The reverse-projected system PSF is convolved with the upwelled radiance from within the heterogeneous GIFOV to determine the radiance recorded for the pixel corresponding to the GIFOV.

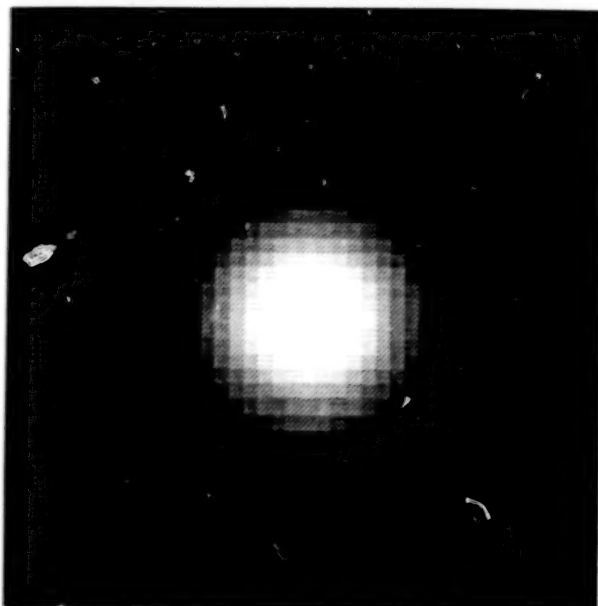


Figure 2. PSF -3 dB limits at 5 m radius.

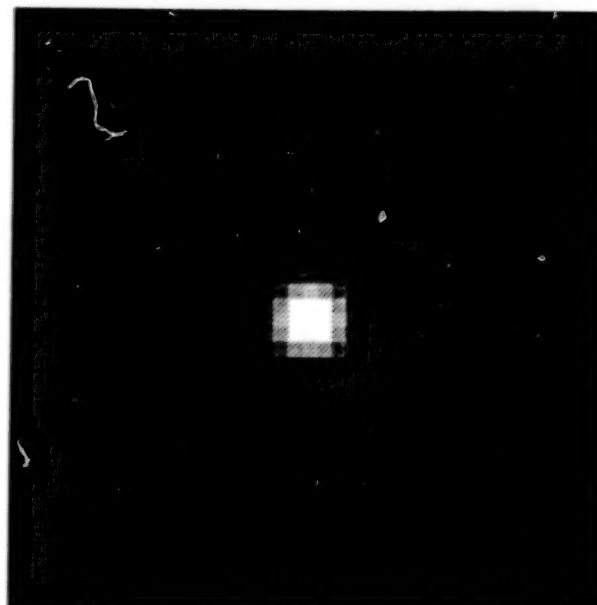


Figure 3. PSF zero power limits at 5 m radius.

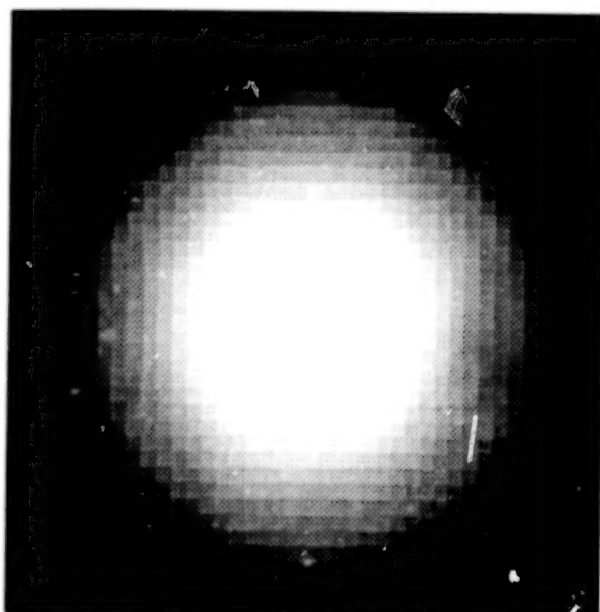


Figure 4. PSF -3 dB limits at 10 m radius.

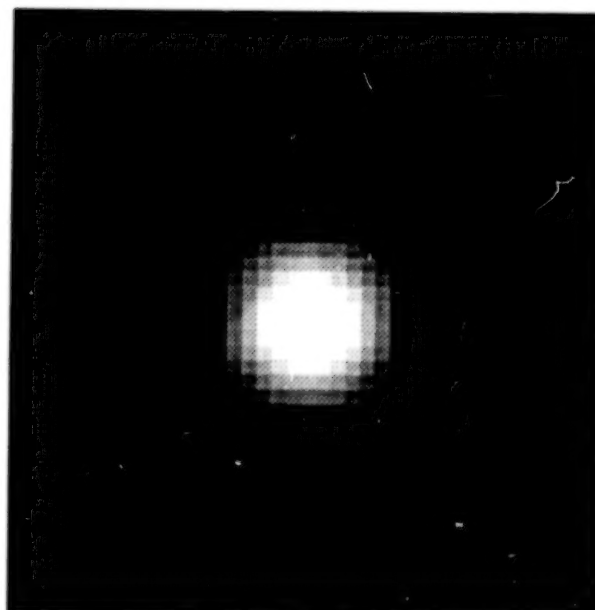


Figure 5. PSF zero power limits at 10 m radius.

BEST COPY AVAILABLE

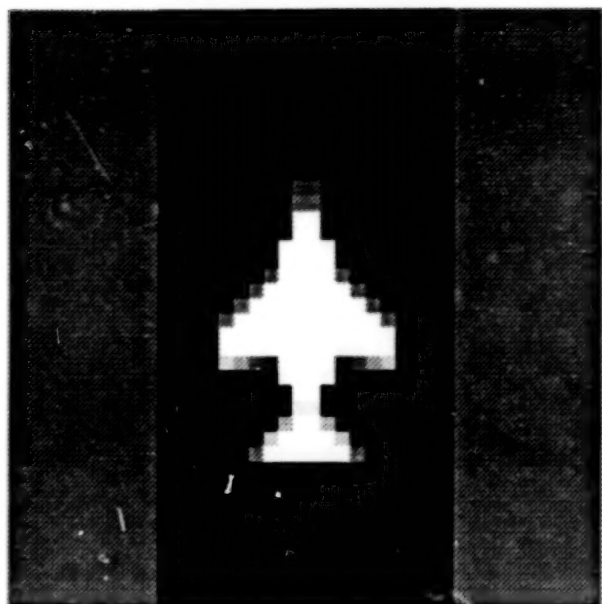


Figure 6. Panchromatic band simulation.

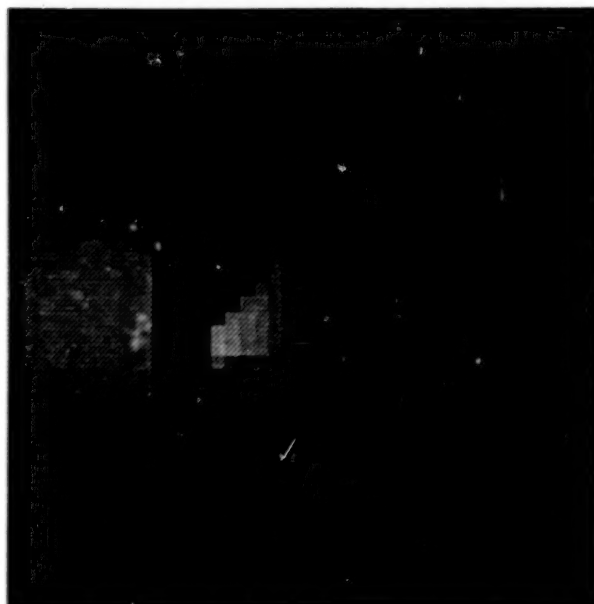


Figure 7. PSF -3 dB radius 10 m located 15 m left of simulated panchromatic image center.

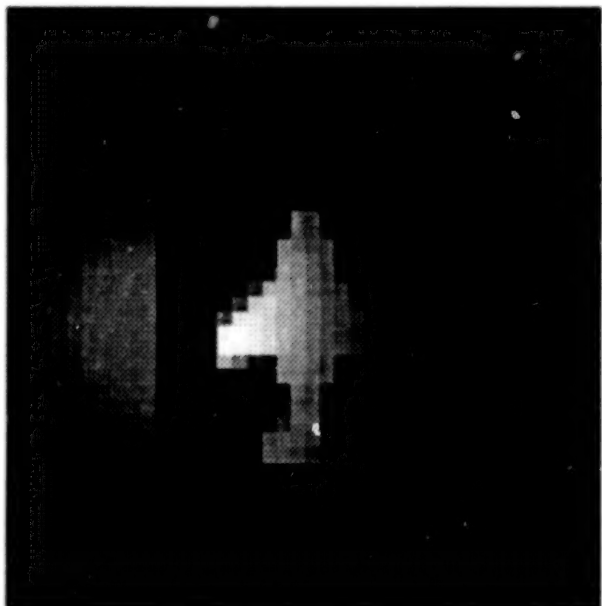


Figure 8. PSF -3 dB radius 10 m located 10 m left of simulated panchromatic image center.

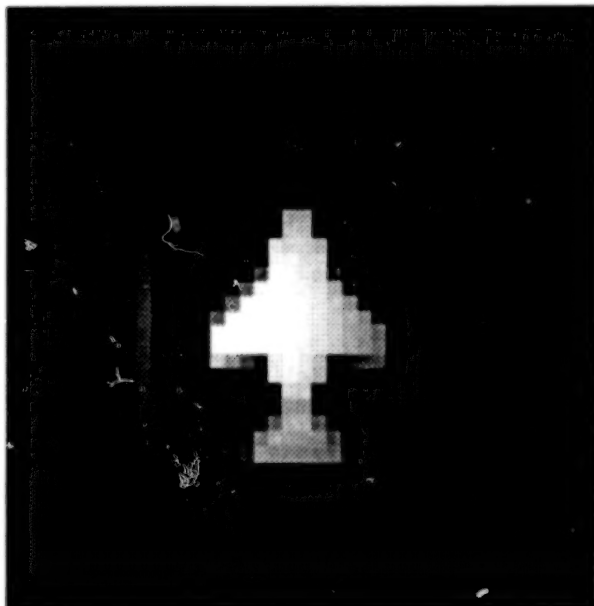


Figure 9. PSF -3 dB radius 10 m located 5 m left of simulated panchromatic image center.

BEST COPY AVAILABLE

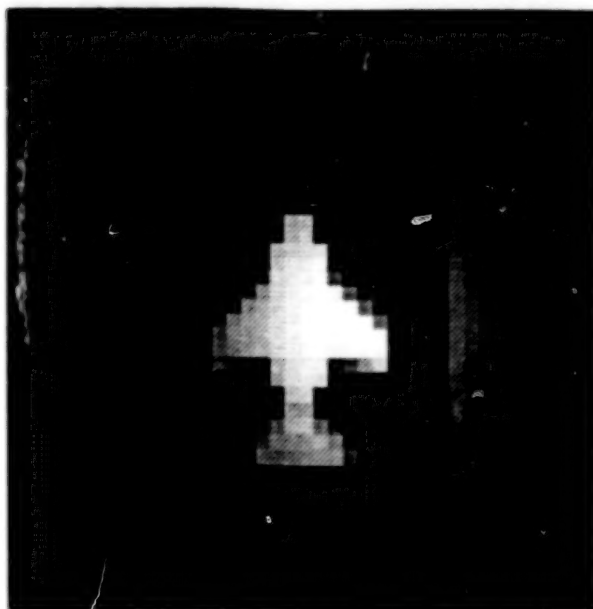


Figure 10. PSF -3 dB radius 10 m at simulated panchromatic image center.

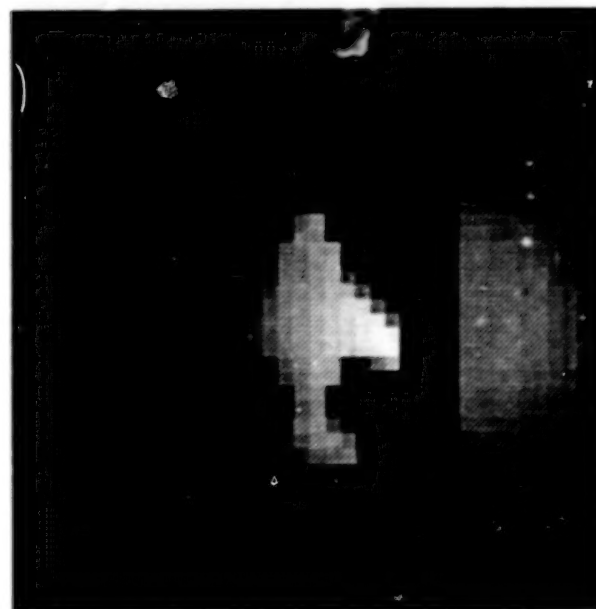


Figure 11. PSF -3 dB radius 10 m located 5 m right of simulated panchromatic image center.

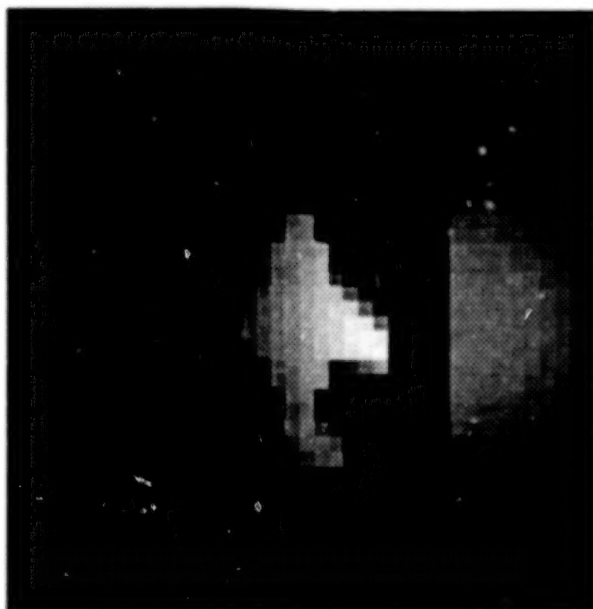


Figure 12. PSF -3 dB radius 10 m located 10 m right of simulated panchromatic image center.

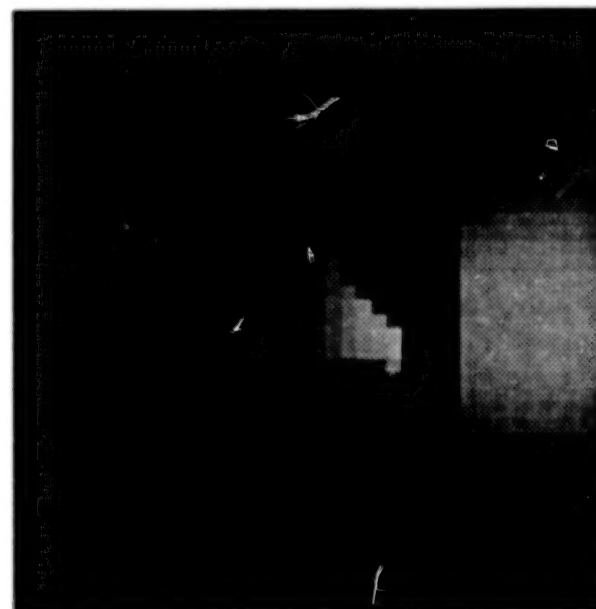


Figure 13. PSF -3 dB radius 10 m located 15 m right of simulated panchromatic image center.

BEST COPY AVAILABLE



Figure 14. PSF 10 m zero power radius 15 m left of simulated panchromatic image center.

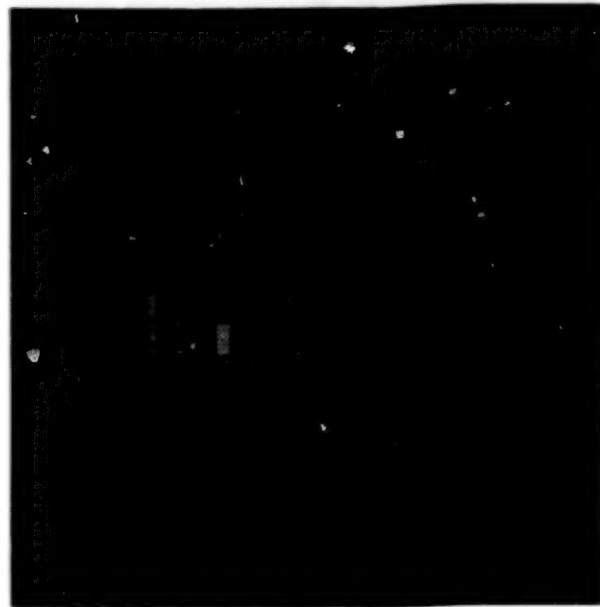


Figure 15. PSF 10 m zero power radius 10 m left of simulated panchromatic image center.

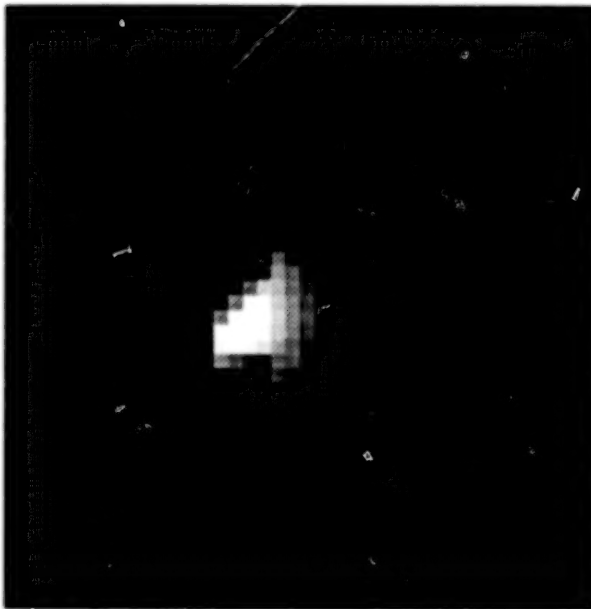


Figure 16. PSF 10 m zero power radius 5 m left of simulated panchromatic image center.

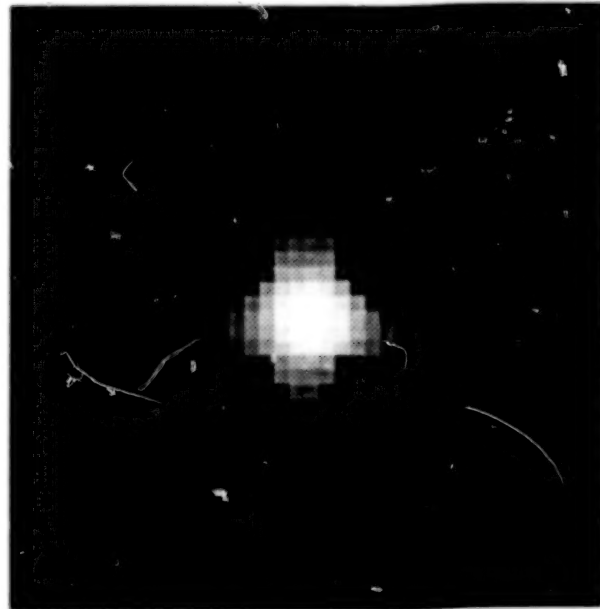


Figure 17. PSF 10 m zero power radius at simulated panchromatic image center.

BEST COPY AVAILABLE

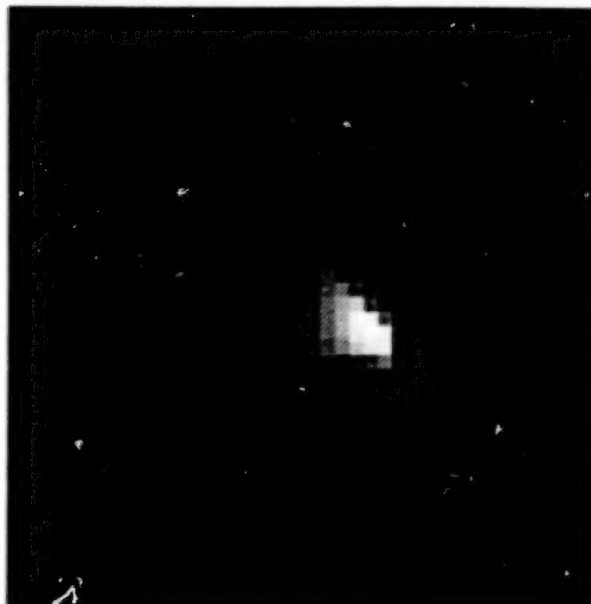


Figure 18. PSF 10 m zero power radius 5 m right of simulated panchromatic image center.



Figure 19. PSF 10 m zero power radius 10 m right of simulated panchromatic image center.

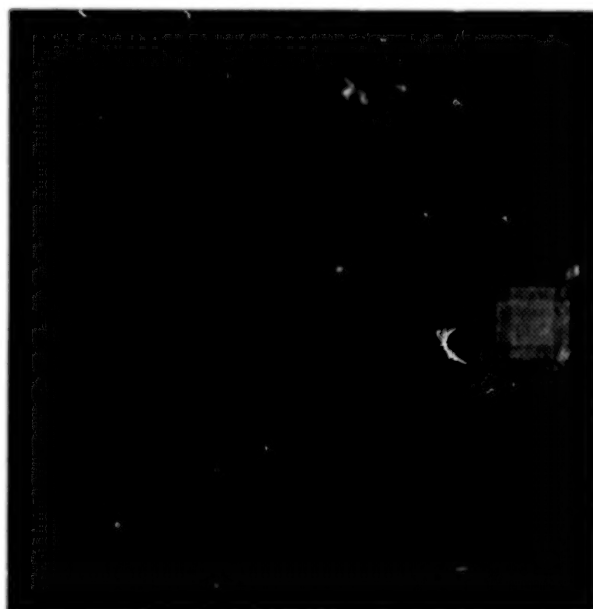


Figure 20. PSF 10 m zero power radius 15 m right of simulated panchromatic image center.

BEST COPY AVAILABLE

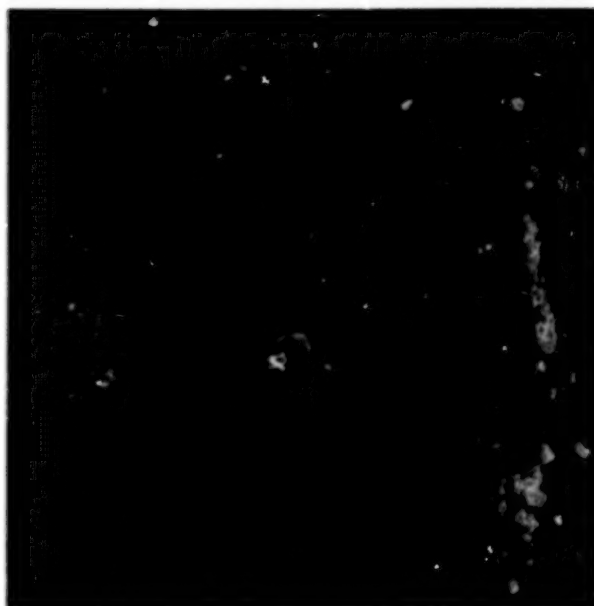


Figure 21. PSF -3 dB radius 5 m located 15 m left of simulated panchromatic image center.

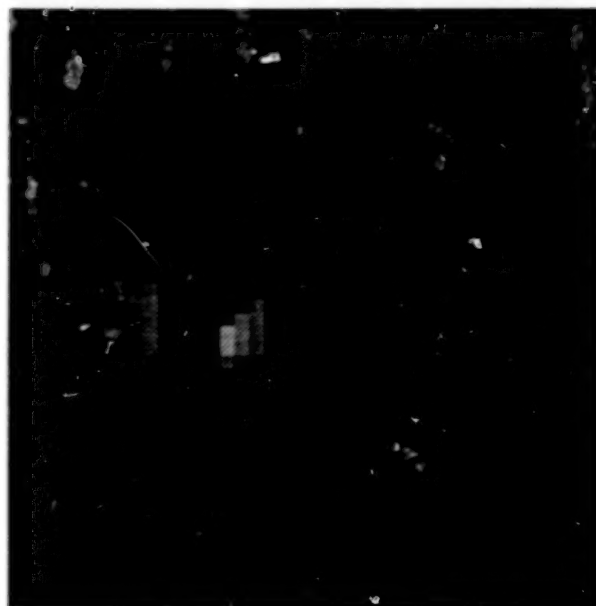


Figure 22. PSF -3 dB radius 5 m located 10 m left of simulated panchromatic image center.

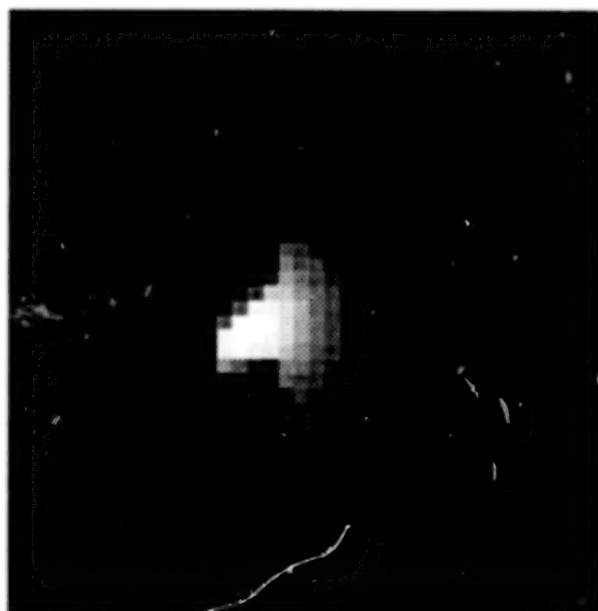


Figure 23. PSF -3 dB radius 5 m located 5 m left of simulated panchromatic image center.

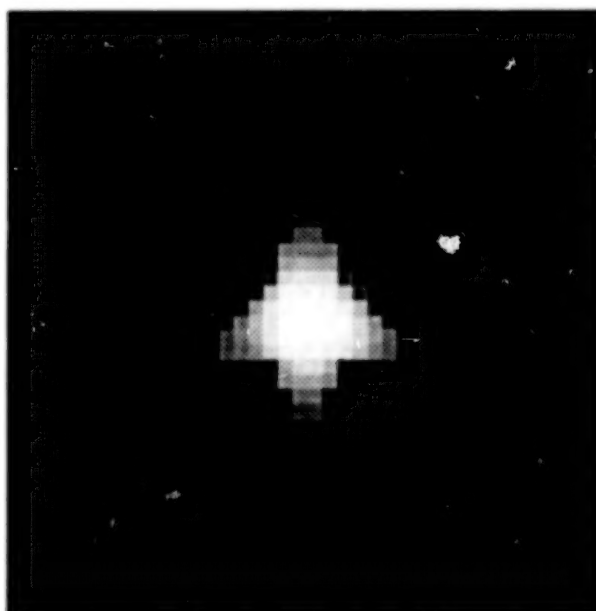


Figure 24. PSF -3 dB radius 5 m located at simulated panchromatic image center.

BEST COPY AVAILABLE



Figure 25. PSF -3 dB radius 5 m located 5 m right of simulated panchromatic image center.

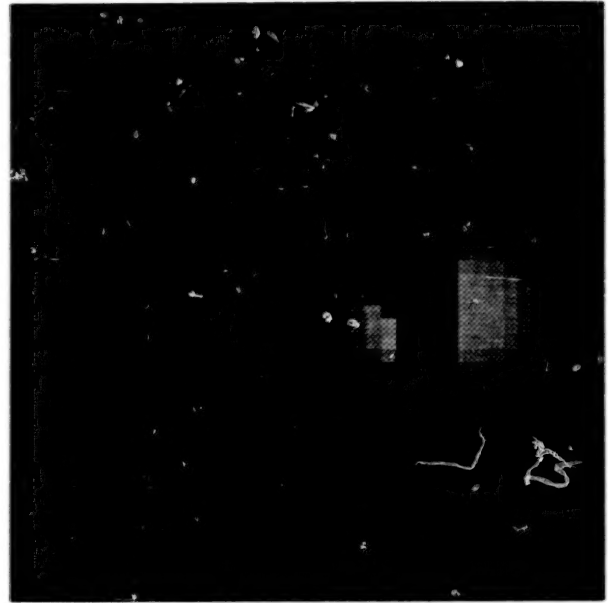


Figure 26. PSF -3 dB radius 5 m located 10 m right of simulated panchromatic image center.

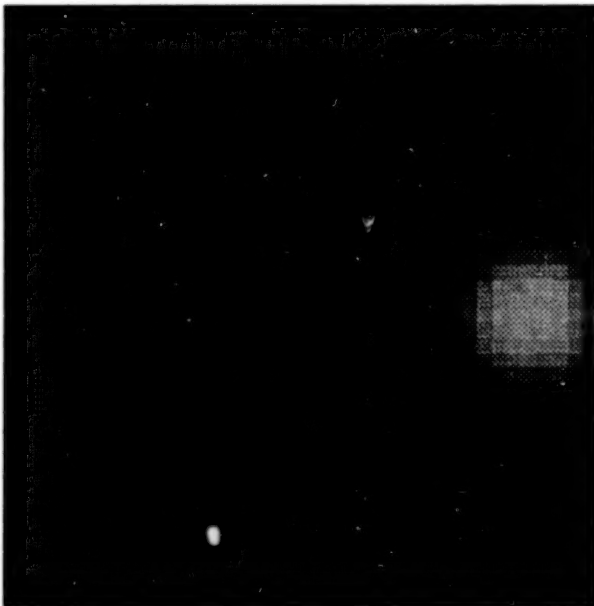


Figure 27. PSF -3 dB radius 5 m located 15 m right of simulated panchromatic image center.

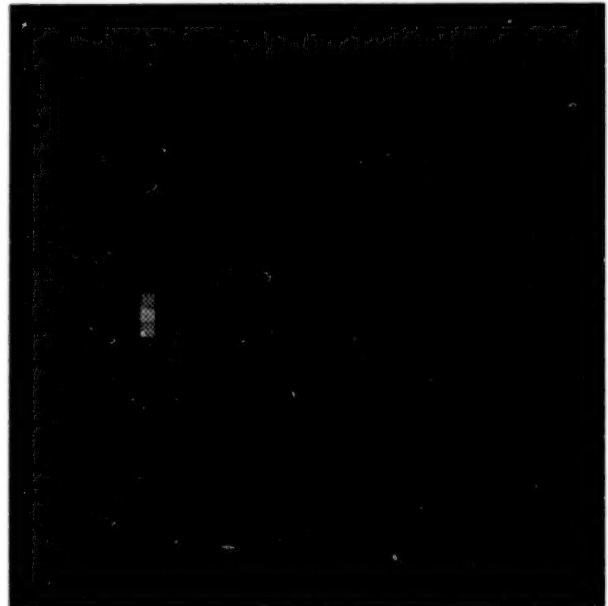


Figure 28. Simulated panchromatic image convolved with PSF 5 m zero power radius 15 m left of simulated panchromatic image center.

BEST COPY AVAILABLE

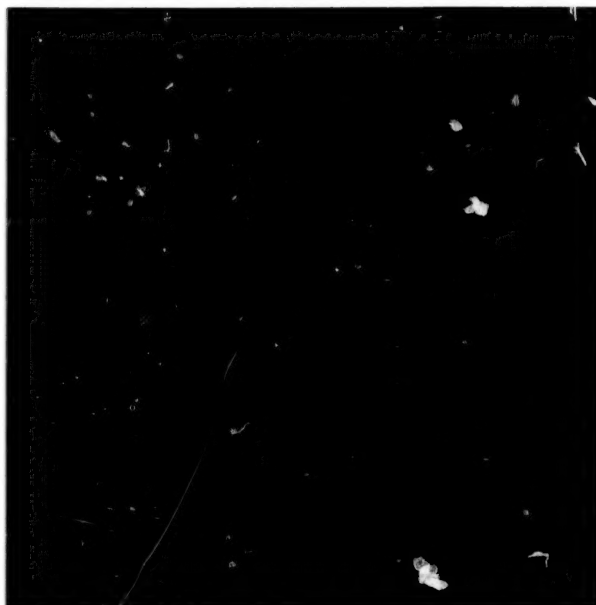


Figure 29. Simulated panchromatic image convolved with PSF 5 m zero power radius 10 m left of simulated panchromatic image center.

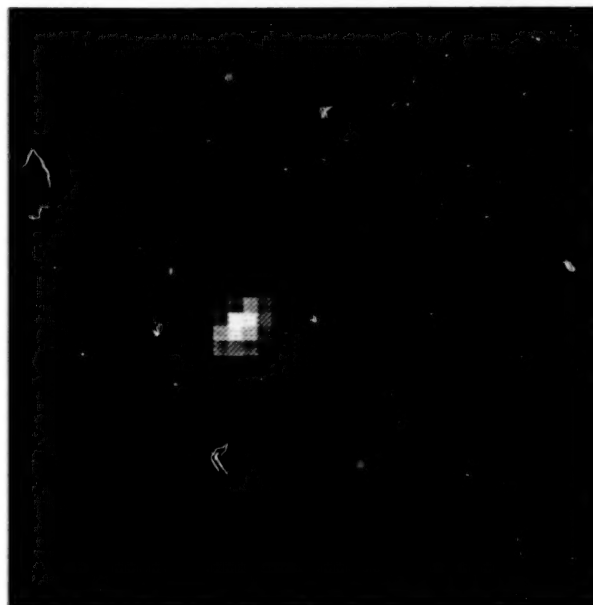


Figure 30. Simulated panchromatic image convolved with PSF 5 m zero power radius 5 m left of simulated panchromatic image center.

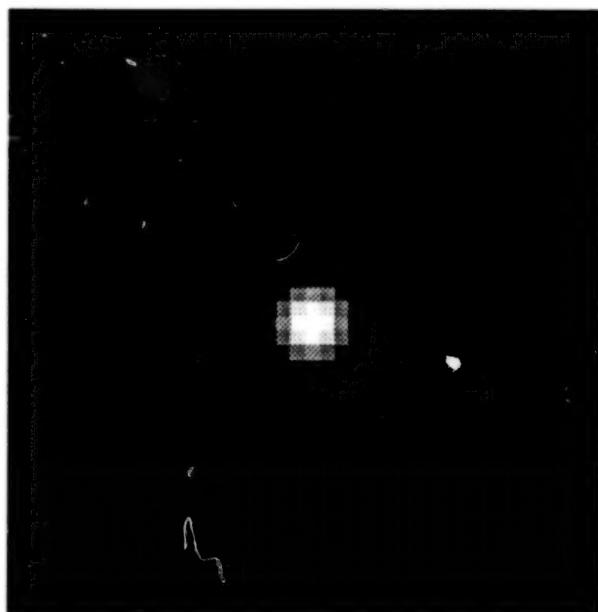


Figure 31. Simulated panchromatic image convolved with PSF 5 m zero power radius at simulated panchromatic image center.

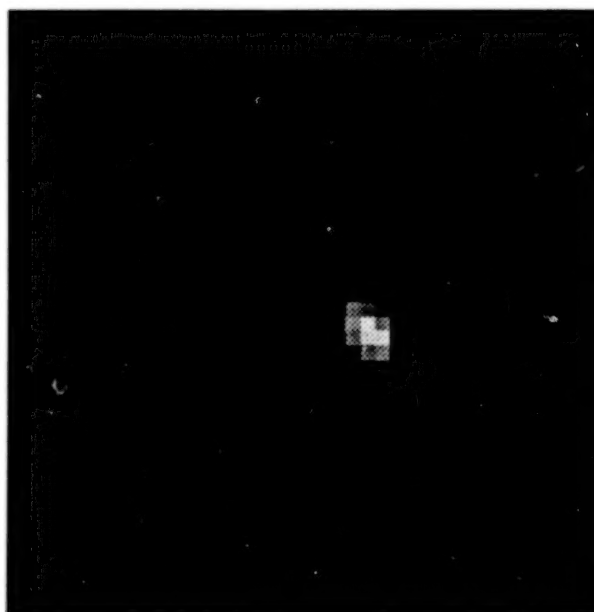


Figure 32. Simulated panchromatic image convolved with PSF 5 m zero power radius 5 m right of simulated panchromatic image center.

BEST COPY AVAILABLE

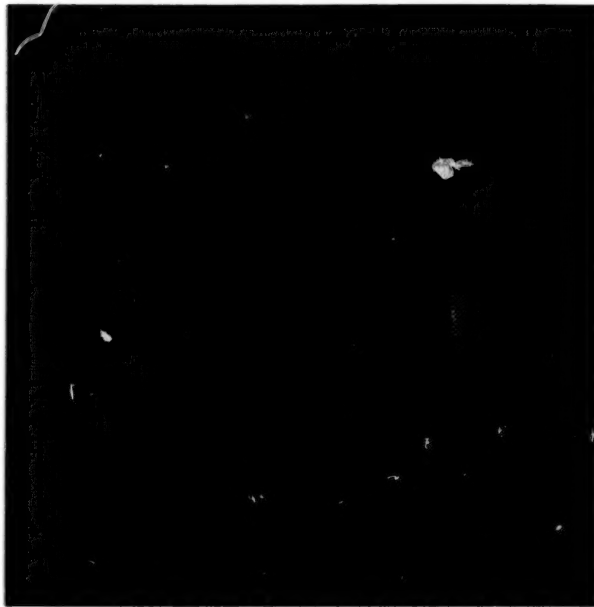


Figure 33. Simulated panchromatic image convolved with PSF 5 m zero power radius 10 m right of simulated panchromatic image center.

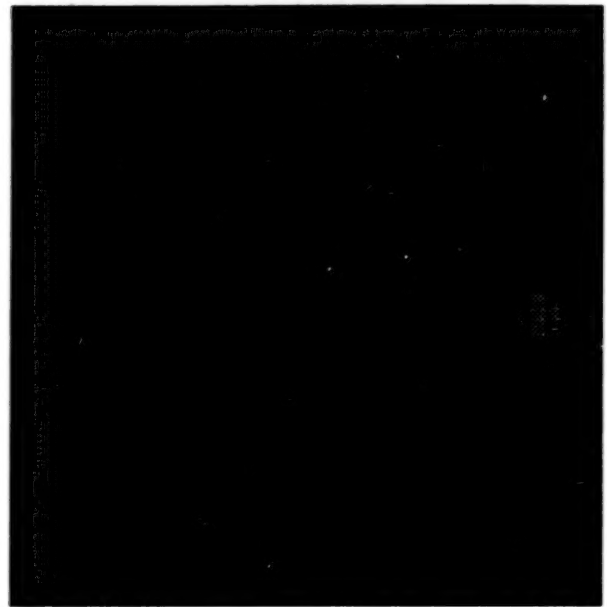


Figure 34. Simulated panchromatic image convolved with PSF 5 m zero power radius 15 m right of simulated panchromatic image center.

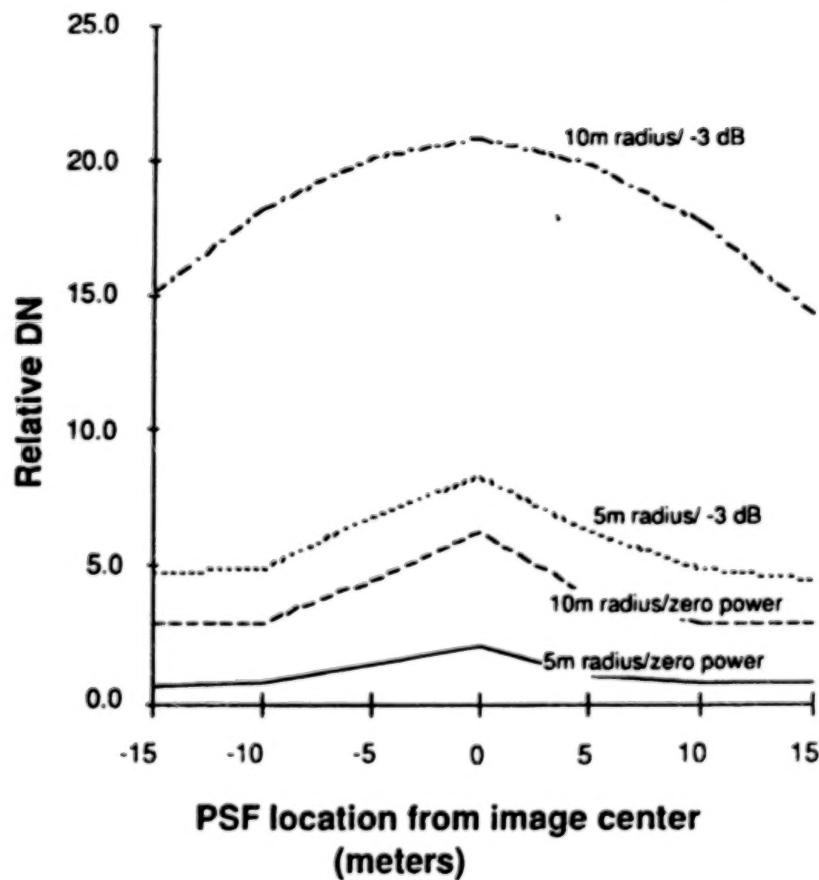


Figure 35. Subpixel target detectability.

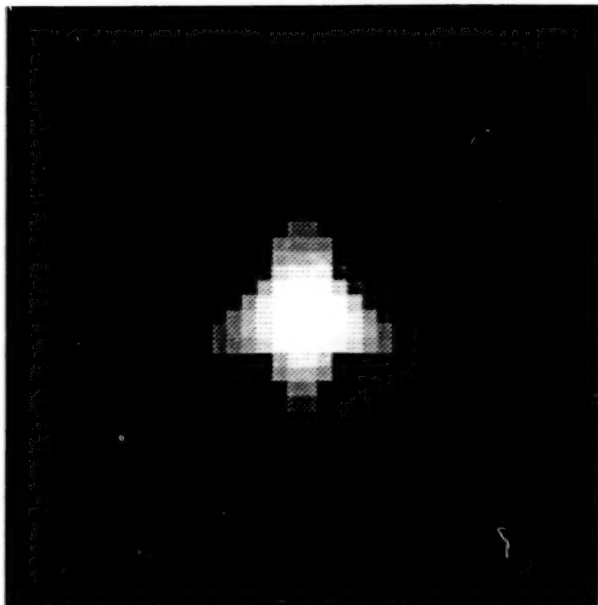


Figure 36. Simulated panchromatic image convolved with PSF with -3 dB radius 5 m, relative energy 8.34.

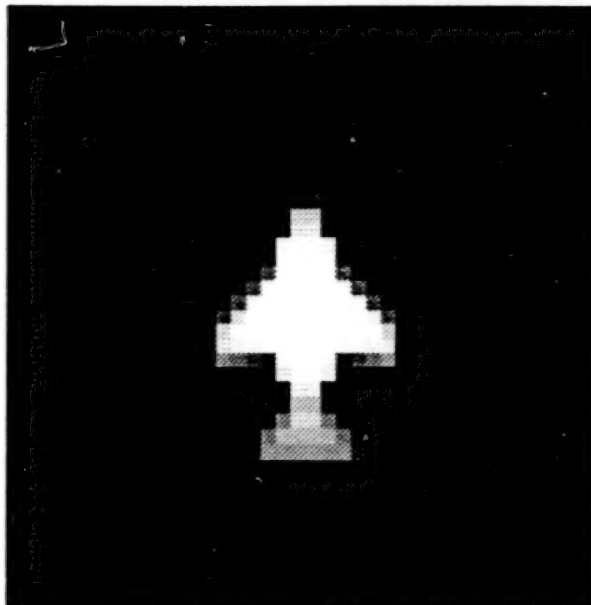


Figure 37. Simulated panchromatic image convolved with PSF with -3 dB radius 10 m, relative energy 20.6.

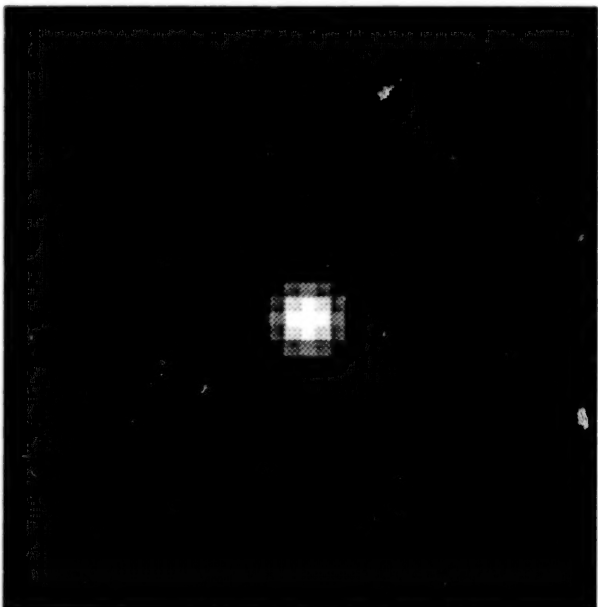


Figure 38. Simulated panchromatic image convolved with PSF with zero power radius 5 m, relative energy 2.10.

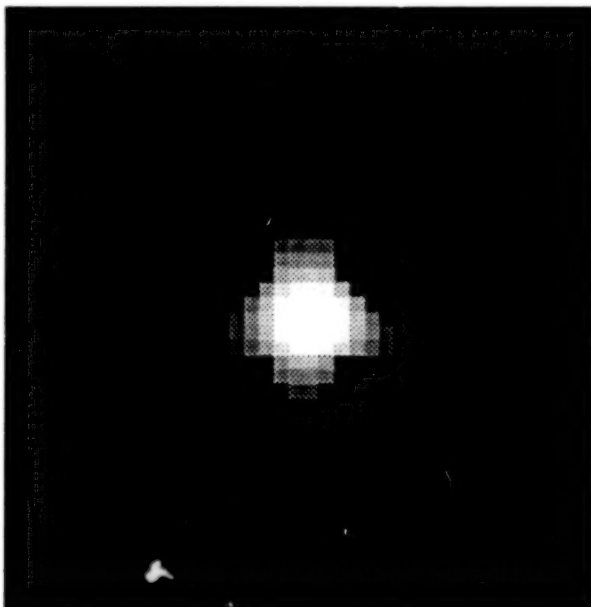


Figure 39. Simulated panchromatic image convolved with PSF with zero power radius 10 m, relative energy 6.15.

BEST COPY AVAILABLE

END

DATE FILMED

07 / 15 / 95